PHOTOCATALYSIS WITH A HETEROSUPRAMOLECULAR ASSEMBLY

A thesis presented to

QUEENSLAND UNIVERSITY OF TECHNOLOGY

In fulfilment of the requirements for the degree of

Doctor of Philosophy

By

GREGORY J. WILSON
Bachelor of Applied Science (Chemistry)
First Class Honours (Chemistry)

Based on research conducted in the

Inorganic Materials Program

School of Physical and Chemical Sciences

Under the supervision of

Dr Geoffrey D. Will

Queensland University of Technology, Brisbane, September 2005

Keywords

Alternative energy storage, coordination complex, dye-sensitised, grey-water, heterosupramolecular, hydrogen gas, kinetic model, organic pollutants, photocatalysis, photo-degradation, photooxidation, titania, titanium dioxide, TiO_2, ruthenium, visible-light.

Declaration of Original Authorship

The work contained in this thesis has not been previously submitted for a degree or diploma at any higher educational institution. To the best of my knowledge and belief, the thesis contains no material previously published or written by another person except where due reference is made.

Gregory J. Wilson
September, 2005

Abstract

Supramolecular chemistry has asserted itself as a significant multidisciplinary field concerned with molecular effects afforded through non-covalent molecular interactions. The increased interest in the literature towards nanoscale devices, through modulation of molecular function, has seen the renaissance of supramolecular chemistry as function progresses from solution to surface. Heterosupramolecular chemistry follows the architectural principles of supramolecular chemistry and embraces both covalent and non-covalent interactions of condensed phase surfaces and molecular components.

A modular approach to device architecture was applied as a novel method of performing photocatalysis under visible light illumination. The application of heterosupramolecular assembly to the design of photoelectrochemical cells capable of visible light induced charge separation allowed the study of interfacial processes by means of electrochemical observations.

Preparation of a series of supramolecular components was undertaken as specific molecular species within a photochemical system. Starting from a synthesised bidentate ligand that incorporated an acidic functional group, 4,4'-bis(methyl)phosphonate-2,2'-bipyridine (**dmpbpy**) as its ethyl ester, was chelated to give the surface sensitisers, bis-(2,2'-bipyridine)-(4,4'-bis(methyl)phosphonato-2,2'-bipyridine)ruthenium(II) dichloride (**[Ru(bpy)$_2$(dmpbpy)]Cl$_2$**) and *cis*-bis-(4,4'-bis-(methyl)phosphonato-2,2'-bipyridine)(2,2'-bipyridine)ruthenium(II) dichloride (**[Ru(dmpbpy)$_2$(bpy)]Cl$_2$**). An electron relay moiety with an acidic functional group, 1-ethyl-1'-(2-phosphonoethyl)-4,4'-bipyridinium dichloride (**EVP**), was also prepared using a procedure developed by the candidate.

The electronic properties of the prepared photosensitisers were examined by theoretical quantum chemical TD-DFT calculations on the molecular structures and singlet excitations were discussed in relation to experimental data. This identified that the lowest lying LUMO states were consistently occupied by 2,2'-bipyridine (**bpy**) and this was speculated to be a factor affecting quantum injection yields.

The effect of microwave modification of colloidal TiO_2 suspensions under extended periods of treatment was investigated. Nanoparticles of TiO_2 were compared and contrast to similar convection hydrothermally treated TiO_2 and a commercial titania product, namely Degussa P25, both of which are utilised in device fabrication. The investigation identified that extended periods of microwave hydrothermal treatment do not greatly enhance the crystallinity and primary grain size of TiO_2.

The heterosupramolecular assembly of a multi-component photochemical system was constructed from prepared molecular and condensed phase components. It was demonstrated that this device was capable of inducing a photochemical reaction in H_2O under irradiation with $\lambda > 420$ nm in the absence of an organic electron donor. Interpretation of the photocurrents obtained from this assembly provided understanding of photochemical reactions under low light intensities. Optimised conditions for the photochemical reaction was determined to be pH = 5 and illumination yielded $\eta = 0.0036\%$ with an apparent quantum yield (AQY) = 1.6%.

Photocatalytic decomposition of organic compounds in a dye-sensitised photoelectrocatalytic cell was investigated for the complete mineralisation of EDTA into CO_2, H_2 and simple amines and interpreted through photocurrent observations. This was extended to a broad range of organic compounds of various solution concentrations as a simulated industrial waste stream. Photooxidation gave unique photocurrent-time profiles which identified two distinct interfacial processes by mathematical treatment of photocurrent transients with a kinetic model. Kinetic parameters were proposed as a factor for qualitative discrimination of the organic compounds.

The implications of these results for heterogeneous catalysis were discussed and the formation of Host-Guest complexes as a method of molecular sensing and as specific photocatalytic receptors was proposed.

Table of Contents

Keywords ---- *ii*

Declaration of Original Authorship ---- *iii*

Abstract ---- *iv*

Table of Contents ---- *iv*

List of Figures ---- *x*

List of Tables ---- *xvi*

List of Schemes ---- *xviii*

Abbreviations and Symbols ---- *xix*

Acknowledgements ---- *xxviii*

Publications Arising From This Work ---- *xxxiii*

Complete List of Publications ---- *xxxiv*

CHAPTER 1 ---- *1*

Introduction and Rationale for Research ---- **1**

1. Description of Research Problem Investigated ---- 3
1.1. Overall Objectives of the Study ---- 3
1.2. Preparation of Condensed Phase Components ---- 4
1.3. Synthesis and Preparation of Molecular Components ---- 5
1.3.1. Ruthenium Polyiimine Complexes ---- 5
1.3.2. Quaternary Diimine Paraquats ---- 6
1.4. Specific Aims of the Study ---- 7
1.5. Account of Research Content and Organisation ---- 8

CHAPTER 2 ---- *11*

Literature Review ---- **11**

2. Introduction ---- 12
2.1. Alternative Energy and Photochemical Systems ---- 14
2.1.1. Introduction to Molecular Photochemical Reactions ---- 15
2.1.2. Model Photochemical Systems ---- 16
2.2. Photocatalysis ---- 19
2.2.1. Photocatalysis on TiO_2 ---- 20
2.2.1.1. Preparation of TiO_2 Photocatalysts ---- 22
2.2.2. Other Metal Oxide Semiconductors ---- 23
2.2.3. Visible-light Photocatalysis ---- 25
2.2.4. Photodegradation of Organic Pollutants ---- 28
2.2.4.1. Photodecomposition of H_2O on TiO_2 ---- 30
2.3. Supramolecular Chemistry ---- 35
2.3.1. Heterosupramolecular Chemistry ---- 37
2.4. Photoelectrochemical (PEC) Cells ---- 39
2.4.1. Alternative Semiconductors in Electrochemical Cells ---- 40

2.4.2. Introduction to the Dye-Sensitised Solar Cell (DSC) ---- 41
2.4.2.1. Modified Grätzel DSC ---- 44
2.4.3. Cell Dynamics of the DSC ---- 47
2.4.3.1. Mathematical Modelling of the DSC ---- 47
2.4.4. Photosensitisers in the DSC ---- 48
2.4.4.1. Organic Dyes ---- 48
2.4.4.2. Coordination Complexes of Organic Dyes ---- 51
2.4.4.3. Ruthenium Complexes ---- 55
2.4.5. Photophysical and Excited State Properties ---- 60
2.4.5.1. Properties of Ligand Anchoring Groups ---- 64
2.5. Conclusions ---- 66

CHAPTER 3 ---- 69

Synthesis of Molecular Components ---- 69

3. Introduction ---- 70
3.1. Materials and Equipment ---- 75
3.2. Discussion of Experimental Procedures ---- 76
3.2.1. Ligand Precursors ---- 76
4,4′-dicarboxy-2,2′-bipyridine (**1**) ---- 77
4,4′-diethoxycarbonyl-2,2′-bipyridine (**2**) ---- 77
4,4′-bis(hydroxymethyl)-2,2′-bipyridine (**3**) ---- 78
4,4′-bis(bromomethyl)-2,2′-bipyridine (**4**) ---- 79
4,4′-bis-diethylphosphonate(methyl)-2,2′-bipyridine (**dempbpy**) ---- 80
4,4′-bis-phosphonato(methyl)-2,2′-bipyridine hydrate (**dmpbpy**) ---- 82
3.2.2. Ruthenium Diimine Coordination Complexes ---- 83
cis-bis-(2,2′-bipyridine)dichlororuthenium(II) hydrate: **[Ru(bpy)$_2$Cl$_2$]** ---- 85
cis-bis-(2,2′-bipyridine)(4,4′-bis-diethylphosphonato(methyl)-2,2′-bipyridine)ruthenium(II) dichloride: **[Ru(bpy)$_2$(dempbpy)]Cl$_2$** ---- 86
cis-bis-(2,2′-bipyridine)(4,4′-bis-phosphonato(methyl)-2,2′-bipyridine)ruthenium(II) dichloride: **[Ru(bpy)$_2$(dmpbpy)]Cl$_2$** ---- 87
cis-bis-(4,4′-bis-diethylphosphonato(methyl)-2,2′-bipyridine)dichlororuthenium(II): **[Ru(dempbpy)$_2$Cl$_2$]** ---- 89
cis-bis-(4,4′-bis-diethylphosphonato(methyl)-2,2′-bipyridine)(2,2′-bipyridine)ruthenium(II) dichloride: **[Ru(dempbpy)$_2$(bpy)]Cl$_2$** ---- 91
cis-bis-(4,4′-bis-phosphonato(methyl)-2,2′-bipyridine)(2,2′-bipyridine)ruthenium(II) dichloride: **[Ru(dmpbpy)$_2$(bpy)]Cl$_2$** ---- 92
cis-bis-(4,4′-bis-phosphonato(methyl)-2,2′-bipyridine)dichlororuthenium(II): **[Ru(dmpbpy)$_2$Cl$_2$]** ---- 93
tris-(4,4′-bis-phosphonato(methyl)-2,2′-bipyridine)ruthenium(II) dichloride: **[Ru(dmpbpy)$_3$]Cl$_2$** ---- 95
3.2.3. Phosphonate Paraquat Sensitiser ---- 97
1-ethyl-4,4′-bipyridinium bromide (**5**) ---- 97
1-ethyl-1′-(2-phosphonoethyl)-4,4′-bipyridinium dichloride (**EVP**) ---- 98
3.3. Conclusions ---- 99

CHAPTER 4 ---- 101

Density-Functional Analysis of the Electronic Structure of Tris-Bipyridyl Ru(II) Sensitisers ---- 101

4. Introduction ---- 102
4.1. Relativistic Considerations ---- 105
4.2. Materials and Equipment ---- 106
4.2.1. Representation of Crystallographic Data ---- 106
4.2.2. Computational Methods ---- 107
4.3. Results and Discussion ---- 109
4.3.1. Structure and Bonding of Optimised Geometries ---- 109
4.3.2. Molecular Orbital Configuration ---- 113
4.3.3. Excited States and Electronic Absorption Spectra ---- 119
4.3.4. Relation to Previous Studies and Electronic Descriptions ---- 128
4.4. Conclusions ---- 129

CHAPTER 5---- 131

Microwave Modification of TiO_2 for Efficient Photocatalysis ---- 131

5. Introduction ---- 132
5.1. Materials and Equipment ---- 134
5.1.1. Preparation of Colloidal TiO_2 Solutions ---- 137
5.1.2. Microwave Hydrothermal Treatment of Colloidal TiO_2 Suspensions ---- 137
5.2. Results and Discussion ---- 138
5.2.1. X-Ray Diffraction Analysis ---- 138
5.2.2. SEM Surface Morphology ---- 141
5.2.3. TEM and Electron Diffraction Investigation ---- 143
5.2.4. Small Angle Neutron Scattering (SANS) Investigation of Colloidal Suspensions ---- 151
5.2.5. Isothermal Nitrogen Adsorption-Desorption ---- 155
5.2.6. Raman Spectroscopy ---- 159
5.3. Further Discussion ---- 161
5.4. Conclusions ---- 164

CHAPTER 6---- 165

Transient Photocurrent Analysis of Visible-Light Water Photolysis ---- 165

6. Introduction ---- 166
6.1. Materials and Equipment ---- 169
6.1.1. Preparation of Catalytic RuO_2 Nanocrystals ---- 170
6.1.2. Preparation of Nanoporous Nanocrystalline TiO_2 Films ---- 170
6.1.3. Electrodeposition of Platinum ---- 170
6.1.4. Chemisorption of Molecular Components to Thin Film Electrodes ---- 171
6.1.5. Photoelectrochemical Measurements ---- 171
6.2. Results and Discussion ---- 174
6.2.1. Investigation of the Photochemical Assembly Using the LED Source 174
6.2.2. Influence of pH on Photocurrent Yield ---- 179
6.2.3. Photoelectrochemical Efficiency of Optimised System ---- 181
6.2.4. The Photoelectrochemical System ---- 182
6.3. Conclusions ---- 186

CHAPTER 7 ---------- *187*

Multi-Step Oxidation and Mineralisation of EDTA with a Photocatalytic Molecular Assembly under Visible Light Irradiation ---------- **187**

7. Introduction ---------- 188
7.1. Materials and Equipment ---------- 191
7.1.1. Preparation of Nanoporous TiO_2 Thin Films ---------- 191
7.1.2. Electrodeposition of Platinum ---------- 192
7.1.3. Sensitisation of TiO_2 Films ---------- 192
7.1.4. Photoelectrochemical Measurements ---------- 192
7.1.5. FTIR-ATR spectroscopy ---------- 194
7.2. Results ---------- 194
7.2.1. Photoelectrochemical Determination of Solution Concentrations 199
7.2.2. Exhaustive Oxidation of EDTA Solutions ---------- 205
7.3. Discussion ---------- 209
7.3.1. Mechanism of Photooxidation and Decarboxylation at a Dye-Sensitised Surface ---------- 209
7.4. Conclusions ---------- 222

CHAPTER 8 ---------- *223*

Chemical Discrimination by a Kinetic Model of Organic Photooxidation in a Heterosupramolecular Assembly ---------- **223**

8. Introduction ---------- 224
8.1. Materials and Equipment ---------- 227
8.1.1. Preparation of Nanoporous TiO_2 Thin Films ---------- 229
8.1.2. Chemisorption of Molecular Sensitiser to Thin Film Electrodes 229
8.1.3. Electrodeposition of Platinum ---------- 229
8.1.4. Photoelectrochemical Measurements ---------- 231
8.2. Results and Discussion ---------- 233
8.2.1. Unbiased Photoelectrolysis in an Open Circuit ---------- 233
8.2.2. In Situ Transient Photocurrent Response ---------- 234
8.2.3. Kinetics of Photoelectrocatalytic Measurements ---------- 244
8.2.4. Quantitative Relationship of Photocurrent Measurements ---- 247
8.2.5. Reproducibility of the Process ---------- 249
8.3. Conclusions ---------- 250

CHAPTER 9 ---------- *251*

Conclusions and Future Work ---------- **251**

9. Conclusions ---------- 252
9.1. Future Work ---------- 257

References ---------- ***261***

APPENDIX I ---------- ***275***

10. Complete TDDFT Transitions for Tris–Bipyridyl Ru(II) Sensitisers - 275

List of Figures

Figure 1-1 – Schematic representation of the heterosupramolecular approach to simultaneous oxidation and reduction. RuO_2 and Pt are specific catalysts, $[Ru(bpy)_2(dmpbpy)]^{2+}$ (where bpy = 2,2′-bipyridine and dmpbpy = 4,4'-di(methyl)phosphonato-2,2′-bipyridine) is a photosensitiser, TiO_2 is a titania nanostructured electrode and EVP (1-ethyl-1′-(2-phosphonoethyl)-4,4′-bipyridinium dichloride) is an electron shuttle molecule ---------- 2
Figure 2-1 – Organic pollution discharge in selected countries in 2000. The values indicate emission of water-borne organics per day (in metric tonnes) and the percentage of total discharge (for selected countries). [Data: World Development Indicators, World Bank 2004][12] ---------- 13
Figure 2-2 – The electromagnetic (EM) spectrum. ---------- 15
Figure 2-3 – Components of the photochemical system: PS = photosensitiser, a molecular species that absorbs visible light, generating an electronically excited species; ES = electron shuttle, a molecule that can be reversibly oxidised or reduced leading to formation of separate charged pairs; Catalyst = specific redox catalyst, a compound that is capable of collecting several electrons for transfer to or from water; D = sacrificial donor, prevents back reaction of PS by sacrificial oxidation and is thus consumed in the process along with water. ---------- 16
Figure 2-4 – Schematic representation of the Orsay model of H_2 production.[14] ----- 17
Figure 2-5 – Band gap energies for various semiconductors in aqueous electrolytes at pH = 1.[29] ---------- 19
Figure 2-6 – Catalytic defect sites of TiO_2 (110).[29] ---------- 21
Figure 2-7 – Valence and conduction band energy and molecular structure showing the relationship between particle size and absorption band broadening a) atomic metal, particles and bulk properties b) change in semiconductor bandgap with structure.[60] ---------- 24
Figure 2-8 – Ternary compounds of the composition ABX_3 have the unit cell of the perovskite lattice e.g. Ca_2TiO_4. ---------- 26
Figure 2-9 – Photodegradation of organics by hydroxyl radical formation on TiO_2. Approximate time scale of the processes induced by ionizing radiation.[93] 28
Figure 2-10 – The principle of charge separation on a composite photocatalytic particle. ---------- 32
Figure 2-11 – The supramolecular 'scorpion' for photochemical electron transfer a) structural geometry as determined at a semi-empirical PM3 model chemistry b) stylised representation of host-guest structure.[129] ---------- 34
Figure 2-12 – Potentiostatic modulation of electron transfer by a heterosupramolecular assembly.[7] ---------- 38
Figure 2-13 – Semiconductor/electrolyte junction of regenerative PEC under illumination. ---------- 39
Figure 2-14 - Schematic of dye sensitised photovoltaic cell. ---------- 43
Figure 2-15 – Schematic representation of the cell and parameters used in the mathematical model of the DSC as described by Ferber. The space between 0 and *d* is the cell free volume occupied by electrolyte. The designators $x = 0$ and $x = d$ indicate the electrolyte/surface interfaces while 0^- and d^+ are interfacial positions within the electrode surface. Under cell illumination, excitation of E_{dye} (1) and subsequent electron injection into the CB of TiO_2 (2) results in ground state quenching by the $E_{electrolyte}$ (3). Electron loss

reactions: (a) excited state relaxation; (b) CB recombination; and (c) Redox electrolyte scavenging of CB electron. Only (c) is considered in the model and is described by an electron relaxation rate constant, k_e.[180] ---- 47
Figure 2-16 – Structure of the coumarin dye NKX-2677. ---- 48
Figure 2-17 – Structure of a) indoline-like dyes; b) Xanthene dye Eosin Y. ---- 49
Figure 2-18 – Structure of the dye Rhodamine B. ---- 50
Figure 2-19 – Structure of perylene. ---- 50
Figure 2-20 – Structure of anthocyanin dye. ---- 51
Figure 2-21 – The porphyrin sensitiser Zn-TCPP. ---- 52
Figure 2-22 – The 'sticky' porphyrin oligomer Zn_5-9. ---- 53
Figure 2-23 – Structure of the mononuclear porphyrin Zn-1b. ---- 54
Figure 2-24 – The efficient DSC sensitiser, $[Ru(dcbpy)_2(NCS)_2]^0$, or N3 dye. ---- 55
Figure 2-25 – The structure of the 'Black dye', $[Ru(tctpy)(NCS)_3]^{1-}$. ---- 56
Figure 2-26 – A selection of amphiphilic ruthenium sensitisers as utilised in the DSC ---- 58
Figure 2-27 – The octahedral geometry of $[Ru(bpy)_3]^{2+}$ depicting the orthogonal correlation of bidentate chelates. Dot surfaces illustrate the Van der Waals radii overlap of Ru–N bonds. ---- 60
Figure 2-28 – Ground state electronic structure of the frontier orbitals of a $[Ru(bpy)_3]^{2+}$ complex as in an octahedral crystal field.[135,224,225] ---- 61
Figure 2-29 – a) Electronic absorption and emission spectra of $[Ru(bpy)_3]^{2+}$ as observed in aqueous media. b) Electronic transitions associated with the frontier molecular orbitals and their relationship to observed absorption phenomena. ---- 62
Figure 2-30 – Acidic linkers associated with heterosupramolecular chemical arrays. ---- 64
Figure 2-31 – Identified and postulated binding modes of acidic groups to the surface of metal oxides: a) identified binding to titania surfaces b) postulated binding to titania surfaces. ---- 65
Figure 3-1 – Schematic representation of the mechanism for formation of coordination complexes of Ru(II) via successive ligand dissociation-association steps. ---- 71
Figure 3-2 –The commercial herbicide Gramoxone. ---- 73
Figure 3-3 – The progression of optical absorption for the formation of tris-heteroleptic diimine complexes of ruthenium(II). All spectra were obtained in methanol and background corrected against solvent and cell absorbance. ---- 83
Figure 4-1 – Ground state structure of $[Ru(bpy)_3]^{2+}$ (depicted with a PF_6^- counter ion) as determined by X-ray crystallography.[273] Structural determination was performed at 295 K, and the structure possesses D_3 symmetry. ---- 103
Figure 4-2 – Radii of *s*, *p* and *d* orbitals for $Z = 3–86$ (Li–Rn) expressed as the ratio of relativistic atomic nodal radii to expected radii in the absence of relativistic effects. [data: Zhang, Cohen and Phillips, Phys. Rev. B, 1987, 36 (11), 5861–5867] ---- 105
Figure 4-3 – Calculated eigenvalues for the frontier orbitals of the four examples of the $[Ru(bpy)_3]^{2+}$ complex. The orbitals are arranged similarly for all examples. ---- 114
Figure 4-4 – Images of frontier molecular orbital densities of the molecular orbitals involved in the primary MLCT transition. The orbitals are labelled with the

numbers from the calculations, Orgel's χ/ψ notation explained in the text, and the symmetry species under the D_3 and C_2 point groups respectively.116
Figure 4-5 – Images of frontier molecular orbital densities of the molecular orbitals involved in the primary MLCT transition. The orbitals are labelled with the numbers from the calculations, Orgel's χ/ψ notation explained in the text, and the symmetry species under the C_2 and D_3 point groups respectively.117
Figure 4-6 – HOMO of the four examples of $[Ru(bpy)_3]^{2+}$ type complexes. The orbitals are labelled with the numbers from the calculations, Orgel's χ/ψ notation explained in the text, and the symmetry species under the D_3 and C_2 point groups respectively.----------118
Figure 4-7 – Calculated excitations of four examples of the $[Ru(bpy)_3]^{2+}$ type complex (vertical lines) and observed absorption spectra (in MeOH). The y axes for the experimental spectra are in arbitrary absorbance units, and are normalised to the maximum oscillator strength in each panel. a) $[Ru(bpy)_3]^{2+}$ b) $[Ru(bpy)_2(dmpbpy)]^{2+}$ c) $[Ru(dmpbpy)_2(bpy)]^{2+}$ d) $[Ru(dmpbpy)_3]^{2+}$. ----------124
Figure 4-8 – Correlation of the observed major UV to visible charge transfer bands vs. calculated excitation wavenumbers (cm^{-1}) for the series of $[Ru(bpy)_3]^{2+}$ type complexes in MeOH.----------126
Figure 5-1 – The mode of hydrothermal bomb recrystallisation a) convection b) microwave. ----------133
Figure 5-2 – Stacked XRD diffraction patterns for investigated TiO_2 powders. Narrowing of the FWHM is observed for increased periods of processing. Traces were digitally smoothed following correction for contribution from Kα_2 radiation. ----------138
Figure 5-3 – SEM images of orthogonal surface structure (left) and structure at the fractured film edge (right) a) Degussa P25 film b) 900 min HT convection film c) 10 min MW film. Scales of images are as indicated.----------140
Figure 5-4 – 900 min HT convection TiO_2 a) ensemble of nanocrystals; b) energy filtered image of a; c) HRTEM showing the (101) lattice planes; d) SAED of nanocrystals e) radial profile of d.----------142
Figure 5-5 – Bright field TEM image of Anatase lath like crystal observed in 900 min HT sample. ----------143
Figure 5-6 – Energy-filtered TEM image of ~17 nm Brookite observed in 10 min MW TiO_2.----------144
Figure 5-7 – 20 min MW treatment a) ensemble of nanocrystals; b) medium magnification energy filtered image; c) HRTEM of microcluster; d) SAED of microcluster; e) radial profile of d.----------145
Figure 5-8 – 120 min MW treatment a) dispersed nanocrystals; b) energy filtered image of a; c) HRTEM of isolated grain; d) SAED of small cluster of nanocrystals; e) radial profile of d. ----------147
Figure 5-9 – 180 min MW treatment a) dispersed nanocrystals with some larger particles present; b) energy filtered image; c) HRTEM showing the multifaceted nanocrystals; d) SAED of nanocrystals; e) radial profile of d. ----------148
Figure 5-10 – 360 min MW treatment a) ensemble of nanocrystals; b) energy filtered image of a; c) HRTEM showing the (101) lattice planes; d) SAED of nanocrystals; e) radial profile of d. ----------149
Figure 5-11 – SANS Porod plot of modified TiO_2 colloidal suspensions prepared by microwave hydrothermal treatment – the Porod slope, P, as determined

from the linear portion (q = 0.02–0.04) of the plot are tabulated opposite. Mole fractions for all samples were in the range 0.49–0.52 M and suspended particles were for acidic conditions. ---------- 152
Figure 5-12 – Representative isotherms for prepared TiO_2 samples a) 180 min MW b) 900 min HT c) Degussa P25; adsorption –×–, desorption –×–. ------ 154
Figure 5-13 – Correlation of the change in pore volume increment with extended period of microwave treatment. ---------- 157
Figure 5-14 – Raman spectra of microwave hydrothermally treated TiO_2. Sample names are given as treatment times with alternative methods of preparation given for comparison. a) 5 min MW; b) 10 min MW; c) 20 min MW; d) 40 min MW; e) 60 min MW; f) 120 min MW; g) 180 min MW; h) 360 min MW; i) 900 min HT; j) Degussa P25. ---------- 158
Figure 6-1 – Photographs of: a) experimental assembly of the DS-PCC b) custom configured LED light source cluster. ---------- 172
Figure 6-2 – Photocurrent observed for a TiO_2/F:SnO_2 cathode against the indicated photoanode irradiated with the white light LED source (3.81 mW·cm^{-2}) in H_2O with Li_2SO_4 (0.5M) as electrolyte (pH = 5.7). ---------- 174
Figure 6-3 – Photocurrent observed for the $[Ru(bpy)_2(dmpbpy)]^{2+}$/RuO_2:TiO_2/F:SnO_2 photoanode irradiated against the indicated cathodes. Experimental conditions are for those described in Figure 6-2. ---------- 176
Figure 6-4 – Photocurrent observed for the $[Ru(bpy)_2(dmpbpy)]^{2+}$/RuO_2:TiO_2/F:SnO_2 photoanode irradiated against the indicated cathodes. Experimental conditions are for those described in Figure 6-2. ---------- 177
Figure 6-5 – Effect of pH on current density. Adjustment to pH was with either HCl or NaOH. Cell assembly: $[Ru(bpy)_2(dmpbpy)]^{2+}$/RuO_2:TiO_2/F:SnO_2|(0.5M Li_2SO_4)|EVP/Pt/TiO_2/F:SnO_2; Xe lamp (12.0 mW·cm^{-2}); AM 1.5 conditions, Oriel cut-off filter (# 66420). ---------- 178
Figure 6-6 – Influence of pH on electron injection for a PS adsorbed on a titania nanostructured electrode. Explanations of terms are given in the text; the zero-zero transition energy, E_{00}, is estimated from the emission maximum of the PS following excitation into the MLCT.---------- 178
Figure 6-7 – Current density-voltage characteristics of DS-PCC at AM 1.5 illumination. Light intensities for light sources examined are as indicated. Active cell area: 0.16 cm^2. ---------- 180
Figure 7-1 – Chemical structure of ethylenediaminetetraacetic acid (EDTA)------ 189
Figure 7-2 – Photograph of experimental instrumentation and setup. ---------- 193
Figure 7-3 – Interaction of solute with electrode surface. ---------- 195
Figure 7-4 – Conceptual model of the transient response of a PEC under an induced potential.---------- 195
Figure 7-5 – Response of DS-PCC under conditions of steady state photooxidation. ---------- 196
Figure 7-6 – Observed transient photocurrent response of the system under an extended period of time (EDTA, 0.1M, pH 2.0). Note should be made of the change in the kinetics over time with system changing from a multi-variable response to that of a single species (inset). ---------- 196
Figure 7-7 – Faradaic Model of photocurrent response over time for a stoichiometric increase in molar concentration of oxidative species A. ---------- 198

Figure 7-8 – Observed oxidation photocurrents for various concentrations of EDTA in solution. ---------- 198
Figure 7-9 – a) Faradaic relationship between concentration and j_{lim}. b) relationship between molar concentration and j_{max}. Experimental data is given as —●—, experimental data corrected for H_2O oxidation as —○— and regression data as ——. Data is for photooxidation of EDTA solutions in the concentration range of 1.000×10^{-1}M–3.125×10^{-3}M. ---------- 200
Figure 7-10 – Model of multi-step oxidation: interaction of solute and photo-products with surface under continuous illumination. ---------- 202
Figure 7-11 – The effect of pH and the photocurrent profile in the degradation of 0.1M EDTA (a) pH 4.5 (b) pH 2.9 (c) pH 2.0. Inset: inhibition of oxidation and photocurrent decline as system evolves gas from the electrode surfaces. ---------- 204
Figure 7-12 – (a) steady-state oxidation of EDTA depicting the periodic fluctuations observed during gas evolution, inset: interval and photocurrent 'spiking' as gas evolves; (b) extended oxidation with the period of fluctuations decreasing over time, inset: the magnitude and period of the photocurrent fluctuations. ---------- 207
Figure 7-13 – Photocurrent observed for the degradation of EDTA by-products: 0.1M ethylene diamine solution —●—, 0.4M glyoxylic acid —O— and a 1:4 mixture of 0.1M ethylene diamine and 0.4M glyoxylic acid—▼—. - 212
Figure 7-14 – Photographs of a) photoanode b) cathode, of a larger scale DS-PCC assembly showing the build up of gaseous degradation products on the electrode surfaces. ---------- 213
Figure 7-15 – Visualisation of secondary film formation on the photoanode surface a) photograph of electrodes: i) unsensitised TiO_2 thin film; ii) fresh dye-sensitised film; iii) photoanode after degradation. b) UV-visible spectra of the dye-sensitised electrodes before – – – and after —— use. A TiO_2 thin film substrate ····· is shown as a reference. Electrodes are from the photooxidation of EDTA depicted in Figure 7-11. ---------- 216
Figure 7-16 – a) Transmission spectra of the photoanode on a glass substrate before and after degradation. Substrates are shown for comparison. b) Transmission spectrum of polymeric film deposited on photoanode depicting the two regions used for analysis of refractive indices and film thickness. ---------- 218
Figure 7-17 – FTIR-ATR of starting organics and the surface of the electrode after extended periods of illumination. Spectra are normalised against the vibration at 1722 cm^{-1} for glyoxylic acid. ---------- 219
Figure 8-1 – Schematic representation of DS-PCC assembly as used in investigation. ---------- 230
Figure 8-2 – The *in situ* effect of concentration on the transient photocurrent for a series of NCS solutions in the DS-PCC. The cell was unbiased and measurements were obtained at pH 5.6 in 0.1M Na_2SO_4 supporting electrolyte; concentrations are as indicated. ---------- 232
Figure 8-3 – *In situ* transient photocurrents for a range of compounds in solution oxidised in the DS-PCC. The cell was unbiased and measurements were obtained in 0.1M Na_2SO_4 supporting electrolyte; solution concentration was 78 μM. ---------- 232

Figure 8-4 – The photocurrent-time decay profile for the oxidation of organic compounds by the DS-PCC assembly; solution concentrations are as indicated with experimental data (___) and the curve fitting data (O) a) EDTA, 156 μM pH 4.5 b) Glu, 625 μM pH 5.5 c) MeOH, 3% v/v, pH 5.8 d) MV, 2500 μM.---------- 236
Figure 8-5 – Plot of the fast (___) and slow (___) current parameters from the fitted data in Figure 8-4. a) EDTA, 156 μM pH 4.5 b) Glu, 625 μM pH 5.5 c) MeOH, 3% v/v, pH 5.8 d) MV, 2500 μM. Solution concentrations are as previously indicated, with the vertical scale normalised between panels. 242
Figure 8-6 – Concentration dependence of k_w for 39–625 μM solutions: dpy (●); NHCS (⊙); NCS (▼). The linear relationship of concentration to k_w is illustrated by the fitting of a linear function: dpy (___); NHCS (___); NCS (___).---------- 246
Figure 8-7 – Transient photocurrent-time profiles depicting the reproducibility of measurements in the DS-PCC a) NHCS b) EDTA.---------- 248
Figure 9-1 – Energy parameters affecting photochemical properties of Ru(II) complexes a) theoretical calculation of ligand LUMO energy [B3LYP/6-311G+(2*d*,*p*) model chemistry] b) experimental reduction potential for the first oxidation of the stated complexes.[54,135,223] Complexes as indicated are (–■–), carboxylate (–▼–) and phosphonate (–●–) analogues.---------- 256
Figure 9-2 – *ex situ* formation of catalytic surface complex and mechanism for bromination of a terminal alkene.---------- 258
Figure 9-3 – The proposed heterosupramolecular structure of a host receptor for controlled photochemical reactions a) chemical structure of the complex b) geometric representation of the Host-Guest inclusion complex depicting 'bound' hexyl-3,5-dihydroxybenzoate as determined at a semi-empirical PM3 model chemistry. ---------- 259

List of Tables

Table 4-1 – Selected calculated bond angles (°) and lengths (Å) for coordination of diimine ligands in the four examples of $[Ru(bpy)_3]^{2+}$ complex. Atom positions are numbered sequentially in a clockwise direction. Individual configurations are: $[Ru(bpy)_3]^{2+}$, R_1–R_3 = H R_1'–R_3' = H; $[Ru(bpy)_2(dmpbpy)]^{2+}$, R_1 and R_2' = mp R_2–R_3 = H R_2'–R_3' = H; $[Ru(dmpbpy)_2(bpy)]^{2+}$, R_1 and R_1' = mp R_3 and R_3' = mp R_2 and R_2' = H; $[Ru(dmpbpy)_3]^{2+}$ R_1–R_3 = mp R_1'–R_3' = mp; where mp = phosphonomethyl. ---------- 110
Table 4-2 – Selected calculated bond lengths (Å) for the four examples of $[Ru(bpy)_3]^{2+}$ Complex. Atom numbering and ligand substitution for the complexes are as in Table 4-1. ---------- 112
Table 4-3 – TDDFT calculated excitation energies, one-electron transitions, and oscillator strengths for optical transitions of $[Ru(bpy)_3]^{2+}$ complex in the gas phase ($\lambda > 400$ nm; $f > 0.01$). ---------- 120
Table 4-4 – TDDFT calculated excitation energies, one-electron transitions, and oscillator strengths for optical transitions of $[Ru(bpy)_2(dmpbpy)]^{2+}$ complex in the gas phase ($\lambda > 400$ nm; $f > 0.01$). ---------- 120
Table 4-5 – TDDFT calculated excitation energies, one-electron transitions, and oscillator strengths for optical transitions of $[Ru(dmpbpy)_2(bpy)]^{2+}$ complex in the gas phase ($\lambda > 400$ nm; $f > 0.01$). ---------- 121
Table 4-6 – TDDFT calculated excitation energies, one-electron transitions, and oscillator strengths for optical transitions of $[Ru(dmpbpy)_3]^{2+}$ complex in the gas phase ($\lambda > 400$ nm; $f > 0.01$). ---------- 121
Table 4-7 – Observed (for series of $[Ru(bpy)_3]^{2+}$ complexes in methanol) and calculated wavenumbers (cm^{-1}) for the UV to visible bands of the substituted complexes. ---------- 126
Table 5-1 – Calculated Scherrer crystallite size (nm) from Anatase 101 (29.53 / °2θ) reflection. ---------- 139
Table 5-2 – Calculated isothermal parameters. ---------- 156
Table 5-3 – Peak characteristics identified for the Anatase E_g band. ---------- 160
Table 6-1 – Scheme for nomenclature and assembly of electrodes. A '/' indicates subsequent treatment, while ':' indicates a composite material. ---------- 171
Table 6-2 – Observed limiting photocurrent (t = 100 s) under visible light illumination with assembled electrodes[a]. ---------- 173
Table 6-3 – Photovoltaic parameters of PCC under different light sources[a] -------- 180
Table 8-1 – Kinetic parameters obtained from fitting of experimental photocatalytic decay profiles with a double exponential expression for the amine structures. For the series of concentrations, $\bar{x}$ is the mean and σ is the standard deviation; definitions of kinetic constants are described in the text. ---------- 238
Table 8-2 – Kinetic parameters obtained from fitting of experimental photocatalytic decay profiles with a double exponential expression for the urea and thiol containing structures. For the series of concentrations, $\bar{x}$ is the mean and σ is the standard deviation; definitions of kinetic constants are described in the text. ---------- 239
Table 8-3 – Kinetic parameters obtained from fitting of experimental photocatalytic decay profiles with a double exponential expression for the alcohol

containing structures. For the series of concentrations, $\bar{x}$ is the mean and σ is the standard deviation; definitions of kinetic constants are described in the text. ---------- 240
Table 10-1 – TDDFT Calculated Excitation Energies, One–Electron Transitions, and Oscillator Strengths for Optical Transitions of $[Ru(bpy)_3]^{2+}$ complex in the Gas Phase.---------- 276
Table 10-2 – TDDFT Calculated Excitation Energies, One–Electron Transitions, and Oscillator Strengths for Optical Transitions of $[Ru(bpy)_2(dmpbpy)]^{2+}$ complex in the Gas Phase. ---------- 289
Table 10-3 – TDDFT Calculated Excitation Energies, One–Electron Transitions, and Oscillator Strengths for Optical Transitions of $[Ru(dmpbpy)_2(bpy)]^{2+}$ complex in the Gas Phase. ---------- 306
Table 10-4 – TDDFT Calculated Excitation Energies, One–Electron Transitions, and Oscillator Strengths for Optical Transitions of $[Ru(dmpbpy)_3]^{2+}$ complex in the Gas Phase. ---------- 324

List of Schemes

Scheme 3-1 – (i) K_2CrO_7/H_2SO_4, HNO_3 reflux 4 h; (ii) $EtOH/H_2SO_4$ (95:5 v/v) reflux 72 h; (iii) EtOH, $NaBH_4$, 50°C, 3 h; (iv) H_2SO_4/HBr (25:75 v/v), reflux 8 h; (v) $P(OEt)_3$, reflux 8 h; (vi) 20% HCl, reflux 18 h, 48% HBr, reflux 4 h. ---------- 76
Scheme 3-2 – (vii) DMF, LiCl, 130°C, 6 h; (viii) MeOH, reflux 13 h; (ix) 20% HCl, reflux 16 h ---------- 84
Scheme 3-3 – (x) DMF, LiCl, 140°C, 8 h; (xi) MeOH, reflux 22 h; (xii) 20% HCl, reflux 16 h ---------- 88
Scheme 3-4 – (xiii) and (xiv) 20 % HCl, reflux 48 h ---------- 94
Scheme 3-5 – (xv) Toluene, bromoethane, reflux 4 h; excess bromoethane, reflux 20 h; (xvi) H_2O, $PO(OEt)_2EtBr$, reflux 48 h; 32 % HCl, reflux 48 h ---------- 97
Scheme 6-1 – Schematic representation of the heterosupramolecular approach to simultaneous O_2 and H_2 production. ---------- 168
Scheme 6-2 – Structure of a) the electron donor ($[Ru(bpy)_2(dmpbpy)]^{2+}$) and b) electron acceptor (EVP) molecules as utilised in the photochemical system. ---------- 169
Scheme 7-1 – Structure of the electron donor $[Ru(dmpbpy)_2(bpy)]^{2+}$ used in the DS-PCC. ---------- 191
Scheme 7-2 – Mechanism of catalytic adsorption and rearrangement where EDTA is degraded to EDTrA and glyoxylic acid in the presence of H_2O. The EDTrA and subsequent amine compounds can then undergo further degradation via this mechanism to give stoichiometric amounts of glyoxylic acid and ethylenediamine. ---------- 210
Scheme 7-3 – Free radical formation via the Kolbe synthetic reaction ---------- 214
Scheme 7-4 – Specific examples of potential radical termination products from Kolbe synthetic reaction. ---------- 215
Scheme 8-1 – Structure of the electron donor $[Ru(bpy)_2(dmpbpy)]^{2+}$ used in the DS-PCC. ---------- 227
Scheme 8-2 – Structure of simulated chemical pollutants studied for their oxidation capacity. Abbreviations used in the text are indicated in brackets. -------- 228

Abbreviations and Symbols

Compounds and Chemicals

$[Ru(bpy)_2(dempbpy)]Cl_2$	*cis*-bis-(2,2′-bipyridine)(4,4′-bis-diethylphosphonato(methyl)-2,2′-bipyridine)ruthenium(II) dichloride
$[Ru(bpy)_2(dmpbpy)]Cl_2$	*cis*-bis-(2,2′-bipyridine)(4,4′-bis-phosphonato(methyl)-2,2′-bipyridine)ruthenium(II) dichloride
$[Ru(bpy)_2(dmpbpy)]^{2+}$	*cis*-bis-(2,2′-bipyridine)(4,4′-bis-phosphonato(methyl)-2,2′-bipyridine)ruthenium(II) dication
$[Ru(bpy)_2Cl_2]$	*cis*-bis-(2,2'-bipyridine)dichlororuthenium(II) hydrate
$[Ru(bpy)_3]Cl_2$	tris-(2,2'-bipyridine)ruthenium(II) dichloride hexahydrate
$[Ru(bpy)_3]^{2+}$	tris-(2,2'-bipyridine)ruthenium(II) dication
$[Ru(dcbpy)_2(NCS)_2]^0$	*cis*-bis-(2,2'-bipyridine-4,4'-dicarboxylato)diisothiocyantoruthenium(II)
$[Ru(dcbpy)_3]Cl_2$	tris-(4,4'-dicarboxy-2,2'-bipyridine)ruthenium(II) dichloride
$[Ru(dcbpy)_3]^{2+}$	tris-(4,4'-dicarboxy-2,2'-bipyridine)ruthenium(II) dication
$[Ru(dempbpy)_2(bpy)]Cl_2$	*cis*-bis-(4,4′-bis-diethylphosphonato(methyl)-2,2′-bipyridine)(2,2′-bipyridine)ruthenium(II) dichloride
$[Ru(dempbpy)_2Cl_2]$	*cis*-bis-(4,4′-bis-diethylphosphonato(methyl)-2,2′-bipyridine)dichlororuthenium(II)
$[Ru(dmpbpy)_2(bpy)]Cl_2$	*cis*-bis-(4,4′-bis-phosphonato(methyl)-2,2′-bipyridine)(2,2′-bipyridine)ruthenium(II) dichloride
$[Ru(dmpbpy)_2(bpy)]^{2+}$	*cis*-bis-(4,4′-bis-phosphonato(methyl)-2,2′-bipyridine)(2,2′-bipyridine)ruthenium(II) dication
$[Ru(dmpbpy)_2Cl_2]$	*cis*-bis-(4,4′-bis-phosphonato(methyl)-2,2′-bipyridine)dichlororuthenium(II)
$[Ru(dmpbpy)_3]Cl_2$	tris-(4,4′-bis-phosphonato(methyl)-2,2′-bipyridine)ruthenium(II) dichloride
$[Ru(dmpbpy)_3]^{2+}$	tris-(4,4′-bis-phosphonato(methyl)-2,2′-bipyridine)ruthenium(II) dication
$[Ru(tctpy)(NCS)_3]^{1-}$	4,4',4"-tricarboxylato-2,2':6,2"-terpyridyl-triisothiocyantoruthenium(II) anion
$[RuCl_2(DMSO)_4]^0$	dichlorotetrakis(dimethylsulphoxide)ruthenium(II)
1	4,4'-dicarboxy-2,2'-bipyridine
2	4,4'-diethoxycarbonyl-2,2'-bipyridine
3	4,4'-bis(hydroxymethyl)-2,2'-bipyridine
4	4,4'-bis(bromomethyl)-2,2'-bipyridine
5	1-ethyl-4,4'-bipyridinium bromide
$(CH_3)_2CO$	acetone
ACN	acetonitrile
biq	2,2'-biquinoline
Black dye	alternate name for $[Ru(tctpy)(NCS)_3]^{1-}$
bpy	2,2'-bipyridine
Carbowax	polyethylene glycol
$CDCl_3$	deuterochloroform
D_2O	deuterium oxide
dcbpy	4,4'-dicarboxy-2,2'-bipyridine

DDT	1,1-bis(4-chlorophenyl)-2,2,2-trichloroethane
dempbpy	4,4′-bis-diethylphosphonate(methyl)-2,2′-bipyridine
dmbpy	4,4'-dimethyl-2,2'-bipyridine
DMF	*N,N'*-dimethylformamide
dmpbpy	4,4′-bis-phosphonato(methyl)-2,2′-bipyridine hydrate
DMSO	dimethylsulphoxide
DMSO-d_6	bis-trideuteromethyl sulphoxide
dpy	4,4'-dipyridyl
dtox	ethanedithioamide (dithiooxamide)
EDTA	ethylenediaminetetraacetic acid disodium
$EDTA^+$	product of EDTA oxidation
EDTrA	ethylenediaminetriacetic acid
en	ethylenediamine
EtGly	ethylene glycol
EtOH	ethanol
EVP	1-ethyl-1'-(2-phosphonoethyl)-4,4'-bipyridinium dichloride
Glu	glucose
Gly	glycerol
HMT	hexamethylenetetramine
MV	methyl viologen (1,1'-methyl-4,4'-bipyridyl dichloride)
N3 dye	alternate name for $[Ru(dcbpy)_2(NCS)_2]^0$
$NaBH_4$	sodium borohydride
NaOD	sodium deuterooxide
NCS	sodium thiocyanate (in photodegradation studies)
NHCO	urea
NHCS	thiourea
phen	phenanthroline
$P(OEt)_2$	triethylphosphite
P25	Degussa P25 titanium dioxide
PET	polyethyleneteraphthalate
$PO(OEt)_2EtBr$	diethylbromoethyl phosphonate
PTFE	polytetrafluoroethylene
$RuCl_3.nH_2O$	ruthenium trichloride hydrate
TBA^+	tetra-*n*-butylammonium cation
TBAOH	tetra-*n*-butylammonium hydroxide
TEOA	triethanolamine

Electrochemical and Kinetic Quantities

η	cell conversion efficiency = $(P_{max} \times ff / P_{in}) \times 100\%$ or refractive index (Chapter 7, indicated in text)
ϕ	quantum injection yield
AQY	apparent quantum yield
LH mechanism	Langmuir-Hinshelwood mechanism of surface-catalysed reactions
LHHW	Langmuir-Hinshelwood-Hougen-Watson expression
C_0	initial molar concentration of oxidisable species
E^0	reduction potential
E^0_{ads}	adsorbed reduction potential
E_{00}	zero-zero spectroscopic energy for emission from MLCT
$E_{½}$	half-wave potential
E_f	fermi potential
ff	fill factor = P_{max}/P_{in}
I_{ph}	photocurrent
j_{lim}	limiting photocurrent density
j_{max}	maximum photocurrent density
j_{sc}	short-circuit current density
P_{in}	incident power intensity
P_{max}	maximum electricity output power density
V_{FB}	flatband potential
V_{oc}	open-circuit potential
V_{ph}	photovoltage
j	designator for type of surface complex or interfacial process
$I_{ph\ j}$	instantaneous photocurrent for the jth event
f	kinetically fast process
s	kinetically slow process
$I^0_{ph\ j}$	initial photocurrent for the jth event at $t = 0$
$I_{ph\ f}$	instantaneous photocurrent for the fast event
$I_{ph\ s}$	instantaneous photocurrent for the slow event
$I_{ss\ water}$	photocurrent for the steady state oxidation of water
$I_{l\ O}$	limiting photocurrent for oxidisable species
k_j	rate constant for the jth kinetic event
k_f	rate constant for the fast kinetic event
k_s	rate constant for the slow kinetic event
k_w	kinetic constant for steady state oxidation of event w
Q	electronic charge
Q^0_j	expected charge for the jth event at $t = 0$
n	number of moles
m_O	mass transfer coefficient

Quantum Chemical Terminology

C_2	symmetry point group identifier
C_3	symmetry operation for 2-fold rotation axis
D_3	symmetry point group identifier
$\tilde{\nu}_{LC}$	transition wavenumber for the LC transition
$\tilde{\nu}_{MC}$	transition wavenumber for the MC transition
$\tilde{\nu}_{MLCT}$	transition wavenumber for the MLCT
χ	Orgel symmetrical orbital
ψ	Orgel anti-symmetrical orbital
ζ	zeta
ab initio	'from the beginning' – in reference to quantum chemical models
AM1	Austin model one, a semi empirical model
B3LYP	Becke 3-Parameter (exchange), Lee, Yang and Parr (correlation) hybrid functional
CT	charge transfer
DFT	density functional theory
ECP	effective core potentials
f	oscillator strength
HOMO	highest unoccupied molecular orbital
INDO/S	intermediate neglect of differential overlap/screened approximation
LanL2DZ	Los Alamos National Laboratory 2-double-ζ basis set
LC	ligand-centred transition
LLCT	ligand-to-ligand charge transfer
LMCT	ligand-to-metal charge transfer
LUMO	lowest unoccupied molecular orbital
MC	metal-centred transition
MLCT	metal-to-ligand charge transfer
^{1}MLCT	singlet metal-to-ligand charge transfer
^{3}MLCT	triplet metal-to-ligand charge transfer
PM3	parametric method three, a semi empirical model
RECP	relativistically parameterized effective core potentials
TD-DFT	time dependant density functional theory

Spectroscopic Expressions

cm^{-1}	wavenumber
δ	chemical shift
ε	molar extinction coefficient or molar absorptivity
Δ	right-hand helical screw of a chiral complex
Λ	left-hand helical screw of a chiral complex
^{13}C	carbon nuclei
$\{^{13}C\}$	carbon decoupled
^{1}H	proton nuclei
$\{^{1}H\}$	proton decoupled
^{31}P	phosphorus nuclei
J	coupling constant
$^{1}J_{PC}$	one bond hetero-coupling constant for $^{31}P–^{13}C$
$^{2}J_{PC}$	two bond hetero-coupling constant for $^{31}P–^{13}C$
$^{2}J_{PH}$	three bond hetero-coupling constant for $^{31}P–^{2}H$
$^{3}J_{PC}$	three bond hetero-coupling constant for $^{31}P–^{13}C$
A_{1g}	irreducible representation or symmetry label for the first one-dimensional symmetrical (gerade) rotation with no change of sign
B_{1g}	irreducible representation or symmetry label for the first one-dimensional symmetrical (gerade) rotation with change of sign
B_{2g}	irreducible representation or symmetry label for the second one-dimensional symmetrical (gerade) rotation with change of sign
B_{3g}	irreducible representation or symmetry label for the third one-dimensional symmetrical (gerade) rotation with change of sign
E_g	irreducible representation or symmetry label for a two-dimensional symmetrical (gerade) rotation
br	broad resonance
d	doublet spin resonance
dd	doublet of doublet spin resonances
dt	double of triplet spin resonances
m	multiplet spin resonance
q	quartet spin resonance
s	singlet spin resonance
t	triplet spin resonance
unr	unresolved coupling
CIS	coordination induced shift

Surface and Material Chemistry Specific Terminology

α	capillary length (LSW theory)
γ_{SL}	solid-liquid interfacial energy (Ostwald-Freundlich equation)
BET	Brunauer–Emmett–Teller isotherm
BJH	Barret–Joyner–Halenda method of adsorption analysis
D_{avg}	average pore diameter
D_m	dispersed phase molecular diffusion coefficient (LSW theory)
$I(q)$	measured quantity of scattered intensity
P	Porod slope, slope of a scattering plot in the Porod region
P	partial pressure (mmHg)
P/P_0	relative pressure
P_0	saturation pressure (mmHg)
P_D	primary crystallite diameter
PV_{SP}	single-point pore volume
q	Fourier spatial frequency
q^{-1}	scattering length (Å)
q_a	Fourier spatial frequency dependant on bond length
q_R	Fourier spatial frequency dependant on radius of gyration
r_c	critical radius (Ostwald ripening)
r_N	average number radius (Ostwald-Freundlich equation)
S	solubility (Ostwald-Freundlich equation)
S_0	flat plate solubility (Ostwald-Freundlich equation)
SA_{BET}	BET surface area
v	ripening rate (LSW theory)
V_I	incremental pore volume
V_m	molar volume

Constants

F	Faraday's constant (96,485.309 $C \cdot mol^{-1}$)
R	gas constant (8.31451 $J \cdot mol^{-1} \cdot K^{-1}$)

General Expressions

σ	statistical standard deviation, $\sigma = \sqrt{\frac{\sum_{i=1}^{N}(x_i - \bar{x})^2}{N-1}}$
$\bar{x}$	statistical mean, $\bar{x} = \frac{\sum_{i=1}^{N} x_i}{N}$
λ	wavelength
°	degree(s)
μA	microampere
μm	micrometre
μs	microsecond
A	ampere
Å	Angstrom units (10^{-10} metres)
AM 1.5	air mass one-and-one half, standard conditions for terrestrial solar spectral irradiance
AR	analytical reagent
ATR	attenuated total reflectance
Catalyst	specific redox catalyst
CB	conduction band
CCD	charge coupled device
CCDC	Cambridge Crystallographic Data Centre
CIF	crystallographic information file
cm^{-1}	wavenumber
CS	crystallographic shear
CV	cyclic voltammogram
CVD	chemical vapour deposition
D	sacrificial donor
DSC	dye-sensitised solar cell
DS-PCC	dye-sensitised photoelectrocatalytic cell
DTGS	deuterated triglycine sulfate (IR detector)
E_g	band gap energy
EM	electromagnetic
ES	electron shuttle
ESEM	environmental scanning electron microscope
ET	electron transfer
eV	electronvolt
fs	femtosecond
FTIR	Fourier transform infrared spectroscopy
FTO	fluoride-doped tin oxide
FWHM	full width at half maximum
GHz	gigahertz
Grätzel solar cell	alternate name for dye-sensitised solar cell (DSC)
H_0	Hammett acidity function

HRTEM	high resolution transmission electron microscopy
HT	hydrothermal
Hz	hertz
IBICVD	ion beam induced chemical vapour deposition
IHP	inner Helmholtz plane
IPCE	incident photon-to-current efficiency
IR	infrared
IRE	internal reflectance element
ITO	indium-doped tin oxide
K	Langmuir adsorption constant for a surface monolayer ($L \cdot mol^{-1}$)
LD_{50}	lethal dose for 50% of the animal population tested
LED	light emitting diode
LOF	Libby Owens Ford
mA	milliampere
MCM	mesoporous crystalline material
MHz	megahertz
MW	molecular weight
MW	Microwave treatment: denoted with a treatment time (min)
Nd-YAG	neodymium (3+)-doped yttrium aluminium garnet laser
NIR	near-infrared
nm	nanometre
NMR	nuclear magnetic resonance spectroscopy
NO_x	nitrous oxides
ns	nanosecond
OHP	outer Helmholtz plane
OPD	optical path difference
PDF	powder diffraction file
PEC	photoelectrochemical
PS	photosensitiser
ps	picosecond
PS I	photosystem I
PS II	photosystem II
PSI	$lb \cdot in^{-2}$
q	Fourier spatial frequency
RSSF	Renishaw super spectral filter
S^+/S	ground state of a sensitiser
S^+/S^*	excited state of a sensitiser
SAED	selected-area electron diffraction
SANS	small-angle neutron scattering
SCE	saturated calomel electrode
SEM	scanning electron microscopy
Sephadex LH–20	commercial polydextrin permeation chromatography gel
SHE	standard hydrogen electrode
TCO	transparent conductive oxide
TE	thermo electric
TEC	thermo electric cooler

TEC15/3	transparent electrical conducting glass ~15 $\Omega \cdot cm^2$, 3 mm thick
TEM	transmission electron microscopy
UHP	ultra high purity
UV	ultra violet
VB	valence band
XRD	X-ray diffraction
Γ	packing density of a Langmuir adsorption isotherm ($mol \cdot cm^{-2}$)

Acknowledgements

The successful preparation, chronicling, justification and compilation of a thesis is a task that is not undertaken lightly and certainly cannot be performed without the assistance of many people – hence, this work is not solely my own. To me the past few years that I have spent undertaking this research project has been one of both career and life-changing proportions. For that immense expenditure on many people's behalf's, I would like to acknowledge and sincerely thank:

"Inspiration" This PhD would not have been without someone's inspirational spark – The essence of Genius is conception. I am sure that for every generation of student, their supervisor beared the weight of conceiving an idea that deserves scientific consideration and could be justified in consuming resources, time, and personnel expenditure to warrant a higher certification. For this I must sincerely thank my supervisor Dr Geoffrey Will for his enthusiastic interest in the work, kind support and encouragement and relentless pursuit of 'the next result'. You have always been a true supporter of my efforts and have inspired me to no end.

Many thanks must also go to my associate supervisor Dr Dennis Arnold who has been a most wonderful addition to my supervisory team. The influence on my standards of work and presentation has certainly been worthwhile. My synthetic adventures would have left me synthetically lost without your subtle guidance.

At a glance performing research seems straightforward, but without funding much of the research undertaken in this thesis would not have been possible. I would like to thank the Queensland Department of Premier and Cabinet for the provision of a Smart State Award in 2003 to complete much of the environmental and chemical energy studies – to my EPA mentors Lindsay Delzoppo and Dr Martin Gellender thank you for your time and patience, and to the assistance of the DPC staff especially Madonna Townsley.

I would also like to extend my thanks to the AINSE committee and ANSTO for the provision of AINSE grant AINGRA04170P – thankyou to Dr Dennis Mather and Ben Thompson for their enthusiastic assistance while I attended the Menai facilities.

To the Australian Partnership for Advanced Computing committee for the provision of funding for projects i64 and g03 under the Merit Allocation Scheme and to the Queensland Partnership for Supercomputing for Partner Share on the project f85. Thanks also to the APAC committee for funding my attendance at the Sydney Gaussian Workshop and the kind invitation and funding to speak at 9th Molecular Graphics Modelling Society Conference 2004.

To the Science Research Committee for the provision of a QUT PRA scholarship – thankyou to the Office of Research staff, Stella Winn and Lois McLaughlin, for assistance during my candidature. To the PCS School Research committee, Inorganic Materials Program and RACI for funding conference attendance/travel – thankyou to Elizabeth Stein, Michelle Rice and Lesley Sands for tracking my 'paper trails'.

I must thank Aaron Matijasevich for his assistance in the lab and preparing many of the samples used for microwave TiO_2 analysis, "you make good titania soup". To Mr Tony Raftery of the Science Faculty's XRD laboratories for his assistance in obtaining and interpreting diffraction patterns of the samples and to Dr Zhe Ding for her welcome discussions on titania preparation and properties. I must also extend my appreciation to Loc Duong (QUT) and Dr Arthur Day (ANSTO) for striving to help me find a 'needle' in a thin-film haystack. When you're dealing with nano-anything's how can I expect to just 'see it'?

Dr Martens, Wayde by any other name, for much assistance in surface characterisation and many informal and fruitful discussions on the inorganic materials aspects of my project. As well as being the 'helmsman' of our research program, Professor Ray Frost has been a helpful collaborator and advisor in much of this work also, thank you. My appreciation to Dr Llew Rintoul for many-a-days discussion over a range of topics but mostly for his 'cool' approach to my sporadic and 'mindless' requirements of Raman vibrational analysis in my project.

Certain key aspects of this project have been highly focused through strong collaborative links. Thanks to Dr David Mitchell and Dr Jamie Schulz (ANSTO) for their collaboration on the microwave modification of TiO_2 and their professional

approach to analysis of TEM and SANS data. There has been much work shared with researchers at Griffith University on the Gold Coast for many years. During this time I have gained practical insight from Dr Shanqing "Eddie" Zhang and a strong acquaintance with Associate Professor Huijun Zhao on the utilisation of TiO_2 for photoelectrochemical applications; I thank them both for their time and knowledge. My appreciation also to Dr Nelsi Zacheroni for her thoughtful insight during her time spent working within our research group while on research sabbatical.

I must sincerely thank the Faculty's "Specialist Sparky", George Racz, who has been so very patient and considerate in preparing the custom electrochemical equipment utilised in this project. All of the electrochemical measurements presented in this thesis would not have been possible without your knowledge and expertise in designing the equipment – you always knew just what I needed.

My appreciation to members of the Synthesis and Molecular Recognition Program for supply of incidental chemicals and advice during the course of this research including Kazuyuki Hosokawa, Farzad Atefi, Meg Hodgson, Daniel Keddie and Ben Morrow. Especially thanks to Oliver Locos, your assistance and advice in synthesis has been crucial over the past 3 years and our afternoon coffee breaks have added a delightful reality disturbance; we have discussed anything from our research to much lighter topics – I remember "this one time, at band camp…", it has been fun. I also extend my appreciation to the former members Dr Regan Hartnell, Dr Craig Smith and Dr Damian Reid for their assistance while they studied. To the Wentrup-Byrne group for their supply of simple alkali salts and ethylene glycol and thanks to John Colwell for his support and friendly aspect to work in E306 over the lifetime of our studies. Thanks also to the members of the Will group, especially Surya Subianto and Adrian Fuchs. To Professor Fabrice Odobel of the University of Nantes and Professor Allan Williams of the University of Geneva, thank you very much for your informal discussions on chemistry relevant to this project.

My sincere appreciation to Dr John Bartley from the Chemistry NMR Facility and Dr Roger Meder of the Physics Magnetic Resonance Suite for their tireless assistance during my synthetic endeavours. John, although you are from the 'unaligned program' you have always made time to assist we less fortunate inorganic chemists

in our dilemmas and Roger, well how many times have I asked you to teach me techniques that are not even in practise here at QUT? Thank you to Dr John McMurtrie for discussion of coordination chemistry of ruthenium and the provision of crystallographic data for analysis of my studied compounds.

The studies during my PhD, although not truly reflected in this thesis, have relied heavily on the support of QUT's High Performance Computing Services and the computational facilities of APAC, QPSF and UQ. For their assistance in all manners of this work I sincerely thank Dr Anthony Rasmussen, Dr Mark Barry, Dr Neil Kelson and Dr Bernadette Savage (QUT, QPSF), Dr Martin Nichol (UQ, QPSF), Dr Rika Kobayashi and Dr David Singleton (APAC) as well as all the other support staff.

My appreciation extends to Mr Pat Stevens for his financial support and assistance and to Dr Chris Carvalho for their knowledge and thoughtful suggestions in instrumental techniques and equipment for my work. Thanks also to Karl Jacques, Eric Martinez, Ronnie McGregor, Shane Russell, Vera Combeer and Nick Ryan, Mark Smith, Kim Larson and Mary Dewar. I am grateful to Stuart Costin and Vern Beecham for IT support; I have at times been very demanding in this area and they, especially Stuart, have always assisted me wholeheartedly. I also need to recognise Jim Drysdale and Bob Organ of the Faculty Workshop for their enthusiasm and assistance when I come to them with a simple task that almost always turned into a crisis that needed to be completed immediately.

My appreciation to Professor Jim Pope, Chris Duncan and the School of PCS for providing adequate laboratory space in E306 and allowing required access to the school facilities of E411. The allocation of office space in H208 during the preparation of my thesis has been a wonderful change that has allowed me to complete my thesis in a timely manner.

"The Family" – to my gorgeous wife Kelly and our darling girl Aisha, there is so much that I have to thank you both for, but so much I cannot express here. Each day has been a struggle but, without fail, you motivate me to face it head on and the thought of you both waiting for me when I come home drives me to take that first step. Each day is a day closer to being with you more – "You make my day".

My appreciation to the whole "are we there yet" gang, our family, – research does not work to an absolute deadline, so neither do I, my thesis will be finished when we "get" there. I do sincerely thank my brothers Andrew and Des, my sister Jeanette and their spouses Tracey, Susie and Scott and also to Amy, Josh and Erin. Thanks also to my Mother and Father, Pam and Clive for their love, support and affection. To Wayne and Sandra I appreciate your thoughtfulness throughout my studies; you have always been there to ask after my well-being and take care of us when we needed it.

To my correspondence colleague at Monash University, George Nikolakopoulos, thanks for keeping in touch and I hope all is progressing well for you. Thanks also to Dr Dalius Sagatys for pure moral support and providing an alternative viewpoint from which to assess life's little troubles.

To those that have seen that my drive can sometimes overcome me, I thank you for understanding; for others, I hope that you can see past my "attitudal" discretions. To all the postgraduates, past and present, I sincerely thankyou for your assistance over the years; if you didn't help me directly there was always that subtle motivation for me to get completed, and move on…

For anyone else who I may have forgotten, I appreciate all that you have done and most of all I appreciate that you stood by me during this time.

_____

Gregory Wilson, September 2005

Publications Arising From This Work

G. J. Wilson, G. D. Will

"Multi-step oxidation and mineralisation of EDTA with a photocatalytic molecular assembly under visible light irradiation"

J. Photochem. Photobiol., A, **2005,** Manuscript in Preparation

G. J. Wilson, A. S. Matijasevich, D. R. G. Mitchell, J. C. Schulz, G. D. Will

"Modification of TiO_2 for efficient photocatalysis: finite Ostwald ripening by a microwave hydrothermal process"

Langmuir, **2005,** Manuscript Accepted

G. J. Wilson, G. D. Will

"Photoelectrochemical measurements of a heterosupramolecular system under visible light irradiation"

Photochem. Photobiol. Sci., **2005,** 4, 602 – 608

G. J. Wilson, G. D. Will

"Photocleavage of water with a photochemical heterosupramolecular assembly"

Curr. Appl. Phys., **2004**, 4, 351–35

Complete List of Publications

Papers

G. J. Wilson, G. D. Will
"Multi-step oxidation and mineralisation of EDTA with a photocatalytic molecular assembly under visible light irradiation"
J. Photochem. Photobiol., A, **2005,** Manuscript in Preparation

G. J. Wilson, A. Matijasevich, D. R. G. Mitchell, J. C. Schulz, G. D. Will
"Modification of TiO_2 for efficient photocatalysis: finite Ostwald ripening by a microwave hydrothermal process"
Langmuir, **2005,** Manuscript Accepted

G. J. Wilson, G. D. Will
"Photoelectrochemical measurements of a heterosupramolecular system under visible light irradiation"
Photochem. Photobiol. Sci. **2005,** 4, 602 – 608

G. J. Wilson, D. P. Arnold
"Time dependent density functional molecular orbital and excited state calculations on bis(porphyrinyl)butadiynes in the monocationic, neutral, monoanionic and dianionic oxidation states"
J. Phys. Chem. A, **2005,** 109, (27), 6104–6113

S. Zhang, D. Jiang, H. Zhao, G. J. Wilson, G. D. Will, R. John
"Photoelectrochemical Characterisation of TiO_2 Thin Films Derived from Microwave Hydrothermally Processed Nanocrystalline Colloids"
J. Photochem. Photobiol., A, Manuscript In Press

G. J. Wilson, G. D. Will
"Photocleavage of water with a photochemical heterosupramolecular assembly"
Curr. Appl. Phys., **2004**, 4, 351–354

G. J. Wilson, G. D. Will, R. L. Frost, S. A. Montgomery
"Efficient microwave hydrothermal preparation of nanocrystalline anatase TiO_2 colloids"
J. Mater. Chem. **2002,** 12, 1787–1791

Lectures

G. J. Wilson, G. D. Will
"Photocatalysis and the photoelectrochemical cell: Pollutant decomposition at the interface"
Interact 2004, Gold Coast, Australia, 2004

G. J. Wilson (invited speaker), A. Fuchs, G. D. Will
"Functional applications of TD-DFT to electronic transitions of supramolecular assemblies"
9th Molecular Graphics Modelling Society Conference 2004, Sydney, Australia, 2004

G. D. Will, G. J. Wilson, A. Fuchs
"Control of size, crystallinity and orientation of TiO_2 nanocrystals"
Asia Pacific Nanotechnology Forum: (Oz Nano 03), Cairns, Australia, 2003

G. J. Wilson, G. D. Will
"Cleaning the environment: just add light"
Inorganic Materials Research Program: Annual Industrial Partners Presentation, Brisbane, Australia, 2003

G. D. Will, G. J. Wilson
"Photocatalytic cleavage of water utilising visible irradiation"
New University of Lisbon, Lisbon, Portugal, 2002
Università degli Studi di Bologna, Italy, 2002

G. J. Wilson, G. D. Will, R. L. Frost
"Raman spectroscopy of microwave hydrothermally treated anatase TiO_2"
4th Australian Conference on Vibrational Spectroscopy, Brisbane, Australia, 2001

Posters

G. J. Wilson, G. D. Will
"Studies of electronic structures of ruthenium d^6 metal centred complexes: a model approach"
RACI National Conference: Conference on Physical Chemistry 2004 (CPC2004), Hobart, Australia, 2004

G. J. Wilson, G. D. Will
"Photocleavage of water with a photochemical heterosupramolecular assembly"
1st International Conference on Advanced Materials and Nanotechnology, Wellington, New Zealand, 2003

G. J. Wilson, G. D. Will, R. L. Frost
"Microwave hydrothermal treatment of colloidal TiO_2 for use in photovoltaic devices"
38th IUPAC World Chemistry Congress, Brisbane, Australia, 2001

Conference Proceedings

G. J. Wilson, G. D. Will, R. L. Frost
"Microwave hydrothermal treatment of colloidal TiO_2 for use in photovoltaic devices"
The Proceedings of the 38th IUPAC World Chemistry Congress, Brisbane, Australia, 2001

Patents

G. J. Wilson, G. D. Will
"Methods for producing nanoparticle oxides and uses thereof"
Provisional patent filed 27th November 2001

Project Funding

G. J. Wilson, T. Tesfamichael, G. D. Will
"Studies of electronic structures of ruthenium d^6 metal-centred complexes for application in the dye-sensitised Solar Cell (DSC)"
QUT, ARC Discovery Incentive Scheme 2004
$1,989 - incentive to compile an ARC Discovery Grant submission

G. J. Wilson, G. D. Will
"Microwave modification of titania nanoparticles"
Australian Institute of Nuclear Science and Engineering (AINSE) Award 2004
Access to Australian Nuclear Science and Technology Organisation (ANSTO) facilities, Lucas Heights, Australia
$11,985 over 12 months

G. J. Wilson, G. D. Will
"Studies of electronic structures of metal-chelated organometallic systems for photoelectrochemical device application"
Australian Partnership for Advanced Computing (APAC) Merit Allocation Scheme and Queensland Parallel Supercomputing Foundation (QPSF) Partner Project 2004
Access to APAC National Facility and QPSF Network, Australian National University, Australia
$54,600 over 18 months

G. J. Wilson, G. D. Will
"Visible light sensitisation for hydrogen fuel generation from waste effluent"
Growing the Smart State 2003: A PhD Research Funding Program, Queensland Government, Department of the Premier and Cabinet
$8,000 over 2 years

CHAPTER 1

Introduction and Rationale for Research

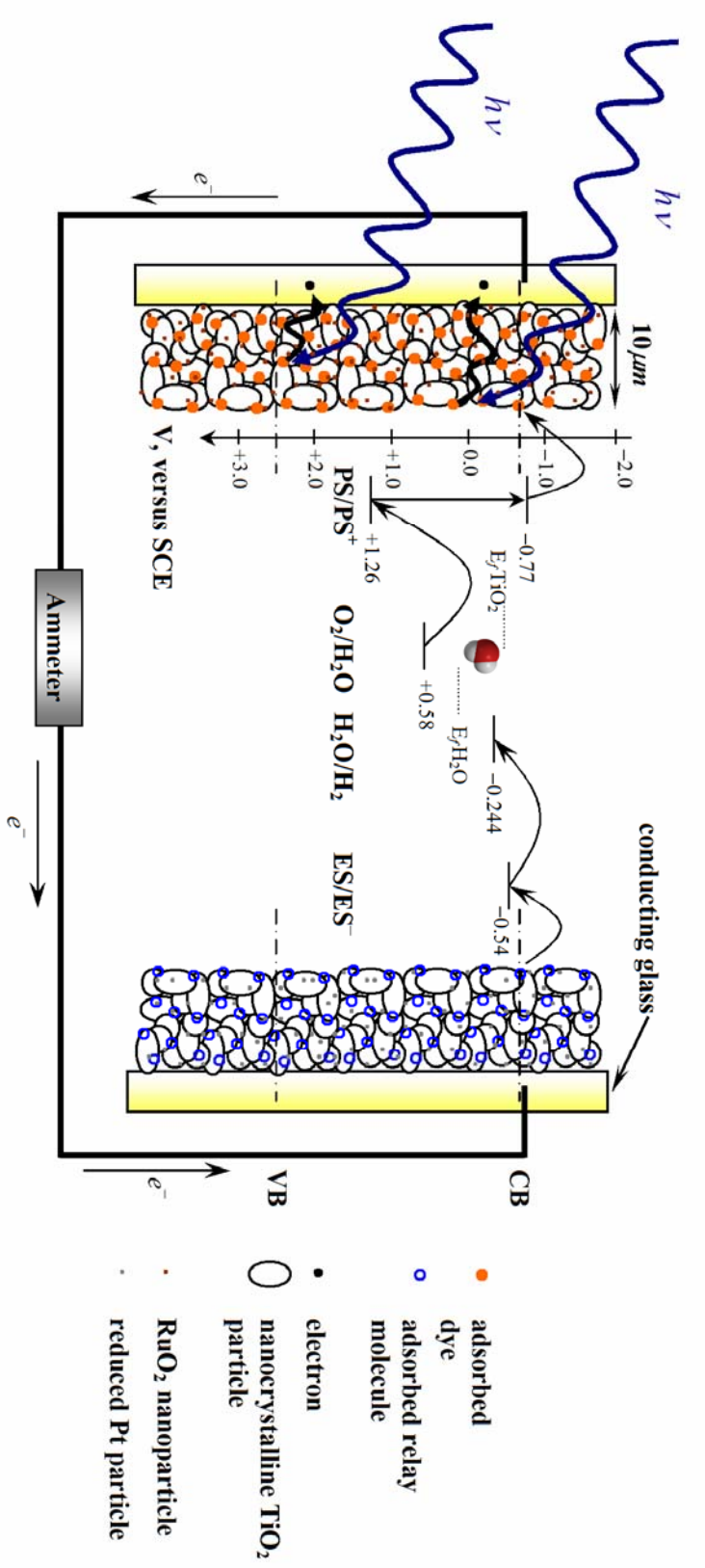

Figure 0-1 – Schematic representation of the heterosupramolecular approach to simultaneous oxidation and reduction. RuO_2 and Pt are specific catalysts, $[Ru(bpy)_2(dmpbpy)]^{2+}$ (where bpy = 2,2′-bipyridine and dmpbpy = 4,4'-di(methyl)phosphonato-2,2′-bipyridine) is a photosensitiser, TiO_2 is a titania nanostructured electrode and EVP (1-ethyl-1′-(2-phosphonoethyl)-4,4′-bipyridinium dichloride) is an electron shuttle molecule

Description of Research Problem Investigated

Global outcome: To investigate a method of eliminating organic pollutants from an aqueous environment as well as reduce and monitor pollutant levels in simulated waste industrial streams.

Overall Objectives of the Study

The scope of the project was to optimise the overall efficiency of an assembled heterosupramolecular array and to gain understanding into the processes that occur at the surface/solution interface of such a device. The assembly of the heterosupramolecular structure involved the selection of suitable materials for the individual functions within the device, these being:

i. Oxidation and reduction catalysts
ii. Electron conduction medium
iii. Light absorption and charge separation
iv. Low energy electron transfer

A heterosupramolecular photochemical system can be assembled on a surface that is capable of performing these functions in an aqueous environment (Figure 0-1). This system follows research presented at the 1st International Conference on Advanced Materials and Nanotechnology and published as a communication describing the capabilities of such a system.[1] This research paper illustrated that cyclic oxidation and reduction are indicated by the observation of a photocurrent within this photoelectrosynthetic cell.

The individual electrodes are assembled in the same configuration as that in the dye-sensitised solar cell.[2] The photoanode and the cathode are spatially separated with each containing specific catalysts for oxidation and reduction in the aqueous environment.

The device principle and configuration is novel with the electron donor and electron acceptor bound to different surfaces to give spatial separation within a macroscopic

framework. The system produces a photocurrent in an aqueous environment indicating that cyclic oxidation and reduction occurs under a steady-state.

The photoelectrochemical system outlined above was prepared from two basic types of materials; condensed phase and molecular components.

Preparation of Condensed Phase Components

The condensed phase material is required to possess several properties. These include:

i. Intrinsic semi-conduction
ii. A high surface area for adsorption of molecular components
iii. Vacant surface sites for the covalent binding of an acidic linker
iv. Stability and durability to varying environmental conditions

Metal oxide semiconductors are versatile, cheap and readily available. One of the most widely reported metal oxides is TiO_2. This material is a known photocatalyst and an efficient medium for electron conduction with a band gap of 3.2 eV. Anatase, a predominant crystalline phase, possesses a reduced surface with vacant surface sites for chemisorption of molecular components. Nanocrystalline particles can be produced with a diameter of ~10 nm via a sol-gel process and can be fabricated into durable thin films that are stable under oxygen evolution with a surface roughness of ~2000 giving a high surface area for chemisorption.

The preparation of titania films is widely investigated and as such, reported literature methods were utilised. However, the hydrothermal modification of TiO_2 nanoparticles is a research field of personal interest[3] and the microwave processing of nanocrystalline TiO_2 will be explored for improved photocatalytic materials.

Synthesis and Preparation of Molecular Components

The requirements of molecular components as outlined above are a light absorber (electron donor), and an electron transfer agent (electron acceptor). In the current study the widely investigated photochemical properties of ruthenium(II) polyiimine complexes and that of the quaternary diimine class of paraquats will be utilised for their electron donor and acceptor properties respectively.

Ruthenium Polyiimine Complexes

Numerous molecular species have been reported that absorb in varying regions of the visible spectrum. These dyes frequently utilise carboxylic acid groups incorporated at the periphery of the heterocyclic ligands to provide an anchoring group for binding to metal oxide surfaces. Previous work has shown that the carboxylated ligands are unstable in aqueous conditions.[4] Thus derivatisation of ligands with a more stable acidic anchoring group will be utilised.

Reports in the literature have shown that the derivatisation of the versatile carboxylate ligand 4,4′-dicarboxylato-2,2′-bipyridine,[5] to a phosphonated analogue is possible under mild conditions in relative high yield.[6,7] The derivatised form, 4,4′-di(methyl)phosphonato-2,2′-bipyridine, can be coordinated under similar conditions to those reported for carboxylated ligands. This has been demonstrated by several researchers.[6-8]

Quaternary Diimine Paraquats

The dichloride salts of quaternary diimines are known as viologens. These possess exceptional electron relay properties in solution and have been shown to exhibit similar properties when adsorbed to a surface.[9] For the purpose of the investigations presented here, a suitable viologen molecule has been reported and a procedure for its preparation was utilised in the current investigation.

The prepared molecules from above were characterised by modern instrumental techniques such as ^{1}H, ^{13}C and ^{31}P NMR, and elemental analysis, in conjunction with UV-visible absorbance and fluorescence emission studies with the details of these reported in Chapter Three.

Specific Aims of the Study

a) Derivatisation of ligands with a pH stabilised anchoring group for versatile application of molecular components in environmental conditions applicable to oxidation and reduction processes
b) Preparation of d^6 ruthenium co-ordination complexes for visible spectral absorption capable of integration in a heterosupramolecular assembly
c) Formation of a novel device from the covalent bonding of molecular components to the surface of TiO_2 to create a heterosupramolecular array
d) Spatial separation of oxidation and reduction specific electrodes incorporating heterosupermolecules to form a dye-sensitised photoelectrocatalytic cell (DS-PCC)
e) Investigation of the phenomenon of water photolysis in the DS-PCC under optimised conditions
f) Investigation of the mechanism for photolysis by a heterosupramolecular assembly
g) The promotion of hydrogen formation via the oxidative degradation of simple organic molecules in solution by the heterosupramolecular assembly
h) The monitoring of the oxidation of simple organic pollutants from a simulated industrial stream to determine the rate and mechanism of degradation
i) Investigation of the steady state current and degradation profiles for the oxidation of organic pollutants
j) Determination of quantum efficiencies of both the water photolysis and pollutant degradation systems

Account of Research Content and Organisation

This Thesis consists of nine chapters. Chapters Three to Eight present laboratory orientated research into photocatalytic processes; hence the general theme of photocatalysis. The integration of solid-state photocatalytic surfaces and molecular components is a unifying theme as the work presented herein has been made possible by the formation of intrinsic heterosupramolecular assemblies; consequently the overall title reflects this unification. Considering the diverse nature of the research project(s) undertaken in this thesis, Chapter Two forms a quite broad literature review of the fields encompassed and the significant progress of researchers in the fields. The remaining Chapters are described briefly as follows:

Chapter Three

Fundamental to the formation of a heterosupramolecular assembly and photocatalysis is the preparation of functionalised molecular components for adsorption to suitable electrode surfaces. Synthetic procedures and methodologies involved in the preparation of several photosensitisers and a molecular electron relay are presented.

Chapter Four

Knowledge of the electronic structure of the prepared photosensitisers is essential to understanding photochemical reactions in which they are involved. Density Functional Theory provides a convenient theoretical basis for interpreting electronic structures and provides good correlation to experimental observations. The electronic transitions and molecular structure are interpreted and presented here as a basis for further electron transfer discussions.

Chapter Five

As well as being an intrinsic semiconductor, TiO_2 possesses excellent photocatalytic properties. To embrace a photocatalytic endeavour without investigating firstly the structural properties of a key component would be unwise. A novel post-synthetic treatment by microwave modification is explored as a means of improving the properties of TiO_2 for photocatalytic applications. A convection hydrothermally treated colloidal gel used for preparation of thin film electrodes in subsequent

Chapters was also prepared and its properties compared to that of the microwave samples.

Chapter Six

Photochemical systems involving multiple electron transfer components have been widely investigated for their ability to 'photolyse' H_2O to H_2 and O_2. Presented here is a photochemical system utilising a modular approach to immobilise the molecular components to spatially separated electrodes. The assembly is characterised through interpretation of photoelectrochemical measurements and the system is discussed in relation to H_2O photolysis under low light intensities in the absence of an organic electron donor.

Chapter Seven

A crucial aspect of photochemical systems is the ability of the photooxidised form of the photosensitiser to degrade organic components; this occurs by electron 'donation' to the oxidised dye complex which leads to the subsequent break down of the organic component to much simpler chemical species. The research here depicts the photodegradation and complete mineralisation of EDTA with a heterosupramolecular assembly to give detectable gaseous products. The observed phenomena are interpreted by photoelectrochemical measurements and empirical mechanistic discussions.

Chapter Eight

The demonstrated ability of the assembled heterosupramolecular DS-PCC to photooxidise organic compounds is further explored on a series of chemically diverse species. For the series of chemical compounds over a range of solution concentrations an exponential decay is identified as a common trait in the photoelectrochemical measurements. By application of a kinetic model to identify specific interfacial processes in the photocurrent transients, speciation and identification of organic compounds were possible.

Chapter Nine

This Chapter highlights the main conclusions from each of the preceding Chapters and how they reinforce a photocatalytic heterosupramolecular assembly.

CHAPTER 2

Literature Review

1. Introduction

The Earth is unique in the Universe; of the known planetary systems there is no evidence to suggest that another planet, other than Earth, supports a biological subsistence. In our Solar System, the 'cradle of life' that is found on Earth has largely been attributed to the presence of one distinctive resource, water. Thus mankind's own search for extraterrestrial existence has revolved around a simple principle, water supports life.

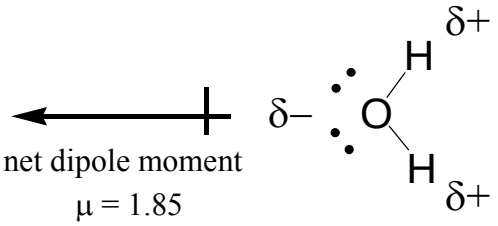

A seemingly simple compound, water is a distinctive combination of hydrogen and oxygen, whose formulation gives a chemical with exceptional properties. Strong polarity dominates the structure due to the O–H covalent bond. Exposed nuclei of hydrogen and non-bonding *p*-orbital lobes of oxygen give regions of positive and negative partial charges and a distorted tetrahedral geometry. This compact structure and the compound's inherent ability to hydrogen bond with like polar groups make it an essential biological agent.

Although H_2O is visibly abundant, covering over 75% of the Earth's surface, the abundance of elemental hydrogen is less than 0.14%, making its presence a finite resource. The modern age has seen vast changes in our technologies but our development has not been easy. The cost to the environment has been significant (Figure 1-1) and indeed can be seen as a threat to our life. It has been predicted that in the ensuing years the demand on our water resources will increase such that water supplies may be threatened over the next two decades.[10,11]

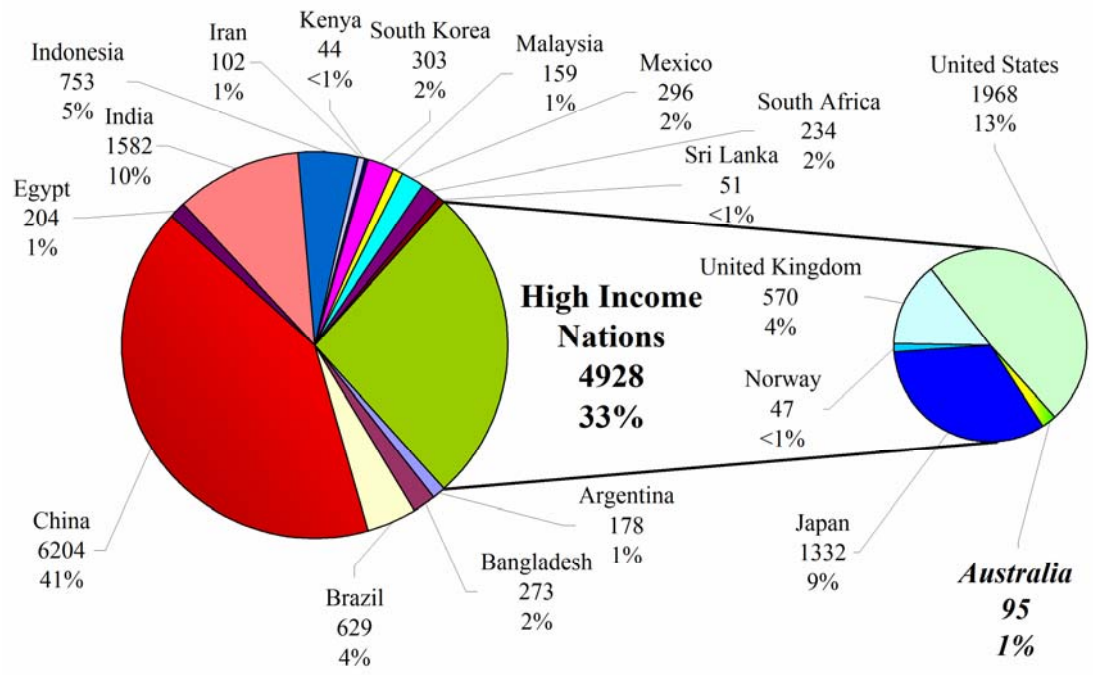

Figure 1-1 – Organic pollution discharge in selected countries in 2000. The values indicate emission of water-borne organics per day (in metric tonnes) and the percentage of total discharge (for selected countries). [Data: World Development Indicators, World Bank 2004][12]

Water remediation and the alternative usage of water is a topical and current area of interest. Sustainability of our natural resources, now and for the future, is of public concern. Globally these have been the forefront for research into alternative energies and the purification of polluted or grey-water sources. It is with these ideals in mind that this thesis is presented.

1.1. Alternative Energy and Photochemical Systems

The abundance and seemingly limitless amount of H_2O, have intrigued scientists for many years. The H_2O photolysis reaction, Equation (1-1), yields H_2 and O_2 in a 2:1 ratio. Hence the generation of two new species 'chemically' stores energy that is released on reformation.

$$H_2O_{(l)} \rightarrow H_{2(g)} + \tfrac{1}{2}O_{2(g)} \qquad (1\text{-}1)$$

Equation (1-2) and (1-3) outline the electrochemical oxidation and reduction processes:

$$2H_2O_{(l)} \rightarrow O_{2(g)} + 4H^+_{(aq)} + 4e^- \qquad E^0 = +0.82V \text{ versus NHE} \qquad (1\text{-}2)$$

$$2H_2O_{(l)} + 2e^- \rightarrow H_{2(g)} + 2OH^-_{(aq)} \qquad E^0 = -0.41V \text{ versus NHE} \qquad (1\text{-}3)$$

The Gibbs free energy change, ΔG = 237.2 kJ/mol, corresponds to a photon with a wavelength of λ < 1008 nm. Thus a photon from the visible region of the solar spectrum has sufficient energy to photolyse water. The electromagnetic (EM) solar spectrum at sea level extends from the NIR (1200 nm) through the visible to the Near UV (~250 nm). The photonic distribution of solar irradiance gives 18% in the NIR, 4 % in the UV and approximately 78% in the visible, that deliver photons with energies up to 3.0 eV.[13]

H_2O itself does not absorb appreciable amounts of radiation in the visible region of the solar spectrum. This property allows H_2O to 'filter' the radiant sun, absorbing infrared energy from the EM spectrum (Figure 1-2) and reflecting or transmitting the remaining wavelengths.

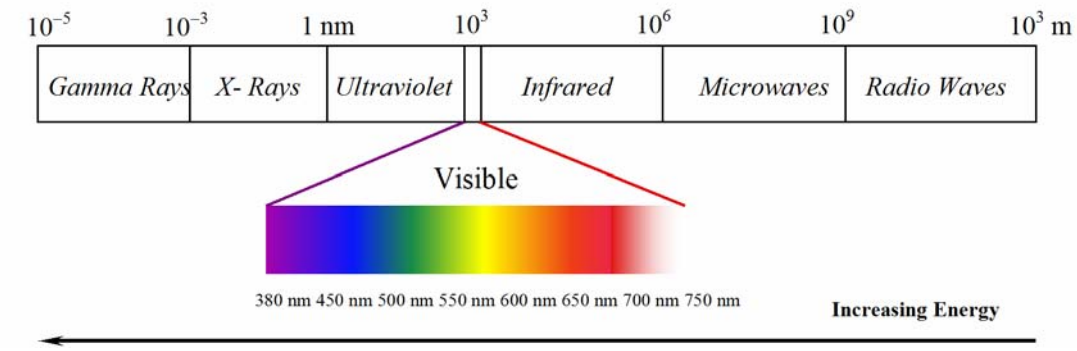

Figure 1-2 – The electromagnetic (EM) spectrum.

To overcome the inability of H_2O to absorb visible light, intermediates can be incorporated. Thus, desirable functions of intermediates include: i) visible light absorption; ii) the ability to convert excitation energy to redox energy; and iii) the transfer of excited electrons to and from H_2O to give H_2 and O_2. The inclusion of intermediates in the photolysis process forms a photochemical system.[14]

1.1.1. Introduction to Molecular Photochemical Reactions

Photoreactions involving the photolysis of H_2O by molecular–chemical processes have long been investigated. The first systems that demonstrated the photochemical photocleavage of H_2O with a ruthenium coordination complex were those described by Whitten *et al.*[15,16] Known as the 'Whitten' experiment, these reports have attracted much interest as the account of molecular gas formation was received with both excitement and scepticism. The experiments could not be repeated and a mixture of impurities was later identified as possible cause for the lack of reproducibility.

The incongruous heterogeneous combination of colloidal catalysts, inorganic chromophore, organic electron-relay, reducing and oxidising agents activated by illumination is sometimes called the "bouillabaisse" technique.[17] This technique was first reported by Lehn and Sauvage.[18] and has been shown to reduce H_2O to H_2 and/or oxidise H_2O to O_2 and is most often regarded as the evolutionary link to photochemical systems **(**Figure 1-3**)**.

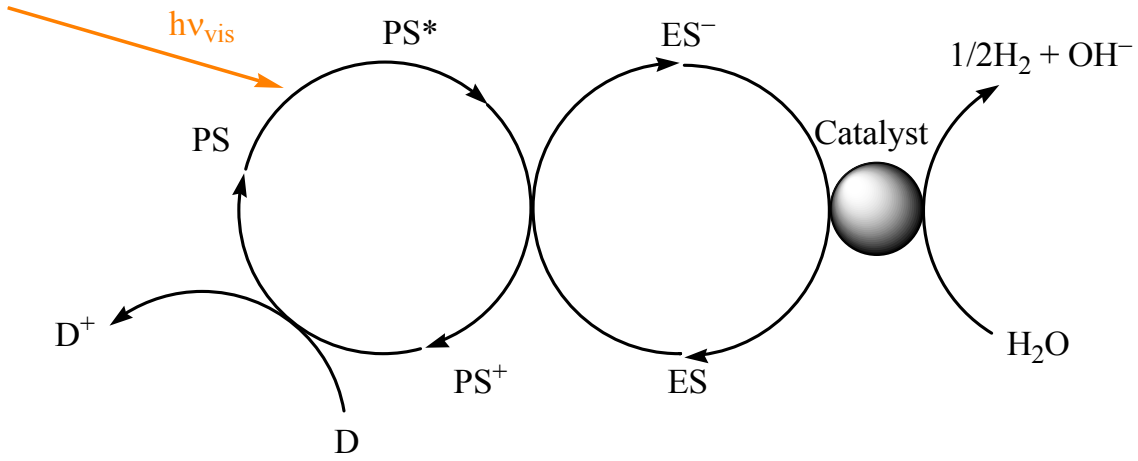

Figure 1-3 – Components of the photochemical system: PS = photosensitiser, a molecular species that absorbs visible light, generating an electronically excited species; ES = electron shuttle, a molecule that can be reversibly oxidised or reduced leading to formation of separate charged pairs; Catalyst = specific redox catalyst, a compound that is capable of collecting several electrons for transfer to or from water; D = sacrificial donor, prevents back reaction of PS by sacrificial oxidation and is thus consumed in the process along with water.

1.1.2. Model Photochemical Systems

The conversion of light to chemical energy is one that is a constant endeavour for many researchers.[14,19-21] These attempts have sought to replicate the most intricate of nature's apparatus, the photosynthetic reaction centres of Photosystem I (PS I) and Photosystem II (PS II). Chemical approaches to artificial photosynthesis have drifted into two schools of thought: the conventional one-step photocatalytic 'cleavage' of H_2O and a two-step biomimetic reaction mechanism, the so-called 'Z-scheme'.[13,22] Photocatalytic systems involving metal oxides are effective in the formation of O_2 and are stable under its evolution whilst meeting the overpotential requirements for H_2 generation. Metal oxides are most effective under UV irradiation and increasing the spectral overlap into the visible region has proven difficult. An example was the use of Eosin Y and derivatised forms of this dye for sensitisers in photochemical H_2 generation systems.[23] This work followed earlier reports by Moser and Grätzel that Eosin Y was capable of favourable electron transfer in colloidal semiconductor solutions.[24]

The classic $[Ru(bpy)_3]^{2+}$ (where bpy = 2,2′-bipyridine) system for the photoconversion of H_2O, in solution, was proposed in 1978 by Alec Moradpour *et al.*[25] from the Université de Paris-Sud, Centre d'Orsay in Orsay, France.

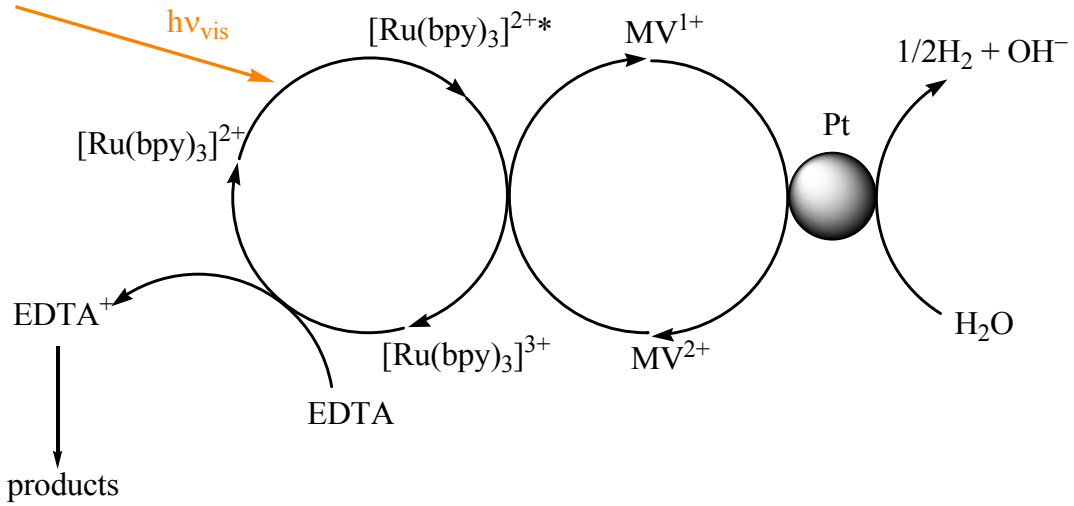

Figure 1-4 – Schematic representation of the Orsay model of H_2 production.[14]

The Orsay group focused on a homogeneous aqueous solution containing a colloidal suspension and dissolved molecular components that produced H_2 efficiently. The Orsay system has become a basis for comparison of other systems and components. In this system (Figure 1-4), the PS is $[Ru(bpy)_3]^{2+}$ and when irradiated with visible light is promoted to an excited state. 1,1′-Dimethyl-4,4′-dipyridyl, methyl viologen (MV) in the form of MV^{2+}, acts as an ES and accepts the excited electron creating the charged pairs MV^+ and $[Ru(bpy)_3]^{3+}$. Ethylenediamine tetraacetic acid (EDTA) reductively quenches the ground state of $[Ru(bpy)_3]^{3+}$ and is decomposed further to glyoxylic acid and glycine. Electron transfer is completed by MV^+ to colloidal platinum, which catalytically reduces H_2O, evolving H_2.

The system is limited by the stability of certain molecular components. The stability of platinum and $[Ru(bpy)_3]^{2+}$ far exceeds the stability of MV, which is often destroyed by hydrogenation. Despite these limitations, their system yielded significant amounts of H_2 through the degradation of simple organic 'pollutants' such as EDTA.

Bamwenda and Arakawa utilised two tandem photosystems that allowed the oxidation and reduction of H_2O at different molecular sites to produce and isolate H_2

and O_2.[26] Sayama *et al.* also describe this so-called 'Z-scheme' to mimic the mechanism of PS I and PS II systems.[13] They utilised a WO_3 surface for light absorption and Fe^{2+}/Fe^{3+} intermediates to facilitate charge transport. Both of these concepts use only visible light and effectively photolyse H_2O in a 2:1 ratio, i.e. $2H_2 + O_2$, yet the overall solar to chemical energy conversion efficiency are still quite low at only 4–5%.[27]

Nevertheless the basis of the photochemical systems and the mechanism of the Z-scheme are fundamentally flawed. Electron-transfer from the relevant species in solution occurs only upon chance collisions of all components within the system thus limiting the effectiveness of the approach.

1.2. Photocatalysis

The study of photocatalytic applications, reactions, mechanisms and catalyst preparation is a broad topic of research in the literature. A search of a well-known chemical database[28] lists the topics related to photocatalysis as 32,275 (3,164 in 2004, 3,216 in 2003, up from 2,688 in 2002 with the lowest being only 1 report in 1908). Of the literature citations, 13,396 pertained specifically to TiO_2 whilst 9021 were in relation to all other metal oxides. For the purposes of this review it is fitting that only relevant examples of the research being conducted in these fields are identified and moreover only authors and articles that relate to the current topic of discussion are included.

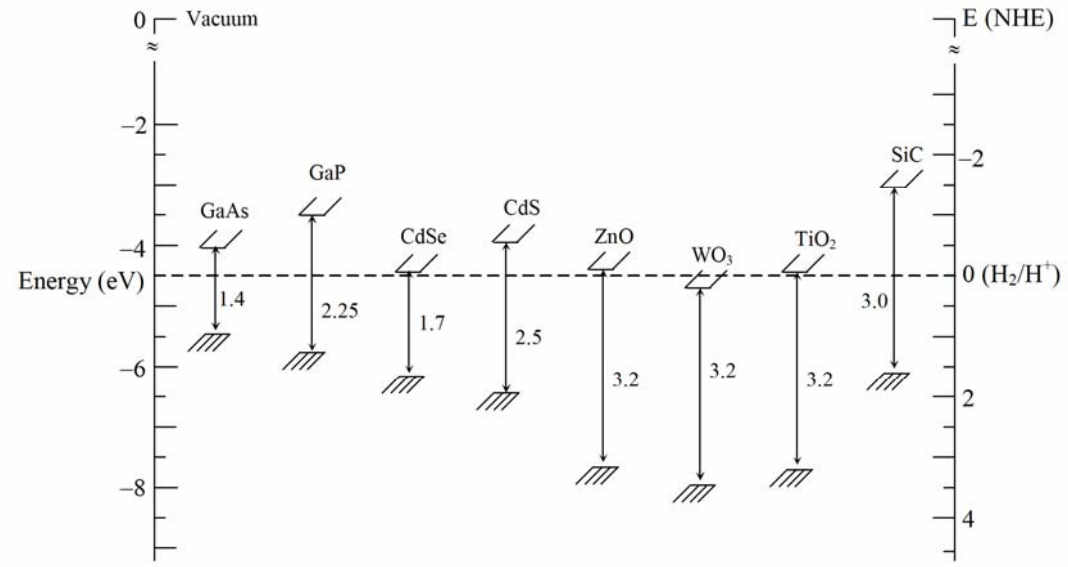

Figure 1-5 – Band gap energies for various semiconductors in aqueous electrolytes at pH = 1.[29]

One-step photochemical processes are initiated by a PS that is capable of both oxidation and reduction and often occur at a surface. These PS surfaces are referred to as photocatalysts. The more prevalent light activated materials used in catalysis are simple oxides of metals, in particular semiconductor metal oxides. Semiconductor nanoparticles have played an increasingly important role in photocatalysis in recent years.[30] This is due in part to their excellent properties and relative ease of preparation. The ability for a semiconductor metal oxide to perform photocatalytically is dependant on its relative band position. The band positions of various semiconductors can be seen in Figure 1-5.

The band structure of metal oxides can be altered through the introduction of free surface states. This has been observed for semiconducting or insulating solids that have been cleaned by ion-bombardment or reduction, and tend to have extra surface states in the band gap evident from structural defects or 'abnormal' valence states.[31] Metal oxides formed from a single metallic element exhibit enhanced catalytic activities when combined in non-stoichiometric ratios, as these give unoccupied regular sites or displacement of atoms from normal positions. These sites allow the insertion of guest ions (doping) that enhances the catalytic activity.

Many metal oxides and multiple elemental compositions have been utilised in photocatalytic processes, these include TiO_2, WO_3, $SrTiO_3$, α-Fe_2O_3, ZnO, ZnS as well as many other combinations in what is an intensely researched field.[32] The most promising of these is the crystalline phases of TiO_2, which are by far the most predominately researched material in the literature.

1.2.3. Photocatalysis on TiO_2

Both Rutile and Anatase crystal phases of TiO_2 are used in photocatalysis, with the activity of Anatase being higher. TiO_2 exhibits catalytic activity when the TiO_6 octahedra in the edge-sharing state are changed to a face-sharing state that converts Ti^{4+} ions to Ti^{3+} ions, with the co-ordination number remaining unchanged at six. This is known as crystallographic shear (CS). The variation in lattice structure gives rise to differing mass densities and electronic band structures. Of particular interest for the chemisorption properties of TiO_2 are the defect sites that results from CS on the surface of the semiconductor (Figure 1-6).

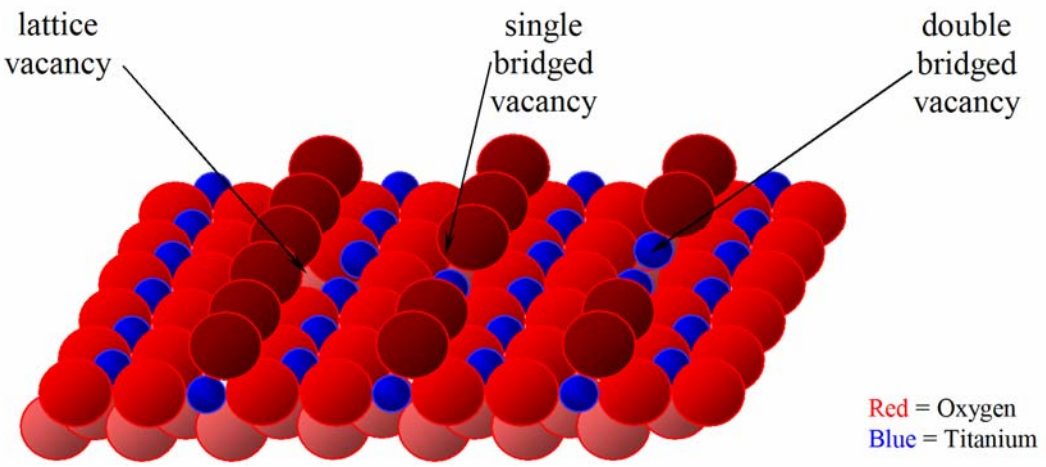

Figure 1-6 – Catalytic defect sites of TiO_2 (110).[29]

In reference to the adsorption of H_2O it has been proposed that H_2O reacts with bridging oxygen atoms of the TiO_2 surface to form two OH groups. Similar effects have been observed for H_2 and O_2 adsorption. The surface defect sites (oxygen vacancies) act as electron donors allowing for the adsorption of H_2 with the adsorption of other molecular species occurring in a like manner.[29]

Preparation of nanoparticle dispersions of semiconductors, such as TiO_2, is important, as nanoparticles exhibit distinct differences to bulk semiconductors in relation to spatial confinement of charge carriers. Formation and confinement of charge carriers in three dimensions on the nanoscale enhance quantum-size effects.[33] Local confinement directs an increase in band gap energies and also the presence of electronic states within the frontier bands or local trap sites.

1.2.3.1. Preparation of TiO_2 Photocatalysts

The method of preparation of TiO_2 is highly dependant upon its final application. Often an amorphous precursor Ti_xO_y is obtained before refining of the material to the desired crystalline phase. There are thee principal polymorphs of TiO_2: anatase, brookite and rutile. The varied optical, dielectric and catalytic properties of these polymorphs provide many useful industrial applications as fine powders, fibres, films and foams.[34] The synthesis and modification of the precursor metal oxide is an important area of interest in the literature as a route to the preparation of structured ceramic materials.

There are numerous methods for the preparation of TiO_2 precursors; however the majority of these processes require harsh conditions with long reaction times and high temperatures (> 1400°C).[35] Alternatively, milder methods include: arrested hydrolysis via reverse micelles in non-polar solvents,[36] hydrothermal synthesis at < 250°C,[37-39] and sol-gel processing.[40-43] Sol-gel processes are broadly researched for hydrolysis and condensation of alkoxide precursors. Following colloidal formation, hydrothermal treatment of the suspended amorphous titania has been shown to produce crystalline products.[37]

Sol-gel processing of titanium dioxide has been investigated since the 19th century, with modern processes developed to refine and control the stability and phase formation of the colloid. Different precursors and peptizing agents have been investigated[40,44-47] where the modification of the alkoxide group and reaction conditions have resulted in the formation of highly crystalline anatase colloidal particles. The generalized reaction for this process is shown by Equations (1-4) and (1-5):[47]

$$Ti(OR)_4 + 4H_2O \rightarrow Ti(OH)_4 + 4ROH \qquad \text{(hydrolysis)} \qquad (1\text{-}4)$$

$$Ti(OH)_4 \rightarrow TiO_2 \cdot xH_2O + (2-x)H_2O \qquad \text{(condensation)} \qquad (1\text{-}5)$$

Where R = an alkyl chain of 2–4 carbon units

The importance of TiO_2 can be seen in its diverse range of applications in industrial, commercial, and increasingly in photoelectrochemical (PEC) and photoelectrochromic cells.[2,27,33,48-56] The application of colloidal nanocrystalline TiO_2 in PEC cells involves dispersion across substrates to produce thin films. These are subsequently calcined to neck the colloidal particles to form a nanostructured percolating network which now possesses electronic interconnects.[31] The mesoporous nature of the resultant films provides a high surface area nanoporous substrate with exceptional qualities for adsorption of dye monolayers or indeed organic pollutants for photocatalytic oxidation.[57]

1.2.4. Other Metal Oxide Semiconductors

Studies of heterogeneous metal oxide photocatalysts, particularly those of transition metals, are motivated by commercial, industrial and community interests. Many of these materials photo-corrode and hence have not gained the same attention as stable photocatalysts such as TiO_2.[58,59] Much of the reported literature contains empirical studies of photocatalytic activity or modification of the metal content by stoichiometric and non-stoichiometric quantities.[29-31] This has allowed the gradual development of the field and understanding of the materials properties and treatment methodologies.

There are various areas of photocatalysis that are studied for novel and interesting functionality. Metal-semiconductor composite nanoparticles exhibit unique electronic and chemical properties (Figure 1-7). The composites show enhanced catalytic properties that influence interfacial charge transfer processes by perturbation of band energetics.[60] The interfacing of noble, rare-earth or transition metals with semiconductors is an essential factor in maximising photocatalytic reactions. The nanocomposite induces a Schottky barrier where the metal acts as a sink and ballistic transport of charge occurs across the interface. Zemski, Justes and Castleman discuss the activities of Group V metal oxide clusters in relation to photocatalytic reactive sites.[61] This gas phase study provided an understanding of bulk surface properties through selection of reactive clusters by Mass Spectrometry and investigation of their reactivity toward organic compounds. Doping of TiO_2 by

rare-earth metals such as the lanthanide series have been shown to extend the absorption properties of the wide band-gap semiconductor and enhance the adsorption of NO_2^-.[62] For exhaustive degradation of nitrates, this preparation showed impressive reactivity in comparison to that of Degussa P25 TiO_2 (P25), which is the most active commercially available titanate.

First row transition metal oxides such as ZnO are also of interest. ZnO shares similar electronic properties to those of TiO_2 yet is not photostable under O_2 evolution. Thin films of ZnO prepared from sol-gel processing give a spongy mesoporous structure that has comparable activity to that of TiO_2.[63] In addition, reduction of the passive oxide layer of second row transition metal with $NaBH_4$ has shown improved quantum efficiencies for Group II–VI semiconductors.[64] The treatment causes exciton recombination allowing some control in this property for photocatalytic and PEC applications.

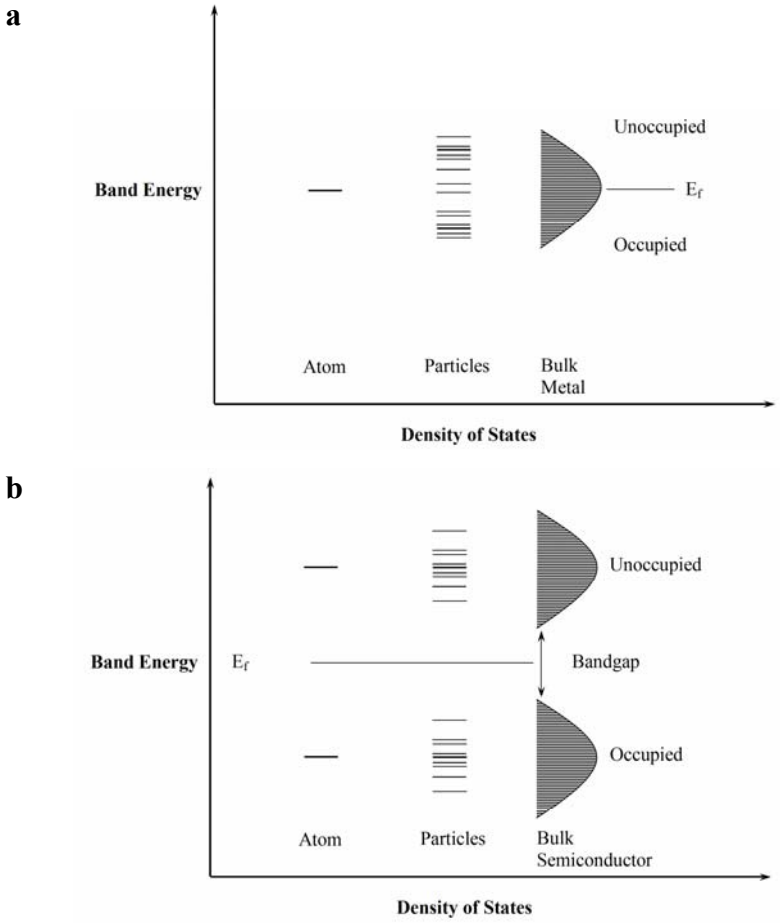

Figure 1-7 – Valence and conduction band energy and molecular structure showing the relationship between particle size and absorption band broadening a) atomic metal, particles and bulk properties b) change in semiconductor bandgap with structure.[60]

In a like manner, binary systems that incorporate hybrid semiconductor composites also show improvement to photocatalytic response. Gopidas, Bohorquez and Kamat showed that coupling of colloidal CdS with TiO_2 or AgI can increase surface recombination or charge transfer between the semiconductors and induce broad spectral responses.[65] Yang *et al.* produced binary TiO_2/SnO_2 particles that exhibited a high affinity for decomposition of methyl orange in solution.[66] Furthermore, sol-gel formation of binary systems of ZnO and TiO_2 has shown improvements in methyl orange photodegradation after sulphating of the surface with H_2SO_4.[67]

Although many formulations of photocatalyst are reported, developments that include TiO_2 are by far the most established method of improving photocatalytic performance. Doping of TiO_2 by nitrogen by a simple mechanochemical method, extends the photocatalytic activity of this material into the visible region.[68] Extended periods of milling and doping of the surface by hexamethylenetetramine (HMT) improved the catalyst's ability for degradation of NO. The most notable modifications for improved photocatalysis increase the region of photonic absorption, thus extending the overlap with the solar spectrum.

1.2.5. Visible-light Photocatalysis

Photocatalysts that are activated by photons from the visible region of the EM spectrum (400–700 nm) are limited to binary semiconductors and smaller band gap materials (< 3.2 eV) such as CdS and WO_3 (which has the same band gap as titania, 3.2 eV). Mixed metal oxides of Bi^{3+} and V^{5+} have been reported as novel catalysts for O_2 evolution.[69] These materials absorb broadly over the visible region and show active H_2O oxidation in comparison to commercial WO_3. $BiVO_4$ exhibits ~30% the efficiency of WO_3 for photocatalytic O_2 evolution yet has potential as a component in the two-photon 'Z scheme' for artificial photosynthetic systems. $BiVO_4$ also exhibits attractive photocatalytic properties for the degradation of alkyl-phenols under visible light irradiation.[70] Impregnation of $BiVO_4$ with Ag gave a passive silver oxide layer, increasing the binary material's adsorption capacity for phenolic compounds, and hence its photocatalytic ability.

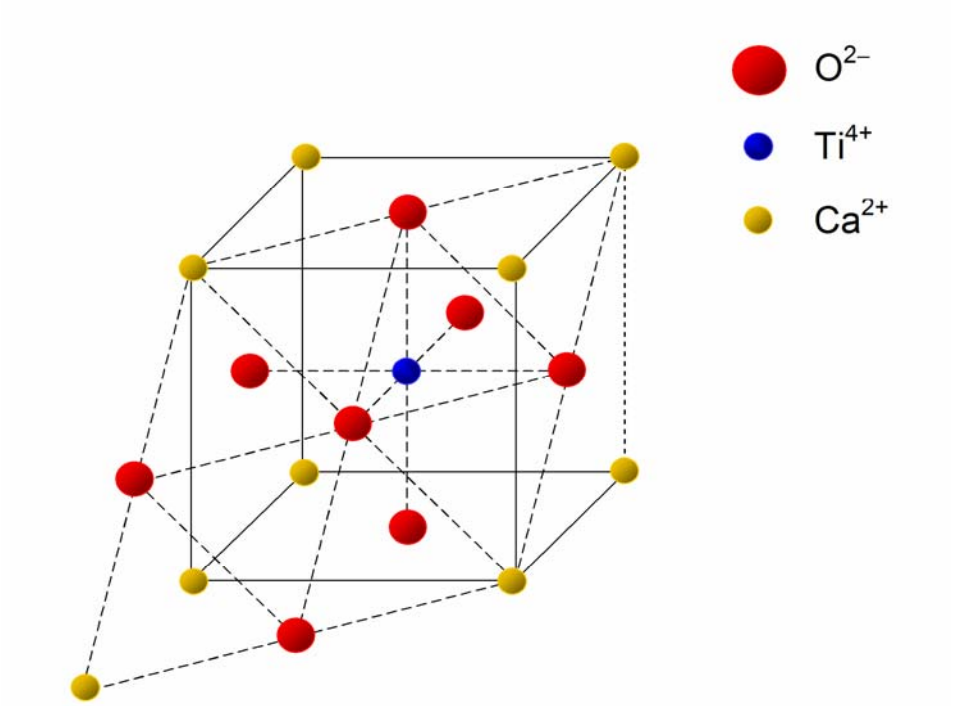

Figure 1-8 – Ternary compounds of the composition ABX_3 have the unit cell of the perovskite lattice e.g. Ca_2TiO_4.

Substitutional doping of perovskite (Figure 1-8), a titanate mineral, also caused a decreased band gap within photocatalytic materials. Hwang *et al.* substituted cations of the layered perovskite, $La_2Ti_2O_7$, to induce hyper valencies and perturb its band gap structure.[71] Exchange of La for Cr and Fe induced active states that demonstrated an affinity for H_2O-methanol decomposition in the visible region. Mesoporous silicates such as MCM-41 and similar cation substituted clay structures have also been modified by cation-substitution. Rodrigues *et al.* report the UV and visible activity of Cr–Al–MCM-41 on the photooxidation of trichloroethylene.[72] Visible light catalysis occurs primarily at Cr^{6+} sites, supported by the silicate framework, and hence has a reaction rate slower than under UV activation where Cr^{3+} is also active.

Photocatalysts involving the Group V metal, Ta, are other highly active materials as reported by Zhang and Gao[73] and Ito *et al.*[74] Ta_3N_5 nanoparticles showed enhanced photocatalytic activity toward methylene blue degradation,[73] whilst meso-microporous TaON had a 20 fold increase in oxidation of methanol under visible light compared to UV-visible activated P25 TiO_2.[74]

Doping of TiO_2 with $ZnFe_2O_4$ gave a minimal shift in the absorption edge > 400 nm,[75] mixed CeO_2–TiO_2 nanopowders show increased spectral response up to 600 nm,[76] however nitrogen-doping of TiO_2 is the prevalent method of increasing the spectral response.[77-81] The preparation of these $TiO_{2-x}N_y$ catalysts involves doping via sputtering in a N_2 or NH_3 atmosphere[77,79] or solvothermal-precipitation from alcoholic solutions containing the desired N-dopant.[78,80,81] These preparations produce materials with desirable absorption properties and are capable of catalytically degradation of methylene blue and 4-chlorophenol, photochemical reduction of Ag^+ ions and the oxidative conversion of NO. Coordination of nitrogen containing ligands has also been described. Slow addition of $TiCl_4$ to a solution of 2,2′–bipyridine afforded a Ti^{4+} complex.[82] Calcination of the isolated complex gave a TiO_2-like catalyst that under visible illumination exhibited high photocatalytic ability for NO_x removal.

Recently, it has been shown that organic dyes can be intercalated into layered titanates.[83] Miyamoto, Kuroda and Ogawa report cyanine dye intercalation compounds with broad spectral response over 300–800 nm. Although the compounds were not used for photocatalytic studies, they are examples of effective surface sensitisation to extend the spectral response of catalysts. Pepe *et al.* describe an alternative heterogeneous catalyst for photooxidation of phenol.[84] Grafting of porphyrins and phthalocyanines to aminopropyl silica and exchange resins gave favourable responses to phenol oxidation, however the macrocycles showed significant (~18–99%) bleaching during the photocatalytic experiments.

There are numerous methods of achieving compounds that are capable of visible photocatalytic response.[57,60,73,74,81,84-86] Predominately these are inorganic solid-state materials yet examples of organic sensitisers for inorganic surfaces do exist.[84,87-90] These compounds, if stable and effective, could prove a simple route to broadening the spectral response of inorganic photocatalysts.

1.2.6. Photodegradation of Organic Pollutants

The treatment of water supplies contaminated with organic pollutants through the use of heterogeneous photocatalysts is a feasible method of grey water remediation. An investigation into the practical application of TiO_2 as a model photocatalyst has been reported by Ljubas.[91] In areas of Croatia the content of naturally occurring organic matter in freshwater lakes is sufficiently high that potable water is unavailable at times of high demand. Treatment of 'naturally' polluted fresh water by chemical disinfection may cause health problems. However by oxidation processes, such as hydroxyl radical ($OH^{\bullet}$) formation at the surface of TiO_2 (Figure 1-9), organic matter is quickly and non-selectively oxidised.[91] This has not been limited to academic interest as commercial ventures, for example Sokang Nano, have also been actively involved in water and air cleaning products that utilise TiO_2 as the active component.[92]

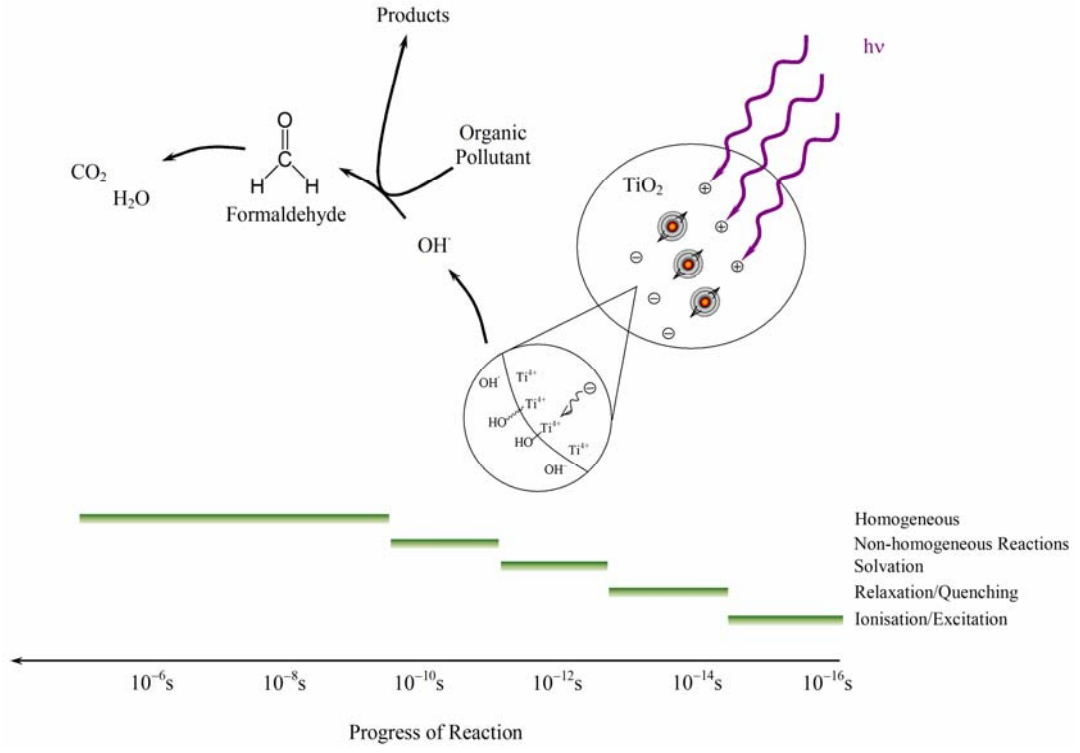

Figure 1-9 – Photodegradation of organics by hydroxyl radical formation on TiO_2. Approximate time scale of the processes induced by ionizing radiation.[93]

Formation of $OH^{\bullet}$ at the surface of TiO_2 can be achieved through band gap excitation.[94] Byrne *et al.* report a novel approach utilising a two-compartment cell to

photooxidise aqueous solutions of formic acid. The acid is strongly adsorbed to the surface of the photocatalyst and electron transport away from the site of oxidation allows the electrowinning of a second solution containing copper ions in a remote compartment. Oxidation at a TiO_2 surface occurs either by an adsorption or free-radical model. The binding of acidic groups to vacant sites on TiO_2 has been discussed earlier (Section 1.2.3) with the formic acid bond being weakened by chelation to free surface states. Oxidation of the molecule occurs by band gap excitation and charge separation. This oxidation process is unique as the degradation of formic acid forms intermediates that are capable of promoting the oxidation of larger organic compounds.

TiO_2 has also proven successful in detoxification of water-borne bacteria and herbicides. Pilot scale plants in Spain have shown that commercial P25 TiO_2 powders in combination with activated carbon/O_3 are capable of total bacteria disinfection[95] and complete mineralisation of 2,4-dichlorophenoxyaceticacid and benzofuran.[96] TiO_2 loaded silicate mineral catalysts have also proven effective in reducing organic pollutant content in aqueous environments. Reddy, Sun and Smirniotis describe the use of MCM-41 catalysts loaded with TiO_2 that are catalytically active under both UV and visible irradiation.[97]

Treatment of sewage water discharge by TiO_2 has also been proposed. Nakahima *et al.* discuss the potential of TiO_2-modified polytetrafluoroethylene (PTFE) mesh for the decomposition of natural estrogens from aquatic environments.[98] Combination of photocatalytic and heat treatment decomposed ~90% of 17β–estradiol and estrone.

The implementation of TiO_2 for the treatment of insecticides,[99] and pesticides,[100] has also been reported. Visible light sensitisation with $[Ru(bpy)_3]^{2+}$ by co-solution with TiO_2 has also been shown to oxidise herbicides,[101] such as 1,1-bis(4-chlorophenyl)-2,2,2-trichloroethane (DDT). Vinodgopal, Wynkoop and Kamat also report the sensitised degradation of azo textile dyes as an effective method of removing coloured pollutants.[102]

Chatterjee and Mahata report similar findings for the visible light assisted photodegradation of aromatic and surfactant pollutants on modified TiO_2 surfaces.[89]

This particulate system utilised methylene blue and rhodamine B to sensitise the TiO_2 surface and demonstrated the wide range of pollutants that can be degraded by binary molecular/condensed phase systems. This approach to the utilisation of visible irradiation allowed irreversible transfer of excited electrons from the dye to the surface, which significantly enhanced the photocatalytic response. Although not covalently bound to the surface, the dye acts as in intermediate in photodegradation, imparting an intrinsic function to the process, extending the capabilities of TiO_2 to a visible light active catalyst.

It has been demonstrated that the photon induced oxidised forms of adsorbed dyes are capable of irreversible degradation of many small organic molecules into CO_2 and H_2O.[89,103] The organic molecules reported to have been degraded range from phenol[89] to EDTA[104] and triethanolamine (TEOA).[105] Often these organic species are present as by-products from industrial processes, whose effluents are expelled into our waterways and their removal is essential for improved water quality in the future.

1.2.6.1. Photodecomposition of H_2O on TiO_2

The electrolysis of water on TiO_2 is due to the photoassisted oxidation of vacant oxygen sites in the crystal lattice,[106,107] with the first study reported by Fujishima and Honda in 1972.[108] Their study involved the use of a single crystal of rutile TiO_2 as a photoanode and a platinum cathode. The cell was irradiated with UV light and assisted by an applied bias (> 0.25 *V*) which resulted in the observation of gaseous H_2 and O_2. The photolysis resulted from the effective separation of photogenerated electron-hole pairs. Holes in the valence band of the TiO_2 anode resulting from band gap excitation are capable of oxidising H_2O to O_2, while the conduction band electrons traverse the external circuit to reduce H_2O at the cathode.

The photocatalytic properties of TiO_2 are modified by the addition of a noble metal such as Pt that changes the distribution of electrons.[109] The resulting properties are due to the formation of a barrier at the metal-semiconductor interface known as a Schottky barrier. The surface of the metal acquires an excess negative charge and as a result of electron migration away from this region, the semiconductor exhibits an

excess positive charge. The insights into the energy and electron-transfer processes that occur at the interface of metal-semiconductor surfaces are of interest to many fields of nanotechnological development especially photocatalysis.[60] The Schottky barrier acts as an effective electron trap, preventing electron-hole recombination.[110]

The use of the Schottky barrier model for trapping of electrons has been seen in many systems.[106,107,111,112] These systems illustrate the effect of platinised TiO_2 particles on the photoassisted production of H_2 from aqueous solutions using microheterogeneous particles of TiO_2 doped with Pt as an active catalyst for the effective reduction of H_2O. The activity of the TiO_2 particles is due to oxygen vacancies in the crystalline lattice of the bulk semiconductor and reduction occurs from the electron-transfer from the TiO_2 to platinum. Another approach to the splitting of water is the use of mixed photocatalysts and the doping of these with rare earth metals. A recent report from Kato, Asakura and Kudo[113] describes a metal oxide/photocatalyst interface that yields large quantities of H_2 and O_2 (750 mL h^{-1}/g) by the separation of active sites for oxidation and reduction of H_2O.

A charge storage mechanism has been reported for some metal oxides, for example RuO_2.[114,115] The build-up of charge has a capacitance effect on RuO_2, and the metal oxide interface of binary semiconductors can be exploited. Effective charge separation leaves electron rich and electron deficient sites on the binary catalyst and hence active sites for the production of H_2 and O_2. As noted in Section 1.2.3, reduction of the rutile structure of TiO_2 improves the catalytic activity of the metal oxide. The reduced form of TiO_2, Anatase, is a more photoactive structure. The use of this more active form of TiO_2 for photolysis of H_2O has been reported. One of the more contentious reports has been that of Kalyanasundaram and Grätzel where they describe the formation of mixed metal oxide photocatalysts for the photolysis of H_2O.[116]

The early photochemical work of the Grätzel group utilised the photocatalytic properties of TiO_2 in combination with other 'charge transfer' molecules in solution to produce H_2 photochemically.[116-121] Their findings involved the use of metal oxides, in particular RuO_2. Their report of light induced water cleavage[118] involved

the use of composite semiconductor particles comprised of TiO_2 with deposited H_2- and O_2- specific catalysts, Pt and RuO_2, respectively (Figure 1-10).

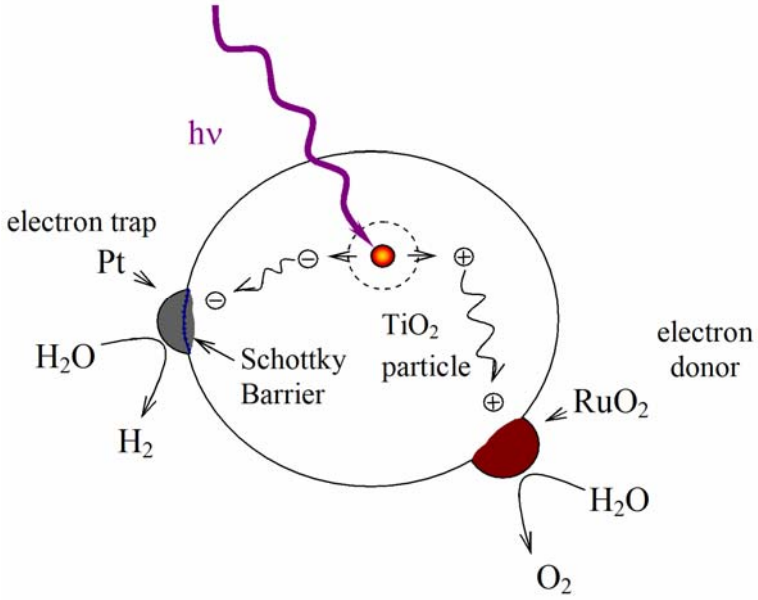

Figure 1-10 – The principle of charge separation on a composite photocatalytic particle.

The composite particle acts as a micro photoelectrochemical cell with RuO_2 as the anode and Pt as the cathode. The overpotential required for the direct photocleavage of H_2O from band-gap excitation of the TiO_2 particles is significantly reduced in the presence of the catalysts. These findings was followed by a further report by Gu, Kiwi and Grätzel.[122] Their work produced significant results, yet not without controversy. Many laboratories have been unable to repeat their findings, which has lead to criticism of the fundamental principle that O_2 and H_2 can be produced at the surface of the same photocatalyst.[14,104]

It can be seen that the limitation of TiO_2 as a photocatalyst is its band gap energy (E_g = 3.2 eV) which is centred in the UV region of the solar spectrum. To increase the photonic efficiency from the available solar spectrum, excitation by photons from the visible region (400–700 nm) is required. Other semiconductors (Figure 1-5) such as CdS have a much smaller band gap (E_g = 2.5 eV), but are unstable to O_2 evolution and degrade over time.[69] Modifying the surface of the semiconductor by forming a composite,[123-126] addition of metals,[127,128] or sensitisation with a dye molecule can overcome this problem.

Hirano *et al.* report the sensitisation of TiO_2 particles with ruthenium-diimine complexes and porphyrins.[90] Irradiation with visible light induces H_2 evolution from aqueous solutions in the presence of a sacrificial donor, EDTA. They note that the electronic coupling of Pt to the surface of TiO_2 is essential for efficient photocatalysis. Although sensitisation of the catalytic surface yielded only small quantum efficiencies, the results were promising.

a

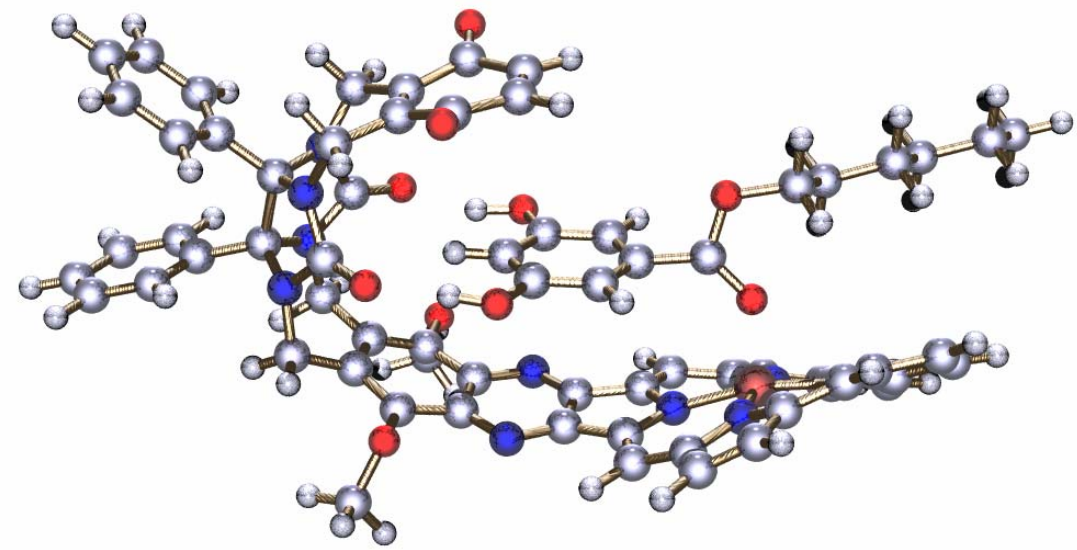

b

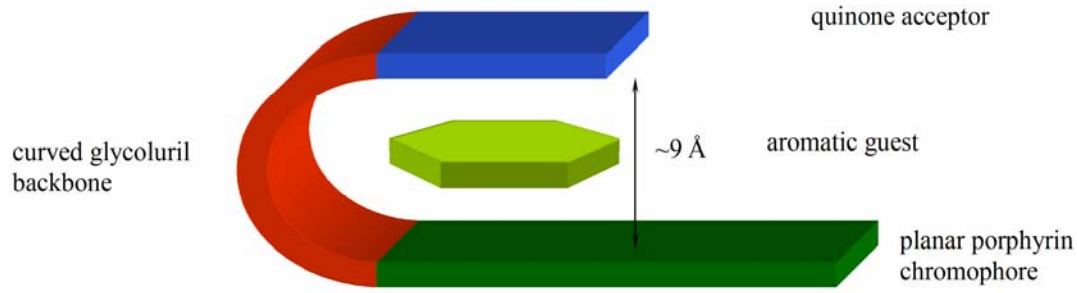

Figure 1-11 – The supramolecular 'scorpion' for photochemical electron transfer a) structural geometry as determined at a semi-empirical PM3 model chemistry b) stylised representation of host-guest structure.[129]

1.3. Supramolecular Chemistry

For a considerable amount of time, the literature has been concerned with molecular structures that go beyond simple covalent bond formation. The covalent linking of molecular fragments introduces significant molecular effects that result in new molecular properties, both physical and chemical. The properties or functions are a result of the new molecular structure. In contrast, the linking of molecular components such that the properties of the linked components are not perturbed gives a higher order function. The resulting supramolecule is said to have a well-defined supramolecular function, which is not a simple superposition of the components.[130] This is an historically recent practice, for science, however biological systems perform this effortlessly and have for billions of years. Modern supramolecular chemistry dates from the late 1960's and early 70's and owes much of its development to macrocyclic researchers and indeed the significant contributions of Jean-Marie Lehn (Nobel Prize, Chemistry 1987).[131]

A feature of supramolecular structures is molecular association involving non-covalent bonding. For electron transfer processes the molecular components rely on collision activation or through-space interactions. Depicted in Figure 1-11 is a representation of a host-guest inclusion complex that utilises π-stacking interactions to mediate electron transfer.[132,133] Prior to binding of a substrate the solvated host structure has only a very long through-bond pathway to facilitate electron transfer from the porphyrin chromophore to the quinone acceptor. The 'scorpion' conformation affords a U-shaped cavity suitable for aromatic guests which can be bound via π–π stacking and hydrogen bonding interactions.[133] Formation of the inclusion complex enhances electron transfer by reducing the distance traversed from chromophore to acceptor. The pillared π–system of chromophore-guest-acceptor imparts a supramolecular function essential to the photochemistry of this assembly.

Supramolecular photochemistry features strongly in the literature with interest in photobiological processes and development of artificial biomimetic systems.[134] Vincenzo Balzani has been an influential researcher into photoinitiated chemical processes and has emphasised the benefits of second-sphere and cage-type

coordination compounds, especially those of ruthenium.[134,135] Together with Lehn *et al.*, Balzani has made associations between the photochemistry of coordination compounds and the supramolecular function of macrocyclic receptors.[136] Labile CN^- ligands of Co^{3+} complexes are quite readily exchanged in a process known as photoaquation. This then allows a second-sphere of coordination to occur between the Co^{3+} complex and the encapsulating macrocyclic receptor. The supramolecular function of these structures exhibited decreased photodissociation as the size of the macrocyclic receptor increased. Their work demonstrated that supramolecular association is a method to enhance and control photochemical reactions.

Sauvage *et al.* demonstrate the change in long-range electronic coupling experienced by bimetallic ruthenium complexes and its dependence on molecular interactions.[137] Control of the spacing of the complexes was regulated by polyaromatic and heteroaromatic subunits.

The photochemical function of supramolecular systems incorporating Ru(II) polypyridyl complexes became a focal point of research late last century when functionalisation of these chromophores allowed their binding to semiconductor surfaces.[2,138] The evolution of supramolecular systems to incorporate inorganic components drew great interest as the possibility of nanoscale devices became apparent. Transfer of molecular function from solution to surface saw the renaissance of supramolecular chemistry and heterosupramolecular chemistry emerged.

1.3.7. Heterosupramolecular Chemistry

The controlled assembly of molecular fragments has long been accomplished by synthetic chemists with heterosupramolecular chemistry following the architectural principles of supramolecular chemistry.

Linking or replacing of molecular components within a supramolecular system with condensed phase materials forms a heterosupramolecular assembly. Analogous to supermolecules, a heterosupermolecule possesses intrinsic properties of the condensed phase and the molecular components which are not a simple superposition of the components.

The field of heterosupramolecular chemistry has been pioneered by the research of Donald Fitzmaurice at University College Dublin who was the first to coin the phrase.[139,140] Their work has included the adaptation of molecular species into heterosupramolecular arrays and the application of this to light-induced processes.[7,141-147]

The heterosupramolecular arrays conceived by Geoffrey Will (see, Figure 1-12) where the charge separation occurred in nanostructured transparent electrodes consisting of Anatase TiO_2 were investigated.[141] The electrodes were modified with adsorbed electron donor and acceptor molecules that exhibited long-lived charge separation properties.[144] The properties of a system that is capable of long-lived charge separation is of general interest, however applications of the phenomenon can be seen in photocatalysis and the development of optoelectronics.[139,140]

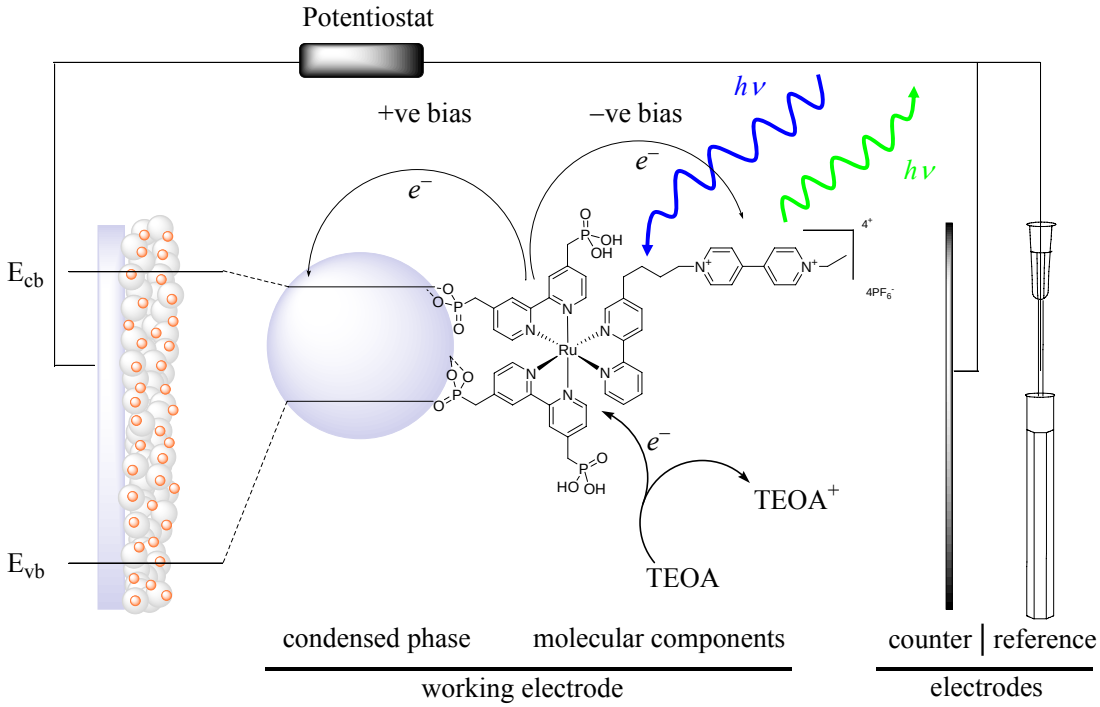

Figure 1-12 – Potentiostatic modulation of electron transfer by a heterosupramolecular assembly.[7]

The covalent linking of a molecular electron acceptor, for example a paraquat derivative,[9] influences electron injection into the condensed phase as the covalently bound electron acceptor is capable of receiving electronic charge following excitation of the molecular complex.[146] In effect, charge separation within the molecular dyad occurs. The lifetime of charge separation can be externally modulated under potentiostatic control and the direction of electron flow determined.[7,142] The exposure of these assemblies to visible light induces a blue coloration which is a direct result of electron transfer from the excited state of the PS to the paraquat moiety, without the need for an applied potential.[147] Under a positive potential bias this assembly injects electrons to the titania substrate, while under a negative bias the conduction band is unfavourable and fluorescence is quenched by the covalently bound paraquat.[7]

The outlined device shows that long-lived intramolecular charge separation and the functions of electron donor and acceptor can be isolated. This approach to device architecture would allow the development of a practical water splitting device.[141,143,144] The assembly of analogous components onto isolated surfaces would exhibit attractive optical and photoelectrochemical properties pertinent to achieving an affective photocatalytic device.

1.4. Photoelectrochemical (PEC) Cells

A photoelectrochemical (PEC) cell produces a space charge layer, similar to the p-n junction of a diode, as a result of the equilibrium between electron exchange at an n-type semiconductor and the redox electrolyte in solution (Figure 1-13). When excited, the semiconductor generates electron-hole pairs in the space charge layer, with the majority of charge carriers (electrons in an n-type) drifting to the bulk of the semiconductor. Minority charge carriers are expelled to the surface of the semi-conductor where they are regenerated by the redox electrolyte. A photo voltage (V_{ph}) results upon completion of the circuit with a counter electrode the redox electrolyte is also regenerated, in a cyclic photo-initiated redox system

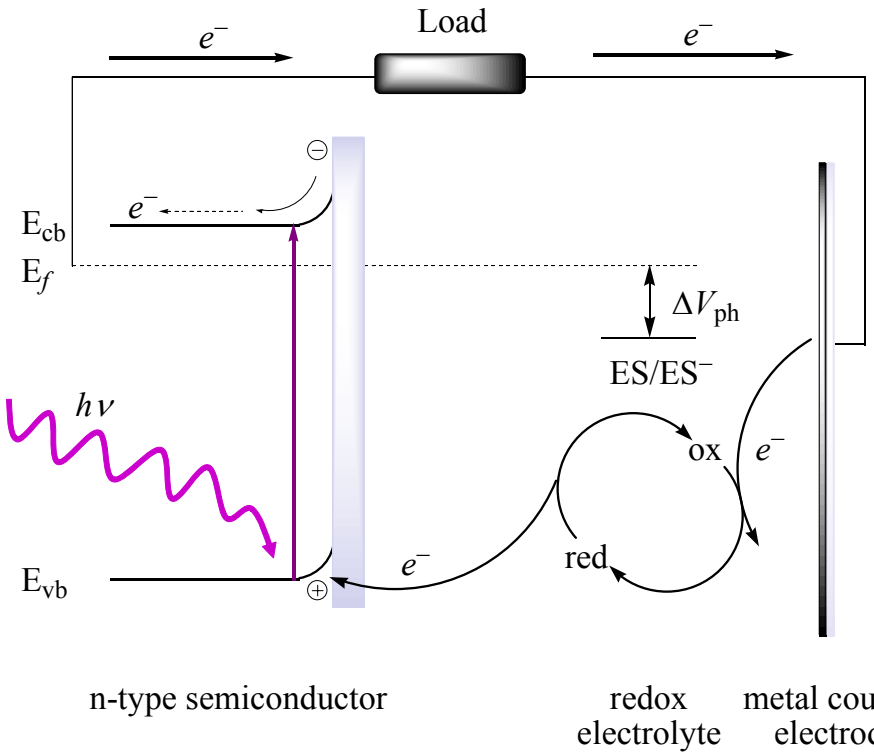

Figure 1-13 – Semiconductor/electrolyte junction of regenerative PEC under illumination.

This forms the basis of many PEC devices and the development and understanding of the properties of these devices have been of interest for a considerable amount of time.[148] The properties of PEC cells allow for a diverse number of applications including photovoltaics,[33,52,149,150] photoelectrochromics[147,151,152] and detection of oxidation processes.[153,154] In recent years interest has focused on development of molecular sensitisers for increased functionalisation of the PEC.[155] The growing

interest in surface bound photo-initiated reactions has been driven, in part, by the success of the dye-sensitised solar cell (DSC) and related PEC devices.

1.4.8. Alternative Semiconductors in Electrochemical Cells

Flexibility in the choice of material for nanostructured metal oxide electrodes is an advantage that photoelectrochemical (PEC) devices have for optimisation of cell parameters. In nanostructured electrodes, there are many secondary properties that need to be considered, not just the intrinsic properties of the bulk material. Surface structure, grain size/shape, film porosity and thickness as well as the relative band gap and band position with respect to surface sensitisers are all important secondary parameters.[156]

The most extensively studied metal oxide for use in the PEC cells is TiO_2. Many of the inefficient processes identified as limiting the performance of the PEC devices can be explored by the well studied TiO_2 model. Identification of acceptable semiconductors, improved substrates and structural properties for nanostructured electrodes are all avenues of research in progress.

Keis *et al.* have compared the thermodynamics, kinetics and charge transport properties of ZnO and TiO_2.[156] ZnO shares similar bulk energetics to TiO_2, yet is photocatalytically less active. Their investigation revealed that adsorption of dye sensitisers to the surface of ZnO does not occur by the same mechanism as for TiO_2. Diffusion of the dye within the porous electrodes is followed by dissolution of Zn atoms from the surface that coordinate with the acid linker of the dye. These aggregates act as a filter and reduce the efficiency of the cell. They identify that dye composition, concentration, pH and sensitisation time must be carefully controlled to avoid this negative effect. Doh *et al.* highlight improvements that can be obtained from the use of indium zinc oxide (IZO) substrates.[157] The short-circuit current density (j_{sc}) and open-circuit photovoltage (V_{oc}) were increased by 40% and 10% respectively over the widely used fluoride-doped tin oxide (FTO) conducting glass.

Controlling charge recombination in the PEC cells has been addressed by Bandara, Divarathne and Nanayakkara.[158] Retardation of interfacial recombination was achieved by the formation of a p-n junction of NiO over SnO_2 on a FTO substrate. Electron tunnelling across the p-n junction reduced electron loss due to trapping and suppressed electron leakage to the electrolyte. Hore *et al.* also note that the use of base peptization rather than the usually employed acidic methods can lead to slower interfacial recombination and increased V_{oc}.[159]

Niobium pentoxide, Nb_2O_5, thin films and coatings have shown potential for use in PEC devices and as catalysts.[160] For a series of Ru(II) photosensitisers adsorbed to Nb_2O_5, the electron transfer (ET) dynamics were shown to be biphasic with an ultrafast component of < 100 fs and a slower component of 300 ps–1 ns.[161] It was also noted that the slow component was an order of magnitude slower for amorphous over crystalline films, although as an alternative to regular semiconductors employed in cells, this material shows comparable properties.

Enhancement to the performance of nanocrystalline TiO_2 films has also been widely studied as the mesoporous nature of the films can affect the cell characteristics.[162] Saito *et al.* make note of the correlation of grain morphology and PEC cell parameters,[163] while light scattering in multi-layered mixed-phase films had a encouraging effect on cell efficiencies.[164]

1.4.9. Introduction to the Dye-Sensitised Solar Cell (DSC)

Although the basis of the PEC effect predates the work of Becquerel in 1839, the use of the effect for energy conversion can be traced to the work of Fujishima and Honda in 1972.[21,108] The use of highly porous metal oxide electrodes for adsorption of high surface concentrations of a PS,[165] has significantly increased the PEC energy efficiency (the amount of electrical energy produced divided by the amount of EM energy incident) and hence its commercial impact. The most widely investigated DSCs are those derived from the work of O'Regan and Grätzel and are often referred to as the Grätzel cell.[2] This cell utilises the semiconducting properties of nanoporous nanocrystalline TiO_2 electrodes and that of a PS adsorbed at the surface. TiO_2 is a n-

type semiconductor with a band gap equivalent to a photon from the UV region of the EM spectrum. Adsorption of a PS extends the absorption region to that of the visible thus increasing the range of radiation which is effective in producing an electrical current.

The preparation of nanoporous nanocrystalline semiconductor surfaces consists of deposition of particles from a suspension onto a conducting substrate, followed by sintering, or calcination, to form Ohmic electrical contact. The necking of particles during calcination increases electron percolation within the mesoporous structure of the film and hence to the substrate. The porous nature of the films allows capillary filling of the pores with an electrolyte and an extremely large surface area for adsorption of PS.

Wide band gap semiconductors, such as TiO_2, have been derivatised by absorbed dye molecules since the late 1960's. Such nanocrystalline semiconductor electrodes distinguish themselves by their high porosity and surface-to-volume ratio.[33] For sensitisation to be successful the PS is bound to the semiconductor such that the excited state of the PS energetically lies above the conduction band (CB) of the semiconductor. This facilitates excited state electron transport to the CB of the semiconductor, electron injection. Electron injection to the semiconductor acts as an excited state quencher for the PS. The PS is regenerated from a redox species (for example, I^-/I_3^-) in the electrolyte, thus preventing recombination (Figure 1-14).

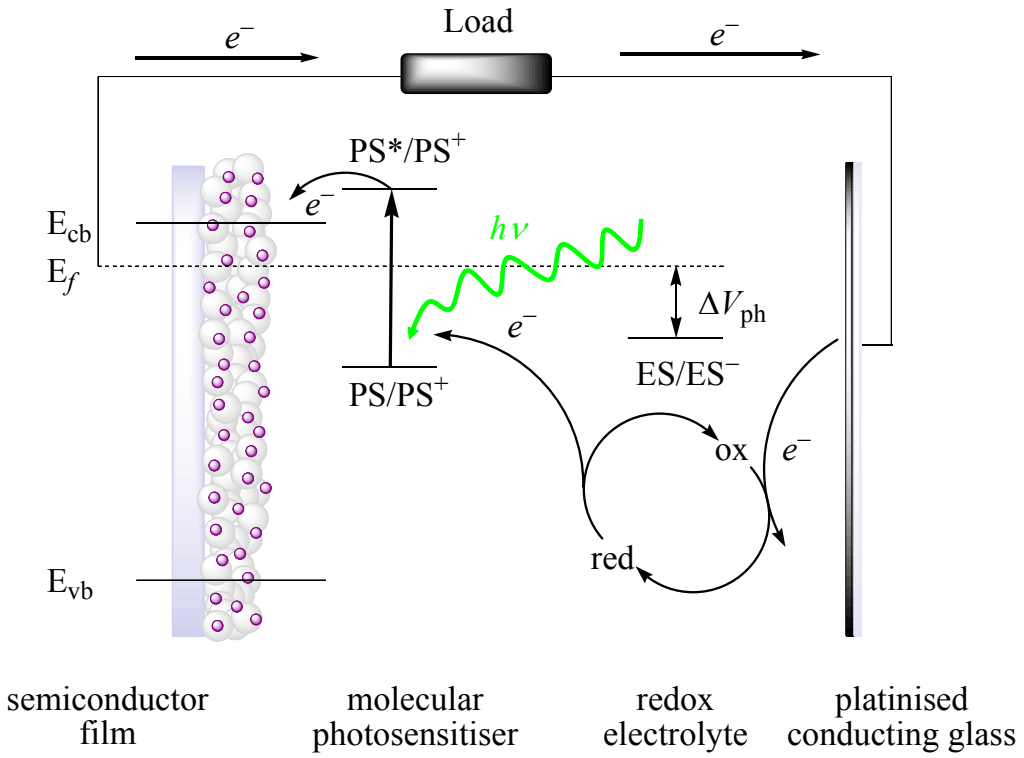

Figure 1-14 - Schematic of dye sensitised photovoltaic cell.

In 1990, O'Regan *et al.*[51] prepared 8 nm colloidal TiO_2 films on conducting glass supports and adsorbed a $[Ru(dcbpy)_3]^{2+}$ chromophore to extend the absorption range to the visible. The system was examined under the influence of an externally applied electric field and a current was observed. As a result, in 1991, O'Regan and Grätzel[2] described a DSC using a 10 μm thick TiO_2 electrode and a PS, $[Ru(dcbpy)_2(\mu(CN)Ru(CN)(bpy)_2)]$. Cell illumination initiated a metal-to-ligand-charge transfer (MLCT) within the PS, transferring electrons to the surface, which gave a photocurrent response. Bond formation between the carboxylate group on the periphery of the PS and TiO_2 particles in the film produces intimate electronic contact between the PS and the semiconductor,[33] facilitating charge injection yielding energy efficiency between 7.1–7.9%.

This heterosupramolecular system is capable of efficient removal of electrons from the site of excitation, at the PS centre, by injection to the semiconductor CB. This partitions the electron in the CB away from the oxidised PS, effecting charge separation.

Hence, these PEC devices can be exploited for the photoproduction of high energy chemicals such as H_2 through a simple modification of the system. The most salient feature of the DSC, and like devices, is irreversible photoinjection and hence charge separation independent of the semiconductor's photoexcitation properties. Treadway, Moss and Meyer describe a PEC cell in a two-electrode assembly utilising an adsorbed bridged dimetallic ruthenium complex as a PS. Connection of the cell against a platinised counter electrode induced photooxidation of short chain alcohols by the oxidised, PS^+, dye and reduction of an acidic solution to H_2 at a spatially separated site.[166]

This cell was a compartmentalised adaptation of the DSC with the photoanode immersed in one compartment and the platinised electrode in the other. The oxidised form of the ruthenium metal centre is reduced by the degradation of the alcohol, whilst H_2 production is promoted by the presence of an excess of H^+ ions in an aqueous 1M $HClO_4$ solution. The more general photolysis of the organic molecules to produce H_2 requires the immersion of the heterosupramolecular assembly in various solvent conditions, some of which may result in desorption of the dye from the surface. The ruthenium complexes are generally bound to the surface through a carboxylate linker on the periphery of a coordinated bipyridine ligand. The bound form of the complex is in equilibrium with the desorbed species which is dependant on the pK_a of the acid (~4.5) on the heterocycle. Thus, in conditions exceeding this pK_a (pH > 5), desorption occurs.[4] By modification of anchoring group for stability in elevated pH conditions, the exploitation of these devices for simultaneous high energy chemical production and oxidation of organic species is possible.

1.4.9.1. Modified Grätzel DSC

Since its conception, the Grätzel DSC has undergone many modifications to minimise the limitations that have been identified over the past decade. These include, and are not limited to, PS-surface and surface-electrolyte recombination, PS desorption, cell impedance, spectral absorption window and the photophysical properties of the PS pertaining to electron injection. Thus, the choices of semiconductor, redox couple, electrolyte solvent, photosensitiser, blocking layers or

molecular co-adsorbates are all essential to attaining an efficient and cost effective device. Even the choice of anatase TiO_2 as the semiconductor medium has its own disadvantage. The anatase crystalline phase of TiO_2 is photoactive and has widespread application as a photocatalyst.[29] Therefore its application in the DSC would induce considerable limitations to the long term stability of the device due to photodegradation of the PS. Photocatalytic degradation of the PS, electrolytes or co-adsorbates is a likely loss or performance limitation.

There have been varied approaches to improve the DSC efficiency. Nasr, Kamat and Hotchandani reported optically transparent coupled SnO_2/TiO_2 electrodes in an effort to suppress the back-electron recombination at the surface-solution interface.[55] This improved several DSC parameters such as the incident photon to current conversion efficiency (IPCE). Hybrid DSC configurations have been reported including modification to the TiO_2 surface structure by formation of aerosol thin films,[167] nanocrystalline nanotube structured electrodes,[168] and single-crystal nanowires.[169] The use of these novel TiO_2 structures was aimed at improving the efficiency of the cell by extending the mesoporous structure of the conductor, increase dye adsorption and improve electron percolation within the nanoporous matrix. Chappel *et al.*[170] proposed that by utilising a transparent nanoporous conduction matrix, coated with a nanometre thin film of TiO_2, losses due to electron trapping and transport would be minimised. Their method consisted of extending the current collector (SnO_2) within the light absorption region of the DSC. Electron transport through the TiO_2 film of only several nanometres rather than several microns reduces charge recombination.

Other hybrid cells have been reported. Plass *et al*. report the use of lead sulphide (PbS) as an inorganic sensitiser in combination with an organic p-type charge transport material.[171] This had mixed influence on the cell with lower energy conversion efficiency η = 0.49%, yet demonstrated that cells involving inorganic heterojunctions are capable of photonic energy conversion. A DSC based on a tandem sensitised anode and cathode also illustrated that new concepts in cell design are required to improve the DSC efficiency in excess of the reported 10%.[172] One suggestion is a cell that incorporates two photoactive semiconductor electrodes. Theoretically this device can achieve up to 43% efficiency through the use of two photon collecting surfaces. Solid-state cells have also proven to be an alternative to

the traditional DSC configuration by substituting the fluid electrolyte with suitable oxide layers or by a polymer gel impregnated with a redox couple. Perera *et al*. report one such multi-layered cell consisting of alternating dye-semiconductor nanostructured layers.[173]Although efficiencies were low (η < 2%) other attempts at solid-state configurations, by Meng *et al.* and O'Regan and Lenzmann, have improved the multi-layered cell and have outlined routes to its further enhancement.[174,175]

Quasi-solid state and flexible nanocrystalline cells are also novel alternatives. These devices require polymeric or cross-linked ionic gels[176] making a solidified cell by eliminating the electrolyte solution. This modification limits the efficiency of the cells, as the polymeric materials are unable to permeate fully to the nanoporous matrix of the thin films. Flexible cells consist of ITO coated PET substrates layered with a thin TiO_2 film. The redox polymeric electrolyte is interpenetrated within the porous films. Haque *et al.*[177] report a high cell efficiency (η = ~5.3%) while Uchilda *et al*., using a microwave modified TiO_2 layer, report a reduced (η = 2.16%) efficiency.[178] The reduced efficiencies of solid-state and flexible cells can be attributed to cell impedance. Longo, Nogueira and De Paoli found that the behaviour of both types of cells in the dark was similar, however the impedance of the flexible DSC was higher than that of the solid-state cell.[179] This can largely be attributed to poor electrical contact between TiO_2 particles due to low calcination temperatures.

As the above examples have illustrated, there are many facets of the DSC and its inherent properties that can be modified to improve cell dynamics and efficiencies. Some of the more pertinent properties that should be considered for improved performance will be discussed.

1.4.10. Cell Dynamics of the DSC

1.4.10.1. Mathematical Modelling of the DSC

Several attempts have been made to describe mathematically the function of the DSC and formulate an electrical model that relates component and material parameters to overall cell performance. A simplified model of DSC operating parameters has been reported by Ferber, Stangl and Luther (Figure 1-15).[180]

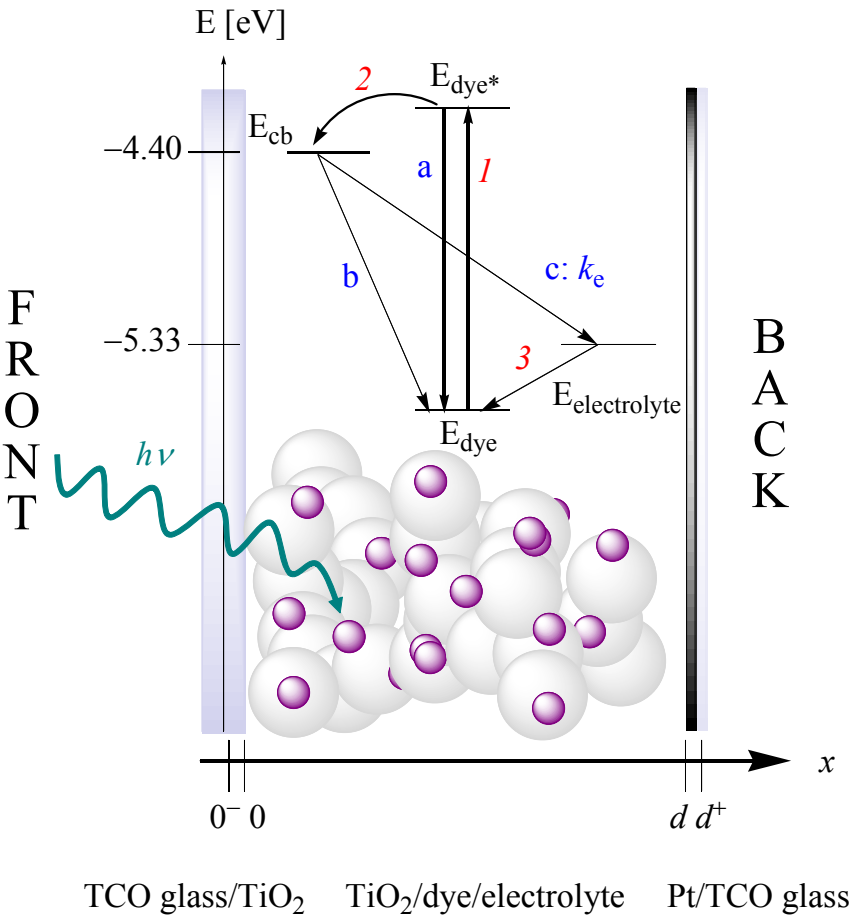

Figure 1-15 – Schematic representation of the cell and parameters used in the mathematical model of the DSC as described by Ferber. The space between 0 and *d* is the cell free volume occupied by electrolyte. The designators *x* = 0 and *x* = *d* indicate the electrolyte/surface interfaces while 0^- and d^+ are interfacial positions within the electrode surface. Under cell illumination, excitation of E_{dye} (1) and subsequent electron injection into the CB of TiO_2 (2) results in ground state quenching by the $E_{electrolyte}$ (3). Electron loss reactions: (a) excited state relaxation; (b) CB recombination; and (c) Redox electrolyte scavenging of CB electron. Only (c) is considered in the model and is described by an electron relaxation rate constant, k_e.[180]

This model allows steady-state properties such as current–voltage (*I–V*) characteristics and internal current flux to be mathematically derived. This simplistic model incorporates a one electron loss mechanism at the surface–solution interface under surface illumination and disregards further recombination pathways as possible mechanisms for efficiency losses. Expanding on the simplistic models, Penny *et al.* have also considered dark current reactions as significant loss mechanisms.[181] Their model further accounts for charge transfer from absorbed species at valence and conduction band as well as surface trap states of the semiconductor. Accordingly, interfacial charge transfer and semiconductor recombination are the identified loss mechanisms. These factors are considered in design of new sensitisers, anchoring groups and semiconductor surfaces for implementation in the DSC.

1.4.11. Photosensitisers in the DSC

Since the early reports of surface sensitisation there has been a wide variety of organic and inorganic dyes and complexes synthesised, isolated or modified for application as photosensitisers in the DSC.[23] The identification of a universal panchromatic sensitiser is a long term aim for increased efficiencies in the DSC.

1.4.11.1. Organic Dyes

Some of the earliest attempts at surface sensitisation came from supramolecular chemistry, hence the photosensitisers, or 'dyes', were often organic based chromophores or macrocyclic structures. Other sensitisers have built on this foundation to investigate broadly absorbing, novel and efficient organic based dyes.

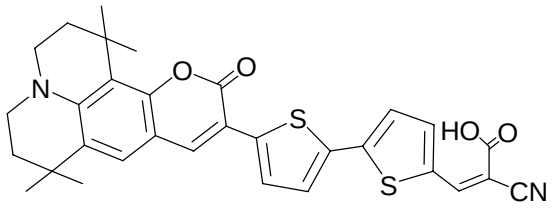

Figure 1-16 – Structure of the coumarin dye NKX-2677.

Hara *et al.* report derivatised coumarin-like dyes for sensitisation of TiO_2 films that attained solar energy conversion of $\eta = 5.6\%$.[182] This was a remarkable achievement

for an organic dye, however an improvement to the coumarin structure by the addition of a thiophene group gave the dye NKX-2677 with an efficiency of η = 7.7%.[183] Grant *et al.* also utilised thiophenes in a conjugated polymeric sensitiser yet the efficiencies that they attained were limited, and were at best η = 0.11%.[184]

Horiuchi, Miura and Uchida discussed the use of indoline dyes as sensitisers obtaining η = 5.1% under AM 1.5 (100 mW·cm^{-2}) conditions.[185] Indoline-type dyes have an intense absorption in the visible region yet show panchromatic spectral broadening on TiO_2 due to strong *J*-aggregate formation. The cell parameters of this class of dyes were highly comparable to the most efficient ruthenium-based sensitisers and were shown to be highly stable under cyclic photoredox processes.

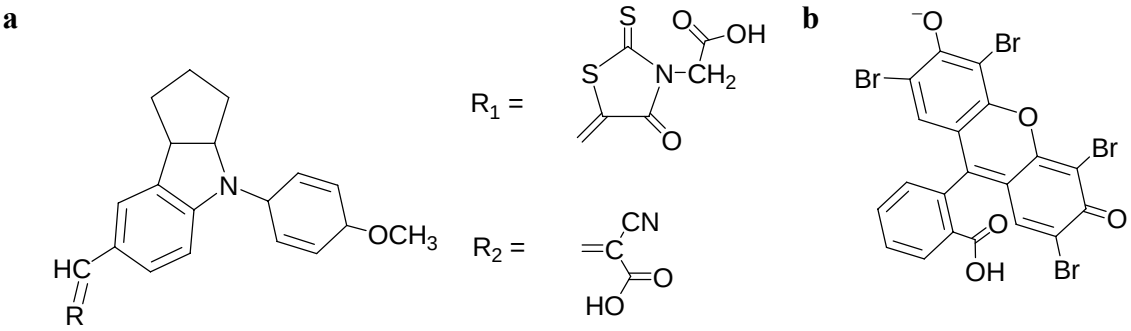

Figure 1-17 – Structure of a) indoline-like dyes; b) Xanthene dye Eosin Y.

Moser and Grätzel were the first to report the use of xanthene based dyes as semiconductor sensitisers.[24] Adsorption of the dye to colloidal TiO_2 nanoparticles gave favourable electron injection rates and quantum yields (38%). The accounts of cyanine and merocyanine structured dyes in the DSC by Sayama *et al.* have also been promising.[186] The co-absorption of yellow, red and blue squarylium cyanine dyes produced cells with efficiencies η = 3.1%. The increased efficiency of the co-adsorbed dyes was attributed to complementary intramolecular electron transfer between dyes, as the blue cyanine dye alone showed minimal efficiency due to *J*-like aggregation.

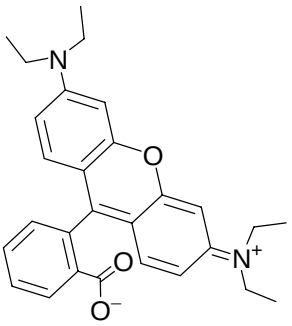

Figure 1-18 – Structure of the dye Rhodamine B.

Perera *et al.* reported the use of Rhodamine B as a co-sensitiser in a DSC incorporating three different organic dyes that absorb over sequential absorption bands.[187] Although ground and excited state energies of the dyes were favourable for electron injection to TiO_2, the broadened spectral absorbance gave only η = 1.67%. The smaller efficiencies were attributed to the heterojunction assembly of the cell. Rhodamine B has also been used in photodegradation[89] and photochemical systems for the generation of H_2.[104,188]

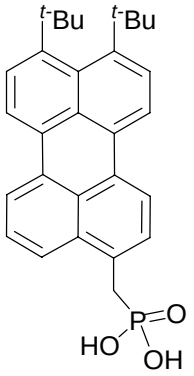

Figure 1-19 – Structure of perylene.

PEC reactions involving the use of perylene have been investigated in the literature with respect to their electron transfer kinetics.[189,190] Time constants of perylene are comparable to ruthenium based photosensitisers, which are on the femtosecond time scale. Kitamura *et al.* relate the use of phenyl-conjugated oligoenes as sensitisers for TiO_2 based cells.[191] Good photovoltaic performance of η = 6.6% was obtained with an IPCE of ~80% for the wavelength of maximum absorption. Other oligoene dyes that have been reported include quinizarin[192] by Ramakrishna *et al.* for electron transfer dynamic studies and xylenol orange by Matsubara *et al.* for a DSC cell that gave η = 1.3%.[193]

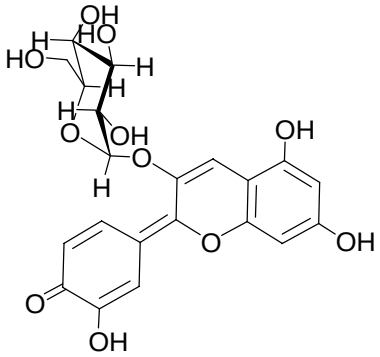

Figure 1-20 – Structure of anthocyanin dye.

The application of natural pigments for use as sensitisers in the DSC has gained attention in the literature.[194,195] The efficiencies of these dyes have not been fully reported however they did display comparable j_{sc} and V_{ph} to many dyes employed in the DSC. Anthocyanin, an extract of Californian blackberries, gave η = 0.56% with reduced efficiencies attributed to electron recapture by the redox mediator and the photon filtering effect of the dye extract. Although the system is not commercially practical, it has proven successful at demonstrating DSC principles to undergraduate students.[196] More recently, Dai and Rabani achieved η = 0.74% for anthocyanins extracted from pomegranate fruits.[197] Garcia, Polo and Murakami Iha also report several natural pigments with promising cell parameters considering the simplicity of the extracts obtained.[198]

1.4.11.2. Coordination Complexes of Organic Dyes

Sensitisers that incorporate a metal-to-ligand-charge-transfer (MLCT) as the photophysical mechanism for electron transfer have proven to be the most efficient class of dyes.[2,199] However, the incorporation of other metal-centred complexes as sensitisers in the DSC has also been investigated. Porphyrinoid species are by far the most numerous and successful macrocyclic dyes employed. These macrocyclic sensitisers are energetically capable of electron charge injection to TiO_2. Porphyrin LUMO states are sufficiently more negative than the CB of TiO_2, with the ground state of the dye sufficiently more positive than the redox mediator in solution.[23] Some of them also exhibit long lived π* singlet excited states (> 1 ns) with limited intersystem crossing of singlet/triplet states.

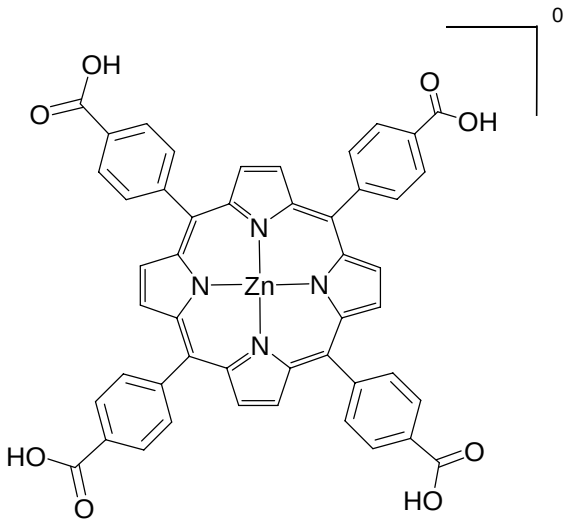

Figure 1-21 – The porphyrin sensitiser Zn-TCPP.

Cherian and Wamser report the use of a porphyrin sensitiser, 5,10,15,20-tetra-(4-carboxyphenyl)porphyrinatozinc(II) (Zn–TCPP), which is currently the most efficient macrocyclic sensitiser investigated.[200] Their efficient use of Zn–TCPP which gave η = 3.5% can be attributed to the use of a co-adsorbate, deoxycholic acid, as other researchers have reported lower efficiencies of η = 1.1%.[23,201]

Modified phthalocyanines have also been reported for use in the DSC. He *et al.* constructed cells of far-visible to NIR sensitised films to achieve η = 0.54%.[202] Amao and Komori discuss aluminium phthalocyanines that gave η > 0.01% yet show that the use of a co-adsorbate, myristic acid, can improve the cell efficiency by 170%.[203]

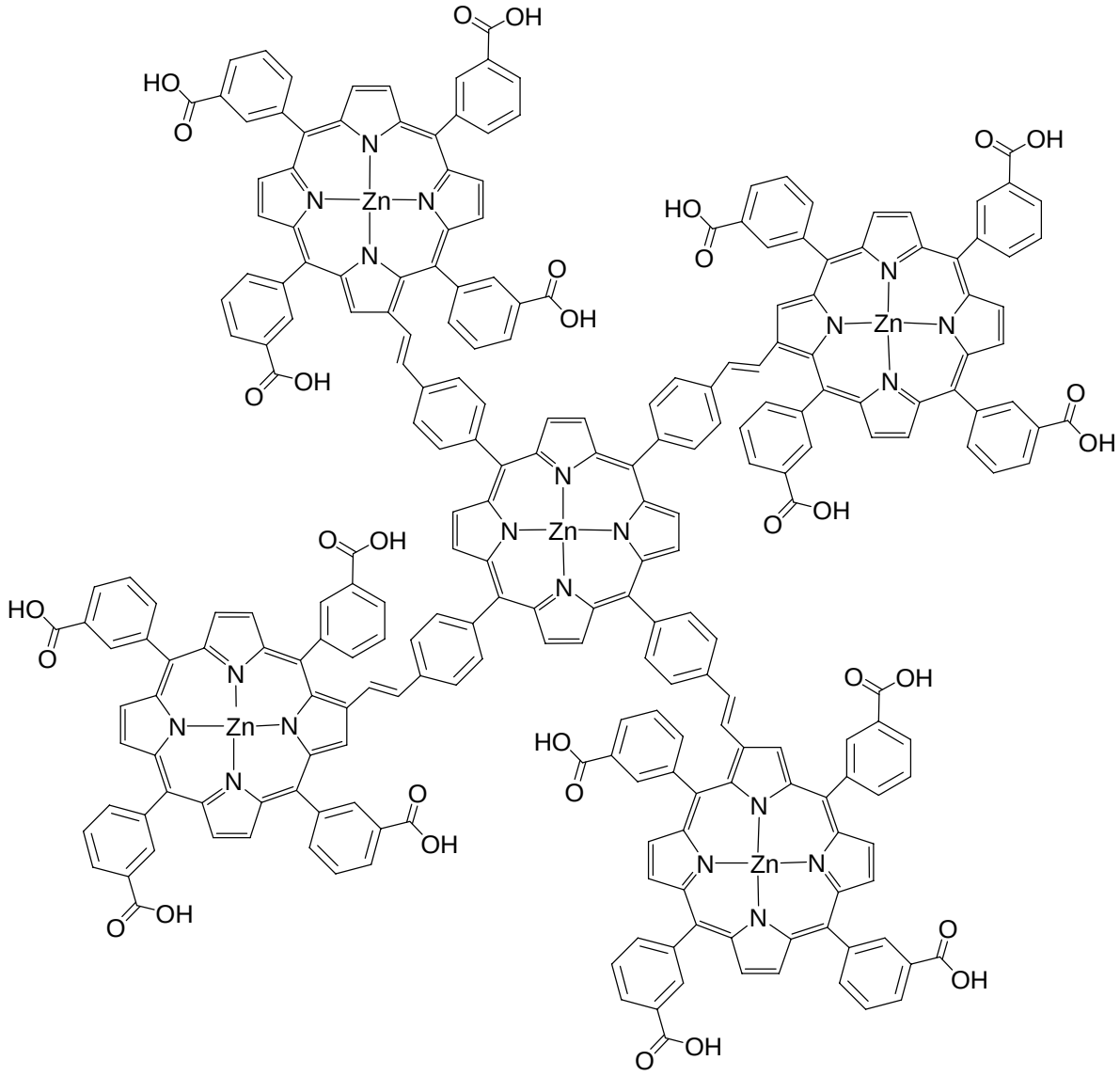

Figure 1-22 – The 'sticky' porphyrin oligomer Zn_5-9.

As an essential component of the photosynthetic reaction centre, porphyrin oligomers act as a light harvester to absorb, convert and transport electron charge in photosynthesis. Researchers have applied this approach for surface sensitisation in the DSC with the preparation of large antennae arrays, for example 5,10,15,20-tetra-{*trans*-4-[5,10,15,20-tetra(3-carboxyphenyl)porphyrin-2-ylatozinc(II)]phenylethenyl}porphyrinatozinc(II) (Zn_5–9).[23] These porphyrin arrays with multiple acidic linkers have been coined 'sticky' porphyrins. Although novel in their approach, these large antennae sensitisers show little improvement over single porphyrin macrocycles.

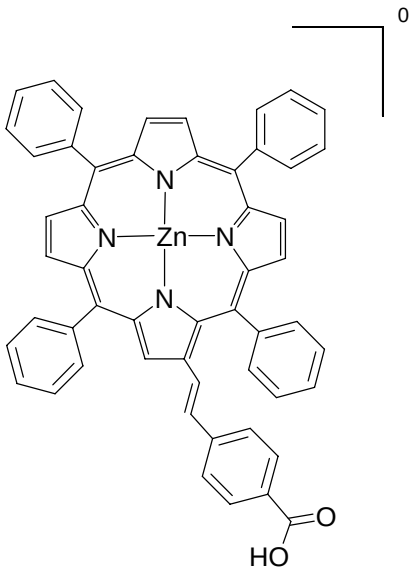

Figure 1-23 – Structure of the mononuclear porphyrin Zn-1b.

Campbell *et al.* have recently reviewed the use of the macrocyclic porphyrin sensitiser in the DSC, including several new sensitisers prepared by their group.[23] The most promising of these is *trans*-2-(4-carboxyphenylethenyl)-5,10,15,20-tetraphenylporphyrinatozinc(II) (Zn−1b) (Figure 1-23). This mononuclear porphyrin shows promising cell parameters for this class of sensitiser with j_{sc} = 1.1 mA·cm^{-2}. Choice of a conjugated linker would explain the increased electronic conduction from the sensitiser/surface interface. However substitution at the β pyrrole position as opposed to the *meso* position could explain the reduced quantum efficiency compared to Zn−TCPP.

Odobel *et al.* report a series of six free base porphyrins for use as sensitisers in the DSC.[204] The significance of their findings is that the choice of acid linker, carboxylate or phosphonate, has little effect on cell parameters however substitution on the macrocyclic periphery has a definite influence. Substitution of linker groups directly to the π aromatic core allows for stronger electronic coupling between the excited state and the TiO_2 *d*-band. They found that sensitisers with the linker substituted remotely from the macrocycle suffered electronic decoupling and exhibited reduced IPCE.

1.4.11.3. Ruthenium Complexes

The most recognised sensitisers for thin film assemblies of the DSC are ruthenium coordination complexes of the diimine ligand, 2,2′-bipyridine and related polypyridyl derivatives. The Ru(II) class of complexes exhibit high molar extinction coefficients of absorption bands in the visible, long excited state lifetimes, are capable of stability in oxidised and reduced states and show minimal aggregation or degradation.[135,205]

Following the early attempts at metal oxide sensitisation with $[Ru(bpy)_3]^{2+}$ by surface aggregation, more elaborate supramolecular structures were prepared.[54,206,207] Bignozzi *et al.* discuss experimental studies of polynuclear systems adsorbed at TiO_2 electrodes.[207] On light absorption, the supramolecular assembly of branched and one dimensional antenna chromophores allow for intercomponent energy transfer – in effect a 'cascade' of electron transfer from the linked components to the surface.

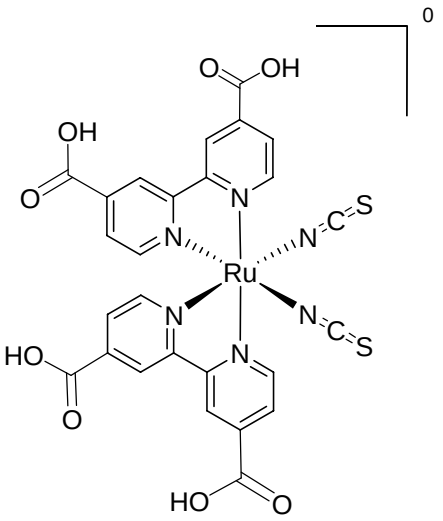

Figure 1-24 – The efficient DSC sensitiser, $[Ru(dcbpy)_2(NCS)_2]^0$, or N3 dye.

Following earlier reports of a highly efficient solar cell,[2] Grätzel's group have investigated many chromophores as sensitisers. Their report on the efficiencies of sensitisers of the form *cis*-X_2-bis-(4,4′-dicarboxylato-2,2′-bipyridyl)ruthenium(II) where X = Cl^-, Br^-, I^-, CN^- and SCN^- has gained the most attention.[54] The thiocyanate analogue, abbreviated as 'N3' in all subsequent references, attained a comparable efficiency to that of silicon-based photovoltaics with η = 10.4%. Many researchers have attempted to replicate this result, with limited success, yet this

remains the highest reported efficiency attained for a charge-transfer sensitiser of this class. The success of this dye has been attributed to its ability to broaden the MLCT band into the far visible region, which is due to a lowering of the energy of t_{2g} orbitals of the metal centre by coordinated thiocyanate ligands.

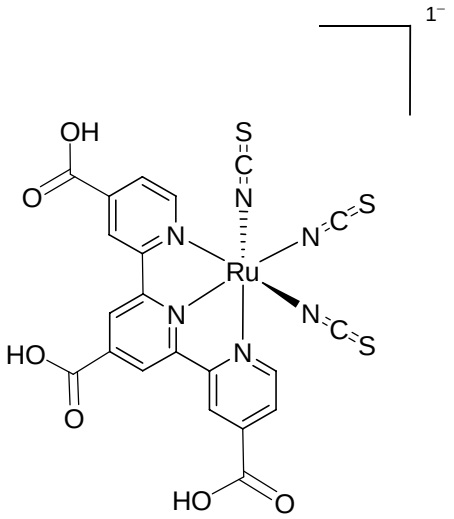

Figure 1-25 – The structure of the 'Black dye', $[Ru(tctpy)(NCS)_3]^{1-}$.

Since reporting the efficiency of this class of sensitisers, panchromatic absorption has been pursued through the use of thiocyanate coordination complexes. Exceptional broad spectral absorption was obtained by a terpyridyl complex with a MLCT that extended into the near-IR as far as 920 nm. The early reports of $Ru(tctpy)(NCS)_3]^{1-}$ (where tctpy = 4,4′,4″-tricarboxylato-2,2′:6,2″-terpyridyl), or the 'black dye' in the literature, gave an IPCE = 80% for much of the 400–700 nm region.[199] In a later report an independent assessment of the cell parameters of a DSC incorporating the 'black dye' gave an overall conversion efficiency of η = 10.4%.[208] This independent assessment confirms that the 'black dye' is an equivalent DSC sensitiser to the N3 dye in relation to cell IPCE.

Yanagida *et al.* compare a series of ruthenium diimine complexes, based on a quinoline derivative, directly with that of the N3 class of sensitiser.[209,210] The best cell configuration gave η = 4.9% (N3 cell gave η = 5.9%) however the amount of dye loading in the two cells was different (as calculated by a Langmuir isotherm). These reports highlight the importance of dye loading to cell performance and that

standardisation with a known dye is often required for comparison of new sensitisers due to cell configuration and testing conditions.

The utilisation of β-diketonate ligands in diimine ruthenium complexes also has a substantial effect on the spectral response of cis-bis configured sensitisers.[211] Sugihara *et al.* introduce β-diketonate as an electron donor in the coordination sphere that significantly lowers the energy of the ruthenium t_{2g} orbital. INDO/S computations showed the contribution of the ketonate ligand to transitions from HOMO–2 to LUMO and LUMO+2 of the dye. The effect of this ligand-to-metal charge transfer (LMCT) improved the longer wavelength response which gave η = 6.9% for the cell.

The molecular configuration and choice of substituents on the periphery of ligands have a profound influence on charge transfer in ruthenium sensitisers. It has been demonstrated that thiophene has a major effect on photophysical properties of sensitisers.[184,212] By modification of the 'black dye' structure by incorporating a second terpyridyl moiety, Figgemeier *et al.* intended extending the absorption of this complex and improve cell efficiencies. However the use of a thiophene on the ligand remote to the surface had a profoundly negative influence. The thiophene motif influenced the energetics of charge transfer with the LUMO residing on the remote ligand, limiting the quantum efficiency. Consideration must therefore be given to the electronic structure of complexes and the respective ligands when engineering the next generation of molecular sensitisers.[212]

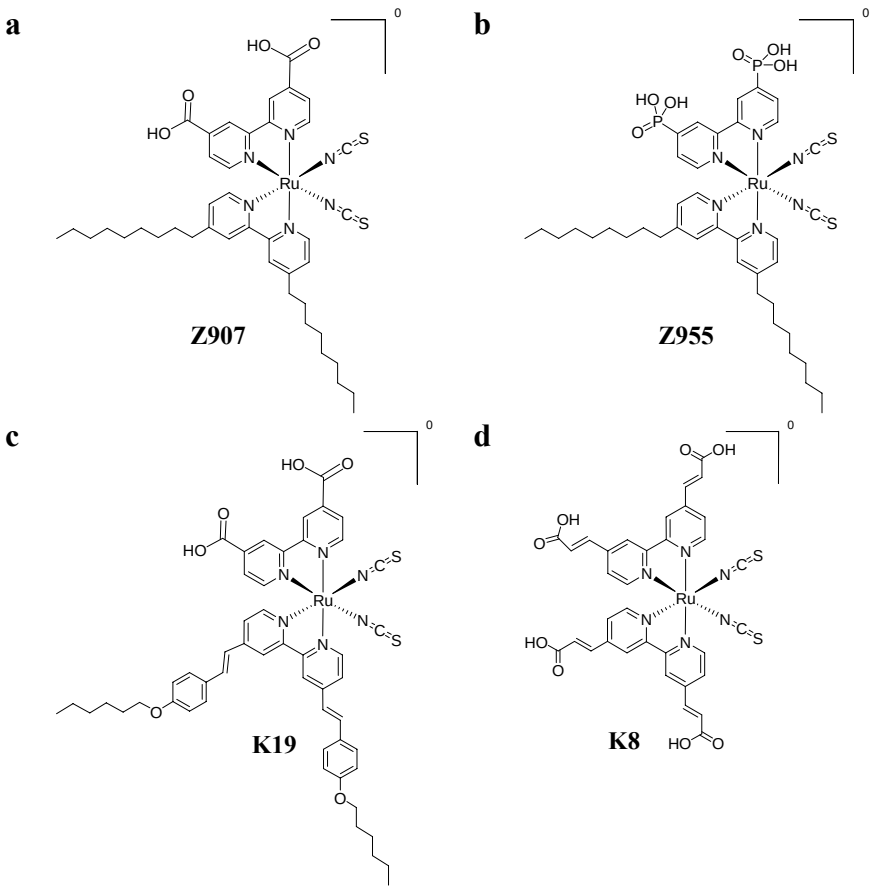

Figure 1-26 – A selection of amphiphilic ruthenium sensitisers as utilised in the DSC
a) *cis*-(4,4′-dinonyl-2,2′-bipyridyl)-(4,4′-dicarboxylato-2,2′-bipyridyl)diisothiocyanatoruthenium(II)
b) *cis*-(4,4′-dinonyl-2,2′-bipyridyl)-(4,4′-diphosphonato-2,2′-bipyridyl)diisothiocyanatoruthenium(II)
c) *cis*-(4,4′-bis(*p*-hexyloxystyryl-2,2′-bipyridyl)-(4,4′-dicarboxylato-2,2′-bipyridyl)diisothiocyanatoruthenium(II)
d) *cis*-bis-(4,4′-bis(carboxyvinyl)-2,2′-bipyridyl)diisothiocyanatoruthenium(II)

Outlined in Figure 1-26 are some of the amphiphilic ruthenium sensitisers synthesised by the Grätzel group.[213-219] These heteroleptic sensitisers are configured in much the same fashion as the N3 class of dyes. The incorporation of ligands that increase the energy of the HOMO of the complex, through σ-donation, or decrease the energy of LUMO states on the anchored ligand should give broader absorption and increased charge injection.[220,221] The amphiphilic sensitisers achieve this while also minimising the recombination effects of I^-/I_3^- at the nanostructured electrode by introducing a strongly hydrophobic ligand to the coordination sphere. Co-grafting of an amphiphilic acid provides a tightly packed mixed monolayer that also retards surface recombination.

Stable DSC sensitisers have been reported that utilise the highly oxophilic phosphonic acid group for strong chemical attachment to nanocrystalline electrodes.

A terpyridyl complex of ruthenium with a phosphonate linkage at the 4-position gave high IPCE for monochromatic excitation about the MLCT.[222] High IPCE in the region of the MLCT has also been reported for phosphonated $[Ru(bpy)_3]^{2+}$ complexes.[8] This study looked at phosphonate linkage effects with and without a methylene spacer between the acid group and the ligand. Introduction of a saturated methylene spacer had a negative influence on the cell performance with decreased photocurrent efficiency and quantum yield of electron injection. Yet, it was encouraging that the acid linker gave enhanced stability over that of carboxylate linkers. Further to this, Zabri *et al*. report the synthesis of phosphonated analogues of the N3 class of sensitisers.[223] The efficiency and injection yield of these phosphonate analogues was comparable to that of the N3 dyes. However the hypsochromic effect of the phosphonate group gave a reduced absorbance in the red region of the spectrum and hence η was 30% lower than the N3 dye.

1.4.12. Photophysical and Excited State Properties

Complexes of ruthenium(II) containing *N*-donor ligands are widely studied for their unique combination of photo- and electrochemical stability. The most prevalent are the diimine complexes of the parent form $[Ru(bpy)_3]^{2+}$.

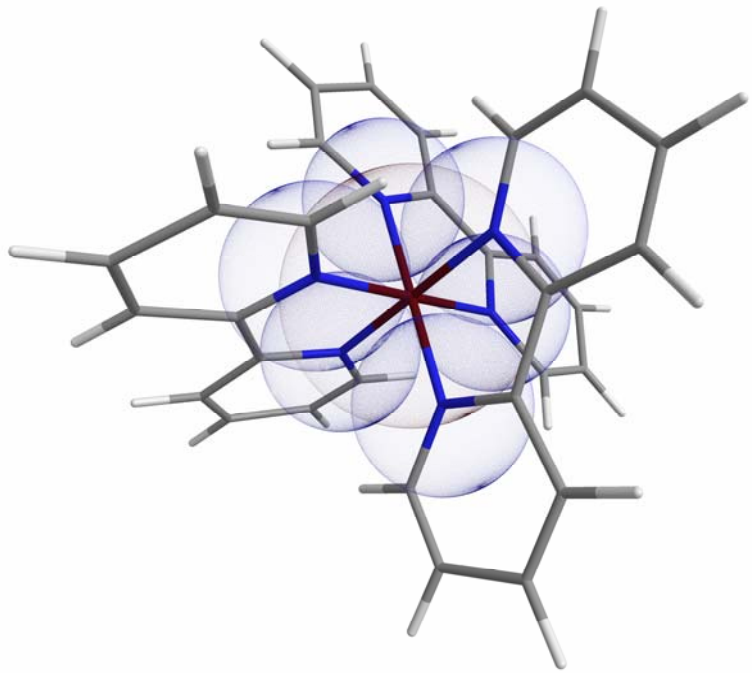

Figure 1-27 – The octahedral geometry of $[Ru(bpy)_3]^{2+}$ depicting the orthogonal correlation of bidentate chelates. Dot surfaces illustrate the Van der Waals radii overlap of Ru–N bonds.

Tris-diimine complexes of Ru(II) have a characteristic d^6 low-spin diamagnetic metal centre and possess D_3 symmetry. Due to the small bite angle of bipyridine, distortion from an octahedral geometry results in a *pseudo*-octahedral ligand crystal field.[224]

Stability of these complexes comes as a result of the π acceptor and σ donor character of diimine ligands. Diimine ligands coordinate through the formation of σ bonds by σ donation to empty d^* orbital whilst forming π bonds with occupied d orbitals and vacant ring π* orbitals (σ–π back-bonding). Significant back-bonding of the diimine ligand to Ru(II) is indicated by the shorter (2.056 Å) Ru–N bond (*c.f.* $Ru–NH_3$, 2.104 Å) and complexes of these ligands are considered essentially substitutionally inert.[135]

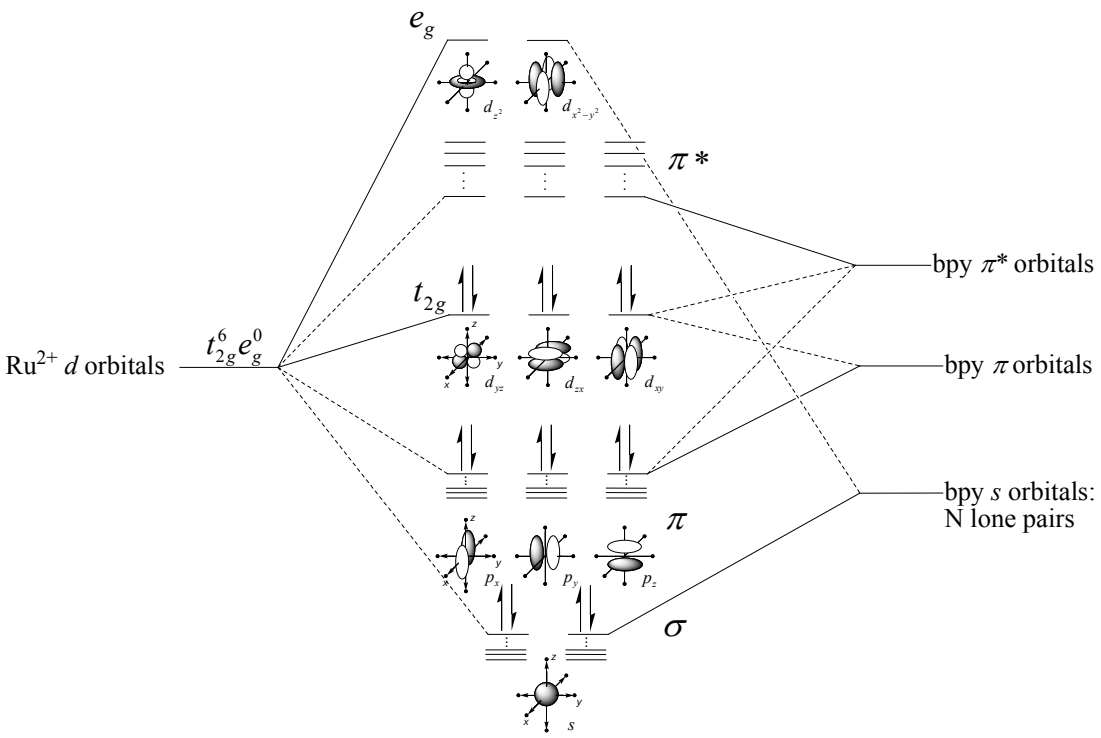

Figure 1-28 – Ground state electronic structure of the frontier orbitals of a $[Ru(bpy)_3]^{2+}$ complex as in an octahedral crystal field.[135,224,225]

The extensive σ–π back-bonding of the diimine ligands leads to six filled σ–bonding orbitals and six unfilled π*–anti-bonding orbitals. Hence, the frontier molecular orbitals (Figure 1-28) are comprised of π–bonding orbitals localised on the diimine ligands, weakly π–bonding orbitals restricted to the Ru(II) centre, π*–anti-bonding orbitals confined to the ligands and σ*–anti-bonding orbitals confined on the metal. Perturbation and redistribution of energies in the octahedral field leads to the fundamental occupied π and *d*–π arrangement and an unoccupied π* and *d*–σ* grouping.

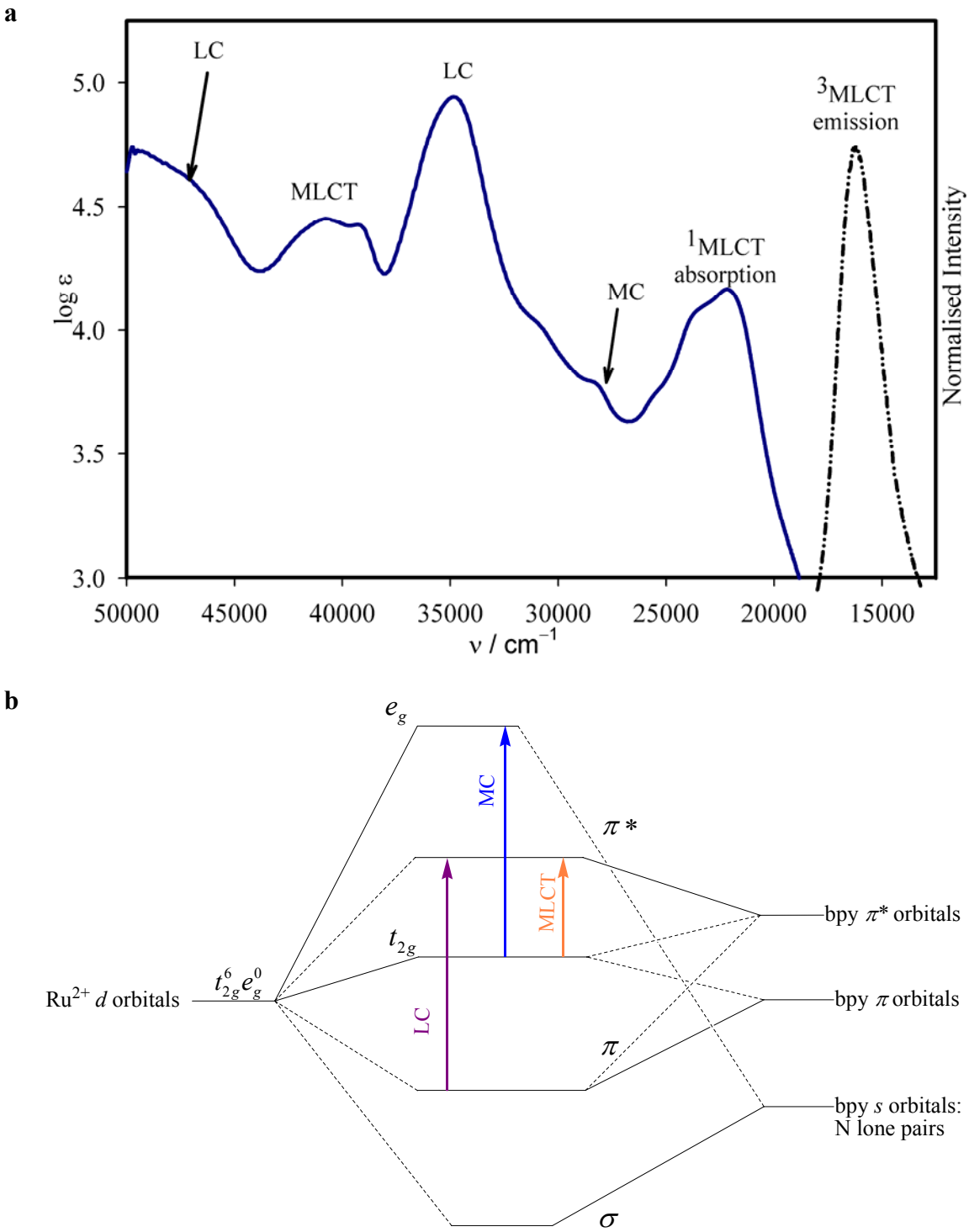

Figure 1-29 – a) Electronic absorption and emission spectra of $[Ru(bpy)_3]^{2+}$ as observed in aqueous media. b) Electronic transitions associated with the frontier molecular orbitals and their relationship to observed absorption phenomena.

The low lying energy of the frontier molecular orbitals allows the accessibility of numerous excited state transitions. The electronic absorption spectrum of $[Ru(bpy)_3]^{2+}$ shows four regions of spectral significance (Figure 1-29a). Also indicated is the proposed assignment of these spectral bands and the relationship to molecular orbital transitions (Figure 1-29b). The dominant feature of the spectrum is an intense MLCT band. In aqueous solution at ambient temperatures this transition has been assigned as singlet $d \rightarrow \pi^*$ while the band at 35000 cm^{-1} has been assigned a ligand-centred (LC) transition. Promotion of an electron from a ligand localised π–bonding orbital to the mainly ligand π^*orbital gives rise to a $\pi \rightarrow \pi^*$ transition that rapidly decays to the t_{2g} manifold.[224] Shoulders of these prominent bands of the UV-visible spectrum at ~31000 and 28000 cm^{-1} have been assigned as most likely metal-centred (MC) transitions.

Excitation of the spin allowed ^{1}MLCT transition results in intersystem crossing and a ^{3}MLCT phosphorescent luminescent state. The bright emission has a lifetime of ~1μs and is sufficiently long-lived for involvement in energy and electron transfer processes in solution.[135] Quenching of the ^{3}MLCT excited state can occur via oxidative or reductive pathways or via direct energy transfer. Linking of Ru(II) complexes to a surface by direct attachment of a ligand leads to excited state quenching through electron transfer to the CB i.e. charge injection. Injection of charge segregates the electron from the photogenerated hole, preventing recombination or excited state relaxation, which leaves the sensitiser as a photoreactive centre, $[Ru(bpy)_3]^{3+}$. The sensitiser in this form is capable of oxidising suitable chemical species in proximity to the reactive centre (E_{ox} = +1.26 V, versus SCE, H_2O),[135] which regenerates $[Ru(bpy)_3]^{2+}$. Consequently, photoexcitation and charge injection facilitates the formation of a surface bound oxidative hole which allows the photophysical properties of this class of complexes to be exploited for heterosupramolecular function.

1.4.12.1. Properties of Ligand Anchoring Groups

Nanoscale device fabrication is fundamentally dependant on the ability to assemble functional ordered structures and arrays. Devices that incorporate inorganic surfaces or involve organic/inorganic interfaces require a binding medium that facilitates the assembly. These are often referred to as linkers or anchoring groups.

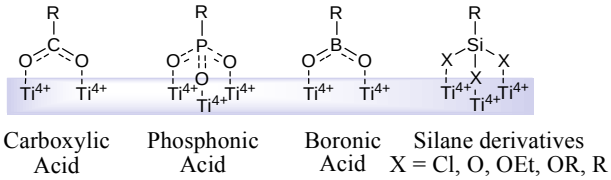

Figure 1-30 – Acidic linkers associated with heterosupramolecular chemical arrays.

The design and choice of appropriate linker groups are important in relation to the application. Considerations when implementing a linker include:[205]

i. Systematic variation of bridge length in linkers can control molecular/surface interactions
ii. Surface aggregation can be prevented by large footprint linkers
iii. Rigid bridge structure, functionality and saturation can influence the chromophore properties
iv. Functional linkers can be used for controlled surface modification

Anchoring groups for binding supramolecules vary depending on the nature of the condensed phase, with common linkers being thiol derivatives for adsorption to metals or silicic acids for glass-like surfaces. The more conventional linkers applied to metal oxide surfaces are those based on carboxylic or salicylate groups.[139] The use of these acidic functional groups to anchor molecules to surfaces is favoured by both ease of preparation and relative ability to facilitate electron transfer. Acid functional groups provide intimate anchoring to condensed phase surfaces with the binding strength dependent on the environment and the acidity of the linker.[4,6] The addition of linker groups to functional moieties allows the fabrication of devices, for example, electrochromic windows utilising viologen chromophores, [226] boronic acid derivatised sensitisers for DSC applications, [227] and surface bound fluorescent probes.[228]

The binding nature of anchoring groups to surfaces is a keen topic of discussion in the literature.[229-234] The more universally accepted modes of adsorption for acidic linkers are summarised in Figure 1-31.

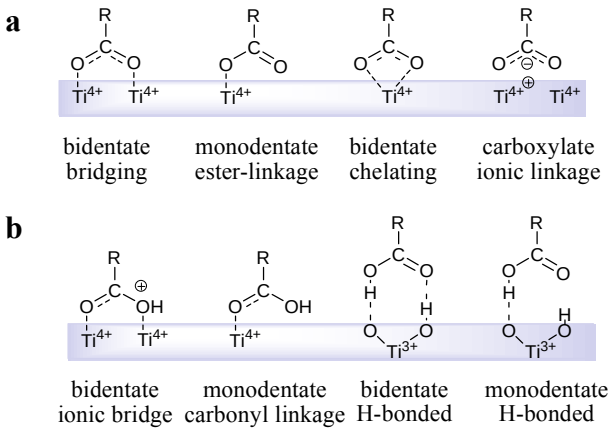

Figure 1-31 – Identified and postulated binding modes of acidic groups to the surface of metal oxides: a) identified binding to titania surfaces b) postulated binding to titania surfaces.

The carboxylate and phosphonate linkers are widely acknowledged as the most suitable anchoring groups. They reversibly bind to oxide surfaces with high equilibrium binding constants ($K \sim 1 \times 10^5$ M^{-1} for carboxylate bound Ru-diimine complexes), and achieve high saturation surface coverage in the range of $\Gamma \sim 1 \times 10^{-10}$ mol cm^{-2}.[6,146,205]

Phosphonate linker groups are tightly bound to metal oxide surfaces that are strong Lewis acids and the former are known to chelate to TiO_2 through vacant surface Ti^{4+} sites and anionic oxygen atoms of the acid.[229,235] In their description of similar carboxylate chelation, Duffy *et al.* depict this as a strong synergic bond between vacant σ orbitals of Ti^{4+} and unpaired electrons of the oxygen atoms.[230] Presumably the same effect would be expected for chelation of other linker groups such as phosphonate. The strong binding of molecular components via acidic linkers is favourable and allows the implementation of devices in a variety of environments.

1.5. Conclusions

The world, as a whole, is progressively finding that it does not have the resources to meet the needs of an ever-growing population. Natural energy resources are becoming increasingly depleted and shortages of fresh water have been forecast in the coming decade.

A review of the literature has shown that research is proactive in achieving environmentally sound solutions to this dilemma. There are numerous groups working in the field of photocatalysis: identifying methods of detoxification of water supplies, developing new catalysts, generating environmentally responsible chemical energy and establishing real-world solutions to fresh water contamination. Continued research into these and other identified areas of concern is of substantial benefit.

Conversion of our most abundant natural resource, terrestrial light, to useable energy has also featured strongly in this review. Solar energy conversion is seen as the most achievable form of sustainable energy in terms of accessibility and cost. As an alternative to silicon based photovoltaic cells, the DSC has emerged as a cost effective PEC device attaining comparable efficiencies of η = 10.4%. The development of this device has been influenced over a considerable amount of time by the chemical architecture of both the condensed phase and molecular components from which it is made. From the first reports of photochemical processes of the DSC, surface/molecular interaction and the role of heterosupramolecular assembly have become apparent as the underlying principles of this and related PEC devices.

Heterosupramolecular assembly is unique in relation to the analogous supramolecular arrays. The covalent interaction of a molecular species with a surface provides an intimate linkage for transfer of electrochemical charge and functions as a means of electron-hole segregation. Charge separation over a large molecular distance can limit recombination and allow the electron and hole to be involved in different chemical reactions.

Photocatalytic reactions at a surface are the basis of function in the DSC. Heterosupramolecular assembly of a photochemical system would enable the investigation of photon induced reactions by means of photoelectrochemical measurements. Investigations into water photolytic reactions, photodegradation of organics, generation of chemical fuels and the identification of photocatalytic processes are all areas that are of benefit to ongoing research into sustainable living practices.

CHAPTER 3

Synthesis of Molecular Components

Introduction

A fundamental aspect of so-called 'molecular engineering' of photosensitisers is the choice of ligand(s), and combination thereof, as the building blocks of coordination complexes.[221,224] With respect to development of surface sensitisers this also involves the choice of binding groups. Consideration of ground state properties, donation and back-bonding effects, as well as the relative energy of excited states must be given to construct effective chromophores with suitable function.

There is a considerable following in the literature for the development of novel ligands and as such methods of preparation of suitable ligands were sourced directly from there. The focus of our synthetic investigation was the preparation of photosensitisers containing functionalised ligands for surface adsorption to titania.

The stability of ligands containing phosphonate acidic linkers has been established.[8,49,223,236,237] These anchoring groups provide intimate connection to the surface, are stable over a wide pH range and under applied electric fields. It is these properties that make the phosphonate linker preferential over other acidic groups, especially the carboxylate linker, which is known to desorb considerably in aqueous environments.

Synthetic preparation of photosensitisers will involve the coordination of ligands to form octahedral complexes with the key 2nd row transition metal, Ruthenium ($^{101}_{44}Ru$). Complexes derived from Ru are important as many of these in the II–IV oxidation states can undergo reversible oxidation/reduction reactions to give structurally similar compounds with different formal charges.[238]

An understanding of the formation of tris(chelate) complexes of Ru(II) is important as it is the basis of research into photoinduced charge separation and energy migration,[7,51,54,189,239] chemiluminescence,[240-244] photocatalysis and photochemical water activation studies.[1,245-247] A schematic representation of the reaction mechanism for octahedral tris chelation of Ru(II) is depicted in Figure 0-1.

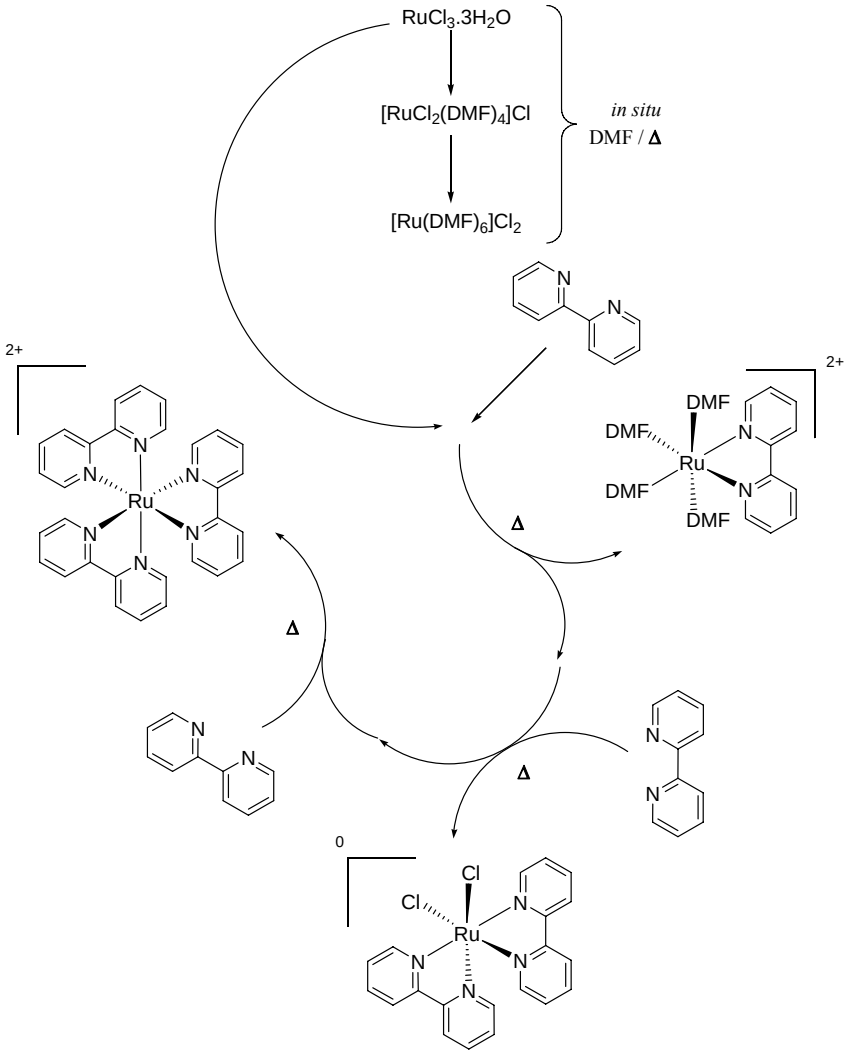

Figure 0-1 – Schematic representation of the mechanism for formation of coordination complexes of Ru(II) via successive ligand dissociation-association steps.

Perhaps the most common starting material for the formation of Ru(II) diimine complexes is a Ru(III) halide complex, the commercially available "$RuCl_3.nH_2O$". Preparations of this type involve refluxing of stoichiometric quantities of ligand and halide precursor in polar aprotic solvents, commonly *N*,*N*-dimethylformamide (DMF). These solvents are chosen due to their weak bonding, increased rate of reaction, and ability to solvate cations effectively.[248]

Initial ligand dissociation gives the Ru^{III} species, $[RuCl_2(DMF)_4]Cl$, as DMF displaces Cl^- in the coordination sphere. This does not change the formal charge on Ru as the *d* valence electron count, d^n, remains 5 and the electron count for the complex also remains unchanged at 17 e^-. Subsequent reductive elimination of HCl leaves the co-ordinately saturated $[Ru(DMF)_6]Cl_2$ with $d^n = 6$ and a formal oxidation state of 2+ as the reactive species in solution.

Josceanu and Moore describe an investigation into the stability of $[Fe(bpy)_3]^{2+}$ dissolved in DMF.[249] In this study the tris(chelate) of Fe(II) is formed from $[Fe(DMF)_6]^{2+}$. Serp, Hernandez and Kalck report similar observations for a red complex under these experimental conditions that upon addition of bis(triphenylphosphino)amine chloride gave the corresponding $[RuCl_5(CO)]^{2-}$ complex.[250] They also found that the addition of 5 equivalents of aqueous HCl gave the corresponding green Ru(II) complex, $[RuCl_4(CO)(DMF)]^{2-}$.

In addition, the analogous, versatile and air-stable complex, dichlorotetrakis(dimethylsulphoxide)ruthenium(II) $[RuCl_2(DMSO)_4]^0$, as reported by Evans, Spencer and Wilkinson displays similar coordination.[251] Dimethyl sulphoxide (DMSO) is a very common polar aprotic solvent used in inorganic syntheses, however the ability for this ligand to bond through the sulphur of the SO group makes it a more strongly bound solvent over DMF.

Under reflux, this reactive species undergoes three chelations by successive ligand dissociation-association. In each of these steps d^n remains 6 and the electron count for the complex is unchanged at 18 e^-. Co-ordination saturation and the chelate effect

impart enhanced stability to these complexes and is the primary reasoning behind the ligand exchange mechanism.

The first 2,2'-bipyridine chelate gives, in solution, $[Ru(bpy)(DMF)_4]^{2+}$ followed by a second chelation to give $[Ru(bpy)_2(DMF)_2]^{2+}$. Josceanu and Moore in their investigation identify the bimolecular addition of the first chelate as a rapid process with a substantial decrease in the rate of reaction for the bis-chelate attributed to a change from a high to low spin state.[249] In addition the analogous $[RuCl_2(bpy)_2(DMSO)_2]^0$ has been reported using DMSO.[251] Due to the weak bonding of aprotic solvents, stoichiometric control of reactants allows the isolation of $[Ru(bpy)_2Cl_2]^0$ following ligand exchange in the coordination sphere.

In an additional experimental step, or by stoichiometric control of the initial reaction, the third chelation also occurs via dissociation-association ligand exchange and the desired *tris*-(2,2'-bipyridine)ruthenium(II) dichloride complex, $[Ru(bpy)_3]Cl_2$, can be isolated by precipitation with a non-polar organic solvent.

Viologens are quaternary salts derived from 4,4′-dipyridyl. The first report of this by Michaelis proposed the naming of these compounds as viologens and covers the range of compounds of type *N*,*N*′-disubstituted-4,4′-bipyridinium dications.[252,253]

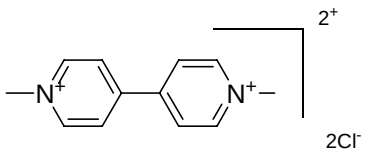

Figure 0-2 –The commercial herbicide Gramoxone.

The 1,1′–dimethyl substituted analogue is the simplest form of viologen and can often be referred to as paraquat, diquat or methyl viologen (MV). The dichloride salt, the commercial herbicide Gramoxone (Figure 0-2), is a toxic water soluble analogue that is lethal to mammals (LD_{50} = 125mg/kg, orally in rats). This has been extensively researched for its oxidation-reduction properties, where a deep coloration is observed for the reduced monocationic form. In more recent years, substituted analogues of this moiety have gained interest as electron-transfer reagents[105,254-257], materials in electrochromic displays[9,147,258] and optically switchable devices.[7,145,259]

Cinnsealach *et al.* have reported the use of modified viologens as redox chromophores.[9] In particular, 1–ethyl–1′–(2–phosphonoethyl)–4,4′–bipyridinium dichloride is of interest as it shares the redox properties of MV whilst gaining the heterosupramolecular function of a electrochemically switchable chromophore. This substance is quite readily prepared, has a first reduction potential $E^{0'} = -0.70\ V$ ($E^{0'}_{ads} = -0.61\ V$) and can be strongly bound to nanostructured electrodes via the phosphonate linker. Development of procedures for the isolation of 4,4'-dipyridyl salts for the explicit application as surface sensitisers has been investigated.[9,49,145,226,258] and will be described in the following procedures.

Materials and Equipment

The molecular components used in subsequent studies, **$[Ru(bpy)_2(dmpbpy)]^{2+}$**, **$[Ru(dmpbpy)_2(bpy)]^{2+}$**, and **EVP** were prepared as depicted in Scheme 1, Scheme 2 and described in detail below. In the experimental procedures, the sensitisers are referred to as their respective chloride salts; however in subsequent reference in proceeding Chapters they will be referred to as cations.

The starting reagents 2,2'-bipyridine (**bpy**) and 4,4'-dipyridyl (**dpy**) were purchased from Sigma-Aldrich, 4,4'-dimethyl-2,2'-bipyridine (**dmbpy**) was purchased from GFS Chemicals and used as received. All other reagents unless otherwise stated, were used as received from Sigma-Aldrich.

The characterisation data of all ligands and molecular components were recorded as ^{1}H ^{13}C, $^{13}C\{^{1}H\}$ or $^{31}P\{^{1}H\}$ NMR spectra on a Bruker NMR spectrometer at 400.162 MHz, 100.630 MHz and 161.994 MHz respectively. ^{1}H or ^{13}C chemical shifts (δ / ppm) are referenced to the residual solvent signal; ^{31}P δ are referenced externally to 85% H_3PO_4. For improved resolution of acidic compounds, a solution of NaOD (20% v/v) in D_2O as solvent was prepared. Absorption spectra were obtained using the Varian Cary 50 UV-Visible Spectrometer and emission spectra obtained on the Varian Eclipse UV-Fluorescence Spectrometer in the indicated solvents. Microanalyses were performed by Microanalytical Service, School of Molecular and Microbial Science, University of Queensland, Brisbane.

Electrochemical characterisation of molecular components was performed using a standard closed compartment three-electrode cell consisting of a carbon paste working and a platinum wire counter electrode referenced to a saturated calomel electrode (SCE) electrode. The electrolyte contained $LiClO_4$ (0.25 M or 0.5 M as indicated) at the stated pH. Potentiostatic control was provided by the EG & G Princeton Applied Research Model 272A Potentiostat/Galvanostat.

Discussion of Experimental Procedures

Ligand Precursors

Preparation of a bidentate ligand containing the stable phosphonate acidic moiety is outlined in Scheme 0-1. The synthetic preparation consists of six functional group transformations from commercially available reagents to give 4,4'-bis-phosphonate(methyl)-2,2'-bipyridine hydrate (**dmpbpy**) in a yield of 48%. Alternatively, the more soluble phosphonate ester, 4,4'-bis-diethylphosphonate(methyl)-2,2'-bipyridine (**dempbpy**), can be prepared in five steps with an overall yield of 53%.

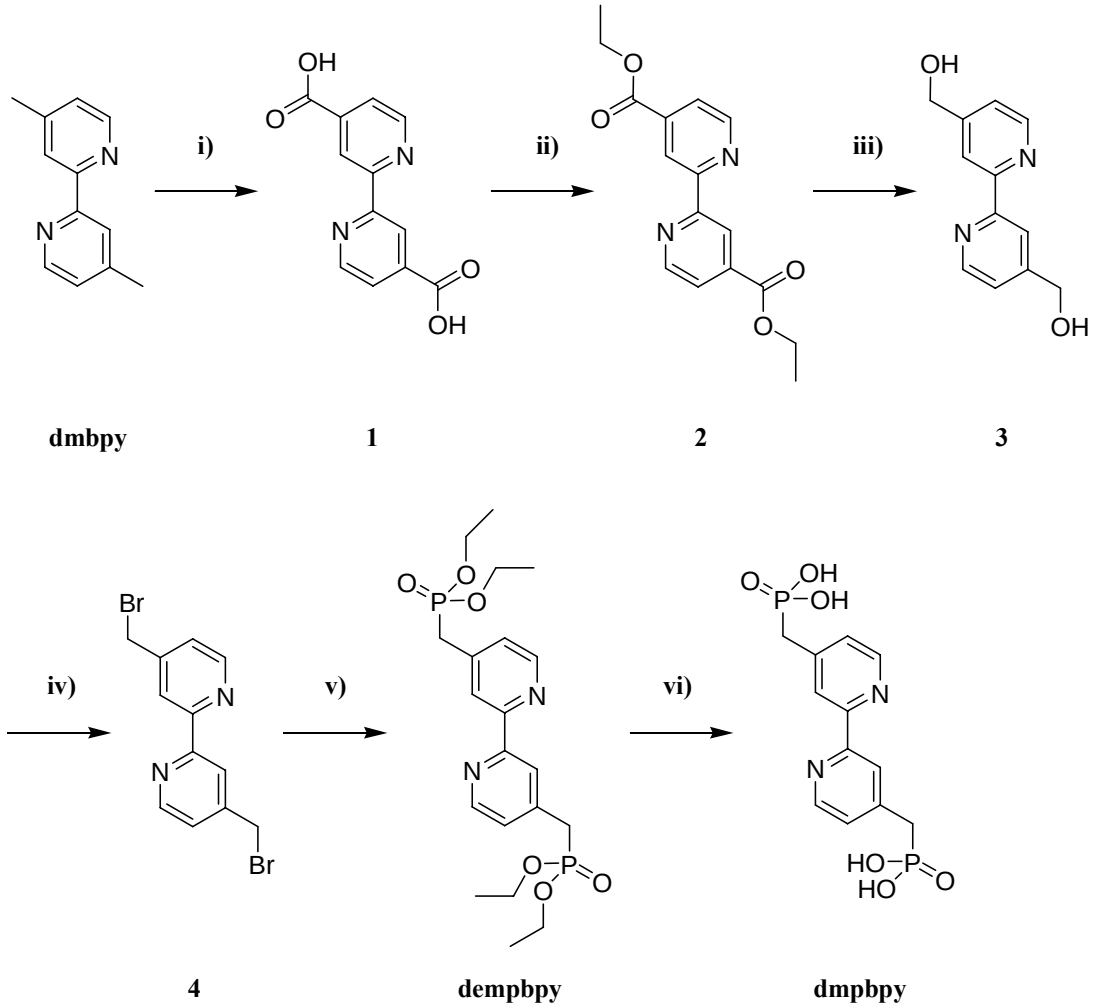

Scheme 0-1 – (i) K_2CrO_7/H_2SO_4, HNO_3 reflux 4 h; (ii) $EtOH/H_2SO_4$ (95:5 v/v) reflux 72 h; (iii) EtOH, $NaBH_4$, 50°C, 3 h; (iv) H_2SO_4/HBr (25:75 v/v), reflux 8 h; (v) $P(OEt)_3$, reflux 8 h; (vi) 20% HCl, reflux 18 h, 48% HBr, reflux 4 h.

Starting from commercially available 4,4'-dimethyl-2,2'-bipyridine, **1** was prepared by a method described by Oki and Morgan.[5]

4,4′-dicarboxy-2,2′-bipyridine (**1**)

To a stirring solution of **dmbpy** (10.99 g, 59.72 mmol) in H_2SO_4 (98%, 250 cm^3), $K_2Cr_2O_7$ (48.00 g, 163.0 mmol) was added in small portions such that the reaction temperature did not exceed 80°C. The reaction temperature was regulated between 70–80°C by cooling in a water bath. Following the addition, the reaction mixture was cooled to < 40°C before pouring over ice (1.60 dm^3) and cooling at 4°C overnight. The crude product was collected by vacuum filtration, air dried and further purified by refluxing in HNO_3 (50%, 340 cm^3) for 4 hours. The resulting solution was poured over an ice/water mixture (2.00 dm^3). The precipitate was collected by vacuum filtration, washed with water (5 × 100 cm^3), followed by $(CH_3)_2CO$ (2 × 40 cm^3). The powdered white product was air dried to give 13.91 g of **1** (95% yield).

^{1}H NMR (400 MHz, D_2O/NaOD, δ): 7.43 (d, J = 4.87 Hz, 2H) H_5, $H_{5'}$; 7.87 (s, 2H) H_3, $H_{3'}$; 8.31 (d, J = 4.87 Hz, 2H) H_6, $H_{6'}$.

Simple acid promoted esterification of **1** gave the fragrant ethyl ester **2** according to Elliot and Hershenhart.[260] Gradual cooling of the pale pink solution afforded needle shaped crystals identified by NMR spectroscopy as **2**. Esterification was confirmed by A_2B_3 spin coupling of proton resonances at 1.44 and 4.46 δ.

4,4′-diethoxycarbonyl-2,2′-bipyridine (**2**)

To a stirring suspension of **1** (7.5 g, 30.7 mmol) in dry absolute EtOH (900 cm^3) was added H_2SO_4 (98%, 8 cm^3). The suspension was refluxed for 72 hours, during which the white suspension changed to a pale pink solution. The solution was cooled to room temperature and further cooled at –24°C overnight. The resulting precipitate was isolated by vacuum filtration, washed with dry EtOH (3 × 50 cm^3) to yield 6.28 g of white needle crystals. The filtrate was further treated by neutralising with NaOH

(0.4M) and the white precipitate collected on a sintered glass frit. The precipitate was washed with dry EtOH (2 × 20 cm^3) before recrystallisation from a minimum of EtOH. The crystalline white product was combined to give 8.97 g of **2** (97% yield).

^{1}H NMR (400 MHz, $CDCl_3$, δ): 1.44 (t, J = 7.13 Hz, 6H) CH_3; 4.46 (q, J = 7.13 Hz, 4H) CH_2; 7.90 (dd, J = 4.96 Hz, 1.58 Hz, 2H) H_5, $H_{5'}$; 8.86 (d, J = 4.96 Hz, 0.68 Hz, 2H) H_3, $H_{3'}$; 8.95 (dd, J = 1.58 Hz, 0.68 Hz, 2H) H_6, $H_{6'}$.

Reduction of the ester, **2**, to a para substituted benzyl alcohol was possible under mild conditions using a procedure reported by Will.[7] The loss of the A_2B_3 spin system and occurrence of a methylene proton resonance at 4.85 δ confirmed the transformation to **3**. This analogue was observed to be stable for up to 12 months at room temperature.

4,4′-bis(hydroxymethyl)-2,2′-bipyridine (**3**)

To a stirring solution of **2** (6.0 g, 19.97 mmol) in dry absolute EtOH (300 cm^3), $NaBH_4$ (4.5 g, 119 mmol) was added. The vigorous reaction was allowed to stir for 30 minutes until all $NaBH_4$ had dissolved and then heated to 50°C for 3 hours. Following the reduction the reaction mixture was cooled to room temperature, H_2O (550 cm^3) was added and stirred overnight. The aqueous suspension was concentrated *in vacuo* to 500 cm^3 and extracted with ethyl acetate (6 × 250 cm^3). The organic extract was dried over $MgSO_4$ and evaporated to dryness to yield a bright white solid. Crystallisation from EtOH gave fine crystalline needles of **3** in a yield of 79% (3.43 g).

^{1}H NMR (400 MHz, $CDCl_3$, δ): 4.85 (s, 4H) CH_2OH; 7.37 (dd, J = 5.0 Hz, 0.6 Hz, 2H) H_5, $H_{5'}$; 8.39 (s, br, 2H) H_3, $H_{3'}$; 8.67 (m, unr, 2H) H_6, $H_{6'}$.

Bromination of **3** by HBr in the presence of H_2SO_4 afforded a reactive species, **4**, in high yield (85%). Modification of the procedure described by Will[7] through Gillaizeau-Gauthier *et al.*[8] gave a modest improvement in the yield. This was confirmed by the upfield shift in the methylene proton resonance to 4.49 δ and the increased solubility in organic solvents. Immediate work-up of the product is required as extended periods in aqueous solutions gave reduced yields. The additional treatment by dissolution in $CHCl_3$, filtering and removal of the solvent gave a compound of improved purity (by NMR). Storage of **3** at sub-ambient temperatures under an inert atmosphere was required if subsequent reaction was not performed.

4,4′-bis(bromomethyl)-2,2′-bipyridine (**4**)

To a stirring solution of **3** (3.37 g, 15.58 mmol) in H_2SO_4 (98%, 8.5 cm^3) was added HBr (48%, 25.5 cm^3) in small portions over several minutes. Care was taken in addition of HBr as the vigorous reaction saw the evolution of $HBr_{(g)}$ in high concentrations. The dark red solution was heated at reflux for 8 hours, cooled to room temperature and quenched with water (50 cm^3). The reaction mixture was neutralised with NaOH (0.4M) and the voluminous white precipitate collected by vacuum filtration. The product was washed with H_2O (neutral, 3 × 50 cm^3), air dried and dissolved in $CHCl_3$ (100 cm^3). The dark yellow solution was dried over anhydrous Na_2SO_4, filtered through a sintered glass frit and dried in vacuo to give 4.54 g of **4** (85% yield).

^{1}H NMR (400 MHz, $CDCl_3$, δ): 4.49 (s, 4H) CH_2Br; 7.36 (dd, J = 5.0 Hz, 1.7 Hz, 2H) H_5, $H_{5'}$; 8.44 (s, br, 2H) H_3, $H_{3'}$; 8.67 (d, br, J = 5.0 Hz, 2H) H_6, $H_{6'}$.

^{13}C NMR (100 MHz, $CDCl_3$, δ): 33.75 (CH_2Br); 121.29 (C_3, $C_{3'}$); 124.07 (C_5, $C_{5'}$); 147.64 (C_4, $C_{4'}$); 149.81 (C_2, $C_{2'}$); 155.21 (C_6, $C_{6'}$).

The diethyl phosphonate ester, **dempbpy**, was prepared by phosphonylation of the benzyl halide **4** via an S_N2 reaction as described by Yan and Hupp.[6] Successful purification of the reaction mixture by 'filtering' through a plug of silica gave deliquescent crystals. Isolation of this compound was confirmed by the emergence of an A_2B_3 spin coupling system in the proton spectrum and the increased up field shift of the methylene resonance to 3.24 δ which showed a distinct $^2J_{PH}$ of 22.3 Hz. The presence of equivalent pentavalent phosphines was substantiated by a single phosphorus resonance at 24.6 δ. The peak displayed second order peak asymmetry due to long range phosphorus coupling.[261] In addition there were distinct $^2J_{PC}$ values of 6.9 and 8.6 Hz for the methylene and aromatic carbons β to P=O and reduced $^3J_{PC}$ of ~5.5–6.8 Hz for the methyl and aromatic carbons γ to P=O. However, as in the proton spectrum, the obvious $^1J_{PC}$ for the methylene group of 137 Hz is the most distinct feature observed in the carbon spectrum. These observations are consistent with the literature.[6-8]

4,4′-bis-diethylphosphonate(methyl)-2,2′-bipyridine (**dempbpy**)

Triethylphosphite (40cm^3) was added to **3** (4.0 g, 11.69 mmol) and the neat solution refluxed at 150°C for 8 hours. The reaction mixture was cooled to room temperature and excess triethylphosphite distilled under high vacuum. The crude product was dissolved in a minimum of $CHCl_3$ and purified on silica gel (Aldrich 230–400 mesh) with ethyl acetate/MeOH (80/20 v/v) as eluent. Evaporation at room temperature gave 4.61 g of crystalline **dempbpy** (86 % yield).

^{1}H NMR (400 MHz, $CDCl_3$, δ): 1.27 (t, J = 7.07 Hz, 12H) CH_3; 3.24 (d, J = 22.27 Hz, 4H) CH_2P; 4.07 (apparent quintet, J = 7.07 Hz, 1.11 Hz, 8H) $POCH_2$; 7.34 (m, unr, 2H) H_5, $H_{5'}$; 8.37 (s, br, 2H) H_3, $H_{3'}$; 8.61 (d, J = 5.05 Hz, 2H) H_6, $H_{6'}$.

^{13}C NMR (100 MHz, $CDCl_3$, δ): 16.40 (d, J = 6.0 Hz, CH_3); 33.67 (d, J = 137.0 Hz, CH_2P); 62.46 (d, J = 6.7 Hz, $POCH_2$); 122.58 (d, J = 6.8 Hz, C_3, $C_{3'}$); 125.03 (d, J = 5.6 Hz, C_5, $C_{5'}$); 142.31 (d, J = 8.6 Hz, C_4, $C_{4'}$); 149.21 (d, J = 2.6 Hz, C_2, $C_{2'}$); 155.95 (d, J = 2.1 Hz, C_6, $C_{6'}$).

^{31}P NMR (162 MHz, $CDCl_3$, δ): 24.61, $CH_2PO_3CH_2CH_3$

The free acid, **dmpbpy**, was obtained by acid promoted hydrolysis in excess H_2O. The attempted isolation of this compound by *in vacuo* removal of the volatile components of the reaction mixture afforded a pale yellow oil that on the addition of H_2O afforded a 'dirty' precipitate. Under reflux the equilibrium concentration of HCl solutions is 20% v/v[262] and due to the extreme acidity of the free acid of the ligand, in excess of H_0 = –8, subsequent treatment in increased concentrations of H^+ is required. Solutions of 48% v/v HBr retain this acid halide content under reflux and treatment of the isolated oil in such a manner, followed by addition of H_2O, afforded the required acid ligand in almost quantitative yield. Gillaizeau-Gauthier *et al.* have also applied a similar technique for the complete hydrolysis of persistent ester derivatives in complexes incorporating phosphonate moieties.[8] Successful hydrolysis of the ester groups was confirmed by the loss of ethyl group resonances in the proton and carbon spectra. In addition, the upfield phosphorus resonance at 17 δ was consistent with pentavalent phosphonates of this type[261] and to those reported for similar structures.[8]

4,4′-bis-phosphonato(methyl)-2,2′-bipyridine hydrate (**dmpbpy**)

A stirring solution of **dempbpy** (1.40 g, 3.08 mmol) in HCl (20 %, 100 cm^3) was heated at reflux for 18 hours, cooled to room temperature and the solvent removed by rotary evaporation. The oily residue was dissolved in H_2O (20 cm^3) and the off-white precipitate collected via vacuum filtration. The crude product was dried in air, then under high vacuum before further hydrolysing in HBr (48%, 20 cm^3) for 4 hours. The solvent was removed *in vacuo* collecting residual HBr in a liquid N_2 trap. On addition of H_2O (100 cm^3) to the isolated compound, a voluminous white precipitate was afforded. The feather shaped crystals were collected by vacuum filtration, washed with H_2O (2 × 20 cm^3) then ether (2 × 20 cm^3) and dried under high vacuum to give 0.95g of **dmpbpy** (90% yield).

^{1}H NMR (400 MHz, D_2O/NaOD, δ): 2.18 (d, J = 20.0 Hz, 4H) CH_2P; 6.59 (d, br, J = 5.0 Hz, 2H) H_5, $H_{5'}$; 6.95 (s, br, 2H) H_3, $H_{3'}$; 7.67 (d, br, J = 5.0 Hz, 2H) H_6, $H_{6'}$.

^{13}C NMR (100 MHz, D_2O/NaOD, δ): 37.84 (d, J = 116.3 Hz, CH_2P); 122.92 (d, J = 3.8 Hz, C_3, $C_{3'}$); 125.28 (d, J = 2.5 Hz, C_5, $C_{5'}$); 148.38 (C_4, $C_{4'}$); 150.24 (d, J = 7.3 Hz, C_2, $C_{2'}$); 154.36 (d, J = 1.8 Hz, C_6, $C_{6'}$).

^{31}P NMR (162 MHz, D_2O/NaOD, δ): 16.96, $CH_2PO_3H_2$.

Calculated for $C_{12}H_{14}N_2O_6P_2 \cdot H_2O$: C, 39.79; H, 4.45; N, 7.73; Found C, 40.30; H, 4.15; N, 7.80.

Ruthenium Diimine Coordination Complexes

The stepwise addition of ligands derivatised with a functional anchoring group to the coordination sphere of $[Ru(bpy)_3]^{2+}$ type analogues is outlined in Scheme 0-2 – Scheme 0-5 with a representative spectral profile for the formation of these complexes depicted in Figure 0-3.

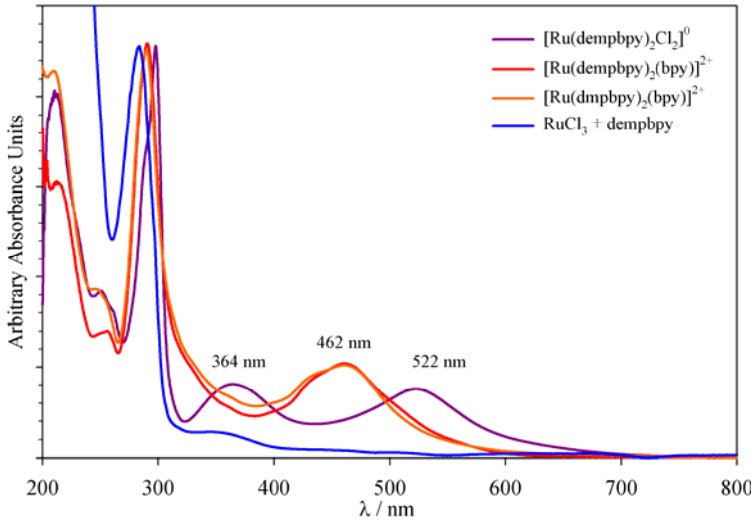

Figure 0-3 – The progression of optical absorption for the formation of tris-heteroleptic diimine complexes of ruthenium(II). All spectra were obtained in methanol and background corrected against solvent and cell absorbance.

The addition of a substituted ligand imparts a supramolecular function to the chromophore without greatly perturbing the ground or excited state properties.

The binding to inorganic surfaces by the peripheral functional groups is known to occur via a bridging acidic linkage, with only one ligand required in the coordination sphere to allow surface sensitisation. The addition of more than one binding ligand to the coordination sphere increases the probability of excited state quenching and would impart subtle variation in the optical properties of the complex.

From the commercially available "$RuCl_3.nH_2O$", dry $RuCl_3.3H_2O$ was prepared by heating in a muffle furnace at 120°C for 3 hours, grinding in a mortar and pestle to yield a fine powder, before returning to the furnace for a further 3 hours.[263] The $RuCl_3$ so prepared was stored at this temperature until required.

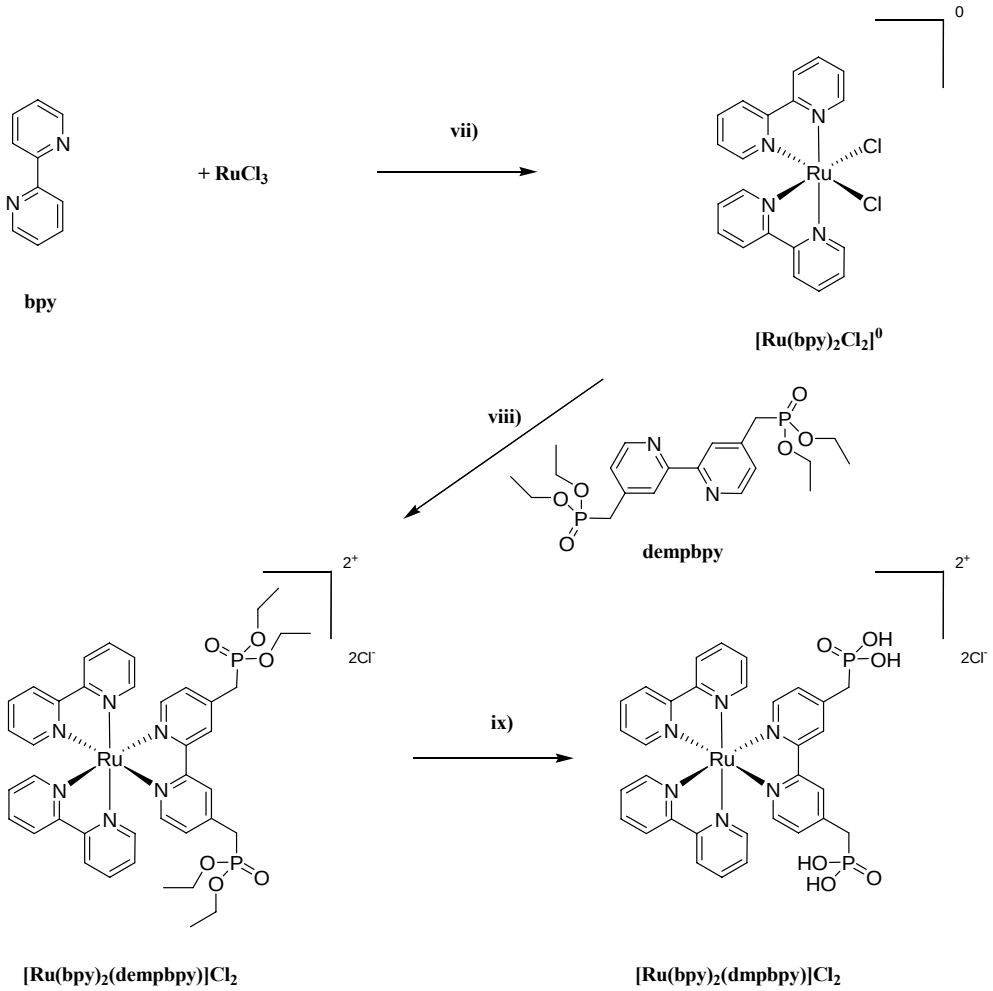

Scheme 0-2 – (vii) DMF, LiCl, 130°C, 6 h; (viii) MeOH, reflux 13 h; (ix) 20% HCl, reflux 16 h

The preparation of a tris-bipyridyl complex with a single bis-substituted phosphonate ligand in the coordination sphere was achieved according to a procedure developed in my previous studies.[264] The procedure is outlined in Scheme 0-2.

Dry $RuCl_3$ (above) was utilised in the procedure with the bis-bipyridine precursor prepared and purified according to Sullivan, Salmon and Meyer.[265]

cis-bis-(2,2′-bipyridine)dichlororuthenium(II) hydrate: **[Ru(bpy)$_2$Cl$_2$]**

Dry DMF (5 cm^3) was added to a Schlenk tube containing **bpy** (448 mg, 2.87 mmol), $RuCl_3$ hydrate (500 mg, 1.91 mmol) and LiCl (542 mg, 12.8 mmol). The solution was evacuated before backfilling with argon. Stirring vigorously, the reaction mixture was heated to reflux at 130°C for 6 hours. The reaction mixture was cooled, $(CH_3)_2CO$ (100 cm^3) was added and allowed stand at 4°C overnight. The deep red solution was filtered and the dark black/green microcrystalline solid washed with $(CH_3)_2CO/H_2O$ (90/10 v/v) until a clear filtrate was obtained. Further purification on silica gel [eluent $(CH_3)_2CO$ (40%):MeOH (30%):CH_2Cl_2 (30%)] gave 515 mg of **[Ru(bpy)$_2$Cl$_2$]** (55% yield).

Absorption (MeOH): λ_{max} = 509 nm ($\varepsilon_{509} = 8.3 \times 10^3$ $dm^3 \cdot mol^{-1} \cdot cm^{-1}$)
Emission (MeOH): λ_{max} = none

The addition of **dempbpy** to the coordination sphere was achieved in a relative high yield of 92%. Chelate ligand addition shows a loss of the LMCT band at 355 nm and shift in the MLCT band from 509 nm to a sharper band at 452 nm consistent with an increase in molecular symmetry. The compound showed significant fluorescence at 612 nm with the structure identified by ^{1}H NMR.

cis-bis-(2,2′-bipyridine)(4,4′-bis-diethylphosphonato(methyl)-2,2′-bipyridine)ruthenium(II) dichloride: **[Ru(bpy)$_2$(dempbpy)]Cl$_2$**

To a solution of **[Ru(bpy)$_2$Cl$_2$]** (106 mg, 0.218 mmol) in methanol (15 cm^3) was added **dempbpy** (150 mg, 0.33 mmol) and the mixture was refluxed for 13 hours. The progress of the reaction was monitored by UV-visible and fluorescence spectroscopy. Completion was determined to be the absence of peaks at 355 nm and 509 nm as well as the appearance of a single intense band at 452 nm. The compound also showed intense fluorescence at 612 nm. The reaction mixture was cooled to room temperature and the solvent removed on a rotary evaporator. The crude product was dissolved in MeOH (2 cm^3), pre-treated by syringe filtration (Teflon, 40 μm) and loaded onto Sephadex LH–20 gel (glass column 2.5 cm × 30 cm, porous glass frit). Elution with MeOH, collection of the major orange band and slow evaporation on a rotary evaporator gave 192 mg of **[Ru(bpy)$_2$(dempbpy)]Cl$_2$** (92% yield) as a hygroscopic dark orange solid.

^{1}H NMR (400 MHz, D_2O, δ): 1.27 (m, unr) CH_3; 3.57 (d, J = 22 Hz, 4H) CH_2P; 4.13 (m, 4H) $POCH_2$; 7.48 (m, unr, 6H); 7.66 (m, unr, 2H); 7.73–7.90 (m, unr, 6H); 8.13 (m, unr, 2H); 8.45 (s, br, 1H); 8.66 (s, br, 1H), 8.72 (d, unr, 4H).

Hydrolysis of the esterified ligand in 20% HCl gave the target compound **[Ru(bpy)$_2$(dempbpy)]Cl$_2$** in high (97%) yield. The ^{31}P spectrum confirmed a single resonance for phosphorus due to the presence of the phosphonated ligand. Coupling of the methylene protons in the ^{1}H spectrum was indicative of $^{2}J_{PH}$ with assignments consistent with that of an analogous complex reported in the literature.[8]

cis-bis-(2,2′-bipyridine)(4,4′-bis-phosphonato(methyl)-2,2′-bipyridine)ruthenium(II) dichloride: **[Ru(bpy)$_2$(dmpbpy)]Cl$_2$**

Cold HCl (20%, 30 cm^3) was added to **[Ru(bpy)$_2$(dempbpy)]Cl$_2$** (140 mg, 0.149 mmol) and the solution refluxed for 16 hours, cooled to room temperature before evaporating to dryness on a rotary evaporator. The crude product was further dried under high vacuum (90°C, 5 hours) to give 117 mg of **[Ru(bpy)$_2$(dmpbpy)]Cl$_2$** as a dark orange hygroscopic solid (97% yield).

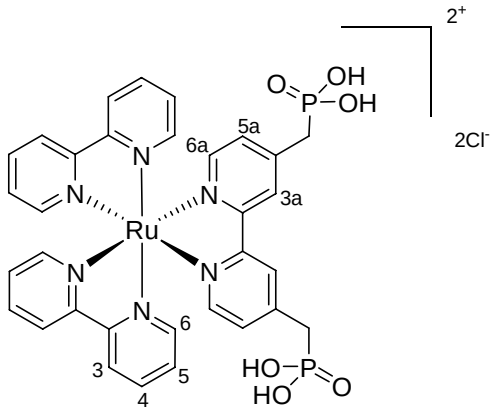

^{1}H NMR (400 MHz, D_2O, δ): 2.84 (d, J = 20 Hz, 4H) CH_2P; 7.04 (m, unr, 2H) H_{5a}, $H_{5a'}$; 7.16 (m, unr, 4H) H_5, $H_{5'}$; 7.28 (m, unr, 1H) $H_{6a'}$; 7.41 (m, unr, 2H) $H_{4'}$; 7.54 (m, unr, 1H) H_{6a}; 7.64 (m, unr, 2H) $H_{6'}$; 7.77 (m, unr, 2H) H_6; 7.84 (m, unr, 2H) H_4; 8.22 (s, br, 2H) H_{3a}; 8.33 (m, unr, 4H) H_3.

^{31}P NMR (162 MHz, D_2O, δ): 15.19, $CH_2PO_3H_2$.

Calculated for $RuC_{32}H_{30}N_6O_6Cl_2P_2{\cdot}9H_2O$: C, 38.80; H, 4.88; N, 8.48; Found C, 38.33; H, 4.12; N, 7.99.

Absorption (MeOH): λ_{max} = 455 nm (ε_{455} = 13.1 × 10^3 dm^3·mol^{-1}·cm^{-1})

Emission (MeOH): λ_{max} = 612 nm

The double substitution of a bis-substituted phosphonate ligand in the coordination sphere is outlined in **Scheme 0-3**.

Following a procedure reported by Will *et al*.[7] the bis-phosphonated *cis*-bis analogue was prepared. The procedure was adapted by the use of a freeze/thaw/degassed and sealed Schlenk tube as opposed to continuous stream of N_2. The formation of **[Ru(dempbpy)$_2$Cl$_2$]** was confirmed by UV-visible and emission spectroscopy as well as ^{1}H NMR that showed the distinct pattern of *cis*-coordinated ligand resonances consistent with literature. Coordination induced shift (CIS) of the aliphatic and aromatic resonances as well as an increased upfield shift for resonances of protons *cis* to Cl^- gave a spectrum consistent with reports of similar cis coordinated complexes.[223,266] The assignment of ^{13}C and ^{31}P spectra with similar CIS shifts compared to free **dempbpy** further supported a *cis* coordination complex with in-equivalent pyridyl fragments.

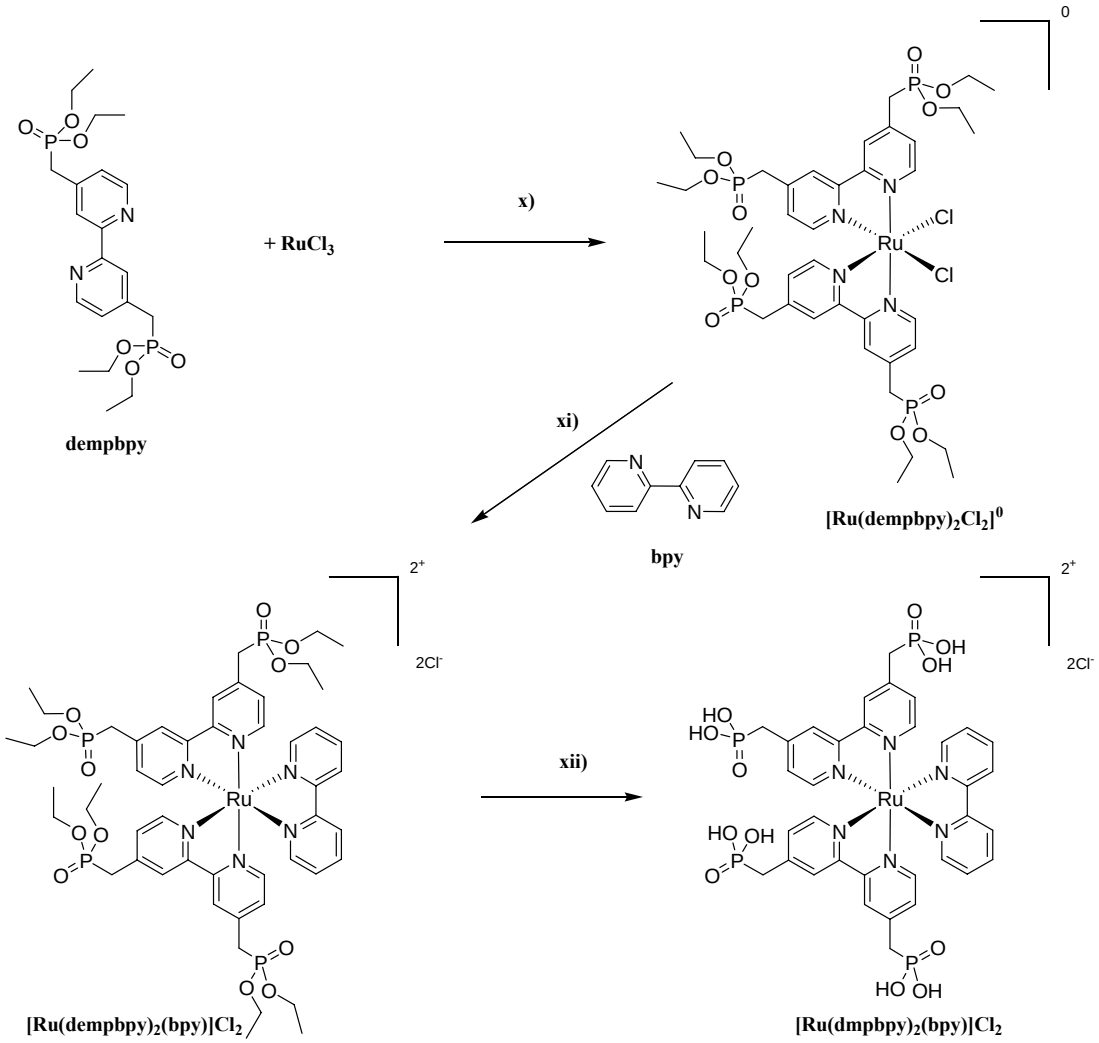

Scheme 0-3 – (x) DMF, LiCl, 140°C, 8 h; (xi) MeOH, reflux 22 h; (xii) 20% HCl, reflux 16 h

cis-bis-(4,4′-bis-diethylphosphonato(methyl)-2,2′-bipyridine)dichlororuthenium(II):
[Ru(dempbpy)$_2$Cl$_2$]

To a Schlenk tube containing **dempbpy** (400 mg, 0.88 mmol) and $RuCl_3$ hydrate (116 mg, 0.44 mmol) was added dry DMF (15 cm^3). Following 4 × freeze/thaw cycles on a vacuum manifold, the Schlenk tube was sealed under argon and the stirring solution heated to reflux at 120°C for 8 hours. The reaction mixture was cooled, poured over $(CH_3)_2CO$ (250 cm^3) and allowed stand at –25°C overnight. The deep purple supernatant solution was filtered and the tris-bipyridyl impurity collected on a sintered glass frit as a deep red microcrystalline solid (81 mg). The filtrate was then concentrated to ~2 cm^3 under high vacuum distillation and purified on a 10 cm plug of silica gel [gradient elution MeOH:$(CH_3)_2CO$ from 20:80 to 50:50]. The deep purple fractions were collected and filtered through a micropore syringe (Teflon, 40 μm) and the complex precipitated by the addition of diethyl ether (250 cm^3). The supernatant was removed and the solid washed several times with fresh ether. Evaporation of the final ethereal wash at room temperature gave a dark purple microcrystalline solid, 170 mg of **[Ru(dempbpy)$_2$Cl$_2$]** (36% yield).

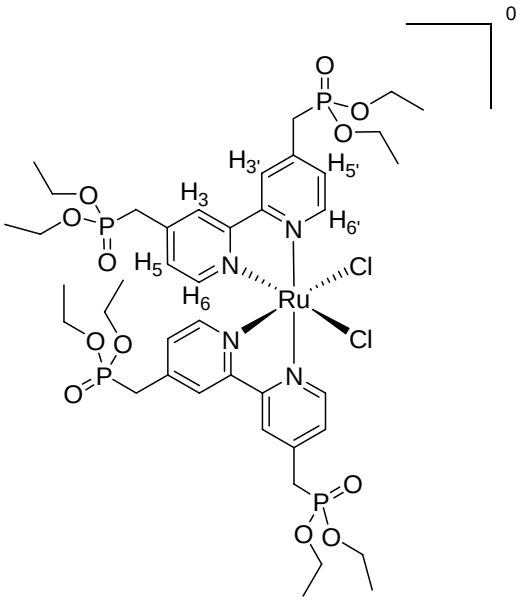

^{1}H NMR (400 MHz, D_2O, δ): 1.12 (dt, J = 7.0 Hz, J = 3.79 Hz 12H) CH_3; 1.29 (dt, J = 7.0 Hz, J = 3.5 Hz 12H) CH_3; 3.29 (d, J = 22.6 Hz, 4H) CH_2P; 3.55 (d, J = 22.6 Hz, 4H) CH_2P; 3.96 (m, unr, 8H) $POCH_2$; 4.14 (m, unr, 8H) $POCH_2$; 6.95 (d, J = 5.8 Hz, 2H) H_5; 7.47 (d, J = 5.8 Hz, 2H) H_6; 7.62 (d, J = 5.8 Hz, 2H) $H_{5'}$; 8.24 (s, br, 2H) H_3; 8.40 (s, br, 2H) $H_{3'}$; 9.87 (d, J = 5.8 Hz, 2H) $H_{6'}$.

^{13}C NMR (100 MHz, D_2O, δ): 16.65 (d, J = 5.8 Hz, CH_3); 16.82 (d, J = 5.8 Hz, CH_3); 33.54 (d, J = 136.0 Hz, CH_2P); 33.02 (d, J = 136.0 Hz, CH_2P); 64.13 (d, J = 5.6 Hz, $POCH_2$); 64.32 (d, J = 5.6 Hz, $POCH_2$); 125.55 (unr, C_3, $C_{3'}$); 128.38 (unr, C_5, $C_{5'}$); 142.51 (d, J = 9.1 Hz, C_4, $C_{4'}$); 143.72 (d, J = 9.1 Hz, C_4, $C_{4'}$); 144.42 (d, J = 9.1 Hz, C_4, $C_{4'}$); 154.04 (d, J = 2.3 Hz, C_2, $C_{2'}$); 154.33 (d, J = 3.3 Hz, C_2, $C_{2'}$); 154.45 (d, J = 2.6 Hz, C_2, $C_{2'}$); 154.70 (d, J = 2.6 Hz, C_2, $C_{2'}$); 159.37 (d, J = 2.7 Hz, C_6, $C_{6'}$); 159.47 (d, J = 2.7 Hz, C_6, $C_{6'}$); 159.69 (d, J = 2.7 Hz, C_6, $C_{6'}$); 159.94 (d, J = 2.7 Hz, C_6, $C_{6'}$).

^{31}P NMR (162 MHz, D_2O, δ): 25.94, 26.43

Calculated for $RuC_{40}H_{60}N_4O_{12}Cl_2P_4 \cdot 7H_2O$: C, 39.68; H, 6.16; N, 4.63; Found C, 39.57; H, 5.19; N, 4.85.

Absorption (MeOH): λ_{max} = 364 nm ($\varepsilon_{364} = 10.8 \times 10^3$ $dm^3 \cdot mol^{-1} \cdot cm^{-1}$)
522 nm ($\varepsilon_{522} = 10.3 \times 10^3$ $dm^3 \cdot mol^{-1} \cdot cm^{-1}$)

Emission (MeOH): λ_{max} = none

Chelation of an additional **bpy** ligand to **[Ru(dempbpy)$_2$Cl$_2$]** showed a loss of the LMCT at 364 nm and a shift in the MLCT from 522 nm to an intense band at 460 nm. The inclusion of **bpy** in the structure and no loss of **dempbpy** were confirmed by ^{1}H and ^{13}P NMR. Hydrolysis of this compound in 20% HCl gave a product consistent with tris-bipyridyl coordination as confirmed by ^{1}H, ^{13}P NMR and optical spectroscopy. Interestingly, close examination and comparison of the optical absorption spectra (Figure 0-3) for **[Ru(dempbpy)$_2$(bpy)]Cl$_2$** and **[Ru(dmpbpy)$_2$(bpy)]Cl$_2$** show a broadening of the MLCT which indicates increased aggregation of the compound in solution even under quite dilute conditions. This may well be a contributing factor in difficulties observed with obtaining and resolving NMR resonances.

cis-bis-(4,4′-bis-diethylphosphonato(methyl)-2,2′-bipyridine)(2,2′-bipyridine)ruthenium(II) dichloride: **[Ru(dempbpy)$_2$(bpy)]Cl$_2$**

[Ru(dempbpy)$_2$Cl$_2$] (35 mg, 0.0289 mmol) and **bpy** (6 mg, 0.0354 mmol) were dissolved in methanol (10 cm^3) and refluxed for 4 hours. Monitoring reaction progress by UV-visible and fluorescence spectroscopy saw the loss of peaks at 364 nm and 522 nm due to the presence of **[Ru(dempbpy)$_2$Cl$_2$]** and the appearance of an intense band at 460 nm. Excitation at this new charge transfer band gave a strong fluorescence signal. The reaction mixture was cooled and the solvent reduced before the addition of $(CH_3)_2CO$ (100 cm^3). The mixture was allowed stand at –25°C overnight and the precipitate collected on a sintered glass frit. The crude product was dissolved in a minimum of MeOH and purified on Sephadex LH–20 as described for **[Ru(bpy)$_2$(dmpbpy)]Cl$_2$**. The first major orange fraction was collected, concentrated and the precipitate collected. The resultant precipitate was washed with $(CH_3)_2CO$ followed by ether before drying at room temperature. Further drying under high vacuum gave 32 mg of **[Ru(dempbpy)$_2$(bpy)]Cl$_2$** as a dark red/brown solid (84% yield).

^{31}P NMR (162 MHz, D_2O, δ): 36.5, 36.8

Calculated for $RuC_{50}H_{68}N_6O_{12}Cl_2P_4 \cdot 5H_2O$: C, 45.12; H, 5.91; N, 6.31; Found C, 44.80; H, 5.66; N, 6.40.

Absorption (MeOH): λ_{max} = 460 nm ($\varepsilon_{460} = 18.5 \times 10^3$ dm^3·mol^{-1}·cm^{-1})
Emission (MeOH): λ_{max} = 620 nm

cis-bis-(4,4′-bis-phosphonato(methyl)-2,2′-bipyridine)(2,2′-bipyridine)ruthenium(II) dichloride: **[Ru(dmpbpy)$_2$(bpy)]Cl$_2$**

A solution of **[Ru(dempbpy)$_2$(bpy)]Cl$_2$** (20 mg, 0.0150 mmol) dissolved in cold HCl (20%, 15 cm^3) was refluxed for 16 hours. The solvent was removed under vacuum and the residue purified on Sephadex LH–20. The crude product was dissolved in methanolic tetra-*n*-butyl ammonium hydroxide (TBAOH) (2 cm^3) and purified on Sephadex LH–20 with MeOH as the eluent. The first major orange fraction was collected, concentrated and a precipitate obtained by the addition of methanolic HCl (0.1M). The resultant precipitate was washed with $(CH_3)_2CO$ followed by ether before drying at room temperature. The complex was further purified by successive two-solvent recrystallisation from MeOH/$(CH_3)_2CO$ to give 16 mg of **[Ru(dmpbpy)$_2$(bpy)]Cl$_2$** as a dark orange/red product (78% yield).

^{1}H NMR (400 MHz, D_2O/NaOD, δ): [0.74 (t, unr, 12H) CH_3; 1.16 (m, unr, 8H) CH_2; 1.44 (m, unr, 8H) CH_2; 2.99 (m, unr, 8H) CH_2]TBA$^+$; 2.81 (d, J = 19.4 Hz, 8H) CH_2P; 7.01 (m, unr, 4H) H_5, $H_{5'}$; 7.13 (m, unr, 2H) H_{5a}, $H_{5a'}$; 7.38 (m, unr, 2H) H_{6a}, $H_{6a'}$; 7.50 (m, unr, 2H) H_{4a}, $H_{4a'}$; 7.76 (m, br, unr, 4H); H_6; 8.18 (s, br, 4H) H_3; 8.27 (m, unr, 2H) H_{3a}.

^{31}P NMR (162 MHz, D_2O, δ): 15.4 (br)

Calculated for (TBA$^+$)[Ru(dmpbpy$^-$)(dmpbpy)(bpy)]Cl$_2$·6H$_2$O

$RuC_{50}H_{71}N_7O_{12}Cl_2P_4$·6H$_2$O: C, 43.96; H, 6.12; N, 7.18;
Found C, 43.68; H, 5.22; N, 7.43

Absorption (MeOH): λ_{max} = 462 nm ($\varepsilon_{462} = 15.9 \times 10^3$ dm^3·mol^{-1}·cm^{-1})
Emission (MeOH): λ_{max} = 617 nm

The specific formation of a tris-substituted coordination sphere with functionalised acid ligands was not required as the desired complex was isolated as an impurity from the preparation of **[Ru(dempbpy)$_2$Cl$_2$]**. The hydrolysis of the esterified complexes to the respective acid analogues is outlined in Scheme 0-4.

Formation and isolation of **[Ru(dempbpy)$_2$Cl$_2$]** in the above procedure gave a 60:40 mixture of the bis and tris analogues. Although not utilised in any further studies, **[Ru(dempbpy)$_2$Cl$_2$]** was hydrolysed to its acid analogue which was confirmed by ^{1}H and ^{31}P NMR as well as by absorption and emission properties. Similarly, the isolated co-product **[Ru(dempbpy)$_3$]$^{2+}$** was hydrolysed under standard acidic conditions with the product confirmed to be **[Ru(dmpbpy)$_3$]$^{2+}$** by ^{1}H, ^{31}P NMR and absorption and emission spectroscopy. The much simplified proton spectrum shows only three resonances in the aromatic region in comparison to the earlier encountered complexes due to increased symmetry of **[Ru(dmpbpy)$_3$]$^{2+}$**.

cis-bis-(4,4′-bis-phosphonato(methyl)-2,2′-bipyridine)dichlororuthenium(II): **[Ru(dmpbpy)$_2$Cl$_2$]**

Cold HCl (20%, 30cm^3) was added to a flask containing **[Ru(dempbpy)$_2$Cl$_2$]** (124 mg, 0.102 mmol) and the solution refluxed for 16 hours, cooled to room temperature before evaporating to dryness on a rotary evaporator. The crude compound was purified by gel permeation on Sephadex LH-20 as described for **[Ru(dmpbpy)$_2$(bpy)]Cl$_2$**. The main purple band was collected, concentrated to ~5cm^3 and pH lowered to 3 with HCl (0.05M methanolic solution). $(CH_3)_2CO$ (50cm^3) was added and the precipitate was washed with $(CH_3)_2CO$ (20cm^3), then ether (2 × 20cm^3) and the dark purple complex dried under vacuum (90°C, 5 hours) to give 28 mg of **[Ru(dmpbpy)$_2$Cl$_2$]** as a dark purple solid (26% yield).

^{31}P NMR (162 MHz, D_2O/NaOD, δ): 6.42 (br)

Calculated for $RuC_{24}H_{28}N_4O_{12}Cl_2P_4 \cdot 4H_2O$: C, 30.91; H, 3.89; N, 6.01; Found C, 30.47; H, 3.54; N, 5.77.

Absorption (H_2O): λ_{max} = 350 nm ($\varepsilon_{350} = 10.2 \times 10^3$ dm^3·mol^{-1}·cm^{-1})
497 nm ($\varepsilon_{497} = 7.32 \times 10^3$ dm^3·mol^{-1}·cm^{-1})

Emission (H_2O): λ_{max} = none

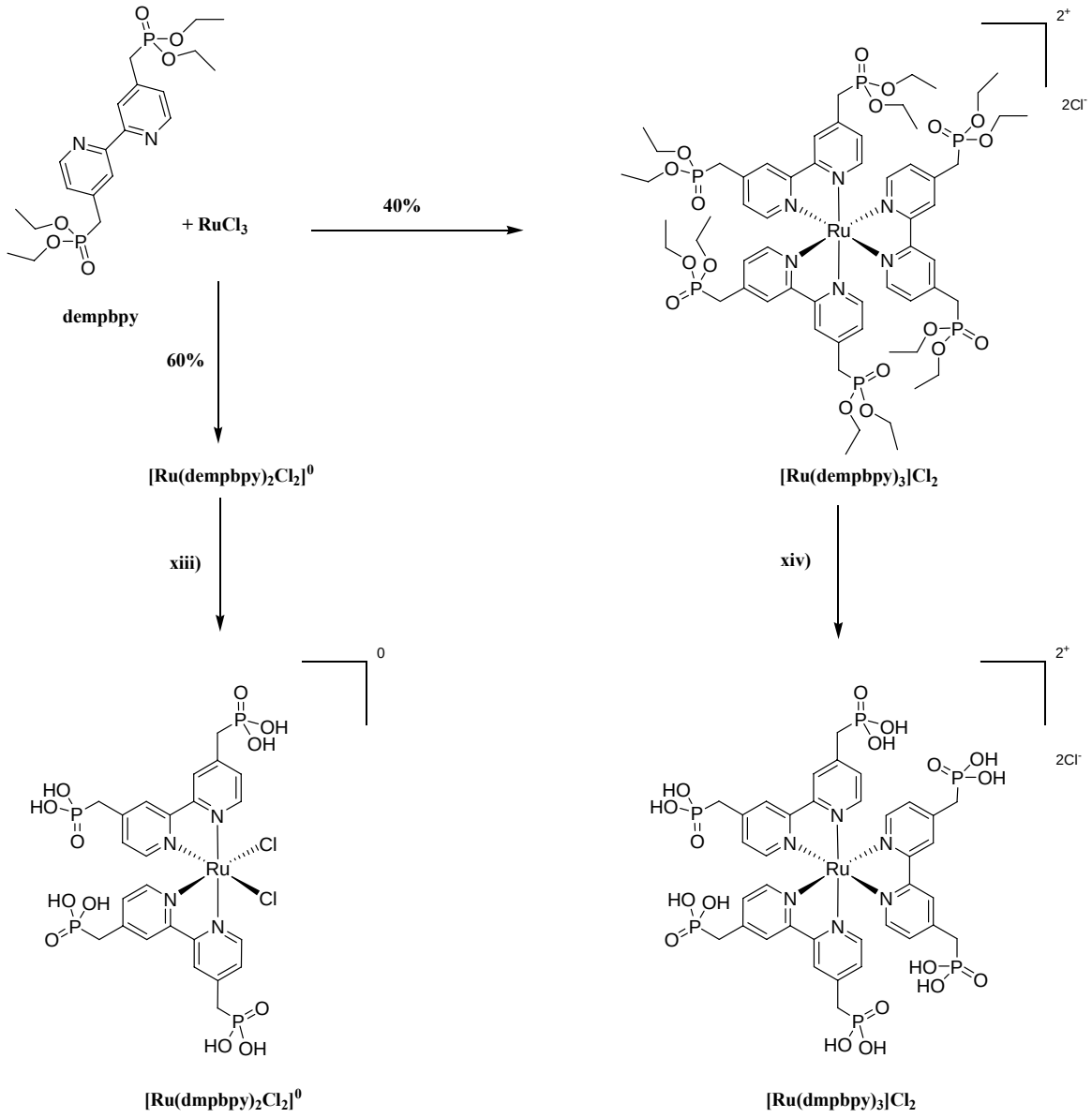

Scheme 0-4 – (xiii) and (xiv) 20 % HCl, reflux 48 h

tris-(4,4′-bis-phosphonato(methyl)-2,2′-bipyridine)ruthenium(II) dichloride:
[Ru(dmpbpy)$_3$]Cl$_2$

Cold HCl (20%, 30cm^3) was added to **[Ru(dempbpy)$_3$]Cl$_2$** (81 mg crude, 0.053 mmol) and the solution was refluxed for 16 hours, cooled to room temperature before evaporating to dryness on a rotary evaporator. Purification of the crude complex by dissolution in TBAOH solution and elution on a Sephadex LH-20 column as described for **[Ru(dmpbpy)$_2$(bpy)]Cl$_2$** gave 42 mg of **[Ru(dmpbpy)$_3$]Cl$_2$** as a deep orange hygroscopic solid (58% yield).

^{1}H NMR (400 MHz, D_2O/NaOD, δ): 2.38 (d, J = 19.2 Hz, 12H) CH_2P; 6.56 (m, unr, 6H) H_5, $H_{5'}$; 7.04 (m, unr, 6H) H_6, $H_{6'}$; 7.74 (m, unr, 6H) H_3, $H_{3'}$.

^{31}P NMR (162 MHz, D_2O/NaOD, δ): 16.7

Calculated for $RuC_{36}H_{42}N_6O_{18}Cl_2P_6 \cdot 9H_2O$: C, 31.64; H, 4.42; N, 6.15; Found C, 31.63; H, 3.59; N, 6.24.

Absorption (H_2O): λ_{max} = 467 nm ($\varepsilon_{467} = 12.8 \times 10^3$ dm^3·mol^{-1}·cm^{-1})
Emission (H_2O): λ_{max} = 627 nm

The difficulty in obtaining high purity compounds and NMR spectra that contain a single species has been discussed with other researchers in this field. A personal communication with Professor Alan Williams (University of Geneva) regarding carboxylate complexes revealed that obtaining spectra requires quite basic conditions to limit broadening due to acidic proton. He also indicated the possibility of oxidation to Ru(III) (a paramagnetic species) under these conditions may also affect spectral acquisition.[267] In another personal communication with Professor Fabrice Odobel (University of Nantes) in specific reference to phosphonate complexes was less encouraging.[268] This group is responsible for the preparation of bis-bipyridine Ru(II) complexes that contain a phosphonate group bound directly to the bipyridine ring.[223] He described difficulties in purification and in obtaining resolved peaks in the NMR. Sufficient deprotonation of the acid group is required to obtain the

spectrum of a ‘single’ species in solution. Difficulties are encountered due to the pKa of the acid where a relatively large concentration of NaOD is required to remove the exchangeable proton fully. This factor is worsened by the increased number of ligands with phosphonate groups in the coordination sphere where obtaining a ‘clean’ spectrum is quite problematic.

Spectral acquisition under these conditions has a number of negative effects as highly basic solutions affect substituents of ligands in the complex and as well as the signal-to-noise of the spectrum due to the much higher concentrations of H_2O in the solution. Watergate gradient solvent suppression was employed as a means of editing the resonance for water at 4.69 ppm; the spectrum is improved, however, due to the coincidence of peaks in this region there is a loss of signal for some proton resonances. The effect of highly basic solvent conditions was identified when obtaining spectra of the free acid ligand in D_2O/NaOD. Immediate acquisition of a spectrum gave the expected doublet resonance for the methylene group and three resonances in the aromatic region. When left to acquire overnight, the corresponding ^1H spectrum showed a distinct *absence* of the methylene resonance however the three resonances in the aromatic region indicative of 4′ substitution were still evident. This indicates that some form of proton exchange occurs to the methylene phosphonate group at the 4′ position. Hence, acquisition in highly basic conditions is not favourable with the consequence of using a less basic media being decreased solubility, the possibility of multiple species and a decreased signal-to-noise. Also, as noted above, aggregation of free-acid complexes can lead to further broadening of the spectrum.

Phosphonate Paraquat Sensitiser

Preparation of the target compound utilised a reported reaction scheme[9] and my previously reported reaction methodologies.[264] Scheme 0-5 depicts the procedure utilised for the preparation of the electron relay component, **EVP**.

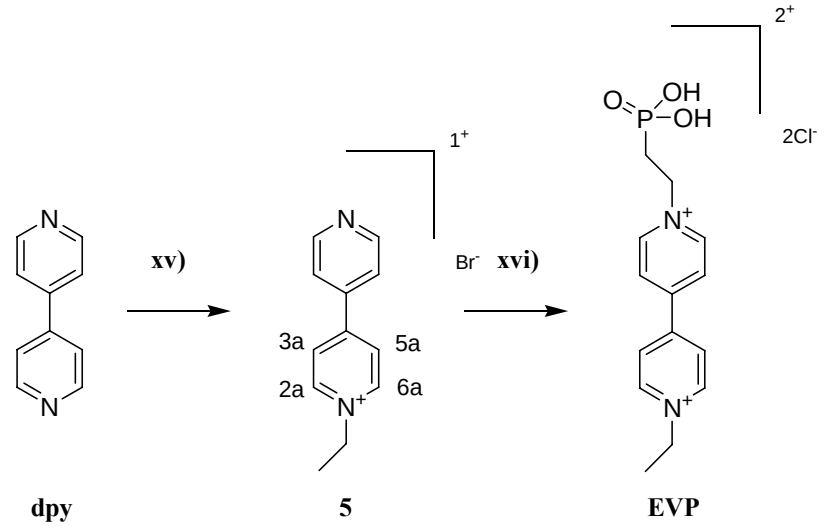

Scheme 0-5 – (xv) Toluene, bromoethane, reflux 4 h; excess bromoethane, reflux 20 h; (xvi) H_2O, $PO(OEt)_2EtBr$, reflux 48 h; 32 % HCl, reflux 48 h

1-ethyl-4,4′-bipyridinium bromide (**5**)

Bromoethane (15.5 cm^3, 97.3 mmol) and **dpy** (10.0 g, 64.1 mmol) were dissolved in toluene (125 cm^3). The vigorously stirred solution was refluxed at 115°C for 4 hours before an excess of bromoethane (35.0 cm^3) was added. Reflux was continued for a further 20 hours. The reaction mixture was cooled and standing at room temperature afforded a pale yellow precipitate. This was isolated via vacuum filtration, washed with toluene (3 × 50 cm^3) and air dried to yield 9.86 g (44%) of **5** as a pale yellow salt.

^{1}H NMR (400 MHz, D_2O, δ): 1.72 (t, J = 7.38 Hz, 3H) CH_3; 4.74 (q, J = 7.38 Hz, 2H) $^+NCH_2CH_3$; 7.88 (dd, J = 4.62 Hz, 1.75 Hz, 2H) $H_{3,5}$; 8.39 (dd, J = 6.80 Hz, 4.62 Hz, 2H) $H_{3a,5a}$; 8.72 (dd, J = 4.62 Hz, 1.75 Hz, 2H) $H_{2,6}$; 9.01 (dd, J = 6.80 Hz, 4.62 Hz, 2H) $H_{2a,6a}$.

1-ethyl-1′-(2-phosphonoethyl)-4,4′-bipyridinium dichloride (**EVP**)

An aqueous solution of **5** (5.86 g, 15.4 mmol) and diethylbromoethyl phosphonate (4.35 cm^3, 23.9 mmol) in H_2O (40 cm^3) was refluxed for 48 hours. Concentrated HCl (40 cm^3) was added to the reaction mixture and reflux continued for a further 48 hours. The reaction mixture was cooled to room temperature and the addition of acetone (250 cm^3) afforded a white precipitate. The compound was isolated by vacuum filtration, washed with toluene (3 × 20 cm^3), EtOH (3 × 20 cm^3) and $(CH_3)_2CO$ (3 × 20 cm^3) and allowed to air dry. The precipitate was recrystallised from aqueous EtOH to yield 4.48 g (80%) of **EVP** as a fine white powder.

^{1}H NMR (400 MHz, DMSO-d_6, δ): 1.58 (t, J = 7.28 Hz, 3H) CH_3; 2.45 (m, unr, 2H) CH_2P; 4.73 (q, J = 7.28 Hz, 2H) $^+NCH_2CH_3$; 4.90 (m, unr, 2H) $^+NCH_2CH_2P$; 8.84 (m, unr, 4H) $H_{3,5}$, $H_{3a,5a}$; 9.46 (m, unr, 4H) $H_{2,6}$, $H_{2a,6a}$.

^{13}C NMR (100 MHz, D_2O, δ): 16.21 CH_3; 29.83 (d, J = 132.98 Hz) CH_2P; 58.16 CH_2CH_2; 58.31 CH_2; 127.58 C_{3a}, C_{5a}; 127.65 C_3, C_5; 145.85 C_{2a}, C_{6a}; 146.31 C_2, C_6; 150.55 C_{4a}; 151.11 C_4.

^{31}P NMR (162 MHz, D_2O, δ): 19.06

Conclusions

The synthesis of molecular components for subsequent applications has been discussed.

Preparation of bidentate ligands as chelation agents that incorporate an acidic functional group, specifically **dmpbpy**, was achieved in six steps with a modest yield of 48%. The incorporation of this ligand within the coordination sphere of Ru(II) complexes imparts an adsorption function to this versatile chromophore. Stepwise addition of ligands to the coordination sphere allowed the assembly of a supramolecular complex with multiple acidic ligands, and hence multiple electron pathways.

Complexes were prepared from the soluble ester of **dmpbpy**, **dempbpy**, which gave compounds in moderate yields, yet were rather hygroscopic and prone to hydrolysis. The difficulties in purification and identification of acidic analogues of these complexes were highlighted and reasoning was proposed for unresolvable NMR resonances due to multiple solution species.

A second type of molecular sensitiser, an electron relay moiety, with an acidic functional group was prepared in modest yield. The synthesis of **EVP** was achieved in two steps and an overall yield of 35%.

The adsorption of these molecular components to a metal oxide semiconductor to form a heterosupramolecular assembly and the investigation of the formed systems will be presented in Chapters 6–8.

CHAPTER 4

Density-Functional Analysis of the Electronic Structure of Tris-Bipyridyl Ru(II) Sensitisers

Introduction

The idealogical goal of achieving efficient solar energy conversion has been enhanced in recent years by the report of O'Regan and Grätzel of a dye-sensitised solar cell (DSC) as a cost effective alternative to silicon-based photovoltaic devices.[2] The DSC, a type of photoelectrochemical cell (PEC), consists of a molecular surface sensitiser and a metal oxide semiconductor as a light absorption antenna and electrical conductor. The spectral overlap of the sensitiser with the terrestrial electromagnetic spectrum has a direct relationship to the PEC device's efficiency and hence there has been considerable discussion in the literature as to choice of surface sensitisers for application in PEC cells. This has normally been through experimental application of such molecular sensitisers until a suitable compound is identified.[220,221,269] The most efficient of these reported to date has been a d^6 Ru(II) coordination complex; namely *cis*-bis-(4,4′-dicarboxylato-2,2′-bipyridine)diisothiocyanatoruthenium(II), or as abbreviated in the literature, the N3 dye.[54]

Substantial electron donation to the Ru(II) t_{2g} orbitals in the ground state is afforded by the *cis*-bis isothiocyanate ligands; lowering the energy required to traverse the HOMO-LUMO gap. The 'back-bonding' effect of coordinated electron donating ligands and the *cis* coordination of π-acceptor ligands (bipyridine) that are lower in energy than the metal centre afford an intense metal-to-ligand-charge-transfer (MLCT) that occurs as a broad spectral band extending over a wide range of the visible region. The charge transfer and subsequent electron injection to a semiconductor substrate occur via a carboxylate linkage at the periphery of the bipyridine ligand. The efficiency of this class of sensitisers is attributed to a cascade of electron density from excitation to injection to the surface with electronic charge transferred due to the inherent potential energy difference between the ligand and the surface.[33] Essentially, electronic charge 'flows' from the sensitiser to the surface unimpeded, which has been attributed to the complementary energy overlap of the surface-linkage-ligand afforded by the carboxylate moiety.

Several groups have studied the lower energy transitions of this important surface sensitiser and have been able to describe accurately the electronic interactions that initiate these transitions.[223,270] More recently, Persson and Lundqvist have reported calculations on the N3 dye–TiO_2 surface interface.[271] A related compound, tris(2,2'-bipyridine)ruthenium(II) dication, $[Ru(bpy)_3]^{2+}$ and its derivatised structures,[7,204,223] have not gained as much attention as surface sensitisers in recent years as their MLCT bands are sharper and occur at higher energy.[138] This compound is considered the 'parent' complex for all bipyridine coordination complexes and much is understood experimentally about this structure (Figure 0-1).[135,272]

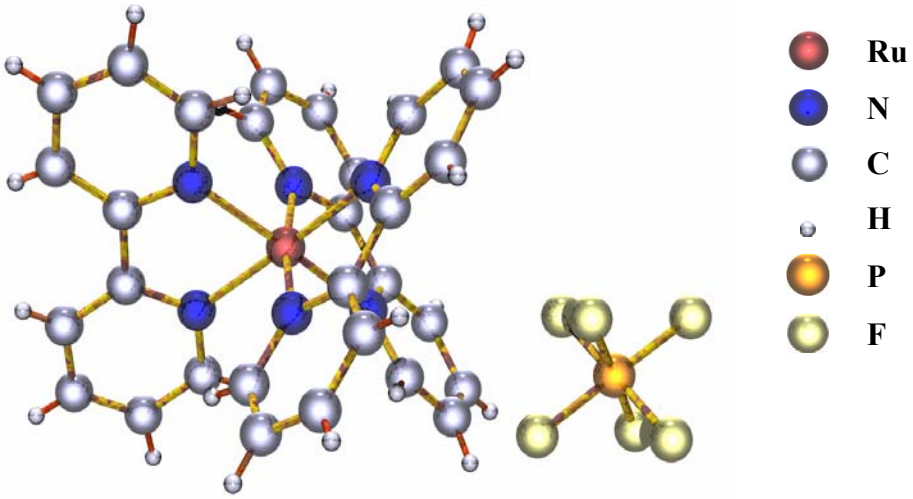

Figure 0-1 – Ground state structure of $[Ru(bpy)_3]^{2+}$ (depicted with a PF_6^- counter ion) as determined by X-ray crystallography.[273] Structural determination was performed at 295 K, and the structure possesses D_3 symmetry.

The nature of the transitions responsible for the MLCT are much simpler than that of N3 type sensitisers with the first singlet state being a t_{2g} to π^* transition and the excited state described as $[Ru(bpy)_2(bpy^-)]^{3+}$ i.e. the electron resides on only *one* of the degenerate bipyridine ligands.[135,225] Which ligand the electron resides on is statistically impossible to predict due to degeneracy of ligand energy, however substitution in the coordination sphere of nonequivalent ligands gives a tendency to 'direct' electron transfer. Watts and Crosby have referred to this as spectral 'fine tuning'.[274] Synthetic modification of coordination complexes to produce a surface sensitiser requires derivatisation of ligands with an acidic anchoring group. As noted above, the N3 dye utilises a carboxylate linkage, however in practice this linkage suffers from considerable desorption from the surface and hence is unstable in

aqueous media. Alternatively the highly oxophilic phosphonate group has been utilised for strong chemical attachment to surfaces.[4,7,204,223] Sensitisers utilising this peripheral anchoring group show comparable charge injection and quantum efficiency compared to sensitisers with a carboxylate group. Although this has been demonstrated for N3 type sensitisers,[223] the non-equivalent ligand effect for trichelated complexes has a different significance. Gillaizeau-Gauthier *et al.* reported phosphonate linkage effects with and without a methylene spacer between the acid group and the ligand.[8] Their study found that introduction of a saturated methylene spacer had a negative influence on the cell performance with decreased photocurrent efficiency and quantum yield of electron injection. They empirically rationalised these effects as "…inductive substituent effects on the π^* levels of the bipyridine ligand and the orientation of the excited state with respect to the semiconductor surface."[8]

However, the phosphonate moiety is not just simply a functional group on the bipyridine ligand. The organometallic fragment imparts considerable influence on the electronic structure of the ligand when substituted in 4 and 4' positions of the ring. This substitution pattern on the diimine ligand has considerable effect on electron transfer with the 4 position allowing for increased interaction with the π^* bonding orbitals of the heterocycle.[275] The saturated linkage between the ring structure and the electropositive phosphorus, decreases the MO overlap of the fragment with the semiconductor surface.[276]

The purpose of the present investigation is to determine the influence of organometallic ligands on the electronic structure of tris-bipyridyl ruthenium(II) complexes. Through interpretation of *ab initio* excited state calculations and molecular orbital descriptions the effect of organometallic phosphonate ligands on the coordination sphere and electronic charge 'directing' will be discussed.

Relativistic Considerations

To determine quantities accurately from *ab initio* calculations requires precise description of the atomic and molecular orbitals. Extending from the theory of relativity, a moving particle experiences a relativistic mass increase in proportion to the square of the speed of light. Due to the proximity of electrons to the nucleus of highly charged heavy atoms, their velocity approaches 10% that of the speed of light and hence heavy atoms experience a relativistic effect. The Schrödinger wavefunction does not entail relativistic terms and thus cannot accurately depict heavy atoms which have a contracted or decontracted valence and sub-valence electrons radius cf. those determined classically. The "heavy atom effect" is depicted in Figure 0-2.

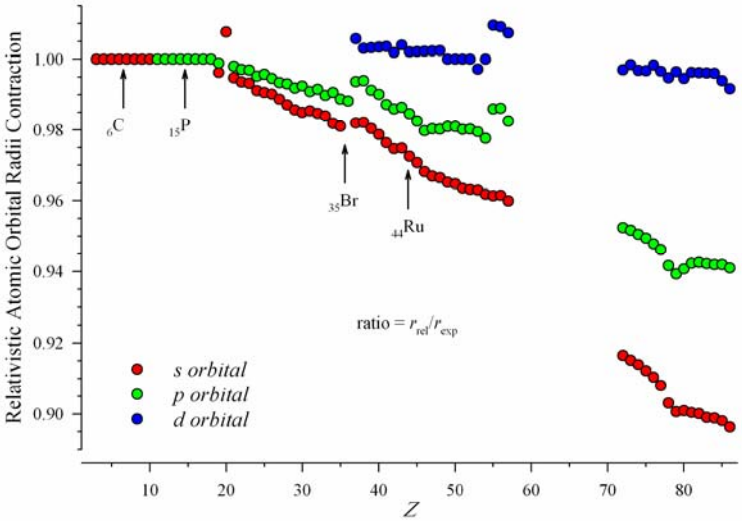

Figure 0-2 – Radii of *s*, *p* and *d* orbitals for Z = 3–86 (Li–Rn) expressed as the ratio of relativistic atomic nodal radii to expected radii in the absence of relativistic effects. [data: Zhang, Cohen and Phillips, Phys. Rev. B, 1987, 36 (11), 5861–5867]

Although the estimates of relativistic contraction of orbital radii in Figure 0-2 have most certainly been improved in recent years the relative estimates suffice for our discussion. The data show a contraction of the 5*s* and 6*s* orbitals for $_{78}$Pt and $_{79}$Au to be ~10%, for $_{44}$Ru this is <3% with contraction of 5*p* orbitals <2%. In the valence shell, for the Ru(II) cation which is a d^6 metal centre, there is no influence from 5*s* with a <0.5% over-estimate of the *d* shell. Certainly contraction of the core electrons will influence the valence shell, which is seen for many heavy atoms. Indeed, it is reported that DFT consistently over-estimates the length of Ru bonds[277] which is

related to the over-estimate of *d* orbital radii illustrated above. However, in relation to the current investigation, this effect on the electronic spectrum is thought to be minimal. The influence on other atoms considered in this study is small with the relativistic effect of $_6$C, $_7$N, $_8$O and $_{15}$P essentially zero. The basis sets employed in this study use relativistically parameterized effective core potentials (RECP) which do not implicitly include relativistic terms but relativistic corrections to the core electrons account for much of the effects.

Materials and Equipment

The compounds $[Ru(bpy)_2(dmpbpy)]^{2+}$, $[Ru(dmpbpy)_2(bpy)]^{2+}$ and $[Ru(dmpbpy)_3]^{2+}$ utilised in this investigation were prepared and described in Chapter 3 with $[Ru(bpy)_3]^{2+}$ available from a previous study.[264]

Representation of Crystallographic Data

Crystallographic data of related tris-bipyridyl structures were obtained from Cambridge Crystallographic Data Centre (CCDC) as a compiled CIF file. Examination of the structures for physical characteristics was performed with Mercury 1.3 (CCDC, Cambridge, UK).[278] For the representation of crystallographic data, thermal ellipsoid plots were generated using ORTEP-3 for Windows (version 1.08, L. J. Farrugia, University of Glasgow)[279] and depicted structures rendered using Persistence of Vision Raytracer (Version 3.6, Persistence of Vision Pty. Ltd. 2004).[280]

Computational Methods

Theoretical *ab initio* calculations of electronic transitions were performed using Density Functional Theory (DFT) as implemented in the Gaussian 03 code.[281] The DFT model consisted of Becke Three Parameter Hybrid Functionals[282] for the exchange with the correlation functional of Lee, Yang, and Parr[283,284] formalised as the B3LYP hybrid functional.

Restricted closed shell calculations were performed for all complexes, which had singlet spin multiplicity. Optimised geometric structures and properties of complexes were obtained using a triple-ζ split valence basis set for the linear combination of three contracted Gaussian functions for each orbital type specified as the LanL2DZ basis set. For the series of structures investigated in this work, we used six primitive *s*-shell functions for hydrogen and three *sp*-shells with three, one and one primitives to describe carbon, nitrogen and oxygen using the Dunning/Huzinaga valence double-ζ basis set.[285] The atomic orbitals of phosphorus and ruthenium were conveyed using Los Alamos Effective Core Potentials (ECP) with valence double-ζ Cartesian *d* functions as described by Hay and Wadt.[286-288] Starting structures were optimised at a semi-empirical level before refinement to the specified B3LYP/*basis* geometry, where *basis* is the implemented basis set as described above.

Optimised geometries were confirmed to be at a stationary point of minimum energy on the potential energy surface by calculation of vibrational frequencies at the stated geometry. Eigenvectors as obtained from this property calculation are the second derivative of the wavefunction. The absence of imaginary (negative) eigenvalues and a threshold of < 50 cm^{-1} were used as confirmation of the geometry's validity for further property calculations.

Calculations of excited states were performed using the optimised geometry of the refined structures by means of the time-dependent (TD) extension of DFT as implemented in the Gaussian code. The electronic structure of the series of complexes was studied over the 40000–10000 cm^{-1} region from the calculation of

120 excited states. Output from the TD-DFT is presented as unbroadened line spectra of electronic transitions in this region.

Single-point energy calculations were obtained for each of the refined structures at the optimised geometry as an indication of the ground state (HOMO) and excited state (LUMO) orbitals of the compounds.

Gas phase experimental absorption spectra were unavailable for the series of compounds investigated. However, the observed spectra for studied species were recorded in methanol (MeOH) solution. The absorbance axes for the observed spectra are depicted in arbitrary absorbance units and are not normalised.

Results and Discussion

Structure and Bonding of Optimised Geometries

The calculations of properties by density functional methods are dependant upon an accurate description of the electron density, hence an accurate depiction of the molecular geometry is essential. To confirm the validity of DFT optimised geometries for all four configurations of "$[Ru(bpy)_3]^{2+}$" as obtained and described in Computational Methods above, a survey of twenty crystallographic structures for Ru(II) diimine complexes was performed. The survey included twelve tris(2,2'-bipyridyl)ruthenium(II) structures crystallized with a range of anionic salts, including Δ and Λ enantiomers, as well as complexes with less than three identical ligands.

The complete details of geometric properties of the modelled compounds can be found in Table 0-1 and Table 0-2. For the full complement of surveyed structures the range of Ru–N bond lengths was 2.017–2.085 Å with an average bond length of 2.055 Å, with the tris complexes alone having 2.046–2.069 Å with an average bond length of 2.056 Å. For the modelled structures, all the bond lengths were ~2% longer at 2.098 Å, which is within the error of relativistic decontraction of the Ru *d* orbital as described in the Introduction. The interatomic distance and bite angle of the nitrogen chelate show little strain and distortion from octahedral symmetry. For the full survey, N–N bond distance was 2.576–2.638 Å with an average of 2.610 Å, while the tris complexes had a tighter range of 2.599–2.631 Å with an average of 2.609 Å. The modelling reproduced this satisfactorily however the overestimate was again ~2% at 2.653 Å.

Table 0-1 – Selected calculated bond angles (°) and lengths (Å) for coordination of diimine ligands in the four examples of $[Ru(bpy)_3]^{2+}$ type complexes. Atom positions are numbered sequentially in a clockwise direction. Individual configurations are: $[Ru(bpy)_3]^{2+}$, R_1–R_3 = H R_1'–R_3' = H; $[Ru(bpy)_2(dmpbpy)]^{2+}$, R_1 and R_2' = mp R_2–R_3 = H R_2'–R_3' = H; $[Ru(dmpbpy)_2(bpy)]^{2+}$, R_1 and R_1' = mp R_3 and R_3' = mp R_2 and R_2' = H; $[Ru(dmpbpy)_3]^{2+}$ R_1–R_3 = mp R_1'–R_3' = mp; where mp = phosphonomethyl.

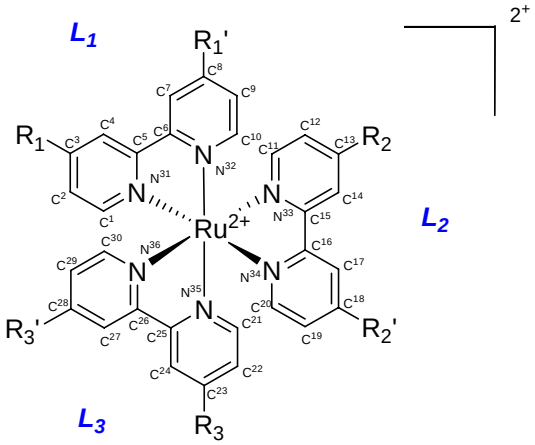

bond	bond angle(°)			
	$[Ru(bpy)_3]^{2+}$	$[Ru(bpy)_2(dmpbpy)]^{2+}$	$[Ru(dmpbpy)_2(bpy)]^{2+}$	$[Ru(dmpbpy)_3]^{2+}$
N^{31}–Ru–N^{32}	78.41	78.36	78.37	78.40
N^{33}–Ru–N^{34}	78.36	78.44	78.50	78.44
N^{35}–Ru–N^{36}	78.40	78.45	78.49	78.49
N^{32}–Ru–N^{34}	88.27	87.66	88.19	87.82
N^{33}–Ru–N^{35}	88.25	88.51	88.92	88.67
N^{36}–Ru–N^{31}	88.49	88.47	89.71	89.28
N^{31}–Ru–N^{33}	96.73	96.72	96.72	96.75
N^{31}–Ru–N^{35}	96.78	96.59	96.59	96.83
N^{32}–Ru–N^{34}	96.90	96.42	96.42	96.39
N^{32}–Ru–N^{36}	96.79	97.21	97.21	97.48
N^{34}–Ru–N^{36}	96.74	94.45	95.45	95.90
N^{33}–Ru–N^{35}	96.89	96.58	96.58	96.62
	bond length (Å)			
N^{31}–Ru	2.099	2.098	2.096	2.095
N^{32}–Ru	2.100	2.097	2.097	2.096
N^{33}–Ru	2.101	2.099	2.099	2.097
N^{34}–Ru	2.100	2.099	2.100	2.098
N^{35}–Ru	2.100	2.099	2.098	2.096
N^{36}–Ru	2.100	2.098	2.093	2.093
N^{31}–N^{32}	2.655	2.650	2.649	2.648
N^{33}–N^{34}	2.654	2.655	2.657	2.652
N^{35}–N^{36}	2.655	2.654	2.651	2.650

The N–Ru–N bite angle for all the crystal structures was 78.23–79.47° with an average of 78.80°, with the tris complexes much the same at 78.41–79.29° and an average of 78.77°. This structural factor was reproduced excellently by the modelling at 78.43° within the range of both symmetrical and asymmetrical complexes. For distortion from octahedral geometry, the angles of adjacent bipyridine fragments would deviate from 90°. This can be seen in crystal structures giving inter-bipyridyl angles of 89.75 and 96.08° for the complete survey and only 89.90 and 95.48° for the homoleptic complexes. Again this factor is reproduced well by the molecular geometries with angles of 88.52 and 96.57°.

The comparison of the optimised geometries to those of crystallographic structures has shown that, in general, the structures have been reproduced well and that the slightly distorted octahedral geometry is maintained. As expected, this gives a structure with alternating orthogonal bis-chelates. Disregarding the partial distortion from octahedral, the parent complex $[Ru(bpy)_3]^{2+}$ is symmetric about each of the bipyridyl ligands (point group D_3, Figure 0-1) however with the addition of the phosphonated ligand the symmetry is lowered. Assuming rotational freedom of the peripheral functional groups, both $[Ru(bpy)_2(dmpbpy)]^{2+}$ and $[Ru(dmpbpy)_2(bpy)]^{2+}$ possess C_2 symmetry while the addition of a third phosphonated ligand returns the symmetry of $[Ru(dmpbpy)_3]^{2+}$ to D_3. These structural observations are consistent with those of Gorelsky and Lever for similar D_3 and C_2 structures.[277,289] The agreement of modelled structures to those of the known crystal structures is a good indication that the geometries are satisfactory for the study of electronic properties.

There is no X-ray crystal structure for tris-bipyridyl structures possessing phosphonate groups. However this factor is not expected to invalidate the major conclusions of this study as the energy of electronic transitions depends on metal-ligand bond distances and on the relative energy of ligand orbitals. Despite addition of the organometallic fragment little change in the ligand is observed structurally; Table 0-2 depicts the individual features of the ligands for each complex. There is a modest change in the aromatic bond lengths in the region of the substitution and only subtle changes in bond angles; essentially the structures are not dissimilar from each other.

Table 0-2 – Selected calculated bond lengths (Å) for the four examples of $[Ru(bpy)_3]^{2+}$ type complexes. Atom numbering and ligand substitution for the complexes are as in Table 0-1.

	bond	bond length (Å)			
		$[Ru(bpy)_3]^{2+}$	$[Ru(bpy)_2(dmpbpy)]^{2+}$	$[Ru(dmpbpy)_2(bpy)]^{2+}$	$[Ru(dmpbpy)_3]^{2+}$
L1	C^5–N^{31}	1.379	1.379	1.380	1.380
	N^{31}–C^1	1.362	1.360	1.360	1.360
	C^1–C^2	1.401	1.399	1.399	1.399
	C^2–C^3	1.408	1.410	1.410	1.410
	C^3–C^4	1.404	1.409	1.409	1.409
	C^4–C^5	1.408	1.403	1.403	2.403
	C^5–C^6	1.478	1.478	1.478	1.478
	C^6–C^7	1.408	1.406	1.406	1.406
	C^7–C^8	1.404	1.407	1.406	1.407
	C^8–C^9	1.408	1.414	1.414	1.412
	C^9–C^{10}	1.401	1.397	1.397	1.397
	C^{10}–N^{32}	1.362	1.362	1.362	1.361
	N^{32}–C^6	1.379	1.377	1.377	1.377
L2	C^{15}-N^{33}	1.379	1.379	1.379	1.379
	N^{33}–C^{11}	1.362	1.362	1.362	1.360
	C^{11}–C^{12}	1.401	1.401	1.401	1.399
	C^{12}–C^{13}	1.408	1.408	1.408	1.410
	C^{13}–C^{14}	1.404	1.404	1.403	1.409
	C^{14}–C^{15}	1.408	1.408	1.408	1.403
	C^{15}–C^{16}	1.478	1.478	1.478	1.478
	C^{16}–C^{17}	1.408	1.408	1.408	1.404
	C^{17}–C^{18}	1.404	1.403	1.404	1.408
	C^{18}–C^{19}	1.408	1.408	1.408	1.411
	C^{19}–C^{20}	1.401	1.401	1.401	1.398
	C^{20}–N^{34}	1.362	1.362	1.363	1.362
	N^{34}–C^{41}	1.379	1.379	1.379	1.378
L3	C^{25}–N^{35}	1.379	1.379	1.378	1.378
	N^{35}–C^{21}	1.362	1.362	1.361	1.360
	C^{21}–C^{22}	1.401	1.401	1.400	1.400
	C^{22}–C^{23}	1.408	1.408	1.410	1.410
	C^{23}–C^{24}	1.404	1.404	1.411	1.410
	C^{24}–C^{25}	1.408	1.408	1.403	1.403
	C^{25}–C^{26}	1.478	1.478	1.477	1.477
	C^{26}–C^{27}	1.408	1.408	1.404	1.404
	C^{27}–C^{28}	1.404	1.404	1.408	1.408
	C^{28}–C^{29}	1.408	1.408	1.411	1.411
	C^{29}–C^{30}	1.401	1.401	1.398	1.398
	C^{30}–N^{36}	1.362	1.362	1.360	1.360
	N^{36}–C^{13}	1.379	1.379	1.379	1.379

Molecular Orbital Configuration

The frontier orbitals of low-spin octahedral complexes can be described in terms of a 5*d* manifold for the t_{2g} and e_g orbitals of Ru(II) and a series of upper storey π^* orbitals to describe the excited state bipyridine manifold. In our discussion the transitions reside within a key number of orbitals, namely the three t_{2g} orbitals of the ground state and three upper storey π^* and the two e_g metal orbitals; essentially an eight orbital manifold. To describe the π^* orbitals of 2,2'-bipyridine and its derivatives it is conventional to use the notation of Orgel,[290] where following rotation about the C_2 axis retained by each of the Ru(bpy) components, the orbitals may be symmetrical (χ) or antisymmetrical (ψ).[135,225]

The irreducible symmetry labels for the D_3 and C_2 point groups are assigned on the basis of the trichelated metal complexes lying along *x*, *y*, *z* coordinates that are coincident with the coordination axes of an O_h symmetrical complex. Due to the increased number of orbitals for each successive complex, MO numbers are inconsistent and the number of transitions encountered makes HOMO and LUMO labels quite cumbersome. Thus in reference to specific transitions of the key orbital manifold, these will be made in terms of orbital shape and using Orgel's notation; hence, the first excited state HOMO-LUMO transition becomes a $\pi_\psi^* \leftarrow d\pi$ transition. The relative eigenvalues of orbitals for the studied complexes as derived from single point energy DFT calculations are depicted in Figure 0-3.

The representation depicts the orbital manifold as described above. For the parent $[Ru(bpy)_3]^{2+}$ the three pseudo-degenerate t_{2g} Ru(II) orbitals are clearly resolved from the bipyridine π-orbitals while the upper storey manifold consists of groupings of low-lying π^* orbitals. The degenerate e_g Ru(II) orbitals can be identified at much higher energy. There is an increased density of electronic states below the frontier molecular orbitals for the complexes that have substituted phosphonate ligands. This is due to the increased number of atomic orbitals and hence electronic states for these ligands; despite this the states show clear distinction for ligand σ and π orbitals for the lower HOMO states and the metal $d\pi$ orbitals are also identifiable. For clarity, the densely occupied bipyridine π-orbitals are depicted as three pseudo degenerate 'columns' which show almost symmetrical states for each ligand

Figure 0-3 – Calculated eigenvalues for the frontier orbitals of the four examples of the $[Ru(bpy)_3]^{2+}$ complex. The orbitals are arranged similarly for all examples.

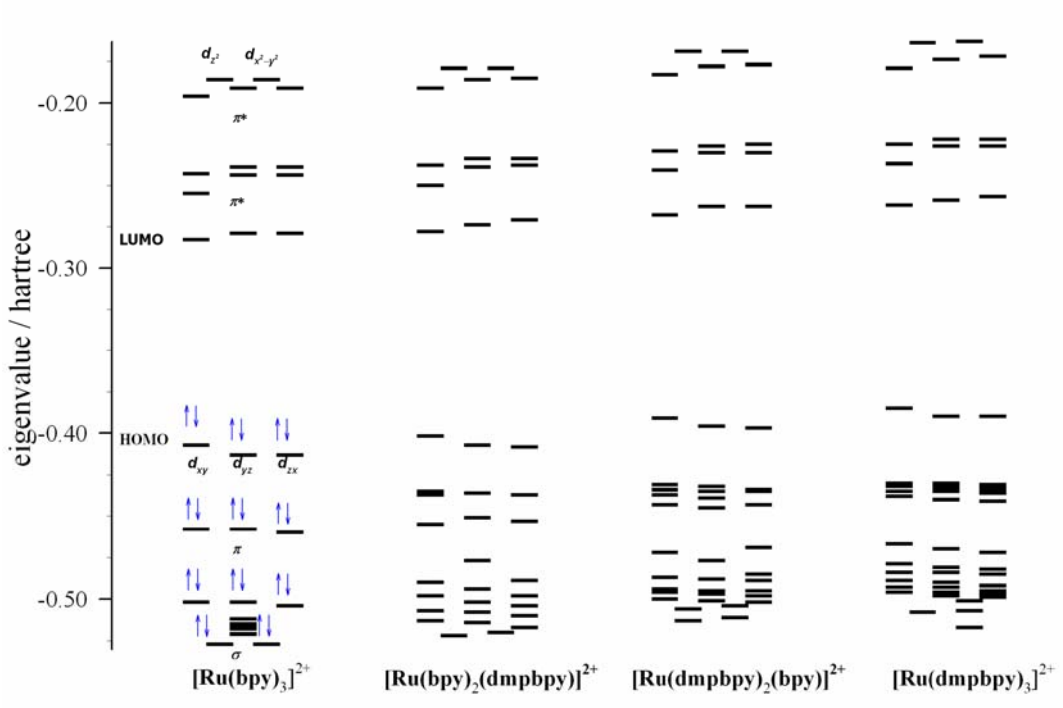

The shapes of MOs involved in the major MLCT transitions are shown for each of the complexes in Figure 0-4 and Figure 0-5. The respective orbital notations are also depicted, with these five orbitals almost exclusively constituting the major MLCT band as listed in the tables of the following section. In the upper storey, the lowest LUMO states are primarily ligand π^* with the metal $d\sigma$ orbitals resolved as the higher LUMO states. Thus, the frontier HOMO states are primarily metal $d\pi$ while the frontier LUMO states are primarily bipyridine π^* in character. However σ–π backbonding leads to mixing of the Ru(II) and bipyridine orbitals.[277,291] The off-axis metal orbitals exhibit π type bonding and due to interaction with the ligand π orbitals can appear distorted from their atomic shape, while the on-axis metal orbitals are less distorted and retain their axial atomic shape despite the strong σ interaction. Similar orbital diagrams have been depicted by others but not as a manifold assembly.[289,292]

Although the complexes show similarity in orbital structure the relative eigenvalues are subtly influenced by the non-equivalent ligands in the coordination sphere. This is seen in the gradual increase in energy of both the HOMO and LUMO orbitals as the number of phosphonated ligands is increased (Figure 0-3, left to right).

Figure 0-4 – Images of frontier molecular orbital densities of the molecular orbitals involved in the primary MLCT transition. The orbitals are labelled with the numbers from the calculations, Orgel's χ/ψ notation explained in the text, and the symmetry species under the D_3 and C_2 point groups respectively.

$[Ru(bpy)_3]^{2+}$	$[Ru(bpy)_2(dmpbpy)]^{2+}$
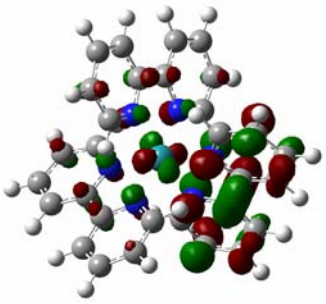	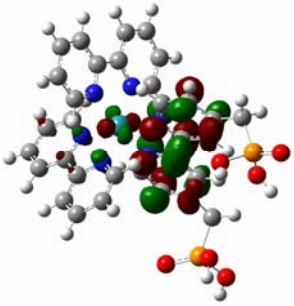
133 (e, π_ψ*)	171 (a, π_ψ*)
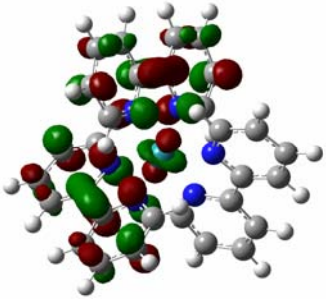	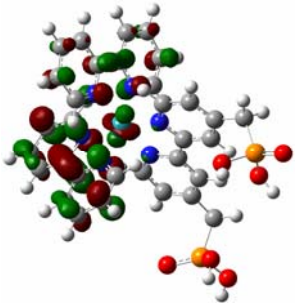
132 (e, π_ψ*)	170 (b, π_ψ*)
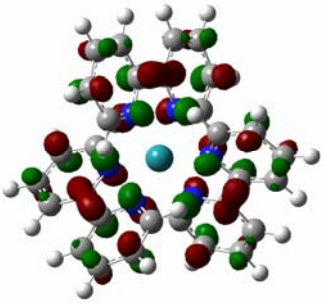	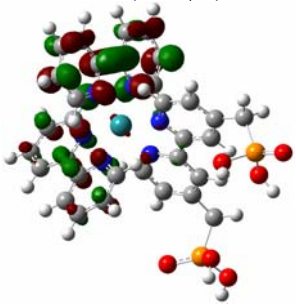
131 (a_2, π_ψ*)	169 (b, π_ψ*)
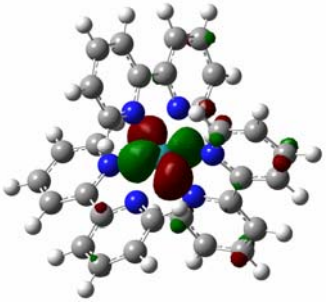	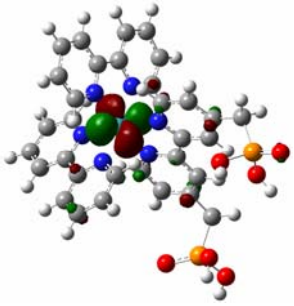
129 (e, $d\pi$)	167 (a, $d\pi$)
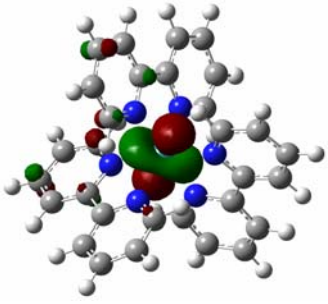	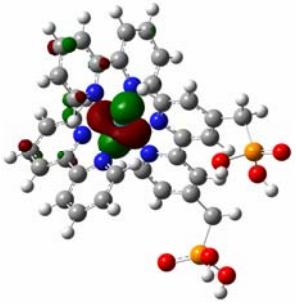
128 (e, $d\pi$)	166 (b, $d\pi$)

Figure 0-5 – Images of frontier molecular orbital densities of the molecular orbitals involved in the primary MLCT transition. The orbitals are labelled with the numbers from the calculations, Orgel's χ/ψ notation explained in the text, and the symmetry species under the C_2 and D_3 point groups respectively.

$[Ru(dmpbpy)_2(bpy)]^{2+}$	$[Ru(dmpbpy)_3]^{2+}$
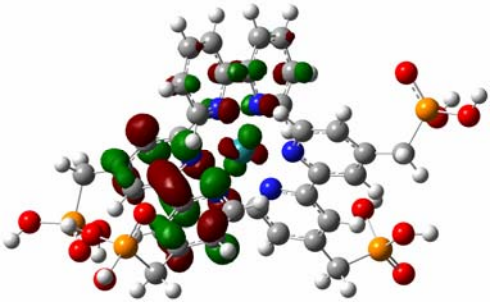	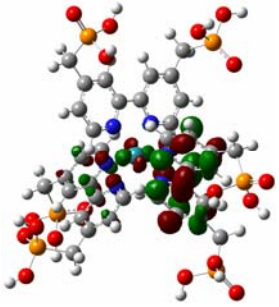
209 (b, π_ψ*)	247 (e, π_ψ*)
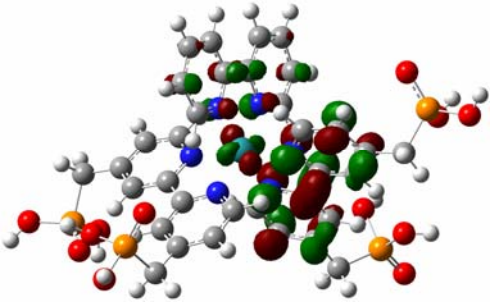	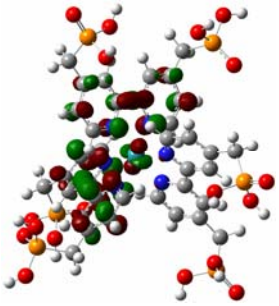
208 (a, π_ψ*)	246 (e, π_ψ*)
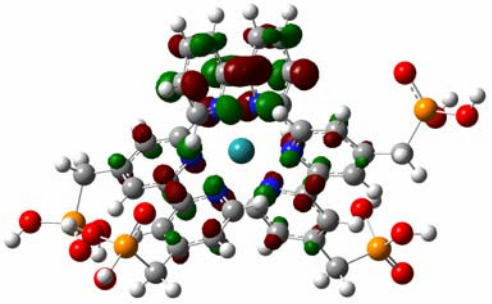	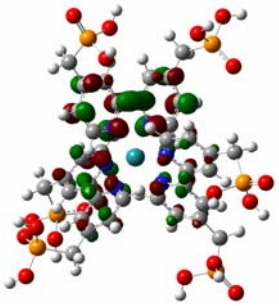
207 (b, π_ψ*)	245 (a_2, π_ψ*)
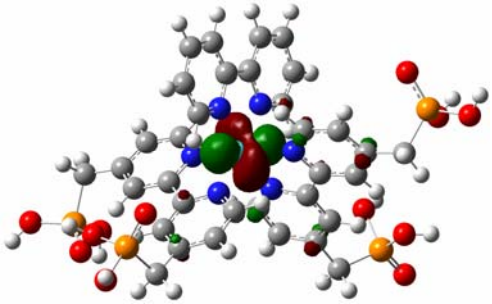	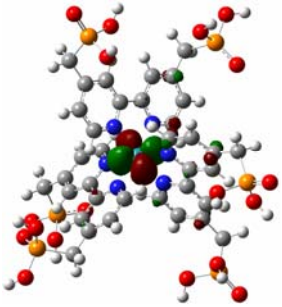
205 (b, $d\pi$)	243 (e, $d\pi$)
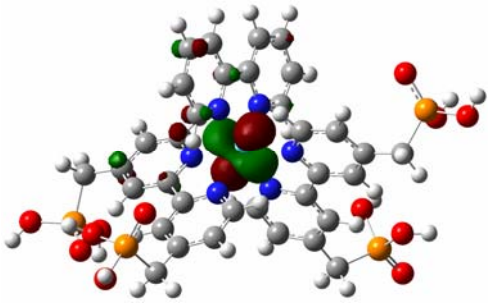	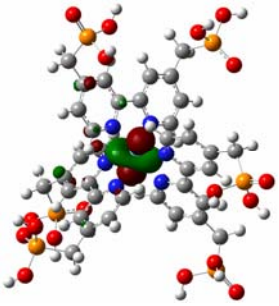
204 (a, $d\pi$)	242 (e, $d\pi$)

Figure 0-6 – HOMO of the four examples of $[Ru(bpy)_3]^{2+}$ type complexes. The orbitals are labelled with the numbers from the calculations, Orgel's χ/ψ notation explained in the text, and the symmetry species under the D_3 and C_2 point groups respectively.

$[Ru(bpy)_3]^{2+}$

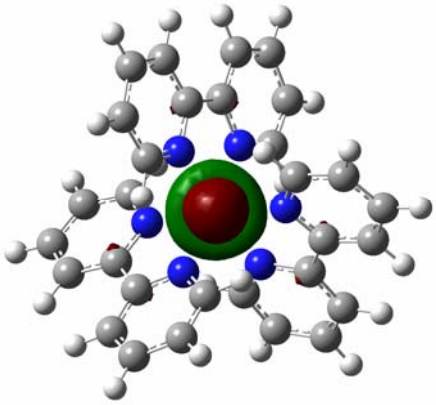

130 (a_1, $d\pi$)

$[Ru(bpy)_2(dmpbpy)]^{2+}$

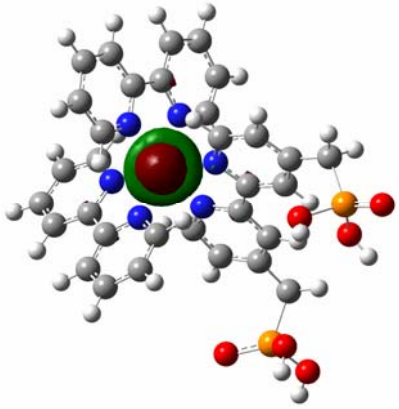

168 (a, $d\pi$)

$[Ru(dmpbpy)_2(bpy)]^{2+}$

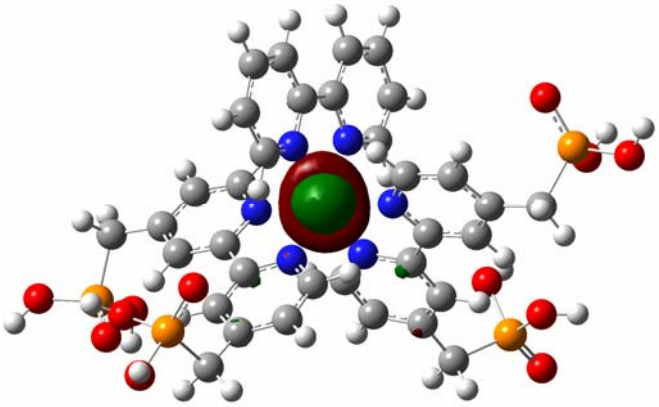

206 (a, $d\pi$)

$[Ru(dmpbpy)_3]^{2+}$

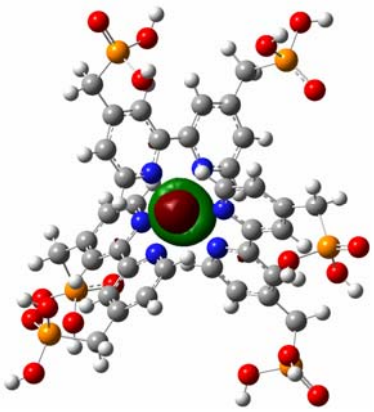

244 (a_1, $d\pi$)

Depicted in Figure 0-6 is the HOMO for each of the complexes. As indicated by the symmetry labels, these metal t_{2g} orbitals are symmetrically different, unlike those observed for degenerate orbitals of homoleptic D_3 complexes, which the modelling reproduces well. For the C_2 complexes, $[Ru(bpy)_2(dmpbpy)]^{2+}$ and $[Ru(dmpbpy)_2(bpy)]^{2+}$ respectively, the HOMO is distorted due to the backbonding interaction with the bipyridine π orbitals. Backbonding favours the low-lying unsubstituted **bpy** ligand. This is consistent with LUMO states as the energetically lowest π_ψ* orbital is an unsubstituted **bpy** for complexes containing non-equivalent ligands. The influence of the phosphonated ligands on molecular transitions is discussed in the following Section.

Excited States and Electronic Absorption Spectra

In this current investigation only singlet spin-allowed transitions having $f \geq 0.01$ have been considered and calculation of the lowest 120 excited states of all four complexes was carried out using TDDFT. The result is a significant amount of data and transitions that allow assignment of charge transfer (CT) bands with the data presented in Appendix I. Relevant visible transitions are listed in a truncated form in Table 0-3 – Table 0-6, as these important CT bands give rise to photoelectron transfer processes. For excited state electron injection, it has been estimated that the lowest-lying states of $[Ru(bpy)_3]^{2+}$ constitute ≤ 10% singlet character, however intersystem crossing of the upper singlet transitions to the triplet manifold enhance triplet transitions in this region.[293] Special note must be made that, although only singlet transitions are included here, the lowest lying excited states can be singlet or triplet transitions.[135,293]

We will concentrate on transitions derived mainly from the *d* orbital and π^* manifold that constitute six key orbitals for HOMO-LUMO transitions. In the interest of reduced repetition, excitation compositions and comparisons of calculated and observed spectra will be discussed concurrently.

Table 0-3 – TDDFT calculated excitation energies, one-electron transitions, and oscillator strengths for optical transitions of $[Ru(bpy)_3]^{2+}$ complex in the gas phase ($\lambda > 400$ nm; $f > 0.01$).

excited state	orbital composition			coefficient	excitation			oscillator strength
					eV	nm	cm^{-1}	
7	131 (a_2, π_ψ*)	←	128 (e, $d\pi$)	0.295	2.89	429	23300	0.110
	132 (e, π_ψ*)	←	128 (e, $d\pi$)	0.152				
	133 (e, π_ψ*)	←	128 (e, $d\pi$)	0.394				
	131 (a_2, π_ψ*)	←	129 (e, $d\pi$)	–0.159				
	132 (e, π_ψ*)	←	129 (e, $d\pi$)	–0.393				
	133 (e, π_ψ*)	←	129 (e, $d\pi$)	0.151				
8	131 (a_2, π_ψ*)	←	128 (e, $d\pi$)	–0.159	2.89	429	23300	0.110
	132 (e, π_ψ*)	←	128 (e, $d\pi$)	0.395				
	133 (e, π_ψ*)	←	128 (e, $d\pi$)	–0.151				
	131 (a_2, π_ψ*)	←	129 (e, $d\pi$)	–0.292				
	132 (e, π_ψ*)	←	129 (e, $d\pi$)	0.151				
	133 (e, π_ψ*)	←	129 (e, $d\pi$)	0.394				

Table 0-4 – TDDFT calculated excitation energies, one-electron transitions, and oscillator strengths for optical transitions of $[Ru(bpy)_2(dmpbpy)]^{2+}$ complex in the gas phase ($\lambda > 400$ nm; $f > 0.01$).

excited state	orbital composition			coefficient	excitation			oscillator strength
					eV	nm	cm^{-1}	
6	169 (b, π_ψ*)	←	166 (a, $d\pi$)	0.503	2.78	446	22400	0.0188
	170 (b, π_ψ*)	←	166 (a, $d\pi$)	–0.191				
	171 (a, π_ψ*)	←	166 (a, $d\pi$)	0.429				
7	169 (b, π_ψ*)	←	166 (a, $d\pi$)	0.365	2.86	434	23000	0.103
	170 (b, π_ψ*)	←	166 (a, $d\pi$)	0.235				
	171 (a, π_ψ*)	←	166 (a, $d\pi$)	–0.367				
	170 (b, π_ψ*)	←	167 (a, $d\pi$)	0.290				
	171 (a, π_ψ*)	←	167 (a, $d\pi$)	0.234				
8	170 (b, π_ψ*)	←	166 (a, $d\pi$)	0.368	2.88	430	23300	0.138
	171 (a, π_ψ*)	←	166 (a, $d\pi$)	0.284				
	169 (b, π_ψ*)	←	167 (a, $d\pi$)	0.225				
	170 (b, π_ψ*)	←	167 (a, $d\pi$)	–0.278				

Table 0-5 – TDDFT calculated excitation energies, one-electron transitions, and oscillator strengths for optical transitions of $[Ru(dmpbpy)_2(bpy)]^{2+}$ complex in the gas phase ($\lambda > 400$ nm; $f > 0.01$).

excited state	orbital composition			coefficient	excitation			oscillator strength
					eV	nm	cm^{-1}	
6	207 (b, π_ψ*)	←	204 (a, $d\pi$)	0.580	2.73	454	22000	0.0149
	208 (a, π_ψ*)	←	204 (a, $d\pi$)	0.303				
	209 (b, π_ψ*)	←	205 (b, $d\pi$)	–0.187				
7	207 (b, π_ψ*)	←	204 (a, $d\pi$)	0.337	2.84	437	23000	0.101
	208 (a, π_ψ*)	←	204 (a, $d\pi$)	–0.347				
	209 (b, π_ψ*)	←	204 (a, $d\pi$)	–0.182				
	208 (a, π_ψ*)	←	205 (b, $d\pi$)	–0.207				
	209 (b, π_ψ*)	←	205 (b, $d\pi$)	0.380				
8	208 (a, π_ψ*)	←	204 (a, $d\pi$)	–0.207	2.87	433	23000	0.184
	209 (b, π_ψ*)	←	204 (a, $d\pi$)	0.387				
	207 (b, π_ψ*)	←	205 (b, $d\pi$)	0.218				
	208 (a, π_ψ*)	←	205 (b, $d\pi$)	0.422				
	209 (b, π_ψ*)	←	205 (b, $d\pi$)	0.208				

Table 0-6 – TDDFT calculated excitation energies, one-electron transitions, and oscillator strengths for optical transitions of $[Ru(dmpbpy)_3]^{2+}$ complex in the gas phase ($\lambda > 400$ nm; $f > 0.01$).

excited state	orbital composition			coefficient	excitation			oscillator strength
					eV	nm	cm^{-1}	
6	245 (a_2, π_ψ*)	←	242 (e, $d\pi$)	0.525	2.74	452	22102	0.0310
	246 (e, π_ψ*)	←	242 (e, $d\pi$)	0.127				
	247 (e, π_ψ*)	←	242 (e, $d\pi$)	–0.414				
	247 (e, π_ψ*)	←	243 (e, $d\pi$)	0.100				
7	245 (a_2, π_ψ*)	←	242 (e, $d\pi$)	0.259	2.83	438	22807	0.156
	246 (e, π_ψ*)	←	242 (e, $d\pi$)	–0.186				
	247 (e, π_ψ*)	←	242 (e, $d\pi$)	0.423				
	245 (a_2, π_ψ*)	←	243 (e, $d\pi$)	–0.213				
	246 (e, π_ψ*)	←	243 (e, $d\pi$)	0.351				
	247 (e, π_ψ*)	←	243 (e, $d\pi$)	0.140				
8	245 (a_2, π_ψ*)	←	242 (e, $d\pi$)	0.135	2.85	435	22998	0.154
	246 (e, π_ψ*)	←	242 (e, $d\pi$)	0.427				
	247 (e, π_ψ*)	←	242 (e, $d\pi$)	0.192				
	245 (a_2, π_ψ*)	←	243 (e, $d\pi$)	0.209				
	246 (e, π_ψ*)	←	243 (e, $d\pi$)	0.185				
	247 (e, π_ψ*)	←	243 (e, $d\pi$)	–0.392				

Observed spectra overlaid with the unbroadened line spectra from excited state calculations are depicted in Figure 0-7. Interestingly, there is strong similarity in the absorption profiles of all four compounds typical of tris-chelation. Although separate CT bands are predicted for complexes with non-equivalent ligands,[220,269,277,289,292,294] the dissimilarity of **bpy** and **dmpbpy** energetically results in little preference for reduction by either ligand. Experimental photophysical properties of $[Ru(bpy)_3]^{2+}$ and related diimine analogues have shown that excited state luminescence, that arises from the excitation into the MLCT, are identical for substituted analogues especially those with 4,4′-substitution.[295,296]

All four compounds show characteristics that are common to diimine chelate complexes with a prominent MLCT transition in the visible and an intense ligand-centred (LC) band in the mid-UV region of the spectra. These bands are both distinct and clearly identifiable. There is also a shoulder between the MLCT and LC that has been attributed to a metal-centred (MC) transition as well as a second peak that occurs in the far-UV that has been described as a secondary MLCT.[135] The 'regions' of excitation bands make it qualitatively possible to dissociate the bands of these spectra and identify specific CT features.

The experimental data depicts a distinct 'two band' spectrum with a third between these, consistent with literature, and calculations reproduce the pattern of the three longest wavelength bands.[135,225] For the parent $[Ru(bpy)_3]^{2+}$ there are three clear regions that can be associated with known charge transfer phenomena. The longest wavelength band ($\tilde{\nu}_{MLCT}$) is symmetry allowed and occurs in the visible region of ~22000 cm^{-1} with a molar absorption coefficient of 8000–20000 L mol^{-1} cm^{-1} and has been assigned to a $\pi_\psi^* \leftarrow d\pi$ transition. This is followed by a band ($\tilde{\nu}_{MC}$) described as a Laporte forbidden MC $d\sigma \leftarrow d\pi$ transition at 27000–31000 cm^{-1} and as such is much weaker. Near the mid-UV of ~35000 cm^{-1} an intense band ($\tilde{\nu}_{LC}$) with a molar absorption coefficient of ~80000 $dm^3 \cdot mol^{-1} \cdot cm^{-1}$ is most certainly of $\pi_\psi^* \leftarrow \pi$ or $\pi_\chi^* \leftarrow \pi$ in origin. All data have these experimental bands and the calculated excitations will be discussed with reference to these transitions.

Comparison of the parent $[Ru(bpy)_3]^{2+}$ to those complexes containing non-equivalent ligands in the coordination sphere shows some distinct similarities and also some subtle differences. The transitions, as depicted in Table 0-3 – Table 0-6, show only those with an oscillator strength ≥ 0.01; hence the first excited states are 6, 7 and 8 and do not involve the HOMO in any of the complexes. Consultation of the unabridged list of transitions in Appendix I shows that the first two to three excited states are true HOMO-LUMO transitions with excitation from these high symmetry $d\pi$ t_{2g} orbitals to one of the low lying π^* orbitals. However, their oscillator strengths are quite small and hence are not deemed to be a large contributor to the observed MLCT. This aberration could be attributed to a common difficulty in calculating transition metal systems and thus could be a wavefunction error. Due to their low-lying excited states there is a risk of spin contamination for unrestricted wave functions; hence restricted open-shell calculations were performed. However the geometries all indicate energy minima for all studied complexes supporting a systematic error. An alternative explanation for this may be that these low-lying excited states are ^{1}MLCT states that contribute to the spin-forbidden ^{3}MLCT states observed and rationalised in the literature.[225,293,296] This reasoning is supported by the somewhat broadened peak at ~22000 cm^{-1} and the low wavenumber shoulder observed in the experimental spectra of Figure 0-7. If this postulate is true, then the presence of non-equivalent ligands in the coordination sphere, for the complexes studied here, increases the population of the low-lying ^{1}MLCT states, hence ^{3}MLCT states, which is observed experimentally as a broadened ^{1}MLCT and stronger ^{3}MLCT bands.

In all the complexes the $\tilde{\nu}_{MLCT}$ is described by several intense excitations all of which originate from the degenerate pair of $d\pi$ orbitals to low lying π^* orbitals. Due to symmetry and energetics of these orbitals these transitions are clearly $\pi_\psi^* \leftarrow d\pi$. Of interest is that in the two homoleptic complexes, $[Ru(bpy)_3]^{2+}$ and $[Ru(dmpbpy)_3]^{2+}$, there appears to be no preference for ligand reduction; however in all cases the first LUMO is lower in energy than the other degenerate pair. This supports the postulate that an instantaneous dipole is formed in the excited state and the electron resides only on a single ligand.[293] For the homoleptic complexes this has no further bearing. However, for the complexes that contain non-equivalent ligands,

spectral 'fine tuning' may be apparent. In the case of $[Ru(bpy)_2(dmpbpy)]^{2+}$ the first (and second) LUMO reside on the **bpy** ligand, a fact which is repeated for $[Ru(dmpbpy)_2(bpy)]^{2+}$. In the 'one-electron' reduction model, this would act as an electron sink if used as light absorption sensitisers in PEC applications. For the excited state on **bpy** to contribute to electron transfer to a surface bound **dmpbpy** ligand would require interligand charge transfer, a phenomenon not observed at the low energy that initiates $\tilde{\nu}_{MLCT}$. For PEC device applications, this factor would significantly contribute to low photocurrent yields and low photochemical efficiency.[8]

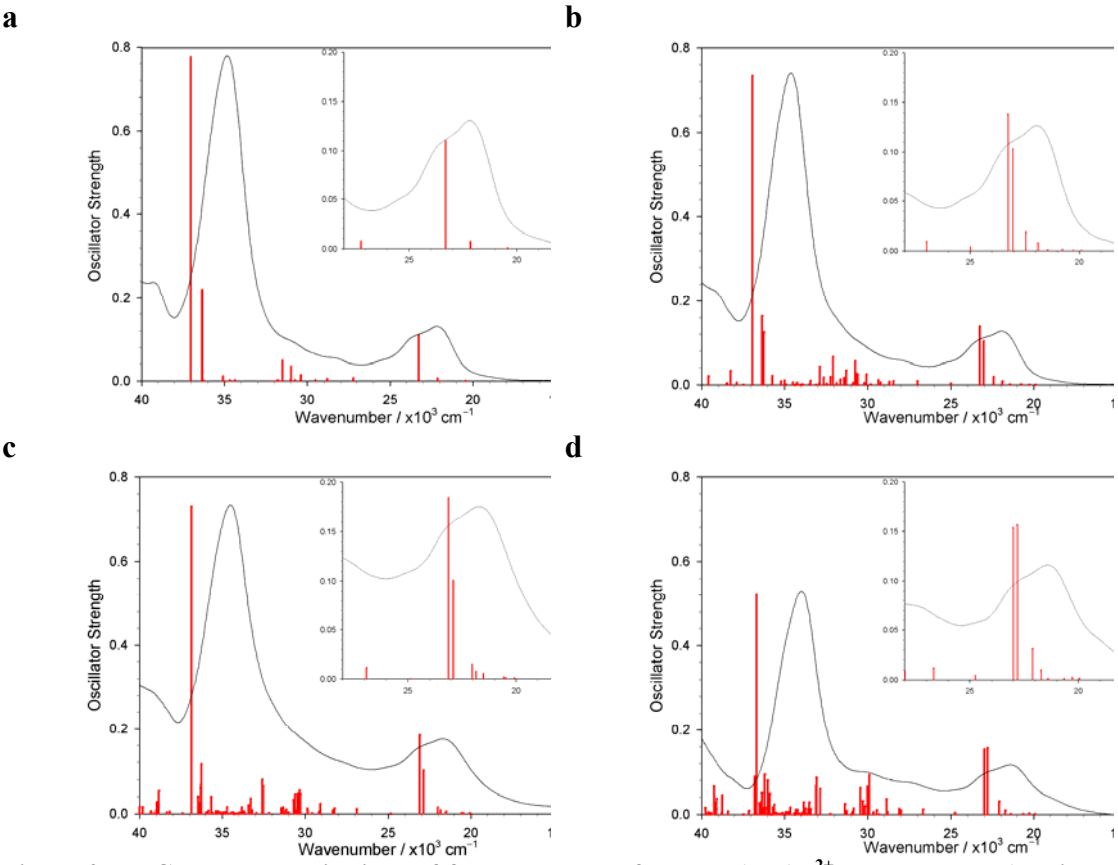

Figure 0-7 – Calculated excitations of four examples of the $[Ru(bpy)_3]^{2+}$ type complex (vertical lines) and observed absorption spectra (in MeOH). The *y* axes for the experimental spectra are in arbitrary absorbance units, and are normalised to the maximum oscillator strength in each panel. a) $[Ru(bpy)_3]^{2+}$ b) $[Ru(bpy)_2(dmpbpy)]^{2+}$ c) $[Ru(dmpbpy)_2(bpy)]^{2+}$ d) $[Ru(dmpbpy)_3]^{2+}$.

Almost exclusively the LC transitions for $\tilde{\nu}_{LC}$ are from π orbitals to the low lying π^* orbitals that have previously been described as ψ^*. There are relatively few transitions outside this upper storey manifold with large oscillator strength; even with the introduction of non-equivalent ligands and the organometallic fragment, transitions can quite clearly be assigned as $\pi_\psi^* \leftarrow \pi$. The magnitude of the oscillator strength corresponds well to that of intraligand charge transfer and indeed compares well in relative intensity to the $\tilde{\nu}_{MLCT}$ band. The energies of vertical excitations correlate quite reasonably to the experimental ones, and are reproduced for all complexes. Also reproduced well are the relative oscillator strengths for the complexes with non-equivalent ligands. The presence of the electropositive phosphorus fragment contributes to destabilisation of the π electron system with a decrease in oscillator strength consistent with the decreased delocalisation.

Between these intense bands is the group of excitations tentatively termed $\tilde{\nu}_{MC}$. There still remains some discrepancy in the literature as to the assignment of this particular band, with ambiguity surrounding a MLCT, a ligand-metal-charge transfer (LMCT) or a MC transition.[135,225] For the simplest case of $[Ru(bpy)_3]^{2+}$, the data in Appendix I support a superposition of two transitions, one being MC $d\sigma \leftarrow d\pi$ and the other MLCT $\pi^* \leftarrow d\pi$. In none of the complexes is the transition a LMCT however all have $d\sigma \leftarrow d\pi$ and $\pi^* \leftarrow d\pi$ transition elements. Suffice to say that the assignment of a mixed $\tilde{\nu}_{MC/MLCT}$ origin for this band would seem the most logical. The data do not clearly support one CT characteristic nor the other and the oscillator strength and experimental ε indicate a relaxed Laporte forbidden $d^* \leftarrow d$ transition due to the instantaneous dipole formation for MLCT transitions as discussed above.

Table 0-7 – Observed (for series of $[Ru(bpy)_3]^{2+}$ type complexes in methanol) and calculated wavenumbers (cm^{-1}) for the UV to visible bands of the substituted complexes.

Complex	$\tilde{\nu}_{MLCT}$ [a]		$\tilde{\nu}_{MC}$ [a]		$\tilde{\nu}_{LC}$ [a]	
	obs.	calc.	obs.	calc.	obs. [b]	calc.
$[Ru(bpy)_3]^{2+}$	22180	23290	28290	31510	34840	37040
$[Ru(bpy)_2(dmpbpy)]^{2+}$	21960	23260	27900	30760	34600	36930
$[Ru(dmpbpy)_2(bpy)]^{2+}$	21650	23110	27780	30330	34540	36860
$[Ru(dmpbpy)_3]^{2+}$	21340	22810	30070	29900	34010	36690

[a]: The terms $\tilde{\nu}_{MLCT}$, $\tilde{\nu}_{MC}$, $\tilde{\nu}_{LC}$ are described in the text

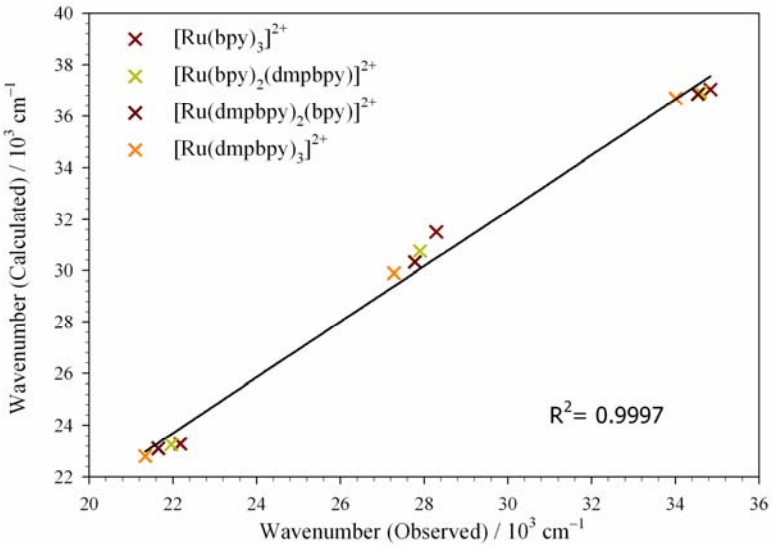

Figure 0-8 – Correlation of the observed major UV to visible charge transfer bands vs. calculated excitation wavenumbers (cm^{-1}) for the series of $[Ru(bpy)_3]^{2+}$ type complexes in MeOH.

As presented, the correlation of absolute vertical excitation energies and observed experimental bands in Figure 0-7 appears limited, although the relative band positions and certainly the spectral characteristics are reproduced well. The LC transitions in the blue region of the spectrum and the MLCT in the visible appear blue shifted from the experimental data. Gas phase calculations, as performed, are unable to reproduce solution spectral features, especially those energy shifts associated with the medium (solvatochromism).[208,270,277] Charge transfer bands, such as the broad MLCT observed here, are sensitive to solvent permittivity and this can indicate a change in the molecular dipole. As has already been discussed, this too indicates an instantaneous electric dipole formation.

A comparison of calculated and observed spectral bands is depicted in Table 0-7 with a linear relationship considered in Figure 0-8. Depicted is the linear correlation of the complexes (R^2 = 0.9997), all with equal agreement. The significance of this correlation is most likely coincidental, yet there is a distinct correlation between calculated and observed energies with all bands agreeing to, at worst 0.33 eV ($\tilde{\nu}_{LC}$, 2600 cm^{-1}), despite not correcting for solvent or other medium effects.

Relation to Previous Studies and Electronic Descriptions

Theoretical calculations on the electronic structure of complexes of the type "$[Ru(bpy)_3]^{2+}$" have previously been performed using TD-DFT,[277,289] Extended Hückel[297] and the semi-empirical INDO method[277,291,298] (and similar variants).[292,294] Much attention has been given to the N3 class of bis chelate diimine complexes due to their strong experimental attention in the literature[223,270,271,299] with these studies highlighting the influence of backbonding effects on the excited states.

For tris chelate complexes there is considerable history in the understanding of excited states. Kober and Meyer proposed that instantaneous dipole formation leads to a delocalised electron model and in their theoretical investigation proposed explicit assignments to the electronic spectrum.[293] The discussion here has followed these assignments, as well as that of Gorelsky and Lever,[277] with the data, we hypothesise, supporting a delocalised electron model. Gorelsky *et al.* using INDO/S have reviewed nicely metal-ligand orbital mixing,[291] and in a later discussion their comparison of DFT and INDO/S models depicted a delocalised system with unequal electron density for complexes with non-equivalent ligands.[277] Much of this effect is evident in our present investigation with a tendency for increased electron density on **bpy** over **dmpbpy** in the low-lying LUMO states.

The explicit description of singlet-triplet excited state manifolds has been a focus of the Crosby group[274,295,296,300] and also Kober and Meyer.[293] Our calculations have concentrated on singlet excited states, however the experimental data in combination with the occurrence of low wavenumber ^{1}MLCT states supports intersystem crossing that enhances ^{3}MLCT states. This factor appears to be strengthened by the inclusion of non-equivalent ligands in the coordination sphere. Further investigation of this, both experimentally and theoretically, is surely warranted through studies of excited state lifetimes, quantum injection yields, and the electronic structure of other heteroleptic complexes of this kind.

Conclusions

The contrast and comparison of a series of $[Ru(bpy)_3]^{2+}$ type complexes have been presented. Experimental data and the theoretical TD-DFT calculations have enabled the testing of non-equivalent ligand substitution on spectral and MO energy properties by the prediction of excited state transitions and energies.

Salient features of experimental electronic spectra (regions of CT bands) have been reproduced well despite gas phase calculations not being corrected for solvent/media effects. The three longest wavelength bands associated with known charge transfer phenomena were identified. The symmetry allowed visible $\tilde{\nu}_{MLCT}$ was assigned as a $\pi_\psi^* \leftarrow d\pi$ transition with the intense UV $\tilde{\nu}_{LC}$ evidently of $\pi_\psi^* \leftarrow \pi$ origin. The ambiguous shoulder on the blue side of $\tilde{\nu}_{MLCT}$ showed $d\sigma \leftarrow d\pi$ and $\pi^* \leftarrow d\pi$ transitional character and would best be described as $\tilde{\nu}_{MC/MLCT}$.

Comparison of observed and calculated vertical excitations showed good correlation; however the bands were blue shifted by, at worst, 0.33 eV (2600 cm^{-1}). The band shape of the MLCT at low wavenumbers was hypothesised as being of increased triplet character as indicated by the enhanced number of singlet states in this region and attributed to the phosphonated ligand, **dmpbpy**, in the coordination sphere. The effect of non-equivalent ligands in the coordination sphere was speculated to contribute to low quantum yields for surface bound sensitisers, with the lowest lying LUMO states consistently occupying **bpy**.

Despite the increased number of atoms in the phosphonated complexes and relativistic contraction of key metal-ligand bonds, the DFT study has quite successfully predicted geometrical and experimental photophysical data. The ECP basis sets and the hybridized *ab initio* model have performed well in studying the influence of ligand substituents on the optical properties of surface sensitisers. These studies attract considerable attention in the literature and this unique contribution may assist other researchers in the development of new surface sensitisers on both a practical and theoretical basis.

CHAPTER 5

Microwave Modification of TiO_2 for Efficient Photocatalysis

2. Introduction

The synthetic processing of titania has been the focal point of a concerted effort to optimise the properties of this important inorganic material.[159,162,301-305] Interest in this wide bandgap semiconductor has been due to the diversity of applications that this material affords; from a whitener in paints, cosmetics and textile dyes,[31] to an abrasive in toothpastes, an efficient photocatalyst[29,306] and more recently as a fundamental component in molecular scale electronics.[7,171,228] One motivation for improved synthetic processing has been the considerable attention that the dye-sensitised solar cell (DSC)[2,157,174] and related photoelectrochemical (PEC) cells has drawn in recent years.[307-309] These PEC cells rely heavily on the properties of a nanocrystalline titania thin film. The performance of nanocrystalline films depends profoundly on the sol-gel processed colloidal suspensions that are used to fabricate the mesoporous coating.[42,59,63]

Sol-gel preparation of nanoparticles is attractive due to its versatility and potential for mass production and has been rigorously investigated to improve the chemistry employed in the nanoparticle synthesis.[42,310] Material properties of the mesoporous films, such as crystalline phase, grain size, surface structure (area and volume), film porosity, optical dispersion and electron transport can be readily controlled by the synthesis procedures.[31] Although the material's final properties are dependant on its synthesis, it has been established that post-synthetic treatments, such as hydrothermal processing, can have significant effects on crystallinity and grain size.[37,39]

Hydrothermal processing of inorganic materials, such as high-pressure convection heat treatment of the colloidal suspension has a distinct effect on the grain morphology and crystalline phase.[39,311,312] Under these conditions Ostwald ripening, where the dissolution of smaller particles occurs in favour of the growth of larger grains, improves the crystallinity of the particles.[313] More recently microwave irradiation has been established to induce the same effect.[314-319]

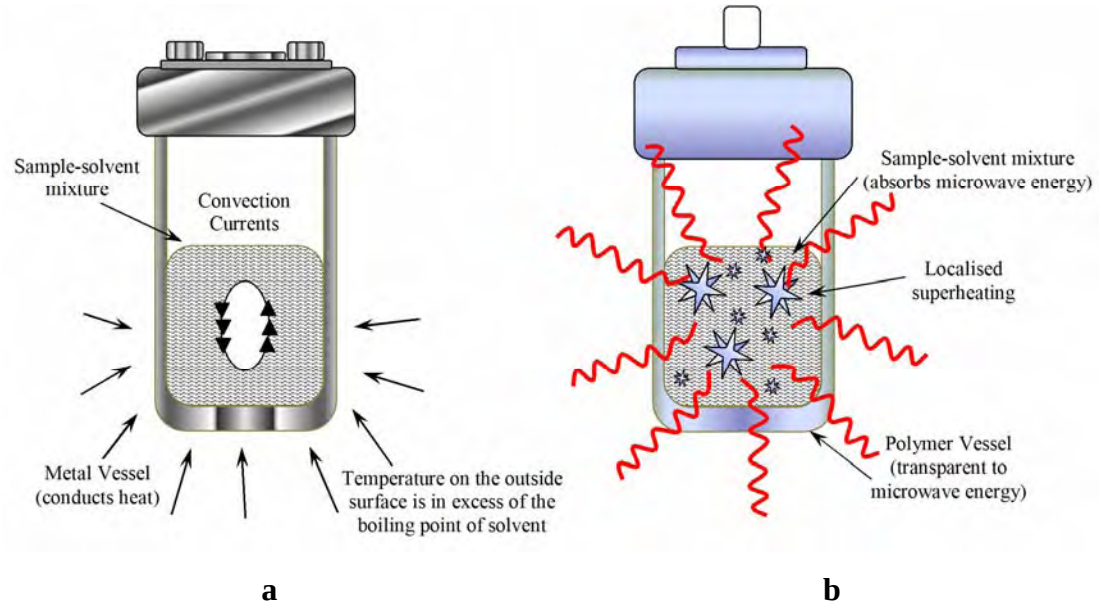

Figure 2-1 – The mode of hydrothermal bomb recrystallisation a) convection b) microwave.

Microwave irradiation is an efficient alternative as it allows for rapid heating to the required temperature and extremely rapid rates of crystallisation.[318,319] In effect this is a high temperature recrystallisation in which the dispersion medium and the dispersed phase are simultaneously affected.[314] High-frequency electromagnetic radiation (2.45×10^9 Hz) interacts with the permanent dipole of the liquid phase which initiates rapid solution heating from the resultant molecular rotation. Likewise permanent or induced dipoles in the dispersed phase cause rapid heating of the particles. These result in a reaction temperature in excess of the surrounding liquid – localised superheating (Figure 2-1).

Previously we have reported the preparation of highly crystalline TiO_2 nanoparticles by microwave irradiation.[3] The mechanism of the solvothermal process should have a profound effect under extended periods of irradiation and the results of such a study are presented here. The resultant powders were characterised to identify the properties pertaining to photocatalysis and PEC device applications and are compared and discussed in relation to commercially available materials.

2.1. Materials and Equipment

All reagents unless otherwise stated were used as received from Sigma-Aldrich.

Degussa P25 TiO_2 powder (TITANDIOXID P25, D-60287, PI-52342) was purchased from Degussa AG, Frankfurt.

The colloidal suspensions were flocculated by thermal dehydration at 80°C and mechanically ground in an agate mortar and pestle to give a finely divided powder. A portion of the powdered product was placed in a mortar and re-suspended in methanol by mild grinding before immersion of a holey carbon support (on a copper grid). The samples were air dried and the copper grid presented for morphology and grain size analysis of particles by transmission electron microscopy (TEM). Specimens were observed on the JEOL 2010F Analytical Scanning Transmission Electron Microscope operating at 200 keV. Selected-area electron diffraction (SAED) patterns were obtained and crystalline phase determined from comparison of identified reflections with those of standard diffraction files.

Nanoporous TiO_2 thin films were prepared by spreading a small quantity of a concentrated dispersion of TiO_2 colloid on a F:SnO_2 substrate as previously described.[7] For commercial Degussa P25, the powder sample was redispersed in H_2O to form a suitable sol by addition of small quantities of liquid in a mortar and pestle. Upon gelation the sample was treated as above to form a thin film for surface porosity analysis. Determination of relative surface porosity was performed on a FEI Quanta 200 environmental scanning electron microscope (ESEM) operating as a conventional high vacuum SEM. Thin films were scored with a diamond edge and fractured to produce an edge profile. Vapour evaporative deposition of a thin (20–25 Å) Au coating was provided by anodic deposition from a plasma source to improve surface charge dissipation and optical resolution.

The dehydrated samples were analysed by X-Ray Diffraction (XRD) using a PHILIPS PW1050 diffractometer with a Long Fine Focus Co Kα radiation source at 40 kV and 32 mA. The LFF Co source had 1° divergence, 1° anti-scatter, a 0.2 mm

receiving slit and one set of solar slits. The samples were presented as a thin film by mechanical treatment of the dehydrated samples, dissolved in a minimum of ethanol and adhered to a thin silicon plate. Data were collected by multiple passes from 26° – 33° 2θ with a 0.02° step at a speed of 0.144°/min. Diffraction patterns were analysed by co-addition and refinement using Diffraction Technology Traces 6.6.10. For calculation of crystallite size, instrumental broadening was corrected against a Boron Lanthanum (B_6La, PDF 03-065-1831) standard by collection and refinement of the 100 (24.85° 2θ) and 110 (35.44° 2θ) *hkl* faces.

Small-angle neutron scattering (SANS) measurements were conducted using the AUSANS instrument at HIFAR, ANSTO, Menai, NSW Australia. Dehydrated samples were suspended in D_2O (99.9%, Aldrich) and presented to the beam in 1 mm path length quartz cuvettes. The SANS data were directly collected using a neutron wavelength of 3.5 Å with spread (FWHM) $\Delta\lambda/\lambda = 0.15\%$. Data were collected at one sample to detector distance, 4.85 m giving a q range of $0.01 < q < 0.23$ Å^{-1}. SANS sample scattering was corrected for background, empty cell scattering, and individual detector pixel sensitivity using NIST SANS Data Reduction Software (National Institute of Standards and Technology (NIST) Center for Neutron Research, Gaithersburg, MD, http://www.ncnr.nist.gov/programs/sans/). Corrected SANS data sets were placed on an absolute scale and circularly averaged using a silica standard and software supplied by NIST.

Raman spectra were obtained by presentation of the dehydrated sample on a stainless steel slide and spectra collected on the Renishaw inVia Raman Microscope, fitted with a RSSF notch filter, and a TE cooled, deep depletion, CCD detector. The excitation source was a Renishaw doubled laser diode-pumped Nd-YAG emitting at a wavelength of 532 nm. Stokes-scattered radiation was corrected against a Si wafer (520.5 cm^{-1}) and spectra collected over an effective Raman shift range of 940–30 cm^{-1}, with instrumental resolution of ~4 cm^{-1}. A laser power of 50% was used with the co-addition of 64 scans to give a high signal-to-noise ratio.

Volumetric analyses of powdered samples for isothermal surface area and pore diameter were performed by a 99 point isotherm on a Micromeritics (Norcross, GA, USA) Tristar 3000 gas adsorption analyser. Samples were presented as a neat powder, dried at 130°C under a constant flow of UHP N_2 on a Micromeritics FlowPrep 060 degasser for 24 hours. Isothermal character, pore volumes and surface areas were calculated by fitting of a Brunauer–Emmett–Teller (BET) isotherm using the Barret–Joyner–Halenda (BJH) method incorporating the Harkins/Jura thickness equation for adsorbed layer thickness. All calculated parameters were standardized against Silica-Alumina (Micromeritics, part number: 004-16821-02).

2.1.1. Preparation of Colloidal TiO_2 Solutions

Colloidal TiO_2 solutions were prepared by hydrolysis of titanium isopropoxide following an experimental procedure adapted from that of O'Regan *et al.*[51] and previously described in detail by our group.[3] Convection hydrothermal treatment of the resultant colloid was performed according to our previous procedure.[3] Briefly, 100 cm^3 of TiO_2 colloid was transferred to a 200 cm^3 Pyrex glass lined stainless steel autoclave Parr-bomb. Treatment of the aliquot was carried out for 15 hours (900 minutes) at 200°C in a convection oven (1300 W, S.E.M.), followed by cooling to room temperature and standing for 24 hours to yield a thick white suspension. This sample is denoted 900 min HT.

2.1.2. Microwave Hydrothermal Treatment of Colloidal TiO_2 Suspensions

A 100 cm^3 aliquot of TiO_2 colloid prepared in Section 2.1.1 was transferred to a Teflon lined polycarbonate vessel. Our previous studies had determined the optimised temperature of the microwave hydrothermal process to be 145°C.[3] Accordingly, microwave processing was performed at 145°C in an ETHOS Synth MicroSynth Labstation (1200 ± 50 W, 2.45 GHz, Milestone MLS) at a setting of 80% power, with a pressure ramp from ambient to the required pressure (60 psi) over a 2 minute period. Temperature in the reaction vessel was automated by the ATC-FO fibre optic temperature probe and pressure maintained by the APC-55E pressure control. The duration of treatment was varied from 5–360 minutes. For each processing batch 15 cm^3 was dehydrated and the sample analysed as detailed below. These samples are denoted by their treatment time and the identifier MW e.g. for 40 minute microwave treatment the sample is 40 min MW.

2.2. Results and Discussion

2.2.3. X-Ray Diffraction Analysis

Wide-angle powder XRD patterns in the region of the anatase (101) d-spacing for the treated and untreated TiO_2 powders are depicted in Figure 2-2. As a point of reference the commercially supplied Degussa P25 is also depicted.

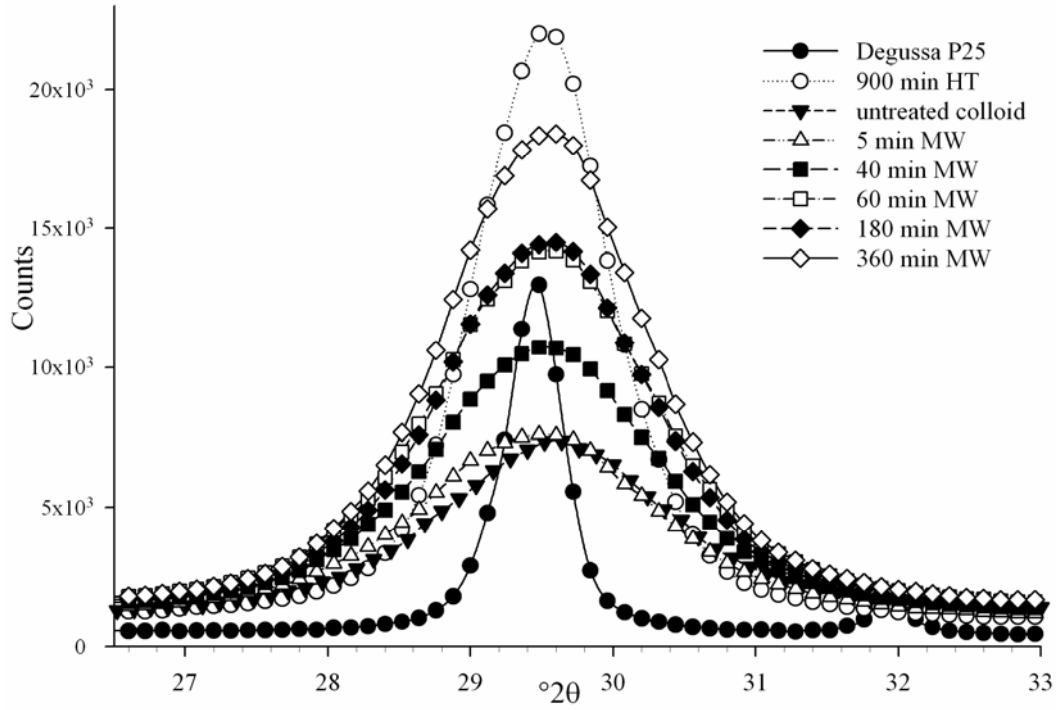

Figure 2-2 – Stacked XRD diffraction patterns for investigated TiO_2 powders. Narrowing of the FWHM is observed for increased periods of processing. Traces were digitally smoothed following correction for contribution from Kα_2 radiation.

The peak intensities obtained from XRD traces for each of the samples correlates both to the quantity of crystalline material and to the grain size of the particles. In comparison to those processed by microwave treatment the peaks obtained for 900 min HT processed TiO_2 and P25 are substantially narrower. However for the untreated colloid and those treated by microwave processing the peak progressively narrows and intensifies indicating a growth in the primary crystallite size. The progression is quantified by measurement of the peak FWHM and the relationship between this quantity and the primary crystallite size (P_D) is identified by application of the Scherrer equation.[320] Good agreement is found with the primary crystallite size

of the commercial Degussa P25[321] (26.7 nm) and also that of the 900 min HT convection treated sample (11.1 nm).[162] Extended periods of processing by microwave treatment appears to have minimal effect on the primary grain size which increases from ~5.7–7.2 nm. The primary crystallite size for the samples is given in Table 2-1.

Table 2-1 – Calculated Scherrer crystallite size (nm) from Anatase 101 (29.53 / °2θ) reflection.

sample	P_D / nm	error
Untreated	5.67	±0.15
5 min MW	5.99	±0.12
10 min MW	6.25	±0.12
20 min MW	6.61	±0.14
40 min MW	6.41	±0.12
60 min MW	6.72	±0.13
120 min MW	6.98	±0.13
180 min MW	6.67	±0.09
360 min MW	7.19	±0.11
900 min HT	11.12	±0.13
Degussa P25	26.71	±0.45

According to the XRD patterns depicted in Figure 2-2, no indication of significant phase transformation from that of Anatase during any of the hydrothermal processing has occurred even under extended periods of irradiation.

The phase compositions of the microwave processed powders were consistent with that of synthetic Anatase (PDF 00-021-1272) with the absence of any further reflections in the 26°–33° 2θ region. An additional inflection in the pattern of Degussa P25 indicates rutile as a polymorphic impurity consistent with literature.[322] Comparison of the reflection to synthetic Rutile (PDF 00-021-1276) and Brookite (PDF 00-029-1360), does not indicate measurable quantities within the structure of the convection or microwave processed powders. XRD data were acquired over a narrow collection range (26° – 33° 2θ) to monitor the FWHM of the Anatase (101) peak only. The strong Brookite (121) peak seen in the TEM data (see later) was outside this scan range (it would occur at ~35.93°). A second much weaker peak, due to Brookite (111), occurs at ~29.92°. However, the broad Anatase peak centred at 29.53° would obscure this feature.

a

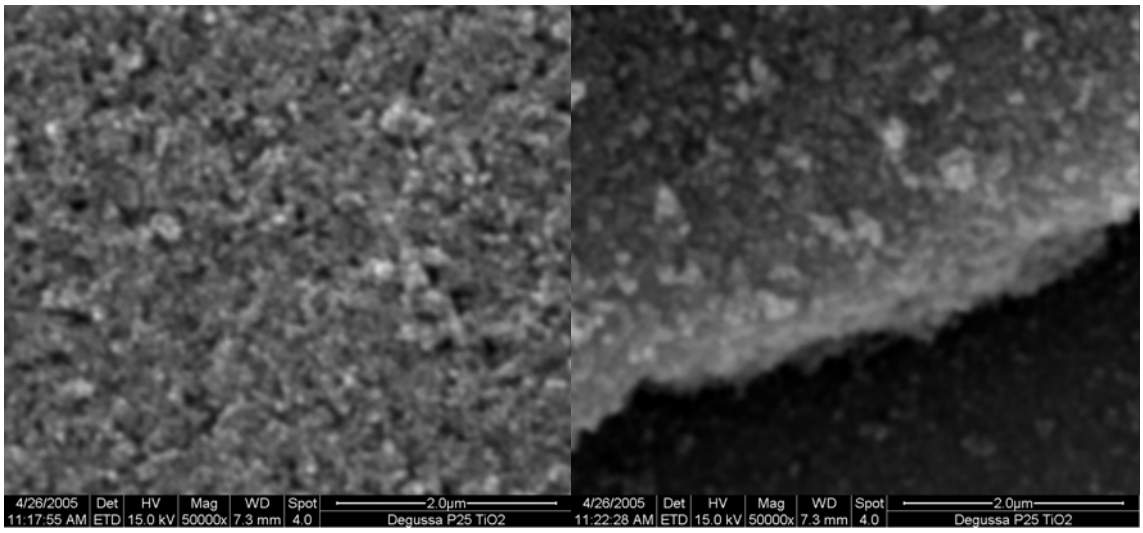

b

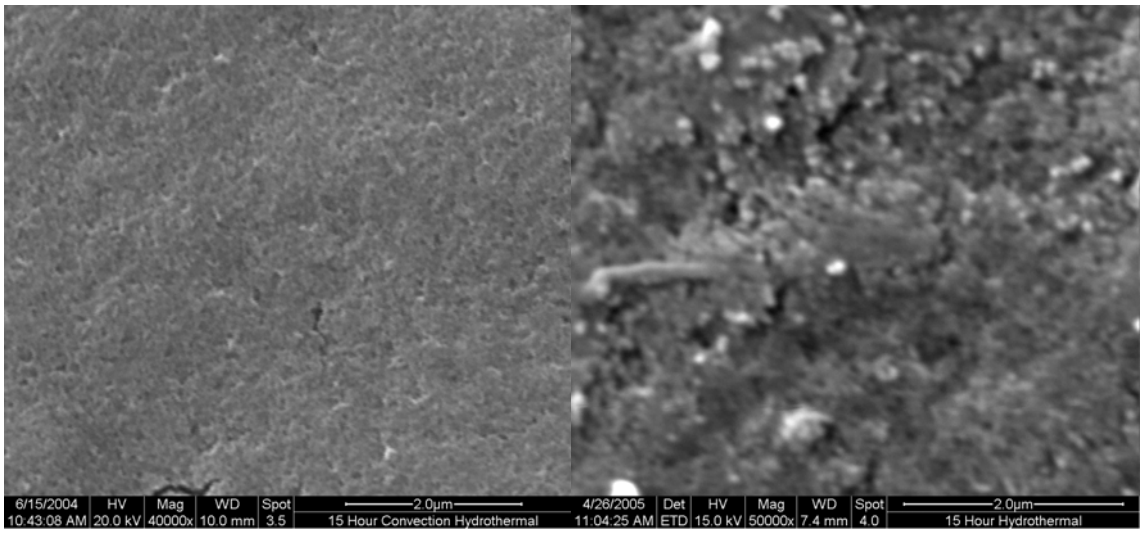

c

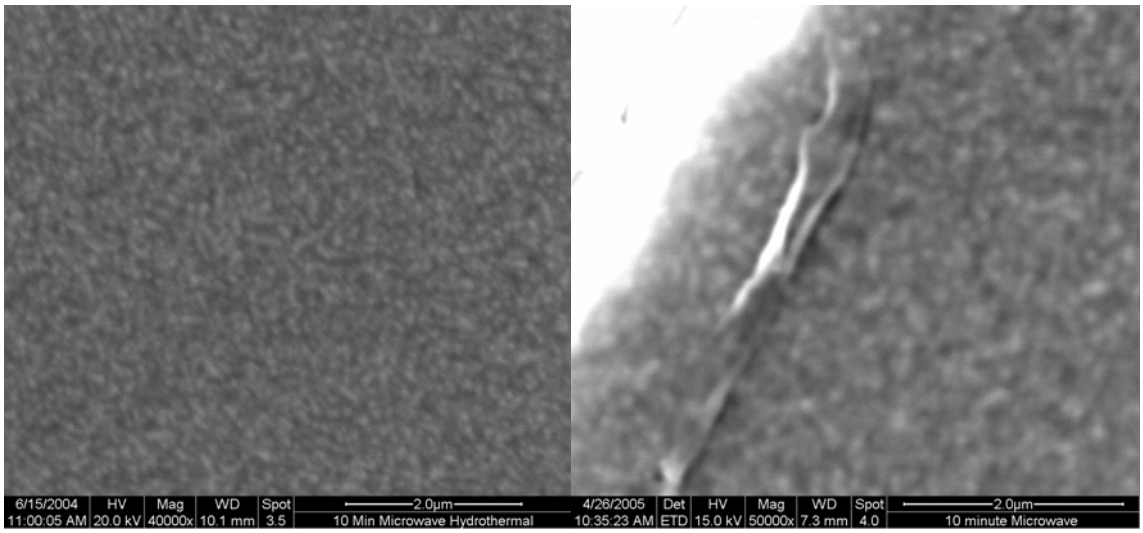

Figure 2-3 – SEM images of orthogonal surface structure (left) and structure at the fractured film edge (right) a) Degussa P25 film b) 900 min HT convection film c) 10 min MW film. Scales of images are as indicated.

2.2.4. SEM Surface Morphology

The morphology of the mesoporous films prepared from the colloidal samples is shown in Figure 2-3. The micrographs indicate that the thin films are continuous and crack free and have a thickness of the order of ~10 μm (not depicted).

The SEM images indicate that commercial Degussa P25 TiO_2 forms relatively large agglomerates during film formation/calcination. These ≈ 260 nm agglomerates form highly irregular clusters and create irregular shaped (≈ 170 nm) pores.

The more regular shaped 900 min HT convection treated nanocrystals give a film structure that has no identifiable agglomerates, however there are distinctive, ≈ 90 nm, pores. The edge profile shows ‘plate-like’ agglomerates arranged to give valleys and ridges in the surface.

The film prepared from microwave processed dispersions (Figure 2-3C) shows a much reduced pore size in comparison to the other films depicted. Certainly there is an inherent porosity to the films, though not easily identified. The image projects a surface that is smooth and uniform apparently due to the dense packing of the nanocrystalline particles. The edge profile shows a similarity to the surface with a consistent structure identified.

A qualitative estimate of surface roughness can be gauged from these images. It can be quite clearly seen that the microwave processed dispersions form a secondary structure that is much denser than that of convection processed dispersions and the commercial Degussa P25.

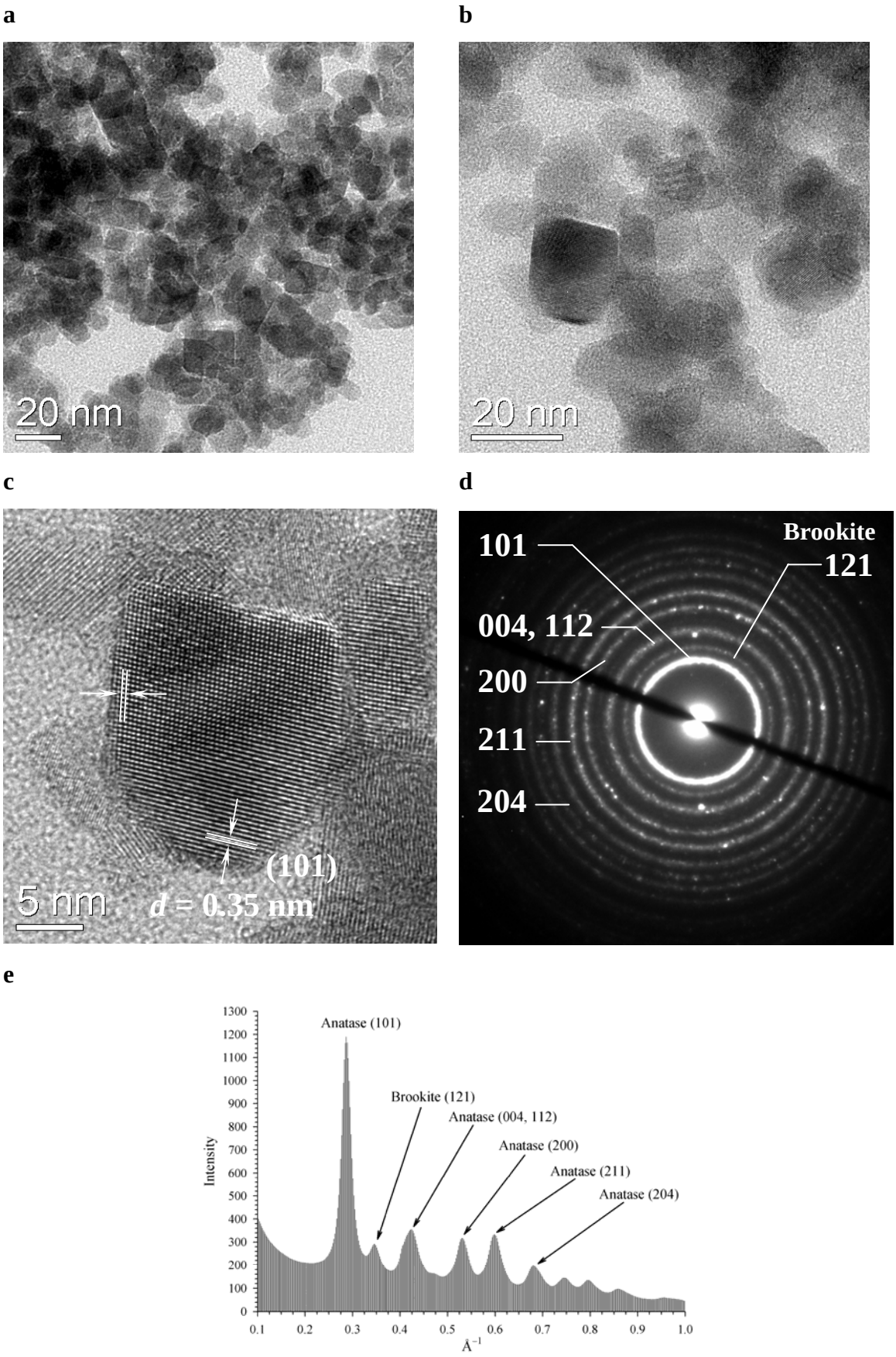

Figure 2-4 – 900 min HT convection TiO_2 a) ensemble of nanocrystals; b) energy filtered image of a; c) HRTEM showing the (101) lattice planes; d) SAED of nanocrystals e) radial profile of d.

2.2.5. TEM and Electron Diffraction Investigation

Images of dispersed nanocrystals as observed by transmission electron microscopy (TEM) for the hydrothermally treated samples are shown in Figure 2-4 – Figure 2-10. The 900 min HT TiO_2 sample is shown in the grouped images of Figure 2-4.

There is distinct polydispersion of particle shapes including spherical and elongated particles of ~10 nm (with some up to 20 nm) that are present in 900 min HT. The sample shows considerable aggregation yet the primary grain size can still be readily distinguished. High resolution TEM (HRTEM) (Figure 2-4C) depict defined nanocrystals with distinct lattice fringes indicative of the Anatase 101 face. The multi-faceted crystals appear to be oriented along the 101 plane with elongated particles observed indicating that, during the Ostwald ripening process, epitaxial growth occurs along this crystal plane. Indeed, for convection hydrothermal treatment Ostwald crystal growth is extensive with large crystals observed such as the >90 nm lath of Figure 2-5.

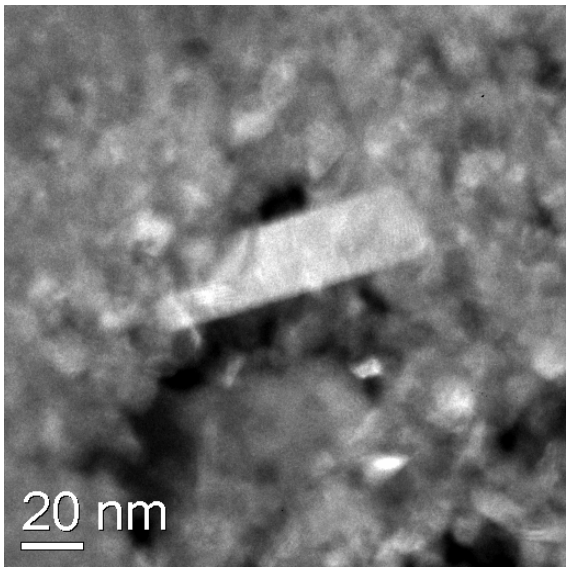

Figure 2-5 – Bright field TEM image of Anatase lath like crystal observed in 900 min HT sample.

In contrast to that observed for convection treated TiO_2, the microwave processed TiO_2 samples show a more uniform grain size. There is only a negligible change in the primary particle size, which remains in the 5–10 nm range, as the time of processing is extended. A complete survey of the microwave samples did not identify lath like crystals such as those observed for convection treated TiO_2, however an

abnormal crystallite was observed in the 10 min MW sample (Figure 2-6). A large particle (~17 nm), in comparison to the average crystallite size (~6 nm) as determined by XRD, was observed. This particle was mostly of Brookite composition (SAED analysis).

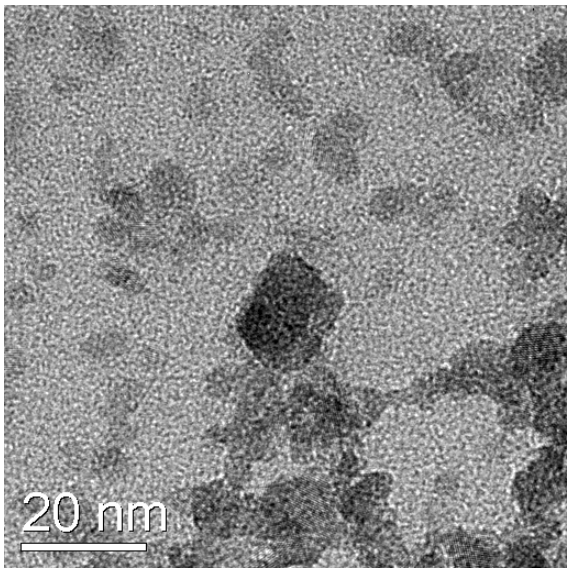

Figure 2-6 – Energy-filtered TEM image of ~17 nm Brookite observed in 10 min MW TiO_2.

Representative 20, 120, 180 and 360 min MW samples are depicted on the following pages. Shown in Figure 2-7 are the TEM images obtained for 20 min MW TiO_2.

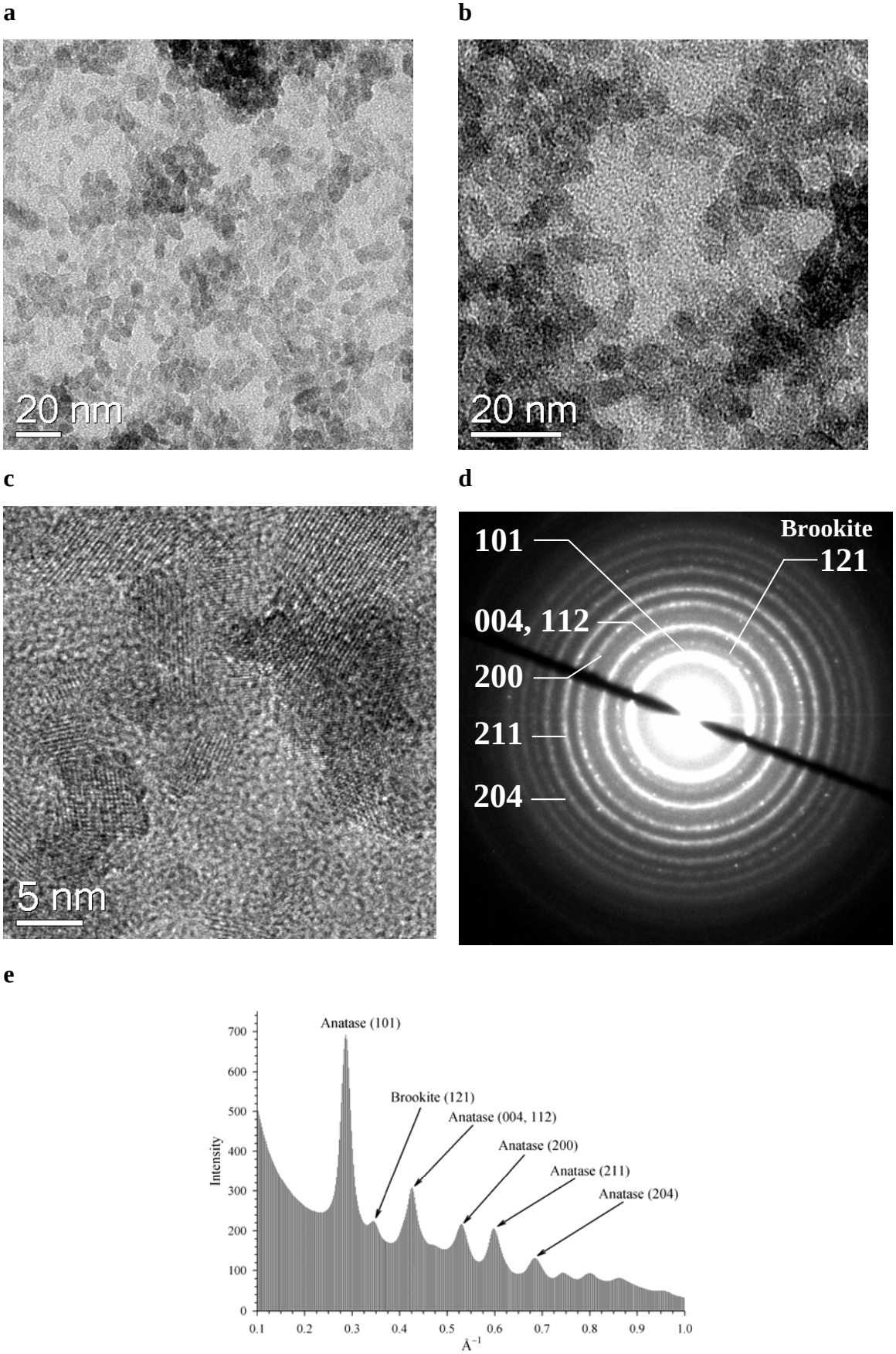

Figure 2-7 – 20 min MW treatment a) ensemble of nanocrystals; b) medium magnification energy filtered image; c) HRTEM of microcluster; d) SAED of microcluster; e) radial profile of d.

In contrast to the lengthy convection treatment in Figure 2-4, the 20 minute microwave treatment gives a comparable colloidal product in appearance. The nanocrystals appear semi-spherical and maintain a dispersed arrangement with minimal amount of aggregation. The mean grain size is substantially smaller and there are elongated particles that indicate growth of the primary crystallite. HRTEM shows nanocrystals that are elongated in one direction with the apex of two lattice planes evident on several of the particles. Selected-area electron diffraction (SAED) of this region gives a pattern consistent with the presence of both Anatase and Brookite crystal phases, with the radial profile identifying the 101, 004, 112, 200, 211 and 204 reflections for Anatase. The Brookite 121 reflection was also identified.

The micrographs for 120, 180 and 360 min MW samples show consistent features to that of the 20 min MW sample. There appears to be a steady increase in the primary crystallite size, however crystallite growth is not directly proportional to the increase in period of irradiation. The HRTEM for 180 min MW and 360 min MW (Figure 2-9C and Figure 2-10C respectively) show distinct lattice fringes attributable to the Anatase 101 plane with the SAED and radial profiles consistent with the above reflections. The frequency of larger particles is evident although the larger particles are increasingly semi-spherical with increased poly-dispersion of the nanocrystals.

In somewhat of a contrast in the 360 min MW sample the nanocrystals are not as dispersed and there appears to be an increased number of larger particles (~10 nm). The appearance of larger particles may simply be a factor of aggregation with aggregates unable to be clearly resolved from single nanocrystals; evidence for this is supported by the Scherrer calculations of primary grain size from XRD traces in Section 2.2.3.

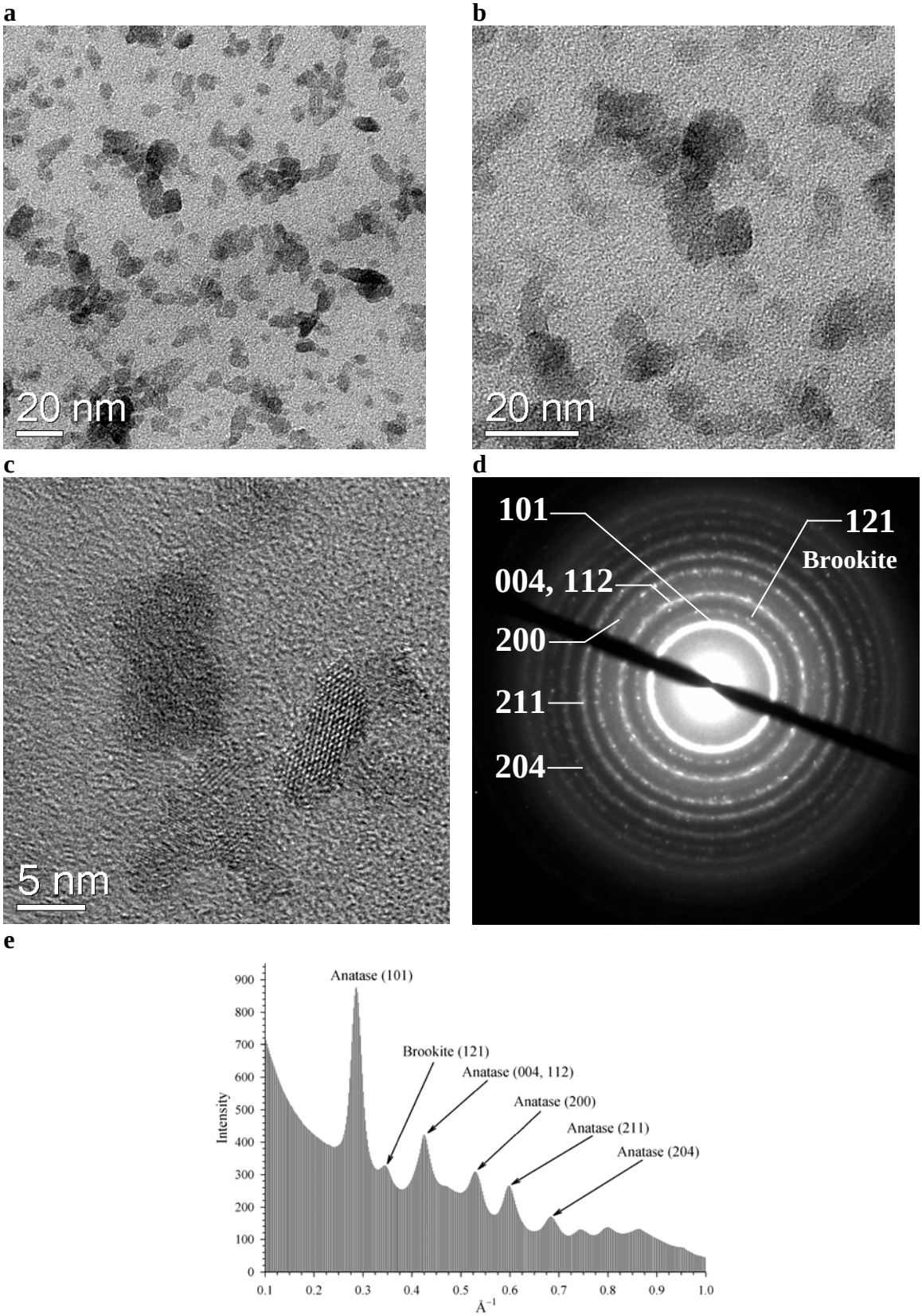

Figure 2-8 – 120 min MW treatment a) dispersed nanocrystals; b) energy filtered image of a; c) HRTEM of isolated grain; d) SAED of small cluster of nanocrystals; e) radial profile of d.

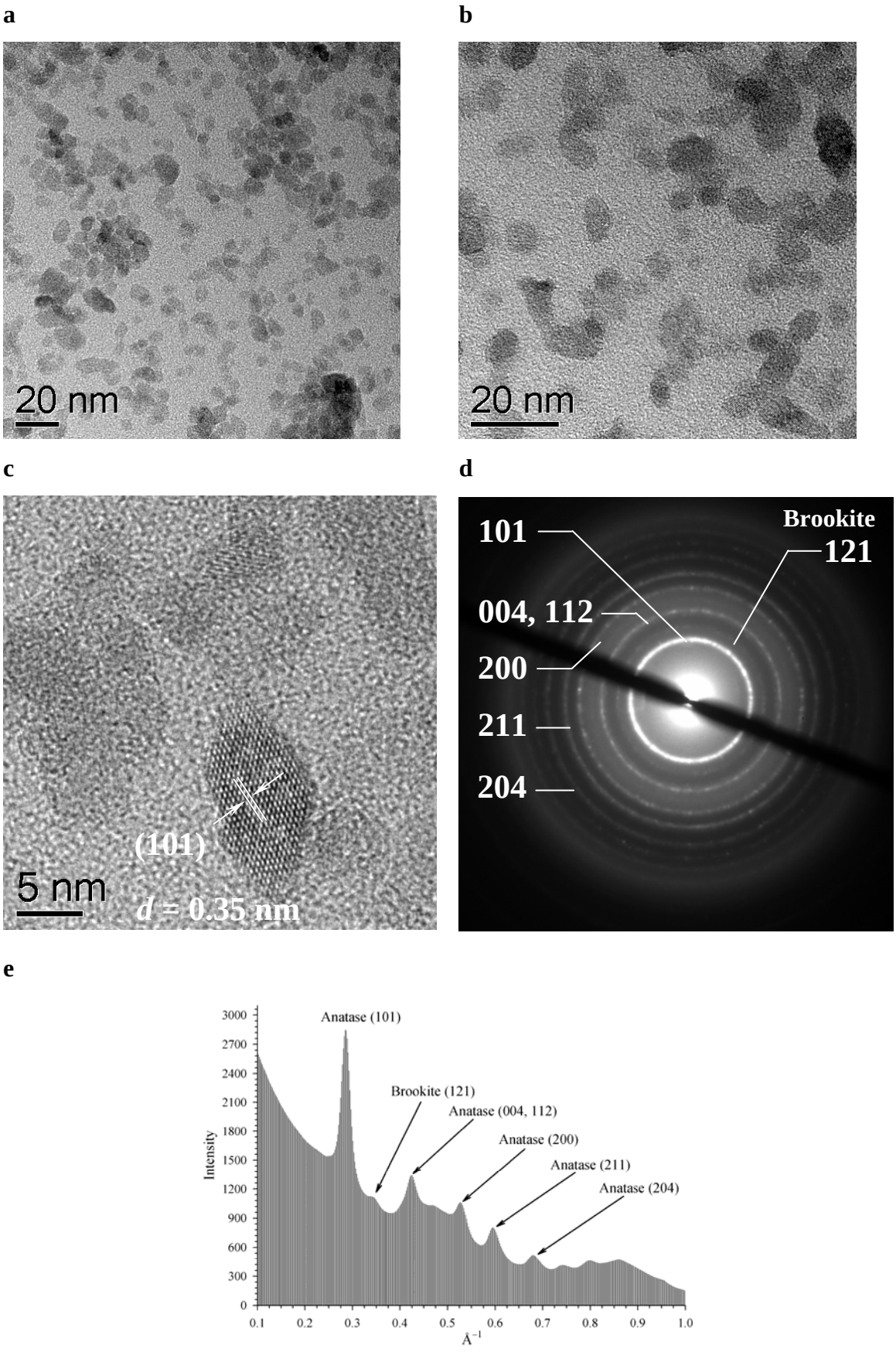

Figure 2-9 – 180 min MW treatment a) dispersed nanocrystals with some larger particles present; b) energy filtered image; c) HRTEM showing the multifaceted nanocrystals; d) SAED of nanocrystals; e) radial profile of d.

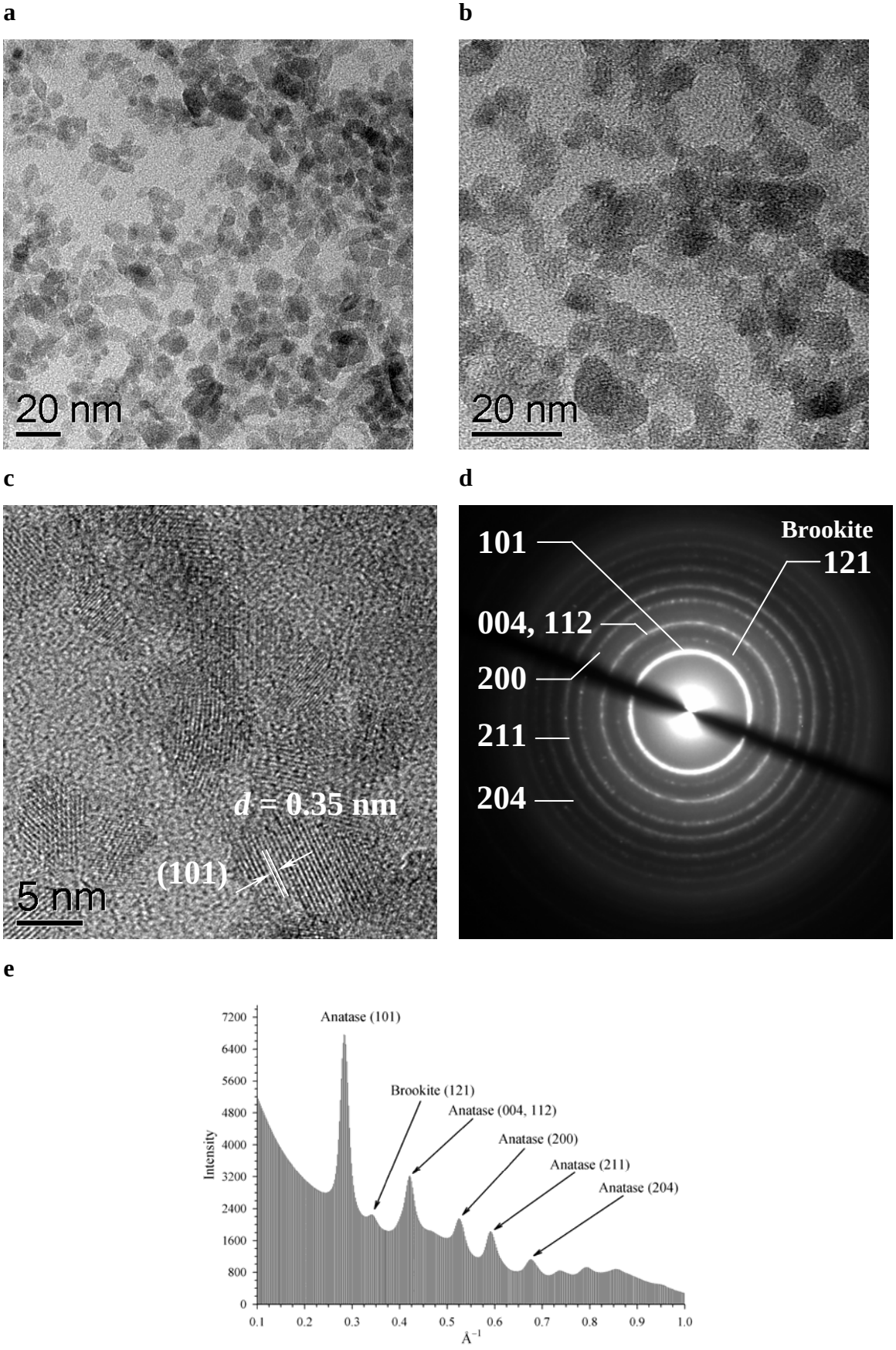

Figure 2-10 – 360 min MW treatment a) ensemble of nanocrystals; b) energy filtered image of a; c) HRTEM showing the (101) lattice planes; d) SAED of nanocrystals; e) radial profile of d.

The grain sizes observed for all the samples analysed by TEM are in good agreement with those determined by XRD, with a small increase in the observed primary grain size with respect to period of irradiation. The tendency of the particles to aggregate may indicate the presence of a heavily hydroxlated surface or to the presence of NO_3^-, residual from peptization, affording an ionic attraction of particles.

Previously we noted that the bright peak, the second sequential peak, in our electron diffraction radial profiles is indicative of Brookite.[3] For the present series of SAED radial profiles the first peak corresponds to Anatase (101) and the second to that of Brookite (121).The subsequent intense peaks correspond to that of Anatase (004 and 112, 200, 211, 204) with the remaining peaks being both unresolved and mutual to Anatase and Brookite. No quantitative determination of phase composition was obtained from these radial profiles. However a qualitative indication of the phase ratio can be obtained by interpolation of the peak intensities of Anatase (101) and Brookite (121) *hkl* reflections.

A ratio of relative intensities of Brookite/Anatase gives an estimate of the binary phase composition for the series of microwave processed colloids to be ~34% compared to ~24% for the convection treated colloid. The binary phase ratio also indicates an increase in Brookite composition proportional to processing time for 180>120>60>20>5 min MW samples before a phase reversal in the 360 min MW powder. This phase composition is highly qualitative only and determination of absolute binary phase composition was inconclusive.

The presence of increased proportions of Brookite in the sample would be indicated by a skewed shoulder in the region of the 101 reflection of XRD patterns (Figure 2-1). Indeed close examination of the diffraction pattern does indicate the presence of a shoulder in the region of the Brookite and this supports the SAED radial profile analysis.

2.2.6. Small Angle Neutron Scattering (SANS) Investigation of Colloidal Suspensions

For small angle diffraction, the scattered intensity can be represented as a function of the Fourier spatial frequency, q [Equation (2-1)]:

$$q = (4\pi/\lambda)\sin(\theta/2) \tag{2-1}$$

Application of Bragg's law allows the relation of q to a characteristic length scale $l = 2\pi/q$, and to the scattering angle of the incident radiation, θ, of wavelength, λ.

Depending on individual sample scattering, four distinct regions in the scattering curve can be observed; namely the limiting, Guinier, Porod and Bragg regions corresponding to limiting, low (q_R ~1), intermediate ($R \leq q^{-1} \geq a$) and large (q_a ~1) scattering angles respectively. Where a is the bond length and R is the radius of gyration.

SANS allows the determination of particle shape and size dependant on the instrumental resolution. The rollover of the AUSANS instrument at q = 0.01 does not allow us to study the gyration length and hence particle size of these colloids in the Guinier region. However observations in the Porod region allow us to examine particle aggregation of the as prepared colloids in solution. SANS data of the Porod region are depicted in Figure 2-11.

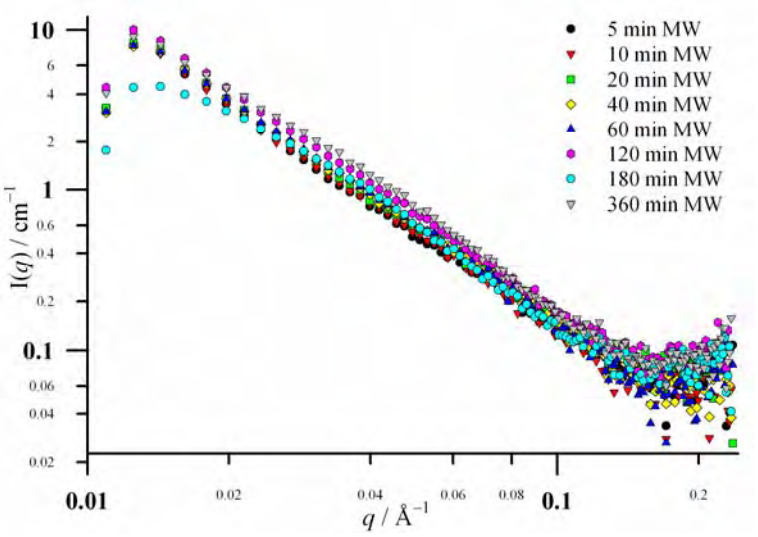

Sample	*P*
5 min MW	–4.7
10 min MW	–4.5
20 min MW	–4.6
40 min MW	–4.4
60 min MW	–4.4
120 min MW	–4.4
180 min MW	–3.7
360 min MW	–4.0

Figure 2-11 – SANS Porod plot of modified TiO_2 colloidal suspensions prepared by microwave hydrothermal treatment – the Porod slope, *P*, as determined from the linear portion (*q* = 0.02–0.04) of the plot are tabulated opposite. Mole fractions for all samples were in the range 0.49–0.52 M and suspended particles were for acidic conditions.

The microwave modification does not appear to have a profound influence on the solution properties of the particles. On examination of the scattered data no peak is observed as an indication of nearest-neighbour interaction. For the relative concentration of the solution (~0.5 M) interaction would be expected due to proximity of particles in solution. What is observed is a change in the slope of the scattered intensity profile that corresponds to ~0.04 $Å^{-1}$ for all treatment times. This change in slope is prominent in the 180 min MW sample where q is related to the average distance between particle centres and is equivalent to a distance, $d = 2\pi/q$ = 15.7 nm.

The magnitude of the Porod slope for each of the samples in the linear region q = 0.02–0.04 is indicated in Figure 2-11 as P. The tabulated values all reduce to a Porod slope of −4, which is indicative of a fractally smooth surface as observed for dispersions of dense colloidal particles. For polydispersed systems, without further knowledge of the extent of polydispersion, it is not possible to derive any meaningful information regarding particle dimension and structure from analysis of scattering intensities in the Porod region.

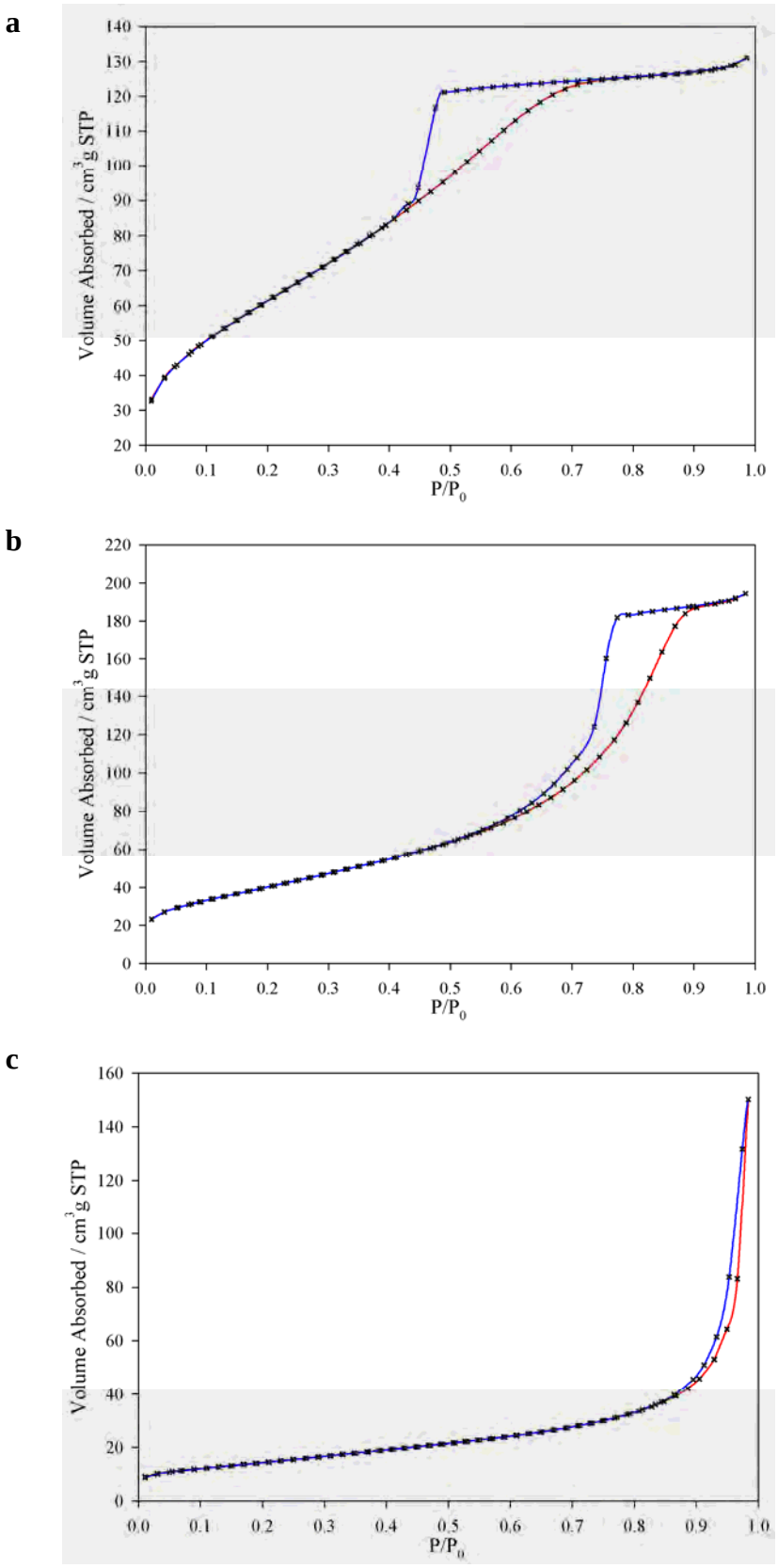

Figure 2-12 – Representative isotherms for prepared TiO_2 samples a) 180 min MW b) 900 min HT c) Degussa P25; adsorption –×–, desorption –×–.

2.2.7. Isothermal Nitrogen Adsorption-Desorption

Surface area and pore size analysis by gas sorption was performed on all prepared samples. In addition the commercially obtained Degussa P25 TiO_2 and a Silica-Alumina sample were analysed. Isothermal characterisation showed an obvious distinction between the different methods of TiO_2 preparation, with the representative N_2 sorption isotherms presented in Figure 2-12.

The samples prepared by hydrothermal processing (Figure 2-12, A and B) exhibit type IV characteristics in the desorption portion of the isotherm which gives rise to type H2 hysteresis, while commercial Degussa P25 is typical of type IV with H3 hysteresis.[323] The H2 hysteresis loop, with limiting adsorption at high P/P_0 shows a distinct level portion to the curve, which indicates a uniform distribution of pore size. The substantial hysteresis is due to hindrance to drainage from the pores through small openings (narrow pore neck), whereas adsorption into these pores occurs quite readily. For the microwave processed TiO_2, the well-defined step between P/P_0 0.45 and 0.75 is formed from the condensation/evaporation of the adsorbate within the mesoporous network during adsorption/desorption respectively. This has been observed to arise from hexagonal-shaped pores from the aggregate of semi-spherical particles.[324] In contrast the ill-defined step of the H3 hysteresis loop (Figure 2-12, C) indicates no limiting adsorption and hence minimal trapping of molecules draining from the pores. While interparticle capillary condensation gives rise to the H3 hysteresis loop at high (> 0.9) P/P_0.

A summary of the isothermal parameters calculated from the gas sorption data is presented in Table 2-2.

Table 2-2 – Calculated isothermal parameters.

sample	area		volume	pore size
	SA_{BET} (m^2/g)	error	PV_{SP} (cm^3/g)	D_{avg} nm
untreated colloid	185.0	±1.7	0.106	2.29
5 min MW	204.7	±1.5	0.121	2.37
10 min MW	204.1	±1.5	0.120	2.36
20 min MW	198.4	±1.3	0.120	2.43
40 min MW	199.3	±1.1	0.125	2.52
60 min MW	198.3	±1.0	0.130	2.61
120 min MW	197.4	±1.0	0.132	2.68
180 min MW	226.0	±1.7	0.203	3.59
360 min MW	213.0	±1.3	0.182	3.42
900 min HT	147.2	±1.2	0.301	8.18
Degussa P25	51.78	±0.25	0.232	17.9
Silica-Alumina	204.5	±0.6	0.589	11.52

The interparticle pores for the hydrothermally treated TiO_2 samples can be observed in the TEM images (Section 2.2.5), however they are not clearly defined. All microwave processed samples have a pore diameter < 4 nm with a small increase in pore diameter proportional to the irradiation time. In contrast to this are the larger pores of the convection hydrothermal sample (three times that of the microwave samples) and the considerably larger commercial Degussa P25. However, the decreased particle size afforded by the microwave processes gives a substantially increased specific surface area (by the BET model) over that of the convection treated and Degussa P25 samples.

The single-point pore volume (PV_{SP}) shows little difference afforded by microwave processing, however at extended periods of irradiation PV_{SP} approaches that of Degussa P25 and the convection treated sample. Of note is the change observed for the 180 min MW sample in comparison to the shorter treatment times and to that of the 360 min MW sample. A plot of differential logarithmic mesopore size distribution emphasises large pores in the structures, with the data depicted in Figure 2-13.

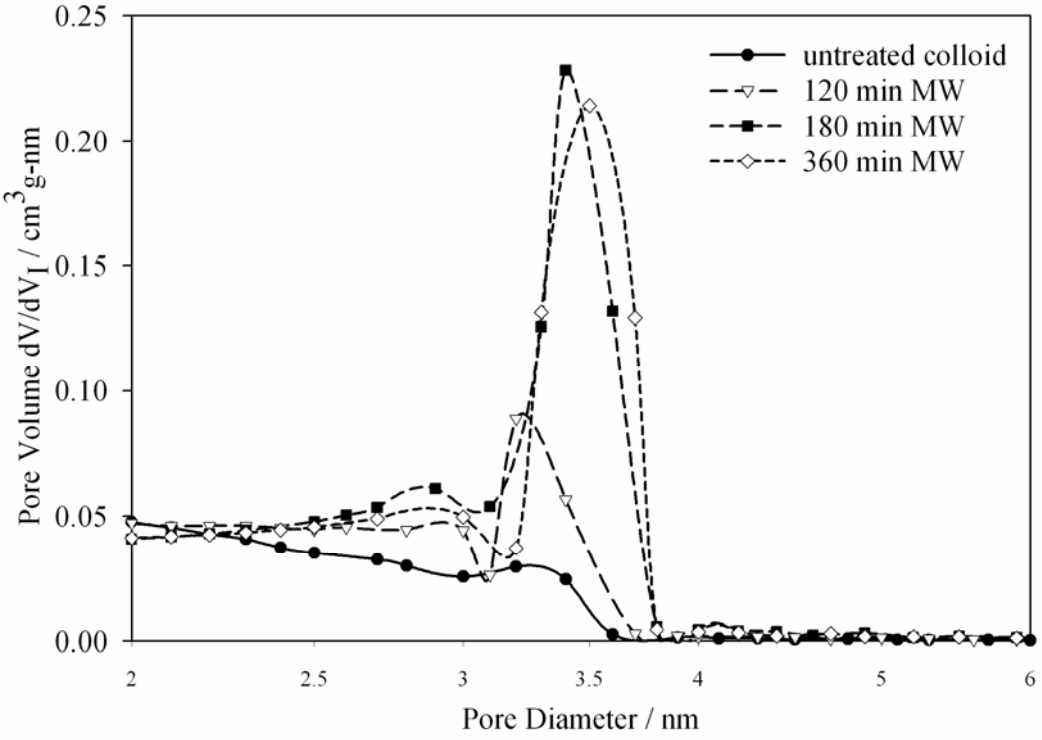

Figure 2-13 – Correlation of the change in pore volume increment with extended period of microwave treatment.

From the data in Table 2-2, all the hydrothermally treated samples emphasise a single pore size with the convection heat treated TiO_2 showing the occurrence of the largest pores compared microwave treated samples. In comparison Degussa P25 shows a bimodal distribution for pores with a reduced pore size (not depicted). Also apparent is a progression in the emphasised pore volume for the period of microwave treatment with a substantial increase at 180 minutes that appears to be reversed by 360 minutes.

This indicates, in association with the other isothermal characteristics, that 180 minutes is an optimum treatment time for microwave processing of TiO_2. The 360 min MW sample appears to show a change in the trend with the microwave processing. The microwave treatment is a thermodynamic equilibrium and reversal of the 360 in MW sample is potentially an outlier as the apparent reversal is unexpected.

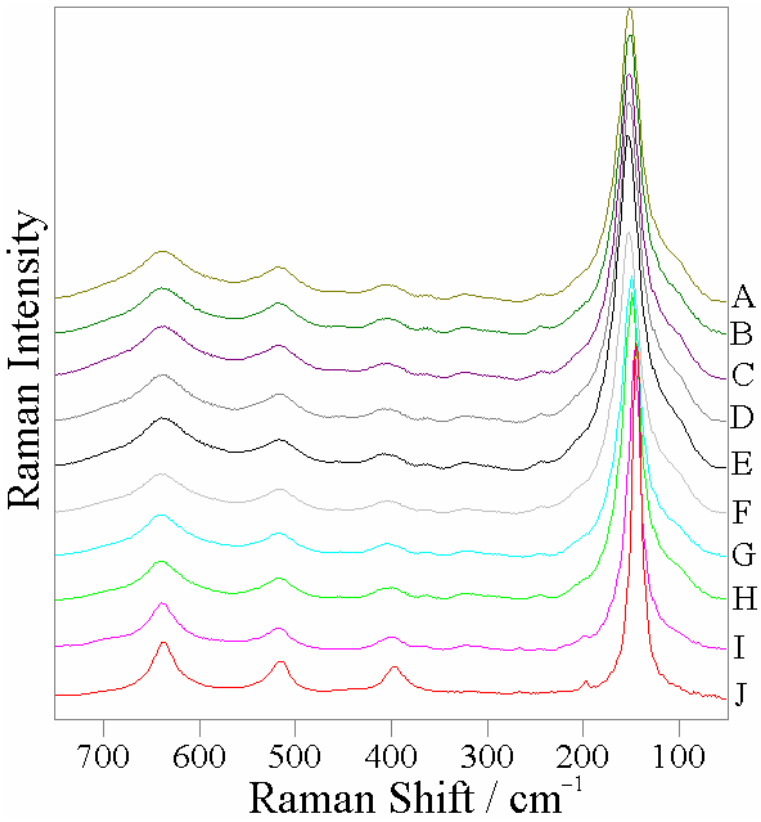

Figure 2-14 – Raman spectra of microwave hydrothermally treated TiO_2. Sample names are given as treatment times with alternative methods of preparation given for comparison. a) 5 min MW; b) 10 min MW; c) 20 min MW; d) 40 min MW; e) 60 min MW; f) 120 min MW; g) 180 min MW; h) 360 min MW; i) 900 min HT; j) Degussa P25.

2.2.8. Raman Spectroscopy

Figure 2-14 depicts the Raman spectra of microwave colloidal TiO_2 samples treated for 5–360 minutes and comparative convection and commercial samples, respectively.

The spectra of samples derived from the colloidal precursor can all be ascribed to a mixture of anatase and Brookite as reported by Gotic *et al*.[46] The composition is predominately Anatase although, the intense band at ~150 cm^{-1} is also observed for Brookite, this may indicate the samples contain some Brookite. However due to the absence of bands at 128 and 636 cm^{-1}, which should also be present for this phase, this is unlikely. The intense vibration at ~150 cm^{-1}, which is common to both Anatase and Brookite, shows an asymmetrical peak shape which can be attributed to polydispersion of particle size. However it also shows a high energy shoulder and this is most likely due to the minor phase impurity. As the length of treatment progresses, the broadness of this shoulder diminishes. There is a notable absence of bands attributable to Rutile; hence the microwave spectra of Figure 2-14 will be interpreted empirically as being of Anatase composition.

The spectra revealed a strong sharp band at 152 cm^{-1}, three mid intensity bands at 401, 516 and 638 cm^{-1}, and a weak band at ~200 cm^{-1} that are consistent with results obtained by Cheng *et al*. for the presence of Anatase TiO_2.[37] The Raman-active phonons have been identified by factor group analysis as $A_{1g} + 2B_{1g}$ and $3E_g$ vibrational modes.[44] These occur at 142 cm^{-1}, 200 cm^{-1} and 639 cm^{-1} for the E_g phonon modes with the 142 cm^{-1} band the most prominent in the spectrum. The fundamental B_{1g} mode occurs at 397 cm^{-1} while the band at 515 cm^{-1} has been assigned to both an A_{1g} and a B_{1g} mode due to the small separation of these phonons. Conversely, Brookite has 36 Raman-active phonons ($9A_{1g}$, $9B_{1g}$, $9B_{2g}$, $9B_{3g}$) and, due to the simplicity of the spectra of microwave modified TiO_2 samples, this factor alone supports the premise of a predominant Anatase phase.

Although bands at 436 cm^{-1}, 611 cm^{-1}, 240 cm^{-1} and 110 cm^{-1} characteristic of the Rutile phase were absent, a weak broad band was present at 245 cm^{-1}. It has been

suggested that this is not due to Rutile, however it results from disorder-induced scattering, second-order scattering, or stoichiometric deficiencies in the oxide.[37,44,46,325]

Due to the relative intensity of the E_g band at low frequency, changes in its peak shape, intensity and position are considered diagnostic of crystallite properties. The collected spectra were normalised to an arbitrary scale and the characteristics of the low frequency band are outlined in Table 2-3. The 900 min HT and Degussa P25 samples are shown as a comparison. These samples indicate high crystallinity and phase purity consistent with the techniques previously described.

Table 2-3 – Peak characteristics identified for the Anatase E_g band.

sample	shift / cm^{-1}	FWHM
5 min MW	151.9	27.0
10 min MW	151.3	27.5
20 min MW	152.2	27.5
40 min MW	152.2	27.5
60 min MW	153.1	28.4
120 min MW	152.7	27.0
180 min MW	149.5	23.0
360 min MW	149.5	21.6
900 min HT	146.4	15.3
Degussa P25	144.6	11.3

The A_{1g} and E_g modes are indicative of crystal lattice vibrations, thus a shift to higher energy and a decrease in peak width are indications of an increase in crystallinity with increasing irradiation of the analysed samples.[326] Considering this logic the microwave processed samples show no apparent change in crystallinity under short treatment periods (< 60 minutes); yet under extended periods there is a small energy shift and narrowing of the FWHM. Doss and Zallen report that an increased low-frequency wing for the Raman band correlates to a particle size distribution that favours a smaller crystallite.[320] The trend with an increase in treatment time is a decrease in the intensity of band at 110 cm^{-1} as the low frequency shoulder of the E_g vibration and a contraction of the band. This is consistent with crystallite growth[326] and an increase in the homogenous size.[320] These observations are consistent with our reasoning from comparative phase and particle characterisation techniques employed above.

2.3. Further Discussion

This investigation was mainly concerned with the effects of microwave hydrothermal treatment on nanocrystalline growth. The XRD analysis in this study was performed with a view to determining the effect of processing on the crystallite size, by measuring the FWHM of the Anatase (101) peak, rather than the phase composition. In our previous work we have measured the proportion of Anatase and Brookite in microwave treated samples identical to these and determined them to contain < 0.1% Brookite for selected *nanocrystals*.[3] The current TEM data also confirmed the presence of Brookite, due to the (121) peak at 2.88 Å, however to give a better representation of the bulk crystalline material this was obtained for *clusters* of nanocrystals. This gave a 30% Brookite composition as determined from SAED profiles and is a more reasonable approximation.

For hydrothermal treatment, the effect of particle size on solubility, *S*, of a particle in a sol-gel system is related to its average number radius, r_N, by the Ostwald-Freundlich equation [Equation (2-2)]:[327]

$$S = S_0 \exp\left(\frac{2\gamma_{SL}V_m}{RTr_N}\right) \qquad (2\text{-}2)$$

Where,
S_0 = solubility of the flat plate
γ_{SL} = solid-liquid interfacial energy
V_m = molar volume of the solid phase
R = ideal gas constant
T = temperature.

Equation (2-2) is a quantitative interpretation of the Kelvin effect, which is a direct consequence of the higher solubility of small particles.

From the above theory the rate of dissolution of particles at a fixed radius slows exponentially with an increase in the temperature of the system; although the particles are dissolving an increase in the temperature does not linearly increase the rate of dissolution. Convention hydrothermal growth occurs over extended periods of time under constant convection heat transfer i.e. the temperature in the reaction

vessel is homogenous at the temperature of the oven. Under microwave irradiation localised superheating provides temperatures well in excess of the reaction vessel and hence solubility of the dispersed phase particles decreases sharply.

Mass conservation in the vessel is observed hence any increase in large particles is due to an equivalent decrease in smaller particles i.e. rate of dissolution equals rate of reprecipitation. Assuming a homogeneous reaction temperature, which would allow for a steady growth rate, and incremental growth of larger particles would occur at the expense of a decrease in small particles. The change in particle size distribution would act to increase r_N which slows the rate of dissolution. Particle growth would then reach a limiting regime.

The implication of these combined factors is that over short periods of microwave irradiation rapid recrystallisation occurs resulting in crystalline particles with a small size distribution. For extended periods of irradiation, little effect on the primary crystallite size would give a material of similar crystallinity and size distribution. The microwave treatment would have a finite effect on the crystallite size as a function of Ostwald ripening due to the fast rate of recrystallisation and the rapid and localised superheating of the reaction mixture.

Hoang, Deriemaeker and Finsy also illustrate succinctly the significance of an independent development of a theory describing the Ostwald ripening process by Lifshitz, Slyozov and Wagner (LSW theory) [Equation (2-3)].[313]

$$S = S_0 \exp(\alpha / r_N) \tag{2-3}$$

For Equation (2-3), α denotes the material dependant capillary length and, for simplicity here, (2-3) is depicted as a derivation of (2-2). This theory shows that a stationary regime is reached, where the ripening rate 'v' is given by Equation (2-4):

$$v = \frac{\mathrm{d}r_N^{\,3}}{dt} = \frac{4}{9}\alpha D_m S_0 \tag{2-4}$$

The dispersed phase molecular diffusion coefficient, D_m, can be determined by experimental measurement of v and knowledge of the bulk solubility, S_0. However, Finsy[328] in his discussion of the critical radius, r_c, in Ostwald ripening showed that as a direct consequence of LSW theory and the law of mass conservation, $r_c = r_N$, illustrating that the relationship of r_c to r_N is independent of whether a stationary regime has been obtained.

The implication of this to our own investigation is seen experimentally in the marginal change in r_N during the course of treatment (5–360 mins) from 5.7–7.2 nm, although, within experimental error for the size determination, r_N increased by ~1.2 nm over the time course of treatment, r_c is limited to 5–10 nm.

The effect of extended periods of microwave irradiation on the dispersed phase remains to be seen, if the microwave process does not give appreciable Ostwald defined growth.

In relation to photocatalytic applications, the percolation of adsorbate molecules within the mesoporous structure is highly dependant on the porosity of the films. The large pores for Degussa P25, D_{avg} = 17.9 nm, would contribute much to its photocatalytic ability. Conversely the tightly packed nanoporous nature of microwave prepared powders would restrict the diffusion of adsorbates to and from the pores.

2.4. Conclusions

The preparation of highly crystalline colloidal dispersions by microwave (2.4 GHz) irradiation has given a material with a bimodal phase composition and a small growth rate over extended periods of treatment. For a treatment time of 5–360 minutes the primary crystallite size increased only marginally from 5.7–7.2 nm. This suggests that the Ostwald mechanism of crystallite growth, often identified for this method of processing, results in a finite crystallite size under microwave irradiation. The apparent high crystallinity was identified by XRD and confirmed by the complementary techniques of electron diffraction and Raman spectroscopy.

The secondary structure of the particles in solution was identified by SANS to be of a smooth non-fractal surface that had an interparticle correlation distance of 15.7 nm. TEM illustrated the primary nanocrystals were multi-faceted, polyhedral or semi-spherical particles that show signs of aggregation into ordered and regular clusters. SEM imaging of thin films of the microwave TiO_2 samples depicted dense packing that gave a visibly smooth surface with non-discernible mesopores.

A similar trend for treatment time was identified for the calculated surface properties of the TiO_2 powders with a small incremental change in the BET surface area, pore volume and diameter as determined by gas sorption in liquid nitrogen at 77 K. The 180 min MW sample had the highest internal and external surface area with SA_{BET} = 226.0 m^2/g, a pore volume PV_{SP} = 0.203 cm^2/g, and an average pore diameter D_{avg} = 3.59 nm. All the microwave processed samples had type IV isotherms with H3 characteristics which indicate hexagonal shaped mesopores.

CHAPTER 6

Transient Photocurrent Analysis of Visible-Light Water Photolysis

Introduction

Photocatalysis using n-type semiconductors is well-established. TiO_2 is often utilised in such systems since it is a robust metal oxide with excellent photocatalytic properties.[31] Electron-hole pair generation affords these attractive properties through charge trapping derived from defect sites of the crystal lattice surface.[29] The crystalline structure of TiO_2 lends itself to these properties with the rutile phase common for this purpose. Research in this field was initiated by the report of Fujishima and Honda.[108] They utilised a single crystal of rutile TiO_2 to achieve photoassisted cleavage of water through bandgap excitation with UV light. Their study involved the use of a TiO_2 photoanode and a platinum cathode irradiated with UV light and assisted by an applied bias (> 0.25 V). TiO_2, due to its photocatalytic properties, is widely studied in relation to the production of hydrogen[329-331] and/or the photodegradation of organic/biological waste in aqueous environments.[88,99,154,332]

Hydrogen generation is an achievable goal for solar energy conversion and storage with TiO_2 a cheap and affordable medium for its production. However TiO_2 is not an efficient photocatalyst (with a bandgap of 3.2 eV). Electron-hole formation necessitates a larger overpotential than is thermodynamically required to achieve water photolysis [Equations (0-1) and (0-2)]:

$$2H_2O_{(l)} \rightarrow O_{2(g)} + 2H^+_{(aq)} + 4e^- \qquad E^0 = +0.82\text{V}^{\S} \qquad (0\text{-}1)$$

$$2H_2O_{(l)} + 2e^- \rightarrow H_{2(g)} + 2OH^-_{(aq)} \qquad E^0 = -0.41\text{V}^{\S} \qquad (0\text{-}2)$$

§ versus SHE at pH = 7

The Gibbs free energy change for the overall photolysis reaction is 237.2 kJ per mole. Thus, the reaction is non-spontaneous and requires an input of energy that corresponds to 2.46 eV per molecule of water to drive the reaction to completion. This equates to 1.23 eV per electron or a photon with a wavelength of $\lambda < 1008$ nm. Hence the photolysis of water can be theoretically and thermodynamically met by a photon from the visible region of the solar spectrum.

An alternative to solid-state photocatalysis is the solution based photochemical production of hydrogen.[105,256,257] This approach involves the use of molecular species in solution, acting as intermediates, to undertake specific functions in the photochemical process. Thus this can effectively overcome the inability of water to absorb appreciable amounts of energy in the visible region of the electromagnetic spectrum. Desirable functions of intermediates include: visible light absorption; conversion of excitation energy to redox energy; and the transfer of excited electrons to and from water to evolve H_2 and O_2.

Many model photochemical systems have been devised, reported and reviewed.[14] In particular Moradpour, Amouyal, Keller and Kagan,[25] and Kalyanasundaram, Kiwi and Grätzel[117] similarly reported the classical and simple $[Ru(bpy)_3]^{2+}$ system for the photoassisted degradation of water. This system utilises a photosensitiser (PS), an electron shuttle molecule and a microheterogeneous catalyst for the photolysis of water using photons of visible light. The system depends on the reduction potentials of the relevant species in solution and the chance collisions of all components.
Further, the reports by Kalyanasundaram[116,117] and Grätzel[118,121] combined the broad spectral response from a PS with that of composite photocatalytic systems. The use of TiO_2 with H_2 and O_2 specific catalysts, Pt and RuO_2 respectively, mediated photoinduced water splitting. These systems describe composite particles imitating a micro-photoelectrochemical (PEC) cell with RuO_2 as the anode and Pt as the cathode. The results of these early reports have been difficult for other laboratories to reproduce.[333,334] Despite this the conclusion that the overpotential required for the direct photolysis of water, under bandgap excitation, is significantly reduced in the presence of mixed catalytic particles has been established.[115,126,335-338] Indeed, a recent study by Currao *et al.* identified stoichiometric quantities of H_2 and O_2, and hence water splitting, by a self-sensitised PEC cell in the presence of noble metals.[339]

This study presents a modular approach to the assembly of a photochemical system, a heterosupramolecular system.[1,139,140] The current investigation presents evidence of photochemical reactions occurring in aqueous media through analysis of photochemical measurements. Further optimisation of the system under the current configuration may provide an effective medium for cyclic water splitting. The concept of this system is represented in Scheme 0-1.

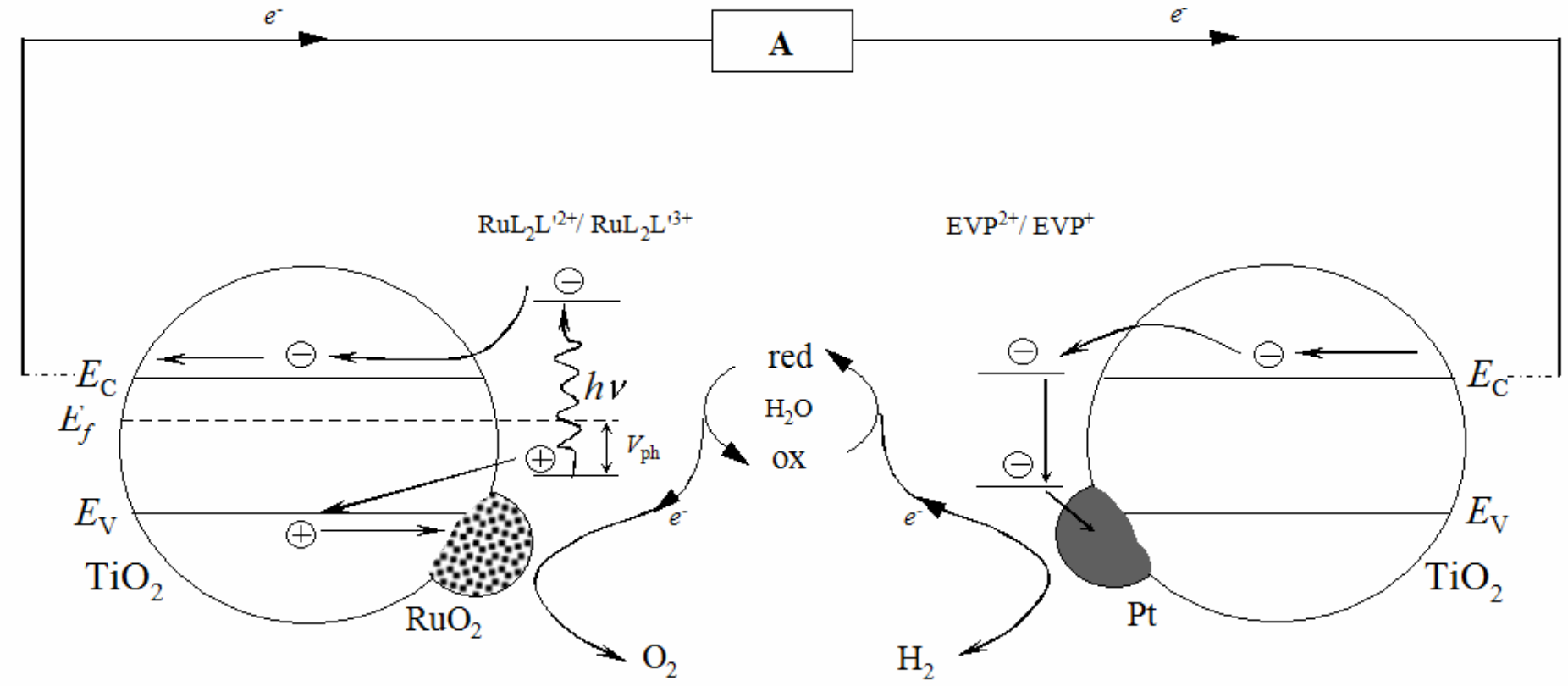

Scheme 0-1 – Schematic representation of the heterosupramolecular approach to simultaneous O_2 and H_2 production.

Materials and Equipment

Molecular components used in the current investigation, **$[Ru(bpy)_2(dmpbpy)]^{2+}$** and **EVP**, were described in Section 0 and 0. The structures of **$[Ru(bpy)_2(dmpbpy)]^{2+}$** and **EVP** are depicted in Scheme 0-2.

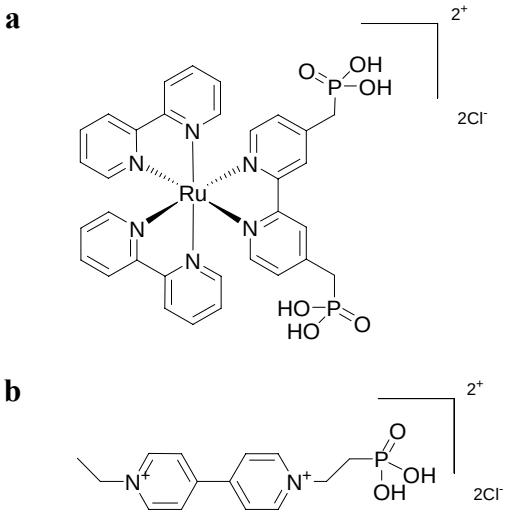

Scheme 0-2 – Structure of a) the electron donor ($[Ru(bpy)_2(dmpbpy)]^{2+}$) and b) electron acceptor (EVP) molecules as utilised in the photochemical system.

All reagents and solutions were prepared from analytical grade reagents (AR) used as received from Sigma-Aldrich. Absorption spectra were obtained using the Varian Cary 50 UV-Visible Spectrometer and emission spectra obtained on the Varian Eclipse UV Fluorescence Spectrometer. Conducting glass substrates were TEC15/3 fluorine doped tin oxide from Libby Owens Ford (LOF) ~3mm thick with a nominal resistivity of 15 Ω/cm^2 abbreviated as $F:SnO_2$. Ultra high purity (UHP) deionised water (18.2 MΩ) was treated by Millipore filtration prior to distillation over $KMnO_4$ to remove ionic and organic contaminants. UHP water so treated was used for all preparations involved in this study. Solution pH was determined using a pH 330i meter and a Sentix 41 pH electrode (WTW, Weilheim) using a conventional two-point calibration. This gave UHP H_2O (pH = 6.2) and 0.5 M Li_2SO_4 (pH = 5.7).

Preparation of Catalytic RuO_2 Nanocrystals

A procedure adapted from Ardizzone, Siviglia, and Trasatti[340] was followed for the preparation of crystalline RuO_2. Briefly, $RuCl_3$ (415 mg) was dissolved in 20% HCl, evaporated at 80°C and redissolved in isopropanol prior to oxidation in a muffle furnace at 350°C for 90 minutes. The crystalline material was ground before returning to the furnace for a further 6 hours at 450°C. The prepared crystalline RuO_2 was washed with high pH, low pH and neutral deionised water and filtered to remove all residual $RuCl_3$. Approximately 200 mg (75%) of RuO_2 was isolated.

Preparation of Nanoporous Nanocrystalline TiO_2 Films

Convection hydrothermally treated colloidal TiO_2 was available from Section 2.1.1. A mixed RuO_2:TiO_2 dispersion was prepared as a 1% w/v mixture of the prepared RuO_2 in the concentrated colloidal TiO_2 dispersion. Nanoporous TiO_2 and mixed metal oxide films were prepared by doctor-blading a small quantity of the concentrated dispersion on a F:SnO_2 substrate.[142] Resulting films were air dried for 45 minutes prior to sintering in a muffle furnace at 450°C in air for 12 hours. The films, denoted TiO_2 and RuO_2:TiO_2 respectively, were stored in a darkened vacuum desiccator until required.

Electrodeposition of Platinum

In a three-electrode system, the working electrode was a F:SnO_2 substrate or modified film, the counter electrode was a Pt wire counter and the reference electrode was a saturated calomel electrode (SCE). Electrodes were immersed in a hexachloroplatinic acid solution (2.1×10^{-3} M) degassed for 10 minutes with high purity N_2 prior to the electroplating sequence. A potential sweep from 0 to $-0.8V$ with deposition for 30 secs at –0.8V over 5 cycles gave a darkened platinised surface. Potentiostatic control was provided by the EG & G Princeton Applied Research Model 272A Potentiostat/Galvanostat. Following the procedure, the electrode surface was rinsed with deionised water and stored in a darkened vacuum desiccator until required.

Chemisorption of Molecular Components to Thin Film Electrodes

To achieve covalent binding of the surface sensitisers, films were heated to 120°C for 20 minutes to remove adsorbed water, before cooling to approximately 80°C. Films were then immersed immediately in an aqueous solution of the molecular component (typically 3.27×10^{-3}M). Chemisorption was achieved after 10 hours; the films were removed and rinsed in deionised water. The films were stored in a darkened vacuum desiccator until required. The assembly of the electrodes for individual experiments is detailed in Table 0-1.

Table 0-1 – Scheme for nomenclature and assembly of electrodes. A '/' indicates subsequent treatment, while ':' indicates a composite material.

Electrode Number	Electrode Assembly
I	TiO_2/F:SnO_2
II	RuO_2:TiO_2/F:SnO_2
III	Pt/TiO_2/F:SnO_2
IV	$[Ru(bpy)_2(dmpbpy)]^{2+}$/TiO_2/F:SnO_2
V	EVP/TiO_2/F:SnO_2
VI	EVP/Pt/TiO_2/F:SnO_2
VII	$[Ru(bpy)_2(dmpbpy)]^{2+}$/RuO_2:TiO_2/F:SnO_2

Photoelectrochemical Measurements

Samples were analysed in a dye-sensitised photoelectrocatalytic cell (DS-PCC) with an exposed electrode surface area (2.30 cm^2) in contact with the electrolyte solution. The cell volume was 100 cm^3 with a spatial distance of 2.8 cm between the electrodes (Figure 0-1). Measurements were obtained in UHP water that contained Li_2SO_4 (0.5M) as electrolyte at pH 5.7. The cell was illuminated using a high intensity white light LED for visible irradiation in the range 400–750 nm. The purpose built LED source consisted of a cluster of 7 × 5 mm round water-clear LED lenses, collimated to a common focal point. The LED source was regulated via a ten position digital resistor, with measurements obtained at 3.81 $mW \cdot cm^{-2}$.

a

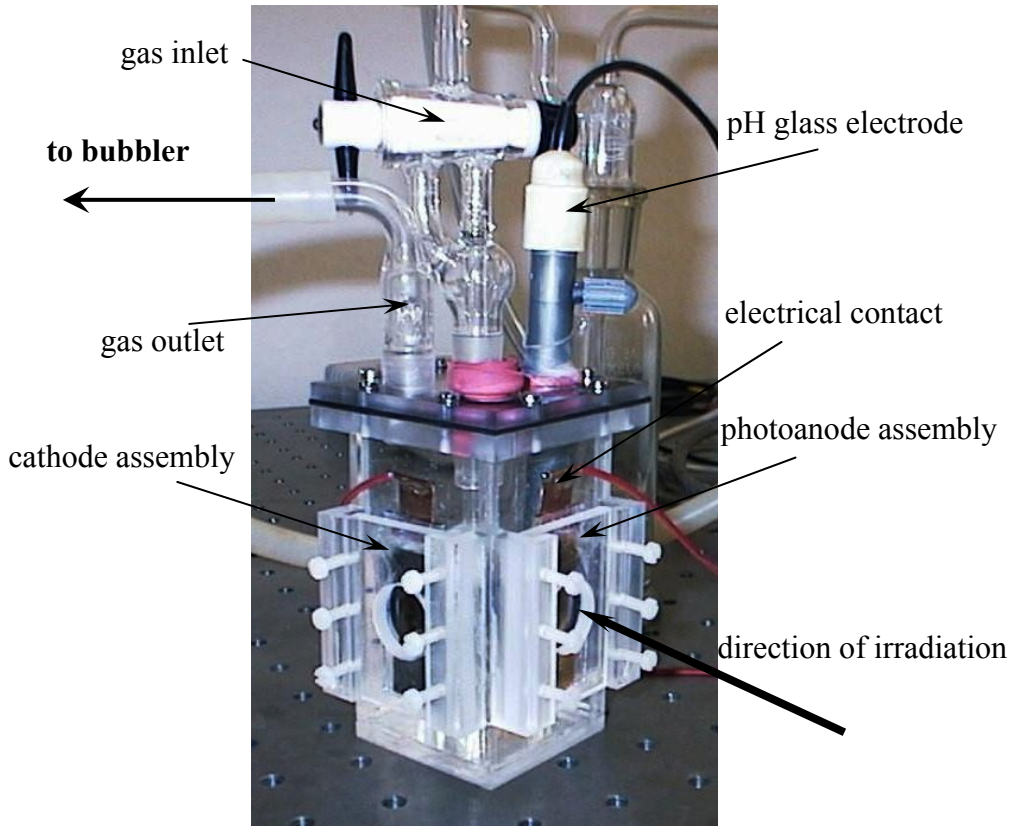

b

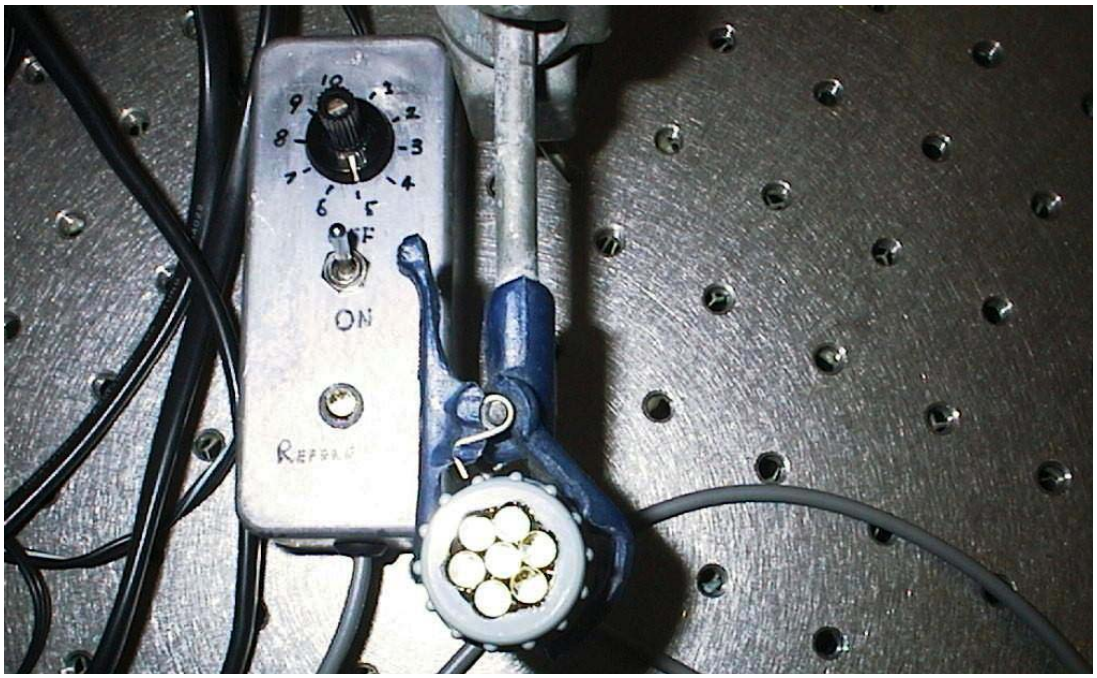

Figure 0-1 – Photographs of: a) experimental assembly of the DS-PCC b) custom configured LED light source cluster.

For increased light intensity the illumination source was a 150-W Xe arc lamp (Oriel) passed through a 90° IR mirror. A Schott KG4 (Oriel #51942) was used to emulate AM1.5 conditions and limited to $\lambda > 420$ nm with a cut-off filter (Oriel # 66420). The beam was focused at the surface of the cell with a spot size of 2.30 cm^2 (12.0 $mW \cdot cm^{-2}$).

Data were recorded using the PT-104 4-channel data logger (Pico Technology Limited, Cambridgeshire United Kingdom) interfaced to an IBM compatible PC. Data were logged (PicoLog for Windows release 5.09.4) at a rate of one sample per second, averaged over the collection period, with a resolution of $\pm 5.2 \times 10^{-5}$ μA. Measurements were collected using a differential 3-wire input with ground across a 3 kΩ resistor. Samples were placed in an optically dark box for several minutes prior to illumination. Light intensities were determined with a Power Max 5100 Laser Power Meter (Molectron Detector Inc.).

Table 0-2 – Observed limiting photocurrent (t = 100 s) under visible light illumination with assembled electrodes[a].

Exp.	Photoanode	Cathode	j_{lim}($\mu A \cdot cm^{-2}$)
1	TiO_2/F:SnO_2	TiO_2/F:SnO_2	*b*
2	"	EVP/TiO_2/F:SnO_2	*b*
3	"	Pt/TiO_2/F:SnO_2	*b*
4	"	EVP/Pt/TiO_2/F:SnO_2	*b*
5	$[Ru(bpy)_2(dmpbpy)]^{2+}$/TiO_2/F:SnO_2	TiO_2/F:SnO_2	0.006
6	"	EVP/TiO_2/F:SnO_2	0.003
7	"	Pt/TiO_2/F:SnO_2	0.010
8	"	EVP/Pt/TiO_2/F:SnO_2	0.008
9	$[Ru(bpy)_2(dmpbpy)]^{2+}$/RuO_2:TiO_2/F:SnO_2	TiO_2/F:SnO_2	0.021
10	"	EVP/TiO_2/F:SnO_2	0.027
11	"	Pt/TiO_2/F:SnO_2	0.104
12	"	EVP/Pt/TiO_2/F:SnO_2	0.157

[a] Illumination with LED source. Incident power intensity = 3.81 $mW \cdot cm^{-2}$

[b] Measured photocurrents were below resolution of instrumentation

Results and Discussion

Investigation of the Photochemical Assembly Using the LED Source

Electrochemical assemblies for individual experiments are summarised in Table 0-2. For each assembly the limiting current density (j_{lim}) under steady-state oxidation after 60 seconds of illumination is detailed.

In our preliminary report we proposed conceptually the use of a photochemical system immobilised on a semiconducting substrate.[1] The following data are for photocurrents obtained, using this photochemical system, in an aqueous medium.

Exp. 1–4 utilise a TiO_2 thin film as a photoanode. TiO_2 (band gap = 3.2 eV for the Anatase crystalline phase) requires a photon of $\lambda < 387$ nm for surface activation, which was unobtainable under the current experimental conditions. The negligible photocurrents obtained provide evidence of the inability of TiO_2 to photooxidise water under white light irradiation.

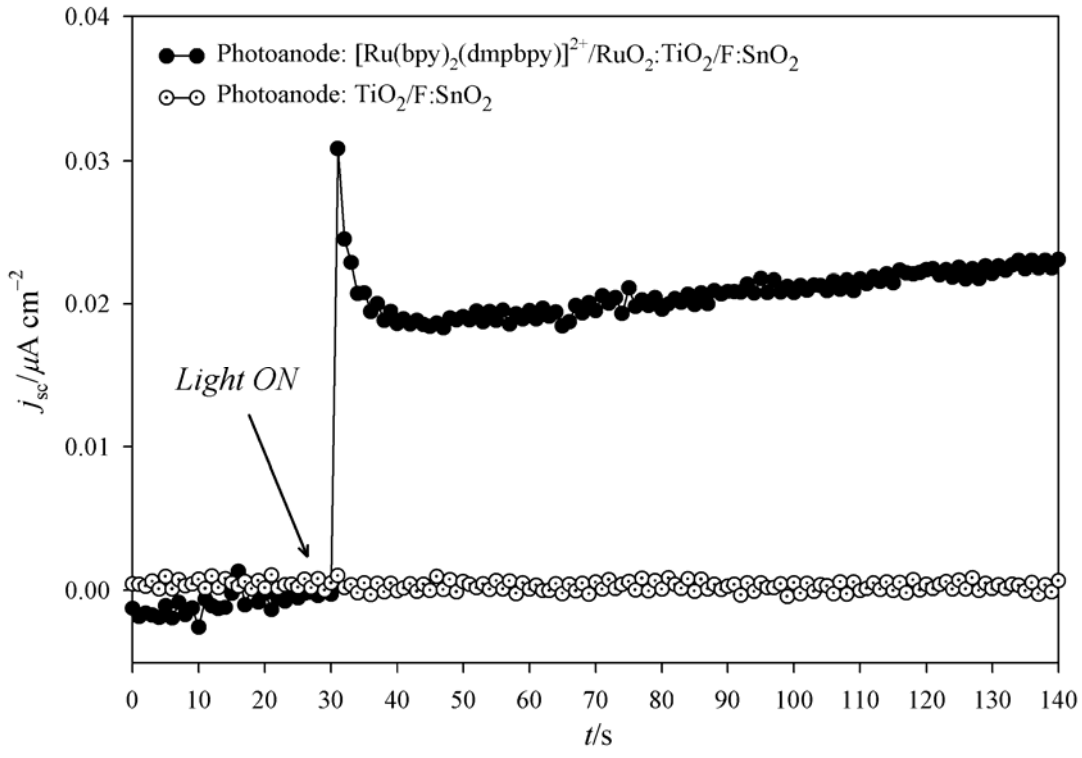

Figure 0-2 – Photocurrent observed for a TiO_2/F:SnO_2 cathode against the indicated photoanode irradiated with the white light LED source (3.81 mW·cm^{-2}) in H_2O with Li_2SO_4 (0.5M) as electrolyte (pH = 5.7).

Surface modification of the TiO_2 electrode by the adsorption of $[Ru(bpy)_2(dmpbpy)]^{2+}$ as a PS provides a spectral response that coincides with that of the illumination source. The peak absorption band for $[Ru(bpy)_2(dmpbpy)]^{2+}$ was centred at 455 nm which corresponds with the peak emission of the white light LED cluster of 462 nm. The adsorption of $[Ru(bpy)_2(dmpbpy)]^{2+}$ to the surface affords several advantages:

i. improved spectral overlap in the visible region;
ii. electron-hole charge separation; and
iii. intimate contact of the PS with TiO_2 for direct electron injection to the conduction band (CB).

The inclusion of $[Ru(bpy)_2(dmpbpy)]^{2+}$ alone to the cell assembly leads to an increase in the observed photocurrent. Therefore the inclusion of the PS (exp. 5) provides efficient charge separation that subsequently increases the photocurrent. In exp. 6, the inclusion of EVP results in a smaller positive photocurrent than in exp. 5, due to the accumulation of negative charge at the cathode from the reduction of EVP. Inclusion of Pt on the surface of the cathode in exp. 7 again improves the performance of the system due to the catalytic nature of Pt. In exp. 8, the inclusion of EVP as an electron shuttle does not have a substantial effect as electronic reduction decreases the photocurrent. The photocurrent measurements obtained in exp. 9–12 are an order of magnitude greater than those discussed in exp. 1–8 showing the importance of the anode catalyst RuO_2.

Figure 0-2 depicts the transient photocurrent of exp. 9 compared with that obtained for exp. 1. The photocurrent yield of exp. 9 was significantly improved over that of exp. 1 with the profile resembling that of a PEC cell. The onset photocurrent on irradiation was sharp indicating charging of the electrical double layer followed by a quasi steady-state current. This was expected since the oxidation species, water, was in relative excess and the system was therefore not concentration-diffusion limited. The photocurrent was observed to increase over time before approaching j_{lim} around 140 seconds.

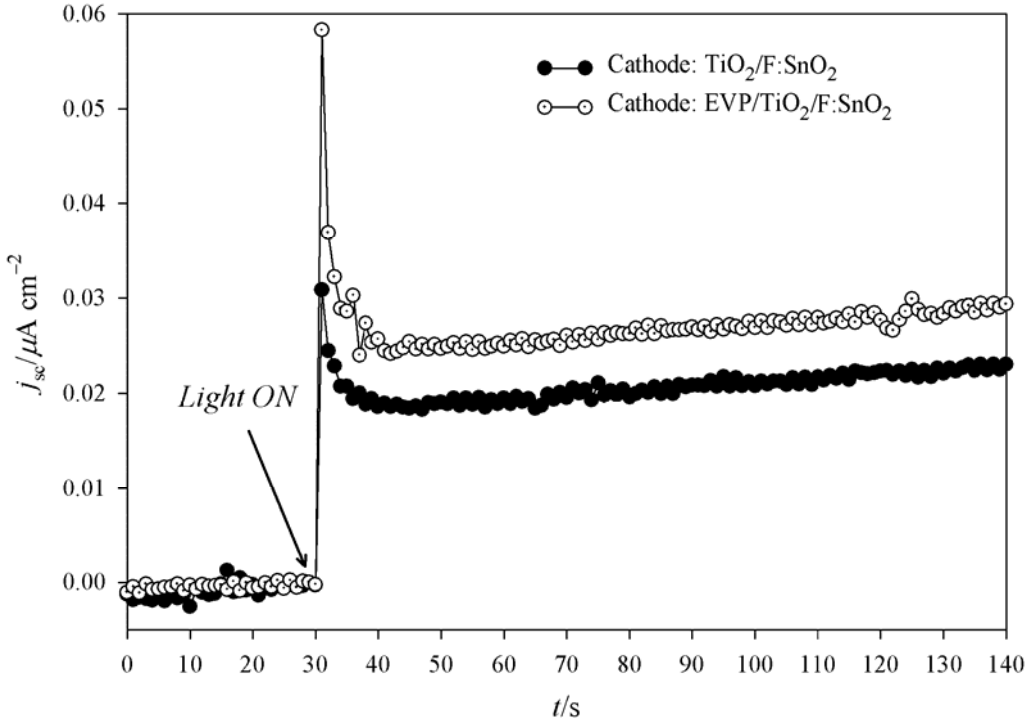

Figure 0-3 – Photocurrent observed for the $[Ru(bpy)_2(dmpbpy)]^{2+}$/RuO_2:TiO_2/F:SnO_2 photoanode irradiated against the indicated cathodes. Experimental conditions are for those described in Figure 0-2.

The observed transient photocurrent of exp. 10 (Figure 0-3) is consistent with that obtained for exp. 9, although a larger peak photocurrent and increased j_{lim}, in comparison, were observed for exp.10. The assembly has been modified by the adsorption of EVP, which allows for charge build up at the surface, providing an alternative electrochemical route for the reduction of water. The increased peak photocurrent results from fast electronic reduction of the EVP species which relaxes into a steady-state electron transfer to water. Analogous to exp. 9, double layer charging was followed by quasi steady-state oxidation.

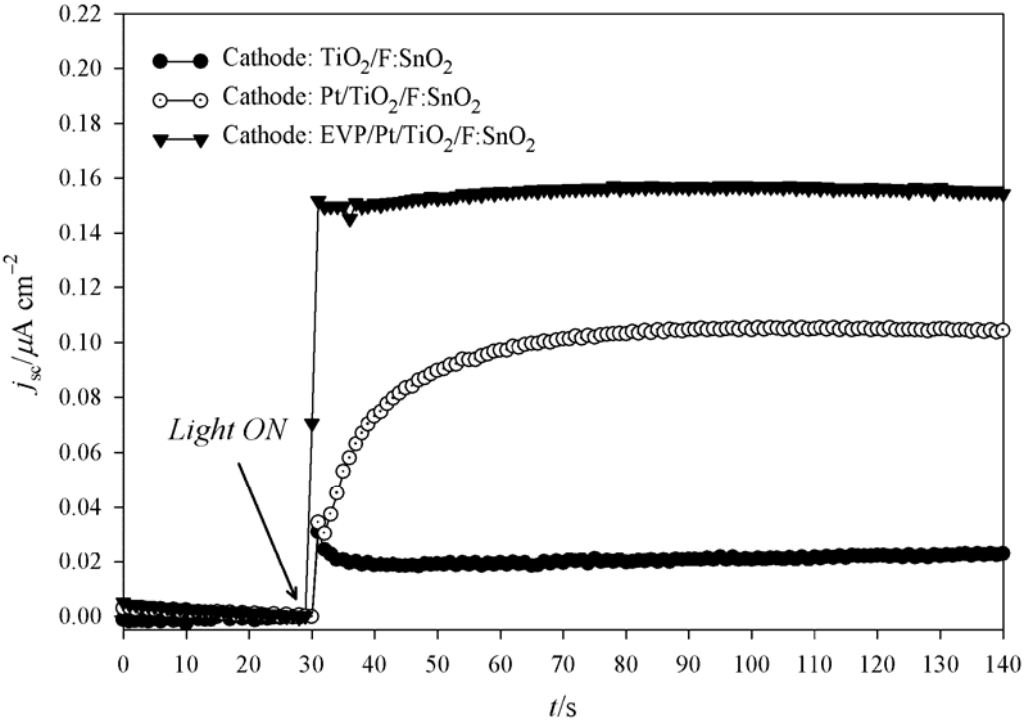

Figure 0-4 – Photocurrent observed for the $[Ru(bpy)_2(dmpbpy)]^{2+}/RuO_2:TiO_2/F:SnO_2$ photoanode irradiated against the indicated cathodes. Experimental conditions are for those described in Figure 0-2.

The transient photocurrents of exp. 11 and 9 are compared in Figure 0-4. The photocurrent onset was intense upon illumination yet there was an apparent absence of charging of the double layer. The inclusion of Pt at the cathode increases the cathodic exchange current density, due to its catalytic nature, and is evident from the increased j_{lim}. The capacitive nature of the assembly was also clear from the gradual increase in j_{sc} from the initial irradiation until j_{lim} was reached.

The transient photocurrent for exp. 12, compared to exp. 9 and 11, yields a large increase in j_{lim} (Figure 0-4). Chemisorption of EVP to the platinised TiO_2 surface gives a favourable and well-defined change in the transient and steady state photocurrent. Surface capacitance was eliminated and steady-state oxidation was apparent from initial illumination. An immediate steady-state process indicates that charging of the double layer and of the assembly components was negligible. This suggests that the process was under activation control with the elimination of the surface charging and build-up of electrons at the two electrodes within the resolution of these experiments.

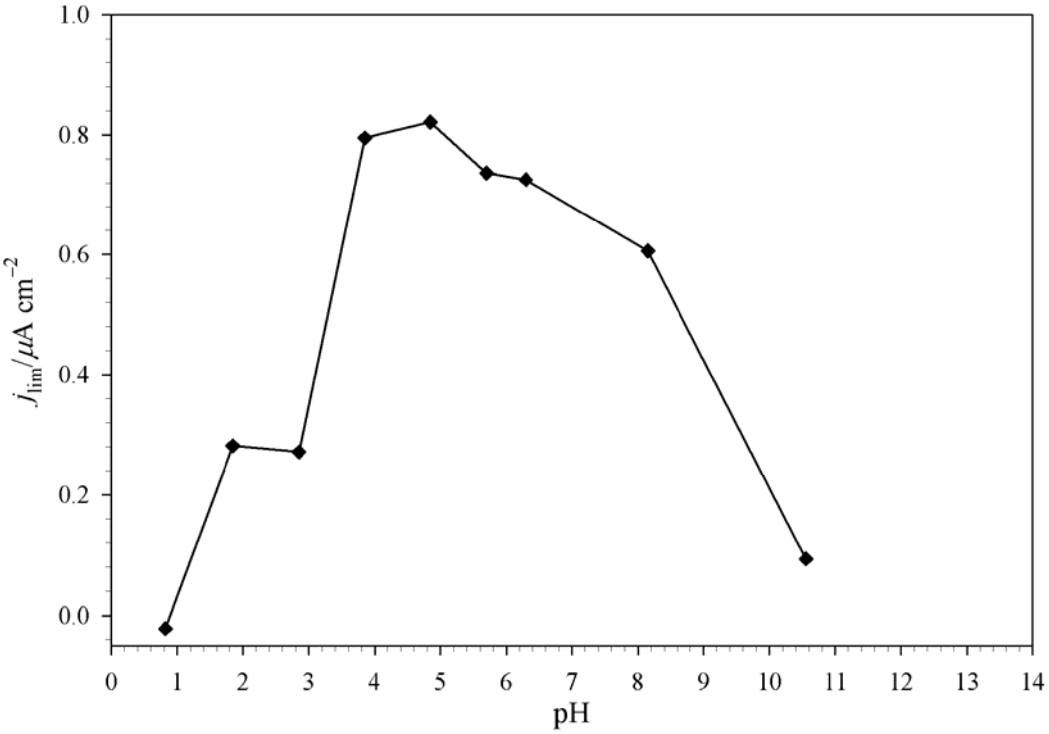

Figure 0-5 – Effect of pH on current density. Adjustment to pH was with either HCl or NaOH. Cell assembly: $[Ru(bpy)_2(dmpbpy)]^{2+}/RuO_2:TiO_2/F:SnO_2|(0.5M\ Li_2SO_4)|EVP/Pt/TiO_2/F:SnO_2$; Xe lamp (12.0 $mW{\cdot}cm^{-2}$); AM 1.5 conditions, Oriel cut-off filter (# 66420).

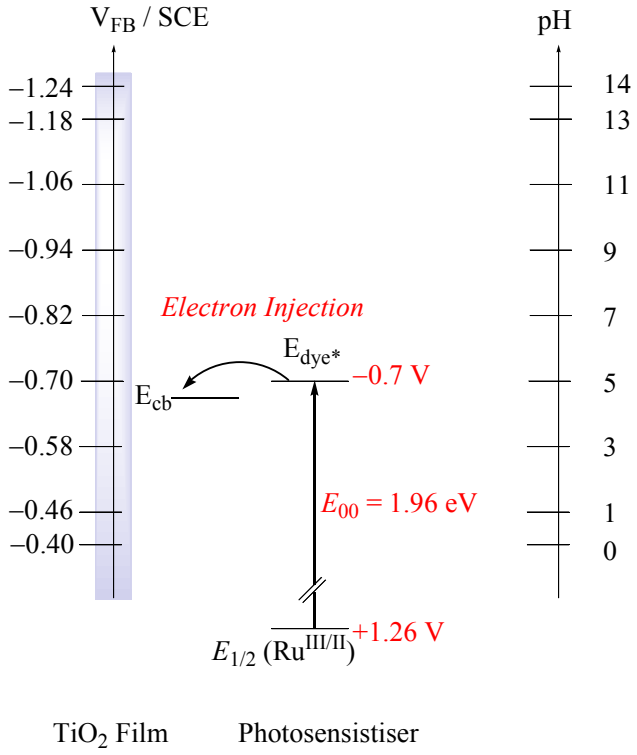

Figure 0-6 – Influence of pH on electron injection for a PS adsorbed on a titania nanostructured electrode. Explanations of terms are given in the text; the zero-zero transition energy, E_{00}, is estimated from the emission maximum of the PS following excitation into the MLCT.

Influence of pH on Photocurrent Yield

The effect of pH on the photocurrent is shown in Figure 0-5. The yield, represented as the j_{lim} from the DS-PCC, showed an optimum at pH 5. This value is consistent with earlier[25] estimations of similar particulate systems although it does conflict with that of Hirano *et al*.[90] For the systems presented in this work, surface protonation affects heterosupramolecular assemblies according to the change in flatband potential, V_{FB} [Equation (0-3)]:[341]

$$V_{FB} = -0.400 - 0.06 \cdot pH \qquad \text{(V/SCE)} \qquad (0\text{-}3)$$

For the PS, $E_{½}$ ($Ru^{III/II}$) = +1.26V and E_{00} = 1.96 eV.[8] Thus at high pH V_{FB} exceeds the energy of the excited electron (Figure 0-6). Hence electron injection into the TiO_2 CB was unfavourable for pH > 5 (V_{FB} < –0.70V). It is feasible that photons with energy exceeding the MLCT are able to inject, however maximum injection efficiency would occur at a pH ≤ 5. It would also be expected that at a pH lower than 5 the potential of the electrons being transferred to the cathode would be lower as these would assume the potential of the CB in the TiO_2. The lowering of the potential would thus reduce the driving force for reduction at the cathode and lower the overall current.

Consequently the pH of the studied solutions, as determined experimentally, provided conditions conducive to effective photochemical reaction.

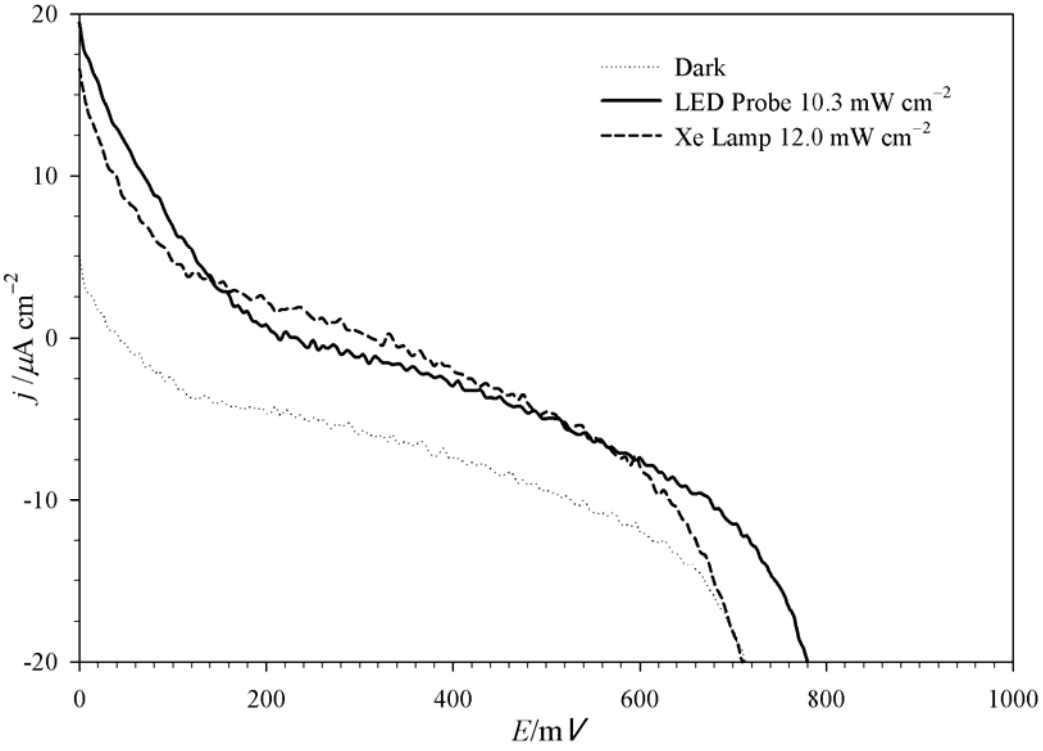

Figure 0-7 – Current density-voltage characteristics of DS-PCC at AM 1.5 illumination. Light intensities for light sources examined are as indicated. Active cell area: 0.16 cm^2.

Table 0-3 – Photovoltaic parameters of PCC under different light sources[a]

Light Source	P_{in} μW·cm^{-2}	j_{sc} μA·cm^{-2}	V_{oc} mV	P_{max} μW·cm^{-2}	*ff*	η (%)
LED Source	10.3	19.5	735	0.736	0.0515	0.0072
Xe Lamp	12.0	15.5	695	0.435	0.0415	0.0036

[a]Incident power intensity P_{in}; short-circuit photocurrent density: j_{sc}; open-circuit photovoltage: V_{oc}; maximum electricity output power density: P_{max}; fill factor: $ff = [P_{max}/(V_{oc} \times j_{sc})]$; conversion efficiency: $\eta = (V_{oc} \times j_{sc} \times ff / P_{in}) \times 100\%$; Active cell area: 0.16 cm^2.

Photoelectrochemical Efficiency of Optimised System

Figure 0-7 presents the current density–voltage characteristics of the photochemical assembly of exp. 12 under AM 1.5 illumination from a Xe arc lamp and that of the LED source (Table 0-3).

The photocurrent density (j_{sc}), open-circuit photovoltage (V_{oc}) and fill factor (*ff*) obtained under different illumination sources give rise to considerable differences in power conversion efficiencies. The LED light source has a peak emission centred at 462 nm while the Xe lamp, simulating AM 1.5 conditions, has a broad photonic spectrum with a small percentage of overall light from the 455 nm region. The absorbed sensitiser has a broad MLCT at 455 nm thus it can be expected for the system to respond favourably to the LED source and accordingly yield higher efficiencies.

The data illustrate that the device does not respond as a simple diode such as the DSC. When the applied potential across the cell was zero, j_{sc} was measured before a sudden change in the current as the applied potential scanned more positive. The drop in current in the light was due to the capacitive nature of the system prior to a positive current flow starting at ~200 mV. The current then further increases until V_{oc} was reached.

A comparative estimation of the photonic yield was obtained using the apparent quantum yield (AQY) in Equation (0-4):[342]

$$AQY(\%) = \frac{Number\ of\ reacted\ electrons\ \ (j_{sc})}{Number\ of\ absorbed\ incident\ \ photons} \times 100 \qquad (0\text{-}4)$$

Efficiency of the device for absorbed photons over the 420–700 nm range under steady-state conditions gives AQY = 1.6% (corrected against substrate attenuation) under AM 1.5 illumination. The calculated quantum yield was comparable to that reported by Tsuji,[342] considering the variation in the experimental conditions between the two systems.

The Photoelectrochemical System

The data presented demonstrate that the measurement of j_{sc} was possible in an aqueous electrolyte under visible light irradiation with no applied potential. The basis of this system can be described as a series of functioning units:

i. light absorption by a PS;
ii. electron injection;
iii. electron transport via a semiconducting substrate;
iv. electronic reduction of an electron shuttle; and
v. subsequent reduction at the cathode.

The linking of each of the individual components, and their intrinsic properties, required for H_2O photolysis constitutes a heterosupramolecular assembly. Hence, the purpose of each component in the assembly can be described and rationalised in terms of its own intrinsic function. While we have not attempted to detect either O_2 or H_2 from water photolysis we have, in accordance with most other work in the field, accepted this as the most likely photoelectrochemical reaction occurring in the cell, and explicitly base our discussion on this assumption.

When a photon of light with sufficient energy to induce charge separation was incident on the adsorbed PS, excitation, ionisation and subsequent oxidation of the PS occur according to Equation (0-5):

$$TiO_2-[Ru(bpy)_2(dmpbpy)]^{2+}+h\nu \rightarrow e^-_{(cb)}+TiO_2-[Ru(bpy)_2(dmpbpy)]^{3+} \quad (0\text{-}5)$$

With the injected electron partitioned in the CB of TiO_2, charge recombination was prevented and the PS^+ was available as a reactive species. Laser flash photolysis experiments have shown that an oxidised PS was capable of direct oxidation of water to O_2.[242] This was illustrated by the photocurrents observed in exp. 5–8. The irreversible photo-oxidation of PS preceding this step was a plausible source of the observed photocurrent. However, in Figure 0-2 – Figure 0-4 the photocurrent was

observed to *increase* with time as opposed to a decrease if the surface concentration of PS^+ was to diminish.[166]

Further to these photocurrent observations, the excited state MLCT of tris-2,2'-bipyridine ruthenium(II) complexes (e.g. $[Ru(bpy)_2(dmpbpy)]^{2+}$) has been described as $[Ru^{III}(bpy^{\bullet-})(bpy)_2]^{2+}$. That is, the electron resides on only one of the three bpy ligands.[242,343] Comparative measurements of injection quantum yields on PSs with substituted bipyridine ligands have shown that $[Ru(bpy)_2(dmpbpy)]^{2+}$, has ϕ = 0.5±0.1. The yield of less than unity, $\phi < 1$, has been attributed to increased π^* energies of the surface bound ligand.[8] This would certainly be a contributing factor to the small photocurrent and efficiencies obtained in this study. However, the fluorescence studies of Will *et al*. have shown that surface adsorption quenches the excited state of the complex i.e. $\phi \approx 1$.[7]

The inclusion of RuO_2 in the photochemical assembly significantly improved the cell performance. Increased photocurrents in exp. 9–12 due to the specific catalytic function of the metal-oxide occur according to Equation (0-6):

$$RuO_{2(bulk)} + H_2O_{(aq)} \rightarrow \tfrac{1}{2}O_{2(ads)} + 2H^+_{(aq)} + 2e^-_{(ads)} \qquad (0\text{-}6)$$

RuO_2 behaves as a hole trap following photo-oxidation of $[Ru(bpy)_2(dmpbpy)]^{2+}$ in Equation (0-5). Although PS^+ was capable of direct oxidation of H_2O, Equation (0-6) and subsequently (0-7) are favoured. The larger (~30 nm) RuO_2 particle is capable of accumulating a significant excess charge and thus acts as an electron donor to regenerate the PS.[116,127]

$$TiO_2 - [Ru(bpy)_2(dmpbpy)]^{3+} + e^-_{(ads)} \rightarrow TiO_2 - [Ru(bpy)_2(dmpbpy)]^{2+} \qquad (0\text{-}7)$$

The preference of the system for Equation (0-6) was evident in the capacitive component present in the system. Sufficient negative charge accumulates on the surface of RuO_2 before partial surface discharge occurs according to Equation (0-8):

$$2 \times \tfrac{1}{2}O_{2(abs)} \rightarrow O_{2(abs)} \rightarrow O_{2(aq)} \qquad (0\text{-}8)$$

However, a limitation of RuO_2 in the system was its capability of catalysing the reversible reaction, Equation (0-9):[127]

$$2OH^-_{(ads)} \overrightarrow{\leftarrow} O_{2(aq)} + 2H^+_{(aq)} + 4e^- \qquad (0\text{-}9)$$

Therefore, in the presence of an oxygenated solution the reverse reaction would suppress oxidation and limit photolysis. This competitive reaction, occurring at the surface of the anode, would act as a short circuit in the cell and reduce the overall photocurrent yield.

The responses of EVP modified electrodes V and VI illustrate that the electron shuttle, EVP, affords an active function in the reduction process. This was facilitated by the presence of a Pt catalyst. Electrons in the CB traverse the external circuit to EVP on the surface, reducing the electron shuttle molecule according to Equation (0-10):

$$e^-_{(cb)} + TiO_2 - EVP^{2+} \rightarrow TiO_2 - EVP^{1+} \qquad (0\text{-}10)$$

Direct electron accumulation from the CB of TiO_2 at surface bound Pt [Equation (0-11)] was supported by the transients in Figure 0-4.

$$e^-_{(cb)} \rightarrow e^-_{(Pt)} \qquad (0\text{-}11)$$

However, the enhanced photocurrents of Figure 0-4 indicate that the presence of EVP provides a more energetically favourable route for the migration of electrons to the surface Pt [Equation (0-12)]. Thus, EVP functions effectively in the system as an electron shuttle contributing to the photochemical assembly.

$$TiO_2 - EVP^{1+} \rightarrow e^-_{(Pt)} + TiO_2 - EVP^{2+} \qquad (0\text{-}12)$$

Increase in the photocurrent yield for experiments involving electrodes V and VI can be rationalised by the presence of Pt.[344] Ballistic transfer of electrons to-and-over the Schottky barrier enhances photocurrent yields. Electrons in the CB and those relayed by EVP accumulate on the surface of Pt and react according to Equation (0-13) – (0-15):[345,346]

$$H^{+}_{(aq)} \rightarrow H^{+}_{(Pt)} \qquad (0\text{-}13)$$

$$H^{+}_{(Pt)} + e^{-}_{(Pt)} \rightarrow H^{\bullet}_{(Pt)} \qquad (0\text{-}14)$$

$$2H^{\bullet}_{(Pt)} \rightarrow H_{2(Pt)} \rightarrow H_{2(aq)} \qquad (0\text{-}15)$$

Diffusion and then migration of hydrogen ions [Equation (0-13)] to the surface of Pt precedes their reduction to the hydrogen radical [Equation (0-14)]. The ease of the reactions described by Equations (0-14) and (0-15) and the decreased overpotenial affords H_2 generation over platinised surfaces.[345] This enables atomic nucleation and subsequent ejection of diatomic H_2 from the surface.

Effectively a single electron ejected from the photo-ionisation of $[Ru(bpy)_2(dmpbpy)]^{2+}$ affords the oxidation of H_2O by RuO_2 and regeneration of $[Ru(bpy)_2(dmpbpy)]^{2+}$. The ejected electron, if sufficient in energy, was all that was required to reduce EVP, accumulate charge on Pt and subsequently reduce H_2O.

Conclusions

The results of a study for a multi-component photochemical system involving molecular and condensed phase components with specific functions have been presented. It has been demonstrated that a heterosupramolecular assembly is capable of inducing a photochemical reaction, in water, under visible irradiation with the process identified and monitored by the measurement of a short circuit current. This process has not been identified previously by the instrumental methods implemented in this work.

$[Ru(bpy)_2(dmpbpy)]^{2+}/RuO_2{:}TiO_2/F{:}SnO_2|(0.5M\ Li_2SO_4)|EVP/Pt/TiO_2/F{:}SnO_2$

was found to be the most efficient cell assembly. Optimised conditions of the electrolyte solution were determined to be pH = 5 where under illumination from the Xe light source, the assembly yielded $\eta = 0.0036\%$ with an apparent quantum yield (AQY) = 1.6%.

CHAPTER 7

Multi-Step Oxidation and Mineralisation of EDTA with a Photocatalytic Molecular Assembly under Visible Light Irradiation

Introduction

Photoelectrochemical (PEC) cells such as the Dye-sensitised Solar Cell (DSC) are efficient devices for the conversion of visible light into electricity.[2] Efficiency in the visible region is afforded by sensitisation of wide bandgap metal oxides with Ru(II)-based photosensitisers. The most frequently studied metal-oxide/photosensitiser combinations are those consisting of TiO_2 and an octahedral ruthenium bis-bipyridine complex. In the DSC, TiO_2 is employed solely as an intrinsic semiconductor to facilitate the transport of electrons away from the site of photoexcitation yet TiO_2, or titania, is widely researched for its photocatalytic properties.[29,94,111,347]

Limitations of TiO_2 in the DSC have been identified as back electron-transfer (ET) and recombination at the surface/sensitiser interface.[348,349] These limitations are attributable to the high surface area nanoporous nanocrystalline film and subsequent occurrence of crystalline defects, surface valence traps and deep inter-valence sites. Surface defect sites, which arise from vacancies in the crystal lattice, facilitate the adsorption of sensitisers through chelation of vacant Ti^{4+} sites with acidic groups on the sensitiser periphery.[350] Yet crystalline defects and surface trap sites enable TiO_2 to also act as a photocatalyst. Hence the use of TiO_2 as a semiconducting medium undoubtedly limits the efficiency of the DSC due to photocatalytic recombination processes at the surface/solution interface. Exploiting the inherent photocatalytic properties of TiO_2 in the DSC in addition to effective electron/hole charge separation that surface/sensitiser chelation affords, PEC devices are capable of broad spectral photocatalysis. The advantage of utilising PEC devices for photocatalysis is the ability to examine the process by electrochemical methods.[153,154]

Energy and electron transfer processes involving Ru(II) polypyridyl photosensitisers have been extensively investigated, which can be attributed to their long-lived excited state (~1μs), the result of an intense metal-to-ligand charge-transfer (MLCT).[135] A photon of light incident with the dye promotes an electron from an occupied *d* orbital of the metal to a ligand acceptor π^* orbital effecting charge separation. Through derivatisation of the bipyridine moiety with an acidic anchoring group the excited electron can be injected 'hot' into the surface substrate within the

picosecond regime.[138] This injection is energetically favourable due to the overlap of π^* orbitals of the carboxylate anchoring group with the *d* orbitals of TiO_2. The linkage provides an efficient pathway for electron transfer in the DSC however, surface desorption limitations of the carboxylate linkage are more problematic when used in a photocatalytic cell.

Carboxylate derivatised bipyridine ligands (pK_a = 4.5) are effectively soluble in aqueous solutions when the pH is greater than ~2.5, thus sensitiser desorption occurs.[350] Also, the favourable orbital overlap that allows efficient electron transfer can also readily aid charge recombination.[351] This limitation can be overcome through use of acidic anchoring groups that resist desorption under these conditions and do not energetically match the surface state. Extending the chemical linkage between sensitiser and surface can physically impede back ET, segregating the excited S^+/S^* state of the dye and physically partitioning the electron in the semiconducting medium.[276]

Effective charge-separation and segregation of the electron-hole pair leaves the oxidised dye and partitioned electron available for photochemical oxidation and electrochemical reduction processes respectively. Treadway, Moss and Meyer found this approach effective and formed a photoelectrosynthetic cell in a two-electrode assembly utilising an adsorbed metal complex against a platinised counter electrode to photodegrade short chain alcohols and electrolytically generate H_2.[166] Nitrogen containing compounds have also shown themselves to be desirable candidates for sacrificial donation in PEC devices.

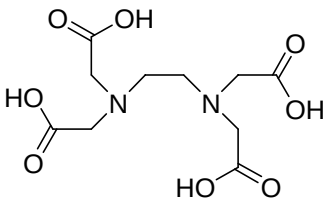

Figure 0-1 – Chemical structure of ethylenediaminetetraacetic acid (EDTA)

Ethylenediaminetetraacetic acid (EDTA) is a tertiary amine containing four acetic acid side chains with the amine centres separated by an ethylene bridge (Figure 0-1). EDTA is a ubiquitous organic pollutant found in many grey water waste steams due

to its common usage in a range of industrial processes, ranging from use as a chelating agent in food preservation (preservative 385) to an additive in cleaning agents used to remove heavy metals from nuclear steam generators. Hence, this compound is present as a range of chemical compounds including, chelated, protonated and anionic forms and due to the extent of usage, quite frequently in our water supplies.

Many examples of organic molecules are present in our waterways as by products from industrial waste streams. Often it is the presence of these organic 'pollutants' that can promote environmental hazards in our waterways such as blue-green algal blooms and, as a consequence, these outbreaks contribute to increased marine-life mortality. Particulate photocatalytic systems, that incorporate metal oxides such as TiO_2, are able to irreversibly photooxidise many organic molecules, such as phenol,[89] EDTA[104] and TEOA,[105] into CO_2 and H_2O.[89,103] In a similar manner, through the supplementation of EDTA as a simulated waste stream contaminant in a PEC device, it should be possible to oxidise EDTA and degrade the pollutant to much simpler amine and organic compounds.

The mechanisms by which aqueous solutions of organics degrade on TiO_2 surfaces have been widely studied.[352] Mechanistic theory is centred upon the formation of surface radicals, peroxy radicals and $O_2^{\bullet}$ free radicals with post-radical reaction rearrangement of the degrading species. Surface sensitisation would significantly change this photocatalytic process with the Ru(II) excited state radical or oxidised Ru(III) dye having a significant role in the degradation whilst limiting the photocatalytic contribution of TiO_2 due to surface chelation. What we propose is that the incorporation of a pollutant within a dye-sensitised PEC forms a dye-sensitised photoelectrocatalytic cell (DS-PCC) and hence a photodegradation system capable of mineralisation of sacrificial pollutants to CO_2, H_2O and other simple species. In addition, in an acidic environment, photogenerated electrons would be available to produce a by-product from the reduction of H_2O, most likely a CO_2/H_2 mixture. This study presents electrochemical observations of a model pollutant, EDTA, in a dye sensitised PEC cell referred to as DS-PCC. We discuss the degradation process in relation to the observed transient photocurrents and propose a mechanism by which the degradation process occurs on sensitised surfaces.

Materials and Equipment

The molecular component used in the current investigation, **$[Ru(dmpbpy)_2(bpy)]^{2+}$**, was described in Section 0. The structure of **$[Ru(dmpbpy)_2(bpy)]^{2+}$** is depicted in Scheme 0-1.

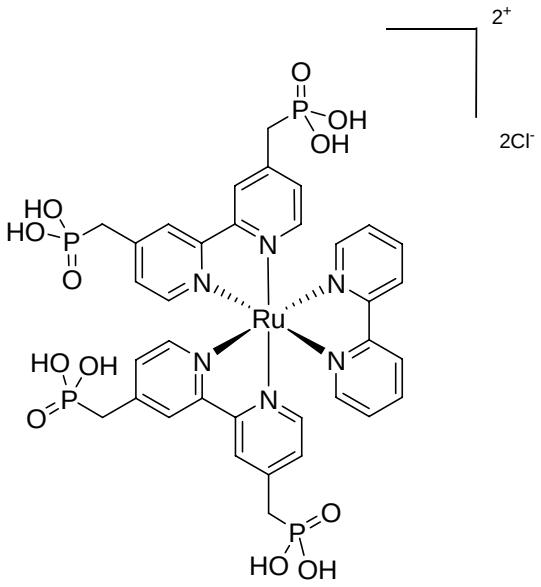

Scheme 0-1 – Structure of the electron donor $[Ru(dmpbpy)_2(bpy)]^{2+}$ used in the DS-PCC.

All reagents and solutions were prepared from analytical (AR) grade reagents used as received from Sigma-Aldrich. The conducting glass was TEC15/3 fluorine doped tin oxide ($F:SnO_2$) from Libby Owens Ford (LOF) ~3.0 mm thick with a nominal resistivity of 15 Ω/square.

Absorption spectra were collected in the solid state in air or in spectroscopic grade MeOH using the Varian Cary 50 UV-visible Spectrometer.

Preparation of Nanoporous TiO_2 Thin Films

Colloidal TiO_2 solution was available from experimental methods described in Section 2.1.1. Nanoporous TiO_2 were prepared by doctor-blading a small quantity of the concentrated dispersion on a $F:SnO_2$ substrate. Resulting films were dried in air for 45 minutes prior to sintering in a muffle furnace at 450°C in air for 12 hours.

Electrodeposition of Platinum

Electrodeposition was performed as described in Section 0. Following the procedure, the platinised surface was rinsed with deionised water, and stored in a vacuum desiccator until required.

Sensitisation of TiO_2 Films

The molecular sensitiser was adsorbed to prepared thin film TiO_2 electrodes by chemisorption as described in Section 0. An aqueous solution of **$[Ru(dmpbpy)_2bpy]Cl_2$** was prepared (3.27×10^{-3} M) and the pH adjusted to 3 with 0.1M HCl. The prepared TiO_2 thin film electrodes were soaked for 48 hours before removing, rinsing in deionised water and storing in a darkened vacuum desiccator.

Photoelectrochemical Measurements

A photoelectrochemical cell was prepared by arranging a chemisorbed $[Ru(dmpbpy)_2bpy]^{2+}/TiO_2$ film and a platinised conducting glass substrate such that they were separated by a neoprene O-ring, and fixed by a heavy clamp to form a tight seal against the surfaces. The respective electrodes of the cell had a predefined area (2.30 cm^2) in contact with the electrolyte solution. The inter-electrode spatial separation was 0.20 cm and the cell volume was 0.459 cm^3. Samples were introduced into the inner cell cavity by piercing the surface of the O-ring with a fine syringe while equalising the pressure via a second syringe. Solutions were prepared in Millipore deionised water (18.2 MΩ·cm) with EDTA (as the disodium salt) constituting the electrolyte (pH = 4.5).

The instrumental setup is depicted in Figure 0-2. The cell assembly was illuminated with a 150W Xe arc lamp passed through a 90° IR filter to remove infra-red radiation. The resulting beam was focused using a two-lens assembly to give an intense spot the size of the exposed electrode surface. A Schott KG4 (Oriel #51942) filter was used to emulate AM1.5 conditions and a Schott 66420 (Edmond Optics) colour filter was used to limit excitation from photons with $\lambda > 420$ nm. The effective lamp power was 41 $mW \cdot cm^{-2}$ at the electrode surface (determined as in Section **0**). Electrode connections were made with a Ag conducting epoxy to a Sn/Cu wire of 20 cm in length. Data were recorded using an ADC200 (Pico Technology Limited, Cambridgeshire United Kingdom) in data logging mode interfaced with a PC. Data points were collected at one sample per second and the short-circuited cell current measured using a differential 3-wire input with ground across a 1 kΩ resistor. Logged data were corrected for the 1 kΩ resistance load according to Ohm's law. The cell setup was subjected to darkness for 10 minutes prior to illumination. Typically, experiments consisted of a sequence of 60 seconds darkness, an illumination period (~5400 seconds, 90 minutes), followed by 60 seconds of darkness. An equilibrium baseline was established in each of the periods of darkness for which the measured current was corrected.

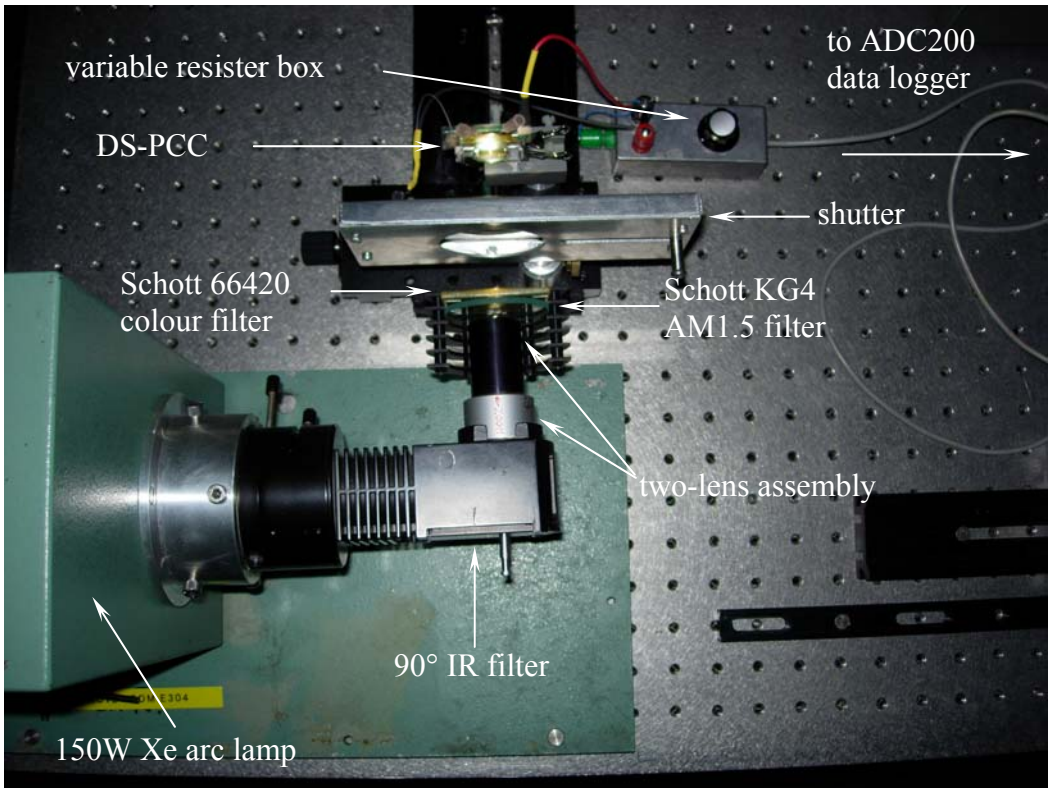

Figure 0-2 – Photograph of experimental instrumentation and setup.

FTIR-ATR spectroscopy

Infrared spectra were obtained using a Nicolet 870 Nexus Fourier Transform infrared spectrometer equipped with a DTGS TEC detector and an ATR objective (Nicolet Instrument Corp., Madison, WI). An Optical Path Difference (OPD) velocity of 0.6329 cm s^{-1} with aperture set to 100, and a gain of 8 were used. The ATR accessory was a Smart Endurance single reflection ATR accessory equipped with a composite diamond IRE with 0.75 mm sampling surface and a ZnSe focusing element. Solid samples of the organic compounds were dried under vacuum and placed directly onto the diamond IRE. Similarly, electrodes used in the degradation process were aligned with the thin film surface on the diamond IRE and the anvil pressurised before spectral collection. Spectra were collected in the spectral range 4000–525 cm^{-1} with the co-addition of 64 scans and 4 cm^{-1} resolution, and were corrected for the wavelength dependence of the ATR experiment.

Results

For a simple one electron oxidation in a photoelectrochemical cell, where the rate of oxidation at the photoanode is equal to the rate of the reduction at the cathode, the single step oxidation can be generalised as Equation (0-1):

$$Rate(mol/s) = dN/dt = I/nF \qquad (0\text{-}1)$$

Thus the oxidation results in a complete transformation of the reactant (A) to a new species, product (B^+), and the transfer of an electron. The oxidation is an interfacial electron transfer process at the electrode surface in contact with the electrolyte solution. Solute interactions at the electrode occur under a potential field, with the removal of the solvation sphere resulting in adsorption of the reactant molecule to the surface (Figure 0-3).

The adsorbed species (A_{abs}) undergoes oxidation with electronic charge transferred to the electrode surface before release of the degraded species (B^+). B^+ is then free to migrate away from the site of oxidation. Under such conditions the expected response of the system when light impinges on the surface of the photoanode can be likened to the application of a potential to the system. The charge separation process induces a potential field and hence can be conceptualised as in Figure 0-4.

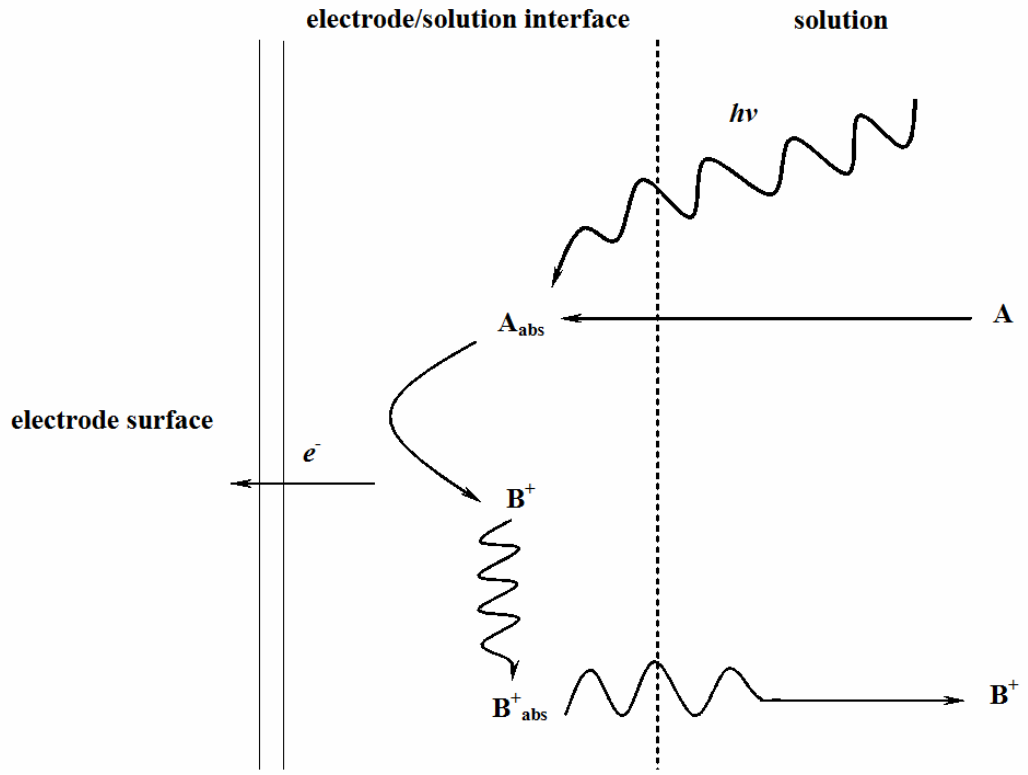

Figure 0-3 – Interaction of solute with electrode surface.

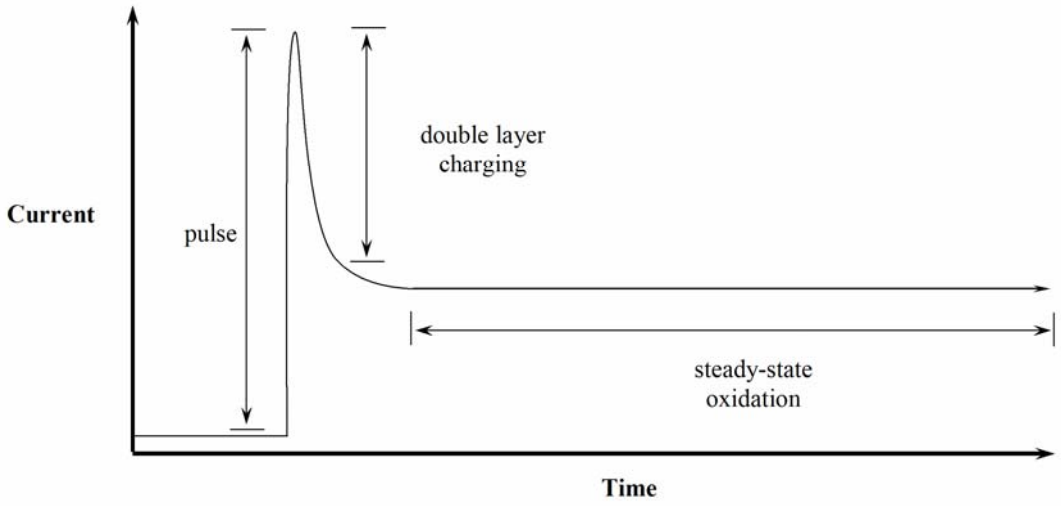

Figure 0-4 – Conceptual model of the transient response of a PEC under an induced potential.

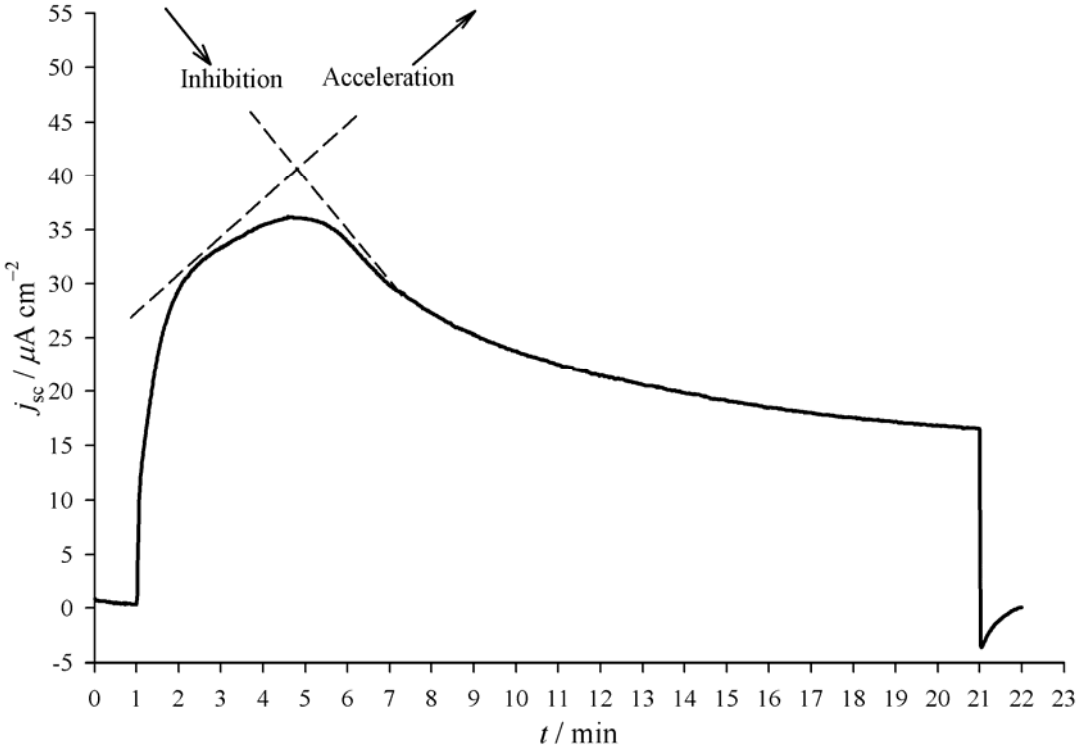

Figure 0-5 – Response of DS-PCC under conditions of steady state photooxidation.

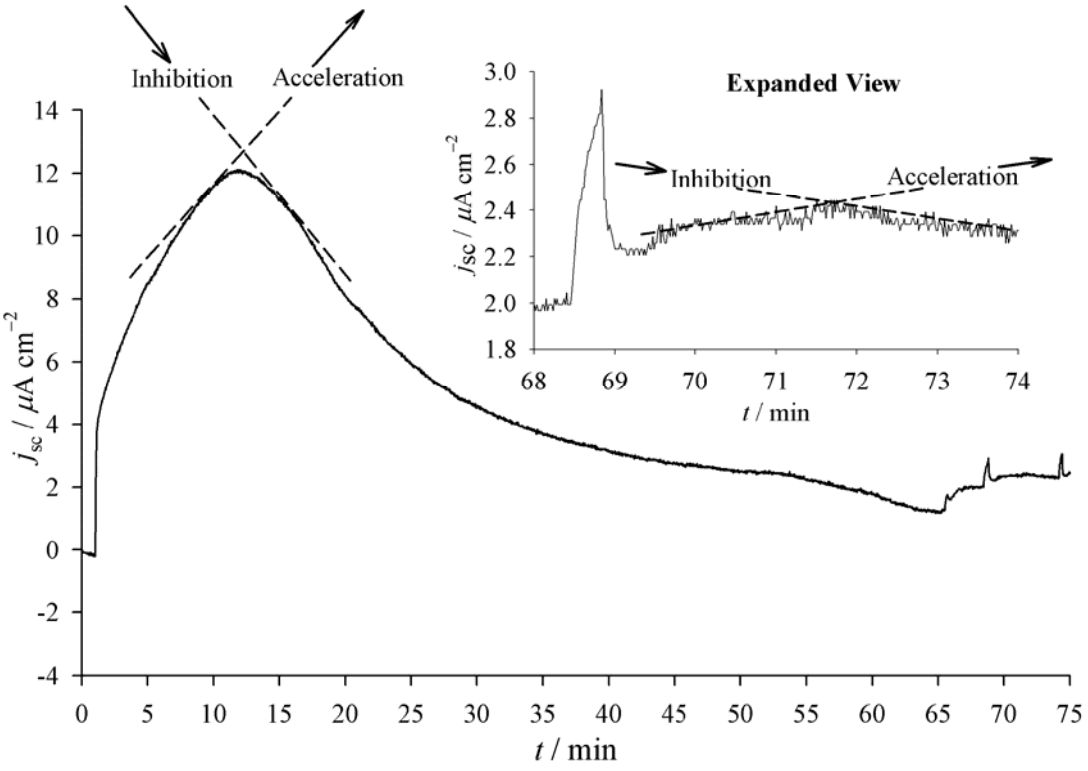

Figure 0-6 – Observed transient photocurrent response of the system under an extended period of time (EDTA, 0.1M, pH 2.0). Note should be made of the change in the kinetics over time with system changing from a multi-variable response to that of a single species (inset).

Light incident on a dye molecule resulting in electron injection is expected to give rise to charging of the electrical double layer before the onset of steady-state oxidation. However, the photocurrent/time response of the system as depicted in Figure 0-4 is a salient feature of oxidation in PEC cells. The response of the PEC cell can be attributed to the consumption of absorbed species and not double layer charging/discharging. An illustrative example is that of Jiang *et al.* for a TiO_2 thin film PEC cell.[153] A sharp photocurrent onset is observed with the steady-state photocurrent dependent on the molar concentration of oxidisable species and independent of adsorption time. Interpolation of the transient photocurrent-time profiles demonstrated that the response followed a Faradaic model for photoelectrochemical oxidation.

Figure 0-5 depicts the response of DS-PCC which quite clearly lacks evidence of a 'sharp' photocurrent onset. The time domain of the measurements precludes the photocurrent transient being the result of double-layer capacitance and the transient spectra display clear regions of photoelectrochemical acceleration and inhibition. A photocurrent maximum (j_{max}) is observed after a period of approximately 5 minutes with the decay of the signal observed over a further 10–15 minutes. The signal decay could in fact be a factor of photoanode stability (i.e. photooxidation of the dye molecule) however due to the high concentration of oxidisable species this was thought to be unlikely. The relatively rapid decline in signal (from 60–65 minutes) indicated another possibility; that surface passivation occurs following the initial system response due to the high concentration of EDTA. Relaxation of the system to a steady-state oxidation and a limiting photocurrent (j_{lim}) takes a considerable amount of time and even under extended periods of time (Figure 0-6) a distinct j_{lim} was not observed. However the lengthy response times of the system and appearance of transient photocurrent fluctuations under extended periods of photodegradation (inset Figure 0-6), prompted our investigation into these observations.

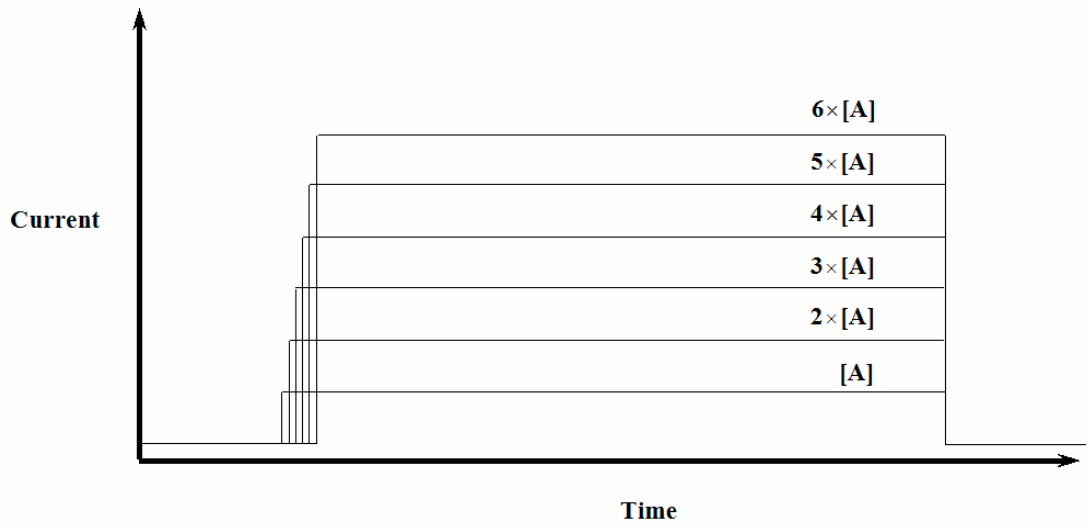

Figure 0-7 – Faradaic Model of photocurrent response over time for a stoichiometric increase in molar concentration of oxidative species A.

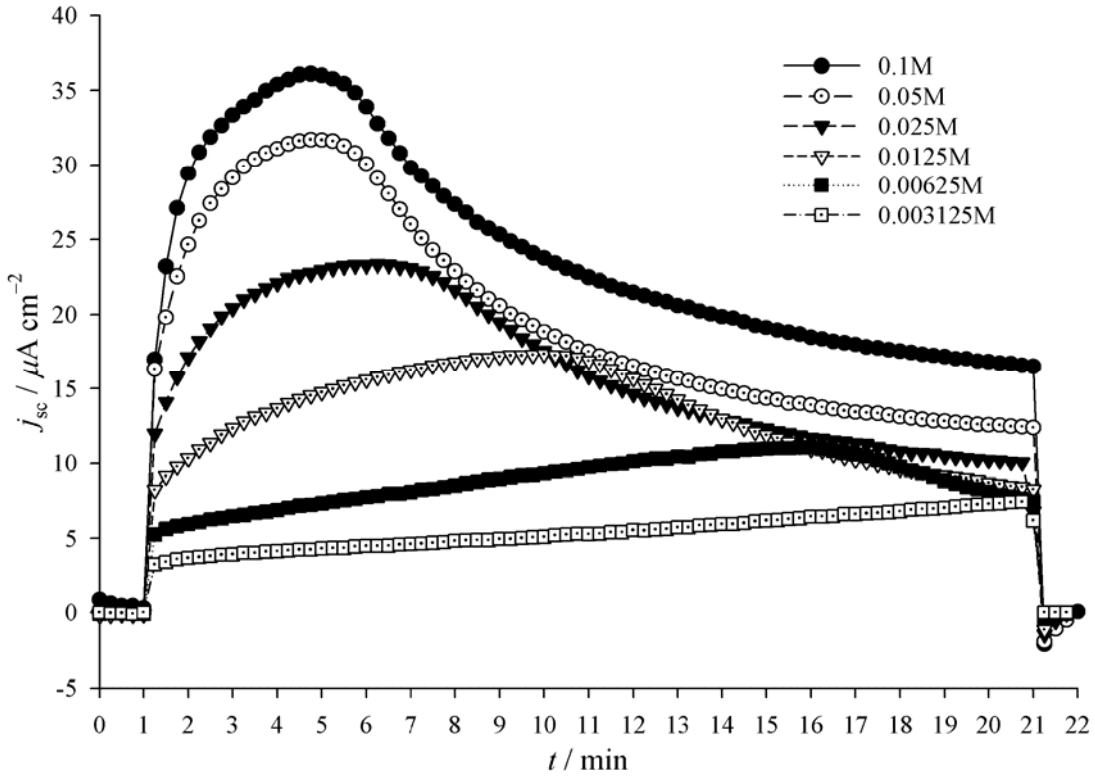

Figure 0-8 – Observed oxidation photocurrents for various concentrations of EDTA in solution.

Photoelectrochemical Determination of Solution Concentrations

Solutions were prepared with incremental concentrations from 1.000×10^{-1}M–3.125×10^{-3}M to investigate the oxidation capacity of the DS-PCC with the electrolyte EDTA. The oxidation of EDTA through sacrificial donation affords the regenerates the ruthenium photosensitiser. Through observation of photocurrent transients insight into the oxidation process can be obtained and relative rates of electron injection determined. If we assume a Faradaic relationship between $j_{\lim}$ for oxidation/electron injection and the molar concentration of oxidisable species in solution (C_0), regardless of the induction period attributable to adsorption of species, an increase in $j_{\lim}$ should be proportional to the molar increase in the oxidisable species according to Equation (0-2):

$$Rate(mol/s) = \frac{dN}{dt} = \frac{j_{\lim}}{nF} \qquad (0\text{-}2)$$

If a single-step oxidation model is assumed, as in Figure 0-3, there should be a linear increase in the observed photocurrent/concentration profile (Figure 0-7). For the oxidation of EDTA the photocurrent response does not adhere to this model under the concentrations used in these experiments (Figure 0-8).

The immediate interpretation of the data in Figure 0-8 is that a high concentration of adsorbed species is present and this impedes the onset of steady state oxidation. Adsorption of EDTA to the free surface states of TiO_2 is logically possible (due to acid groups present) and may indeed lead to a decrease in the oxidation rate for photosensitiser catalysis. However the response of the system at high molar concentrations of EDTA (0.1M and 0.05M) show remarkable homology in the transient profile. The changes to $j_{\max}$ and $j_{\lim}$ are logical with respect to the decrease in concentration and suggest a concentration/diffusion controlled system.

a

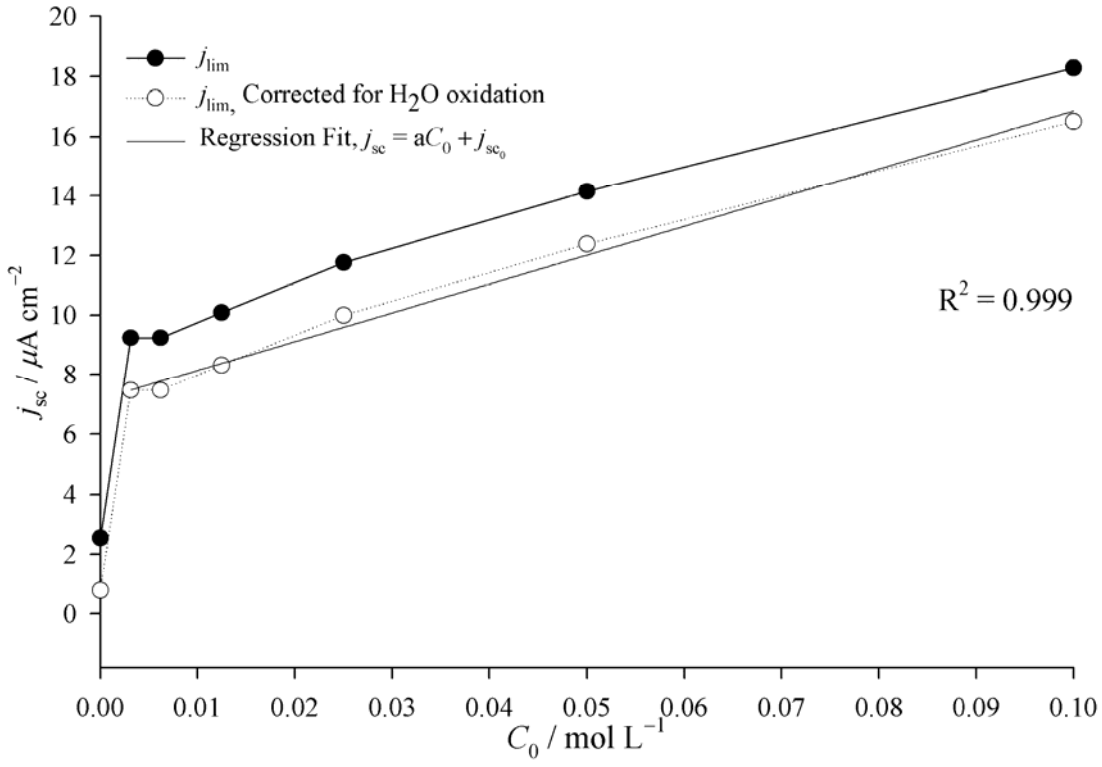

b

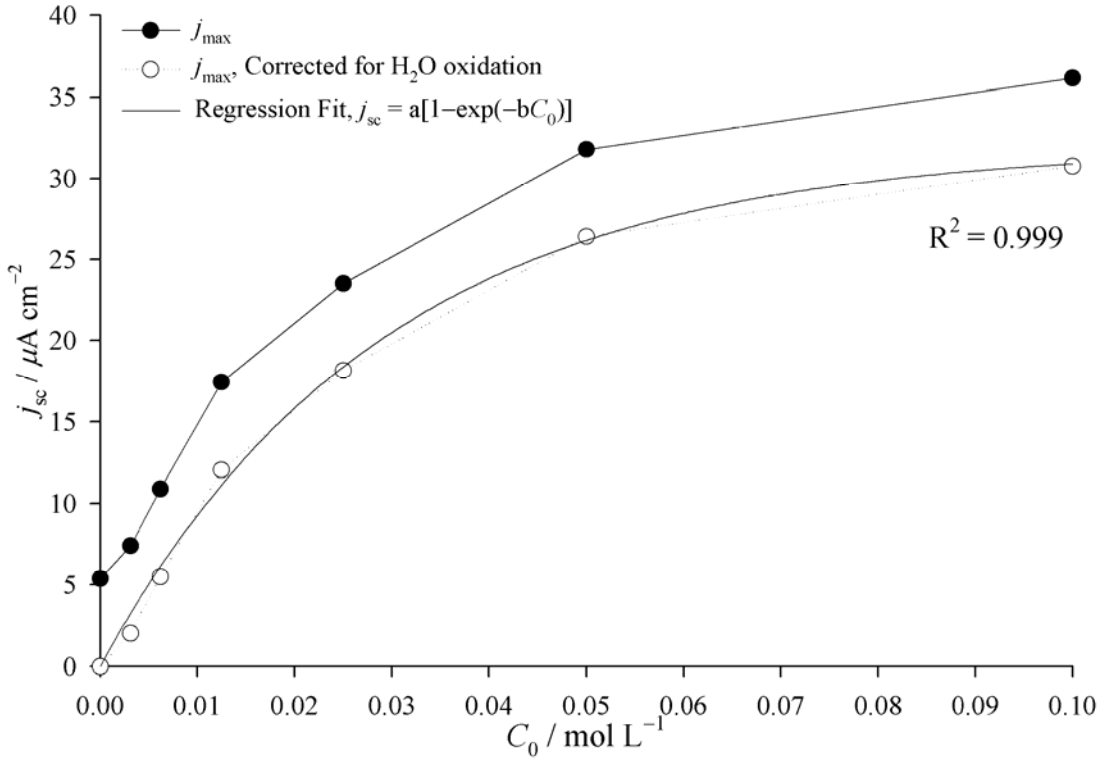

Figure 0-9 – a) Faradaic relationship between concentration and j_{lim}. b) relationship between molar concentration and j_{max}. Experimental data is given as —●—, experimental data corrected for H_2O oxidation as —○— and regression data as ——. Data is for photooxidation of EDTA solutions in the concentration range of 1.000×10^{-1}M–3.125×10^{-3}M.

The response of the system, from initial illumination to j_{max}, is depicted in the data as a period of rapid oxidation. The relationship of j_{lim} and j_{max} to molar concentration of oxidisable species is depicted in Figure 0-9a and Figure 0-9b respectively.

A linear fit to the data (Figure 0-9a, j_{lim} versus C_0) is only obtained at high concentration, with the intercept in the absence of EDTA non-zero. Considering the data in Figure 0-9b, with subtraction of j_{sc} for H_2O oxidation, there appears to be a logarithmic relationship between concentration and j_{max} attained for each solution. From Figure 0-8 it can be seen that incremental decreases in EDTA concentration leads to an increase in time to reach j_{max}. This indicates that as the concentration of EDTA increases there is an exponential increase in the rate of oxidation or that the oxidation is a superposition of several oxidation steps. For the data presented, this does not fit a single step oxidation model. However, if the degradation of EDTA $\rightarrow$ $EDTA^+$ gives a discrete amount of current and $EDTA^+$ is also capable of being oxidised, the observed flux of electrons would yield a current larger than expected.

The data shown in Figure 0-9 present an inconclusive relationship between the photocurrent and concentration for EDTA if a one electron process is considered. Indeed the photocurrents show a superposition of multiple oxidations that are most likely due to multiple reaction pathways for the mineralisation of EDTA. Hence, the single-step model for photodegradation at the electrode surface is invalid as expected for the chemical structure of EDTA.

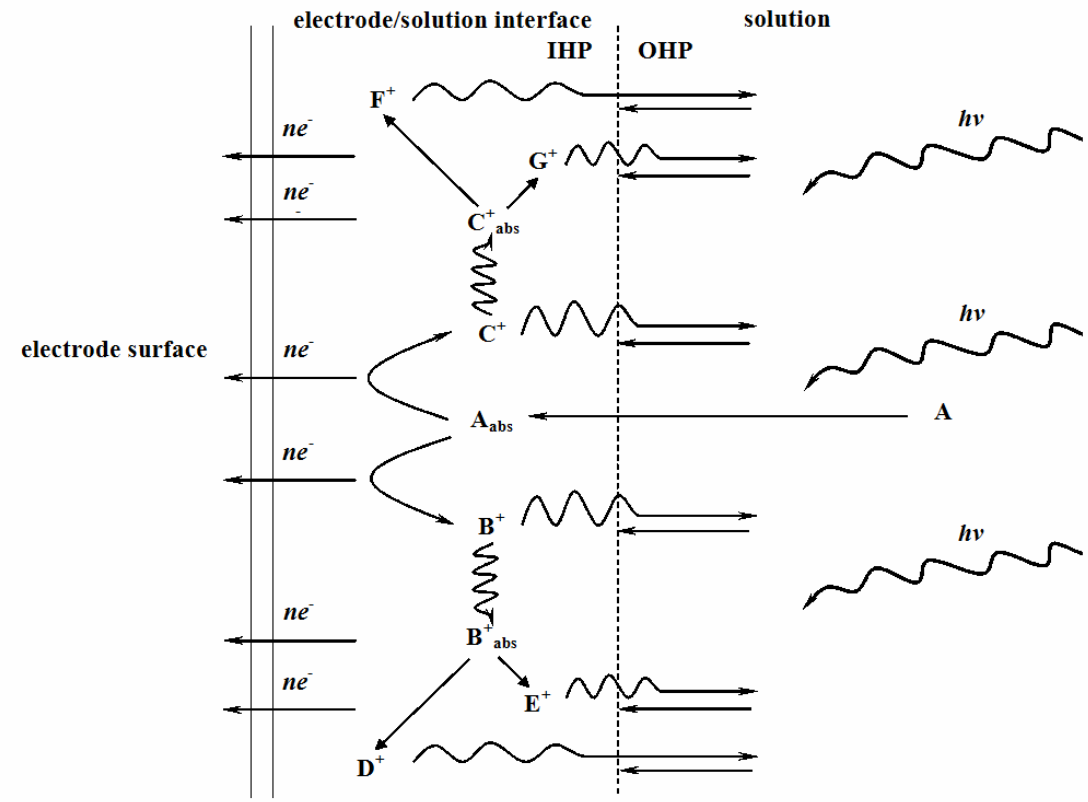

Figure 0-10 – Model of multi-step oxidation: interaction of solute and photo-products with surface under continuous illumination.

A plausible explanation for EDTA is a multi-step oxidation model (Figure 0-10) which would be supported by multiple electron rich functional groups that can lead to an array of degradant compounds. This oxidation process involves diffusion and adsorption of the parent oxidisable species (A) to the electrode surface. Following oxidation, the reaction products, B^+ and C^+, are free to migrate back to the solution bulk, through the nanoporous matrix and reabsorbed or be directly oxidised. Subsequently the reactant products, B^+ and C^+, do not undergo interfacial diffusion from the electrode surface to the bulk but contribute further to the charge transfer and hence the photocurrent signal. Oxidation of B^+ and C^+ gives further oxidised compounds D^+, E^+, F^+ and G^+, all of which add to the photocurrent. As would be expected, oxidation via the multi-step model leads to a cascade of electron transfer to the substrate and simultaneous accumulation of degradation products. These degradation products actively participate in the oxidation and mineralisation of EDTA which will be elaborated in the discussion of Section 0.

It was noted following the concentration experiments that a discoloration of the photoanode surface could be observed by inspection. There was no apparent change to the sensitised surface after each experiment; however a gradual change or loss of dye from the sensitised surface was confirmed by optical spectroscopy. Desorption of the dye from the electrode surface was unexpected due to stability of the phosphonic acid anchoring group hence the discolouration was recognized as a direct result of the oxidation process. The photoanodes were monitored before and after each irradiation sequence with an *increase* in visible absorption over the entire spectrum (see Figure 0-15). Consideration of acid-base equilibria in the bulk of the solution does not explain desorption of the dye, although microscale pH fluctuations are expected in the adsorbed interfacial electrode region from amine species as products of photooxidation. A new electrode was used for each of the solution concentrations, performed in duplicate, with discoloration observed after each measurement. Attempts to re-adsorb dye to the surface had no effect on absorption spectra for the electrodes, with no change in their photoactivity. The electrodes were subsequently used in long term degradation experiments and gave reproducible photocurrent profiles.

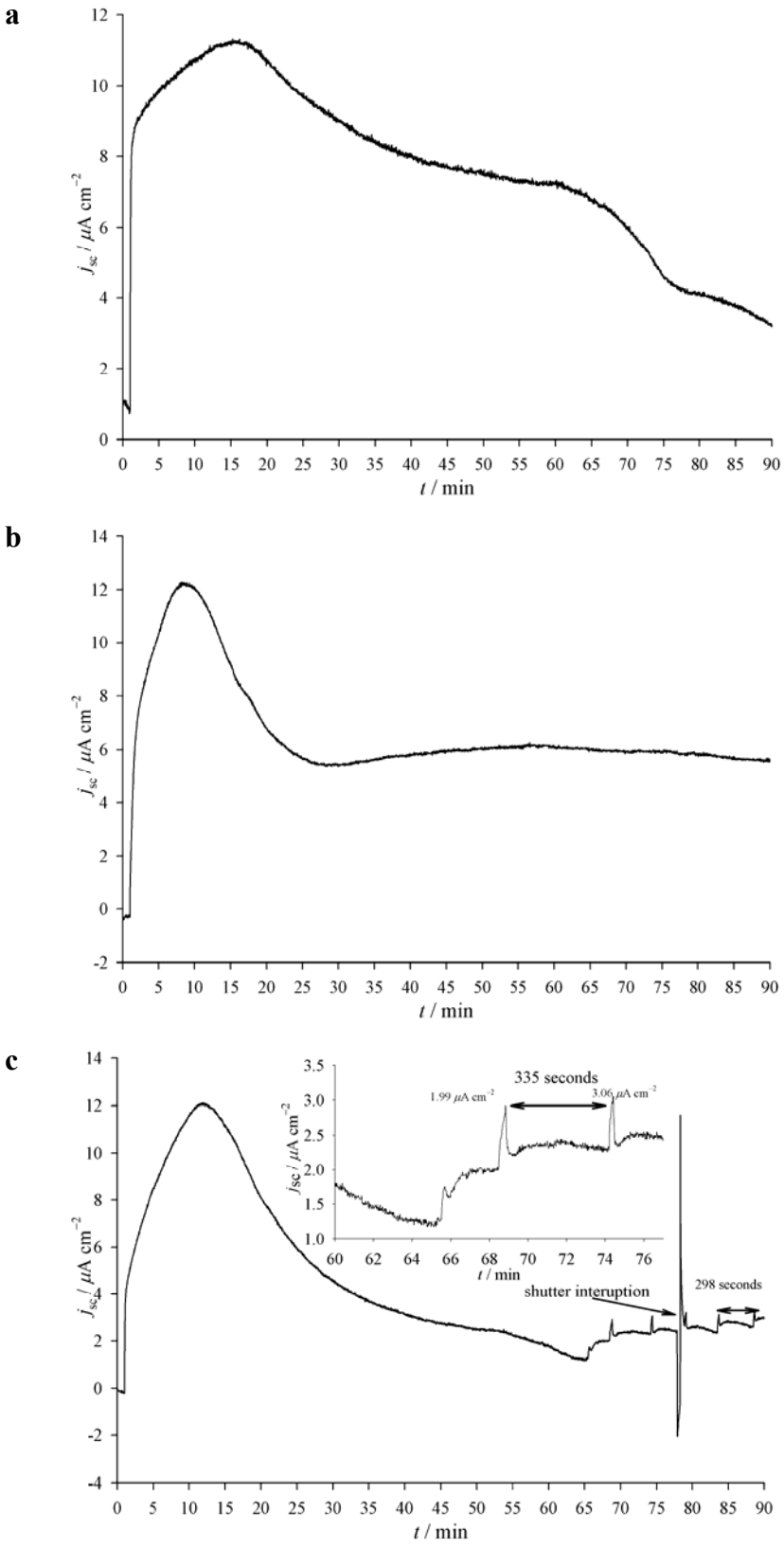

Figure 0-11 – The effect of pH and the photocurrent profile in the degradation of 0.1M EDTA (a) pH 4.5 (b) pH 2.9 (c) pH 2.0. Inset: inhibition of oxidation and photocurrent decline as system evolves gas from the electrode surfaces.

Exhaustive Oxidation of EDTA Solutions

The process by which EDTA degrades in the DS-PCC changes quite dramatically with respect to pH (Figure 0-11). At the buffered pH 4.5 of the EDTA solution (Figure 0-11a) degradation proceeds quite slowly with an increase in photocurrent to j_{max} reached within 15 minutes. Electrochemical studies into the complete oxidation of EDTA detect the presence of formic acid, oxalic acid and ultimately decarboxylation (CO_2) products.[353] No attempt was made to determine the presence of the degradation products; however the observation of a gaseous decomposition product would indicate mineralisation of EDTA in these experiments.

The photocurrent transients of Figure 0-11b and Figure 0-11c show similar profiles to that at pH = 4.5 with an increased photooxidation rate for pH 2.9 and 2.0 requiring 9 and 11 minutes respectively to reach j_{max}. The degradation as depicted in Figure 0-11b would benefit from enhanced concomitant oxidation/reduction as reduction of H_2O at the counter electrode would be favoured at pH =2.9. The equilibrium between the protonated and anionic forms of EDTA at pH =2.0 is considered the cause of the slower oxidation in Figure 0-12c. Due to the presence of the tetraacetic acid groups the molecule is expected to exist in both anionic and protonated forms (pK_{a1} = 1.70, pK_{a2} = 2.60, pK_{a3} = 6.30, pK_{a4} = 10.60) at this pH. The buffering character of the electrolyte allows the molecule to resist significant change in pH, inhibiting the degradation process as the protonated form has lower solubility and its insolubility hinders oxidisation. Although the integration of photocurrent profiles over the 90 minute period indicates that oxidation at pH = 4.5 has occurred to a greater extent, if the photocurrent decrease is due to surface passivation then the process is affected by solution pH, and not simply a change in reaction kinetics. In addition the observation of photocurrent fluctuations depicted in the inset of Figure 0-11c require further discussion of the obtained photocurrent profile.

Between 60 and 65 minutes there is a rapid decrease in the photocurrent that is not observed for the other experiments. Following the decline in the photocurrent, a sharp spike and gradual increase in observed j_{sc} coincided with the visual observation of gaseous reaction products on the surface of both the photoanode and cathode

surfaces. The coincidental rapid decrease in j_{sc} subsequently followed by observation of gas evolution suggests a decrease in the effective electrode surface area as gas nucleation inhibits the exposed electrode. The fluctuation could thus be a result of sudden solution mixing as the bubble is liberated from the electrode surface. The initial spike in the photocurrent at 66 minutes was not unique, with periodic fluctuations in the photocurrent profile occurring several minutes apart.

After the periodic fluctuations were observed over 10 minutes it was assumed that they were an artefact of the instrumentation. The manual shutter was used to interrupt illumination whilst data collection was continued as indicated in Figure 0-11c. The photocurrent diminished instantaneously and was assumed to reset the system. After a period of 30 seconds of darkness the shutter was removed and illumination continued. However, the fluctuations recommenced with the frequency of the spikes remaining unchanged.

Oxidation was continued for a further 14 minutes, with observation of the periodic fluctuations, before a second shutter interruption to cell illumination. Following a period of darkness, illumination of the cell saw the reappearance of the spikes with no change in the periodic fluctuations. These fluctuations must then be considered a true component of the photocurrent measurements and consequently be factored into our understanding of the degradation process. Observations of the cell during this time showed that, unlike the experiment conducted at pH = 4.5, that there was an increased rate of formation and evolution of gaseous products from the surface. Small bubbles could be seen on the surface of both electrodes with gas evolution from the surface corresponding with the fluctuation in current measurements.

Two interesting aspects of these fluctuations become apparent; specifically, the frequency with which they occur and the change in the current that coincides with the fluctuation (inset Figure 0-11c and Figure 0-12).

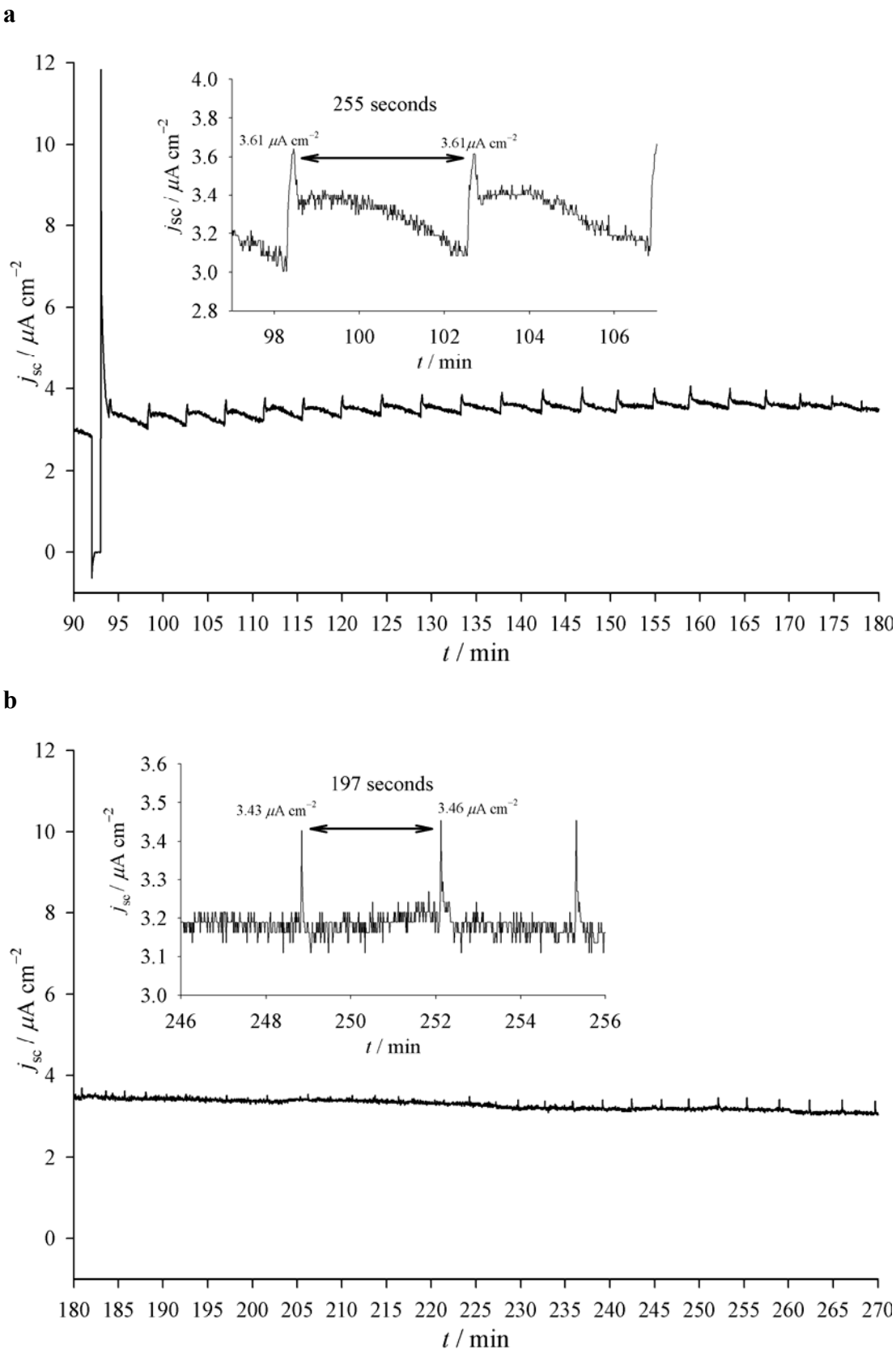

Figure 0-12 – (a) steady-state oxidation of EDTA depicting the periodic fluctuations observed during gas evolution, inset: interval and photocurrent 'spiking' as gas evolves; (b) extended oxidation with the period of fluctuations decreasing over time, inset: the magnitude and period of the photocurrent fluctuations.

On close assessment the fluctuations in photocurrent are not instantaneous but occur over a 50 second period that decreases with prolonged irradiation. Also, the frequency of photocurrent fluctuations diminishes with prolonged time of irradiation. The frequencies decrease from the initial onset of gas evolution (Figure 0-11c, 335 seconds for the period 68–74 minutes), to a recurrent fluctuation over a period of 90 minutes (Figure 0-12a, 255 seconds for the period 98–103 minutes) and significantly diminish at the end of the oxidation experiment (Figure 0-12b, 197 seconds for the period 249–252 minutes). The onset of gas evolution, the periodic photocurrent frequency and the gradual increase in j_{lim} (*c.f.* Figure 0-11c to Figure 0-12a) may provide evidence to the process by which EDTA degrades within the DS-PCC.

The periodic fluctuations that coincide with gas evolution may represent agitation of the electrode surface and subsequent mixing or increase in surface area of the electrode in contact with the solution. An explanation for the diminishing photocurrent prior to the evolution of gas may be the result of an increase in surface concentration of decomposition products or a masking of the exposed surface through bubble formation and nucleation. As the oxidation of EDTA proceeds there is an increase in concentration of decomposition products at the surface of the electrode, essentially a blocking layer, which impedes mass transport. Surface adsorbed species would be preferentially degraded with many of these capable of decarboxylation which leads to gas bubble formation. When the critical dimension of the micro-bubbles is such that they overcome attractive forces of the surface, they spontaneously evolve and the exposed surface area rapidly increases.

Discussion

Mechanism of Photooxidation and Decarboxylation at a Dye-Sensitised Surface

In dye-sensitised PEC devices the photo- and electrochemical reactions that occur on a discrete molecular level translate to concerted properties in the bulk cell. Assuming a one-dimensional model, a photon of light incident with an adsorbed dye molecule excites an electron from a t_{2g} *d* orbital of the Ru^{2+} ion to the LUMO, a π* orbital, of a coordinated bipyridine ligand.[242] Intimate contact of peripheral anchoring groups of the bipyridine with the surface provides a physical route for electron transfer via the $[Ru(dmpbpy)_2(bpy)]^{3+}$–TiO_2 potential gradient, effecting charge separation/segregation. The electron transfer process leaves $[Ru(dmpbpy)_2(bpy)]^{3+}$ in a highly oxidative state.

Ground state regeneration is often afforded by electron donation from a sacrificial species. For a similar surface bound sensitiser, $E_{½}$ ($Ru^{III/II}$) is +1.26V and E_{00} = 1.96eV (see Figure 0-6 p178).[8] Thus for the flatband potential of TiO_2 (–0.7V at pH = 5) the energy of the excited state electron is sufficient for injection to the TiO_2 CB and is favourable only for pH < 5.[341] The Ru(III) state of the sensitiser is a strong Lewis acid with an oxidation capacity of +1.26V. EDTA, a tertiary amine, is Lewis base in character thus nucleophilic attack on the Ru(III) occurs and, following rearrangement, $EDTA^+$ is ejected as an iminium ion. During post-catalytic rearrangement in the presence of H_2O two species emerge: ethylenediaminetriacetic acid (EDTrA) and glyoxylic acid (Scheme 0-2).

The presence of both of these species as by-products from the oxidation of EDTA by tris-diimine Ru(II) complexes has been reported.[334] Oxidation of the EDTrA moiety via the mechanism of Scheme 0-2 is feasible with prolonged irradiation leading to the formation of stoichiometric quantities of ethylenediamine and glyoxylic acid (0.1mol and 0.4mol respectively for 0.1mol of EDTA). The possibility of these compounds being present in the extended oxidation experiments prompted us to explore their electron donation capability. Figure 0-13 depicts the photocurrent transients obtained from stoichiometric quantities of these two degradation products.

Scheme 0-2 – Mechanism of catalytic adsorption and rearrangement where EDTA is degraded to EDTrA and glyoxylic acid in the presence of H_2O. The EDTrA and subsequent amine compounds can then undergo further degradation via this mechanism to give stoichiometric amounts of glyoxylic acid and ethylenediamine.

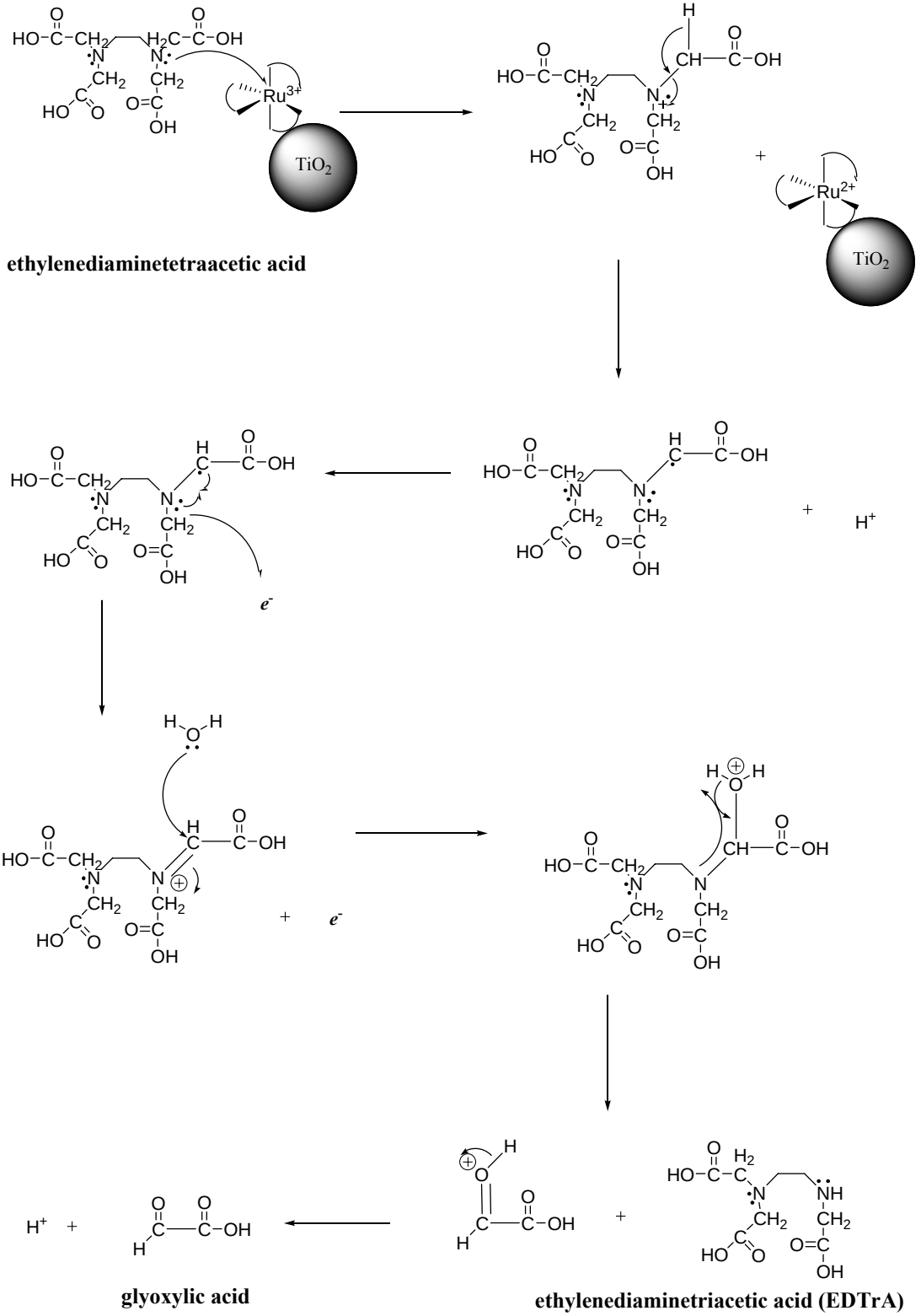

Glyoxylic acid, in its protonated form ($pK_a = 3.18$), shows no oxidative capacity (see Figure 0-13) however may aid the decomposition process as a source of H^+ for reduction at the cathode. In fact the response from the DS-PCC with glyoxylic acid is less than that of H_2O alone. Ethylenediamine shows some improvement over glyoxylic acid yet interestingly a 1:4 mixture of these two compounds lead to a marked improvement in the observed photocurrent. Also of note is that upon mixing of ethylene diamine and glyoxylic acid (both clear aqueous solutions) the mixed solution darkened over several minutes and when observed standing for a week, darkened considerably to an intense brown/red solution. The darkening is most likely the formation of a polymeric compound as amines readily react in the presence of aldehydes. The presence of either of these compounds at the site of oxidation would contribute negligibly to the observed photocurrent under extended irradiation (~3 $\mu A \cdot cm^{-2}$).

Although the pH of the 1:4 solution was initially ~2.5 the molecular pH at the surface following oxidation is dependent on the nature of species present. The basicity of ethylenediamine would be sufficient to deprotonate the glyoxylic acid moiety giving the corresponding anion and corresponding cation pair. The electron transfer process as described above induces an electrochemical potential field that would be capable of oxidising the glyoxylic anion. Under these conditions decarboxylation of the glyoxylic anion according to the Kolbe electrosynthetic mechanism can occur,[354] resulting in the evolution of a gaseous product, CO_2 (Figure 0-14 and Scheme 0-3). This mechanism is supported by the photooxidation experiment for ethylenediamine and glyoxylic acid (Figure 0-13), indicating that a mixture of the two components is the only photoactive solution.

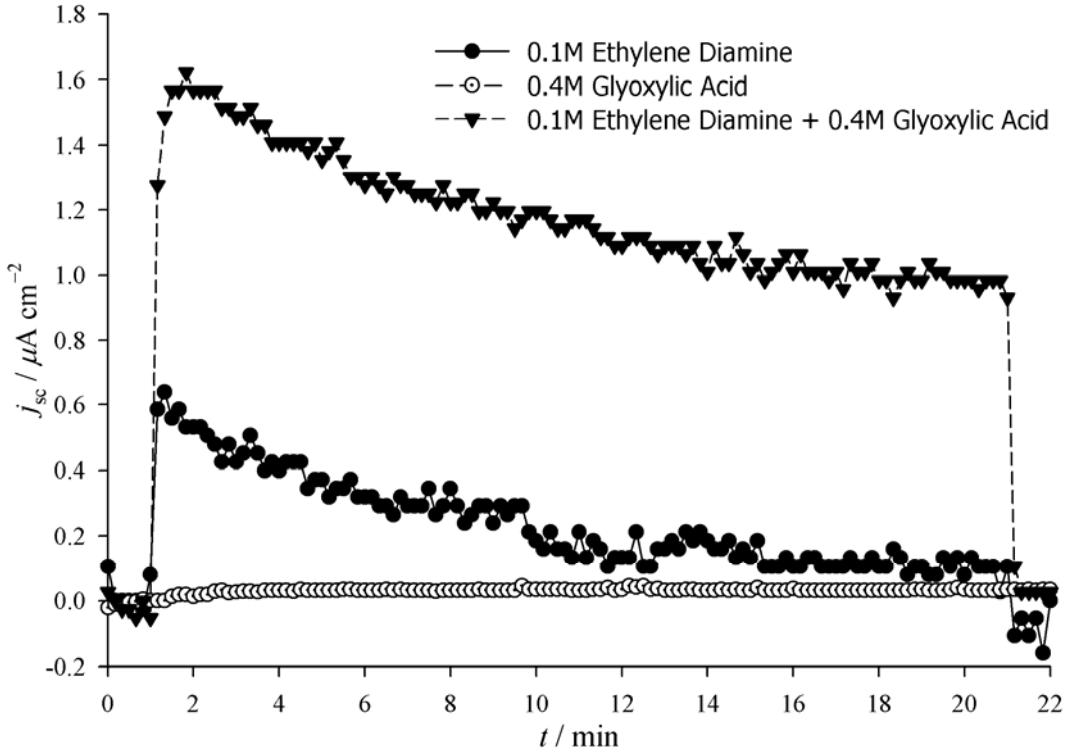

Figure 0-13 – Photocurrent observed for the degradation of EDTA by-products: 0.1M ethylene diamine solution —●—, 0.4M glyoxylic acid —o— and a 1:4 mixture of 0.1M ethylene diamine and 0.4M glyoxylic acid—▼—.

a

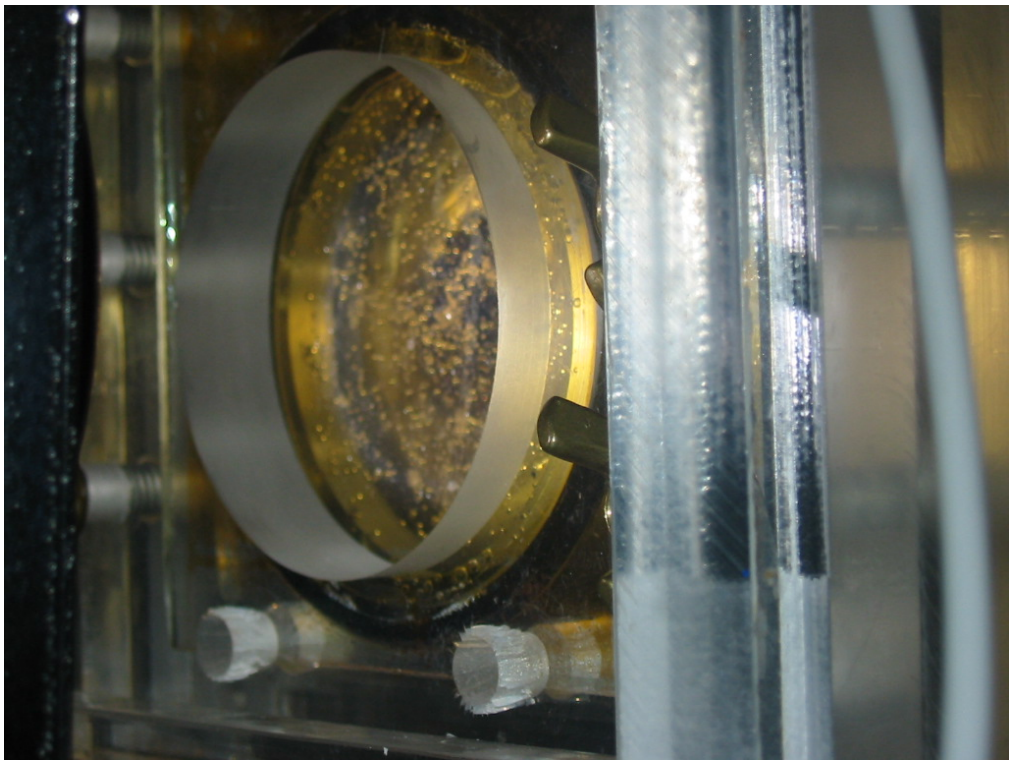

b

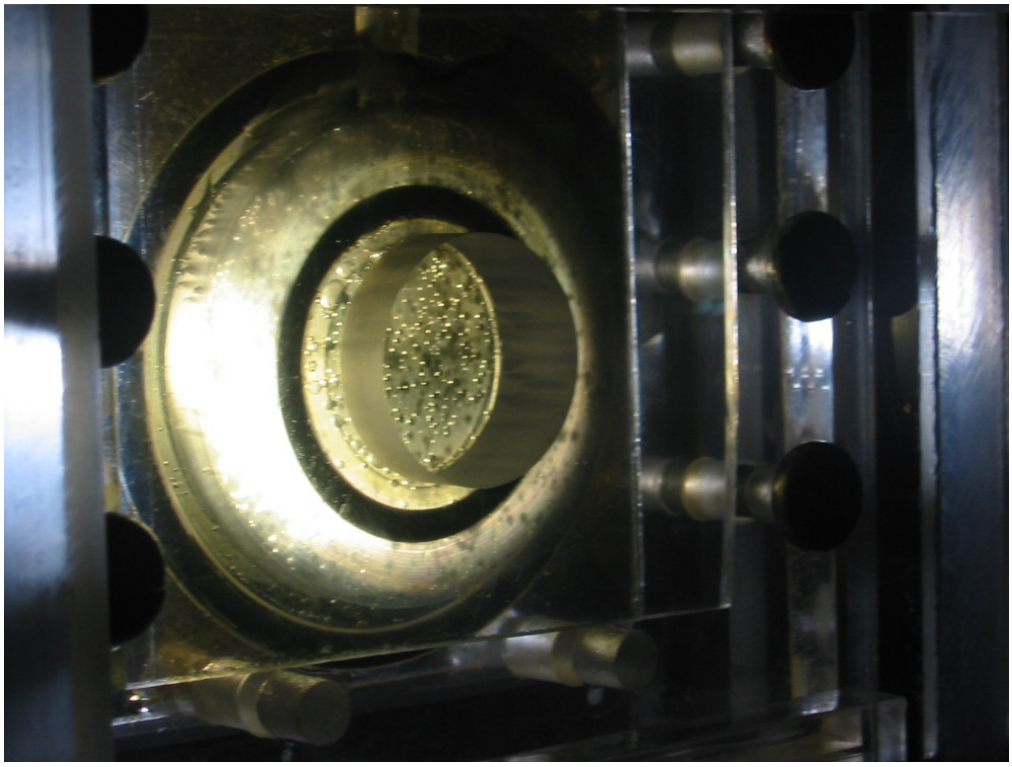

Figure 0-14 – Photographs of a) photoanode b) cathode, of a larger scale DS-PCC assembly showing the build up of gaseous degradation products on the electrode surfaces.

Scheme 0-3 – Free radical formation via the Kolbe synthetic reaction

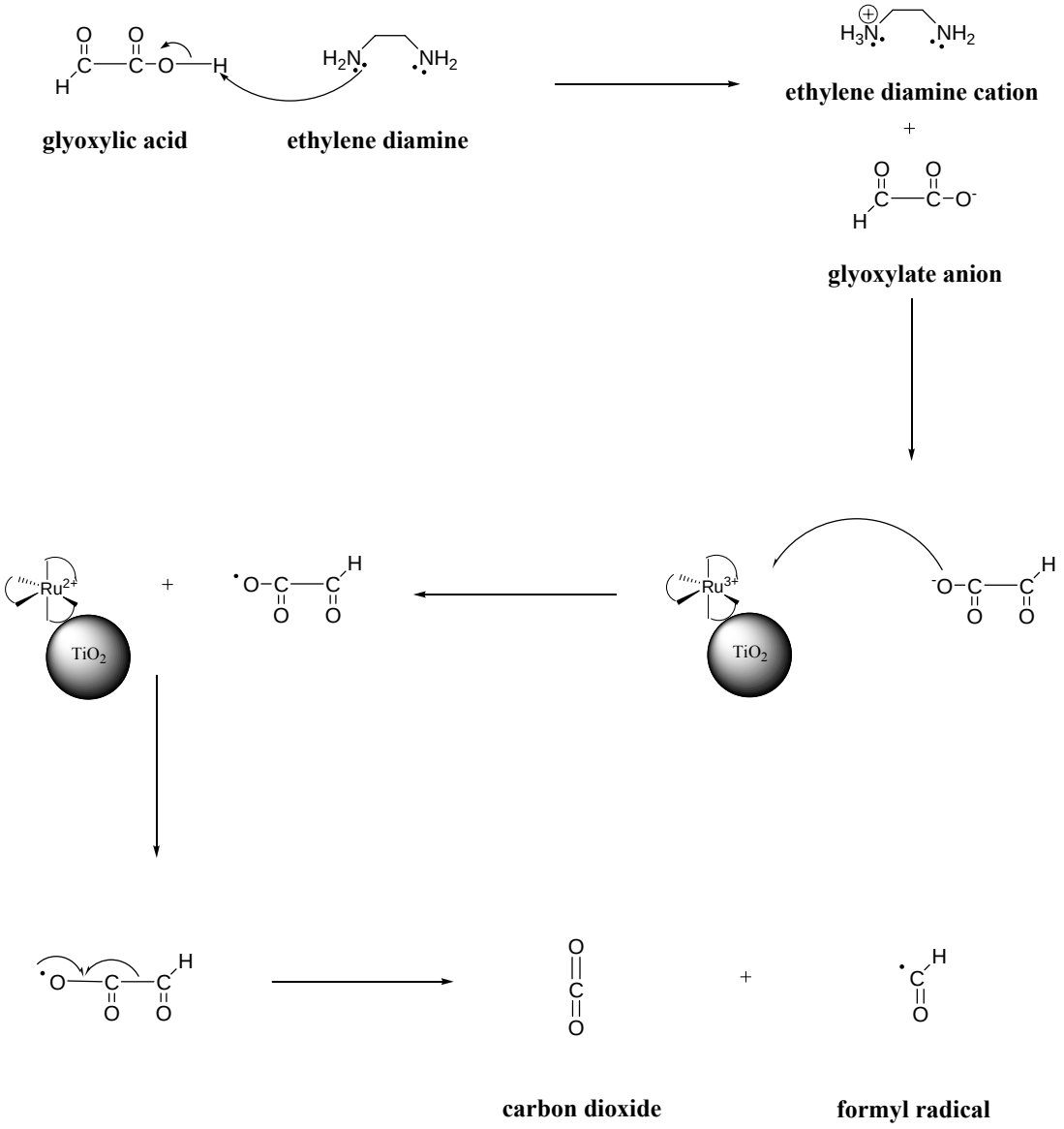

Ethylenediamine initiates a mechanism by which glyoxylic acid can be oxidised within the DS-PCC. This leads to an increased observed photocurrent affording the loss of CO_2 from the glyoxylate moiety and formation of the formyl radical. Combined voltammomeric and HPLC studies have shown the presence of formic acid, oxalic acid and CO_2 as degradation components from EDTA oxidation.[353] The formyl radical is highly reactive and a known initiator in free-radical polymerisation. Studies into the Kolbe electrosynthesis reaction have demonstrated the existence of species associated with the termination of this radical, namely: R–H, R–OH, R–COO–R and R–R, where R is the radical formed. Assuming the formation of these termination products. Scheme 0-4 depicts products from formyl radical termination.

Scheme 0-4 – Specific examples of potential radical termination products from Kolbe synthetic reaction.

formaldehyde

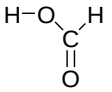

formic acid

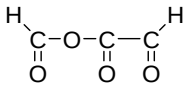

formyl-glyoxylic anhydride

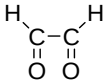

ethanedial

In aqueous media a significant termination product would be formic acid or, in the presence of amines, imine formation through reaction of the formyl radical to give a polymeric structure. In addition, the observation of gas evolution and the transformation of the electrode surface under extended periods of illumination provide evidence to support the proposed mechanism. Figure 0-15a depicts images of the electrode before and after the degradation experiments.

a

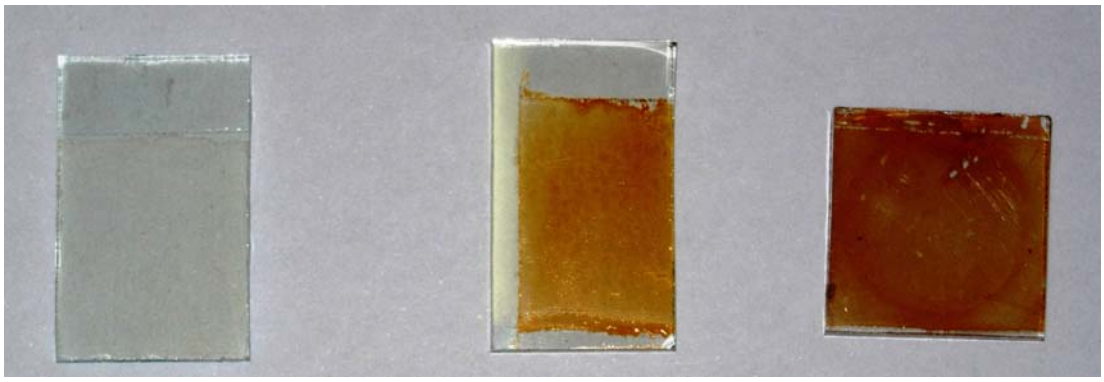

i **ii** **iii**

b

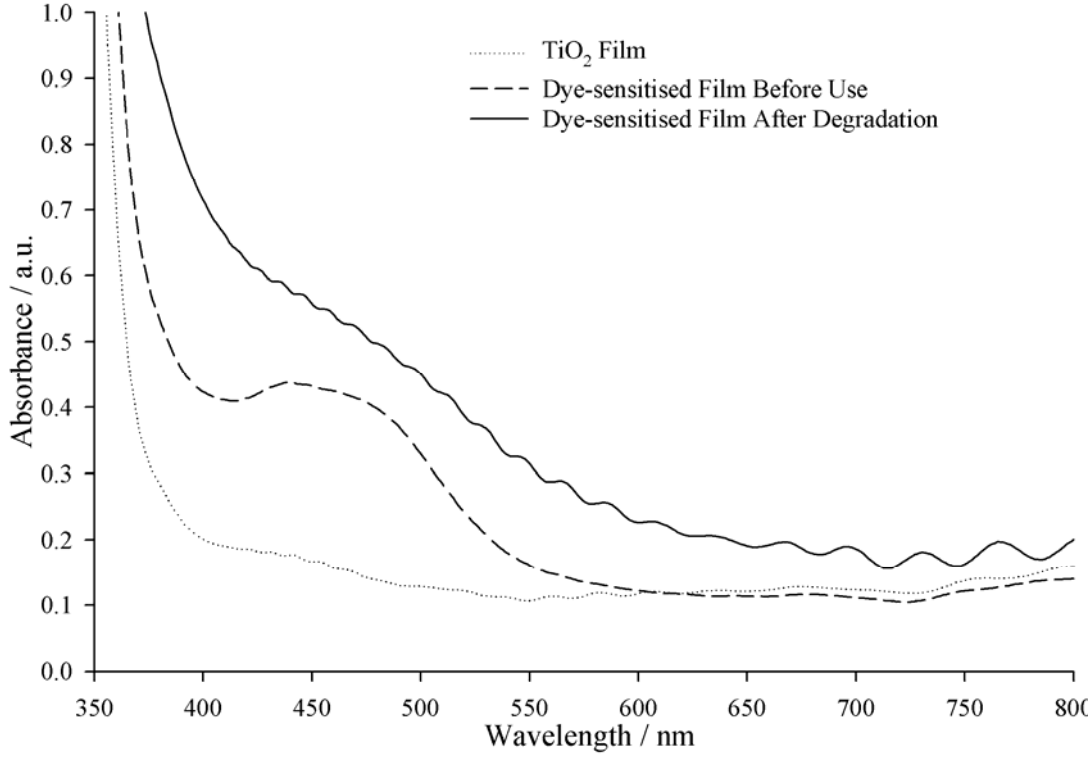

Figure 0-15 – Visualisation of secondary film formation on the photoanode surface a) photograph of electrodes: i) unsensitised TiO_2 thin film; ii) fresh dye-sensitised film; iii) photoanode after degradation. b) UV-visible spectra of the dye-sensitised electrodes before – – – and after —— use. A TiO_2 thin film substrate ····· is shown as a reference. Electrodes are from the photooxidation of EDTA depicted in Figure 0-11.

Visual discoloration of the photoanode following use in the degradation experiments is clearly evident. Additionally Figure 0-15b depicts the change in the electrode surface as monitored by solid state UV-visible spectroscopy during the degradation process.

An absorption maximum at 460 nm for the dye-sensitised electrode before use in the cell is indicative of the chemisorbed ruthenium complex. Following illumination for some time in the DS-PCC, this absorption band is obscured by a much larger absorption with a distinct interference pattern dominating the longer wavelength region. Initially, there was believed to be loss of dye from the surface of the electrode in increasingly alkaline conditions. As speculated above, the presence of ethylene diamine from continued oxidation of EDTA would result in a micro-alkaline environment sufficient to cause dye desorption. Interestingly, under extended periods of illumination the absorption band of the dye is no longer discernable in the UV-visible spectrum. However, a new species with an *increased* absorption in the region of the chromophore becomes the more dominant feature, obscuring the spectrum of the dye.

As depicted in Figure 0-15a no apparent change in the dye is evident, yet a darker orange hue to the surface is noted. We hypothesize that the presence of ethylenediamine (as a product from further oxidation of EDTrA) and glyoxylic acid affords reactive intermediates able to polymerise with other (amine) degradation species. This leads to an increased molecular weight, long chain compound representative of a ‘polyglyoxal-imine’ polymer. Furthermore, the observed interference pattern in the electrode spectrum indicates the formation of a secondary film on the dye-sensitised electrode surface after extended periods of oxidation. Figure 0-16a depicts solid-state UV-vis transmission spectra for the various electrode substrates with Figure 0-16b indicating two regions of the post degradation dye-sensitised electrode surface used for analysis.

a

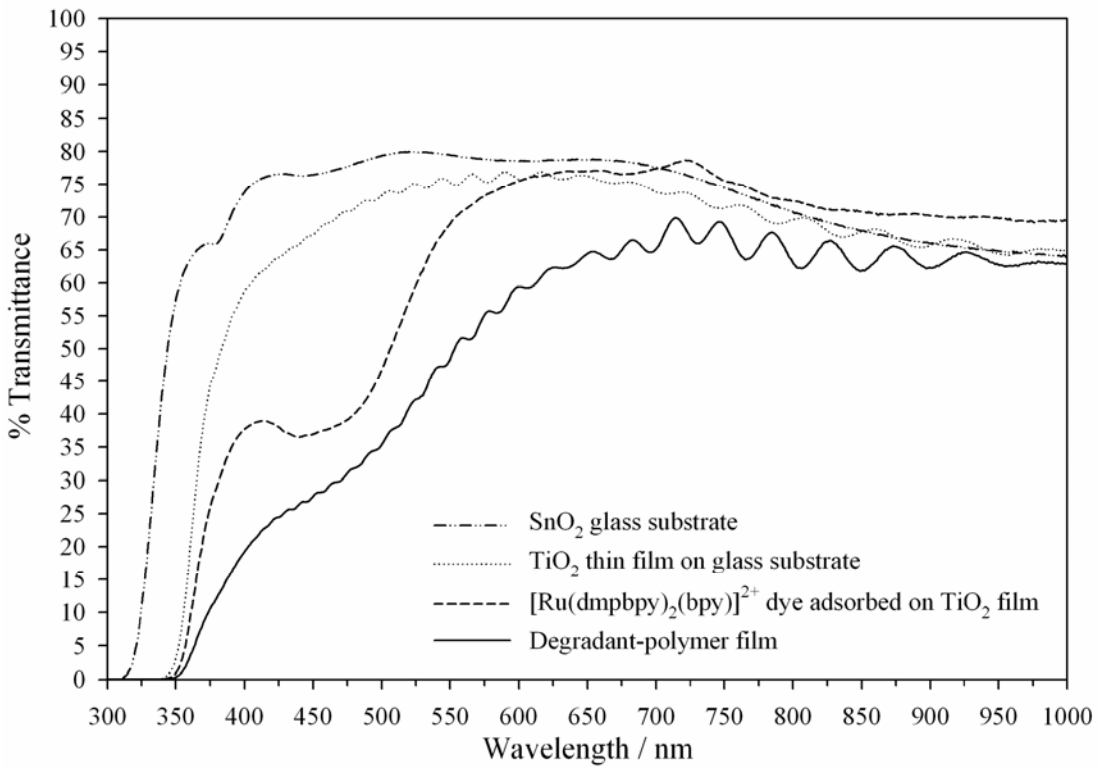

b

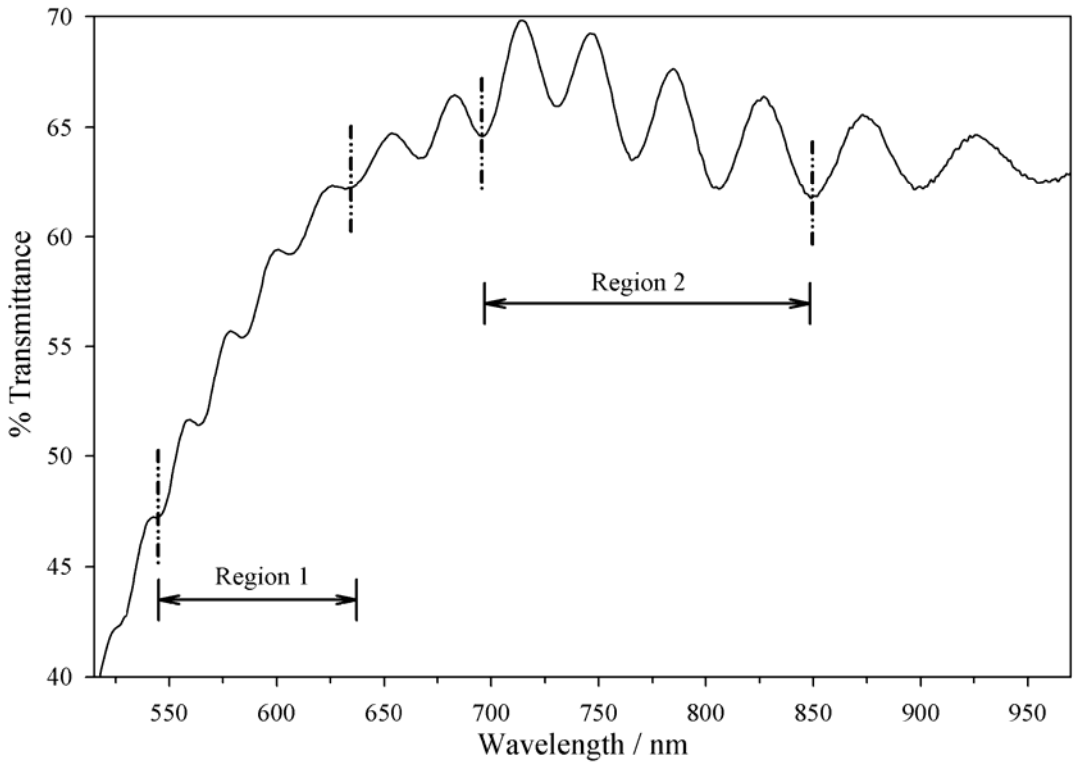

Figure 0-16 – a) Transmission spectra of the photoanode on a glass substrate before and after degradation. Substrates are shown for comparison. b) Transmission spectrum of polymeric film deposited on photoanode depicting the two regions used for analysis of refractive indices and film thickness.

Interpretation of the interference pattern[355] reveals a change in the refractive index for TiO_2 from η = 2.023 to η = 2.174 for the photoanode used in the degradation study. Calculation of the film thickness from the interference pattern in the transmission data indicates the formation of a secondary thin film, 2.73 ± 0.65 μm, during the photocatalytic degradation. Reliability in this estimation is limited as the nanoporous nanocrystalline film has a highly irregular surface morphology however the interference pattern and the change in η are indicative of the presence of a secondary film.

Closer examination of the electrode surface by FT-IR ATR spectroscopy reveals features of the surface residue. Figure 0-17 depicts the spectra of EDTA, some possible degradation species and the electrode surface.

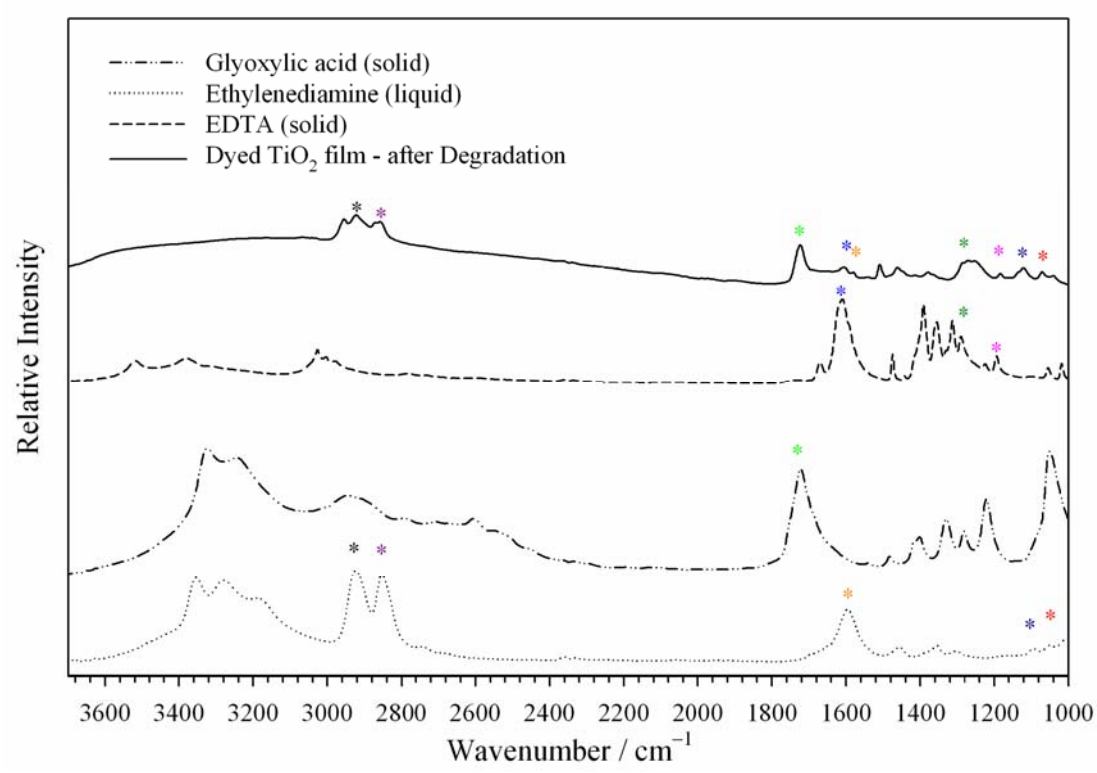

Figure 0-17 – FTIR-ATR of starting organics and the surface of the electrode after extended periods of illumination. Spectra are normalised against the vibration at 1722 cm^{-1} for glyoxylic acid.

The spectrum of glyoxylic acid in the high frequency region around 3400 cm^{-1} and tailing to around 2200 cm^{-1} is indicative of extensive hydrogen bonding from carboxylic acid and carboxylate ions. A broad >C=O stretch (1600–1800 cm^{-1}) from the presence of aldehyde and carboxylate chelated and H-bonded dimers is also observed in addition to –OH bending and C–O stretching in the fingerprint region.

The spectrum of ethylenediamine has three distinct vibrational regions: 2800–2960 cm^{-1} indicative of $-CH_2$ stretching; 3240–3400 cm^{-1} indicative of $-NH_2$ stretches; and the presence of broad featureless vibrations 3080–3200 cm^{-1} from $-NH_3^+$ stretching.

In comparison to ethylenediamine and glyoxylic acid, EDTA shows some spectral similarities with the presence of vibrations due to –OH bonding, as well as $-CH_2$ and $-NH_2$ stretches. Moreover, comparisons of these three compounds to that of the electrode surface exhibit distinct similarities. The spectrum for the electrode surface was corrected for a TiO_2 substrate background, which was essentially featureless, similarly for the spectrum of the dye-sensitised electrode surface before degradation. The dye-sensitised electrode surface appeared featureless during the examination by the ATR crystal due to the instrumental penetration depth and hence does not contribute to the bands discussed. Common features in the electrode surface are denoted by '*'.

The dye-sensitised electrode after degradation exhibited high surface concentration of contaminant species and the interference fringes indicate a secondary film obscuring the underlying substrate. Specifically vibrations attributable to: $-CH_2$ stretching (2780–2980 cm^{-1}); a medium >C=O stretch (1680–1730 cm^{-1}) most likely due to aldehydes; conjugated imine >C=N– stretches (1580–1620 cm^{-1}) and –OH bending and C–O stretching in the fingerprint region were observed.

Common spectral features indicate that the deposited material is most likely attributable to the reaction between glyoxylic acid, ethylenediamine and further decomposition products. Interestingly, the prominent >C=O stretch of glyoxylic acid at 1726 cm^{-1}, which is not observed in EDTA, is present in the surface bound residue

yet other distinct bands of glyoxylic acid are absent. The absence of clear vibrations of terminal $-NH_2$ and $-COOH$ present the case of a linear chain polymer comprising >C=O and >C=N– subunits.

Indeed the formation of thin polymeric films from ethylene diamine and related primary amines via electrochemical oxidation has been described. Herlem *et al.*[356] report surface passivation of metallic and semi-conducting electrodes with a film visible to the naked eye. They describe the formation of 'polyethyleneimine-like' coatings formed under free radical polymerisation in the presence of $R-NH_2^{+\bullet}$ cations. In comparison, our mechanism supports passivation of the electrode surface by thin film formation.

Conclusions

The non-Faradaic response from the oxidation of EDTA was examined. Photocurrent transients exhibited a superposition of multiple oxidations that is most likely due to multiple reaction pathways. A non-linear relationship between concentration and electron flux can be attributed to high concentrations of oxidisable species in comparison to linear relationships for significantly smaller concentrations reported previously. This was explained via a multi-step oxidation process for high-concentrations of EDTA. Observations of complete mineralisation of EDTA to CO_2 and the appearance of surface discoloration under extended periods of oxidation prompted explanation of these phenomena.

The transient photocurrent profiles obtained for the degradation of EDTA at high solution concentration (1.000×10^{-1}M) depict a steady decrease in the observed current which could not be explained by depletion of oxidisable species. The decline in photocurrent and the observation of surface discoloration were explained in terms of surface passivation by decomposition products; passivation was accounted for both by gas bubble nucleation and the formation of a secondary film.

Postulation of a mechanism for photocatalytic decomposition of EDTA on a dye-sensitised surface posed above has allowed our understanding of irregular photocurrent transients and secondary film formation. Extended oxidation of EDTA generates the glyoxylate anion that upon donation of an electron to the oxidised Ru(III) complex forms a free radical capable of polymerisation. Formation of the formyl radical evolves CO_2, observed in the experiment, and affords a free radical reaction forming a polymeric film that passivates the electrode surface. Surface passivation impedes interfacial surface diffusion and inhibits charge transfer and oxidation, as observed in photocurrent measurements.

CHAPTER 8

Chemical Discrimination by a Kinetic Model of Organic Photooxidation in a Heterosupramolecular Assembly

Introduction

Indoor and outdoor air-quality and the sustainability of water sources for the next generation are fundamental concerns. Rapid identification of organic molecules as aerosols or as contaminants in waterways is therefore useful as an indicator of air and water quality. Organic species are readily oxidised by catalytic processes and due to the discrete quantity of electrons transferred they may be detected via electrochemical and photoelectrochemical (PEC) observations. Detection of volatile organics,[357] organic dyes,[358] and organic acids[153] adsorbed at the surface of TiO_2 has been reported. Organic sensors of this type allow the determination of adsorbed organic molecules by monitoring the current under an applied potential or illumination. The oxidation of an organic molecule at the electrode surface results in a known number of electrons being injected to the TiO_2 nanocrystallites.[153] The number of electrons injected depends on the mechanism of oxidation which is also dependent on the chemical nature and relative concentration of organics present.[353,356,359-361]

For surface catalysed reactions, the rate of reaction can be represented by the Langmuir-Hinshelwood mechanism (LH mechanism)[62,362] or derivations such as the Langmuir-Hinshelwood-Hougen-Watson expression (LHHW).[363,364] This is commonly the approach employed to determine reaction kinetics and concentration of species consumed in the oxidation. The LHHW expression for this mechanism is given in Equation (0-1):

$$\frac{dC}{dt} = \frac{kKC}{\kappa\left(1+\left(K/\kappa\right)C\right)} \qquad (0\text{-}1)$$

Where C is the concentration of adsorbed species, t is time, K is the Langmuir isotherm adsorption constant, k is the pseudo-first-order rate constant and κ is a constant related to the kinetics of adsorption of O_2 to the surface of TiO_2 and dissolved O_2 in solution.

Catalysed reaction mechanisms for degradation of organic species require the physisorption or chemisorption to the catalytic surface prior to photooxidation.[57,70,154,365] The adsorption of a chemical species to the catalytic surface has a significant effect on the electron transport properties of semiconductors employed as photocatalysts, such as TiO_2, which can be fabricated into thin films and coatings on TCO glass supports.[123,308,322,366-368]

For a thin film photocatalytic surface in an electrochemical cell, diffusion or flux of oxidisable species to the electrode surface from the bulk is given by the current density, j, according to the Butler-Volmer Equation (0-2):[369]

$$j = j_0\{\exp((1-\alpha)f\eta) - \exp(-\alpha f\eta)\} \quad (0\text{-}2)$$

Where, j is the current density, α is the transfer coefficient, $f = F/RT$ and η is the overpotential of the cell.

It also follows that for an electrochemical reaction, there is a Faradaic relationship between current and concentration [Equation (0-3)]:[370]

$$I_{l\,O} = nFAm_O C_0 \quad (0\text{-}3)$$

Where, $I_{l\,O}$ is the limiting photocurrent for oxidisable species, C_0, is the initial bulk solution concentration at $t = 0$, n is the number of moles of electrons transferred in the oxidation, F is Faraday's constant, A is the electrode surface area and m_O is the mass transfer coefficient.

Incorporation of a thin film electrode in an electrochemical cell allows the monitoring of steady-state currents from the oxidation process. Through experimental determination of the steady-state photooxidation current and consideration of Equations (0-2) and (0-3) for a given molecular species, the initial concentration of species oxidised can be readily determined.

The altering of the physical properties of TiO_2 by surface absorbed species has a measurable effect on transient photocurrents.[153] Interpretation of the transient profiles provides understanding of processes that occur at the surface of

nanostructured TiO_2 electrodes. Indeed Jiang *et al.* have described a technique for determination of rates of oxidation of species adsorbed at titania surfaces.[154] The technique relies on analysing the characteristic decay profile observed in photocurrent transients.

There have been no reports of the use of sensitised electrodes for the determination of organic pollutant concentrations in solution. For these surfaces, the mechanism is altered compared to bare TiO_2 catalyst surfaces since oxidation occurs at an oxidised metal centre where organic molecules degrade due to the hole scavenging effect of such compounds.[371] However the electron injection and transport properties of titania nanostructured electrodes are not affected by the adsorption of a photosensitiser to the electrode surface. In fact, Nakade *et al.* report increased electron transport in nanostructured titania electrodes from the removal of charge trap sites due to dye adsorption.[372] Their study also indicated that surface charge traps are evident throughout the mesoporous structure of the electrode and that dye adsorption significantly increases the diffusion coefficient in these electrodes.

In the present study, transient photocurrents obtained from the photooxidation of organic species in solution will be interpreted using a kinetic model. This should provide an insight into the mechanism of oxidation and hence chemical speciation of compounds. This kinetic model may enable the discrimination of molecules in solution through interpretation of kinetic parameters related to organic structure and/or concentration.

Materials and Equipment

The molecular sensitiser used in the current investigation, **$[Ru(bpy)_2(dmpbpy)]^{2+}$**, was described in Section 0. The structure of **$[Ru(bpy)_2(dmpbpy)]^{2+}$** is depicted in Scheme 0-1.

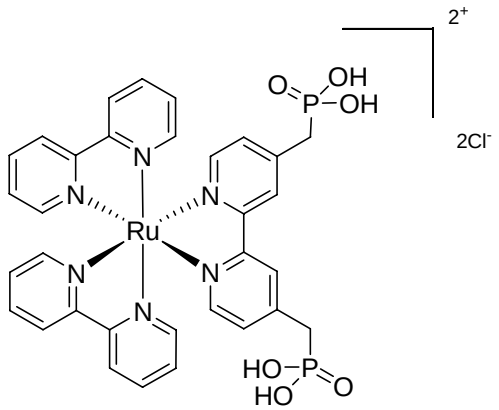

Scheme 0-1 – Structure of the electron donor $[Ru(bpy)_2(dmpbpy)]^{2+}$ used in the DS-PCC.

All reagents (unless otherwise stated) were of analytical reagent (AR) grade and were used as supplied from Sigma-Aldrich. Solvents were AR grade and were used as received. The organic compounds investigated for their oxidation rates are depicted in Scheme 0-2. Solutions were prepared in a range of concentrations (39 μM–200000 μM or 1–10% v/v as indicated) in Millipore ultra high purity (UHP) deionised water (18.2 MΩ) with 0.1M Na_2SO_4 as the supporting electrolyte.

Conducting glass substrates were TEC15/3 fluorine doped tin oxide (F:SnO_2) from Libby Owens Ford (LOF) ~3mm thick with a nominal resistivity of 15 Ω/cm^2 abbreviated as F:SnO_2.

Absorption spectra were collected in the solid state in air or in spectroscopic grade methanol using the Varian Cary 50 UV-visible Spectrometer.

Scheme 0-2 – Structure of simulated chemical pollutants studied for their oxidation capacity. Abbreviations used in the text are indicated in brackets.

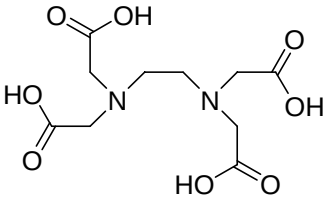

Ethylenediaminetetraacetic Acid (EDTA)

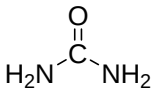

Urea (NHCO)

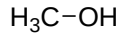

Methanol (MeOH)

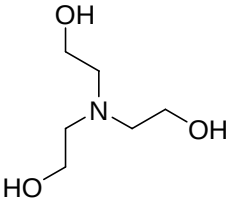

Triethanolamine (TEOA)

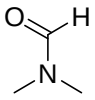

Dimethyl Formamide (DMF)

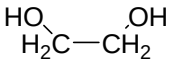

Ethylene Glycol (EtGly)

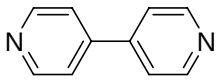

4,4'-dipyridyl (dpy)

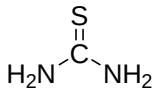

Thiourea (NHCS)

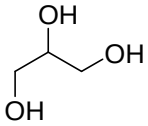

Glycerol (Gly)

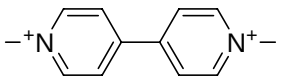

Methyl Viologen (MV)

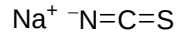

Sodium Thiocyanate (NCS)

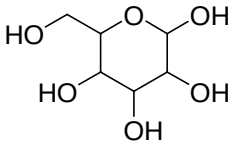

Glucose (Glu)

Preparation of Nanoporous TiO_2 Thin Films

Colloidal TiO_2 solution was available from experimental methods described in Section 2.1.1. Nanoporous TiO_2 films were prepared by doctor-blading a small quantity of the concentrated dispersion on a F:SnO_2 substrate. Resulting films were dried in air for 45 minutes prior to sintering in a muffle furnace at 450°C in air for 12 hours.

Chemisorption of Molecular Sensitiser to Thin Film Electrodes

The molecular sensitiser was adsorbed to prepared thin film TiO_2 electrodes by chemisorption as described in Section 0. The aqueous solution was 4.68×10^{-4}M and following chemisorption the films were removed and rinsed in deionised water. The films were stored in a darkened vacuum desiccator until required.

Electrodeposition of Platinum

Electrodeposition on conducting glass substrates for use as a counter electrode was performed as described in Section 0. Following the procedure, the platinised surface was rinsed with deionised water, and the electrode was stored in a vacuum desiccator until required.

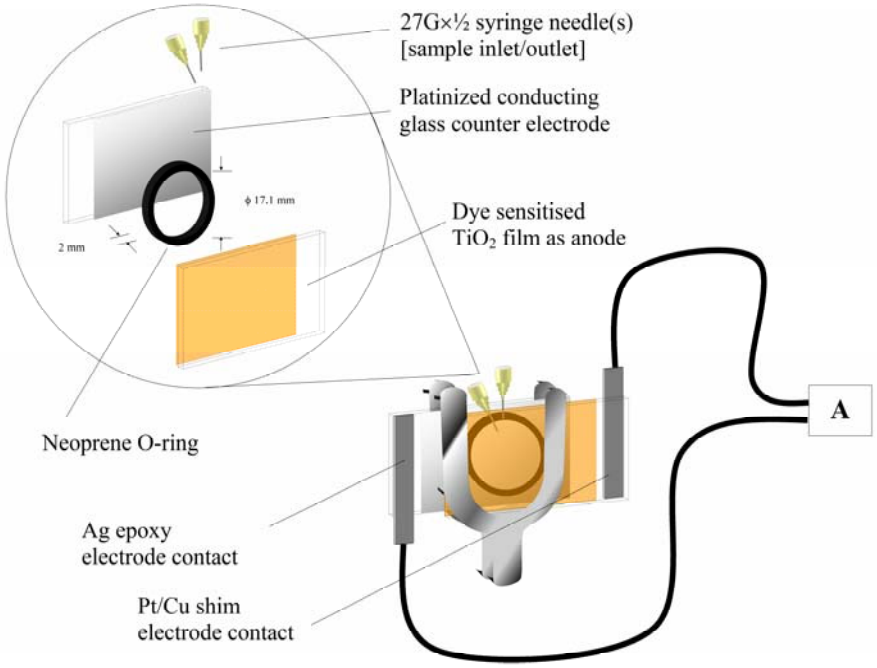

Figure 0-1 – Schematic representation of DS-PCC assembly as used in investigation.

Photoelectrochemical Measurements

A dye-sensitised photoelectrocatalytic cell (DS-PCC) was prepared by staggering a chemisorbed $[Ru(bpy)_2(dmpbpy)]^{2+}/TiO_2$ film and a platinised conducting glass substrate such that they overlapped, separated by a neoprene O-ring, and fixed by a heavy clamp to form a tight seal against the surfaces. The respective electrodes of the cell had a predefined area (2.30 cm^2) in contact with the electrolyte solution. The inter-electrode spatial separation was 0.20 cm and the cell volume was 0.459 cm^3. Samples were introduced into the inner cell cavity by piercing the surface of the O-ring with a fine syringe while equalising the pressure via a second syringe.

The optical illumination of the cell was as described in Section **0** with the effective lamp power 41 $mW \cdot cm^{-2}$ at the electrode surface. The cell assembly is depicted in Figure 0-2. For the ready exchange of films in the DS-PCC, electrode connection to the photoanode was via a pressurised Pt/Cu shim while the cathode was made with a Ag conducting epoxy. Both electrodes consisted of a Sn/Cu wire of 20 cm in length for connection to the recording device. Data were recorded using an ADC200 (Pico Technology Limited, Cambridgeshire United Kingdom) in data logging mode interfaced with a PC. Data points were collected at one sample per second and the short-circuited cell current measured using a differential 3-wire input with ground across a 1 kΩ resistor. The logged data were corrected for the resistance load according to Ohm's law. Experiments consisted of a sequence of 200 seconds darkness, an illumination period of 600 seconds, followed by 200 seconds of darkness. No attempt was made to baseline correct samples and the following mathematical treatment was performed on the raw data as collected.

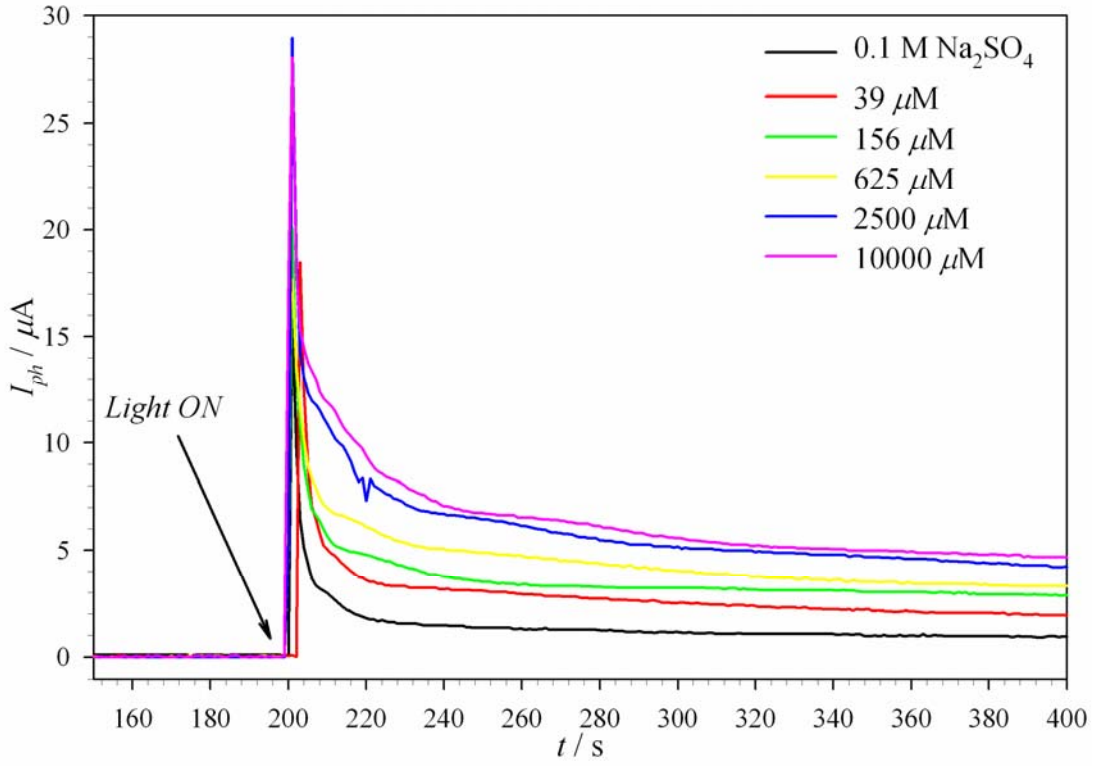

Figure 0-2 – The *in situ* effect of concentration on the transient photocurrent for a series of NCS solutions in the DS-PCC. The cell was unbiased and measurements were obtained at pH 5.6 in 0.1M Na_2SO_4 supporting electrolyte; concentrations are as indicated.

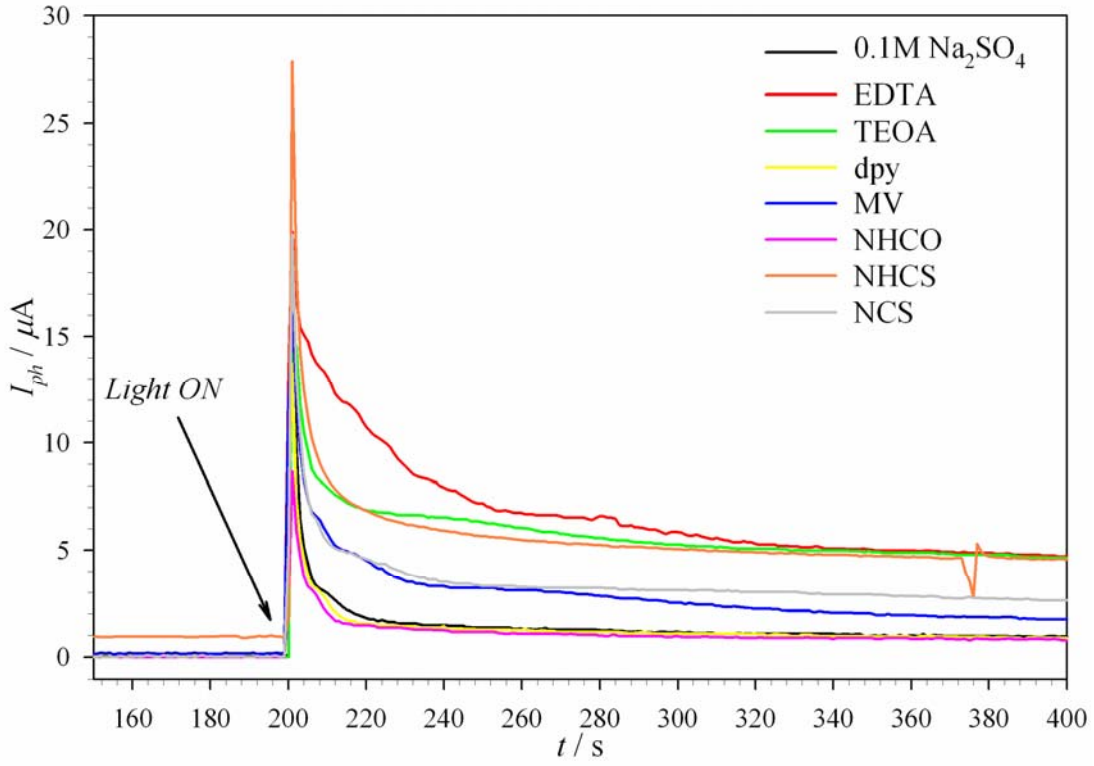

Figure 0-3 – *In situ* transient photocurrents for a range of compounds in solution oxidised in the DS-PCC. The cell was unbiased and measurements were obtained in 0.1M Na_2SO_4 supporting electrolyte; solution concentration was 78 μM.

Results and Discussion

Unbiased Photoelectrolysis in an Open Circuit

The effect of applying a potential bias has often been utilised to considerably enhance photocatalytic processes.[94,153,154,363,373] In the DSC, a device under no external potential bias, the photoelectrochemical effect occurs as a cascade of electron transfer processes and has been shown to be photochemically efficient.[2,51] In an unbiased PEC, photochemical events rely upon interfacial electron transfer and the turnover of the adsorbed PS.[33] Under these conditions, the driving force for electron transfer is both the strength of the oxidising agent (the excited state PS) and the relative electron donating ability of the species being oxidised. Observation of the electrochemical reaction would demonstrate the relative flux of species undergoing oxidation and thus would enable the study of the kinetics of the major interfacial processes.

In a simple model of the DS-PCC the factors influencing photodegradation would be: (1) the chemical nature of the species being oxidised; and (2) the available concentration of the species for photooxidation. To investigate the effect of both these factors a series of chemically similar and dissimilar organic compounds were chosen that were water soluble and capable of oxidation. These were prepared in a range of solution concentrations (39–10000μM). The effect of solution concentration is explored in Figure 0-2 and the effect of chemical nature on photocurrent (I_{ph}) transients depicted in Figure 0-3.

For the series of NCS solutions there is evidence of a relationship between concentration and the observed I_{ph} (Figure 0-2). Both the onset I_{ph} and the steady-state I_{ph} vary with an increase in concentration. The I_{ph} versus time profiles all show evidence of a biexponential process, yet as depicted in Figure 0-3. Therefore for a range of compounds at the same solution concentration, both the onset I_{ph} and the steady-state I_{ph} are influenced by the chemical species undergoing photooxidation.

The data in Figure 0-2 and Figure 0-3 demonstrate the influence of concentration and chemical nature on the photocurrent transients. In the following Sections the observation of a biexponential process evident in the transient data will be further explored in the anticipation of identifying compounds uniquely from their photooxidation profiles.

In Situ Transient Photocurrent Response

A similar transient photocurrent and kinetic study for a titania based PEC has been reported by Jiang *et al*.[154] In their investigation Jiang *et al*. were primarily interested in the kinetics of oxidation for surface bound complexes that form on titania surfaces. The strong adsorption of carboxylate groups of such organic compounds as oxalic acid to titania surfaces enabled the study of photooxidation kinetics. The overall observed photocatalytic oxidation current can be modelled as an accumulation of individual photocurrents attributed to multiple photocatalytic processes, Equation (0-4):

$$I_{ph} = \sum_{j=1}^{n} I_{ph\ j} \tag{0-4}$$

Where I_{ph} is the instantaneous photocurrent and $I_{ph\ j}$ is the instantaneous photocurrent for the oxidation of j type of surface complex. This relationship assumed an exhaustive photodegradation model with no contribution of species from the bulk of solution. However, an analogous assumption can be made for photooxidation by a non-exhaustive model, where I_{ph} is the sum of j type of *interfacial processes* occurring at the electrode surface, each contributing an instantaneous photocurrent $I_{ph\ j}$.

In our investigation, the surface photooxidative hole, $[h^+]_s$, that Jiang *et al*. describe for TiO_2 is substituted by the oxidised PS complex adsorbed to the surface. The chemisorption of the complex via the stable phosphonate group to free surface sites hinders the photocatalytic activity of TiO_2 and under visible light illumination photooxidation occurs only at the Ru(III) metal centre. Under these conditions there is limited evidence to suggest surface adsorption by degrading species due to the high surface loading of the PS complex occupying vacant Ti^{4+} sites. Thus the

observed interfacial processes would be photooxidation following *transfer from* the dye at the surface and photooxidation of species as they *transfer to* the dye from the bulk of the solution. In the preceding Chapter, we studied the oxidation of EDTA at much higher solution concentrations and a non-Faradaic response was observed. This was attributed to the chemical species being degraded, its mechanism of degradation and the solution concentration.

In the present investigation the concentration of organic species in solution is considerably lower by several orders of magnitude and the result gives the photocurrent decay profiles observed in Figure 0-2 and Figure 0-3. In Section 0, Equation (0-1) was presented to describe the proportional relationship of the observed current to the rate of oxidation (Equation (0-5)):[374]

$$Rate(mol/s) = \frac{dN}{dt} = \frac{I}{nF} \tag{0-5}$$

Jiang *et al*. demonstrated that, considering this relationship, the observed photocurrent, I_{ph} can be related to the total photocurrent decay profile as a sum of individual exponential components corresponding to the individual degradation processes (Equations (0-6) and (0-7)):

$$I_{ph} = \sum_{j=1}^{n} I_{ph\,j}^{0} \exp(-k_j t) \tag{0-6}$$

$$I_{ph} = \sum_{j=1}^{n} k_j Q_j^0 \exp(-k_j t) \tag{0-7}$$

Where $I_{ph\,j}^{0}$ is the initial photocurrent at $t = 0$, Q_j^0 is the expected charge from the complete mineralisation arising from the *j*th process and k_j is the rate constant for the *j*th kinetic process.

These findings have provided significant influence on the understanding of the kinetic processes occurring in the DS-PCC utilised here. Appreciating this kinetic model the experimental data (such as those obtained in Figure 0-2 and Figure 0-3) can be fitted to a double exponential expression. Representative curve fitted decay profiles are presented in Figure 0-4.

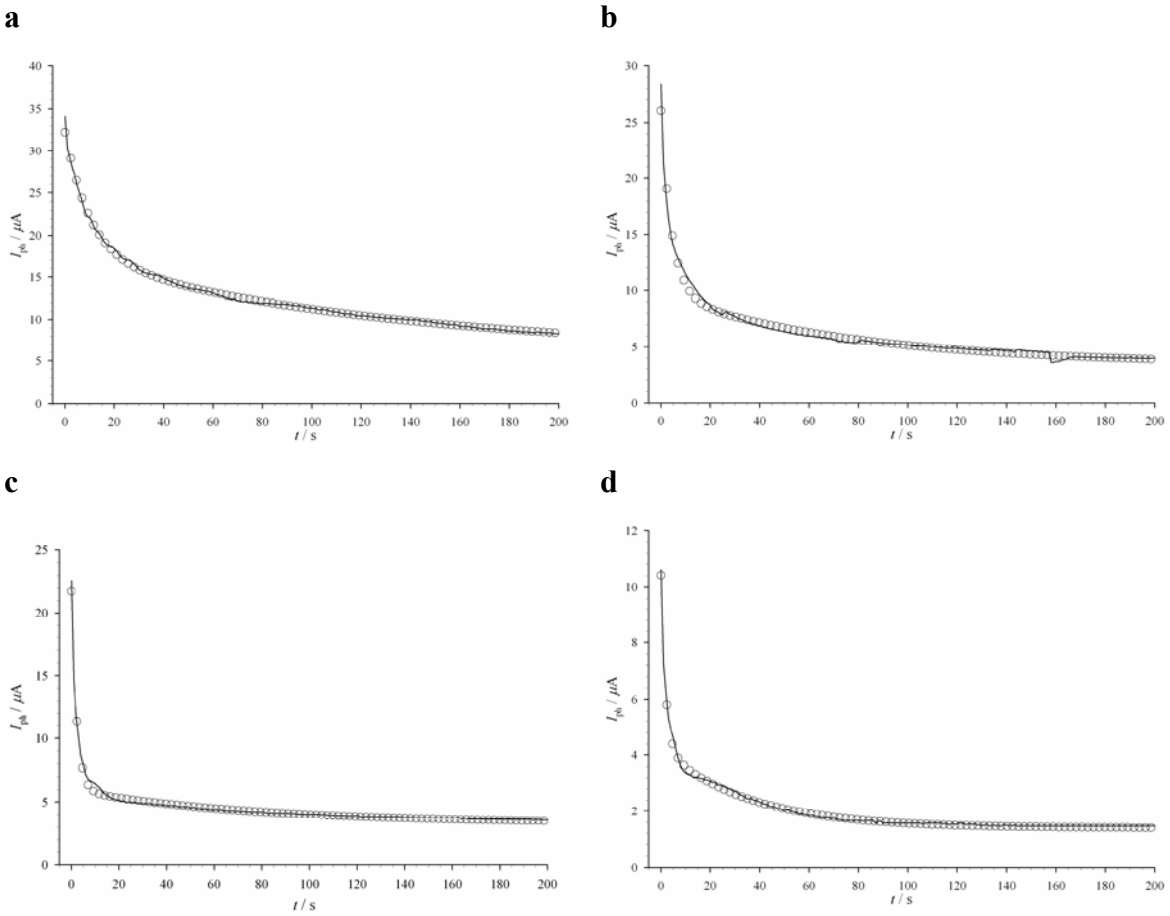

Figure 0-4 – The photocurrent-time decay profile for the oxidation of organic compounds by the DS-PCC assembly; solution concentrations are as indicated with experimental data (——) and the curve fitting data (O) a) EDTA, 156 μM pH 4.5 b) Glu, 625 μM pH 5.5 c) MeOH, 3% v/v, pH 5.8 d) MV, 2500 μM.

In attempting to fit the decay profiles, both single and multiple exponential expressions were trialled unsuccessfully. To obtain a tight convergence on the experimental data and a good fit ($R^2 > 0.95$) only a five parameter double exponential curve was satisfactory. This is consistent with the findings of Jiang *et al*. They identified two distinct kinetic decay processes, a fast (denoted *f*) and a slow process (denoted *s*), which are related to the decay profile by Equations (0-8) and (0-9):

$$I_{ph} = I^0_{ph_f} \exp\left(-k_f t\right) + I^0_{ph_s} \exp\left(-k_s t\right) + k_w \tag{0-8}$$

$$I_{ph} = k_f Q^0_f \exp\left(-k_f t\right) + k_s Q^0_s \exp\left(-k_s t\right) + k_w \tag{0-9}$$

The two distinct kinetic processes have different half-lives and can be represented by the k_f and k_s rate constants for the fast and slow process respectively. As stated by Jiang *et al*. these kinetic process are independent of the amount adsorbed; hence are equally attributable to the non-exhaustive model. The fifth parameter, k_w, has previously been described as independent of the chemical nature and surface coverage; Jiang *et al*. attributed this to the steady-state oxidation of H_2O.[154] In our study, the data demonstrates that this conclusion is not supported by dye-sensitised photooxidation. The extensive data from the curve fitting of the decay profiles are tabulated in Table 0-1 – Table 0-3.

Table 0-1 – Kinetic parameters obtained from fitting of experimental photocatalytic decay profiles with a double exponential expression for the amine structures. For the series of concentrations, $\bar{x}$ is the mean and σ is the standard deviation; definitions of kinetic constants are described in the text.

Compound	Constant	Concentration										$\bar{x}$	σ
		H_2O	39 μM	78 μM	156 μM	312 μM	625 μM	1250 μM	2500 μM	5000 μM	10000 μM		
EDTA	k_w	2.78	2.53	3.01	5.97	10.1	13.4	21.1	16.2	23.2	21.6	13.0	8.07
	$I_{ph\,f}$	14.5	11.4	9.52	14.8	19.4	18.9	11.6	56.9	70.7	73.3	31.8	26.9
	k_f	0.264	0.335	0.0569	0.0956	0.0556	0.0298	0.0390	0.0509	0.0817	0.0841	0.0920	0.0936
	$I_{ph\,s}$	3.66	3.71	4.78	11.4	14.8	17.2	30.8	55.3	55.4	69.3	29.2	24.7
	k_s	0.00880	0.0102	0.00550	0.00780	0.00660	0.00450	0.00560	0.00330	0.00410	0.00460	0.00580	0.00213
TEOA	k_w	1.46	3.18	3.11	3.07	3.56	*a*	17.4	15.7	29.7	41.0	13.1	14.2
	$I_{ph\,f}$	4.82	10.4	8.46	5.96	3.82	*a*	7.89	24.8	45.5	81.7	21.5	26.3
	k_f	0.331	0.339	0.265	0.443	0.0278	*a*	0.00460	0.0183	0.0212	0.0455	0.166	0.175
	$I_{ph\,s}$	0.56	3.90	3.96	3.87	4.58	*a*	6.97	59.1	61.2	66.8	23.4	29.3
	k_s	0.00820	0.00880	0.00510	0.00460	0.00210	*a*	0.00460	0.00340	0.00360	0.00510	0.00506	0.00218
dpy	k_w	0.897	0.579	0.769	0.778	0.985	0.961	0.909	0.950	0.765	0.887	0.848	0.125
	$I_{ph\,f}$	12.3	8.79	11.0	11.2	11.6	12.5	8.01	8.81	6.98	6.49	9.77	2.22
	k_f	0.578	0.455	0.491	0.542	0.463	0.568	0.351	0.357	0.341	0.307	0.445	0.101
	$I_{ph\,s}$	2.32	1.18	1.20	1.38	1.37	1.55	0.986	1.89	0.979	0.796	1.37	0.459
	k_s	0.0213	0.0161	0.0136	0.0170	0.0144	0.0199	0.00990	0.0161	0.00960	0.00820	0.0146	0.00438
MV	k_w	1.40	1.12	1.56	1.52	1.50	1.46	1.40	1.39	1.39	1.33	1.41	0.12
	$I_{ph\,f}$	7.90	10.4	10.3	10.1	8.59	9.27	6.79	6.14	6.03	7.29	8.29	1.70
	k_f	0.598	0.599	0.335	0.434	0.436	0.556	0.351	0.546	0.555	0.448	0.486	0.098
	$I_{ph\,s}$	2.87	4.32	3.59	3.43	3.31	3.12	3.04	2.89	2.78	3.96	3.33	0.51
	k_s	0.0256	0.0339	0.0140	0.0172	0.0156	0.0209	0.0218	0.0287	0.0291	0.0232	0.0230	0.00642

[a] Function did not converge on experimental data

Table 0-2 – Kinetic parameters obtained from fitting of experimental photocatalytic decay profiles with a double exponential expression for the urea and thiol containing structures. For the series of concentrations, $\bar{x}$ is the mean and σ is the standard deviation; definitions of kinetic constants are described in the text.

Compound	Constant	Concentration										$\bar{x}$	σ
		H_2O	39 μM	78 μM	156 μM	312 μM	625 μM	1250 μM	2500 μM	5000 μM	10000 μM		
NHCO	k_w	0.648	*b*	0.616	0.708	0.637	1.76	*b*	*b*	*b*	*b*	0.929	0.552
	$I_{ph\,f}$	6.25	*b*	6.64	6.39	4.65	4.14	*b*	*b*	*b*	*b*	5.46	1.24
	k_f	0.333	*b*	0.300	0.265	0.255	0.396	*b*	*b*	*b*	*b*	0.304	0.0643
	$I_{ph\,s}$	0.879	*b*	0.870	0.820	0.842	2.45	*b*	*b*	*b*	*b*	1.25	0.806
	k_s	0.0115	*b*	0.0083	0.00660	0.00740	0.0181	*b*	*b*	*b*	*b*	0.0101	0.00538
DMF	k_w	1.09	1.37	*b*	*b*	*b*	*b*	3.09	1.33	1.28	*b*	1.77	0.882
	$I_{ph\,f}$	7.68	9.55	*b*	*b*	*b*	*b*	9.53	9.25	5.91	*b*	8.56	1.77
	k_f	0.626	0.622	*b*	*b*	*b*	*b*	0.374	0.760	0.941	*b*	0.675	0.239
	$I_{ph\,s}$	0.991	3.27	*b*	*b*	*b*	*b*	2.71	3.45	3.51	*b*	3.23	0.366
	k_s	0.0371	0.0163	*b*	*b*	*b*	*b*	0.00700	0.0483	0.103	*b*	0.0437	0.0434
NHCS	k_w	1.87	*b*	3.90	4.73	5.65	7.56	7.75	9.19	11.1	13.5	7.92	3.25
	$I_{ph\,f}$	10.1	*b*	19.3	11.5	25.8	23.2	25.4	23.7	26.8	27.0	22.8	5.22
	k_f	0.352	*b*	0.402	0.279	0.468	0.324	0.476	0.452	0.172	0.152	0.341	0.130
	$I_{ph\,s}$	2.35	*b*	3.18	3.07	4.69	7.13	8.14	8.08	11.4	10.7	7.05	3.19
	k_s	0.0185	*b*	0.00900	0.00680	0.00880	0.00490	0.00630	0.00560	0.00780	0.00690	0.00701	0.00145
NCS	k_w	0.788	1.57	1.55	1.91	2.39	2.93	3.03	3.43	3.64	3.67	2.68	0.856
	$I_{ph\,f}$	13.5	14.0	14.3	14.4	15.1	10.6	12.3	18.1	17.7	14.4	14.5	2.33
	k_f	0.510	0.461	0.367	0.350	0.368	0.339	0.450	0.513	0.367	0.262	0.386	0.0754
	$I_{ph\,s}$	1.52	2.49	2.77	2.54	2.64	3.66	3.75	6.18	7.14	6.09	4.14	1.83
	k_s	0.0147	0.00980	0.00510	0.00550	0.00760	0.0117	0.0133	0.0123	0.0116	0.0108	0.00974	0.00299

[b] Experimental data not obtained

Table 0-3 – Kinetic parameters obtained from fitting of experimental photocatalytic decay profiles with a double exponential expression for the alcohol containing structures. For the series of concentrations, $\bar{x}$ is the mean and σ is the standard deviation; definitions of kinetic constants are described in the text.

Compound	Constant	Concentration											$\bar{x}$	σ
		H_2O	1%	2%	3%	4%	5%	6%	7%	8%	9%	10%		
MeOH	k_w	1.41	2.93	3.27	3.34	3.86	3.88	3.30	3.30	3.44	4.09	3.17	3.46	0.367
	$I_{ph\,f}$	11.0	14.0	14.7	15.8	19.7	16.2	14.0	14.0	12.8	14.0	11.1	14.6	2.29
	k_f	0.560	0.516	0.515	0.457	0.383	0.341	0.361	0.361	0.344	0.327	0.288	0.389	0.0794
	$I_{ph\,s}$	2.96	3.56	2.55	2.63	2.26	2.19	2.41	2.41	2.13	2.09	2.41	2.46	0.424
	k_s	0.0278	0.0297	0.0189	0.0137	0.00490	0.00420	0.00290	0.00290	0.00420	0.00510	0.00310	0.00896	0.00904
EtGly	k_w	0.499	1.18	1.30	1.45	1.51	1.48	1.50	1.58	1.49	1.55	1.58	1.46	0.128
	$I_{ph\,f}$	12.6	8.42	12.3	10.9	12.6	7.53	10.8	11.0	9.37	7.42	8.10	9.84	1.92
	k_f	0.615	0.563	0.760	0.676	0.690	0.611	0.647	0.523	0.563	0.541	0.409	0.598	0.100
	$I_{ph\,s}$	1.59	1.95	3.49	2.27	2.29	2.72	2.40	2.03	2.22	1.95	2.01	2.33	0.472
	k_s	0.0155	0.0397	0.0598	0.0212	0.0204	0.0555	0.0258	0.0254	0.0129	0.0168	0.00620	0.0284	0.0178
Gly	k_w	1.06	1.04	1.39	1.49	1.55	1.59	1.54	1.47	1.62	1.70	1.87	1.53	0.214
	$I_{ph\,f}$	8.45	8.55	12.5	10.6	9.81	8.82	10.1	9.74	9.58	9.26	10.7	9.98	1.13
	k_f	0.393	0.432	0.965	0.701	0.573	0.562	0.685	0.548	0.518	0.435	0.426	0.585	0.165
	$I_{ph\,s}$	0.953	0.861	3.44	2.43	2.18	2.03	2.19	1.99	1.89	1.93	1.96	2.09	0.630
	k_s	0.0117	0.0148	0.0693	0.0280	0.0172	0.0153	0.0218	0.0100	0.0145	0.00640	0.00540	0.0203	0.0185
		H_2O				**625 μM**	**1250 μM**	**2500 μM**	**5000 μM**	**10000 μM**	**100000 μM**	**200000 μM**		
Glu	k_w	3.25	–	–	–	3.38	3.52	4.42	4.02	4.48	3.81	4.49	4.02	0.465
	$I_{ph\,f}$	15.6	–	–	–	16.4	16.1	20.8	14.9	26.2	13.2	18.1	18.0	4.37
	k_f	0.246	–	–	–	0.231	0.189	0.295	0.323	0.287	0.246	0.349	0.274	0.0555
	$I_{ph\,s}$	5.91	–	–	–	6.32	5.33	7.47	4.36	7.97	4.41	5.72	5.94	1.41
	k_s	0.0132	–	–	–	0.0128	0.0106	0.0100	0.0137	0.0128	0.0108	0.0140	0.0121	0.00161

For non-exhaustive photooxidation the kinetic model appears to fit well, with the parameters obtained showing distinct trends both in chemical nature of organic compound under photooxidation and the initial solution concentration. It is at this point that the interpretation of the non-exhaustive model deviates from that of the exhaustive model.

The decay profiling allows the direct determination of five kinetic parameters; namely, $I_{ph\,f}$, $I_{ph\,s}$, k_f, k_s, and k_w. Figure 0-5 shows the deconvoluted kinetic processes as determined from the theoretical curve fits. Note should be taken that the photooxidation of the supporting electrolyte, 0.1M Na_2SO_4, constitutes the oxidation of H_2O. These data also could be fitted only by a double exponential decay, hence is not a simple first-order oxidation. This suggests that each of the five kinetic parameters is affected by the photooxidation of H_2O and no *single* parameter is independent. Due to the non-exhaustive model of photooxidation investigated here, k_w is inherently dependant on the chemical nature of the solute and can be related to the bulk solution concentration (see Section 0).

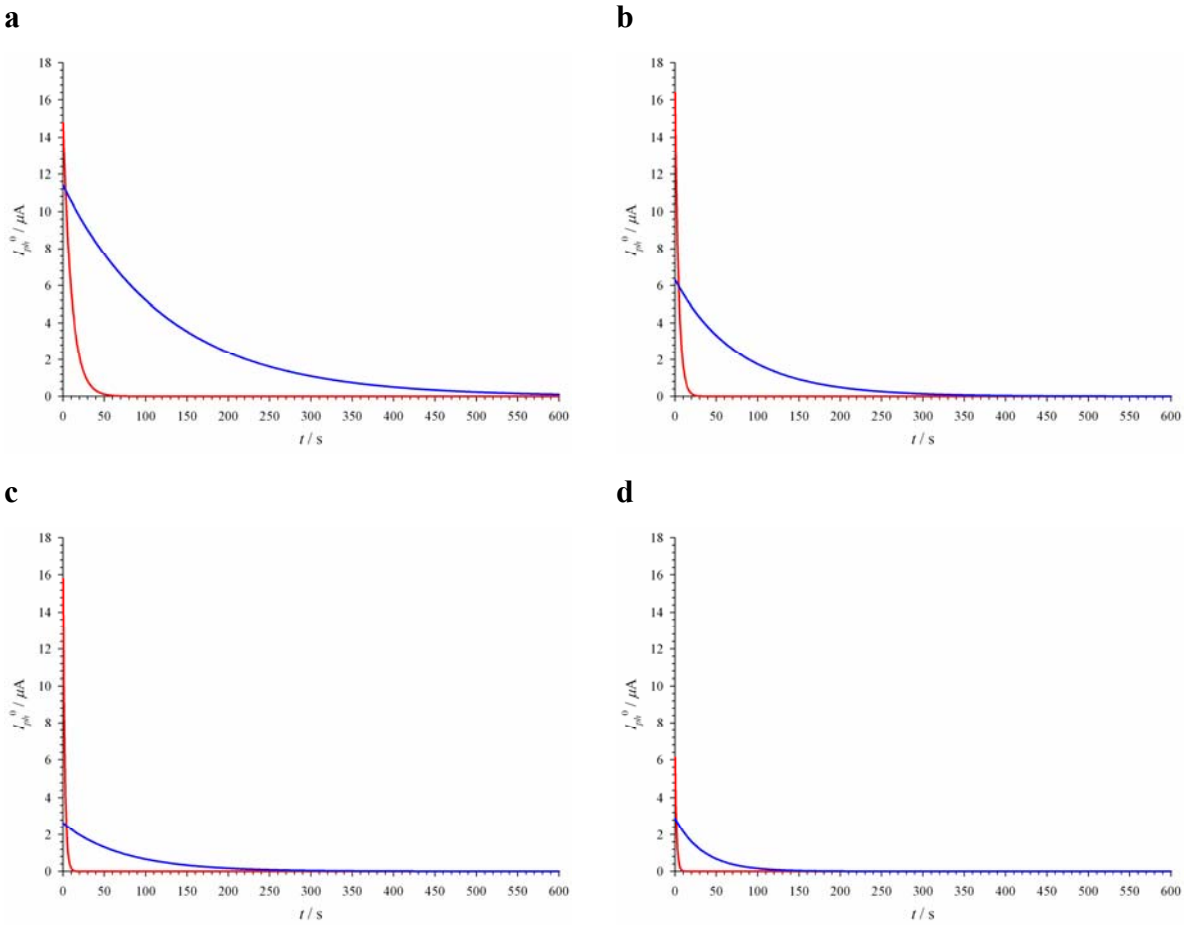

Figure 0-5 – Plot of the fast (——) and slow (——) current parameters from the fitted data in Figure 0-4. a) EDTA, 156 μM pH 4.5 b) Glu, 625 μM pH 5.5 c) MeOH, 3% v/v, pH 5.8 d) MV, 2500 μM. Solution concentrations are as previously indicated, with the vertical scale normalised between panels.

The deconvoluted profiles indeed depict two kinetically distinct interfacial processes. The fast process occurs over a very short period of time and is responsible for the large photocurrent upon initial irradiation. Due to the 200 second period of darkness prior to cell illumination, this interfacial process can be attributed to the rapid oxidation of solute species in close proximity to the PS; either adsorbed on the PS or near the surface. The time domain for the slow process is almost ten fold longer and can be attributed to a diffusion controlled process from the bulk of the solution prior to oxidation at the surface. As indicated by the deconvoluted data in Figure 0-5, the two processes behave in a similar manner for all chemical species yet differ as a function of concentration and species. As presented, with only the fast and slow processes plotted, these interfacial currents are observed to relax over time to zero i.e. they are not responsible for the entire photocurrent profile. A significant proportion of the experimental data indicates that the interfacial processes occur at a steady-state.

The fifth parameter, k_w, can be related to a steady-state oxidation however is not solely due to the oxidation of H_2O. This is supported by the magnitude of the photocurrents obtained for 0.1M Na_2SO_4 and of the values of k_w as obtained for the solutions of organic species, especially at higher solution concentrations. The value of k_w obtained for the photooxidation of organic solutions constitutes an aggregate of *more than one* steady-state process. The first of these processes is the steady-state oxidation of H_2O as described by Jiang *et al*. However, for non-exhaustive oxidation, the second steady-state oxidation is of the bulk solution hence is related to the limiting current, I_l. Thus, the aggregate parameter k_w should be redefined as, $k_w = I_{ss\ water} + I_{l\ O}$, where $I_{ss\ water}$ is the photocurrent for the steady state oxidation of H_2O and $I_{l\ O}$ is the limiting photocurrent for oxidisable species occurring at a steady state.

The kinetic model of (0-8) predicts that, according to (0-9), the instantaneous photocurrent should be directly proportional to the amount of charge (Q) generated from the oxidation. The ratio of I_{ph}/k expresses the charge generated from oxidation and the data in Table 0-1 – Table 0-3 show a strong relationship for both the fast and slow processes with respect to chemical structure and concentration.

At increased concentrations (and hence Q) there is significant variance in the data and as such these values do not give a true indication of oxidation kinetics. The variance in data with respect to individual compounds and concentrations can be attributed to their specific effect on the 'sense' electrode in the cell, the photoanode. As observed in the EDTA photooxidation study in the preceding Chapter some compounds have an adverse effect on the photoanode under illumination. The effect observed in the previous Chapter, that of a secondary film passivation of the surface was not observed in this investigation due to the decreased solution concentration. However dye desorption was observed for compounds at increased solution pH i.e. TEOA and NHCO. This was determined by optical spectroscopy and due to this factor, the photocurrents were unsatisfactory for analysis (hence the absence of experimental data for these compounds).

The initial photocurrent or rate of oxidation for the fast process follows a proportional relationship to the net charge generated within experimental variance. This is consistent with rapid oxidation of species in close proximity to the photooxidation centre. Yet only a limited quantity of species can be chemically adsorbed to the surface, thus the species must still undergo some form of migration to the Ru(III) metal centre prior to oxidation; hence individual mass transfer properties for the compounds and concentrations contribute to the experimental variance.

Equally for the slow interfacial process a proportional relationship between I_{ph} and Q exists; however, in comparison to the fast interfacial process the agreement of I_{ph} to Q is more consistent. This suggests that the process is a much more controlled

oxidation, which can be associated with the description of this kinetic process as the transfer of oxidisable species from the bulk to the surface.

Examination of kinetic rate constants, despite experimental variance in the data, shows two distinct kinetic processes. For example, the oxidation of Urea (**NHCO**) over the concentration range of 39–10000μM gave two distinct rate constants; 0.30±0.07 s^{-1} for the fast process and 0.010±0.006 s^{-1} for the slow process. The rates of oxidation are shown to vary between compounds with the oxidation of methyl viologen (**MV**) over the same concentration range giving a rate constant of 0.49±0.1 s^{-1} for the fast process and 0.023±0.007 s^{-1} for the slow process.

Comparison of the two kinetic rate constants shows there are on average ~40 fold difference between the interfacial processes for a given species. The fast interfacial process has a first-order rate constant in the order of 0.4 s^{-1} which is comparable to that identified by Jiang *et al*. (0.61 s^{-1}) for the oxidation of a surface complex.[154] The decreased rate of photooxidation supports migration of the species from the bulk to adsorbed dye; a kinetically slower process to photooxidation of species at the electrode surface. The slow process with a first-order rate constant in the order of 0.01 s^{-1} is an order of magnitude slower than the analogous oxidation identified by Jiang *et al*. (0.10 s^{-1}).[154] Jiang *et al*. describe both the fast and slow processes as oxidation of two types of surface adsorbed species with only a 6 fold difference in oxidation rate. For the slow process identified in this study, the oxidation rate is consistent with transfer from the solution bulk prior to photooxidation.

It should be noted that there is a large degree of variance for the rate constants as presented. Due to the kinetic rates of each chemical species, there is indication from the mean and standard deviation of rate constants in Table 0-1 – Table 0-3 that these parameters can be used to discriminate between chemical structure and/or concentration.

Close inspection of the kinetic parameters for individual species and concentrations indicates there are several calculated values that have a much higher variance for k_f; specifically for the increased concentrations of EDTA and TEOA. These solutions

gave the largest I_{ph} response however the oxidation rate for the fast process was an order of magnitude smaller than any of the other species or solutions. The value of k_f for these solutions approached that of k_s. In relation to the studies in Chapter 7 this may indicate that the DS-PCC experiences a saturation effect due to the ability of EDTA and TEOA to be readily oxidised. Both these compounds are chemically similar (saturated tertiary amines) and are known as strong electron donors.[7,25,145,334] Despite this there is clear indication of two distinct interfacial electron processes that are kinetically discernable from one another.

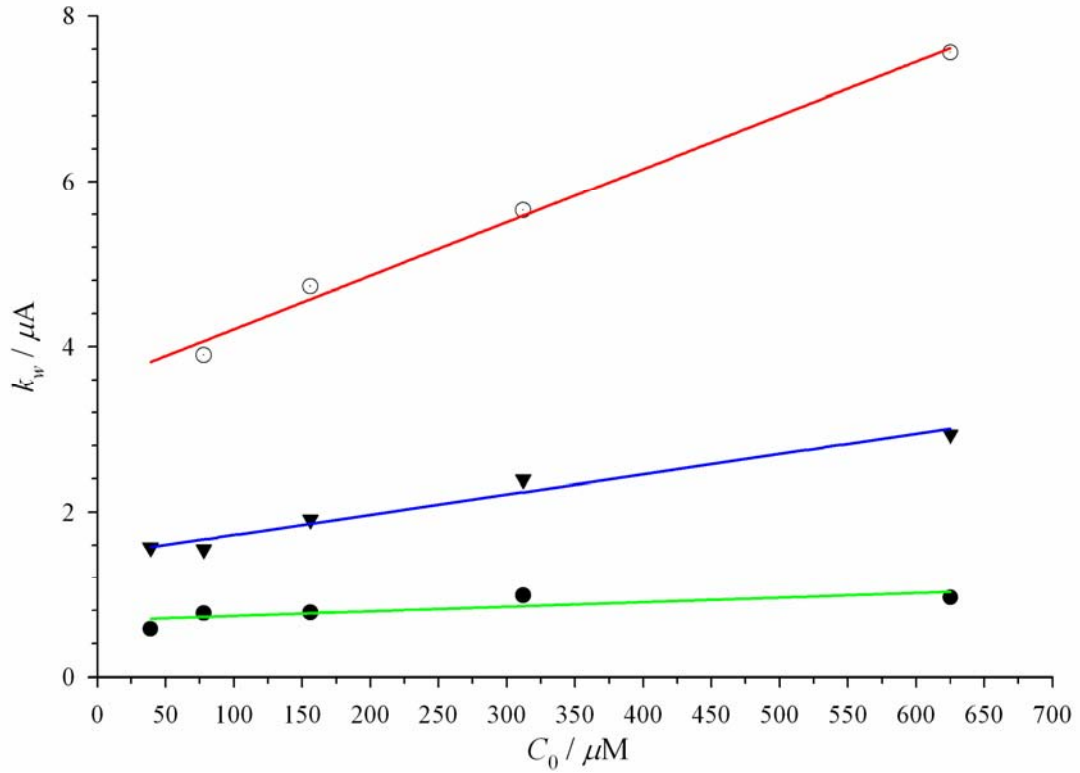

Figure 0-6 – Concentration dependence of k_w for 39–625 μM solutions: dpy (●); NHCS (⊙); NCS (▼). The linear relationship of concentration to k_w is illustrated by the fitting of a linear function: dpy (—); NHCS (—); NCS (—).

Quantitative Relationship of Photocurrent Measurements

From cursory inspection of the tabulated data the two rate constants do not differ significantly between species and/or concentration, however the deconvoluted photocurrent parameters show some correlation, in particular k_w. The aggregate steady-state oxidation parameter, k_w, incorporates $I_{l\,O}$ which is related to the initial bulk solution concentration at $t = 0$, C_0, according to Equation (0-3):[370]

$$I_{l\,O} = nFAm_O C_0$$

Where, n is the number of moles of electrons transferred in the oxidation, F is Faraday's constant, A is the electrode surface area and m_O is the mass transfer coefficient.

As can be seen in Figure 0-6 it is this relationship that may allow the discrimination of chemical compounds however the chemical nature of the oxidisable species affects the proportion of k_w responsible for H_2O oxidation. The data are uncorrected for the H_2O photooxidation component and attempts to perform this correction (by subtraction of I_{ph} for H_2O) did not give the same linear relationship as depicted. Thus there may be a solvation effect as the more hydrophilic compounds would be hydrated to a greater extent than the hydrophobic compounds. The implication of this is a linear relationship with change in concentration yet a non zero intercept that deviates from Equation (0-3).

Although mass transfer coefficients cannot be derived directly from the data of Figure 0-6 the presented linear relationship and unique gradient for each compound are encouraging for speciation and identification. In combination with the identified kinetic parameters this may provide a means by which to discriminate organic compounds and solution concentrations.

a

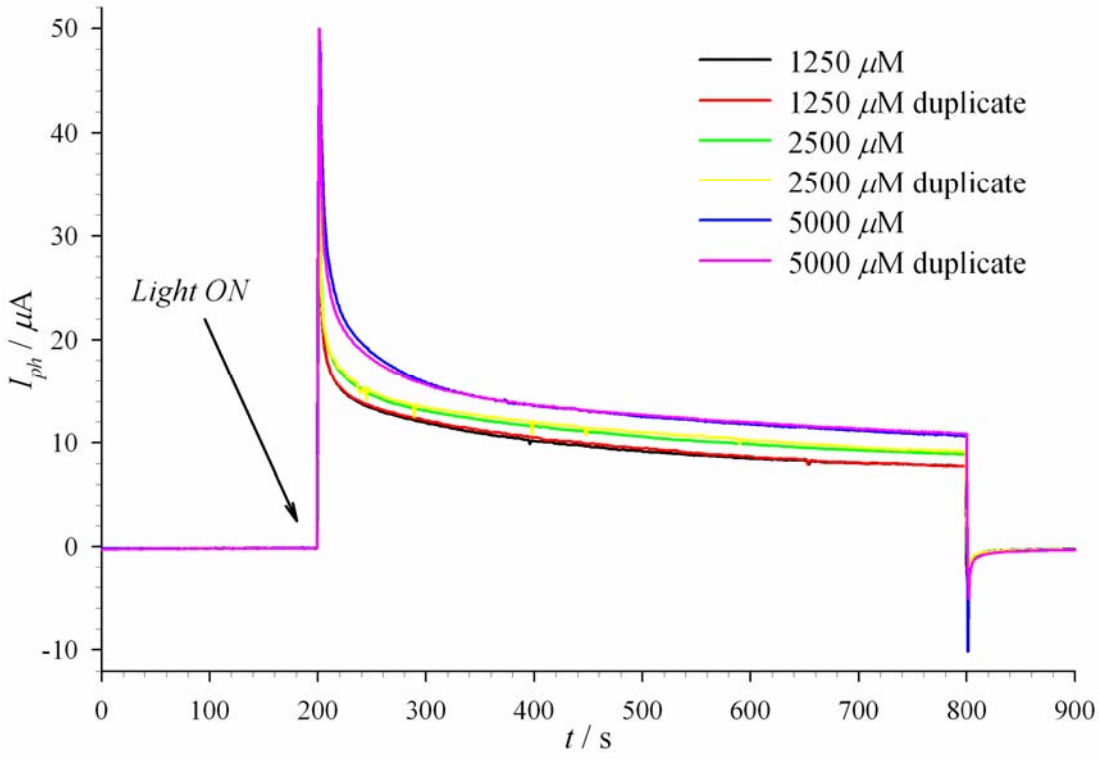

b

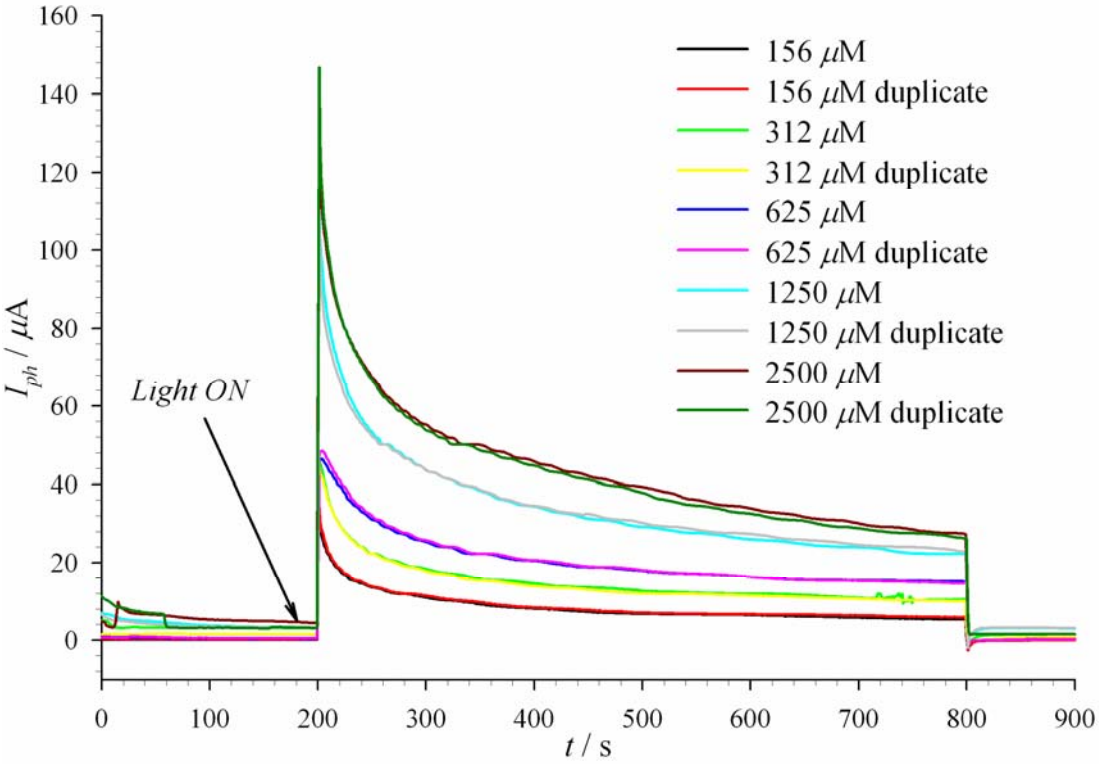

Figure 0-7 – Transient photocurrent-time profiles depicting the reproducibility of measurements in the DS-PCC a) NHCS b) EDTA.

Reproducibility of the Process

Depicted in Figure 0-7a are the raw transient photocurrent data for NHCS at three concentrations overlaid with replicate measurements of these solutions. In the kinetic discussion of Section 0 dispersion in the kinetic rates determined may imply that the measurements suffer from consistency and that the observed kinetic phenomena are an artefact of irreproducibility. For the representative transient profiles depicted the data are contrary to this speculation and assert that experimental measurements can be duplicated. Photooxidation of NHCS gave an I_{ph} profile that exhibited distinction from other compounds at each of these concentrations. The fast oxidation component for NHCS was rapid and constituted an above average k_f for the concentration range as well as a large value for $I_{ph\ f}$ (Table 0-2). Conversely, the slow component displayed below average k_s and a fast relaxation of $I_{ph\ s}$ into k_w. This indicates that steady state oxidation is characteristic of sulphur affecting electron donation as it is a poor oxidation candidate. This is supported by the negative current observed when illumination of the cell is ceased, indicative of dissipation of charge.

Figure 0-7b are the observed photocurrent transients for the photooxidation of EDTA over a much wider concentration range. In a like manner to NHCS, the data indicate reproducibility of observations by duplicate measurements. Contrasting to NHCS, the I_{ph} profile is distinct for this compound. The fast component has a below average k_f which is an order of magnitude lower for some concentrations and a much larger $I_{ph\ f}$ in comparison to NHCS (Table 0-1). Relaxation of the slow component to steady-state oxidation is consistent throughout the concentration range maintaining an almost average k_s however the magnitude of $I_{ph\ s}$ and indeed k_w are much larger in comparison to other compounds. The trend in these parameters is shared by the chemically similar TEOA as both are readily oxidised,[7,25,145,334] and is supported by the reduced negative transient indicative of decreased surface charging.

These compounds illustrate the reproducibility of experimental observations (±4% of the measured Coulomb charge) and propose that the kinetic parameters $I_{ph\ f}$, k_f, $I_{ph\ s}$, k_s, k_w, constitute a transient photocurrent 'signature' that allows for qualitative discrimination of compounds photooxidised in the DS-PCC.

Conclusions

For a range of chemically dissimilar organic compounds and solution concentrations, two distinct interfacial processes have been identified that occur during photooxidation within the DS-PCC.

Deconvolution of transient photocurrents observed for the oxidation process by the mathematical fit of a five-parameter double exponential decay function produced evidence of numerous interfacial processes. Consistent with a kinetic model for photooxidation in titania PEC cells, the analysis revealed a biphasic kinetic relationship for photooxidation in the analogous DS-PCC. Rapid oxidation of species in close proximity to the photooxidation centre, the oxidised Ru(II) dye, was proposed as the kinetically fast interfacial process with a first-order rate constant of the order 0.4 s^{-1}. The much slower interfacial process (by a factor of ~30) was attributed to transfer of oxidisable species from the solution bulk to the surface prior to oxidation with a first-order rate constant of the order 0.01 s^{-1}.

Theoretical profiling of the kinetic events supported the biphasic assignment of interfacial processes and indicated that non-exhaustive oxidation occurs for the solution concentrations examined. The fast event occurs over a very short period of time and is responsible for the large onset photocurrent, whilst the slow event occurs over a considerably longer time before relaxing into a steady-state oxidation of the bulk solution. The steady-state oxidation, k_w, was related to the bulk solution concentration by $k_w = I_{ss\ water} + I_{l\ O}$, which indicated that the limiting current suffered from contributions due to photooxidation of H_2O and hence prevented its easy deconvolution.

Reproducible observations supported unique photocurrent profiles for chemical species with complete kinetic parameters identified as contributing to a transient photocurrent ‘signature’. This allows qualitative discrimination of organic compounds and concentrations when all kinetic parameters are considered.

CHAPTER 9

Conclusions and Future Work

Conclusions

The scope of this thesis was to investigate novel methods of photocatalysis capable of performing water remediation through the degradation of organic species in solution.

Heterosupramolecular assembly was identified as a unique approach to photocatalysis as the covalent interaction of a molecular species with an inorganic surface provides an intimate linkage for transfer of electrochemical charge and functions as a means of electron-hole segregation. Charge separation over a large molecular distance can limit recombination and allows the electron and hole to perform discrete functions.

The synthesis of condensed phase and molecular components was performed.

Highly crystalline colloidal TiO_2 dispersions were prepared by a novel microwave hydrothermal process. Irradiation of colloidal dispersions in a microwave hydrothermal vessel over extended periods of time had significant effects on the material's surface and structural properties. The new material's properties were characterised by isothermal gas sorption, XRD, TEM, SEM, SANS and confirmed by the complementary techniques of ED and Raman spectroscopy. The titania had a bimodal phase composition and experienced a remarkably small crystallite growth rate; for a treatment time of 5–360 minutes the primary crystallite size increased only marginally from 6.0–7.2 nm. Interestingly the 180 min microwave treated sample had the highest internal and external surface area with SA_{BET} = 226.0 m^2/g, a pore volume PV_{SP} = 0.203 cm^2/g, and an average pore diameter D_{avg} = 3.59 nm. It was proposed that the mechanism of crystallite growth, Ostwald ripening, was limited by microwave irradiation and hence the sols experienced a limiting growth rate. The investigation demonstrated good correlation amongst the techniques employed for characterisation. The effect of microwave over that of convection hydrothermal treatment was insufficient to justify its use in preparation of thin film assemblies; in addition the pore size would prevent sufficient dye penetration and loading. Thus during the remainder of the studies, convection hydrothermal titania was employed as the condensed phase substrate for electrochemical assemblies.

For the subsequent electrochemical applications, synthesis of specific molecular components was required. A bidentate ligand incorporating an acidic functional group, specifically 4,4'-bis-phosphonate(methyl)-2,2'-bipyridine (**dmpbpy**), was obtained in six steps in a yield of 48%. Stepwise addition of the soluble ester of **dmpbpy**, 4,4'-bis-diethylphosphonate(methyl)-2,2'-bipyridine (**dempbpy**) to Ru allowed the assembly of a series of supramolecular complexes capable of chemisorption to thin film electrodes. Difficulties in purification and identification of acidic analogues of these complexes were highlighted and reasoning was proposed for unresolvable NMR resonances due to multiple solution species. The complexes of interest for electrochemical investigations were *cis*-bis-(2,2'-bipyridine)-(4,4'-bis-phosphonato(methyl)-2,2'-bipyridine)ruthenium(II) dichloride (**[Ru(bpy)$_2$(dmpbpy)]Cl$_2$**) and *cis*-bis-(4,4'-bis-phosphonato(methyl)-2,2'-bipyridine)(2,2'-bipyridine)ruthenium(II) dichloride (**[Ru(dmpbpy)$_2$(bpy)]Cl$_2$**).

An electron relay moiety with an acidic functional group capable of chemisorption to thin film electrodes was prepared through modification of a method from the literature. The synthesis of 1-ethyl-1'-(2-phosphonoethyl)-4,4'-bipyridinium dichloride (**EVP**) was obtained in two steps and an overall yield of 35%.

For the series of molecular sensitisers synthesised, complexes of the type $[Ru(bpy)_3]^{2+}$, where **bpy** is derivatised with an acidic linker, were compared and contrasted for effects of ligand substitution on electronic properties. Theoretical TD-DFT calculations of molecular structures and singlet excitations were discussed in relation to experimental data. Salient features of the electronic spectra were reproduced well without correction for solvent/media effects. The three longest wavelength bands associated with known charge transfer phenomena were identified. The symmetry allowed visible $\tilde{\nu}_{MLCT}$ was assigned a $\pi_\psi^* \leftarrow d\pi$ transition with the intense UV $\tilde{\nu}_{LC}$ evidently of $\pi_\psi^* \leftarrow \pi$ origin. The ambiguous shoulder on the blue side of $\tilde{\nu}_{MLCT}$ showed $d\sigma \leftarrow d\pi$ and $\pi^* \leftarrow d\pi$ transition character and was described as a $\tilde{\nu}_{MC/MLCT}$ band.

It was recognised that the lowest lying LUMO states were consistently localised on 2,2'-bipyridine (**bpy**) and this was speculated to be a factor identified in the literature affecting quantum injection yields of these sensitisers.

Utilising the molecular sensitisers, **[Ru(bpy)$_2$(dmpbpy)]$^{2+}$** and **EVP**, as well as thin film electrode assemblies incorporating RuO_2 and Pt as co-catalysts on the corresponding electrodes, a multi-component photochemical system was prepared. It was demonstrated, through interpretation of photoelectrochemical measurements, that the heterosupramolecular assembly was capable of inducing a photochemical reaction in H_2O under visible irradiation in the absence of an organic electron donor. The optimised electrode assembly was identified as:

[Ru(bpy)$_2$(dmpbpy)]$^{2+}$/RuO_2:TiO_2/F:SnO_2|(0.5M Li_2SO_4)|**EVP**/Pt/TiO_2/F:SnO_2

Optimised pH for the observed photochemical reaction was determined to be 5, yielding η = 0.0036% with an apparent quantum yield (AQY) = 1.6%. The dye-sensitised photoelectrocatalytic cell (DS-PCC) exhibited unique photocurrents profiles that were discussed in relation to molecular function and modulation that are afforded by heterosupramolecular assembly. The observed photochemical phenomena were rationalised by charge capacitance and electron migration reported by other researchers investigating similar molecular-solution/colloidal-dispersion systems.

The complete mineralisation of the model electron donor, ethylenediaminetetraacetic acid disodium (EDTA), was investigated by photodegradation in the DS-PCC. The cell employed in this aspect of study incorporated **[Ru(dmpbpy)$_2$(bpy)]$^{2+}$** adsorbed to a titania thin film electrode as the degradation of organic components via electron donation does not require a co-catalyst. The counter electrode was a Pt coated FTO substrate with solution of EDTA (as the disodium salt) utilised as the electrolyte for charge compensation. The exhaustive oxidation of EDTA gave a non-linear response for incremental change in concentration, however over extended periods of time quantities of gas(s) were observed to evolve from the respective electrodes. This was proposed to be a CO_2/H_2 mixture due to the complete mineralisation of EDTA and reduction of H_2O at the photoanode and cathode respectively.

An explanation of the non-Faradaic relationship was discussed in relation to experimental photocurrent transients as a superposition of multiple oxidations that occurs as EDTA degrades to smaller organic species. The resultant organic species were responsible for CO_2 formation and surface discoloration of the photoanode. A mechanism was postulated for the photocatalytic decomposition of EDTA in the DS-PCC, supported by mechanisms and experimental data of other researchers in the literature.

Photodegradation in the DS-PCC was extended over a wide range of chemically dissimilar organic compounds and solution concentrations as a representation of simulated water pollution. The photoanode electrode assembly was modified to incorporate **$[Ru(bpy)_2(dmpbpy)]^{2+}$** as the photosensitiser, with no other modification to the DS-PCC to that utilised in the complete mineralisation of EDTA. This demonstrated the range of compounds capable of photooxidation by a heterosupramolecular assembly and identified two distinct interfacial processes for dye-sensitised surfaces by mathematical treatment of photocurrent transients with a kinetic model.

A five-parameter double exponential decay function was well fit ($R^2 > 0.95$) to the experimental data which was consistent with a kinetic model for photooxidation in titania PEC cells. Photooxidation of all compounds was identified as a biphasic reaction constituting a fast and slow component. The fast interfacial process had a first order rate constant of the order 0.40 s^{-1} and was attributed to rapid oxidation of species in close proximity to the oxidised Ru(II) dye. Transfer of oxidisable species from the solution bulk to the surface prior to oxidation was proposed as the slow interfacial process with a first order rate constant of the order 0.01 s^{-1}.

Theoretical profiling supported these postulates and reproducible observations demonstrated the unique photocurrent profiles for organic compounds and concentrations. It was proposed that the identified parameters, $I_{ph\,f}$, k_f , $I_{ph\,s}$, k_s and k_w constitute a transient photocurrent 'signature' that allows qualitative discrimination of organic compounds and concentrations.

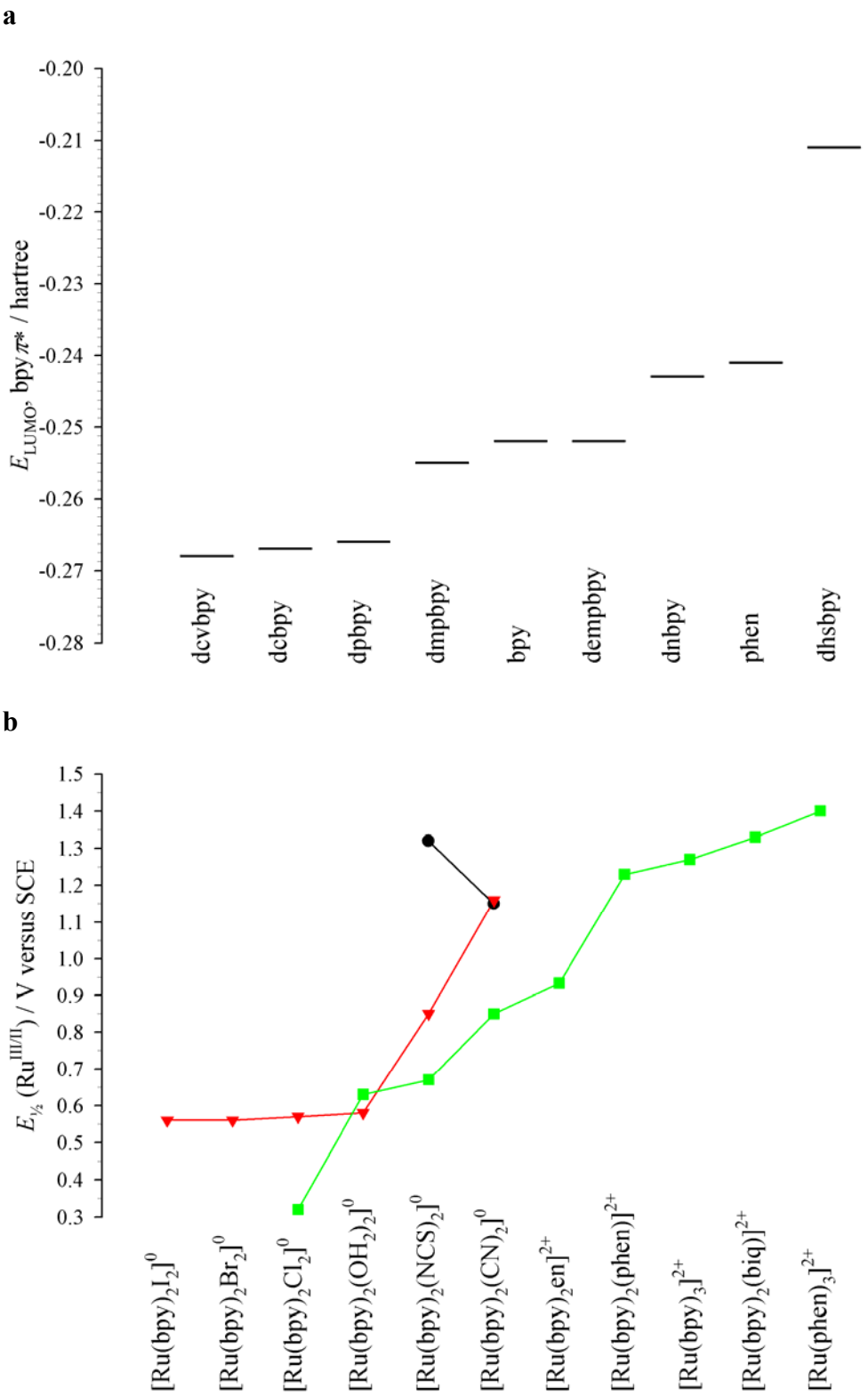

Figure 0-1 – Energy parameters affecting photochemical properties of Ru(II) complexes a) theoretical calculation of ligand LUMO energy [B3LYP/6-311G+(2*d*,*p*) model chemistry] b) experimental reduction potential for the first oxidation of the stated complexes.[54,135,223] Complexes as indicated are (–■–), carboxylate (–▼–) and phosphonate (–●–) analogues.

Future Work

Heterosupramolecular chemistry is still in early development as a research entity of its own. Yet in the past decade, since its beginnings as a niche application field, many interesting aspects have been investigated. Just like its 'older brother', supramolecular chemistry, some 40 years earlier, the formative years can be the most exciting and challenging. Thus there is much work to be accomplished and much more to be discovered.

The findings presented in this Thesis encourage further developments and research into applications of heterosupramolecular modulation and heterogeneous catalysis. Some examples are detailed below.

Surface bound formation of heterogeneous catalysts

For complexes that contain labile ligands, such as $[Ru(dmpbpy)_2Cl_2]^0$, the *ex situ* formation of a catalytic 'film' may allow the preparation of a reusable catalytic surface. By immersion of the film in a solution containing a suitable ligand, it may be possible to exchange the labile Cl^- ligands by reflux for several hours.

Many homogeneous catalytic reactions are performed with ruthenium complexes and formation of catalytic compounds on a surface with ligands capable of exchange would allow for reaction selectivity e.g. halide addition to a terminal alkene due to the hindered conformation of the bound complex (Figure 0-2). Following the catalytic reaction, the surface could be regenerated by returning to a solution of the required labile ligand for regeneration or exchange. Also by the use of electrode bound catalysts, such as Ru(II) dyes with phosphonated linkers, there is the possibility of control of an oxidation/reduction process by application of a suitable potential bias as an additional reaction driving force.

Tuneable photocatalytic surfaces

Presented in Figure 0-1 are representative coordination compounds and ligands with the calculated HOMO-LUMO energies for comparison.

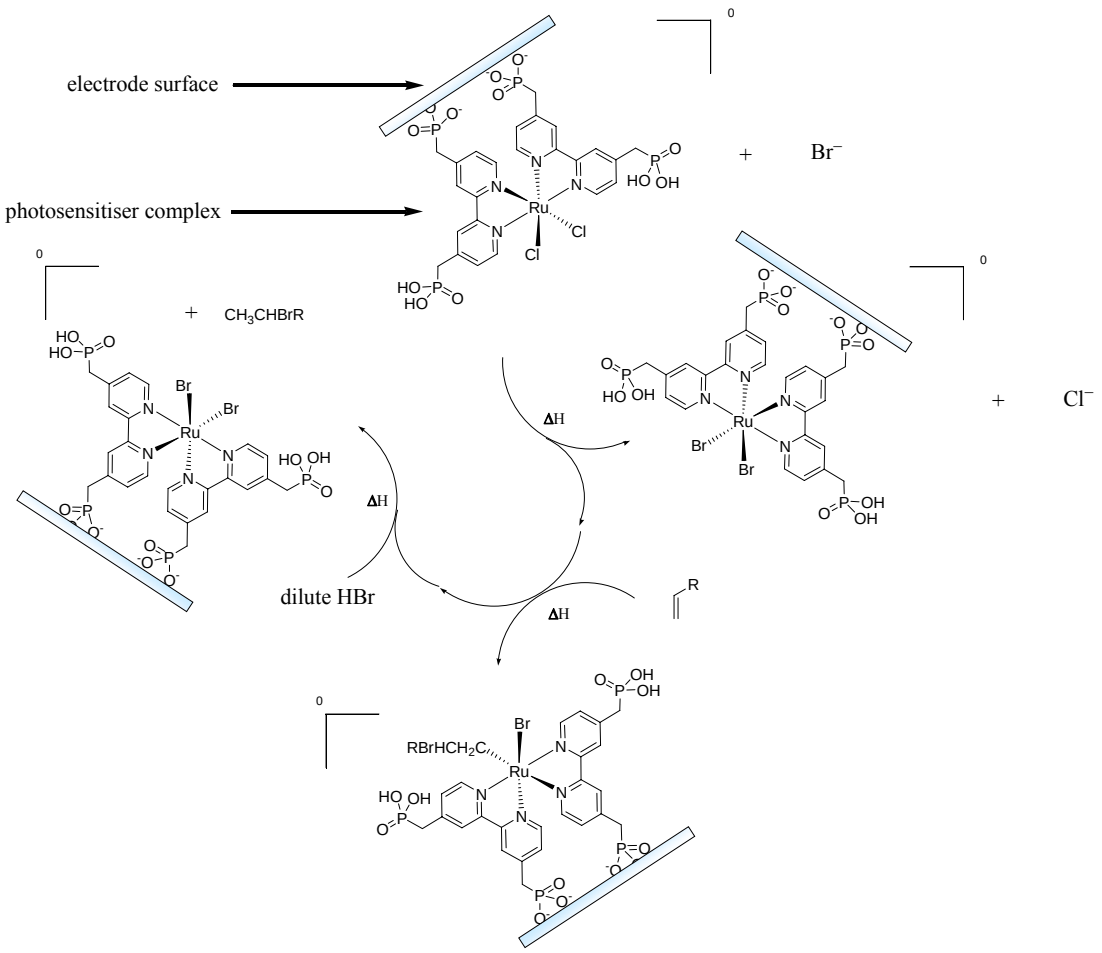

Figure 0-2 – *ex situ* formation of catalytic surface complex and mechanism for bromination of a terminal alkene.

a

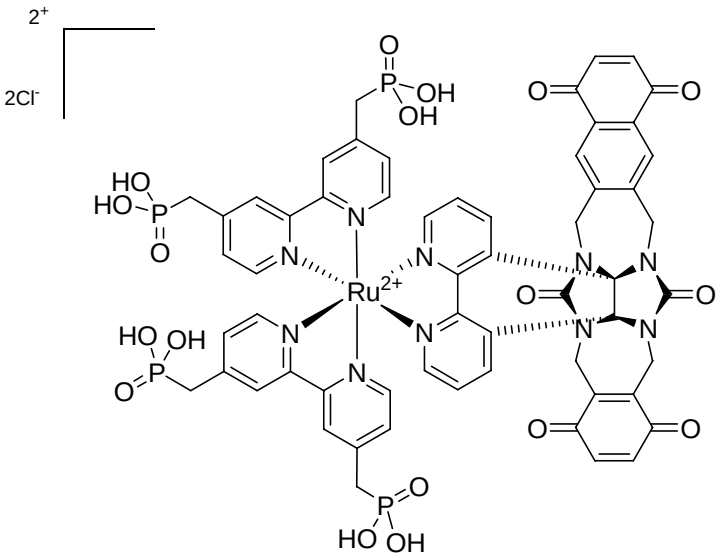

b

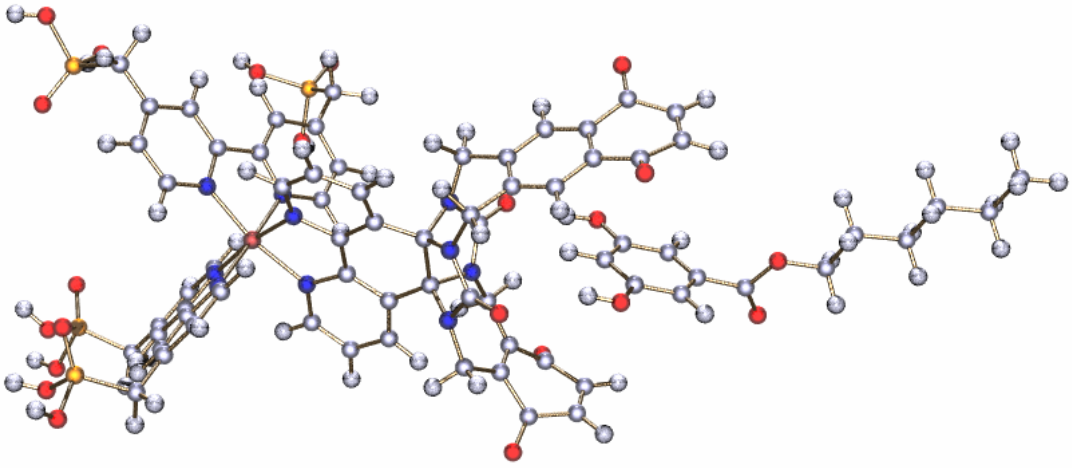

Figure 0-3 – The proposed heterosupramolecular structure of a host receptor for controlled photochemical reactions a) chemical structure of the complex b) geometric representation of the Host-Guest inclusion complex depicting 'bound' hexyl-3,5-dihydroxybenzoate as determined at a semi-empirical PM3 model chemistry.

By judicious choice of the coordination ligand, the statistical probability of the destination of an ejected electron from MLCT excitation can be estimated based on relative ligand (LUMO) energy. Coordination of ligands, in an assortment of monodentate, bidentate or polydentate forms, influences the redox potential of the metal centre. As can be seen in Figure 0-1b, there is a broad range of oxidation potentials (0.3–1.4 V) that can be obtained from the suitable choice of ligand type.

Thus, this has a 'tuning' effect on the oxidation potential for catalytic or photocatalytic applications. This would allow more specific targeting of species in solution. Another approach would be the use of the 'host-guest' model by preparing or utilising ligands with specific functionality to enable binding to target species in

solution. Depicted in Figure 0-3 is a proposed structure of a Host receptor complex as well as a pictorial representation of a Host-Guest inclusion complex as an aromatic compound (hexyl-3,5-dihydroxybenzoate) interacts with the cage structure of a glycoluril moiety. This design is reminiscent of the supramolecular 'scorpion' of Section 1.3.[132]

The potential of this type of supramolecular or heterosupramolecular assembly could see applications as a specific photocatalyst for targeting, for instance, biological contaminants such as steroidal or pharmaceutical discharges. This structure of photocatalyst could also find application in medical research as a specific binder or agonists or antagonists. Due to the inherent photophysical properties, this structure could prove a worthwhile chemotherapy agent with the ability to bind to cellular structures or perhaps DNA fragments prior to therapeutic photocatalytic treatment.[375,376]

Lastly, heterosupramolecular structures of this kind could find application as a versatile sensor as inspired by the modulation of function investigated by Will *et al*.[7,142,145,377] The structure of Figure 0-3 presents a means for selective binding of compounds to target species for identification or photocatalysis. The heterosupermolecule contains a quinone moiety in the guest 'cage'. When a substrate is bound the fluorescence might be quenched by electron transfer to the guest allowing the structure to act as a sensor. In addition, binding of a substrate could initiate electron transfer for photocatalytic degradation by the application of a suitable potential bias to prevent electron transfer to the electrode surface.[7]

The conceptual applications proposed above illustrate the flexibility of heterosupramolecular chemistry to address current research problems. The formative years still lie ahead in this discipline; the work presented in this Thesis highlights just a small part that heterosupramolecular chemistry plays in device architecture. The further application of heterosupramolecular chemistry not only in photocatalysis but also in other photo driven processes highlights the versatility of this important chemical field to on-going materials, synthetic, medicinal and environmental research.

References

(1) G. J. Wilson; G. Will, *Curr. Appl. Phys.*, 2004, **4,** 351-354.
(2) B. O'Regan; M. Grätzel, *Nature*, 1991, **353,** 737-740.
(3) G. J. Wilson; G. D. Will; R. L. Frost; S. A. Montgomery, *J. Mater. Chem.*, 2002, **12,** 1787-1791.
(4) P. Pechy; F. P. Rotzinger; M. K. Nazeeruddin; O. Kohle; S. M. Zakeeruddin; R. Humphry-Baker; M. Grätzel, *J. Chem. Soc., Chem. Comm.*, 1995**,** 65-66.
(5) A. R. Oki; R. J. Morgan, *Synthetic Comm.*, 1995, **25,** 4093-4097.
(6) S. G. Yan; J. T. Hupp, *J. Phys. Chem.*, 1996, **100,** 6867-6870.
(7) G. Will; G. Boschloo; S. N. Rao; D. Fitzmaurice, *J. Phys. Chem. B*, 1999, **103,** 8067-8079.
(8) I. Gillaizeau-Gauthier; F. Odobel; M. Alebbi; R. Argazzi; E. Costa; C. A. Bignozzi; P. Qu; G. J. Meyer, *Inorg. Chem.*, 2001, **40,** 6073-6079.
(9) R. Cinnsealach; G. Boschloo; S. Nagaraja Rao; D. Fitzmaurice, *Sol. Energy Mater. Sol. Cells*, 1999, **57,** 107-125.
(10) P. Aldhous, *Nature*, 2003, **422,** 251.
(11) Q. Schiermeier, *Nature*, 2003, **424,** 359.
(12) T. W. Bank *2004 World Bank Indicators*; International Bank for Reconstruction and Development: Washington, 2004; p 136-139.
(13) K. Sayama; K. Mukasa; R. Abe; Y. Abe; H. Arakawa, *J. Photochem. Photobiol., A*, 2002, **148,** 71-77.
(14) E. Amouyal, *Sol. Energy Mater. Sol. Cells*, 1995, **38,** 249-276.
(15) G. Sprintschnik; H. W. Sprintschnik; P. P. Kirsch; D. G. Whitten, *J. Am. Chem. Soc.*, 1976, **98,** 2337-2338.
(16) G. Sprintschnik; H. W. Sprintschnik; P. P. Kirsch; D. G. Whitten, *J. Am. Chem. Soc.*, 1977, **99,** 4947-4954.
(17) E. A. Seddon; K. R. Seddon, Topics in Inorganic and General Chemistry, Vol. 19: The Chemistry of Ruthenium. In 1984; p1240-1252.
(18) J. M. Lehn; J. P. Sauvage, *Nouv. J. Chim.*, 1977, **1,** 449-451.
(19) T. J. Meyer, *Acc. Chem. Res.*, 1989, **22,** 163-170.
(20) W. Ruttinger; G. C. Dismukes, *Chem. Rev.*, 1997, **97,** 1-24.
(21) A. J. Bard; M. A. Fox, *Acc. Chem. Res.*, 1995, **28,** 141-145.
(22) L. Hammarstrom; L. Sun; B. Akermark; S. Styring, *Spect. Acta, A: Mol. Biomol. Spect.*, 2001, **57A,** 2145-2160.
(23) W. M. Campbell; A. K. Burrell; D. L. Officer; K. W. Jolley, *Coord. Chem. Rev.*, 2004, **248,** 1363-1379.
(24) J. Moser; M. Grätzel, *J. Am. Chem. Soc.*, 1984, **106,** 6557-6564.
(25) A. Moradpour; E. Amouyal; P. Keller; H. Kagan, *Nouv. J. Chim.*, 1978, **2,** 547-549.
(26) G. R. Bamwenda; K. Sayama; H. Arakawa, *J. Photochem. Photobiol., A*, 1999, **122,** 175-183.
(27) M. Grätzel, *Prog. Photovoltaics*, 2000, **8,** 171-185.
(28) A. C. Society *SciFinder Scholar*, 2004.2; American Chemical Society: 2004.
(29) A. L. Linsebigler; G. Lu; J. T. Yates, Jr., *Chem. Rev.*, 1995, **95,** 735-758.
(30) A. Mills; R. H. Davies; D. Worsley, *Chem. Soc. Rev.*, 1993, **22,** 417-425.
(31) U. Diebold, *Surf. Sci. Rep.*, 2003, **48,** 53-229.
(32) D. Beydoun; R. Amal; G. Low; S. Mcevoy, *J. Nanopart. Res.*, 1999, **1,** 439-458.

(33) A. Hagfeldt; M. Grätzel, *Chem. Rev.*, 1995, **95,** 49-68.
(34) A. Yamamoto; H. Imai, *J. Catal.*, 2004, **226,** 462-465.
(35) K. Nagaveni; M. S. Hegde; N. Ravishankar; G. N. Subbanna; G. Madras, *Langmuir*, 2004, **20,** 2900-2907.
(36) M. Niederberger; G. Garnweitner; F. Krumeich; R. Nesper; H. Colfen; M. Antonietti, *Chem. Mater.*, 2004, **16,** 1202-1208.
(37) H. Cheng; J. Ma; Z. Zhao; L. Qi, *Chem. Mater.*, 1995, **7,** 663-671.
(38) N. Uekawa; J. Kajiwara; K. Kakegawa; Y. Sasaki, *J. Colloid. Interf. Sci.*, 2002, **250,** 285-290.
(39) D. V. Bavykin; V. N. Parmon; A. A. Lapkin; F. C. Walsh, *J. Mater. Chem.*, 2004, **14,** 3370-3377.
(40) K. Terabe; K. Kato; H. Miyazaki; S. Yamaguchi; A. Imai; Y. Iguchi, *J. Mater. Sci.*, 1994, **29,** 1617-1622.
(41) S. R. Dhage; R. Pasricha; V. Ravi, *Mater. Res. Bull.*, 2003, **38,** 1623-1628.
(42) X. S. Li; G. E. Fryxell; J. C. Birnbaum; C. Wang, *Langmuir*, 2004, **20,** 9095-9102.
(43) K. Kanie; T. Sugimoto, *Chem. Commun.*, 2004**,** 1584-1585.
(44) P. A. Venz; J. T. Kloprogge; R. L. Frost, *Langmuir*, 2000, **16,** 4962-4968.
(45) P. A. Venz; R. L. Frost; J. R. Bartlett; J. L. Woolfrey, *Spect. Acta, A: Mol. Biomol. Spect.*, 1997, **53,** 969-977.
(46) M. Gotic; M. Ivanda; S. Popovic; S. Music; A. Sekulic; A. Turkovic; K. Furic, *J. Raman Spectrosc.*, 1997, **28,** 555-558.
(47) D. Vorkapic; T. Matsoukas, *J. Am. Ceram. Soc.*, 1998, **81,** 2815-2820.
(48) C. Bechinger; S. Ferrere; A. Zaban; J. Sprague; B. A. Gregg, *Nature*, 1996, **383,** 608-610.
(49) F. Campus; P. Bonhote; M. Grätzel; S. Heinen; L. Walder, *Sol. Energy Mater. Sol. Cells*, 1999, **56,** 281-297.
(50) Z. Wang; X. Hu; U. Helmersson, *J. Mater. Chem.*, 2000, **10,** 2396-2400.
(51) B. O'Regan; J. Moser; M. Anderson; M. Grätzel, *J. Phys. Chem.*, 1990, **94,** 8720-8726.
(52) A. Hagfeldt; M. Grätzel, *Acc. Chem. Res.*, 2000, **33,** 269-277.
(53) M. Grätzel, *Coord. Chem. Rev.*, 1998, **171,** 245-250.
(54) M. K. Nazeeruddin; A. Kay; I. Rodicio; R. Humphrybaker; E. Muller; P. Liska; N. Vlachopoulos; M. Grätzel, *J. Am. Chem. Soc.*, 1993, **115,** 6382-6390.
(55) C. Nasr; P. V. Kamat; S. Hotchandani, *J. Phys. Chem. B*, 1998, **102,** 10047-10056.
(56) R. Gruenwald; H. Tributsch, *J. Phys. Chem. B*, 1997, **101,** 2564-2575.
(57) H. Ding; H. Sun; Y. Shan, *J. Photochem. Photobiol., A*, 2004, **169,** 101-107.
(58) L. Spanhel; H. Weller; A. Henglein, *J. Am. Chem. Soc.*, 1987, **109,** 6632-6635.
(59) L. Spanhel; M. A. Anderson, *J. Am. Chem. Soc.*, 1991, **113,** 2826-2833.
(60) P. V. Kamat, *J. Phys. Chem. B*, 2002, **106,** 7729-7744.
(61) K. A. Zemski; D. R. Justes; A. W. Castleman, *J. Phys. Chem. B*, 2002, **106,** 6136-6148.
(62) A.-W. Xu; Y. Gao; H.-Q. Liu, *J. Catal.*, 2002, **207,** 151-157.
(63) B. Pal; M. Sharon, *Mater. Chem. Phys.*, 2002, **76,** 82-87.
(64) E. Jang; S. Jun; Y. Chung; L. Pu, *J. Phys. Chem. B*, 2004, **108,** 4597-4600.
(65) K. R. Gopidas; M. Bohorquez; P. V. Kamat, *J. Phys. Chem.*, 1990, **94,** 6435-6440.

(66) J. Yang; D. Li; X. Wang; X. Yang; L. Lu, *J. Solid State Chem.*, 2002, **165,** 193-198.
(67) S. Liao; H. Donggen; D. Yu; Y. Su; G. Yuan, *J. Photochem. Photobiol., A*, 2004, **168,** 7-13.
(68) S. Yin; H. Yamaki; M. Komatsu; Q. W. Zhang; J. S. Wang; Q. Tang; F. Saito; T. Sato, *J. Mater. Chem.*, 2003, **13,** 2996-3001.
(69) A. Kudo; K. Ueda; H. Kato; I. Mikami, *Catal. Lett.*, 1998, **53,** 229-230.
(70) S. Kohtani; J. Hiro; N. Yamamoto; A. Kudo; K. Tokumura; R. Nakagaki, *Catal. Comm.*, 2005, **6,** 185-189.
(71) D. W. Hwang; H. G. Kim; J. S. Jang; S. W. Bae; S. M. Ji; J. S. Lee, *Catal. Today*, 2004, **93-95,** 845-850.
(72) S. Rodrigues; K. T. Ranjit; S. Uma; I. N. Martyanov; K. J. Klabunde, *J. Catal.*, 2005, **230,** 158-165.
(73) Q. Zhang; L. Gao, *Langmuir*, 2004, **20,** 9821-9827.
(74) S. Ito; K. R. Thampi; P. Comte; P. Liska; M. Grätzel, *Chem. Commun.*, 2005**,** 268-270.
(75) P. Cheng; W. Li; T. Zhou; Y. Jin; M. Gu, *J. Photochem. Photobiol., A*, 2004, **168,** 97-101.
(76) S. Pavasupree; Y. Suzuki; S. Pivsa-Art; S. Yoshikawa, *J. Solid State Chem.*, 2005, **178,** 128-134.
(77) R. Asahi; T. Morikawa; T. Ohwaki; K. Aoki; Y. Taga, *Science*, 2001, **293,** 269-271.
(78) S. Sakthivel; M. Janczarek; H. Kisch, *J. Phys. Chem. B*, 2004, **108,** 19384-19387.
(79) O. Diwald; T. L. Thompson; T. Zubkov; E. G. Goralski; S. D. Walck; J. T. Yates, *J. Phys. Chem. B*, 2004, **108,** 6004-6008.
(80) Y. Aita; M. Komatsu; S. Yin; T. Sato, *J. Solid State Chem.*, 2004, **177,** 3235-3238.
(81) S. Yin; Y. Aita; M. Komatsu; J. Wang; Q. Tang; T. Sato, *J. Mater. Chem.*, 2005, **15,** 674-682.
(82) T. Sano; N. Negishi; K. Koike; K. Takeuchi; S. Matsuzawa, *J. Mater. Chem.*, 2004, **14,** 380-384.
(83) N. Miyamoto; K. Kuroda; M. Ogawa, *J. Phys. Chem. B*, 2004, **108,** 4268-4274.
(84) E. Pepe; O. Abbas; C. Rebufa; M. Simon; S. Lacombe; M. Julliard, *J. Photochem. Photobiol., A*, 2005, **170,** 143-149.
(85) M. Y. Liu; W. S. You; Z. B. Lei; G. H. Zhou; J. J. Yang; G. P. Wu; G. J. Ma; G. Y. Luan; T. Takata; M. Hara; K. Domen; L. Can, *Chem. Commun.*, 2004**,** 2192-2193.
(86) T. Takata; A. Tanaka; M. Hara; J. N. Kondo; K. Domen, *Catal. Today*, 1998, **44,** 17-26.
(87) R. Abe; K. Sayama; H. Arakawa, *J. Photochem. Photobiol., A*, 2004, **166,** 115-122.
(88) T. Tachikawa; S. Tojo; M. Fujitsuka; T. Majima, *Langmuir*, 2004, **20,** 2753-2759.
(89) D. Chatterjee; A. Mahata, *J. Photochem. Photobiol., A*, 2002, **153,** 199-204.
(90) K. Hirano; E. Suzuki; A. Ishikawa; T. Moroi; H. Shiroishi; M. Kaneko, *J. Photochem. Photobiol., A*, 2000, **136,** 157-161.
(91) D. Ljubas, *Energy (Amsterdam, Netherlands)*, 2005, **30,** 1699-1710.
(92) Sokang Nano. http://www.sokangnano.com (24th June 2005),

(93) B. C. Garrett; D. A. Dixon; D. M. Camaioni; D. M. Chipman; M. A. Johnson; C. D. Jonah; G. A. Kimmel; J. H. Miller; T. N. Rescigno; P. J. Rossky; S. S. Xantheas; S. D. Colson; A. H. Laufer; D. Ray; P. F. Barbara; D. M. Bartels; K. H. Becker; H. Bowen; S. E. Bradforth; I. Carmichael; J. V. Coe; L. R. Corrales; J. P. Cowin; M. Dupuis; K. B. Eisenthal; J. A. Franz; M. S. Gutowski; K. D. Jordan; B. D. Kay; J. A. Laverne; S. V. Lymar; T. E. Madey; C. W. Mccurdy; D. Meisel; S. Mukamel; A. R. Nilsson; T. M. Orlando; N. G. Petrik; S. M. Pimblott; J. R. Rustad; G. K. Schenter; S. J. Singer; A. Tokmakoff; L. S. Wang; C. Wittig; T. S. Zwier, *Chem. Rev.*, 2005, **105,** 355-389.
(94) J. A. Byrne; A. Davidson; P. S. M. Dunlop; B. R. Eggins, *J. Photochem. Photobiol., A*, 2002, **148,** 365-374.
(95) J. Arana; J. A. Herrera Melian; J. M. Dona Rodriguez; O. Gonzalez Diaz; A. Viera; J. Perez Pena; P. M. Marrero Sosa; V. Espino Jimenez, *Catal. Today*, 2002, **76,** 279-289.
(96) J.-M. Herrmann; J. Disdier; P. Pichat; S. Malato; J. Blanco, *Appl. Catal., B*, 1998, **17,** 15-23.
(97) E. P. Reddy; B. Sun; P. G. Smirniotis, *J. Phys. Chem. B*, 2004, **108,** 17198-17205.
(98) T. Nakashima; Y. Ohko; Y. Kubota; A. Fujishima, *J. Photochem. Photobiol., A*, 2003, **160,** 115-120.
(99) A. Topalov; D. Molnar-Gabor; B. Abramovic; S. Korom; D. Pericin, *J. Photochem. Photobiol., A*, 2003, **160,** 195-201.
(100) I. Losito; A. Amorisco; F. Palmisano; P. G. Zambonin, *Appl. Surf. Sci.*, 2005, **240,** 180-188.
(101) J. Lobedank; E. Bellmann; J. Bendig, *J. Photochem. Photobiol., A*, 1997, **108,** 89-93.
(102) K. Vinodgopal; D. E. Wynkoop; P. V. Kamat, *Environ. Sci. Technol.*, 1996, **30,** 1660-1666.
(103) K. T. Ranjit; I. Willner; S. Bossmann; A. Braun, *Res. Chem. Intermed.*, 1999, **25,** 733-756.
(104) Y. Li; G. Lu; S. Li, *J. Photochem. Photobiol., A*, 2002, **152,** 219-228.
(105) M. Suzuki; C. C. Waraksa; T. E. Mallouk; H. Nakayama; K. Hanabusa, *J. Phys. Chem. B*, 2002, **106,** 4227-4231.
(106) S. Sato; J. M. White, *J. Am. Chem. Soc.*, 1980, **102,** 7206-7210.
(107) S. Sato; J. M. White, *J. Phys. Chem.*, 1981, **85,** 592-594.
(108) A. Fujishima; K. Honda, *Nature*, 1972, **238,** 37-38.
(109) D. Tafalla; P. Salvador, *Ber. Bunsen-Ges. Phys. Chem.*, 1987, **91,** 475-479.
(110) V. P. Zhdanov, *Surf. Sci.*, 2002, **512,** L331-L334.
(111) U. Siemon; D. Bahnemann; J. J. Testa; D. Rodriguez; M. I. Litter; N. Bruno, *J. Photochem. Photobiol., A*, 2002, **148,** 247-255.
(112) D. Hufschmidt; D. Bahnemann; J. J. Testa; C. A. Emilio; M. I. Litter, *J. Photochem. Photobiol., A*, 2002, **148,** 223-231.
(113) H. Kato; K. Asakura; A. Kudo, *J. Am. Chem. Soc.*, 2003, **125,** 3082-3089.
(114) L. M. Doubova; S. Daolio; A. De Battisti, *J. Electroanal. Chem.*, 2002, **532,** 25-33.
(115) P. Keller; A. Moradpour; E. Amouyal, *J. Chem. Soc., Faraday Trans. 1*, 1982, **78,** 3331-3340.
(116) K. Kalyanasundaram; M. Grätzel, *Angew. Chem., Int. Ed.*, 1979, **18,** 701-702.

(117) K. Kalyanasundaram; J. Kiwi; M. Grätzel, *Helv. Chim. Acta*, 1978, **61,** 2720-2730.
(118) D. Duonghong; E. Borgarello; M. Grätzel, *J. Am. Chem. Soc.*, 1981, **103,** 4685-4690.
(119) V. H. Houlding; M. Grätzel, *J. Am. Chem. Soc.*, 1983, **105,** 5695-5696.
(120) J. Kiwi; E. Borgarello; D. Duonghong; M. Grätzel, *Stud. Surf. Sci. Catal.*, 1983, **16,** 135-146.
(121) D. Duonghong; N. Serpone; M. Grätzel, *Sci. Pap. Inst. Phys. Chem. Res. (Jpn.)*, 1984, **78,** 232-236.
(122) B. Gu; J. Kiwi; M. Grätzel, *Nouv. J. Chim.*, 1985, **9,** 539-543.
(123) A. Yasumori; K. Ishizu; S. Hayashi; K. Okada, *J. Mater. Chem.*, 1998, **8,** 2521-2524.
(124) S. K. Das; P. K. Dutta, *Micro. Meso. Mater.*, 1998, **22,** 475-483.
(125) Y. I. Kim; S. W. Keller; J. S. Krueger; E. H. Yonemoto; G. B. Saupe; T. E. Mallouk, *J. Phys. Chem. B*, 1997, **101,** 2491-2500.
(126) S. Licht; B. Wang; S. Mukerji; T. Soga; M. Umeno; H. Tributsch, *J. Phys. Chem. B*, 2000, **104,** 8920-8924.
(127) N. Serpone; E. Pelizzetti; M. Grätzel, *Coord. Chem. Rev.*, 1985, **64,** 225-245.
(128) J. Kiwi; M. Grätzel, *J. Phys. Chem.*, 1986, **90,** 637-640.
(129) J. W. Steed; J. L. Atwood, Supramolecular Chemistry. In John Wiley & Sons: West Sussex, 2000; p593.
(130) J. M. Lehn, *Science*, 1985, **227,** 849-856.
(131) J. W. Steed; J. L. Atwood, Supramolecular Chemistry. In John Wiley & Sons: West Sussex, 2000; p4.
(132) M. D. Ward, *Chem. Soc. Rev.*, 1997, **26,** 365-376.
(133) J. W. Steed; J. L. Atwood, Supramolecular Chemistry. In John Wiley & Sons: West Sussex, 2000; p592.
(134) V. Balzani, *Pure Appl. Chem.*, 1990, **62,** 1099-1102.
(135) A. Juris; V. Balzani; F. Barigelletti; S. Campagna; P. Belser; A. Von Zelewsky, *Coord. Chem. Rev.*, 1988, **84,** 85-277.
(136) M. F. Manfrin; L. Moggi; V. Castelvetro; V. Balzani; M. W. Hosseini; J. M. Lehn, *J. Am. Chem. Soc.*, 1985, **107,** 6888-6892.
(137) C. Patoux; J.-P. Launay; M. Beley; S. Chodorowski-Kimmes; J.-P. Collin; S. James; J.-P. Sauvage, *J. Am. Chem. Soc.*, 1998, **120,** 3717-3725.
(138) N. Vlachopoulos; P. Liska; J. Augustynski; M. Grätzel, *J. Am. Chem. Soc.*, 1988, **110,** 1216-1220.
(139) X. Marguerettaz; R. O'neill; D. Fitzmaurice, *J. Am. Chem. Soc.*, 1994, **116,** 2629-2630.
(140) X. Marguerettaz; D. Fitzmaurice, *J. Am. Chem. Soc.*, 1994, **116,** 5017-5018.
(141) R. Hoyle; J. Sotomayor; G. Will; D. Fitzmaurice, *J. Phys. Chem. B*, 1997, **101,** 10791-10800.
(142) G. Will; G. Boschloo; R. Hoyle; S. N. Rao; D. Fitzmaurice, *J. Phys. Chem. B*, 1998, **102,** 10272-10278.
(143) J. Sotomayor; R. W. Hoyle; G. Will; D. Fitzmaurice, *J. Mater. Chem.*, 1998, **8,** 105-110.
(144) R. Hoyle; G. Will; D. Fitzmaurice, *J. Mater. Chem.*, 1998, **8,** 2033-2036.
(145) G. Will; J. S. S. Nagaraja Rao; D. Fitzmaurice, *J. Mater. Chem.*, 1999, **9,** 2297-2299.
(146) A. Merrins; C. Kleverlaan; G. Will; S. N. Rao; F. Scandola; D. Fitzmaurice, *J. Phys. Chem. B*, 2001, **105,** 2998-3004.

(147) J. Sotomayor; G. Will; D. Fitzmaurice, *J. Mater. Chem.*, 2000, **10,** 685-692.
(148) B. Parkinson, *Acc. Chem. Res.*, 1984, **17,** 431-437.
(149) A. Goetzberger; J. Luther; G. Willeke, *Sol. Energy Mater. Sol. Cells*, 2002, **74,** 1-11.
(150) A. Goetzberger; C. Hebling, *Sol. Energy Mater. Sol. Cells*, 2000, **62,** 1-19.
(151) A. Hauch; A. Georg; S. Baumgartner; U. Opara Krasovec; B. Orel, *Electrochim. Acta*, 2001, **46,** 2131-2136.
(152) S. K. Deb; S. H. Lee; C. Edwin Tracy; J. Roland Pitts; B. A. Gregg; H. M. Branz, *Electrochim. Acta*, 2001, **46,** 2125-2130.
(153) D. Jiang; H. Zhao; S. Zhang; R. John; G. D. Will, *J. Photochem. Photobiol., A*, 2002, **156,** 201-206.
(154) D. L. Jiang; H. J. Zhao; S. Q. Zhang; R. John, *J. Catal.*, 2004, **223,** 212-220.
(155) R. Argazzi; N. Y. Murakami Iha; H. Zabri; F. Odobel; C. A. Bignozzi, *Coord. Chem. Rev.*, 2004, **248,** 1299-1316.
(156) K. Keis; C. Bauer; G. Boschloo; A. Hagfeldt; K. Westermark; H. Rensmo; H. Siegbahn, *J. Photochem. Photobiol., A*, 2002, **148,** 57-64.
(157) J. G. Doh; J. S. Hong; R. Vittal; M. G. Kang; N. G. Park; K. J. Kim, *Chem. Mater.*, 2004, **16,** 493-497.
(158) J. Bandara; C. M. Divarathne; S. D. Nanayakkara, *Sol. Energy Mater. Sol. Cells*, 2004, **81,** 429-437.
(159) S. Hore; E. Palomares; H. Smit; N. J. Bakker; P. Comte; P. Liska; K. R. Thampi; J. M. Kroon; A. Hinsch; J. R. Durrant, *J. Mater. Chem.*, 2005, **15,** 412-418.
(160) M. A. Aegerter, *Sol. Energy Mater. Sol. Cells*, 2001, **68,** 401-422.
(161) X. Ai; J. C. Guo; N. A. Anderson; T. Q. Lian, *J. Phys. Chem. B*, 2004, **108,** 12795-12803.
(162) K. G. Brooks; S. D. Burnside; V. Shklover; P. Comte; F. Arendse; A. Mcevoy; M. Grätzel, *Ceram. Trans.*, 2000, **109,** 115-122.
(163) Y. Saito; S. Kambe; T. Kitamura; Y. Wada; S. Yanagida, *Sol. Energy Mater. Sol. Cells*, 2004, **83,** 1-13.
(164) S. Ngamsinlapasathian; T. Sreethawong; Y. Suzuki; S. Yoshikawa, *Sol. Energy Mater. Sol. Cells*, 2005, **86,** 269-282.
(165) J. Desilvestro; M. Grätzel; L. Kavan; J. Moser; J. Augustynski, *J. Am. Chem. Soc.*, 1985, **107,** 2988-2990.
(166) J. A. Treadway; J. A. Moss; T. J. Meyer, *Inorg. Chem.*, 1999, **38,** 4386-4387.
(167) C. L. Huisman; A. Goossens; J. Schoonman, *Chem. Mater.*, 2003, **15,** 4617-4624.
(168) S. Ngamsinlapasathian; S. Sakulkhaemaruethai; S. Pavasupree; A. Kitiyanan; T. Sreethawong; Y. Suzuki; S. Yoshikawa, *J. Photochem. Photobiol., A*, 2004, **164,** 145-151.
(169) M. Adachi; Y. Murata; J. Takao; J. T. Jiu; M. Sakamoto; F. M. Wang, *J. Am. Chem. Soc.*, 2004, **126,** 14943-14949.
(170) S. Chappel; L. Grinis; A. Ofir; A. Zaban, *J. Phys. Chem. B*, 2005, **109,** 1643-1647.
(171) R. Plass; S. Pelet; J. Krueger; M. Grätzel; U. Bach, *J. Phys. Chem. B*, 2002, **106,** 7578-7580.
(172) J. He; H. Lindstrom; A. Hagfeldt; S. E. Lindquist, *Sol. Energy Mater. Sol. Cells*, 2000, **62,** 265-273.
(173) V. P. S. Perera; P. Pitigala; P. V. V. Jayaweera; K. M. P. Bandaranayake; K. Tennakone, *J. Phys. Chem. B*, 2003, **107,** 13758-13761.

(174) Q. B. Meng; K. Takahashi; X. T. Zhang; I. Sutanto; T. N. Rao; O. Sato; A. Fujishima; H. Watanabe; T. Nakamori; M. Uragami, *Langmuir*, 2003, **19,** 3572-3574.
(175) B. C. O'Regan; F. Lenzmann, *J. Phys. Chem. B*, 2004, **108,** 4342-4350.
(176) S. Murai; S. Mikoshiba; H. Sumino; T. Kato; S. Hayase, *Chem. Commun.*, 2003**,** 1534-1535.
(177) S. A. Haque; E. Palomares; H. M. Upadhyaya; L. Otley; R. J. Potter; A. B. Holmes; J. R. Durrant, *Chem. Commun.*, 2003**,** 3008-3009.
(178) S. Uchida; M. Tomiha; H. Takizawa; M. Kawaraya, *J. Photochem. Photobiol., A*, 2004, **164,** 93-96.
(179) C. Longo; A. F. Nogueira; M.-A. De Paoli; H. Cachet, *J. Phys. Chem. B*, 2002, **106,** 5925-5930.
(180) J. Ferber; R. Stangl; J. Luther, *Sol. Energy Mater. Sol. Cells*, 1998, **53,** 29-54.
(181) M. Penny; T. Farrell; G. Will; J. Bell, *J. Photochem. Photobiol., A*, 2004, **164,** 41-46.
(182) K. Hara; K. Sayama; H. Arakawa; Y. Ohga; A. Shinpo; S. Suga, *Chem. Commun.*, 2001**,** 569-570.
(183) K. Hara; M. Kurashige; Y. Dan-Oh; C. Kasada; A. Shinpo; S. Suga; K. Sayama; H. Arakawa, *New J. Chem.*, 2003, **27,** 783-785.
(184) C. D. Grant; A. M. Schwartzberg; G. P. Smestad; J. Kowalik; L. M. Tolbert; J. Z. Zhang, *J. Electroanal. Chem.*, 2002, **522,** 40-48.
(185) T. Horiuchi; H. Miura; S. Uchida, *J. Photochem. Photobiol., A*, 2004, **164,** 29-32.
(186) K. Sayama; S. Tsukagoshi; T. Mori; K. Hara; Y. Ohga; A. Shinpou; Y. Abe; S. Suga; H. Arakawa, *Sol. Energy Mater. Sol. Cells*, 2003, **80,** 47-71.
(187) V. P. S. Perera; P. K. D. D. P. Pitigala; M. K. I. Senevirathne; K. Tennakone, *Sol. Energy Mater. Sol. Cells*, 2005, **85,** 91-98.
(188) K. Gurunathan, *J. Mol. Catal. A: Chem.*, 2000, **156,** 59-67.
(189) K. Schwarzburg; R. Ernstorfer; S. Felber; F. Willig, *Coord. Chem. Rev.*, 2004, **248,** 1259-1270.
(190) B. Burfeindt; T. Hannappel; W. Storck; F. Willig, *J. Phys. Chem.*, 1996, **100,** 16463-16465.
(191) T. Kitamura; M. Ikeda; K. Shigaki; T. Inoue; N. A. Anderson; X. Ai; T. Q. Lian; S. Yanagida, *Chem. Mater.*, 2004, **16,** 1806-1812.
(192) G. Ramakrishna; A. K. Singh; D. K. Palit; H. N. Ghosh, *J. Phys. Chem. B*, 2004, **108,** 4775-4783.
(193) T. Matsubara; Y. Ichikawa; K. Aramaki; A. Katagiri, *Sol. Energy Mater. Sol. Cells*, 2004, **85,** 269-275.
(194) N. J. Cherepy; G. P. Smestad; M. Grätzel; J. Z. Zhang, *J. Phys. Chem. B*, 1997, **101,** 9342-9351.
(195) K. Tennakone; G. Kumara; I. R. M. Kottegoda; V. P. S. Perera; P. Weerasundara, *J. Photochem. Photobiol., A*, 1998, **117,** 137-142.
(196) G. P. Smestad; M. Grätzel, *J. Chem. Educ.*, 1998, **75,** 752-756.
(197) Q. Dai; J. Rabani, *Chem. Commun.*, 2001**,** 2142-2143.
(198) C. G. Garcia; A. S. Polo; N. Y. Murakami Iha, *J. Photochem. Photobiol., A*, 2003, **160,** 87-91.
(199) M. K. Nazeeruddin; P. Pechy; M. Grätzel, *Chem. Commun.*, 1997, **18,** 1705-1706.
(200) S. Cherian; C. C. Wamser, *J. Phys. Chem. B*, 2000, **104,** 3624-3629.

(201) J. Jasieniak; M. Johnston; E. R. Waclawik, *J. Phys. Chem. B*, 2004, **108,** 12962-12971.
(202) J. He; G. Benkoe; F. Korodi; T. Polivka; R. Lomoth; B. Kermark; L. Sun; A. Hagfeldt; V. Sundstroem, *J. Am. Chem. Soc.*, 2002, **124,** 4922-4932.
(203) Y. Amao; T. Komori, *Langmuir*, 2003, **19,** 8872-8875.
(204) F. Odobel; E. Blart; M. Lagree; M. Villieras; H. Boujtita; N. El Murr; S. Caramori; C. Alberto Bignozzi, *J. Mater. Chem.*, 2003, **13,** 502-510.
(205) E. Galoppini, *Coord. Chem. Rev.*, 2004, **248,** 1283-1297.
(206) M. K. Nazeeruddin; P. Liska; J. Moser; N. Vlachopoulos; M. Grätzel, *Helv. Chim. Acta*, 1990, **73,** 1788-1803.
(207) C. A. Bignozzi; R. Argazzi; J. R. Schoonover; G. J. Meyer; F. Scandola, *Sol. Energy Mater. Sol. Cells*, 1995, **38,** 187-198.
(208) M. K. Nazeeruddin; P. Pechy; T. Renouard; S. M. Zakeeruddin; R. Humphry-Baker; P. Comte; P. Liska; L. Cevey; E. Costa; V. Shklover; L. Spiccia; G. B. Deacon; C. A. Bignozzi; M. Grätzel, *J. Am. Chem. Soc.*, 2001, **123,** 1613-1624.
(209) M. Yanagida; T. Yamaguchi; M. Kurashige; K. Hara; R. Katoh; H. Sugihara; H. Arakawa, *Inorg. Chem.*, 2003, **42,** 7921-7931.
(210) M. Yanagida; T. Yamaguchi; M. Kurashige; G. Fujihashi; K. Hara; R. Katoh; H. Sugihara; H. Arakawa, *Inorg. Chim. Acta*, 2003, **351,** 283-290.
(211) H. Sugihara; S. Sano; T. Yamaguchi; M. Yanagida; T. Sato; Y. Abe; Y. Nagao; H. Arakawa, *J. Photochem. Photobiol., A*, 2004, **166,** 81-90.
(212) E. Figgemeier; V. Aranyos; E. C. Constable; R. W. Handel; C. E. Housecroft; C. Risinger; A. Hagfeldt; E. Mukhtar, *Inorg. Chem. Commun.*, 2004, **7,** 117-121.
(213) P. Wang; S. M. Zakeeruddin; P. Comte; R. Charvet; R. Humphry-Baker; M. Grätzel, *J. Phys. Chem. B*, 2003, **107,** 14336-14341.
(214) P. Wang; S. M. Zakeeruddin; J. E. Moser; M. K. Nazeeruddin; T. Sekiguchi; M. Grätzel, *Nat. Mater.*, 2003, **2,** 498-498.
(215) C. Klein; K. Nazeeruddin; D. Di Censo; P. Liska; M. Grätzel, *Inorg. Chem.*, 2004, **43,** 4216-4226.
(216) M. K. Nazeeruddin; S. M. Zakeeruddin; J.-J. Lagref; P. Liska; P. Comte; C. Barolo; G. Viscardi; K. Schenk; M. Grätzel, *Coord. Chem. Rev.*, 2004, **248,** 1317-1328.
(217) P. Wang; C. Klein; J. E. Moser; R. Humphry-Baker; N. L. Cevey-Ha; R. Charvet; P. Comte; S. M. Zakeeruddin; M. Grätzel, *J. Phys. Chem. B*, 2004, **108,** 17553-17559.
(218) P. Wang; R. Humphry-Baker; J. E. Moser; S. M. Zakeeruddin; M. Grätzel, *Chem. Mater.*, 2004, **16,** 3246-3251.
(219) P. Wang; C. Klein; R. Humphry-Baker; S. M. Zakeeruddin; M. Grätzel, *J. Am. Chem. Soc.*, 2005, **127,** 808-809.
(220) P. A. Anderson; G. F. Strouse; J. A. Treadway; F. R. Keene; T. J. Meyer, *Inorg. Chem.*, 1994, **33,** 3863-3864.
(221) P. A. Anderson; F. R. Keene; T. J. Meyer; J. A. Moss; G. F. Strouse; J. A. Treadway, *J. Chem. Soc., Dalton Trans.*, 2002**,** 3820-3831.
(222) S. M. Zakeeruddin; M. K. Nazeeruddin; P. Pechy; F. P. Rotzinger; R. Humphry-Baker; K. Kalyanasundaram; M. Grätzel; V. Shklover; T. Haibach, *Inorg. Chem.*, 1997, **36,** 5937-5946.
(223) H. Zabri; I. Gillaizeau; C. A. Bignozzi; S. Caramori; M. F. Charlot; J. Cano-Boquera; F. Odobel, *Inorg. Chem.*, 2003, **42,** 6655-6666.

(224) J. A. Treadway. Creation and Utilization of Highly Unsymmetric Complexes of Ruthenium(II). Dissertation, University of North Carolina, Chapel Hill, 1998.
(225) E. A. Seddon; K. R. Seddon, Topics in Inorganic and General Chemistry, Vol. 19: The Chemistry of Ruthenium. In 1984; p1173-1205.
(226) R. Cinnsealach; G. Boschloo; S. N. Rao; D. Fitzmaurice, *Sol. Energy Mater. Sol. Cells*, 1998, **55,** 215-223.
(227) S. Altobello; C. A. Bignozzi; S. Caramori; G. Larramona; S. Quici; G. Marzanni; R. Lakhmiri, *J. Photochem. Photobiol., A*, 2004, **166,** 91-98.
(228) W. J. E. Beek; R. A. J. Janssen, *J. Mater. Chem.*, 2004, **14,** 2795-2800.
(229) G. Redmond; D. Fitzmaurice; M. Grätzel, *J. Phys. Chem.*, 1993, **97,** 6951-6954.
(230) N. W. Duffy; K. D. Dobson; K. C. Gordon; B. H. Robinson; A. J. Mcquillan, *Chem. Phys. Lett.*, 1997, **266,** 451-455.
(231) M. Li; Z. Xiao; Z. Huan; Z. Lu, *Appl. Surf. Sci.*, 1998, **125,** 217-220.
(232) Y.-X. Weng; L. Li; Y. Liu; L. Wang; G.-Z. Yang, *J. Phys. Chem. B*, 2003, **107,** 4356-4363.
(233) K. Kils; E. I. Mayo; B. S. Brunschwig; H. B. Gray; N. S. Lewis; J. R. Winkler, *J. Phys. Chem. B*, 2004, **108,** 15640-15651.
(234) P. Pitigala; M. K. I. Seneviratne; V. P. S. Perera; K. Tennakone, *Langmuir*, 2004, **20,** 5100-5103.
(235) U. Koelle; J. Moser; M. Grätzel, *Inorg. Chem.*, 1985, **24,** 2253-2258.
(236) M. K. Nazeeruddin; R. Humphry-Baker; D. L. Officer; W. M. Campbell; A. K. Burrell; M. Grätzel, *Langmuir*, 2004, **20,** 6514-6517.
(237) R. S. Loewe; A. Ambroise; K. Muthukumaran; K. Padmaja; A. B. Lysenko; G. Mathur; Q. L. Li; D. F. Bocian; V. Misra; J. S. Lindsey, *J. Org. Chem.*, 2004, **69,** 1453-1460.
(238) F. A. Cotton; G. Wilkinson; M. Bochmann; C. Murillo, Advanced Inorganic Chemistry, 6th Edition. In 1998; p1012.
(239) J. X. Pan; Y. H. Xu; G. Benko; Y. Feyziyev; S. Styring; L. C. Sun; B. Akermark; T. Polivka; V. Sundstrom, *J. Phys. Chem. B*, 2004, **108,** 12904-12910.
(240) Y. F. Zhuang; H. X. Ju, *Electroanal.*, 2004, **16,** 1401-1405.
(241) D. V. Kozlov; D. S. Tyson; C. Goze; R. Ziessel; F. N. Castellano, *Inorg. Chem.*, 2004, **43,** 6083-6092.
(242) M. Goez; D. Von Ramin-Marro; M. H. O. Musa; M. Schiewek, *J. Phys. Chem. A*, 2004, **108,** 1090-1100.
(243) Y.-Q. Fang; N. J. Taylor; G. S. Hanan; F. Loiseau; R. Passalacqua; S. Campagna; H. Nierengarten; A. Van Dorsselaer, *J. Am. Chem. Soc.*, 2002, **124,** 7912-7913.
(244) M. Montalti; S. Wadhwa; W. Y. Kim; R. A. Kipp; R. H. Schmehl, *Inorg. Chem.*, 2000, **39,** 76-84.
(245) S. H. Bossmann; S. Jockusch; P. Schwarz; B. Baumeister; S. Gob; C. Schnabel; L. Payawan; M. R. Pokhrel; M. Worner; A. M. Braun; N. J. Turro, *Photochem. Photobiol. Sci.*, 2003, **2,** 477-486.
(246) S. Bonnet; J. P. Collin; N. Gruber; J. P. Sauvage; E. R. Schofield, *Dalton T.*, 2003**,** 4654-4662.
(247) T. Kojima; T. Sakamoto; Y. Matsuda, *Inorg. Chem.*, 2004, **43,** 2243-2245.
(248) G. Solomons; C. Fryhle, Organic Chemistry, 8th Edition. In 2004; p262-263.
(249) A. M. Josceanu; P. Moore, *J. Chem. Soc., Dalton Trans.*, 1998**,** 369-374.

(250) P. Serp; M. Hernandez; P. Kalck, *Comptes Rendus de l'Academie des Sciences, Serie IIc: Chimie*, 1999, **2,** 267-272.
(251) I. P. Evans; A. Spencer; G. Wilkinson, *J. Chem. Soc., Dalton Trans.*, 1973**,** 204-209.
(252) L. Michaelis, *Biochem. Z.*, 1932, **250,** 564-567.
(253) L. Michaelis; E. S. Hill, *J. Am. Chem. Soc.*, 1933, **55,** 1481-1494.
(254) Y. Amao; Y. Tomonou; I. Okura, *Sol. Energy Mater. Sol. Cells*, 2003, **79,** 103-111.
(255) R. Toba; J. Maria Quintela; C. Peinador; E. Roman; A. E. Kaifer, *Chem. Commun.*, 2001**,** 857-858.
(256) M. Sakamoto; T. Kamachi; I. Okura; A. Ueno; H. Mihara, *Biopolymers*, 2001, **59,** 103-109.
(257) N. Asakura; T. Hiraishi; T. Kamachi; I. Okura, *J. Mol. Catal. A: Chem.*, 2001, **172,** 1-7.
(258) R. Cinnsealach; G. Boschloo; S. N. Rao; D. Fitzmaurice, *Sol. Energy Mater. Sol. Cells*, 1999, **57,** 107-125.
(259) B. Long; K. Nikitin; D. Fitzmaurice, *J. Am. Chem. Soc.*, 2003, **125,** 15490-15498.
(260) C. M. Elliott; E. J. Hershenhart, *J. Am. Chem. Soc.*, 1982, **104,** 7519-7526.
(261) J. H. Nelson, in *Nuclear Magnetic Resonance Spectroscopy*. Prentice Hall: Upper Saddle River, NJ, 2003; p 464.
(262) in *The Merck Index*. 11th; Merck Co. Inc.: New Jersey, USA, 1999; p 1606.
(263) J. A. Broomhead; C. G. Young, *Inorg. Synth.*, 1990, **28,** 338-340.
(264) G. J. Wilson. Photocleavage of water into hydrogen and oxygen utilising the electron relay properties of a covalently linked molecular and condensed phase component assembly. Dissertation, Queensland University of Technology, Brisbane, 2001.
(265) B. P. Sullivan; D. J. Salmon; T. J. Meyer, *Inorg. Chem.*, 1978, **17,** 3334-3341.
(266) M. Yanagida; L. P. Singh; K. Sayama; K. Hara; R. Katoh; A. Islam; H. Sugihara; H. Arakawa; M. K. Nazeeruddin; M. Grätzel, *Dalton*, 2000**,** 2817-2822.
(267) A. Williams, Email, *"Email Subject: Carbon 13 NMR of ruthenium dicarboxy-2,2-bipyridyl complexes"*, 2005.
(268) F. Odobel, Email, *"Email Subject: Recent Article in Inorganic Chemistry"*, 2003.
(269) K. Kalyanasundaram; M. K. Nazeeruddin, *Chem. Phys. Lett.*, 1992, **193,** 292-297.
(270) S. Fantacci; F. De Angelis; A. Selloni, *J. Am. Chem. Soc.*, 2003, **125,** 4381-4387.
(271) P. Persson; M. J. Lundqvist, *J. Phys. Chem. B*, 2005, **109,** 11918-11924.
(272) E. A. Seddon; K. R. Seddon, Topics in Inorganic and General Chemistry, Vol. 19: The Chemistry of Ruthenium. In 1984; p414-475.
(273) D. P. Rillema; D. S. Jones; H. A. Levy, *Chem. Commun.*, 1979**,** 849.
(274) G. A. Crosby; R. J. Watts, *J. Am. Chem. Soc.*, 1971, **93,** 3184-3188.
(275) M. K. Nazeeruddin; K. Kalyanasundaram; M. Grätzel, *Inorg. Synth.*, 1998, **32,** 181-186.
(276) S. G. Yan; J. S. Prieskorn; Y. J. Kim; J. T. Hupp, *J. Phys. Chem. B*, 2000, **104,** 10871-10877.
(277) S. I. Gorelsky; A. B. P. Lever, *J. Organomet. Chem.*, 2001, **635,** 187-196.

(278) I. J. Bruno, Cole, J. C., Edgington, P. R., Kessler, M. K., Macrae, C.F., Mccabe, P., Pearson, J.,Taylor, R., *Acta Crystallogr.*, 2002, **B58,** 389-397.
(279) L. J. Farrugia, *J. Appl. Cryst*, 1997, **30,** 565.
(280) *Persistence of Vision Raytracer*, v3.6; Persistence of Vision Pty. Ltd.: Williamstown, Victoria, Australia, 2004.
(281) M. J. Frisch; G. W. Trucks; H. B. Schlegel; G. E. Scuseria; M. A. Robb; J. R. Cheeseman; J. J. A. Montgomery; T. Vreven; N. Kudin; J. C. Burant; J. M. Millam; S. S. Iyengar; J. Tomasi; V. Barone; B. Mennucci; M. Cossi; G. Scalmani; N. Rega; G. A. Petersson; H. Nakatsuji; M. Hada; M. Ehara; K. Toyota; R. Fukuda; J. Hasegawa; M. Ishida; T. Nakajima; Y. Honda; O. Kitao; H. Nakai; M. Klene; X. Li; J. E. Knox; H. P. Hratchian; J. B. Cross; C. Adamo; J. Jaramillo; R. Gomperts; R. E. Stratmann; O. Yazyev; A. J. Austin; R. Cammi; C. Pomelli; J. W. Ochterski; P. Y. Ayala; K. Morokuma; G. A. Voth; P. Salvador; J. J. Dannenberg; V. G. Zakrzewski; S. Dapprich; A. D. Daniels; M. C. Strain; O. Farkas; D. K. Malick; A. D. Rabuck; K. Raghavachari; J. B. Foresman; J. V. Ortiz; Q. Cui; A. G. Baboul; S. Clifford; J. Cioslowski; B. B. Stefanov; G. Liu; A. Liashenko; P. Piskorz; I. Komaromi; R. L. Martin; D. J. Fox; T. Keith; M. A. Al-Laham; C. Y. Peng; A. Nanayakkara; M. Challacombe; P. M. W. Gill; B. Johnson; W. Chen; M. W. Wong; C. Gonzalez; J. A. Pople *Gaussian 03, Revision B.05*, Gaussian 03, Revision B.05; Gaussian, Inc.: Pittsburgh PA, 2003.
(282) A. D. Becke, *J. Chem. Phys.*, 1993, **98,** 5648-5652.
(283) C. Lee; W. Yang; R. G. Parr, *Phys. Rev. B: Condens. Matter Mater. Phys.*, 1988, **37,** 785-789.
(284) B. Miehlich; A. Savin; H. Stoll; H. Preuss, *Chem. Phys. Lett.*, 1989, **157,** 200-206.
(285) T. H. Dunning, Jr.; P. J. Hay, *Mod. Theor. Chem.*, 1977, **3,** 1-27.
(286) P. J. Hay; W. R. Wadt, *J. Chem. Phys.*, 1985, **82,** 270-283.
(287) W. R. Wadt; P. J. Hay, *J. Chem. Phys.*, 1985, **82,** 284-298.
(288) P. J. Hay; W. R. Wadt, *J. Chem. Phys.*, 1985, **82,** 299-310.
(289) S. R. Stoyanov; J. M. Villegas; D. P. Rillema, *Inorg. Chem.*, 2002, **41,** 2941-2945.
(290) L. E. Orgel, *J. Chem. Soc. Abs.*, 1961**,** 3683-3686.
(291) S. I. Gorelsky; E. S. Dodsworth; A. B. P. Lever; A. A. Vlcek, *Coord. Chem. Rev.*, 1998, **174,** 469-494.
(292) G. Pourtois; D. Beljonne; C. Moucheron; S. Schumm; A. Kirsch-De Mesmaeker; R. Lazzaroni; J. L. Bredas, *J. Am. Chem. Soc.*, 2004, **126,** 683-692.
(293) E. M. Kober; T. J. Meyer, *Inorg. Chem.*, 1982, **21,** 3967-3977.
(294) H. E. Toma; R. M. Serrasqueiro; R. C. Rocha; G. J. F. Demets; H. Winnischofer; K. Araki; P. E. A. Ribeiro; C. L. Donnici, *J. Photochem. Photobiol., A*, 2000, **135,** 185-191.
(295) G. D. Hager; G. A. Crosby, *J. Am. Chem. Soc.*, 1975, **97,** 7031-7037.
(296) G. D. Hager; R. J. Watts; G. A. Crosby, *J. Am. Chem. Soc.*, 1975, **97,** 7037-7042.
(297) G. Calzaferri; R. Rytz, *J. Phys. Chem.*, 1995, **99,** 12141-12150.
(298) A. Broo; P. Lincoln, *Inorg. Chem.*, 1997, **36,** 2544-2553.
(299) J.-F. Guillemoles; V. Barone; L. Joubert; C. Adamo, *J. Phys. Chem. A*, 2002, **106,** 11354-11360.
(300) G. A. Crosby, *Acc. Chem. Res.*, 1975, **8,** 231-238.

(301) A. Usami; H. Ozaki, *J. Phys. Chem. B*, 2005, **109,** 2591-2596.
(302) D. P. Serrano; G. Calleja; R. Sanz; P. Pizarro, *Chem. Commun.*, 2004**,** 1000-1001.
(303) M. Salmi; N. Tkachenko; V. Vehmanen; R. J. Lamminmaki; S. Karvinen; H. Lemmetyinen, *J. Photochem. Photobiol., A*, 2004, **163,** 395-401.
(304) K. L. Yeung; S. T. Yau; A. J. Maira; J. M. Coronado; J. Soria; P. L. Yue, *J. Catal.*, 2003, **219,** 107-116.
(305) J. Lin; Y. Lin; P. Liu; M. J. Meziani; L. F. Allard; Y. P. Sun, *J. Am. Chem. Soc.*, 2002, **124,** 11514-11518.
(306) K. Rajeshwar; C. R. Chenthamarakshan; S. Goeringer; M. Djukic, *Pure Appl. Chem.*, 2001, **73,** 1849-1860.
(307) I. Mora-Sero; T. L. Villarreal; J. Bisquert; A. Pitarch; R. Gomez; P. Salvador, *J. Phys. Chem. B*, 2005, **109,** 3371-3380.
(308) G. R. Torres; T. Lindgren; J. Lu; C. G. Granqvist; S. E. Lindquist, *J. Phys. Chem. B*, 2004, **108,** 5995-6003.
(309) N. G. Park; M. G. Kang; K. M. Kim; K. S. Ryu; S. H. Chang; D. K. Kim; J. Van De Lagemaat; K. D. Benkstein; A. J. Frank, *Langmuir*, 2004, **20,** 4246-4253.
(310) J. C. Yu; W. K. Ho; J. G. Yu; S. K. Hark; K. Iu, *Langmuir*, 2003, **19,** 3889-3896.
(311) L. Kavan; M. Kalbac; M. Zukalova; I. Exnar; V. Lorenzen; R. Nesper; M. Grätzel, *Chem. Mater.*, 2004, **16,** 477-485.
(312) T. Oekermann; D. Zhang; T. Yoshida; H. Minoura, *J. Phys. Chem. B*, 2004, **108,** 2227-2235.
(313) T. K. N. Hoang; L. Deriemaeker; V. B. La; R. Finsy, *Langmuir*, 2004, **20,** 8966-8969.
(314) C. R. Patra; A. Gedanken, *New J. Chem.*, 2004, **28,** 1060-1065.
(315) F. Bensebaa; N. Patrito; Y. Le Page; P. L'ecuyer; D. Wang, *J. Mater. Chem.*, 2004, **14,** 3378-3384.
(316) T.-Z. Ren; Z.-Y. Yuan; B.-L. Su, *Langmuir*, 2004, **20,** 1531-1534.
(317) E. Vigil; J. A. Ayllon; A. M. Peiro; R. Rodriguez-Clemente; X. Domenech; J. Peral, *Langmuir*, 2001, **17,** 891-896.
(318) J. A. Ayllon; A. M. Peiro; L. Saadoun; E. Vigil; X. Domenech; J. Peral, *J. Mater. Chem.*, 2000, **10,** 1911-1914.
(319) S. Komarneni; R. K. Rajha; H. Katsuki, *Mater. Chem. Phys.*, 1999, **61,** 50-54.
(320) C. J. Doss; R. Zallen, *Phys. Rev. B: Condens. Matter*, 1993, **48,** 15626-15637.
(321) T. A. Egerton; I. R. Tooley, *J. Phys. Chem. B*, 2004, **108,** 5066-5072.
(322) T. K. Kim; M. N. Lee; S. H. Lee; Y. C. Park; C. K. Jung; J. H. Boo, *Thin Solid Films*, 2005, **475,** 171-177.
(323) K. S. W. Sing; D. H. Everett; R. A. W. Haul; L. Moscou; R. A. Pierotti; J. Rouquerol; T. Siemieniewska, *Pure Appl. Chem.*, 1985, **57,** 603-619.
(324) S. J. S. Gregg, Kenneth S W, Adsorption, Surface Area, and Porosity. In 2nd; Academic Press, Inc.: London, 1982; p21-23.
(325) R. J. Betsch; H. L. Park; W. B. White, *Mater. Res. Bull.*, 1991, **26,** 613-622.
(326) N. G. Park; G. Schlichthorl; J. Van De Lagemaat; H. M. Cheong; A. Mascarenhas; A. J. Frank, *J. Phys. Chem. B*, 1999, **103,** 3308-3314.
(327) C. Brinker; G. Scherer, Sol-Gel Science: The Physics and Chemistry of Sol-Gel Processing. In 1990; p237.
(328) R. Finsy, *Langmuir*, 2004, **20,** 2975-2976.
(329) T. Sreethawong; Y. Suzuki; S. Yoshikawa, *Catal. Comm.*, 2005, **6,** 119-124.

(330) Q.-L. Zhang; L.-C. Du; Y.-X. Weng; L. Wang; H.-Y. Chen; J.-Q. Li, *J. Phys. Chem. B*, 2004, **108,** 15077-15083.
(331) T.-V. Nguyen; S. Kim; O.-B. Yang, *Catal. Comm.*, 2004, **5,** 59-62.
(332) N. Serpone; J. Martin; S. Horikoshi; H. Hidaka, *J. Photochem. Photobiol., A*, 2005, **169,** 235-251.
(333) A. Harriman, *Platinum Met. Rev.*, 1991, **35,** 22-23.
(334) P. Keller; A. Moradpour; E. Amouyal; H. B. Kagan, *Nouv. J. Chim.*, 1980, **4,** 377-384.
(335) J. Sato; H. Kobayashi; K. Ikarashi; N. Saito; H. Nishiyama; Y. Inoue, *J. Phys. Chem. B*, 2004, **108,** 4369-4375.
(336) K. Ikarashi; J. Sato; H. Kobayashi; N. Saito; H. Nishiyama; Y. Inoue, *J. Phys. Chem. B*, 2002, **106,** 9048-9053.
(337) J. M. Kleijn; G. K. Boschloo, *J. Electroanal. Chem. Interfacial Electrochem.*, 1991, **300,** 595-606.
(338) J. M. Kleijn; J. Lyklema, *Colloid Polym. Sci.*, 1987, **265,** 1105-1113.
(339) A. Currao; V. Raja Reddy; M. K. Van Veen; R. E. I. Schropp; G. Calzaferri, *Photochem. Photobiol. Sci.*, 2004, **3,** 1017-1025.
(340) S. Ardizzone; P. Siviglia; S. Trasatti, *J. Electroanal. Chem. Interfacial Electrochem.*, 1981, **122,** 395-401.
(341) G. Rothenberger; D. Fitzmaurice; M. Grätzel, *J. Phys. Chem.*, 1992, **96,** 5983-5986.
(342) I. Tsuji; H. Kato; H. Kobayashi; A. Kudo, *J. Am. Chem. Soc.*, 2004, **126,** 13406-13413.
(343) P. S. Braterman; A. Harriman; G. A. Heath; L. J. Yellowlees, *J. Chem. Soc., Dalton Trans.*, 1983**,** 1801-1803.
(344) E. W. Mcfarland; J. Tang, *Nature*, 2003, **421,** 616-618.
(345) R. Fretwell; P. Douglas, *Photochem. Photobiol. Sci.*, 2002, **1,** 793-798.
(346) P. Pichat; M. N. Mozzanega; J. Disdier; J. M. Herrmann, *Nouv. J. Chim.*, 1982, **6,** 559-564.
(347) Y. K. Du; J. Rabani, *J. Phys. Chem. B*, 2003, **107,** 11970-11978.
(348) D. C. Hurum; K. A. Gray; T. Rajh; M. C. Thurnauer, *J. Phys. Chem. B*, 2005, **109,** 977-980.
(349) L. Q. Song; H. Y. Ding; X. S. Wang; B. W. Zhang; Y. Cao; J. Feng; X. C. Ai; J. P. Zhang, *J. Photochem. Photobiol., A*, 2004, **165,** 137-142.
(350) E. Bae; W. Choi; J. Park; H. S. Shin; S. B. Kim; J. S. Lee, *J. Phys. Chem. B*, 2004, **108,** 14093-14101.
(351) J. B. Asbury; N. A. Anderson; E. Hao; X. Ai; T. Lian, *J. Phys. Chem. B*, 2003, **107,** 7376-7386.
(352) S. Devipriya; S. Yesodharan, *Sol. Energy Mater. Sol. Cells*, 2005, **86,** 309-348.
(353) L. Ouattara; I. Duo; T. Diaco; A. Ivandini; K. Honda; T. Rao; A. Fujishima; C. Comninellis, *New Diam. Front. C. Tec.*, 2003, **13,** 97-108.
(354) M. B. Smith; J. March, March's Advanced Organic Chemistry: Reactions, Mechanisms, and Structure. In 5th; John Wiley & Sons, Inc.: New York, 2001; p942.
(355) R. Swanepoel, *J. Phys. E Sci. Intrum.*, 1983, **16,** 1214-1222.
(356) G. Herlem; K. Reybier; A. Trokourey; B. Fahys, *J. Electrochem. Soc.*, 2000, **147,** 597-601.
(357) L. R. Skubal; N. K. Meshkov; M. C. Vogt, *J. Photochem. Photobiol., A*, 2002, **148,** 103-108.

(358) E. Stathatos; P. Lianos; C. Tsakiroglou, *Langmuir*, 2004, **20,** 9103-9107.
(359) R. Nakamura; T. Tanaka; Y. Nakato, *J. Phys. Chem. B*, 2004, **108,** 10617-10620.
(360) H. Yamada; F. Siems William; T. Koike; K. Hurst James, *J. Am. Chem. Soc.*, 2004, **126,** 9786-9795.
(361) G. M. Liu; X. Z. Li; J. C. Zhao; S. Horikoshi; H. Hidaka, *J. Mol. Catal. A-Chem.*, 2000, **153,** 221-229.
(362) M. Bettoni; T. Del Giacco; C. Rol; G. V. Sebastiani, *J. Photochem. Photobiol., A*, 2004, **163,** 481-487.
(363) R. J. Candal; W. A. Zeltner; M. A. Anderson, *Environ. Sci. Technol.*, 2000, **34,** 3443-3451.
(364) P. W. Atkins, In *Physical Chemistry, 6th Edition*, 1998; p866-867.
(365) M. Sokmen; A. Ozkan, *J. Photochem. Photobiol., A*, 2002, **147,** 77-81.
(366) H. J. Nam; T. Amemiya; M. Murabayashi; K. Toh, *J. Phys. Chem. B*, 2004, **108,** 8254-8259.
(367) S. Gelover; P. Mondragon; A. Jimenez, *J. Photochem. Photobiol., A*, 2004, **165,** 241-246.
(368) D. Huang; Z.-D. Xiao; J.-H. Gu; N.-P. Huang; C.-W. Yuan, *Thin Solid Films*, 1997, **305,** 110-115.
(369) P. W. Atkins, In *Physical Chemistry, 6th Edition*, 1998; p880-883.
(370) A. J. Bard; L. R. Faulkner, Electrochemical Methods: Fundamentals and Applications. In 2nd; 2001; p31.
(371) J. Nelson; A. M. Eppler; I. M. Ballard, *J. Photochem. Photobiol., A*, 2002, **148,** 25-31.
(372) S. Nakade; Y. Saito; W. Kubo; T. Kanzaki; T. Kitamura; Y. Wada; S. Yanagida, *Electrochem. Commun.*, 2003, **5,** 804-808.
(373) M. E. Calvo; R. J. Candal; S. A. Bilmes, *Environ. Sci. Technol.*, 2001, **35,** 4132-4138.
(374) A. J. Bard; L. R. Faulkner, Electrochemical Methods: Fundamentals and Applications. In 2nd; 2001; p28.
(375) H. Xu; K. C. Zheng; H. Deng; L. J. Lin; Q. L. Zhang; L. N. Ji, *New J. Chem.*, 2003, **27,** 1255-1263.
(376) R. Caspar; L. Musatkina; A. Tatosyn; H. Amouri; M. Gruselle; C. Guyard-Duhayon; R. Duval; C. Cordier, *Inorg. Chem.*, 2004, **43,** 7986-7993.
(377) G. Will; E. Kudryashov; E. Duggan; D. Fitzmaurice; V. Buckin; E. Waghorne; S. Mukherjee, *Spect. Acta, A: Mol. Biomol. Spect.*, 1999, **55A,** 2711-2717.

APPENDIX I

Complete TDDFT Transitions for Tris–Bipyridyl Ru(II) Sensitisers

Table 0-1 – TDDFT Calculated Excitation Energies, One–Electron Transitions, and Oscillator Strengths for Optical Transitions of $[Ru(bpy)_3]^{2+}$ complex in the Gas Phase.

excited state	orbital composition			coefficient	excitation			oscillator strength
					eV	nm	cm^{-1}	
1	132 (e, π_ψ*)	←	130 (a_1, $d\pi$)	0.683	2.53	490	20402	0.0001
2	131 (a_2, π_ψ*)	←	130 (a_1, $d\pi$)	0.278	2.53	490	20410	0.0002
	132 (e, π_ψ*)	←	130 (a_1, $d\pi$)	–0.112				
	133 (e, π_ψ*)	←	130 (a_1, $d\pi$)	0.625				
3	131 (a_2, π_ψ*)	←	130 (a_1, $d\pi$)	0.641	2.53	489	20434	0.0012
	133 (e, π_ψ*)	←	130 (a_1, $d\pi$)	–0.280				
4	133 (e, π_ψ*)	←	128 (e, $d\pi$)	0.470	2.71	458	21852	0.0002
	132 (e, π_ψ*)	←	129 (e, $d\pi$)	0.498				
5	132 (e, π_ψ*)	←	128 (e, $d\pi$)	0.247	2.74	452	22125	0.0074
	131 (a_2, π_ψ*)	←	129 (e, $d\pi$)	0.608				
	133 (e, π_ψ*)	←	129 (e, $d\pi$)	0.241				
6	131 (a_2, π_ψ*)	←	128 (e, $d\pi$)	0.605	2.75	452	22145	0.0075
	133 (e, π_ψ*)	←	128 (e, $d\pi$)	–0.272				
	132 (e, π_ψ*)	←	129 (e, $d\pi$)	0.221				
7	131 (a_2, π_ψ*)	←	128 (e, $d\pi$)	0.295	2.89	429	23287	0.1104
	132 (e, π_ψ*)	←	128 (e, $d\pi$)	0.152				
	133 (e, π_ψ*)	←	128 (e, $d\pi$)	0.394				
	131 (a_2, π_ψ*)	←	129 (e, $d\pi$)	–0.159				
	132 (e, π_ψ*)	←	129 (e, $d\pi$)	–0.393				
	133 (e, π_ψ*)	←	129 (e, $d\pi$)	0.151				
8	131 (a_2, π_ψ*)	←	128 (e, $d\pi$)	–0.159	2.89	429	23288	0.1102
	132 (e, π_ψ*)	←	128 (e, $d\pi$)	0.395				
	133 (e, π_ψ*)	←	128 (e, $d\pi$)	–0.151				
	131 (a_2, π_ψ*)	←	129 (e, $d\pi$)	–0.292				
	132 (e, π_ψ*)	←	129 (e, $d\pi$)	0.151				
	133 (e, π_ψ*)	←	129 (e, $d\pi$)	0.394				
9	132 (e, π_ψ*)	←	128 (e, $d\pi$)	–0.432	3.11	398	25110	0.0000
	133 (e, π_ψ*)	←	129 (e, $d\pi$)	0.435				
	137	←	130 (a_1, $d\pi$)	0.261				
10	134	←	130 (a_1, $d\pi$)	0.698	3.37	368	27211	0.0079
11	134	←	129 (e, $d\pi$)	0.696	3.57	347	28793	0.0063
12	134	←	128 (e, $d\pi$)	0.696	3.57	347	28805	0.0063
13	135	←	130 (a_1, $d\pi$)	0.675	3.66	339	29507	0.0031
	143	←	130 (a_1, $d\pi$)	–0.124				
14	136	←	130 (a_1, $d\pi$)	0.675	3.66	339	29516	0.0032
	144	←	130 (a_1, $d\pi$)	0.124				
15	135	←	128 (e, $d\pi$)	–0.163	3.73	332	30120	0.0000
	139	←	128 (e, $d\pi$)	0.183				
	136	←	129 (e, $d\pi$)	–0.165				
	138	←	129 (e, $d\pi$)	–0.184				
	137	←	130 (a_1, $d\pi$)	0.578				
16	135	←	129 (e, $d\pi$)	0.102	3.77	329	30371	0.0146
	137	←	129 (e, $d\pi$)	–0.289				
	138	←	130 (a_1, $d\pi$)	0.612				
17	137	←	128 (e, $d\pi$)	0.294	3.77	329	30380	0.0152
	139	←	130 (a_1, $d\pi$)	0.616				
18	135	←	128 (e, $d\pi$)	0.210	3.81	325	30746	0.0025
	136	←	128 (e, $d\pi$)	0.103				
	143	←	128 (e, $d\pi$)	–0.193				
	144	←	128 (e, $d\pi$)	0.158				

excited state	orbital composition			coefficient	excitation			oscillator strength
					eV	nm	cm^{-1}	
	135	←	129 (e, $d\pi$)	0.112				
	136	←	129 (e, $d\pi$)	–0.200				
	143	←	129 (e, $d\pi$)	–0.163				
	144	←	129 (e, $d\pi$)	–0.184				
	135	←	130 (a_1, $d\pi$)	0.129				
	143	←	130 (a_1, $d\pi$)	0.470				
19	135	←	128 (e, $d\pi$)	–0.110	3.81	325	30759	0.0037
	136	←	128 (e, $d\pi$)	0.187				
	143	←	128 (e, $d\pi$)	0.160				
	144	←	128 (e, $d\pi$)	0.180				
	135	←	129 (e, $d\pi$)	0.210				
	136	←	129 (e, $d\pi$)	0.112				
	143	←	129 (e, $d\pi$)	–0.192				
	144	←	129 (e, $d\pi$)	0.163				
	136	←	130 (a_1, $d\pi$)	–0.124				
	144	←	130 (a_1, $d\pi$)	0.473				
20	136	←	128 (e, $d\pi$)	0.158	3.84	323	30980	0.0361
	137	←	129 (e, $d\pi$)	0.606				
	138	←	130 (a_1, $d\pi$)	0.250				
21	135	←	128 (e, $d\pi$)	–0.139	3.84	323	30990	0.0350
	137	←	128 (e, $d\pi$)	0.600				
	136	←	129 (e, $d\pi$)	0.112				
	139	←	130 (a_1, $d\pi$)	–0.247				
22	131 (a_2, π_ψ*)	←	125	–0.113	3.85	322	31024	0.0045
	135	←	128 (e, $d\pi$)	0.130				
	136	←	128 (e, $d\pi$)	–0.441				
	135	←	129 (e, $d\pi$)	0.456				
	136	←	129 (e, $d\pi$)	0.131				
23	135	←	128 (e, $d\pi$)	0.378	3.88	320	31296	0.0000
	136	←	128 (e, $d\pi$)	0.110				
	139	←	128 (e, $d\pi$)	0.256				
	135	←	129 (e, $d\pi$)	–0.120				
	136	←	129 (e, $d\pi$)	0.417				
	138	←	129 (e, $d\pi$)	–0.270				
24	136	←	128 (e, $d\pi$)	0.404	3.91	317	31505	0.0471
	138	←	128 (e, $d\pi$)	–0.143				
	144	←	128 (e, $d\pi$)	–0.115				
	135	←	129 (e, $d\pi$)	0.396				
	139	←	129 (e, $d\pi$)	0.135				
	143	←	129 (e, $d\pi$)	0.119				
	138	←	130 (a_1, $d\pi$)	–0.148				
	143	←	130 (a_1, $d\pi$)	–0.119				
	144	←	130 (a_1, $d\pi$)	–0.198				
25	135	←	128 (e, $d\pi$)	0.407	3.91	317	31516	0.0496
	137	←	128 (e, $d\pi$)	0.131				
	139	←	128 (e, $d\pi$)	0.151				
	143	←	128 (e, $d\pi$)	0.120				
	136	←	129 (e, $d\pi$)	–0.380				
	138	←	129 (e, $d\pi$)	0.126				
	144	←	129 (e, $d\pi$)	0.117				
	139	←	130 (a_1, $d\pi$)	–0.154				
	143	←	130 (a_1, $d\pi$)	–0.193				
	144	←	130 (a_1, $d\pi$)	0.120				

excited state	orbital composition			coefficient	excitation			oscillator strength
					eV	nm	cm^{-1}	
26	138	←	128 (e, $d\pi$)	0.354	3.94	315	31760	0.0025
	143	←	128 (e, $d\pi$)	–0.122				
	144	←	128 (e, $d\pi$)	–0.230				
	138	←	129 (e, $d\pi$)	–0.106				
	139	←	129 (e, $d\pi$)	0.423				
	143	←	129 (e, $d\pi$)	–0.238				
	144	←	129 (e, $d\pi$)	0.130				
27	131 (a_2, π_ψ*)	←	126	–0.117	3.95	314	31861	0.0021
	138	←	128 (e, $d\pi$)	–0.214				
	139	←	128 (e, $d\pi$)	0.404				
	138	←	129 (e, $d\pi$)	0.406				
	139	←	129 (e, $d\pi$)	0.199				
28	131 (a_2, π_ψ*)	←	127	0.116	3.95	314	31863	0.0024
	136	←	128 (e, $d\pi$)	0.102				
	138	←	128 (e, $d\pi$)	0.437				
	139	←	128 (e, $d\pi$)	0.215				
	138	←	129 (e, $d\pi$)	0.197				
	139	←	129 (e, $d\pi$)	–0.369				
29	131 (a_2, π_ψ*)	←	125	–0.104	3.99	311	32143	0.0002
	138	←	128 (e, $d\pi$)	0.243				
	143	←	128 (e, $d\pi$)	0.185				
	144	←	128 (e, $d\pi$)	0.347				
	139	←	129 (e, $d\pi$)	0.264				
	143	←	129 (e, $d\pi$)	0.343				
	144	←	129 (e, $d\pi$)	–0.186				
30	133 (e, π_ψ*)	←	125	0.151	4.26	291	34367	0.0029
	132 (e, π_ψ*)	←	126	–0.205				
	131 (a_2, π_ψ*)	←	127	0.613				
	133 (e, π_ψ*)	←	127	0.212				
31	132 (e, π_ψ*)	←	125	0.157	4.26	291	34376	0.0029
	131 (a_2, π_ψ*)	←	126	0.610				
	133 (e, π_ψ*)	←	126	–0.190				
	132 (e, π_ψ*)	←	127	–0.225				
32	133 (e, π_ψ*)	←	126	–0.215	4.27	291	34407	0.0000
	132 (e, π_ψ*)	←	127	0.186				
	135	←	128 (e, $d\pi$)	0.166				
	139	←	128 (e, $d\pi$)	–0.302				
	136	←	129 (e, $d\pi$)	0.164				
	138	←	129 (e, $d\pi$)	0.308				
	137	←	130 (a_1, $d\pi$)	0.235				
	140	←	130 (a_1, $d\pi$)	–0.127				
33	131 (a_2, π_ψ*)	←	125	0.580	4.30	288	34682	0.0026
	132 (e, π_ψ*)	←	126	0.295				
	133 (e, π_ψ*)	←	127	0.273				
34	133 (e, π_ψ*)	←	126	–0.430	4.33	286	34950	0.0001
	132 (e, π_ψ*)	←	127	0.480				
	139	←	128 (e, $d\pi$)	0.127				
	138	←	129 (e, $d\pi$)	–0.124				
	137	←	130 (a_1, $d\pi$)	–0.112				
35	132 (e, π_ψ*)	←	125	0.470	4.35	285	35079	0.0117
	131 (a_2, π_ψ*)	←	126	0.110				
	133 (e, π_ψ*)	←	126	0.390				
	132 (e, π_ψ*)	←	127	0.324				

excited state	orbital composition			coefficient	excitation			oscillator strength
					eV	nm	cm^{-1}	
36	133 (e, π_ψ*)	←	125	0.478	4.35	285	35096	0.0120
	132 (e, π_ψ*)	←	126	0.350				
	131 (a_2, π_ψ*)	←	127	0.112				
	133 (e, π_ψ*)	←	127	–0.357				
37	143	←	128 (e, $d\pi$)	0.314	4.49	276	36209	0.0001
	144	←	128 (e, $d\pi$)	–0.174				
	143	←	129 (e, $d\pi$)	0.172				
	144	←	129 (e, $d\pi$)	0.316				
	143	←	130 (a_1, $d\pi$)	0.364				
	144	←	130 (a_1, $d\pi$)	–0.112				
38	143	←	128 (e, $d\pi$)	–0.178	4.49	276	36237	0.0010
	144	←	128 (e, $d\pi$)	–0.319				
	143	←	129 (e, $d\pi$)	0.316				
	144	←	129 (e, $d\pi$)	–0.169				
	143	←	130 (a_1, $d\pi$)	0.108				
	144	←	130 (a_1, $d\pi$)	0.358				
39	132 (e, π_ψ*)	←	125	0.444	4.51	275	36336	0.2203
	131 (a_2, π_ψ*)	←	126	–0.208				
	133 (e, π_ψ*)	←	126	–0.228				
	134	←	126	–0.147				
	132 (e, π_ψ*)	←	127	–0.226				
	137	←	128 (e, $d\pi$)	0.112				
40	133 (e, π_ψ*)	←	125	0.442	4.51	275	36347	0.2208
	132 (e, π_ψ*)	←	126	–0.227				
	131 (a_2, π_ψ*)	←	127	–0.205				
	133 (e, π_ψ*)	←	127	0.230				
	134	←	127	–0.147				
	137	←	129 (e, $d\pi$)	–0.113				
41	131 (a_2, π_ψ*)	←	125	–0.306	4.59	270	37036	0.7776
	134	←	125	–0.103				
	132 (e, π_ψ*)	←	126	0.334				
	133 (e, π_ψ*)	←	127	0.336				
	136	←	128 (e, $d\pi$)	0.104				
	138	←	128 (e, $d\pi$)	–0.104				
	135	←	129 (e, $d\pi$)	–0.104				
	139	←	129 (e, $d\pi$)	–0.105				
42	143	←	128 (e, $d\pi$)	–0.393	4.64	267	37386	0.0000
	144	←	128 (e, $d\pi$)	0.216				
	143	←	129 (e, $d\pi$)	0.212				
	144	←	129 (e, $d\pi$)	0.401				
43	131 (a_2, π_ψ*)	←	123	0.126	4.99	249	40222	0.0292
	134	←	126	0.627				
	140	←	128 (e, $d\pi$)	–0.150				
44	131 (a_2, π_ψ*)	←	124	–0.125	4.99	249	40223	0.0293
	134	←	127	0.627				
	140	←	129 (e, $d\pi$)	0.150				
45	132 (e, π_ψ*)	←	123	–0.114	5.04	246	40613	0.0610
	133 (e, π_ψ*)	←	124	0.112				
	134	←	125	0.640				
	142	←	128 (e, $d\pi$)	0.102				
	141	←	129 (e, $d\pi$)	0.101				
46	140	←	130 (a_1, $d\pi$)	0.647	5.04	246	40638	0.0000
47	132 (e, π_ψ*)	←	122	0.134	5.09	244	41068	0.0005

excited state	orbital composition			coefficient	excitation			oscillator strength
					eV	nm	cm^{-1}	
	138	←	125	–0.128				
	137	←	126	0.210				
	141	←	130 (a_1, $d\pi$)	0.202				
	142	←	130 (a_1, $d\pi$)	–0.538				
48	133 (e, π_ψ*)	←	122	0.131	5.09	243	41069	0.0006
	139	←	125	0.126				
	137	←	127	0.215				
	141	←	130 (a_1, $d\pi$)	0.540				
	142	←	130 (a_1, $d\pi$)	0.202				
49	135	←	126	0.120	5.17	240	41660	0.0017
	134	←	127	–0.162				
	136	←	127	0.115				
	140	←	129 (e, $d\pi$)	0.620				
	142	←	130 (a_1, $d\pi$)	–0.184				
50	134	←	126	0.162	5.17	240	41671	0.0017
	136	←	126	0.110				
	135	←	127	–0.119				
	140	←	128 (e, $d\pi$)	0.621				
	141	←	130 (a_1, $d\pi$)	0.179				
51	131 (a_2, π_ψ*)	←	122	0.331	5.18	239	41771	0.0000
	133 (e, π_ψ*)	←	123	0.116				
	132 (e, π_ψ*)	←	124	0.119				
	137	←	125	–0.220				
	136	←	126	–0.248				
	138	←	126	0.197				
	135	←	127	–0.245				
	139	←	127	–0.196				
	141	←	128 (e, $d\pi$)	0.129				
	142	←	129 (e, $d\pi$)	–0.133				
	140	←	130 (a_1, $d\pi$)	0.172				
52	133 (e, π_ψ*)	←	122	0.244	5.23	237	42200	0.0078
	133 (e, π_ψ*)	←	123	–0.121				
	132 (e, π_ψ*)	←	124	0.114				
	135	←	125	0.181				
	138	←	126	0.158				
	137	←	127	0.332				
	139	←	127	0.162				
	141	←	128 (e, $d\pi$)	–0.159				
	142	←	129 (e, $d\pi$)	–0.156				
	141	←	130 (a_1, $d\pi$)	–0.305				
53	132 (e, π_ψ*)	←	122	0.252	5.23	237	42208	0.0084
	133 (e, π_ψ*)	←	124	0.125				
	136	←	125	0.179				
	137	←	126	0.334				
	139	←	126	–0.149				
	136	←	127	0.104				
	138	←	127	0.168				
	142	←	128 (e, $d\pi$)	–0.137				
	141	←	129 (e, $d\pi$)	0.173				
	142	←	130 (a_1, $d\pi$)	0.306				
54	132 (e, π_ψ*)	←	123	0.151	5.24	236	42289	0.0373
	133 (e, π_ψ*)	←	124	–0.132				
	134	←	125	0.202				

excited state	orbital composition			coefficient	excitation			oscillator strength
					eV	nm	cm^{-1}	
	135	←	126	0.359				
	139	←	126	–0.133				
	136	←	127	–0.349				
	138	←	127	–0.105				
	142	←	128 (e, $d\pi$)	–0.228				
	141	←	129 (e, $d\pi$)	–0.206				
55	132 (e, π_ψ*)	←	122	–0.140	5.26	236	42444	0.0248
	131 (a_2, π_ψ*)	←	124	–0.283				
	138	←	125	0.113				
	135	←	126	0.338				
	134	←	127	–0.102				
	136	←	127	0.334				
	142	←	128 (e, $d\pi$)	–0.103				
	140	←	129 (e, $d\pi$)	–0.240				
	141	←	129 (e, $d\pi$)	0.105				
	142	←	130 (a_1, $d\pi$)	–0.128				
56	133 (e, π_ψ*)	←	122	0.146	5.26	236	42453	0.0247
	131 (a_2, π_ψ*)	←	123	0.283				
	139	←	125	0.114				
	136	←	126	–0.340				
	135	←	127	0.340				
	140	←	128 (e, $d\pi$)	0.239				
	141	←	130 (a_1, $d\pi$)	–0.132				
57	135	←	125	0.392	5.29	234	42704	0.0004
	137	←	125	–0.158				
	138	←	126	0.108				
	135	←	127	0.344				
	137	←	127	–0.333				
	141	←	128 (e, $d\pi$)	–0.129				
	142	←	129 (e, $d\pi$)	–0.164				
58	136	←	125	0.430	5.30	234	42720	0.0003
	135	←	126	–0.171				
	137	←	126	–0.394				
	136	←	127	–0.191				
	142	←	128 (e, $d\pi$)	–0.163				
	141	←	129 (e, $d\pi$)	0.167				
59	131 (a_2, π_ψ*)	←	122	0.113	5.30	234	42729	0.0001
	135	←	125	–0.180				
	137	←	125	–0.361				
	135	←	126	–0.105				
	136	←	126	0.417				
	135	←	127	0.243				
	137	←	127	0.181				
	139	←	127	–0.119				
	141	←	128 (e, $d\pi$)	0.104				
60	131 (a_2, π_ψ*)	←	118	0.116	5.33	233	42977	0.0000
	131 (a_2, π_ψ*)	←	122	0.262				
	141	←	128 (e, $d\pi$)	–0.419				
	142	←	129 (e, $d\pi$)	0.464				
61	132 (e, π_ψ*)	←	122	–0.156	5.34	232	43042	0.0004
	132 (e, π_ψ*)	←	123	–0.104				
	131 (a_2, π_ψ*)	←	124	0.191				
	133 (e, π_ψ*)	←	124	–0.131				

excited state	orbital composition			coefficient	excitation			oscillator strength
					eV	nm	cm^{-1}	
	136	←	125	–0.198				
	141	←	128 (e, $d\pi$)	0.137				
	142	←	128 (e, $d\pi$)	–0.354				
	141	←	129 (e, $d\pi$)	0.403				
	142	←	129 (e, $d\pi$)	0.128				
62	133 (e, π_ψ*)	←	122	0.153	5.34	232	43044	0.0002
	131 (a_2, π_ψ*)	←	123	–0.189				
	133 (e, π_ψ*)	←	123	–0.122				
	132 (e, π_ψ*)	←	124	0.117				
	135	←	125	0.195				
	141	←	128 (e, $d\pi$)	0.405				
	142	←	128 (e, $d\pi$)	0.122				
	141	←	129 (e, $d\pi$)	–0.141				
	142	←	129 (e, $d\pi$)	0.355				
63	132 (e, π_ψ*)	←	123	0.197	5.34	232	43101	0.0380
	133 (e, π_ψ*)	←	124	–0.183				
	135	←	126	0.153				
	136	←	127	–0.152				
	142	←	128 (e, $d\pi$)	0.446				
	141	←	129 (e, $d\pi$)	0.389				
64	135	←	126	0.166	5.41	229	43595	0.0103
	139	←	126	0.422				
	136	←	127	–0.166				
	138	←	127	0.479				
65	135	←	125	–0.349	5.42	229	43681	0.0013
	138	←	126	0.381				
	139	←	126	0.128				
	137	←	127	–0.243				
	138	←	127	–0.103				
	139	←	127	0.361				
66	136	←	125	0.350	5.42	229	43685	0.0013
	137	←	126	0.237				
	138	←	126	–0.127				
	139	←	126	0.401				
	138	←	127	–0.341				
	139	←	127	–0.106				
67	131 (a_2, π_ψ*)	←	118	0.177	5.43	228	43774	0.0000
	131 (a_2, π_ψ*)	←	122	0.190				
	137	←	125	0.475				
	136	←	126	0.122				
	138	←	126	0.255				
	135	←	127	0.132				
	139	←	127	–0.282				
68	132 (e, π_ψ*)	←	118	–0.152	5.44	228	43867	0.0209
	132 (e, π_ψ*)	←	122	–0.244				
	131 (a_2, π_ψ*)	←	124	–0.122				
	138	←	125	0.479				
	135	←	126	–0.179				
	137	←	126	0.265				
	136	←	127	–0.169				
69	131 (a_2, π_ψ*)	←	118	0.156	5.44	228	43877	0.0174
	133 (e, π_ψ*)	←	118	0.139				
	131 (a_2, π_ψ*)	←	122	0.122				

excited state	orbital composition			coefficient	excitation			oscillator strength
					eV	nm	cm^{-1}	
	133 (e, π_ψ*)	←	122	0.222				
	131 (a_2, π_ψ*)	←	123	0.107				
	139	←	125	0.444				
	136	←	126	0.147				
	138	←	126	–0.165				
	135	←	127	–0.155				
	137	←	127	–0.254				
70	131 (a_2, π_ψ*)	←	118	0.359	5.44	228	43888	0.0030
	131 (a_2, π_ψ*)	←	122	0.268				
	133 (e, π_ψ*)	←	123	–0.147				
	132 (e, π_ψ*)	←	124	–0.139				
	139	←	125	–0.189				
	138	←	126	–0.180				
	137	←	127	0.103				
	139	←	127	0.250				
	141	←	128 (e, $d\pi$)	0.137				
	142	←	129 (e, $d\pi$)	–0.116				
71	131 (a_2, π_ψ*)	←	116	0.121	5.47	227	44121	0.0080
	132 (e, π_ψ*)	←	118	0.326				
	132 (e, π_ψ*)	←	122	0.372				
	131 (a_2, π_ψ*)	←	124	–0.224				
	138	←	125	0.269				
72	131 (a_2, π_ψ*)	←	115	–0.121	5.47	227	44129	0.0080
	133 (e, π_ψ*)	←	118	0.328				
	133 (e, π_ψ*)	←	122	0.377				
	131 (a_2, π_ψ*)	←	123	–0.222				
	139	←	125	–0.267				
73	132 (e, π_ψ*)	←	118	0.123	5.53	224	44627	0.0595
	132 (e, π_ψ*)	←	123	0.264				
	131 (a_2, π_ψ*)	←	124	0.454				
	133 (e, π_ψ*)	←	124	0.261				
	138	←	125	0.267				
74	133 (e, π_ψ*)	←	118	0.124	5.53	224	44640	0.0603
	131 (a_2, π_ψ*)	←	123	0.452				
	133 (e, π_ψ*)	←	123	–0.253				
	132 (e, π_ψ*)	←	124	0.275				
	139	←	125	–0.265				
75	131 (a_2, π_ψ*)	←	118	0.242	5.59	222	45055	0.0001
	133 (e, π_ψ*)	←	123	0.438				
	132 (e, π_ψ*)	←	124	0.443				
76	132 (e, π_ψ*)	←	113	–0.119	5.59	222	45072	0.0322
	133 (e, π_ψ*)	←	114	–0.116				
	132 (e, π_ψ*)	←	115	0.100				
	131 (a_2, π_ψ*)	←	119	–0.285				
	132 (e, π_ψ*)	←	121	0.101				
	132 (e, π_ψ*)	←	123	0.360				
	133 (e, π_ψ*)	←	124	–0.340				
	135	←	126	–0.135				
	136	←	127	0.129				
77	131 (a_2, π_ψ*)	←	113	–0.101	5.60	221	45201	0.0083
	131 (a_2, π_ψ*)	←	115	0.115				
	132 (e, π_ψ*)	←	119	–0.215				
	131 (a_2, π_ψ*)	←	121	0.184				

excited state	orbital composition			coefficient	excitation			oscillator strength
					eV	nm	cm^{-1}	
	131 (a_2, π_ψ*)	←	123	0.173				
	133 (e, π_ψ*)	←	123	0.327				
	132 (e, π_ψ*)	←	124	–0.304				
	135	←	125	0.157				
	139	←	125	–0.145				
78	131 (a_2, π_ψ*)	←	114	–0.104	5.61	221	45207	0.0090
	131 (a_2, π_ψ*)	←	116	0.112				
	133 (e, π_ψ*)	←	119	–0.216				
	131 (a_2, π_ψ*)	←	120	0.181				
	132 (e, π_ψ*)	←	123	0.307				
	131 (a_2, π_ψ*)	←	124	–0.172				
	133 (e, π_ψ*)	←	124	0.326				
	136	←	125	–0.156				
	138	←	125	–0.145				
79	133 (e, π_ψ*)	←	118	–0.121	5.68	218	45781	0.0026
	131 (a_2, π_ψ*)	←	121	0.593				
	131 (a_2, π_ψ*)	←	123	–0.116				
80	132 (e, π_ψ*)	←	118	0.121	5.68	218	45784	0.0028
	131 (a_2, π_ψ*)	←	120	0.592				
	131 (a_2, π_ψ*)	←	124	0.113				
81	131 (a_2, π_ψ*)	←	117	–0.198	5.71	217	46089	0.0000
	131 (a_2, π_ψ*)	←	118	0.371				
	132 (e, π_ψ*)	←	120	0.174				
	133 (e, π_ψ*)	←	121	–0.177				
	131 (a_2, π_ψ*)	←	122	–0.310				
	137	←	125	–0.132				
	138	←	126	0.137				
	139	←	127	–0.137				
82	133 (e, π_ψ*)	←	118	0.346	5.75	216	46383	0.0254
	132 (e, π_ψ*)	←	120	0.286				
	131 (a_2, π_ψ*)	←	121	0.211				
	133 (e, π_ψ*)	←	121	0.308				
	133 (e, π_ψ*)	←	122	–0.252				
	139	←	125	0.101				
83	132 (e, π_ψ*)	←	113	0.100	5.75	216	46386	0.0265
	132 (e, π_ψ*)	←	118	0.364				
	131 (a_2, π_ψ*)	←	120	–0.214				
	133 (e, π_ψ*)	←	120	0.257				
	132 (e, π_ψ*)	←	121	–0.300				
	132 (e, π_ψ*)	←	122	–0.258				
	138	←	125	–0.104				
84	132 (e, π_ψ*)	←	112	0.114	5.76	215	46450	0.0003
	131 (a_2, π_ψ*)	←	113	0.508				
	133 (e, π_ψ*)	←	113	0.180				
	132 (e, π_ψ*)	←	114	0.176				
	131 (a_2, π_ψ*)	←	115	–0.117				
	132 (e, π_ψ*)	←	116	–0.107				
	132 (e, π_ψ*)	←	120	–0.131				
	131 (a_2, π_ψ*)	←	121	0.130				
	133 (e, π_ψ*)	←	122	–0.105				
	132 (e, π_ψ*)	←	124	–0.103				
85	133 (e, π_ψ*)	←	112	0.112	5.76	215	46452	0.0003
	132 (e, π_ψ*)	←	113	0.183				

excited state	orbital composition			coefficient	excitation			oscillator strength
					eV	nm	cm^{-1}	
	131 (a_2, π_ψ*)	←	114	0.503				
	133 (e, π_ψ*)	←	114	–0.169				
	132 (e, π_ψ*)	←	115	–0.103				
	131 (a_2, π_ψ*)	←	116	–0.105				
	131 (a_2, π_ψ*)	←	120	0.130				
	132 (e, π_ψ*)	←	121	–0.128				
	132 (e, π_ψ*)	←	122	0.112				
	132 (e, π_ψ*)	←	123	0.103				
86	131 (a_2, π_ψ*)	←	118	–0.211	5.77	215	46498	0.0000
	132 (e, π_ψ*)	←	120	0.431				
	133 (e, π_ψ*)	←	121	–0.395				
	131 (a_2, π_ψ*)	←	122	0.136				
	134	←	122	0.117				
87	133 (e, π_ψ*)	←	114	–0.138	5.77	215	46562	0.0005
	131 (a_2, π_ψ*)	←	119	0.205				
	133 (e, π_ψ*)	←	120	0.414				
	132 (e, π_ψ*)	←	121	0.481				
88	132 (e, π_ψ*)	←	113	–0.180	5.78	214	46640	0.0100
	133 (e, π_ψ*)	←	114	0.117				
	131 (a_2, π_ψ*)	←	116	0.148				
	132 (e, π_ψ*)	←	118	–0.311				
	133 (e, π_ψ*)	←	120	0.410				
	132 (e, π_ψ*)	←	121	–0.292				
	132 (e, π_ψ*)	←	122	0.186				
89	133 (e, π_ψ*)	←	113	0.150	5.78	214	46648	0.0122
	132 (e, π_ψ*)	←	114	0.144				
	131 (a_2, π_ψ*)	←	115	–0.147				
	133 (e, π_ψ*)	←	118	–0.337				
	132 (e, π_ψ*)	←	120	0.322				
	133 (e, π_ψ*)	←	121	0.365				
	133 (e, π_ψ*)	←	122	0.205				
90	131 (a_2, π_ψ*)	←	112	0.139	5.81	213	46852	0.0005
	132 (e, π_ψ*)	←	113	0.403				
	133 (e, π_ψ*)	←	114	0.414				
	132 (e, π_ψ*)	←	115	–0.131				
	133 (e, π_ψ*)	←	116	–0.126				
	133 (e, π_ψ*)	←	120	0.162				
	132 (e, π_ψ*)	←	121	0.136				
	132 (e, π_ψ*)	←	123	0.116				
	133 (e, π_ψ*)	←	124	–0.119				
91	131 (a_2, π_ψ*)	←	119	0.574	5.87	211	47372	0.0044
	133 (e, π_ψ*)	←	120	–0.108				
	132 (e, π_ψ*)	←	121	–0.106				
	132 (e, π_ψ*)	←	123	0.104				
	133 (e, π_ψ*)	←	124	–0.102				
	135	←	126	–0.120				
	136	←	127	0.119				
92	133 (e, π_ψ*)	←	115	0.101	5.89	210	47515	0.0000
	132 (e, π_ψ*)	←	116	–0.106				
	131 (a_2, π_ψ*)	←	117	0.631				
	131 (a_2, π_ψ*)	←	122	–0.134				
	134	←	122	–0.118				
93	131 (a_2, π_ψ*)	←	113	0.107	5.92	209	47767	0.0030

excited state	orbital composition			coefficient	excitation			oscillator strength
					eV	nm	cm^{-1}	
	133 (e, π_ψ*)	←	113	–0.205				
	132 (e, π_ψ*)	←	114	–0.235				
	131 (a_2, π_ψ*)	←	115	–0.139				
	132 (e, π_ψ*)	←	116	0.101				
	133 (e, π_ψ*)	←	118	–0.136				
	132 (e, π_ψ*)	←	119	0.503				
94	132 (e, π_ψ*)	←	113	–0.225	5.92	209	47787	0.0034
	131 (a_2, π_ψ*)	←	114	0.114				
	133 (e, π_ψ*)	←	114	0.238				
	132 (e, π_ψ*)	←	115	0.105				
	131 (a_2, π_ψ*)	←	116	–0.155				
	133 (e, π_ψ*)	←	116	–0.107				
	132 (e, π_ψ*)	←	118	0.143				
	133 (e, π_ψ*)	←	119	0.482				
95	132 (e, π_ψ*)	←	113	0.175	5.95	208	48024	0.0056
	131 (a_2, π_ψ*)	←	114	–0.113				
	133 (e, π_ψ*)	←	114	–0.170				
	131 (a_2, π_ψ*)	←	115	–0.105				
	131 (a_2, π_ψ*)	←	116	0.341				
	132 (e, π_ψ*)	←	117	–0.245				
	132 (e, π_ψ*)	←	118	–0.157				
	133 (e, π_ψ*)	←	119	0.377				
96	131 (a_2, π_ψ*)	←	113	–0.102	5.96	208	48038	0.0061
	133 (e, π_ψ*)	←	113	0.173				
	132 (e, π_ψ*)	←	114	0.195				
	131 (a_2, π_ψ*)	←	115	0.354				
	133 (e, π_ψ*)	←	115	–0.101				
	131 (a_2, π_ψ*)	←	116	0.111				
	132 (e, π_ψ*)	←	116	–0.103				
	133 (e, π_ψ*)	←	117	0.252				
	133 (e, π_ψ*)	←	118	0.158				
	132 (e, π_ψ*)	←	119	0.348				
97	132 (e, π_ψ*)	←	113	0.171	5.96	208	48100	0.0039
	131 (a_2, π_ψ*)	←	114	–0.211				
	133 (e, π_ψ*)	←	114	–0.164				
	132 (e, π_ψ*)	←	117	0.568				
	133 (e, π_ψ*)	←	119	0.122				
98	131 (a_2, π_ψ*)	←	113	0.209	5.97	208	48119	0.0042
	133 (e, π_ψ*)	←	113	–0.161				
	132 (e, π_ψ*)	←	114	–0.179				
	133 (e, π_ψ*)	←	117	0.565				
	132 (e, π_ψ*)	←	119	–0.129				
99	133 (e, π_ψ*)	←	113	0.443	5.98	207	48223	0.0001
	132 (e, π_ψ*)	←	114	–0.416				
	133 (e, π_ψ*)	←	115	–0.195				
	132 (e, π_ψ*)	←	116	0.179				
	131 (a_2, π_ψ*)	←	118	–0.181				
100	131 (a_2, π_ψ*)	←	114	0.290	6.04	205	48697	0.0269
	132 (e, π_ψ*)	←	115	0.207				
	133 (e, π_ψ*)	←	115	0.107				
	131 (a_2, π_ψ*)	←	116	0.435				
	132 (e, π_ψ*)	←	116	0.112				
	133 (e, π_ψ*)	←	116	–0.194				

excited state	orbital composition			coefficient	excitation			oscillator strength
					eV	nm	cm^{-1}	
	132 (e, π_ψ*)	←	117	0.183				
101	131 (a_2, π_ψ*)	←	113	0.295	6.04	205	48704	0.0254
	131 (a_2, π_ψ*)	←	115	0.429				
	132 (e, π_ψ*)	←	115	–0.111				
	133 (e, π_ψ*)	←	115	0.205				
	132 (e, π_ψ*)	←	116	0.206				
	133 (e, π_ψ*)	←	116	0.110				
	133 (e, π_ψ*)	←	117	–0.182				
102	132 (e, π_ψ*)	←	113	0.175	6.09	204	49091	0.0001
	133 (e, π_ψ*)	←	114	0.166				
	132 (e, π_ψ*)	←	115	0.426				
	133 (e, π_ψ*)	←	115	–0.156				
	132 (e, π_ψ*)	←	116	0.155				
	133 (e, π_ψ*)	←	116	0.432				
103	133 (e, π_ψ*)	←	113	0.150	6.11	203	49240	0.0006
	132 (e, π_ψ*)	←	114	–0.189				
	132 (e, π_ψ*)	←	115	0.124				
	133 (e, π_ψ*)	←	115	0.272				
	132 (e, π_ψ*)	←	116	–0.340				
	134	←	117	0.136				
	134	←	122	0.357				
104	132 (e, π_ψ*)	←	113	–0.187	6.11	203	49310	0.0460
	133 (e, π_ψ*)	←	114	0.185				
	132 (e, π_ψ*)	←	115	–0.340				
	133 (e, π_ψ*)	←	116	0.355				
	132 (e, π_ψ*)	←	117	0.106				
	134	←	120	0.199				
	134	←	124	–0.118				
105	133 (e, π_ψ*)	←	113	0.207	6.11	203	49311	0.0455
	132 (e, π_ψ*)	←	114	0.167				
	133 (e, π_ψ*)	←	115	0.372				
	132 (e, π_ψ*)	←	116	0.315				
	133 (e, π_ψ*)	←	117	0.107				
	134	←	121	–0.198				
	134	←	123	–0.124				
106	145	←	130 (a_1, $d\pi$)	0.703	6.15	202	49573	0.0024
107	133 (e, π_ψ*)	←	115	–0.151	6.19	200	49949	0.0000
	132 (e, π_ψ*)	←	116	0.148				
	134	←	118	0.377				
	135	←	120	0.101				
	136	←	121	0.101				
	134	←	122	0.422				
108	134	←	124	0.644	6.22	199	50151	0.0174
109	134	←	123	0.643	6.22	199	50160	0.0167
110	147	←	130 (a_1, $d\pi$)	0.699	6.26	198	50455	0.0001
111	146	←	130 (a_1, $d\pi$)	0.699	6.26	198	50456	0.0001
112	145	←	129 (e, $d\pi$)	0.703	6.32	196	51003	0.0019
113	145	←	128 (e, $d\pi$)	0.703	6.33	196	51017	0.0018
114	134	←	113	–0.122	6.38	194	51493	0.0175
	134	←	114	0.104				
	135	←	118	–0.171				
	136	←	118	0.129				
	134	←	120	–0.195				

excited state	orbital composition			coefficient	excitation			oscillator strength
					eV	nm	cm^{-1}	
	134	←	121	0.236				
	135	←	122	–0.341				
	136	←	122	0.256				
	140	←	127	0.117				
115	134	←	113	–0.105	6.38	194	51494	0.0173
	134	←	114	–0.123				
	135	←	118	0.130				
	136	←	118	0.170				
	134	←	120	0.232				
	134	←	121	0.198				
	135	←	122	0.261				
	136	←	122	0.338				
	140	←	126	–0.118				
116	135	←	113	–0.121	6.40	194	51589	0.0020
	136	←	114	0.135				
	137	←	118	0.256				
	134	←	119	–0.267				
	137	←	122	0.483				
	135	←	123	–0.138				
	136	←	124	–0.152				
117	134	←	117	0.205	6.41	193	51696	0.0000
	134	←	118	0.477				
	135	←	120	–0.102				
	136	←	121	–0.106				
	134	←	122	–0.281				
	140	←	125	–0.172				
	142	←	126	0.112				
	141	←	127	–0.117				
118	146	←	128 (e, $d\pi$)	–0.266	6.43	193	51832	0.0006
	147	←	129 (e, $d\pi$)	0.645				
119	147	←	128 (e, $d\pi$)	–0.357	6.43	193	51844	0.0017
	146	←	129 (e, $d\pi$)	0.597				
120	146	←	128 (e, $d\pi$)	0.644	6.43	193	51847	0.0018
	147	←	129 (e, $d\pi$)	0.265				

Table 0-2 – TDDFT Calculated Excitation Energies, One–Electron Transitions, and Oscillator Strengths for Optical Transitions of $[Ru(bpy)_2(dmpbpy)]^{2+}$ complex in the Gas Phase.

excited state	orbital composition			coefficient	excitation			oscillator strength
					eV	nm	cm^{-1}	
1	169 (b, π_ψ*)	←	168 (a, $d\pi$)	0.516	2.47	502	19909	0.0005
	170 (b, π_ψ*)	←	168 (a, $d\pi$)	0.454				
2	169 (b, π_ψ*)	←	168 (a, $d\pi$)	–0.387	2.51	493	20270	0.0006
	170 (b, π_ψ*)	←	168 (a, $d\pi$)	0.492				
	171 (a, π_ψ*)	←	168 (a, $d\pi$)	0.302				
3	169 (b, π_ψ*)	←	168 (a, $d\pi$)	0.270	2.58	481	20769	0.0015
	170 (b, π_ψ*)	←	168 (a, $d\pi$)	–0.174				
	171 (a, π_ψ*)	←	168 (a, $d\pi$)	0.615				
4	169 (b, π_ψ*)	←	166 (a, $d\pi$)	–0.219	2.66	466	21441	0.0010
	171 (a, π_ψ*)	←	166 (a, $d\pi$)	0.171				
	169 (b, π_ψ*)	←	167 (a, $d\pi$)	0.443				
	170 (b, π_ψ*)	←	167 (a, $d\pi$)	0.447				
5	169 (b, π_ψ*)	←	166 (a, $d\pi$)	0.187	2.71	457	21888	0.0079
	170 (b, π_ψ*)	←	166 (a, $d\pi$)	–0.239				
	171 (a, π_ψ*)	←	166 (a, $d\pi$)	–0.214				
	169 (b, π_ψ*)	←	167 (a, $d\pi$)	0.475				
	170 (b, π_ψ*)	←	167 (a, $d\pi$)	–0.319				
	171 (a, π_ψ*)	←	167 (a, $d\pi$)	–0.145				
6	169 (b, π_ψ*)	←	166 (a, $d\pi$)	0.503	2.78	446	22441	0.0188
	170 (b, π_ψ*)	←	166 (a, $d\pi$)	–0.191				
	171 (a, π_ψ*)	←	166 (a, $d\pi$)	0.429				
7	169 (b, π_ψ*)	←	166 (a, $d\pi$)	0.365	2.86	434	23039	0.1032
	170 (b, π_ψ*)	←	166 (a, $d\pi$)	0.235				
	171 (a, π_ψ*)	←	166 (a, $d\pi$)	–0.367				
	170 (b, π_ψ*)	←	167 (a, $d\pi$)	0.290				
	171 (a, π_ψ*)	←	167 (a, $d\pi$)	0.234				
8	170 (b, π_ψ*)	←	166 (a, $d\pi$)	0.368	2.88	430	23263	0.1383
	171 (a, π_ψ*)	←	166 (a, $d\pi$)	0.284				
	169 (b, π_ψ*)	←	167 (a, $d\pi$)	0.225				
	170 (b, π_ψ*)	←	167 (a, $d\pi$)	–0.278				
	171 (a, π_ψ*)	←	167 (a, $d\pi$)	0.353				
9	170 (b, π_ψ*)	←	166 (a, $d\pi$)	–0.379	3.10	400	24993	0.0038
	171 (a, π_ψ*)	←	167 (a, $d\pi$)	0.470				
	175	←	168 (a, $d\pi$)	0.248				
10	172	←	168 (a, $d\pi$)	0.698	3.35	370	27000	0.0093
11	172	←	167 (a, $d\pi$)	0.695	3.53	352	28445	0.0085
12	172	←	166 (a, $d\pi$)	0.691	3.56	349	28691	0.0070
13	173	←	168 (a, $d\pi$)	0.567	3.62	342	29220	0.0062
	174	←	168 (a, $d\pi$)	–0.372				
14	173	←	168 (a, $d\pi$)	0.369	3.64	341	29350	0.0109
	174	←	168 (a, $d\pi$)	0.538				
	175	←	168 (a, $d\pi$)	–0.199				
15	174	←	166 (a, $d\pi$)	–0.180	3.70	335	29821	0.0016
	176	←	166 (a, $d\pi$)	–0.151				
	174	←	167 (a, $d\pi$)	–0.126				
	175	←	167 (a, $d\pi$)	–0.159				
	177	←	167 (a, $d\pi$)	–0.165				
	174	←	168 (a, $d\pi$)	0.155				
	175	←	168 (a, $d\pi$)	0.521				
	177	←	168 (a, $d\pi$)	0.167				

excited state	orbital composition		coefficient	excitation			oscillator strength
				eV	nm	cm^{-1}	
16	175	← 166 (a, $d\pi$)	–0.200	3.73	333	30067	0.0252
	176	← 168 (a, $d\pi$)	0.623				
	177	← 168 (a, $d\pi$)	0.134				
17	175	← 166 (a, $d\pi$)	0.115	3.74	331	30200	0.0044
	176	← 166 (a, $d\pi$)	0.103				
	173	← 167 (a, $d\pi$)	0.173				
	175	← 167 (a, $d\pi$)	–0.301				
	175	← 168 (a, $d\pi$)	–0.151				
	176	← 168 (a, $d\pi$)	–0.113				
	177	← 168 (a, $d\pi$)	0.502				
18	174	← 166 (a, $d\pi$)	–0.132	3.79	327	30599	0.0250
	173	← 167 (a, $d\pi$)	0.300				
	175	← 167 (a, $d\pi$)	0.518				
	177	← 168 (a, $d\pi$)	0.235				
	182	← 168 (a, $d\pi$)	0.127				
19	174	← 166 (a, $d\pi$)	–0.146	3.81	326	30702	0.0275
	175	← 166 (a, $d\pi$)	–0.111				
	173	← 167 (a, $d\pi$)	–0.251				
	174	← 167 (a, $d\pi$)	0.473				
	181	← 167 (a, $d\pi$)	0.103				
	182	← 167 (a, $d\pi$)	0.108				
	177	← 168 (a, $d\pi$)	0.262				
	182	← 168 (a, $d\pi$)	–0.188				
20	173	← 166 (a, $d\pi$)	0.201	3.81	326	30709	0.0170
	174	← 166 (a, $d\pi$)	–0.185				
	175	← 166 (a, $d\pi$)	–0.111				
	181	← 166 (a, $d\pi$)	–0.126				
	173	← 167 (a, $d\pi$)	0.347				
	174	← 167 (a, $d\pi$)	0.173				
	175	← 167 (a, $d\pi$)	–0.186				
	181	← 167 (a, $d\pi$)	–0.120				
	182	← 167 (a, $d\pi$)	0.111				
	177	← 168 (a, $d\pi$)	–0.184				
	181	← 168 (a, $d\pi$)	–0.337				
21	174	← 166 (a, $d\pi$)	0.174	3.81	325	30763	0.0560
	175	← 166 (a, $d\pi$)	0.545				
	174	← 167 (a, $d\pi$)	0.121				
	175	← 167 (a, $d\pi$)	0.106				
	182	← 167 (a, $d\pi$)	0.150				
	176	← 168 (a, $d\pi$)	0.188				
	181	← 168 (a, $d\pi$)	–0.107				
	182	← 168 (a, $d\pi$)	–0.119				
22	173	← 166 (a, $d\pi$)	0.537	3.83	324	30878	0.0048
	174	← 166 (a, $d\pi$)	0.204				
	175	← 166 (a, $d\pi$)	–0.120				
	182	← 166 (a, $d\pi$)	0.105				
	174	← 167 (a, $d\pi$)	–0.172				
	182	← 168 (a, $d\pi$)	–0.189				
23	174	← 166 (a, $d\pi$)	0.234	3.83	324	30899	0.0020
	175	← 166 (a, $d\pi$)	–0.118				
	176	← 166 (a, $d\pi$)	–0.120				
	182	← 166 (a, $d\pi$)	0.185				
	173	← 167 (a, $d\pi$)	0.346				

excited state	orbital composition			coefficient	excitation			oscillator strength
					eV	nm	cm^{-1}	
	174	←	167 (a, $d\pi$)	0.197				
	175	←	167 (a, $d\pi$)	–0.106				
	177	←	167 (a, $d\pi$)	–0.234				
	181	←	167 (a, $d\pi$)	0.129				
	181	←	168 (a, $d\pi$)	0.278				
	182	←	168 (a, $d\pi$)	–0.162				
24	173	←	166 (a, $d\pi$)	0.291	3.88	319	31300	0.0339
	174	←	166 (a, $d\pi$)	–0.120				
	175	←	166 (a, $d\pi$)	0.127				
	176	←	166 (a, $d\pi$)	0.121				
	181	←	166 (a, $d\pi$)	0.133				
	174	←	167 (a, $d\pi$)	0.227				
	176	←	167 (a, $d\pi$)	0.365				
	182	←	167 (a, $d\pi$)	–0.186				
	176	←	168 (a, $d\pi$)	0.122				
	181	←	168 (a, $d\pi$)	0.167				
	182	←	168 (a, $d\pi$)	0.189				
25	173	←	166 (a, $d\pi$)	–0.146	3.89	319	31389	0.0156
	176	←	166 (a, $d\pi$)	–0.115				
	177	←	166 (a, $d\pi$)	0.119				
	181	←	166 (a, $d\pi$)	–0.123				
	182	←	166 (a, $d\pi$)	0.139				
	174	←	167 (a, $d\pi$)	–0.138				
	176	←	167 (a, $d\pi$)	0.488				
	177	←	167 (a, $d\pi$)	0.175				
	176	←	168 (a, $d\pi$)	–0.106				
	182	←	168 (a, $d\pi$)	–0.234				
26	174	←	166 (a, $d\pi$)	0.368	3.90	318	31440	0.0165
	175	←	166 (a, $d\pi$)	–0.163				
	176	←	166 (a, $d\pi$)	–0.288				
	177	←	166 (a, $d\pi$)	–0.162				
	173	←	167 (a, $d\pi$)	–0.138				
	174	←	167 (a, $d\pi$)	0.110				
	176	←	167 (a, $d\pi$)	0.133				
	181	←	167 (a, $d\pi$)	–0.230				
	181	←	168 (a, $d\pi$)	–0.212				
	182	←	168 (a, $d\pi$)	0.157				
27	169 (b, π_ψ*)	←	165	0.128	3.92	316	31655	0.0128
	171 (a, π_ψ*)	←	165	0.124				
	174	←	166 (a, $d\pi$)	0.119				
	176	←	166 (a, $d\pi$)	0.392				
	177	←	166 (a, $d\pi$)	0.215				
	176	←	167 (a, $d\pi$)	0.107				
	177	←	167 (a, $d\pi$)	–0.375				
28	176	←	166 (a, $d\pi$)	–0.171	3.95	314	31881	0.0041
	177	←	166 (a, $d\pi$)	0.587				
	181	←	166 (a, $d\pi$)	0.127				
	182	←	166 (a, $d\pi$)	–0.104				
	177	←	167 (a, $d\pi$)	0.167				
29	169 (b, π_ψ*)	←	164	0.149	3.98	312	32096	0.0662
	169 (b, π_ψ*)	←	165	0.449				
	170 (b, π_ψ*)	←	165	–0.215				
	171 (a, π_ψ*)	←	165	0.219				

excited state	orbital composition			coefficient	excitation			oscillator strength
					eV	nm	cm^{-1}	
	177	←	166 (a, $d\pi$)	–0.155				
	181	←	166 (a, $d\pi$)	0.119				
	182	←	166 (a, $d\pi$)	–0.152				
	181	←	167 (a, $d\pi$)	0.192				
	182	←	167 (a, $d\pi$)	0.125				
30	169 (b, π_ψ*)	←	165	0.232	4.00	310	32243	0.0191
	170 (b, π_ψ*)	←	165	–0.105				
	181	←	166 (a, $d\pi$)	–0.231				
	182	←	166 (a, $d\pi$)	0.347				
	176	←	167 (a, $d\pi$)	–0.201				
	181	←	167 (a, $d\pi$)	–0.299				
	182	←	167 (a, $d\pi$)	–0.227				
31	169 (b, π_ψ*)	←	162	0.477	4.03	308	32473	0.0027
	170 (b, π_ψ*)	←	162	–0.278				
	171 (a, π_ψ*)	←	162	0.390				
	169 (b, π_ψ*)	←	164	–0.134				
32	169 (b, π_ψ*)	←	162	0.130	4.05	306	32657	0.0176
	169 (b, π_ψ*)	←	164	0.534				
	170 (b, π_ψ*)	←	164	–0.147				
	171 (a, π_ψ*)	←	164	0.250				
	171 (a, π_ψ*)	←	165	–0.269				
33	169 (b, π_ψ*)	←	161	–0.144	4.08	304	32880	0.0429
	171 (a, π_ψ*)	←	164	0.306				
	169 (b, π_ψ*)	←	165	–0.308				
	171 (a, π_ψ*)	←	165	0.509				
34	169 (b, π_ψ*)	←	163	0.522	4.08	304	32912	0.0030
	170 (b, π_ψ*)	←	163	–0.176				
	171 (a, π_ψ*)	←	163	0.416				
35	169 (b, π_ψ*)	←	161	0.148	4.11	302	33118	0.0006
	170 (b, π_ψ*)	←	161	0.154				
	169 (b, π_ψ*)	←	164	0.117				
	170 (b, π_ψ*)	←	164	0.250				
	169 (b, π_ψ*)	←	165	0.203				
	170 (b, π_ψ*)	←	165	0.556				
36	171 (a, π_ψ*)	←	162	–0.102	4.15	299	33436	0.0097
	169 (b, π_ψ*)	←	164	–0.322				
	170 (b, π_ψ*)	←	164	–0.315				
	171 (a, π_ψ*)	←	164	0.415				
	169 (b, π_ψ*)	←	165	0.170				
	170 (b, π_ψ*)	←	165	0.160				
	171 (a, π_ψ*)	←	165	–0.142				
37	169 (b, π_ψ*)	←	162	–0.328	4.15	299	33494	0.0021
	170 (b, π_ψ*)	←	162	0.203				
	171 (a, π_ψ*)	←	162	0.558				
	170 (b, π_ψ*)	←	164	–0.133				
38	169 (b, π_ψ*)	←	163	0.455	4.20	295	33893	0.0007
	170 (b, π_ψ*)	←	163	0.311				
	171 (a, π_ψ*)	←	163	–0.429				
39	169 (b, π_ψ*)	←	162	–0.110	4.21	295	33953	0.0012
	169 (b, π_ψ*)	←	164	–0.103				
	170 (b, π_ψ*)	←	164	0.490				
	171 (a, π_ψ*)	←	164	0.350				
	170 (b, π_ψ*)	←	165	–0.250				

excited state	orbital composition			coefficient	excitation			oscillator strength
					eV	nm	cm^{-1}	
	171 (a, π_ψ*)	←	165	–0.159				
40	169 (b, π_ψ*)	←	162	0.339	4.22	294	34035	0.0002
	170 (b, π_ψ*)	←	162	0.581				
	170 (b, π_ψ*)	←	164	0.112				
41	169 (b, π_ψ*)	←	160	–0.218	4.24	292	34221	0.0006
	169 (b, π_ψ*)	←	161	–0.124				
	170 (b, π_ψ*)	←	161	–0.202				
	170 (b, π_ψ*)	←	162	–0.143				
	170 (b, π_ψ*)	←	163	–0.120				
	174	←	166 (a, $d\pi$)	0.151				
	176	←	166 (a, $d\pi$)	0.260				
	177	←	167 (a, $d\pi$)	0.279				
	175	←	168 (a, $d\pi$)	0.192				
	178	←	168 (a, $d\pi$)	0.110				
42	169 (b, π_ψ*)	←	160	0.139	4.25	292	34261	0.0050
	170 (b, π_ψ*)	←	160	0.179				
	171 (a, π_ψ*)	←	160	0.108				
	169 (b, π_ψ*)	←	161	0.558				
	170 (b, π_ψ*)	←	163	–0.159				
	169 (b, π_ψ*)	←	165	–0.100				
	177	←	167 (a, $d\pi$)	0.133				
43	169 (b, π_ψ*)	←	160	0.114	4.26	291	34381	0.0001
	170 (b, π_ψ*)	←	163	0.553				
	171 (a, π_ψ*)	←	163	0.328				
	177	←	167 (a, $d\pi$)	0.111				
44	169 (b, π_ψ*)	←	159	0.125	4.28	290	34507	0.0061
	169 (b, π_ψ*)	←	160	0.523				
	169 (b, π_ψ*)	←	161	–0.230				
	170 (b, π_ψ*)	←	161	0.137				
	171 (a, π_ψ*)	←	161	0.158				
	170 (b, π_ψ*)	←	163	–0.138				
45	169 (b, π_ψ*)	←	159	–0.250	4.33	286	34931	0.0010
	170 (b, π_ψ*)	←	160	–0.376				
	170 (b, π_ψ*)	←	161	0.474				
	170 (b, π_ψ*)	←	164	–0.103				
	170 (b, π_ψ*)	←	165	–0.123				
46	169 (b, π_ψ*)	←	159	0.374	4.34	286	35007	0.0107
	170 (b, π_ψ*)	←	159	–0.346				
	169 (b, π_ψ*)	←	160	–0.186				
	170 (b, π_ψ*)	←	160	0.206				
	171 (a, π_ψ*)	←	160	–0.189				
	170 (b, π_ψ*)	←	161	0.316				
47	169 (b, π_ψ*)	←	159	0.181	4.37	284	35220	0.0082
	170 (b, π_ψ*)	←	159	–0.274				
	170 (b, π_ψ*)	←	160	–0.217				
	171 (a, π_ψ*)	←	160	0.439				
	171 (a, π_ψ*)	←	161	0.353				
48	169 (b, π_ψ*)	←	159	0.105	4.43	280	35741	0.0214
	171 (a, π_ψ*)	←	159	0.571				
	171 (a, π_ψ*)	←	160	–0.300				
	171 (a, π_ψ*)	←	161	0.175				
49	170 (b, π_ψ*)	←	159	0.104	4.49	276	36248	0.1245
	171 (a, π_ψ*)	←	159	–0.275				

excited state	orbital composition			coefficient	excitation			oscillator strength
					eV	nm	cm^{-1}	
	171 (a, π_ψ*)	←	160	–0.246				
	170 (b, π_ψ*)	←	161	–0.121				
	171 (a, π_ψ*)	←	161	0.275				
	172	←	161	–0.102				
	182	←	166 (a, $d\pi$)	–0.171				
	181	←	167 (a, $d\pi$)	–0.207				
	181	←	168 (a, $d\pi$)	0.176				
	182	←	168 (a, $d\pi$)	–0.108				
50	181	←	166 (a, $d\pi$)	–0.351	4.50	275	36300	0.0012
	182	←	166 (a, $d\pi$)	0.111				
	181	←	167 (a, $d\pi$)	0.113				
	182	←	167 (a, $d\pi$)	0.328				
	181	←	168 (a, $d\pi$)	0.157				
	182	←	168 (a, $d\pi$)	0.353				
51	169 (b, π_ψ*)	←	159	0.128	4.50	275	36321	0.1127
	170 (b, π_ψ*)	←	159	0.300				
	171 (a, π_ψ*)	←	159	–0.196				
	169 (b, π_ψ*)	←	160	–0.126				
	171 (a, π_ψ*)	←	161	0.185				
	182	←	166 (a, $d\pi$)	0.224				
	181	←	167 (a, $d\pi$)	0.235				
	182	←	167 (a, $d\pi$)	–0.107				
	181	←	168 (a, $d\pi$)	–0.225				
	182	←	168 (a, $d\pi$)	0.106				
52	170 (b, π_ψ*)	←	159	0.331	4.51	275	36347	0.1638
	171 (a, π_ψ*)	←	159	0.175				
	169 (b, π_ψ*)	←	160	–0.151				
	170 (b, π_ψ*)	←	160	0.130				
	171 (a, π_ψ*)	←	160	0.248				
	170 (b, π_ψ*)	←	161	0.131				
	182	←	166 (a, $d\pi$)	–0.164				
	181	←	167 (a, $d\pi$)	–0.175				
	181	←	168 (a, $d\pi$)	0.155				
53	169 (b, π_ψ*)	←	159	–0.319	4.58	271	36926	0.7337
	170 (b, π_ψ*)	←	159	–0.112				
	170 (b, π_ψ*)	←	160	0.334				
	171 (a, π_ψ*)	←	161	0.302				
54	181	←	166 (a, $d\pi$)	0.374	4.65	267	37468	0.0006
	182	←	166 (a, $d\pi$)	0.277				
	181	←	167 (a, $d\pi$)	–0.241				
	182	←	167 (a, $d\pi$)	0.360				
55	172	←	164	0.218	4.70	264	37869	0.0053
	172	←	165	0.572				
	174	←	165	0.162				
	175	←	165	–0.144				
	176	←	165	–0.109				
	177	←	165	0.114				
56	172	←	164	0.564	4.74	261	38243	0.0330
	173	←	164	0.188				
	174	←	164	0.179				
	172	←	165	–0.228				
	173	←	165	–0.109				
57	172	←	162	–0.248	4.77	260	38458	0.0037

excited state	orbital composition		coefficient	excitation			oscillator strength
				eV	nm	cm^{-1}	
	172	← 163	0.531				
	173	← 163	0.231				
	174	← 163	0.197				
	175	← 163	0.107				
	176	← 163	0.103				
	172	← 164	0.108				
58	172	← 162	0.551	4.77	260	38476	0.0035
	174	← 162	0.176				
	175	← 162	–0.174				
	176	← 162	–0.136				
	177	← 162	0.138				
	172	← 163	0.250				
59	172	← 160	–0.123	4.91	253	39582	0.0205
	172	← 161	0.327				
	175	← 164	0.158				
	176	← 164	0.136				
	177	← 164	–0.124				
	172	← 165	0.232				
	174	← 165	–0.163				
	175	← 165	0.259				
	176	← 165	0.215				
	177	← 165	–0.242				
60	169 (b, π_ψ*)	← 158	–0.218	4.97	250	40056	0.0055
	170 (b, π_ψ*)	← 158	0.136				
	171 (a, π_ψ*)	← 158	–0.182				
	172	← 160	0.135				
	172	← 161	0.420				
	172	← 164	–0.114				
	175	← 165	–0.174				
	176	← 165	–0.146				
	178	← 168 (a, $d\pi$)	0.101				
61	172	← 160	–0.241	4.99	249	40219	0.0098
	173	← 165	–0.111				
	178	← 168 (a, $d\pi$)	0.561				
62	169 (b, π_ψ*)	← 158	0.122	5.00	248	40290	0.0162
	171 (a, π_ψ*)	← 158	0.163				
	172	← 160	0.490				
	178	← 166 (a, $d\pi$)	0.141				
	178	← 168 (a, $d\pi$)	0.178				
63	172	← 160	–0.114	5.00	248	40322	0.0353
	172	← 164	–0.287				
	173	← 164	0.375				
	174	← 164	0.242				
	175	← 164	0.153				
	176	← 164	0.179				
	173	← 165	–0.123				
	175	← 165	–0.119				
	176	← 165	–0.126				
	178	← 168 (a, $d\pi$)	–0.187				
64	172	← 159	–0.123	5.01	247	40415	0.0030
	172	← 160	0.110				
	172	← 161	–0.119				
	172	← 162	0.283				

excited state	orbital composition		coefficient	excitation			oscillator strength
				eV	nm	cm^{-1}	
	174	← 162	–0.144				
	175	← 162	0.307				
	176	← 162	0.264				
	177	← 162	–0.277				
	173	← 165	–0.183				
65	172	← 159	0.109	5.02	247	40500	0.0050
	172	← 162	0.150				
	175	← 162	0.171				
	176	← 162	0.144				
	177	← 162	–0.140				
	172	← 163	–0.140				
	173	← 163	0.132				
	175	← 163	0.101				
	176	← 163	0.114				
	173	← 164	0.136				
	173	← 165	0.347				
	174	← 165	0.147				
	178	← 168 (a, $d\pi$)	0.123				
	179	← 168 (a, $d\pi$)	–0.216				
66	171 (a, π_ψ*)	← 158	0.132	5.03	246	40599	0.0377
	172	← 159	0.509				
	173	← 165	–0.252				
	178	← 166 (a, $d\pi$)	–0.111				
	179	← 166 (a, $d\pi$)	0.102				
67	172	← 159	–0.140	5.04	246	40636	0.0060
	172	← 163	–0.322				
	173	← 163	0.368				
	174	← 163	0.223				
	175	← 163	0.184				
	176	← 163	0.202				
	179	← 168 (a, $d\pi$)	0.126				
68	169 (b, π_ψ*)	← 158	–0.198	5.05	245	40762	0.0015
	174	← 161	0.157				
	173	← 164	–0.122				
	174	← 164	0.168				
	175	← 164	0.112				
	173	← 165	–0.228				
	174	← 165	0.395				
	175	← 165	0.217				
	177	← 165	–0.114				
	179	← 168 (a, $d\pi$)	–0.205				
69	169 (b, π_ψ*)	← 158	–0.222	5.06	245	40791	0.0038
	170 (b, π_ψ*)	← 158	0.121				
	175	← 160	0.110				
	172	← 161	–0.199				
	173	← 165	0.134				
	179	← 168 (a, $d\pi$)	0.317				
	180	← 168 (a, $d\pi$)	0.333				
70	169 (b, π_ψ*)	← 158	0.301	5.07	245	40891	0.0053
	170 (b, π_ψ*)	← 158	–0.109				
	171 (a, π_ψ*)	← 158	0.110				
	172	← 159	–0.150				
	172	← 161	0.213				

excited state	orbital composition			coefficient	excitation			oscillator strength
					eV	nm	cm^{-1}	
	175	←	161	0.105				
	177	←	161	–0.100				
	173	←	165	–0.145				
	174	←	165	0.210				
	178	←	167 (a, $d\pi$)	–0.150				
	179	←	168 (a, $d\pi$)	0.181				
	180	←	168 (a, $d\pi$)	0.279				
71	169 (b, π_ψ*)	←	158	0.152	5.08	244	40986	0.0040
	171 (a, π_ψ*)	←	158	–0.125				
	174	←	160	–0.103				
	176	←	160	0.103				
	173	←	164	0.139				
	173	←	165	0.173				
	174	←	165	0.235				
	175	←	165	0.147				
	179	←	168 (a, $d\pi$)	0.312				
	180	←	168 (a, $d\pi$)	–0.313				
72	172	←	161	0.147	5.11	243	41236	0.0040
	178	←	166 (a, $d\pi$)	–0.103				
	178	←	167 (a, $d\pi$)	0.613				
	179	←	168 (a, $d\pi$)	0.119				
	180	←	168 (a, $d\pi$)	0.116				
73	169 (b, π_ψ*)	←	158	–0.184	5.13	242	41376	0.0008
	170 (b, π_ψ*)	←	158	0.110				
	171 (a, π_ψ*)	←	158	0.370				
	172	←	159	–0.113				
	177	←	161	–0.115				
	174	←	164	0.217				
	176	←	164	–0.113				
	178	←	166 (a, $d\pi$)	–0.124				
	179	←	168 (a, $d\pi$)	0.156				
	180	←	168 (a, $d\pi$)	–0.289				
74	171 (a, π_ψ*)	←	158	–0.111	5.13	242	41402	0.0002
	173	←	162	0.605				
	177	←	162	0.153				
	173	←	164	–0.134				
	174	←	164	0.170				
75	171 (a, π_ψ*)	←	158	–0.158	5.14	241	41430	0.0026
	173	←	162	–0.280				
	173	←	164	–0.138				
	174	←	164	0.447				
	175	←	164	–0.159				
	176	←	164	–0.105				
	174	←	165	–0.211				
	175	←	165	0.120				
	180	←	168 (a, $d\pi$)	0.107				
76	169 (b, π_ψ*)	←	157	–0.140	5.14	241	41480	0.0079
	169 (b, π_ψ*)	←	158	–0.179				
	170 (b, π_ψ*)	←	158	–0.139				
	175	←	159	–0.107				
	172	←	160	–0.141				
	175	←	164	–0.146				
	178	←	166 (a, $d\pi$)	0.496				

excited state	orbital composition			coefficient	excitation			oscillator strength
					eV	nm	cm^{-1}	
	178	←	167 (a, $d\pi$)	0.127				
77	170 (b, π_ψ*)	←	158	0.109	5.15	241	41534	0.0044
	171 (a, π_ψ*)	←	158	0.111				
	173	←	164	–0.172				
	175	←	164	0.398				
	177	←	164	–0.131				
	173	←	165	0.192				
	175	←	165	–0.178				
	176	←	165	–0.144				
	178	←	166 (a, $d\pi$)	0.286				
78	169 (b, π_ψ*)	←	157	–0.124	5.16	240	41606	0.0029
	171 (a, π_ψ*)	←	157	–0.111				
	169 (b, π_ψ*)	←	158	–0.146				
	170 (b, π_ψ*)	←	158	–0.176				
	176	←	161	0.133				
	173	←	164	–0.257				
	174	←	164	0.122				
	175	←	164	0.135				
	176	←	164	0.170				
	175	←	165	–0.210				
	176	←	165	0.329				
	177	←	165	0.193				
79	174	←	162	0.574	5.16	240	41651	0.0019
	175	←	162	0.295				
	176	←	162	–0.112				
	177	←	162	–0.171				
80	169 (b, π_ψ*)	←	158	0.217	5.17	240	41659	0.0045
	170 (b, π_ψ*)	←	158	0.356				
	175	←	164	–0.144				
	176	←	164	0.123				
	177	←	164	0.144				
	176	←	165	0.290				
	177	←	165	0.188				
	178	←	166 (a, $d\pi$)	0.165				
81	170 (b, π_ψ*)	←	158	–0.127	5.18	239	41774	0.0041
	175	←	161	0.159				
	174	←	163	–0.130				
	175	←	163	0.142				
	174	←	164	–0.114				
	175	←	164	0.200				
	177	←	164	0.163				
	174	←	165	–0.131				
	175	←	165	0.327				
	176	←	165	–0.109				
	177	←	165	0.356				
82	170 (b, π_ψ*)	←	158	–0.134	5.19	239	41842	0.0003
	173	←	163	–0.181				
	174	←	163	0.561				
	175	←	163	–0.224				
	176	←	163	–0.132				
83	169 (b, π_ψ*)	←	154	0.156	5.19	239	41892	0.0001
	169 (b, π_ψ*)	←	157	–0.194				
	169 (b, π_ψ*)	←	158	0.112				

excited state	orbital composition			coefficient	excitation			oscillator strength
					eV	nm	cm^{-1}	
	170 (b, π_ψ*)	←	158	0.297				
	173	←	159	0.130				
	175	←	159	–0.198				
	173	←	160	–0.105				
	174	←	163	0.126				
	173	←	164	–0.125				
	175	←	164	0.121				
	174	←	165	–0.117				
	176	←	165	–0.141				
	177	←	165	0.130				
	179	←	167 (a, $d\pi$)	0.155				
	179	←	168 (a, $d\pi$)	–0.127				
84	173	←	163	–0.394	5.21	238	42003	0.0009
	174	←	163	0.146				
	175	←	163	0.500				
	177	←	163	–0.166				
85	170 (b, π_ψ*)	←	154	0.194	5.22	237	42132	0.0073
	170 (b, π_ψ*)	←	157	–0.112				
	170 (b, π_ψ*)	←	158	–0.138				
	173	←	159	0.107				
	173	←	160	0.298				
	175	←	160	0.230				
	176	←	160	–0.170				
	176	←	161	–0.164				
	177	←	165	0.122				
	180	←	166 (a, $d\pi$)	–0.238				
	179	←	168 (a, $d\pi$)	–0.105				
	180	←	168 (a, $d\pi$)	–0.128				
86	169 (b, π_ψ*)	←	154	–0.100	5.23	237	42201	0.0203
	171 (a, π_ψ*)	←	157	–0.160				
	172	←	159	0.141				
	173	←	160	0.110				
	174	←	160	–0.141				
	173	←	161	0.377				
	174	←	161	0.132				
	175	←	161	0.115				
	174	←	164	–0.105				
	176	←	165	–0.139				
	178	←	166 (a, $d\pi$)	0.105				
	179	←	166 (a, $d\pi$)	–0.154				
	180	←	166 (a, $d\pi$)	–0.114				
	179	←	167 (a, $d\pi$)	–0.134				
87	169 (b, π_ψ*)	←	157	0.204	5.24	237	42284	0.0106
	170 (b, π_ψ*)	←	158	0.145				
	173	←	160	0.126				
	174	←	160	–0.129				
	174	←	161	–0.238				
	177	←	164	0.112				
	179	←	167 (a, $d\pi$)	0.330				
	180	←	167 (a, $d\pi$)	0.320				
88	171 (a, π_ψ*)	←	158	–0.206	5.25	236	42353	0.0040
	175	←	161	0.143				
	177	←	161	–0.126				

excited state	orbital composition		coefficient	excitation			oscillator strength
				eV	nm	cm^{-1}	
	176	← 162	0.111				
	179	← 166 (a, $d\pi$)	–0.138				
	179	← 167 (a, $d\pi$)	0.404				
	180	← 167 (a, $d\pi$)	–0.347				
89	169 (b, π_ψ*)	← 157	–0.101	5.25	236	42380	0.0003
	175	← 164	0.206				
	176	← 164	–0.284				
	177	← 164	0.457				
	176	← 165	0.138				
	177	← 165	–0.233				
90	174	← 162	0.223	5.26	236	42416	0.0010
	176	← 162	0.539				
	177	← 162	0.270				
	177	← 164	–0.160				
91	169 (b, π_ψ*)	← 154	–0.168	5.27	235	42478	0.0059
	169 (b, π_ψ*)	← 157	–0.151				
	172	← 159	–0.137				
	174	← 159	–0.240				
	176	← 159	–0.119				
	174	← 160	0.274				
	173	← 161	0.183				
	178	← 166 (a, $d\pi$)	0.118				
	179	← 166 (a, $d\pi$)	0.345				
	179	← 167 (a, $d\pi$)	0.198				
92	173	← 161	–0.169	5.28	235	42593	0.0009
	174	← 161	0.145				
	175	← 161	0.140				
	175	← 162	–0.106				
	176	← 162	0.147				
	173	← 164	–0.143				
	175	← 164	–0.117				
	176	← 164	0.383				
	177	← 164	0.239				
	173	← 165	0.124				
	176	← 165	–0.198				
	177	← 165	–0.140				
	179	← 166 (a, $d\pi$)	0.164				
	180	← 167 (a, $d\pi$)	0.111				
93	174	← 160	–0.184	5.28	235	42604	0.0025
	173	← 161	–0.219				
	174	← 161	0.268				
	175	← 161	0.262				
	177	← 162	–0.128				
	173	← 164	0.140				
	176	← 164	–0.268				
	177	← 164	–0.219				
	175	← 165	–0.108				
	176	← 165	0.110				
	179	← 166 (a, $d\pi$)	0.123				
	180	← 167 (a, $d\pi$)	0.152				
94	175	← 159	–0.163	5.29	234	42668	0.0056
	173	← 160	0.106				
	174	← 160	0.118				

excited state	orbital composition			coefficient	excitation			oscillator strength
					eV	nm	cm^{-1}	
	175	←	160	–0.314				
	174	←	161	0.358				
	175	←	161	–0.172				
	175	←	162	0.148				
	177	←	162	0.175				
	179	←	166 (a, $d\pi$)	–0.159				
	179	←	167 (a, $d\pi$)	0.122				
	180	←	167 (a, $d\pi$)	0.148				
95	174	←	160	–0.135	5.29	234	42697	0.0001
	175	←	160	0.162				
	175	←	161	0.129				
	173	←	162	–0.127				
	174	←	162	–0.107				
	175	←	162	0.417				
	176	←	162	–0.121				
	177	←	162	0.426				
	179	←	166 (a, $d\pi$)	0.131				
96	169 (b, π_ψ*)	←	155	0.101	5.31	234	42800	0.0098
	169 (b, π_ψ*)	←	157	0.122				
	174	←	159	0.120				
	173	←	160	–0.106				
	175	←	163	0.229				
	176	←	163	–0.260				
	177	←	163	0.453				
	180	←	166 (a, $d\pi$)	0.160				
	180	←	167 (a, $d\pi$)	0.108				
97	170 (b, π_ψ*)	←	154	0.123	5.31	234	42812	0.0101
	169 (b, π_ψ*)	←	155	0.103				
	169 (b, π_ψ*)	←	157	0.162				
	173	←	160	–0.105				
	174	←	160	0.115				
	175	←	160	0.131				
	173	←	161	0.109				
	175	←	163	–0.142				
	176	←	163	0.153				
	177	←	163	–0.306				
	180	←	166 (a, $d\pi$)	0.346				
	180	←	167 (a, $d\pi$)	0.217				
98	169 (b, π_ψ*)	←	154	0.221	5.31	233	42828	0.0135
	170 (b, π_ψ*)	←	157	0.121				
	174	←	159	0.273				
	174	←	160	–0.111				
	173	←	161	0.111				
	175	←	161	–0.108				
	177	←	163	–0.129				
	179	←	166 (a, $d\pi$)	0.411				
	180	←	166 (a, $d\pi$)	–0.200				
99	169 (b, π_ψ*)	←	154	0.105	5.32	233	42922	0.0102
	173	←	159	–0.299				
	175	←	159	–0.293				
	173	←	160	0.384				
	176	←	161	0.114				
	179	←	166 (a, $d\pi$)	0.110				

excited state	orbital composition			coefficient	excitation			oscillator strength
					eV	nm	cm^{-1}	
	180	←	166 (a, $d\pi$)	0.231				
100	173	←	163	–0.226	5.33	233	42996	0.0009
	175	←	163	–0.121				
	176	←	163	0.520				
	177	←	163	0.334				
101	170 (b, π_ψ*)	←	154	0.141	5.33	232	43014	0.0141
	169 (b, π_ψ*)	←	155	–0.130				
	173	←	159	0.392				
	174	←	159	0.112				
	173	←	160	0.104				
	174	←	160	–0.142				
	175	←	160	–0.215				
	176	←	163	0.120				
	177	←	163	0.119				
	180	←	166 (a, $d\pi$)	0.292				
	180	←	167 (a, $d\pi$)	–0.128				
102	169 (b, π_ψ*)	←	155	0.126	5.35	232	43188	0.0497
	171 (a, π_ψ*)	←	155	0.249				
	169 (b, π_ψ*)	←	157	–0.126				
	170 (b, π_ψ*)	←	157	0.124				
	171 (a, π_ψ*)	←	158	0.225				
	174	←	160	–0.235				
	175	←	160	0.154				
	174	←	161	0.126				
	175	←	161	–0.196				
	180	←	166 (a, $d\pi$)	0.142				
	179	←	167 (a, $d\pi$)	0.161				
	180	←	167 (a, $d\pi$)	–0.184				
103	169 (b, π_ψ*)	←	156	0.353	5.38	230	43409	0.0020
	170 (b, π_ψ*)	←	156	–0.174				
	171 (a, π_ψ*)	←	156	0.390				
	171 (a, π_ψ*)	←	157	0.101				
	173	←	159	0.125				
	175	←	159	0.105				
	174	←	160	0.100				
	175	←	160	0.166				
	176	←	160	0.201				
	176	←	161	0.128				
104	169 (b, π_ψ*)	←	156	–0.227	5.38	230	43416	0.0021
	171 (a, π_ψ*)	←	156	–0.278				
	173	←	159	0.158				
	174	←	159	0.172				
	175	←	159	0.121				
	173	←	160	0.150				
	174	←	160	0.166				
	175	←	160	0.184				
	176	←	160	0.303				
	176	←	161	0.253				
105	169 (b, π_ψ*)	←	157	–0.177	5.39	230	43493	0.0094
	170 (b, π_ψ*)	←	157	0.210				
	171 (a, π_ψ*)	←	157	0.103				
	174	←	159	0.216				
	174	←	160	0.197				

excited state	orbital composition			coefficient	excitation			oscillator strength
					eV	nm	cm^{-1}	
	176	←	160	–0.159				
	177	←	160	0.139				
	175	←	161	0.152				
	177	←	161	0.410				
106	169 (b, π_ψ*)	←	146	–0.106	5.40	230	43550	0.0116
	169 (b, π_ψ*)	←	147	0.192				
	169 (b, π_ψ*)	←	157	0.293				
	171 (a, π_ψ*)	←	157	–0.195				
	173	←	159	0.116				
	175	←	159	–0.141				
	174	←	160	0.125				
	177	←	160	0.190				
	175	←	161	0.108				
	177	←	161	0.277				
	180	←	167 (a, $d\pi$)	–0.169				
107	171 (a, π_ψ*)	←	157	–0.136	5.41	229	43604	0.0075
	173	←	159	0.101				
	176	←	160	–0.265				
	177	←	160	–0.178				
	173	←	161	–0.180				
	175	←	161	–0.187				
	176	←	161	0.423				
	177	←	161	0.194				
108	170 (b, π_ψ*)	←	147	0.174	5.41	229	43656	0.0244
	170 (b, π_ψ*)	←	154	–0.100				
	170 (b, π_ψ*)	←	155	0.155				
	170 (b, π_ψ*)	←	157	0.351				
	173	←	159	0.157				
	174	←	159	–0.106				
	175	←	160	0.144				
	176	←	160	–0.196				
	177	←	160	0.127				
	175	←	161	–0.170				
	177	←	161	–0.188				
	179	←	167 (a, $d\pi$)	–0.102				
109	169 (b, π_ψ*)	←	155	–0.167	5.42	229	43717	0.0072
	170 (b, π_ψ*)	←	157	–0.201				
	173	←	159	–0.142				
	175	←	159	0.236				
	177	←	159	0.121				
	175	←	160	0.161				
	177	←	160	0.411				
	174	←	161	0.162				
	175	←	161	–0.138				
110	169 (b, π_ψ*)	←	147	–0.191	5.46	227	44049	0.0123
	169 (b, π_ψ*)	←	154	0.158				
	169 (b, π_ψ*)	←	155	–0.122				
	169 (b, π_ψ*)	←	157	0.171				
	173	←	159	0.110				
	174	←	159	–0.249				
	176	←	159	0.402				
	177	←	159	0.120				
	176	←	160	–0.146				

excited state	orbital composition			coefficient	excitation			oscillator strength
					eV	nm	cm^{-1}	
	177	←	160	–0.128				
111	169 (b, π_ψ*)	←	147	0.232	5.47	227	44142	0.0207
	169 (b, π_ψ*)	←	148	–0.106				
	169 (b, π_ψ*)	←	150	–0.112				
	169 (b, π_ψ*)	←	151	–0.127				
	169 (b, π_ψ*)	←	154	–0.106				
	169 (b, π_ψ*)	←	155	0.188				
	169 (b, π_ψ*)	←	157	–0.141				
	170 (b, π_ψ*)	←	157	–0.135				
	171 (a, π_ψ*)	←	157	0.160				
	176	←	159	0.395				
	176	←	160	–0.136				
112	171 (a, π_ψ*)	←	147	–0.246	5.50	225	44378	0.0579
	171 (a, π_ψ*)	←	148	0.142				
	171 (a, π_ψ*)	←	150	0.123				
	171 (a, π_ψ*)	←	151	0.162				
	171 (a, π_ψ*)	←	154	0.237				
	171 (a, π_ψ*)	←	155	–0.182				
	169 (b, π_ψ*)	←	157	–0.144				
	171 (a, π_ψ*)	←	157	–0.162				
	175	←	159	0.125				
	176	←	159	0.258				
	177	←	159	–0.123				
	176	←	161	–0.125				
113	170 (b, π_ψ*)	←	157	–0.102	5.51	225	44419	0.0125
	175	←	159	–0.198				
	177	←	159	0.558				
	177	←	160	–0.171				
114	169 (b, π_ψ*)	←	145	0.112	5.51	225	44435	0.0171
	169 (b, π_ψ*)	←	147	0.103				
	170 (b, π_ψ*)	←	147	–0.277				
	170 (b, π_ψ*)	←	148	0.113				
	170 (b, π_ψ*)	←	151	0.131				
	170 (b, π_ψ*)	←	154	0.316				
	170 (b, π_ψ*)	←	155	–0.109				
	170 (b, π_ψ*)	←	157	0.308				
	171 (a, π_ψ*)	←	157	0.143				
	177	←	159	0.121				
	176	←	160	0.114				
115	169 (b, π_ψ*)	←	152	0.160	5.55	223	44781	0.0369
	169 (b, π_ψ*)	←	154	0.238				
	171 (a, π_ψ*)	←	154	0.120				
	169 (b, π_ψ*)	←	155	0.388				
	170 (b, π_ψ*)	←	155	0.132				
	169 (b, π_ψ*)	←	156	0.214				
	171 (a, π_ψ*)	←	156	–0.162				
	176	←	159	–0.131				
	177	←	159	0.185				
116	169 (b, π_ψ*)	←	154	–0.205	5.56	223	44872	0.0313
	169 (b, π_ψ*)	←	156	0.463				
	170 (b, π_ψ*)	←	156	0.139				
	171 (a, π_ψ*)	←	156	–0.279				
	171 (a, π_ψ*)	←	157	–0.212				

excited state	orbital composition			coefficient	excitation			oscillator strength
					eV	nm	cm^{-1}	
	176	←	159	0.109				
117	169 (b, π_ψ*)	←	152	0.132	5.58	222	44993	0.0422
	170 (b, π_ψ*)	←	154	–0.113				
	171 (a, π_ψ*)	←	154	0.167				
	171 (a, π_ψ*)	←	155	–0.243				
	169 (b, π_ψ*)	←	156	0.125				
	170 (b, π_ψ*)	←	156	0.116				
	171 (a, π_ψ*)	←	156	–0.176				
	171 (a, π_ψ*)	←	157	0.308				
	173	←	161	0.117				
	174	←	161	0.142				
	177	←	161	0.146				
118	170 (b, π_ψ*)	←	144	–0.108	5.61	221	45231	0.0045
	169 (b, π_ψ*)	←	149	–0.104				
	169 (b, π_ψ*)	←	152	–0.150				
	170 (b, π_ψ*)	←	152	0.133				
	170 (b, π_ψ*)	←	154	0.238				
	171 (a, π_ψ*)	←	154	–0.119				
	170 (b, π_ψ*)	←	155	0.431				
	171 (a, π_ψ*)	←	155	–0.141				
	177	←	160	–0.122				
119	169 (b, π_ψ*)	←	152	–0.102	5.62	221	45307	0.0026
	170 (b, π_ψ*)	←	154	–0.133				
	171 (a, π_ψ*)	←	154	0.191				
	171 (a, π_ψ*)	←	155	0.222				
	170 (b, π_ψ*)	←	156	0.540				
	171 (a, π_ψ*)	←	156	0.201				
120	169 (b, π_ψ*)	←	151	–0.136	5.63	220	45413	0.0060
	169 (b, π_ψ*)	←	152	0.509				
	169 (b, π_ψ*)	←	153	–0.152				
	171 (a, π_ψ*)	←	154	–0.217				
	169 (b, π_ψ*)	←	155	–0.166				
	170 (b, π_ψ*)	←	156	0.167				
	171 (a, π_ψ*)	←	156	0.129				

Table 0-3 – TDDFT Calculated Excitation Energies, One–Electron Transitions, and Oscillator Strengths for Optical Transitions of $[Ru(dmpbpy)_2(bpy)]^{2+}$ complex in the Gas Phase.

excited state	orbital composition		coefficient	excitation			oscillator strength
				eV	nm	cm^{-1}	
1	207 (b, π_ψ*)	← 206 (a, $d\pi$)	0.568	2.49	498	20075	0.0011
	208 (a, π_ψ*)	← 206 (a, $d\pi$)	–0.321				
	209 (b, π_ψ*)	← 206 (a, $d\pi$)	–0.243				
2	207 (b, π_ψ*)	← 206 (a, $d\pi$)	0.274	2.54	489	20466	0.0014
	208 (a, π_ψ*)	← 206 (a, $d\pi$)	0.606				
	209 (b, π_ψ*)	← 206 (a, $d\pi$)	–0.176				
3	207 (b, π_ψ*)	← 206 (a, $d\pi$)	0.301	2.55	486	20562	0.0020
	209 (b, π_ψ*)	← 206 (a, $d\pi$)	0.620				
4	207 (b, π_ψ*)	← 204 (a, $d\pi$)	0.133	2.67	465	21503	0.0054
	208 (a, π_ψ*)	← 204 (a, $d\pi$)	–0.237				
	207 (b, π_ψ*)	← 205 (b, $d\pi$)	0.483				
	208 (a, π_ψ*)	← 205 (b, $d\pi$)	–0.245				
	209 (b, π_ψ*)	← 205 (b, $d\pi$)	–0.336				
5	208 (a, π_ψ*)	← 204 (a, $d\pi$)	0.356	2.71	458	21841	0.0079
	209 (b, π_ψ*)	← 204 (a, $d\pi$)	–0.275				
	207 (b, π_ψ*)	← 205 (b, $d\pi$)	0.427				
	209 (b, π_ψ*)	← 205 (b, $d\pi$)	0.307				
6	207 (b, π_ψ*)	← 204 (a, $d\pi$)	0.580	2.73	454	22015	0.0149
	208 (a, π_ψ*)	← 204 (a, $d\pi$)	0.303				
	209 (b, π_ψ*)	← 205 (b, $d\pi$)	–0.187				
7	207 (b, π_ψ*)	← 204 (a, $d\pi$)	0.337	2.84	437	22885	0.1010
	208 (a, π_ψ*)	← 204 (a, $d\pi$)	–0.347				
	209 (b, π_ψ*)	← 204 (a, $d\pi$)	–0.182				
	208 (a, π_ψ*)	← 205 (b, $d\pi$)	–0.207				
	209 (b, π_ψ*)	← 205 (b, $d\pi$)	0.380				
8	208 (a, π_ψ*)	← 204 (a, $d\pi$)	–0.207	2.87	433	23111	0.1842
	209 (b, π_ψ*)	← 204 (a, $d\pi$)	0.387				
	207 (b, π_ψ*)	← 205 (b, $d\pi$)	0.218				
	208 (a, π_ψ*)	← 205 (b, $d\pi$)	0.422				
	209 (b, π_ψ*)	← 205 (b, $d\pi$)	0.208				
9	208 (a, π_ψ*)	← 204 (a, $d\pi$)	0.174	3.08	402	24866	0.0002
	209 (b, π_ψ*)	← 204 (a, $d\pi$)	0.407				
	208 (a, π_ψ*)	← 205 (b, $d\pi$)	–0.373				
	209 (b, π_ψ*)	← 205 (b, $d\pi$)	0.179				
	212	← 206 (a, $d\pi$)	–0.123				
	213	← 206 (a, $d\pi$)	0.234				
10	210	← 206 (a, $d\pi$)	0.696	3.33	372	26898	0.0112
11	210	← 205 (b, $d\pi$)	0.694	3.50	354	28233	0.0126
12	210	← 204 (a, $d\pi$)	0.696	3.51	353	28340	0.0082
13	211	← 206 (a, $d\pi$)	0.681	3.61	344	29090	0.0234
14	212	← 206 (a, $d\pi$)	0.639	3.62	343	29168	0.0050
	213	← 206 (a, $d\pi$)	0.230				
15	212	← 204 (a, $d\pi$)	–0.181	3.67	338	29592	0.0015
	214	← 204 (a, $d\pi$)	–0.181				
	213	← 205 (b, $d\pi$)	–0.186				
	215	← 205 (b, $d\pi$)	–0.167				
	212	← 206 (a, $d\pi$)	–0.130				
	213	← 206 (a, $d\pi$)	0.536				
	214	← 206 (a, $d\pi$)	–0.130				
16	213	← 204 (a, $d\pi$)	–0.105	3.70	335	29838	0.0058

excited state	orbital composition		coefficient	excitation			oscillator strength
				eV	nm	cm^{-1}	
	212	← 205 (b, $d\pi$)	0.147				
	213	← 205 (b, $d\pi$)	–0.287				
	214	← 206 (a, $d\pi$)	0.113				
	215	← 206 (a, $d\pi$)	0.570				
17	212	← 204 (a, $d\pi$)	0.147	3.70	335	29865	0.0117
	213	← 204 (a, $d\pi$)	–0.249				
	214	← 204 (a, $d\pi$)	–0.106				
	211	← 205 (b, $d\pi$)	0.158				
	212	← 206 (a, $d\pi$)	–0.114				
	213	← 206 (a, $d\pi$)	0.101				
	214	← 206 (a, $d\pi$)	0.555				
18	213	← 204 (a, $d\pi$)	0.234	3.75	330	30280	0.0458
	212	← 205 (b, $d\pi$)	0.458				
	213	← 205 (b, $d\pi$)	–0.297				
	214	← 206 (a, $d\pi$)	0.144				
	215	← 206 (a, $d\pi$)	–0.251				
	219	← 206 (a, $d\pi$)	–0.115				
19	211	← 204 (a, $d\pi$)	0.229	3.76	330	30331	0.0544
	212	← 204 (a, $d\pi$)	–0.223				
	213	← 204 (a, $d\pi$)	0.457				
	211	← 205 (b, $d\pi$)	0.122				
	212	← 205 (b, $d\pi$)	–0.151				
	213	← 205 (b, $d\pi$)	0.136				
	214	← 206 (a, $d\pi$)	0.252				
	215	← 206 (a, $d\pi$)	0.165				
20	211	← 204 (a, $d\pi$)	0.294	3.78	328	30451	0.0464
	213	← 204 (a, $d\pi$)	–0.141				
	211	← 205 (b, $d\pi$)	0.528				
	212	← 205 (b, $d\pi$)	0.176				
	214	← 206 (a, $d\pi$)	–0.160				
21	211	← 204 (a, $d\pi$)	0.443	3.78	328	30510	0.0072
	213	← 204 (a, $d\pi$)	–0.164				
	211	← 205 (b, $d\pi$)	–0.340				
	212	← 205 (b, $d\pi$)	0.239				
	213	← 205 (b, $d\pi$)	0.215				
	215	← 205 (b, $d\pi$)	–0.119				
22	211	← 204 (a, $d\pi$)	–0.342	3.80	326	30632	0.0447
	212	← 204 (a, $d\pi$)	–0.179				
	219	← 204 (a, $d\pi$)	0.100				
	212	← 205 (b, $d\pi$)	0.274				
	213	← 205 (b, $d\pi$)	0.382				
	220	← 205 (b, $d\pi$)	–0.127				
	215	← 206 (a, $d\pi$)	0.158				
	220	← 206 (a, $d\pi$)	0.199				
23	212	← 204 (a, $d\pi$)	0.456	3.81	326	30715	0.0326
	213	← 204 (a, $d\pi$)	0.271				
	214	← 204 (a, $d\pi$)	–0.122				
	220	← 204 (a, $d\pi$)	–0.115				
	213	← 205 (b, $d\pi$)	0.131				
	215	← 205 (b, $d\pi$)	–0.215				
	214	← 206 (a, $d\pi$)	–0.107				
	219	← 206 (a, $d\pi$)	–0.227				
24	212	← 204 (a, $d\pi$)	–0.209	3.85	322	31017	0.0037

excited state	orbital composition		coefficient	excitation			oscillator strength
				eV	nm	cm^{-1}	
	214	← 204 (a, $d\pi$)	0.109				
	220	← 204 (a, $d\pi$)	–0.164				
	214	← 205 (b, $d\pi$)	0.386				
	219	← 205 (b, $d\pi$)	–0.176				
	219	← 206 (a, $d\pi$)	–0.372				
	220	← 206 (a, $d\pi$)	–0.196				
25	214	← 204 (a, $d\pi$)	–0.308	3.86	321	31156	0.0097
	219	← 204 (a, $d\pi$)	0.163				
	220	← 204 (a, $d\pi$)	–0.102				
	212	← 205 (b, $d\pi$)	–0.120				
	215	← 205 (b, $d\pi$)	0.376				
	220	← 205 (b, $d\pi$)	–0.153				
	219	← 206 (a, $d\pi$)	–0.198				
	220	← 206 (a, $d\pi$)	0.274				
26	214	← 204 (a, $d\pi$)	0.137	3.87	320	31209	0.0065
	215	← 204 (a, $d\pi$)	0.412				
	214	← 205 (b, $d\pi$)	–0.264				
	215	← 205 (b, $d\pi$)	–0.304				
	219	← 205 (b, $d\pi$)	–0.142				
	220	← 205 (b, $d\pi$)	–0.174				
	219	← 206 (a, $d\pi$)	–0.196				
27	207 (b, π_ψ*)	← 195	0.105	3.89	319	31347	0.0148
	212	← 204 (a, $d\pi$)	0.159				
	214	← 204 (a, $d\pi$)	–0.142				
	215	← 204 (a, $d\pi$)	0.479				
	220	← 204 (a, $d\pi$)	0.150				
	214	← 205 (b, $d\pi$)	0.312				
	219	← 205 (b, $d\pi$)	0.100				
	219	← 206 (a, $d\pi$)	0.164				
28	214	← 204 (a, $d\pi$)	0.340	3.90	318	31450	0.0136
	215	← 204 (a, $d\pi$)	–0.106				
	219	← 204 (a, $d\pi$)	0.195				
	212	← 205 (b, $d\pi$)	–0.153				
	213	← 205 (b, $d\pi$)	–0.106				
	214	← 205 (b, $d\pi$)	0.314				
	220	← 205 (b, $d\pi$)	–0.221				
	220	← 206 (a, $d\pi$)	0.272				
29	215	← 204 (a, $d\pi$)	–0.124	3.99	311	32195	0.0020
	219	← 204 (a, $d\pi$)	–0.280				
	220	← 204 (a, $d\pi$)	0.367				
	219	← 205 (b, $d\pi$)	–0.362				
	220	← 205 (b, $d\pi$)	–0.274				
30	207 (b, π_ψ*)	← 201	0.168	4.04	307	32546	0.0637
	207 (b, π_ψ*)	← 202	–0.264				
	209 (b, π_ψ*)	← 202	–0.232				
	207 (b, π_ψ*)	← 203	0.490				
	208 (a, π_ψ*)	← 203	0.216				
31	207 (b, π_ψ*)	← 201	–0.152	4.04	307	32593	0.0797
	209 (b, π_ψ*)	← 201	–0.128				
	207 (b, π_ψ*)	← 202	0.436				
	209 (b, π_ψ*)	← 202	0.262				
	207 (b, π_ψ*)	← 203	0.335				
	208 (a, π_ψ*)	← 203	0.169				

excited state	orbital composition			coefficient	excitation			oscillator strength
					eV	nm	cm^{-1}	
32	207 (b, π_ψ*)	←	200	0.540	4.09	303	32968	0.0022
	208 (a, π_ψ*)	←	200	0.404				
	209 (b, π_ψ*)	←	200	–0.117				
	207 (b, π_ψ*)	←	201	–0.108				
33	209 (b, π_ψ*)	←	193	0.103	4.12	301	33211	0.0080
	209 (b, π_ψ*)	←	194	0.121				
	207 (b, π_ψ*)	←	196	–0.120				
	209 (b, π_ψ*)	←	196	–0.139				
	207 (b, π_ψ*)	←	197	0.383				
	209 (b, π_ψ*)	←	197	0.291				
	207 (b, π_ψ*)	←	198	0.309				
	209 (b, π_ψ*)	←	198	0.216				
	207 (b, π_ψ*)	←	201	0.152				
	208 (a, π_ψ*)	←	203	–0.125				
34	207 (b, π_ψ*)	←	197	–0.218	4.12	301	33249	0.0030
	209 (b, π_ψ*)	←	197	–0.191				
	207 (b, π_ψ*)	←	198	0.437				
	209 (b, π_ψ*)	←	198	0.332				
	207 (b, π_ψ*)	←	201	–0.168				
	207 (b, π_ψ*)	←	202	–0.127				
	208 (a, π_ψ*)	←	203	0.190				
35	207 (b, π_ψ*)	←	194	0.105	4.13	300	33296	0.0356
	207 (b, π_ψ*)	←	197	0.211				
	209 (b, π_ψ*)	←	197	0.182				
	207 (b, π_ψ*)	←	198	–0.127				
	207 (b, π_ψ*)	←	201	–0.202				
	207 (b, π_ψ*)	←	202	–0.118				
	207 (b, π_ψ*)	←	203	–0.204				
	208 (a, π_ψ*)	←	203	0.485				
36	207 (b, π_ψ*)	←	200	0.101	4.14	299	33419	0.0201
	207 (b, π_ψ*)	←	201	0.373				
	208 (a, π_ψ*)	←	201	0.325				
	207 (b, π_ψ*)	←	202	0.197				
	208 (a, π_ψ*)	←	202	0.220				
	207 (b, π_ψ*)	←	203	–0.175				
	208 (a, π_ψ*)	←	203	0.264				
37	207 (b, π_ψ*)	←	199	0.533	4.17	297	33650	0.0029
	208 (a, π_ψ*)	←	199	0.445				
38	207 (b, π_ψ*)	←	193	–0.150	4.18	297	33707	0.0059
	207 (b, π_ψ*)	←	194	–0.143				
	207 (b, π_ψ*)	←	196	0.214				
	209 (b, π_ψ*)	←	196	0.146				
	207 (b, π_ψ*)	←	197	0.132				
	209 (b, π_ψ*)	←	198	–0.117				
	207 (b, π_ψ*)	←	201	0.196				
	209 (b, π_ψ*)	←	201	–0.222				
	207 (b, π_ψ*)	←	202	–0.257				
	209 (b, π_ψ*)	←	202	0.409				
39	207 (b, π_ψ*)	←	196	0.429	4.19	296	33828	0.0153
	209 (b, π_ψ*)	←	196	0.371				
	207 (b, π_ψ*)	←	197	0.132				
	209 (b, π_ψ*)	←	197	0.100				
	209 (b, π_ψ*)	←	201	0.128				

excited state	orbital composition			coefficient	excitation			oscillator strength
					eV	nm	cm^{-1}	
	209 (b, π_ψ*)	←	202	–0.120				
	214	←	204 (a, $d\pi$)	–0.109				
	215	←	205 (b, $d\pi$)	–0.130				
40	207 (b, π_ψ*)	←	196	0.128	4.21	294	33976	0.0026
	209 (b, π_ψ*)	←	196	0.129				
	207 (b, π_ψ*)	←	200	–0.218				
	208 (a, π_ψ*)	←	200	0.348				
	207 (b, π_ψ*)	←	202	0.132				
	209 (b, π_ψ*)	←	202	–0.151				
	214	←	204 (a, $d\pi$)	0.231				
	215	←	205 (b, $d\pi$)	0.201				
	213	←	206 (a, $d\pi$)	0.146				
41	207 (b, π_ψ*)	←	200	–0.299	4.23	293	34082	0.0005
	208 (a, π_ψ*)	←	200	0.407				
	209 (b, π_ψ*)	←	200	0.107				
	207 (b, π_ψ*)	←	201	0.117				
	208 (a, π_ψ*)	←	202	–0.140				
	209 (b, π_ψ*)	←	203	0.122				
	214	←	204 (a, $d\pi$)	–0.167				
	215	←	205 (b, $d\pi$)	–0.158				
	213	←	206 (a, $d\pi$)	–0.119				
42	209 (b, π_ψ*)	←	194	–0.117	4.24	292	34190	0.0004
	207 (b, π_ψ*)	←	195	0.176				
	209 (b, π_ψ*)	←	195	0.181				
	209 (b, π_ψ*)	←	202	0.113				
	207 (b, π_ψ*)	←	203	0.101				
	209 (b, π_ψ*)	←	203	0.583				
43	208 (a, π_ψ*)	←	193	0.116	4.25	292	34286	0.0003
	207 (b, π_ψ*)	←	194	0.122				
	208 (a, π_ψ*)	←	194	0.137				
	208 (a, π_ψ*)	←	197	–0.145				
	208 (a, π_ψ*)	←	198	–0.112				
	208 (a, π_ψ*)	←	201	–0.283				
	208 (a, π_ψ*)	←	202	0.521				
	209 (b, π_ψ*)	←	202	0.113				
44	207 (b, π_ψ*)	←	193	0.131	4.26	291	34362	0.0033
	207 (b, π_ψ*)	←	194	0.255				
	207 (b, π_ψ*)	←	197	–0.194				
	209 (b, π_ψ*)	←	197	0.279				
	207 (b, π_ψ*)	←	198	–0.119				
	209 (b, π_ψ*)	←	198	0.147				
	207 (b, π_ψ*)	←	201	–0.111				
	208 (a, π_ψ*)	←	201	0.335				
	207 (b, π_ψ*)	←	202	–0.230				
	209 (b, π_ψ*)	←	202	0.161				
45	207 (b, π_ψ*)	←	193	0.116	4.28	290	34496	0.0018
	207 (b, π_ψ*)	←	194	0.131				
	207 (b, π_ψ*)	←	195	0.124				
	207 (b, π_ψ*)	←	197	–0.213				
	209 (b, π_ψ*)	←	197	0.143				
	207 (b, π_ψ*)	←	198	–0.113				
	209 (b, π_ψ*)	←	198	0.159				
	207 (b, π_ψ*)	←	201	0.342				

excited state	orbital composition			coefficient	excitation			oscillator strength
					eV	nm	cm^{-1}	
	208 (a, π_ψ*)	←	201	–0.301				
	208 (a, π_ψ*)	←	202	–0.265				
	209 (b, π_ψ*)	←	202	0.112				
46	207 (b, π_ψ*)	←	194	–0.117	4.30	288	34687	0.0004
	207 (b, π_ψ*)	←	197	0.190				
	209 (b, π_ψ*)	←	197	–0.199				
	207 (b, π_ψ*)	←	198	–0.379				
	209 (b, π_ψ*)	←	198	0.492				
47	208 (a, π_ψ*)	←	193	–0.129	4.30	288	34710	0.0158
	209 (b, π_ψ*)	←	193	–0.118				
	208 (a, π_ψ*)	←	194	0.129				
	209 (b, π_ψ*)	←	194	0.144				
	207 (b, π_ψ*)	←	195	0.533				
	207 (b, π_ψ*)	←	199	0.100				
	208 (a, π_ψ*)	←	199	–0.137				
	208 (a, π_ψ*)	←	201	0.153				
	207 (b, π_ψ*)	←	203	–0.103				
	209 (b, π_ψ*)	←	203	–0.160				
48	207 (b, π_ψ*)	←	193	–0.284	4.32	287	34855	0.0035
	207 (b, π_ψ*)	←	194	0.306				
	207 (b, π_ψ*)	←	195	0.135				
	208 (a, π_ψ*)	←	195	0.248				
	209 (b, π_ψ*)	←	195	0.217				
	209 (b, π_ψ*)	←	197	–0.126				
	207 (b, π_ψ*)	←	199	–0.235				
	208 (a, π_ψ*)	←	199	0.281				
49	207 (b, π_ψ*)	←	193	0.185	4.33	286	34945	0.0032
	207 (b, π_ψ*)	←	194	–0.237				
	208 (a, π_ψ*)	←	195	–0.145				
	209 (b, π_ψ*)	←	195	–0.121				
	207 (b, π_ψ*)	←	199	–0.377				
	208 (a, π_ψ*)	←	199	0.428				
50	208 (a, π_ψ*)	←	193	–0.155	4.35	285	35074	0.0011
	208 (a, π_ψ*)	←	194	–0.198				
	208 (a, π_ψ*)	←	197	0.447				
	208 (a, π_ψ*)	←	198	0.306				
	208 (a, π_ψ*)	←	201	–0.142				
	209 (b, π_ψ*)	←	201	0.105				
	208 (a, π_ψ*)	←	202	0.218				
51	209 (b, π_ψ*)	←	197	–0.166	4.35	285	35120	0.0034
	209 (b, π_ψ*)	←	201	0.578				
	209 (b, π_ψ*)	←	202	0.248				
	209 (b, π_ψ*)	←	203	–0.128				
52	208 (a, π_ψ*)	←	193	–0.203	4.37	284	35255	0.0057
	208 (a, π_ψ*)	←	194	0.159				
	209 (b, π_ψ*)	←	194	–0.105				
	208 (a, π_ψ*)	←	195	0.323				
	209 (b, π_ψ*)	←	195	–0.286				
	207 (b, π_ψ*)	←	200	0.108				
	209 (b, π_ψ*)	←	200	0.424				
53	208 (a, π_ψ*)	←	193	0.129	4.38	283	35308	0.0061
	209 (b, π_ψ*)	←	193	–0.116				
	208 (a, π_ψ*)	←	194	–0.119				

excited state	orbital composition		coefficient	excitation			oscillator strength
				eV	nm	cm^{-1}	
	209 (b, π_ψ*)	← 194	0.136				
	208 (a, π_ψ*)	← 195	–0.237				
	209 (b, π_ψ*)	← 195	0.187				
	209 (b, π_ψ*)	← 197	–0.105				
	208 (a, π_ψ*)	← 198	–0.156				
	207 (b, π_ψ*)	← 200	0.140				
	209 (b, π_ψ*)	← 200	0.510				
54	208 (a, π_ψ*)	← 197	–0.351	4.38	283	35331	0.0011
	208 (a, π_ψ*)	← 198	0.576				
55	207 (b, π_ψ*)	← 193	0.260	4.39	283	35390	0.0058
	207 (b, π_ψ*)	← 194	0.159				
	209 (b, π_ψ*)	← 194	–0.131				
	209 (b, π_ψ*)	← 195	–0.161				
	207 (b, π_ψ*)	← 196	–0.339				
	209 (b, π_ψ*)	← 196	0.355				
	207 (b, π_ψ*)	← 197	0.186				
	209 (b, π_ψ*)	← 197	–0.201				
56	209 (b, π_ψ*)	← 199	0.671	4.41	281	35580	0.0018
57	207 (b, π_ψ*)	← 193	–0.275	4.42	280	35668	0.0396
	207 (b, π_ψ*)	← 194	–0.281				
	208 (a, π_ψ*)	← 195	0.100				
	209 (b, π_ψ*)	← 195	0.152				
	207 (b, π_ψ*)	← 196	–0.293				
	209 (b, π_ψ*)	← 196	0.331				
	207 (b, π_ψ*)	← 197	–0.105				
	209 (b, π_ψ*)	← 197	0.200				
	209 (b, π_ψ*)	← 199	–0.136				
58	207 (b, π_ψ*)	← 193	–0.165	4.44	279	35831	0.0072
	209 (b, π_ψ*)	← 193	–0.170				
	209 (b, π_ψ*)	← 194	0.443				
	209 (b, π_ψ*)	← 195	–0.336				
	209 (b, π_ψ*)	← 199	0.135				
	209 (b, π_ψ*)	← 201	0.103				
	209 (b, π_ψ*)	← 203	0.219				
59	208 (a, π_ψ*)	← 193	–0.159	4.46	278	35957	0.0032
	208 (a, π_ψ*)	← 194	–0.215				
	208 (a, π_ψ*)	← 196	0.579				
	209 (b, π_ψ*)	← 196	0.116				
	208 (a, π_ψ*)	← 197	–0.238				
60	208 (a, π_ψ*)	← 193	–0.182	4.50	276	36258	0.1164
	209 (b, π_ψ*)	← 193	0.318				
	208 (a, π_ψ*)	← 194	0.356				
	209 (b, π_ψ*)	← 194	0.160				
	208 (a, π_ψ*)	← 195	–0.166				
	209 (b, π_ψ*)	← 195	0.150				
	208 (a, π_ψ*)	← 196	0.165				
	208 (a, π_ψ*)	← 197	0.104				
61	208 (a, π_ψ*)	← 193	–0.129	4.50	276	36285	0.0676
	209 (b, π_ψ*)	← 193	0.296				
	208 (a, π_ψ*)	← 194	–0.263				
	208 (a, π_ψ*)	← 196	–0.159				
	219	← 204 (a, $d\pi$)	0.211				
	220	← 205 (b, $d\pi$)	–0.196				

excited state	orbital composition			coefficient	excitation			oscillator strength
					eV	nm	cm^{-1}	
	220	←	206 (a, $d\pi$)	–0.269				
62	209 (b, π_ψ*)	←	193	0.313	4.50	275	36304	0.0596
	208 (a, π_ψ*)	←	194	–0.205				
	208 (a, π_ψ*)	←	196	–0.121				
	219	←	204 (a, $d\pi$)	–0.265				
	220	←	205 (b, $d\pi$)	0.244				
	219	←	206 (a, $d\pi$)	–0.127				
	220	←	206 (a, $d\pi$)	0.292				
63	208 (a, π_ψ*)	←	193	0.391	4.51	275	36384	0.0252
	208 (a, π_ψ*)	←	196	0.201				
	208 (a, π_ψ*)	←	197	0.168				
	220	←	204 (a, $d\pi$)	0.235				
	219	←	205 (b, $d\pi$)	0.264				
	219	←	206 (a, $d\pi$)	–0.195				
	220	←	206 (a, $d\pi$)	–0.109				
64	208 (a, π_ψ*)	←	193	0.329	4.52	274	36458	0.0401
	209 (b, π_ψ*)	←	193	0.211				
	208 (a, π_ψ*)	←	196	0.151				
	220	←	204 (a, $d\pi$)	–0.258				
	219	←	205 (b, $d\pi$)	–0.298				
	219	←	206 (a, $d\pi$)	0.241				
65	207 (b, π_ψ*)	←	193	0.262	4.57	271	36863	0.7300
	207 (b, π_ψ*)	←	194	–0.117				
	208 (a, π_ψ*)	←	194	–0.104				
	209 (b, π_ψ*)	←	194	0.302				
	208 (a, π_ψ*)	←	195	0.329				
	209 (b, π_ψ*)	←	195	0.147				
	215	←	204 (a, $d\pi$)	0.108				
66	219	←	204 (a, $d\pi$)	0.373	4.64	267	37398	0.0011
	220	←	204 (a, $d\pi$)	0.282				
	219	←	205 (b, $d\pi$)	–0.259				
	220	←	205 (b, $d\pi$)	0.338				
67	210	←	201	–0.219	4.73	262	38168	0.0051
	213	←	201	–0.127				
	210	←	202	0.538				
	211	←	202	0.150				
	213	←	202	0.252				
	215	←	202	0.106				
68	210	←	203	0.599	4.75	261	38343	0.0037
	212	←	203	–0.235				
	214	←	203	0.175				
69	210	←	196	–0.111	4.81	258	38813	0.0530
	210	←	197	0.404				
	212	←	197	0.220				
	210	←	198	0.201				
	210	←	201	0.355				
	213	←	201	–0.104				
70	210	←	198	0.449	4.82	257	38882	0.0219
	211	←	198	0.108				
	213	←	198	0.216				
	210	←	201	–0.333				
	211	←	201	–0.152				
	210	←	202	–0.170				

excited state	orbital composition			coefficient	excitation			oscillator strength
					eV	nm	cm^{-1}	
71	210	←	197	0.316	4.83	257	38936	0.0268
	212	←	197	0.119				
	210	←	198	–0.310				
	211	←	198	–0.119				
	213	←	198	–0.184				
	210	←	200	0.268				
	212	←	200	–0.129				
	214	←	200	0.109				
	210	←	201	–0.234				
	211	←	201	–0.108				
	210	←	202	–0.147				
72	210	←	197	–0.197	4.83	257	38966	0.0073
	210	←	200	0.526				
	212	←	200	–0.241				
	214	←	200	0.184				
	210	←	201	0.121				
	210	←	203	–0.104				
73	210	←	199	0.592	4.85	255	39141	0.0016
	211	←	199	0.268				
	213	←	199	–0.230				
74	210	←	196	0.555	4.87	254	39315	0.0058
	211	←	196	–0.114				
	212	←	196	0.322				
	214	←	196	0.119				
	210	←	197	0.151				
75	207 (b, π_ψ*)	←	192	0.121	4.93	251	39802	0.0159
	210	←	194	0.209				
	210	←	195	–0.238				
	210	←	203	–0.149				
	212	←	203	–0.217				
	214	←	203	0.239				
	216	←	206 (a, $d\pi$)	0.373				
76	209 (b, π_ψ*)	←	192	0.117	4.96	250	39989	0.0159
	210	←	193	0.136				
	210	←	195	0.319				
	210	←	203	0.107				
	212	←	203	0.166				
	214	←	203	–0.157				
	216	←	206 (a, $d\pi$)	0.374				
	217	←	206 (a, $d\pi$)	–0.126				
77	207 (b, π_ψ*)	←	192	0.218	4.97	250	40053	0.0138
	209 (b, π_ψ*)	←	192	0.162				
	210	←	193	0.140				
	210	←	194	0.349				
	211	←	197	–0.105				
	212	←	197	0.145				
	210	←	202	0.138				
	211	←	202	–0.122				
	213	←	202	–0.130				
	216	←	206 (a, $d\pi$)	–0.293				
78	207 (b, π_ψ*)	←	191	–0.128	4.98	249	40135	0.0028
	207 (b, π_ψ*)	←	192	–0.149				
	209 (b, π_ψ*)	←	192	–0.134				

excited state	orbital composition			coefficient	excitation			oscillator strength
					eV	nm	cm^{-1}	
	210	←	194	0.109				
	210	←	195	0.318				
	211	←	202	–0.122				
	210	←	203	–0.103				
	212	←	203	–0.120				
	214	←	203	0.112				
	216	←	204 (a, $d\pi$)	0.157				
	216	←	205 (b, $d\pi$)	–0.118				
	216	←	206 (a, $d\pi$)	0.108				
	217	←	206 (a, $d\pi$)	0.211				
79	207 (b, π_ψ*)	←	191	–0.105	5.00	248	40337	0.0150
	210	←	193	–0.210				
	210	←	195	0.224				
	210	←	197	–0.105				
	211	←	201	–0.120				
	213	←	201	–0.112				
	210	←	202	–0.209				
	211	←	202	0.264				
	213	←	202	0.208				
	215	←	202	0.143				
	214	←	203	0.117				
	216	←	206 (a, $d\pi$)	–0.200				
80	207 (b, π_ψ*)	←	191	0.158	5.02	247	40482	0.0277
	208 (a, π_ψ*)	←	191	0.227				
	207 (b, π_ψ*)	←	192	–0.132				
	209 (b, π_ψ*)	←	192	–0.107				
	210	←	193	–0.252				
	210	←	194	0.299				
	212	←	195	0.118				
	216	←	206 (a, $d\pi$)	0.121				
	217	←	206 (a, $d\pi$)	–0.180				
	218	←	206 (a, $d\pi$)	0.148				
81	207 (b, π_ψ*)	←	192	0.176	5.03	246	40599	0.0053
	210	←	194	0.104				
	213	←	195	0.111				
	210	←	201	0.119				
	210	←	203	0.171				
	211	←	203	–0.243				
	212	←	203	0.126				
	214	←	203	–0.223				
	216	←	205 (b, $d\pi$)	0.220				
	217	←	206 (a, $d\pi$)	0.281				
	218	←	206 (a, $d\pi$)	–0.119				
82	209 (b, π_ψ*)	←	190	0.106	5.05	245	40749	0.0101
	207 (b, π_ψ*)	←	192	0.169				
	209 (b, π_ψ*)	←	192	0.107				
	210	←	193	0.188				
	210	←	202	–0.136				
	211	←	202	0.147				
	212	←	202	0.102				
	217	←	206 (a, $d\pi$)	0.111				
	218	←	206 (a, $d\pi$)	0.443				
83	207 (b, π_ψ*)	←	192	–0.325	5.06	245	40774	0.0176

excited state	orbital composition		coefficient	excitation			oscillator strength
				eV	nm	cm^{-1}	
	210	← 193	0.268				
	210	← 194	0.115				
	211	← 202	0.184				
	216	← 204 (a, $d\pi$)	0.168				
	216	← 205 (b, $d\pi$)	0.337				
84	207 (b, π_ψ*)	← 190	–0.122	5.07	245	40884	0.0115
	207 (b, π_ψ*)	← 191	–0.161				
	210	← 193	–0.129				
	210	← 197	–0.132				
	211	← 197	–0.132				
	212	← 197	0.105				
	210	← 200	0.113				
	212	← 200	0.120				
	214	← 200	–0.127				
	212	← 202	–0.110				
	211	← 203	–0.170				
	216	← 204 (a, $d\pi$)	–0.196				
	216	← 205 (b, $d\pi$)	0.145				
	218	← 206 (a, $d\pi$)	0.310				
85	210	← 193	0.109	5.07	244	40921	0.0135
	210	← 197	–0.136				
	211	← 197	–0.112				
	212	← 197	0.155				
	210	← 200	–0.238				
	212	← 200	–0.238				
	213	← 200	0.122				
	214	← 200	0.300				
	212	← 201	0.116				
	211	← 203	–0.104				
	216	← 205 (b, $d\pi$)	–0.199				
	217	← 206 (a, $d\pi$)	0.218				
86	210	← 194	–0.151	5.08	244	40934	0.0032
	210	← 200	–0.203				
	212	← 200	–0.228				
	214	← 200	0.264				
	211	← 202	–0.101				
	216	← 205 (b, $d\pi$)	0.404				
	217	← 206 (a, $d\pi$)	–0.104				
	218	← 206 (a, $d\pi$)	0.109				
87	208 (a, π_ψ*)	← 192	0.119	5.08	244	41000	0.0043
	210	← 201	0.110				
	211	← 201	–0.170				
	213	← 201	0.106				
	211	← 202	–0.117				
	211	← 203	–0.169				
	216	← 204 (a, $d\pi$)	0.442				
	216	← 205 (b, $d\pi$)	–0.138				
	217	← 206 (a, $d\pi$)	–0.280				
88	210	← 198	0.171	5.09	244	41061	0.0139
	211	← 198	–0.205				
	213	← 198	–0.169				
	215	← 198	–0.129				
	210	← 201	–0.233				

excited state	orbital composition			coefficient	excitation			oscillator strength
					eV	nm	cm^{-1}	
	211	←	201	0.274				
	213	←	201	–0.171				
	211	←	202	0.110				
	213	←	202	–0.136				
	211	←	203	–0.270				
	216	←	204 (a, $d\pi$)	0.124				
	216	←	205 (b, $d\pi$)	–0.115				
89	210	←	197	0.141	5.10	243	41099	0.0003
	210	←	198	–0.256				
	211	←	198	0.327				
	213	←	198	0.245				
	215	←	198	0.185				
	211	←	203	–0.285				
	212	←	203	–0.123				
	217	←	206 (a, $d\pi$)	–0.157				
90	210	←	193	–0.184	5.10	243	41155	0.0130
	210	←	194	–0.144				
	210	←	196	0.105				
	211	←	197	–0.188				
	213	←	197	–0.168				
	210	←	198	–0.134				
	211	←	198	0.117				
	211	←	203	0.191				
	216	←	204 (a, $d\pi$)	0.317				
	217	←	206 (a, $d\pi$)	0.222				
91	207 (b, π_ψ*)	←	191	0.326	5.11	243	41234	0.0029
	207 (b, π_ψ*)	←	192	0.114				
	210	←	193	0.109				
	210	←	194	–0.142				
	210	←	195	0.233				
	212	←	195	0.147				
	213	←	203	0.312				
	214	←	203	0.110				
	218	←	206 (a, $d\pi$)	0.121				
92	207 (b, π_ψ*)	←	191	–0.148	5.12	242	41287	0.0025
	207 (b, π_ψ*)	←	192	0.166				
	208 (a, π_ψ*)	←	192	0.154				
	209 (b, π_ψ*)	←	192	–0.163				
	213	←	194	–0.133				
	210	←	195	–0.104				
	213	←	195	0.111				
	211	←	201	0.135				
	210	←	203	0.115				
	211	←	203	0.153				
	212	←	203	0.213				
	213	←	203	0.353				
	217	←	206 (a, $d\pi$)	–0.174				
93	209 (b, π_ψ*)	←	192	–0.101	5.13	242	41388	0.0007
	210	←	199	–0.321				
	211	←	199	0.393				
	212	←	199	0.156				
	213	←	199	–0.272				
	214	←	199	–0.136				

excited state	orbital composition			coefficient	excitation			oscillator strength
					eV	nm	cm^{-1}	
	215	←	199	–0.141				
94	207 (*b*, π_ψ*)	←	190	0.119	5.13	241	41411	0.0055
	210	←	196	0.179				
	211	←	196	0.205				
	212	←	196	–0.175				
	213	←	196	0.113				
	214	←	196	–0.111				
	211	←	197	–0.169				
	212	←	197	0.129				
	210	←	199	0.124				
	211	←	199	–0.144				
	213	←	199	0.109				
	212	←	201	–0.114				
	212	←	202	0.309				
	217	←	206 (*a*, *dπ*)	–0.107				
95	207 (*b*, π_ψ*)	←	190	–0.108	5.14	241	41432	0.0008
	208 (*a*, π_ψ*)	←	191	0.149				
	207 (*b*, π_ψ*)	←	192	–0.210				
	209 (*b*, π_ψ*)	←	192	0.218				
	211	←	197	–0.100				
	211	←	201	–0.124				
	212	←	201	–0.123				
	213	←	201	0.113				
	211	←	202	0.105				
	212	←	202	0.277				
	213	←	202	–0.132				
	214	←	202	0.100				
	213	←	203	0.250				
	218	←	206 (*a*, *dπ*)	–0.132				
96	207 (*b*, π_ψ*)	←	192	–0.147	5.15	241	41528	0.0081
	209 (*b*, π_ψ*)	←	192	0.167				
	213	←	193	0.108				
	211	←	196	0.144				
	211	←	201	0.155				
	213	←	201	–0.152				
	211	←	202	–0.287				
	213	←	202	0.347				
	213	←	203	0.163				
97	207 (*b*, π_ψ*)	←	191	0.112	5.16	240	41636	0.0050
	208 (*a*, π_ψ*)	←	191	–0.201				
	207 (*b*, π_ψ*)	←	192	–0.133				
	209 (*b*, π_ψ*)	←	192	0.107				
	210	←	193	–0.137				
	213	←	195	0.105				
	210	←	196	–0.182				
	211	←	196	–0.231				
	212	←	196	0.195				
	213	←	196	–0.119				
	214	←	196	0.127				
	213	←	197	–0.103				
	212	←	202	0.232				
	213	←	202	0.105				
	218	←	206 (*a*, *dπ*)	0.154				

excited state	orbital composition			coefficient	excitation			oscillator strength
					eV	nm	cm^{-1}	
98	207 (b, π_ψ*)	←	191	–0.169	5.17	240	41674	0.0059
	208 (a, π_ψ*)	←	191	0.241				
	207 (b, π_ψ*)	←	192	0.142				
	209 (b, π_ψ*)	←	192	–0.217				
	212	←	193	0.107				
	210	←	194	–0.172				
	211	←	194	–0.119				
	211	←	195	–0.106				
	214	←	195	–0.106				
	210	←	196	–0.148				
	211	←	196	–0.180				
	212	←	196	0.167				
	212	←	197	0.113				
	218	←	206 (a, $d\pi$)	–0.137				
99	207 (b, π_ψ*)	←	190	–0.173	5.18	239	41799	0.0069
	207 (b, π_ψ*)	←	191	0.188				
	208 (a, π_ψ*)	←	192	0.369				
	211	←	194	0.131				
	210	←	195	0.116				
	215	←	195	0.129				
	211	←	200	0.115				
	213	←	201	–0.105				
	212	←	202	0.101				
	211	←	203	0.186				
	213	←	203	–0.182				
	215	←	203	0.128				
	218	←	204 (a, $d\pi$)	–0.105				
	217	←	205 (b, $d\pi$)	–0.157				
100	211	←	200	0.624	5.19	239	41864	0.0023
	212	←	200	0.180				
	214	←	200	0.104				
	215	←	200	–0.139				
101	207 (b, π_ψ*)	←	190	0.215	5.20	239	41912	0.0043
	208 (a, π_ψ*)	←	192	0.308				
	209 (b, π_ψ*)	←	192	0.144				
	212	←	193	0.108				
	211	←	197	–0.114				
	212	←	197	–0.102				
	213	←	197	–0.175				
	212	←	201	–0.167				
	211	←	202	0.162				
	212	←	202	–0.289				
102	209 (b, π_ψ*)	←	190	–0.151	5.20	238	41973	0.0099
	208 (a, π_ψ*)	←	192	0.219				
	209 (b, π_ψ*)	←	192	0.129				
	210	←	193	0.126				
	212	←	194	–0.193				
	211	←	195	–0.171				
	211	←	197	0.185				
	212	←	197	0.122				
	213	←	197	0.108				
	212	←	202	0.187				
	214	←	203	0.113				

excited state	orbital composition			coefficient	excitation			oscillator strength
					eV	nm	cm^{-1}	
	218	←	204 (a, $d\pi$)	0.198				
103	209 (b, π_ψ*)	←	192	0.175	5.21	238	42041	0.0028
	211	←	203	0.114				
	215	←	203	0.213				
	217	←	205 (b, $d\pi$)	0.525				
104	208 (a, π_ψ*)	←	191	–0.112	5.21	238	42061	0.0030
	212	←	195	0.186				
	212	←	201	–0.128				
	214	←	202	0.113				
	211	←	203	–0.180				
	212	←	203	0.383				
	213	←	203	–0.135				
	214	←	203	0.333				
	215	←	203	–0.158				
	217	←	205 (b, $d\pi$)	0.133				
105	207 (b, π_ψ*)	←	190	–0.148	5.22	237	42129	0.0020
	207 (b, π_ψ*)	←	191	–0.104				
	212	←	193	–0.108				
	211	←	195	0.166				
	212	←	197	0.123				
	212	←	198	0.135				
	211	←	201	0.170				
	212	←	201	–0.336				
	214	←	201	0.107				
	214	←	203	–0.130				
	218	←	205 (b, $d\pi$)	0.346				
106	207 (b, π_ψ*)	←	191	–0.145	5.23	237	42155	0.0042
	208 (a, π_ψ*)	←	191	0.137				
	212	←	195	0.170				
	212	←	198	–0.147				
	211	←	201	–0.137				
	212	←	201	0.324				
	218	←	204 (a, $d\pi$)	–0.199				
	218	←	205 (b, $d\pi$)	0.352				
107	207 (b, π_ψ*)	←	190	0.183	5.23	237	42191	0.0011
	208 (a, π_ψ*)	←	191	0.116				
	211	←	197	–0.144				
	213	←	197	0.152				
	217	←	204 (a, $d\pi$)	0.523				
	217	←	205 (b, $d\pi$)	–0.126				
108	211	←	193	0.150	5.24	237	42223	0.0011
	211	←	194	0.111				
	211	←	197	–0.237				
	213	←	197	0.246				
	211	←	198	–0.146				
	212	←	198	–0.100				
	213	←	198	0.165				
	214	←	201	0.105				
	213	←	202	0.160				
	214	←	202	–0.193				
	215	←	202	–0.201				
	217	←	204 (a, $d\pi$)	–0.242				
	218	←	204 (a, $d\pi$)	0.171				

excited state	orbital composition			coefficient	excitation			oscillator strength
					eV	nm	cm^{-1}	
109	208 (a, π_ψ*)	←	192	–0.111	5.24	237	42261	0.0108
	212	←	197	–0.127				
	212	←	198	0.132				
	211	←	201	–0.180				
	212	←	201	–0.154				
	213	←	201	–0.261				
	215	←	201	0.114				
	212	←	203	0.111				
	214	←	203	0.144				
	215	←	203	0.378				
	218	←	204 (a, $d\pi$)	–0.107				
110	212	←	200	0.185	5.24	237	42283	0.0015
	213	←	200	0.559				
	215	←	200	–0.183				
	213	←	201	–0.142				
	215	←	203	–0.125				
111	212	←	197	–0.200	5.24	236	42293	0.0004
	212	←	198	0.511				
	214	←	198	0.120				
	215	←	198	0.142				
	215	←	203	–0.255				
112	212	←	197	–0.143	5.25	236	42342	0.0039
	213	←	197	–0.122				
	212	←	198	0.130				
	213	←	200	0.240				
	211	←	201	0.183				
	212	←	201	0.186				
	213	←	201	0.338				
	211	←	202	0.142				
	213	←	202	0.169				
	215	←	203	0.225				
	217	←	205 (b, $d\pi$)	–0.114				
113	207 (b, π_ψ*)	←	190	–0.141	5.26	236	42408	0.0028
	209 (b, π_ψ*)	←	190	0.242				
	211	←	194	–0.102				
	213	←	201	–0.113				
	218	←	204 (a, $d\pi$)	0.439				
	218	←	205 (b, $d\pi$)	0.241				
114	209 (b, π_ψ*)	←	192	0.113	5.26	236	42441	0.0022
	210	←	193	–0.132				
	213	←	197	0.303				
	212	←	198	0.162				
	213	←	198	0.149				
	214	←	201	–0.111				
	211	←	202	–0.148				
	212	←	202	–0.125				
	214	←	202	0.138				
	215	←	202	0.192				
	217	←	204 (a, $d\pi$)	–0.169				
	217	←	205 (b, $d\pi$)	–0.162				
115	212	←	194	0.147	5.27	235	42493	0.0014
	212	←	195	0.141				
	213	←	197	0.222				

excited state	orbital composition		coefficient	excitation			oscillator strength
				eV	nm	cm^{-1}	
	211	← 198	0.352				
	213	← 198	–0.328				
	214	← 198	0.140				
	214	← 202	–0.187				
116	212	← 193	–0.134	5.27	235	42525	0.0002
	212	← 194	0.133				
	212	← 195	0.201				
	213	← 198	0.103				
	211	← 199	–0.222				
	212	← 199	0.487				
	214	← 199	–0.188				
117	212	← 193	0.147	5.27	235	42541	0.0005
	211	← 194	0.121				
	212	← 194	–0.184				
	211	← 195	0.144				
	212	← 195	–0.299				
	211	← 197	–0.159				
	213	← 197	0.104				
	211	← 198	0.139				
	213	← 198	–0.176				
	211	← 199	–0.146				
	212	← 199	0.319				
	214	← 199	–0.123				
	214	← 201	–0.110				
	214	← 202	0.142				
118	209 (b, π_ψ*)	← 190	–0.120	5.28	235	42588	0.0026
	210	← 193	0.111				
	211	← 193	0.119				
	212	← 193	–0.198				
	211	← 195	–0.199				
	212	← 195	0.194				
	213	← 196	0.115				
	211	← 197	–0.201				
	213	← 198	–0.130				
	214	← 201	–0.125				
	215	← 201	–0.116				
	214	← 202	0.288				
	215	← 202	0.144				
119	207 (b, π_ψ*)	← 191	–0.149	5.29	234	42667	0.0283
	209 (b, π_ψ*)	← 191	–0.166				
	208 (a, π_ψ*)	← 192	0.121				
	211	← 195	0.212				
	212	← 195	0.138				
	213	← 196	–0.111				
	215	← 197	0.110				
	215	← 201	0.101				
	213	← 202	0.108				
	214	← 202	0.275				
	215	← 202	–0.228				
	217	← 204 (a, $d\pi$)	0.117				
	218	← 204 (a, $d\pi$)	0.144				
	218	← 205 (b, $d\pi$)	–0.171				
120	208 (a, π_ψ*)	← 192	0.121	5.29	234	42685	0.0100

excited state	orbital composition	coefficient	excitation			oscillator strength
			eV	nm	cm^{-1}	
211	← 195	0.273				
212	← 196	0.141				
213	← 196	0.215				
215	← 197	–0.128				
211	← 199	0.116				
213	← 199	0.169				
215	← 201	–0.128				
211	← 202	–0.123				
214	← 202	–0.179				
215	← 202	0.205				

Table 0-4 – TDDFT Calculated Excitation Energies, One–Electron Transitions, and Oscillator Strengths for Optical Transitions of $[Ru(dmpbpy)_3]^{2+}$ complex in the Gas Phase.

excited state	orbital composition		coefficient	excitation			oscillator strength
				eV	nm	cm^{-1}	
1	245 (a_2, π_ψ*)	← 244 (a_1, $d\pi$)	–0.470	2.47	501	19955	0.0015
	246 (e, π_ψ*)	← 244 (a_1, $d\pi$)	0.491				
	247 (e, π_ψ*)	← 244 (a_1, $d\pi$)	–0.130				
2	245 (a_2, π_ψ*)	← 244 (a_1, $d\pi$)	0.445	2.51	493	20279	0.0025
	246 (e, π_ψ*)	← 244 (a_1, $d\pi$)	0.478				
	247 (e, π_ψ*)	← 244 (a_1, $d\pi$)	0.236				
3	245 (a_2, π_ψ*)	← 244 (a_1, $d\pi$)	–0.263	2.56	484	20653	0.0013
	247 (e, π_ψ*)	← 244 (a_1, $d\pi$))	0.637				
4	245 (a_2, π_ψ*)	← 242 (e, $d\pi$)	–0.342	2.65	468	21390	0.0013
	246 (e, π_ψ*)	← 242 (e, $d\pi$)	0.179				
	247 (e, π_ψ*)	← 242 (e, $d\pi$)	–0.228				
	245 (a_2, π_ψ*)	← 243 (e, $d\pi$)	–0.238				
	246 (e, π_ψ*)	← 243 (e, $d\pi$)	0.464				
5	246 (e, π_ψ*)	← 242 (e, $d\pi$)	–0.196	2.69	461	21715	0.0099
	245 (a_2, π_ψ*)	← 243 (e, $d\pi$)	0.568				
	246 (e, π_ψ*)	← 243 (e, $d\pi$)	0.289				
	247 (e, π_ψ*)	← 243 (e, $d\pi$)	0.185				
6	245 (a_2, π_ψ*)	← 242 (e, $d\pi$)	0.525	2.74	452	22102	0.0310
	246 (e, π_ψ*)	← 242 (e, $d\pi$)	0.127				
	247 (e, π_ψ*)	← 242 (e, $d\pi$)	–0.414				
	247 (e, π_ψ*)	← 243 (e, $d\pi$)	0.100				
7	245 (a_2, π_ψ*)	← 242 (e, $d\pi$)	0.259	2.83	438	22807	0.1564
	246 (e, π_ψ*)	← 242 (e, $d\pi$)	–0.186				
	247 (e, π_ψ*)	← 242 (e, $d\pi$)	0.423				
	245 (a_2, π_ψ*)	← 243 (e, $d\pi$)	–0.213				
	246 (e, π_ψ*)	← 243 (e, $d\pi$)	0.351				
	247 (e, π_ψ*)	← 243 (e, $d\pi$)	0.140				
8	245 (a_2, π_ψ*)	← 242 (e, $d\pi$)	0.135	2.85	435	22998	0.1536
	246 (e, π_ψ*)	← 242 (e, $d\pi$)	0.427				
	247 (e, π_ψ*)	← 242 (e, $d\pi$)	0.192				
	245 (a_2, π_ψ*)	← 243 (e, $d\pi$)	0.209				
	246 (e, π_ψ*)	← 243 (e, $d\pi$)	0.185				
	247 (e, π_ψ*)	← 243 (e, $d\pi$)	–0.392				
9	246 (e, π_ψ*)	← 242 (e, $d\pi$)	0.352	3.07	404	24755	0.0045
	247 (e, π_ψ*)	← 242 (e, $d\pi$)	0.155				
	246 (e, π_ψ*)	← 243 (e, $d\pi$)	–0.102				
	247 (e, π_ψ*)	← 243 (e, $d\pi$)	0.451				
	249	← 244 (a_1, $d\pi$)	0.163				
	251	← 244 (a_1, $d\pi$)	–0.220				
10	248	← 244 (a_1, $d\pi$)	0.698	3.31	375	26670	0.0118
11	248	← 243 (e, $d\pi$)	0.697	3.47	357	27993	0.0094
12	248	← 242 (e, $d\pi$)	0.693	3.48	356	28107	0.0136
13	249	← 244 (a_1, $d\pi$)	0.473	3.57	347	28805	0.0058
	250	← 244 (a_1, $d\pi$)	0.416				
	251	← 244 (a_1, $d\pi$)	0.271				
14	249	← 244 (a_1, $d\pi$)	–0.393	3.58	346	28862	0.0363
	250	← 244 (a_1, $d\pi$)	0.538				
	251	← 244 (a_1, $d\pi$)	–0.130				
15	250	← 242 (e, $d\pi$)	–0.128	3.63	341	29293	0.0006
	251	← 242 (e, $d\pi$)	–0.159				

excited state	orbital composition		coefficient	excitation			oscillator strength
				eV	nm	cm^{-1}	
	252	← 242 (e, $d\pi$)	0.102				
	253	← 242 (e, $d\pi$)	–0.123				
	252	← 243 (e, $d\pi$)	–0.175				
	249	← 244 (a_1, $d\pi$)	–0.172				
	251	← 244 (a_1, $d\pi$)	0.518				
	253	← 244 (a_1, $d\pi$)	0.182				
16	251	← 242 (e, $d\pi$)	0.152	3.65	340	29442	0.0106
	249	← 243 (e, $d\pi$)	0.236				
	250	← 243 (e, $d\pi$)	0.112				
	251	← 243 (e, $d\pi$)	–0.216				
	252	← 244 (a_1, $d\pi$)	0.574				
17	249	← 242 (e, $d\pi$)	0.286	3.68	337	29655	0.0050
	250	← 242 (e, $d\pi$)	0.127				
	251	← 242 (e, $d\pi$)	–0.195				
	253	← 242 (e, $d\pi$)	0.111				
	249	← 243 (e, $d\pi$)	0.195				
	249	← 244 (a_1, $d\pi$)	0.101				
	251	← 244 (a_1, $d\pi$)	–0.130				
	252	← 244 (a_1, $d\pi$)	–0.102				
	253	← 244 (a_1, $d\pi$)	0.469				
18	249	← 242 (e, $d\pi$)	–0.119	3.71	334	29900	0.0927
	249	← 243 (e, $d\pi$)	0.427				
	251	← 243 (e, $d\pi$)	–0.332				
	252	← 244 (a_1, $d\pi$)	–0.298				
	253	← 244 (a_1, $d\pi$)	–0.234				
19	249	← 242 (e, $d\pi$)	0.481	3.72	333	30013	0.0652
	251	← 242 (e, $d\pi$)	–0.248				
	252	← 244 (a_1, $d\pi$)	0.105				
	253	← 244 (a_1, $d\pi$)	–0.380				
20	249	← 242 (e, $d\pi$)	–0.102	3.74	332	30159	0.0199
	251	← 242 (e, $d\pi$)	–0.141				
	250	← 243 (e, $d\pi$)	0.650				
	252	← 244 (a_1, $d\pi$)	–0.102				
21	249	← 243 (e, $d\pi$)	0.400	3.75	331	30234	0.0188
	251	← 243 (e, $d\pi$)	0.529				
22	249	← 242 (e, $d\pi$)	–0.277	3.76	330	30291	0.0320
	250	← 242 (e, $d\pi$)	0.529				
	251	← 242 (e, $d\pi$)	–0.247				
	250	← 243 (e, $d\pi$)	–0.136				
	252	← 243 (e, $d\pi$)	–0.118				
23	249	← 242 (e, $d\pi$)	0.203	3.77	329	30432	0.0623
	250	← 242 (e, $d\pi$)	0.314				
	251	← 242 (e, $d\pi$)	0.460				
	252	← 242 (e, $d\pi$)	0.125				
	253	← 242 (e, $d\pi$)	–0.136				
	252	← 243 (e, $d\pi$)	–0.162				
	252	← 244 (a_1, $d\pi$)	–0.107				
	257	← 244 (a_1, $d\pi$)	0.150				
24	252	← 242 (e, $d\pi$)	0.503	3.83	324	30854	0.0140
	252	← 243 (e, $d\pi$)	0.388				
	253	← 243 (e, $d\pi$)	–0.166				
	258	← 244 (a_1, $d\pi$)	–0.134				
25	247 (e, π_ψ*)	← 230	0.102	3.83	323	30922	0.0069

excited state	orbital composition		coefficient	excitation			oscillator strength
				eV	nm	cm^{-1}	
	252	← 242 (e, $d\pi$)	0.274				
	253	← 242 (e, $d\pi$)	0.297				
	257	← 242 (e, $d\pi$)	0.105				
	252	← 243 (e, $d\pi$)	–0.304				
	253	← 243 (e, $d\pi$)	0.334				
	258	← 244 (a_1, $d\pi$)	–0.254				
26	252	← 242 (e, $d\pi$)	0.120	3.84	323	30993	0.0010
	253	← 242 (e, $d\pi$)	–0.391				
	253	← 243 (e, $d\pi$)	0.463				
	257	← 243 (e, $d\pi$)	0.122				
	257	← 244 (a_1, $d\pi$)	–0.229				
27	249	← 242 (e, $d\pi$)	–0.108	3.88	320	31272	0.0080
	251	← 242 (e, $d\pi$)	–0.114				
	253	← 242 (e, $d\pi$)	–0.236				
	258	← 242 (e, $d\pi$)	–0.270				
	252	← 243 (e, $d\pi$)	0.135				
	253	← 243 (e, $d\pi$)	0.132				
	257	← 243 (e, $d\pi$)	–0.224				
	257	← 244 (a_1, $d\pi$)	0.418				
	258	← 244 (a_1, $d\pi$)	–0.117				
28	250	← 242 (e, $d\pi$)	–0.120	3.89	319	31371	0.0249
	252	← 242 (e, $d\pi$)	0.212				
	253	← 242 (e, $d\pi$)	0.210				
	257	← 242 (e, $d\pi$)	–0.269				
	249	← 243 (e, $d\pi$)	0.110				
	258	← 243 (e, $d\pi$)	0.268				
	257	← 244 (a_1, $d\pi$)	0.135				
	258	← 244 (a_1, $d\pi$)	0.392				
29	257	← 242 (e, $d\pi$)	0.334	4.00	310	32256	0.0009
	258	← 242 (e, $d\pi$)	–0.328				
	257	← 243 (e, $d\pi$)	0.323				
	258	← 243 (e, $d\pi$)	0.331				
30	246 (e, π_ψ*)	← 237	–0.102	4.08	304	32869	0.0596
	245 (a_2, π_ψ*)	← 238	0.307				
	246 (e, π_ψ*)	← 238	0.214				
	247 (e, π_ψ*)	← 238	0.102				
	245 (a_2, π_ψ*)	← 239	0.404				
	246 (e, π_ψ*)	← 239	0.299				
	247 (e, π_ψ*)	← 239	0.131				
	245 (a_2, π_ψ*)	← 241	–0.122				
31	245 (a_2, π_ψ*)	← 235	–0.238	4.10	302	33084	0.0863
	246 (e, π_ψ*)	← 235	0.105				
	245 (a_2, π_ψ*)	← 237	0.351				
	246 (e, π_ψ*)	← 237	–0.189				
	245 (a_2, π_ψ*)	← 238	0.159				
	245 (a_2, π_ψ*)	← 241	0.366				
	246 (e, π_ψ*)	← 241	0.128				
	247 (e, π_ψ*)	← 241	–0.209				
32	245 (a_2, π_ψ*)	← 235	0.192	4.11	302	33110	0.0674
	245 (a_2, π_ψ*)	← 237	–0.322				
	246 (e, π_ψ*)	← 237	0.141				
	246 (e, π_ψ*)	← 238	0.107				
	245 (a_2, π_ψ*)	← 239	0.110				

excited state	orbital composition			coefficient	excitation			oscillator strength
					eV	nm	cm^{-1}	
	245 (a_2, π_ψ*)	←	241	0.416				
	246 (e, π_ψ*)	←	241	0.127				
	247 (e, π_ψ*)	←	241	–0.261				
33	245 (a_2, π_ψ*)	←	230	0.140	4.14	299	33427	0.0125
	245 (a_2, π_ψ*)	←	240	0.552				
	246 (e, π_ψ*)	←	240	0.150				
	247 (e, π_ψ*)	←	240	–0.316				
34	245 (a_2, π_ψ*)	←	234	0.156	4.15	298	33509	0.0290
	246 (e, π_ψ*)	←	234	0.144				
	245 (a_2, π_ψ*)	←	235	0.198				
	245 (a_2, π_ψ*)	←	237	0.246				
	245 (a_2, π_ψ*)	←	238	–0.149				
	245 (a_2, π_ψ*)	←	239	0.197				
	247 (e, π_ψ*)	←	239	–0.101				
	247 (e, π_ψ*)	←	241	–0.135				
	252	←	242 (e, $d\pi$)	–0.124				
	253	←	242 (e, $d\pi$)	0.188				
	252	←	243 (e, $d\pi$)	0.192				
	253	←	243 (e, $d\pi$)	0.161				
	251	←	244 (a_1, $d\pi$)	0.131				
35	245 (a_2, π_ψ*)	←	233	–0.148	4.16	298	33584	0.0130
	246 (e, π_ψ*)	←	233	–0.111				
	245 (a_2, π_ψ*)	←	234	0.467				
	246 (e, π_ψ*)	←	234	0.370				
	247 (e, π_ψ*)	←	234	0.166				
36	245 (a_2, π_ψ*)	←	231	0.434	4.17	298	33601	0.0039
	246 (e, π_ψ*)	←	231	–0.220				
	245 (a_2, π_ψ*)	←	232	0.243				
	246 (e, π_ψ*)	←	232	–0.193				
	245 (a_2, π_ψ*)	←	235	0.268				
	246 (e, π_ψ*)	←	235	–0.120				
	245 (a_2, π_ψ*)	←	237	0.105				
	245 (a_2, π_ψ*)	←	238	0.162				
37	246 (e, π_ψ*)	←	227	–0.111	4.18	297	33673	0.0008
	246 (e, π_ψ*)	←	229	0.118				
	246 (e, π_ψ*)	←	231	–0.215				
	245 (a_2, π_ψ*)	←	232	0.419				
	246 (e, π_ψ*)	←	232	0.130				
	245 (a_2, π_ψ*)	←	235	–0.250				
	245 (a_2, π_ψ*)	←	238	–0.111				
	245 (a_2, π_ψ*)	←	239	0.144				
	247 (e, π_ψ*)	←	239	–0.116				
	247 (e, π_ψ*)	←	240	0.109				
	247 (e, π_ψ*)	←	241	–0.123				
38	246 (e, π_ψ*)	←	228	0.107	4.19	296	33754	0.0145
	245 (a_2, π_ψ*)	←	231	0.351				
	245 (a_2, π_ψ*)	←	232	–0.159				
	246 (e, π_ψ*)	←	232	–0.184				
	245 (a_2, π_ψ*)	←	233	0.125				
	245 (a_2, π_ψ*)	←	235	–0.294				
	246 (e, π_ψ*)	←	235	0.218				
	245 (a_2, π_ψ*)	←	237	–0.112				
	245 (a_2, π_ψ*)	←	238	–0.146				

excited state	orbital composition			coefficient	excitation			oscillator strength
					eV	nm	cm^{-1}	
39	245 (a_2, π_ψ*)	←	229	–0.140	4.20	295	33846	0.0286
	245 (a_2, π_ψ*)	←	230	0.203				
	246 (e, π_ψ*)	←	231	0.103				
	246 (e, π_ψ*)	←	232	–0.192				
	245 (a_2, π_ψ*)	←	233	–0.100				
	245 (a_2, π_ψ*)	←	238	–0.183				
	246 (e, π_ψ*)	←	238	–0.132				
	247 (e, π_ψ*)	←	238	0.184				
	245 (a_2, π_ψ*)	←	239	0.296				
	247 (e, π_ψ*)	←	239	–0.170				
	246 (e, π_ψ*)	←	240	–0.115				
	246 (e, π_ψ*)	←	241	0.125				
	247 (e, π_ψ*)	←	241	0.111				
	252	←	243 (e, $d\pi$)	–0.107				
40	245 (a_2, π_ψ*)	←	230	0.353	4.20	295	33879	0.0010
	247 (e, π_ψ*)	←	230	0.120				
	245 (a_2, π_ψ*)	←	236	0.155				
	245 (a_2, π_ψ*)	←	237	–0.109				
	245 (a_2, π_ψ*)	←	238	0.269				
	247 (e, π_ψ*)	←	238	–0.180				
	246 (e, π_ψ*)	←	239	–0.163				
	247 (e, π_ψ*)	←	240	0.201				
	247 (e, π_ψ*)	←	241	–0.131				
41	245 (a_2, π_ψ*)	←	231	–0.127	4.21	295	33948	0.0046
	245 (a_2, π_ψ*)	←	233	0.534				
	246 (e, π_ψ*)	←	233	–0.266				
	245 (a_2, π_ψ*)	←	234	0.171				
	246 (e, π_ψ*)	←	234	–0.112				
	245 (a_2, π_ψ*)	←	239	0.104				
	246 (e, π_ψ*)	←	239	–0.134				
42	245 (a_2, π_ψ*)	←	227	–0.139	4.22	294	34006	0.0003
	245 (a_2, π_ψ*)	←	230	0.322				
	245 (a_2, π_ψ*)	←	233	0.160				
	246 (e, π_ψ*)	←	233	–0.106				
	245 (a_2, π_ψ*)	←	235	0.106				
	245 (a_2, π_ψ*)	←	236	0.142				
	245 (a_2, π_ψ*)	←	237	0.112				
	246 (e, π_ψ*)	←	237	–0.113				
	245 (a_2, π_ψ*)	←	238	–0.189				
	246 (e, π_ψ*)	←	238	0.128				
	247 (e, π_ψ*)	←	238	0.102				
	245 (a_2, π_ψ*)	←	239	–0.168				
	246 (e, π_ψ*)	←	239	0.256				
	247 (e, π_ψ*)	←	240	0.180				
	246 (e, π_ψ*)	←	241	–0.142				
43	245 (a_2, π_ψ*)	←	230	–0.170	4.23	293	34107	0.0019
	245 (a_2, π_ψ*)	←	236	0.511				
	246 (e, π_ψ*)	←	236	0.110				
	247 (e, π_ψ*)	←	236	–0.406				
44	245 (a_2, π_ψ*)	←	230	0.103	4.24	292	34207	0.0112
	246 (e, π_ψ*)	←	230	–0.120				
	247 (e, π_ψ*)	←	240	0.106				
	245 (a_2, π_ψ*)	←	241	0.345				

excited state	orbital composition			coefficient	excitation			oscillator strength
					eV	nm	cm^{-1}	
	247 (e, π_ψ*)	←	241	0.504				
45	245 (a_2, π_ψ*)	←	229	–0.321	4.25	292	34299	0.0065
	246 (e, π_ψ*)	←	229	–0.312				
	247 (e, π_ψ*)	←	229	–0.127				
	246 (e, π_ψ*)	←	230	0.338				
	245 (a_2, π_ψ*)	←	232	0.111				
	246 (e, π_ψ*)	←	232	0.118				
	246 (e, π_ψ*)	←	240	0.281				
	247 (e, π_ψ*)	←	240	0.150				
46	245 (a_2, π_ψ*)	←	227	0.113	4.26	291	34321	0.0112
	245 (a_2, π_ψ*)	←	229	0.298				
	246 (e, π_ψ*)	←	229	0.262				
	247 (e, π_ψ*)	←	229	0.120				
	246 (e, π_ψ*)	←	230	0.331				
	246 (e, π_ψ*)	←	235	0.128				
	246 (e, π_ψ*)	←	238	–0.129				
	245 (a_2, π_ψ*)	←	239	0.116				
	246 (e, π_ψ*)	←	239	–0.112				
	246 (e, π_ψ*)	←	240	0.203				
	247 (e, π_ψ*)	←	240	0.102				
	245 (a_2, π_ψ*)	←	241	0.105				
	247 (e, π_ψ*)	←	241	0.131				
47	246 (e, π_ψ*)	←	235	0.126	4.26	291	34398	0.0002
	246 (e, π_ψ*)	←	237	–0.134				
	246 (e, π_ψ*)	←	239	0.114				
	245 (a_2, π_ψ*)	←	241	–0.135				
	246 (e, π_ψ*)	←	241	0.592				
48	245 (a_2, π_ψ*)	←	228	–0.188	4.27	290	34424	0.0026
	246 (e, π_ψ*)	←	228	–0.152				
	246 (e, π_ψ*)	←	230	–0.120				
	245 (a_2, π_ψ*)	←	235	0.163				
	246 (e, π_ψ*)	←	235	0.308				
	247 (e, π_ψ*)	←	235	–0.188				
	245 (a_2, π_ψ*)	←	237	–0.175				
	246 (e, π_ψ*)	←	237	–0.285				
	247 (e, π_ψ*)	←	237	0.148				
	246 (e, π_ψ*)	←	238	–0.124				
	246 (e, π_ψ*)	←	240	–0.117				
	247 (e, π_ψ*)	←	240	–0.118				
	246 (e, π_ψ*)	←	241	–0.196				
49	247 (e, π_ψ*)	←	227	0.100	4.30	289	34658	0.0163
	245 (a_2, π_ψ*)	←	230	–0.107				
	247 (e, π_ψ*)	←	232	0.140				
	247 (e, π_ψ*)	←	235	–0.145				
	245 (a_2, π_ψ*)	←	238	–0.198				
	246 (e, π_ψ*)	←	239	–0.214				
	247 (e, π_ψ*)	←	239	0.481				
	245 (a_2, π_ψ*)	←	240	0.102				
	247 (e, π_ψ*)	←	240	0.167				
50	245 (a_2, π_ψ*)	←	227	0.205	4.31	288	34768	0.0056
	245 (a_2, π_ψ*)	←	228	0.111				
	245 (a_2, π_ψ*)	←	231	–0.107				
	245 (a_2, π_ψ*)	←	232	0.228				

excited state	orbital composition			coefficient	excitation			oscillator strength
					eV	nm	cm^{-1}	
	246 (e, π_ψ*)	←	232	–0.190				
	247 (e, π_ψ*)	←	232	–0.126				
	246 (e, π_ψ*)	←	237	–0.159				
	245 (a_2, π_ψ*)	←	238	–0.243				
	246 (e, π_ψ*)	←	238	0.298				
	247 (e, π_ψ*)	←	238	–0.279				
51	245 (a_2, π_ψ*)	←	228	0.114	4.31	287	34787	0.0008
	245 (a_2, π_ψ*)	←	230	0.131				
	246 (e, π_ψ*)	←	230	0.124				
	245 (a_2, π_ψ*)	←	231	–0.126				
	246 (e, π_ψ*)	←	231	0.104				
	245 (a_2, π_ψ*)	←	232	0.192				
	246 (e, π_ψ*)	←	232	–0.151				
	246 (e, π_ψ*)	←	237	0.106				
	247 (e, π_ψ*)	←	238	0.279				
	245 (a_2, π_ψ*)	←	239	–0.158				
	246 (e, π_ψ*)	←	239	0.121				
	247 (e, π_ψ*)	←	239	0.168				
	245 (a_2, π_ψ*)	←	240	–0.243				
	247 (e, π_ψ*)	←	240	–0.278				
52	245 (a_2, π_ψ*)	←	228	0.117	4.32	287	34837	0.0050
	245 (a_2, π_ψ*)	←	230	–0.223				
	246 (e, π_ψ*)	←	230	–0.116				
	247 (e, π_ψ*)	←	230	–0.103				
	245 (a_2, π_ψ*)	←	231	–0.107				
	246 (e, π_ψ*)	←	232	–0.155				
	247 (e, π_ψ*)	←	238	0.245				
	245 (a_2, π_ψ*)	←	239	–0.193				
	246 (e, π_ψ*)	←	239	0.149				
	247 (e, π_ψ*)	←	239	–0.134				
	245 (a_2, π_ψ*)	←	240	0.231				
	247 (e, π_ψ*)	←	240	0.329				
53	247 (e, π_ψ*)	←	227	–0.116	4.33	286	34924	0.0056
	245 (a_2, π_ψ*)	←	228	0.141				
	246 (e, π_ψ*)	←	228	0.174				
	247 (e, π_ψ*)	←	228	0.151				
	246 (e, π_ψ*)	←	235	–0.156				
	247 (e, π_ψ*)	←	235	–0.398				
	247 (e, π_ψ*)	←	237	0.414				
54	245 (a_2, π_ψ*)	←	234	–0.108	4.35	285	35101	0.0032
	246 (e, π_ψ*)	←	235	0.237				
	245 (a_2, π_ψ*)	←	237	0.159				
	246 (e, π_ψ*)	←	237	0.273				
	246 (e, π_ψ*)	←	238	0.393				
	247 (e, π_ψ*)	←	238	0.123				
	246 (e, π_ψ*)	←	239	–0.197				
	247 (e, π_ψ*)	←	239	–0.179				
	246 (e, π_ψ*)	←	240	0.122				
55	245 (a_2, π_ψ*)	←	234	0.291	4.35	285	35122	0.0040
	246 (e, π_ψ*)	←	234	–0.268				
	246 (e, π_ψ*)	←	235	–0.187				
	246 (e, π_ψ*)	←	237	–0.241				
	246 (e, π_ψ*)	←	238	0.237				

excited state	orbital composition			coefficient	excitation			oscillator strength
					eV	nm	cm^{-1}	
	247 (e, π_ψ*)	←	238	0.216				
	246 (e, π_ψ*)	←	239	–0.267				
56	246 (e, π_ψ*)	←	230	–0.316	4.36	285	35136	0.0018
	245 (a_2, π_ψ*)	←	234	0.157				
	246 (e, π_ψ*)	←	234	–0.179				
	246 (e, π_ψ*)	←	236	–0.117				
	246 (e, π_ψ*)	←	238	–0.114				
	247 (e, π_ψ*)	←	238	–0.156				
	245 (a_2, π_ψ*)	←	240	–0.146				
	246 (e, π_ψ*)	←	240	0.462				
57	246 (e, π_ψ*)	←	230	–0.158	4.36	285	35141	0.0014
	246 (e, π_ψ*)	←	232	–0.132				
	245 (a_2, π_ψ*)	←	234	–0.272				
	246 (e, π_ψ*)	←	234	0.317				
	245 (a_2, π_ψ*)	←	235	–0.117				
	246 (e, π_ψ*)	←	235	–0.152				
	245 (a_2, π_ψ*)	←	237	–0.158				
	246 (e, π_ψ*)	←	237	–0.240				
	247 (e, π_ψ*)	←	238	0.102				
	246 (e, π_ψ*)	←	239	–0.161				
	246 (e, π_ψ*)	←	240	0.233				
58	245 (a_2, π_ψ*)	←	236	0.408	4.37	284	35260	0.0020
	246 (e, π_ψ*)	←	236	–0.306				
	247 (e, π_ψ*)	←	236	0.458				
59	245 (a_2, π_ψ*)	←	231	0.243	4.39	282	35424	0.0021
	246 (e, π_ψ*)	←	231	0.381				
	247 (e, π_ψ*)	←	231	–0.361				
	245 (a_2, π_ψ*)	←	232	0.147				
	246 (e, π_ψ*)	←	232	0.208				
	247 (e, π_ψ*)	←	232	–0.281				
60	246 (e, π_ψ*)	←	227	–0.120	4.40	282	35508	0.0042
	247 (e, π_ψ*)	←	227	0.123				
	247 (e, π_ψ*)	←	228	0.119				
	246 (e, π_ψ*)	←	231	0.164				
	247 (e, π_ψ*)	←	231	–0.215				
	246 (e, π_ψ*)	←	232	–0.202				
	247 (e, π_ψ*)	←	232	0.319				
	247 (e, π_ψ*)	←	234	0.118				
	247 (e, π_ψ*)	←	235	–0.156				
	246 (e, π_ψ*)	←	237	–0.110				
	247 (e, π_ψ*)	←	237	–0.143				
	247 (e, π_ψ*)	←	238	–0.192				
	247 (e, π_ψ*)	←	239	–0.259				
61	245 (a_2, π_ψ*)	←	227	–0.172	4.42	281	35618	0.0234
	245 (a_2, π_ψ*)	←	228	0.279				
	247 (e, π_ψ*)	←	228	–0.151				
	247 (e, π_ψ*)	←	230	0.146				
	245 (a_2, π_ψ*)	←	233	0.143				
	246 (e, π_ψ*)	←	233	0.266				
	246 (e, π_ψ*)	←	235	0.178				
	246 (e, π_ψ*)	←	236	0.327				
	247 (e, π_ψ*)	←	236	0.165				
62	245 (a_2, π_ψ*)	←	228	–0.161	4.42	281	35646	0.0054

excited state	orbital composition			coefficient	excitation			oscillator strength
					eV	nm	cm^{-1}	
	247 (e, π_ψ*)	←	230	–0.104				
	245 (a_2, π_ψ*)	←	233	–0.123				
	246 (e, π_ψ*)	←	233	–0.222				
	245 (a_2, π_ψ*)	←	236	0.109				
	246 (e, π_ψ*)	←	236	0.497				
	247 (e, π_ψ*)	←	236	0.266				
63	245 (a_2, π_ψ*)	←	227	0.124	4.43	280	35698	0.0162
	245 (a_2, π_ψ*)	←	228	–0.256				
	247 (e, π_ψ*)	←	230	–0.116				
	245 (a_2, π_ψ*)	←	233	0.247				
	246 (e, π_ψ*)	←	233	0.471				
	246 (e, π_ψ*)	←	234	0.156				
	246 (e, π_ψ*)	←	235	–0.161				
64	247 (e, π_ψ*)	←	233	–0.156	4.44	279	35812	0.0002
	246 (e, π_ψ*)	←	234	–0.221				
	247 (e, π_ψ*)	←	234	0.560				
	247 (e, π_ψ*)	←	235	0.207				
	247 (e, π_ψ*)	←	237	0.233				
65	245 (a_2, π_ψ*)	←	227	0.266	4.45	279	35880	0.0484
	245 (a_2, π_ψ*)	←	228	0.188				
	245 (a_2, π_ψ*)	←	229	–0.220				
	246 (e, π_ψ*)	←	229	0.215				
	247 (e, π_ψ*)	←	230	–0.219				
	246 (e, π_ψ*)	←	231	–0.140				
	246 (e, π_ψ*)	←	232	0.162				
	247 (e, π_ψ*)	←	234	0.155				
	247 (e, π_ψ*)	←	235	–0.192				
	247 (e, π_ψ*)	←	237	–0.253				
66	245 (a_2, π_ψ*)	←	227	–0.117	4.45	278	35912	0.0064
	246 (e, π_ψ*)	←	228	0.155				
	245 (a_2, π_ψ*)	←	229	0.294				
	246 (e, π_ψ*)	←	229	–0.288				
	247 (e, π_ψ*)	←	231	0.107				
	245 (a_2, π_ψ*)	←	232	0.108				
	247 (e, π_ψ*)	←	232	–0.232				
	247 (e, π_ψ*)	←	234	0.180				
	247 (e, π_ψ*)	←	235	–0.226				
	247 (e, π_ψ*)	←	237	–0.286				
67	245 (a_2, π_ψ*)	←	227	–0.104	4.47	278	36014	0.0795
	247 (e, π_ψ*)	←	227	–0.115				
	245 (a_2, π_ψ*)	←	228	–0.194				
	245 (a_2, π_ψ*)	←	229	–0.256				
	246 (e, π_ψ*)	←	229	0.254				
	247 (e, π_ψ*)	←	230	0.296				
	247 (e, π_ψ*)	←	231	0.164				
	247 (e, π_ψ*)	←	232	–0.203				
	247 (e, π_ψ*)	←	235	–0.158				
	247 (e, π_ψ*)	←	237	–0.127				
68	245 (a_2, π_ψ*)	←	227	0.140	4.48	277	36150	0.0166
	246 (e, π_ψ*)	←	228	–0.147				
	245 (a_2, π_ψ*)	←	231	0.164				
	246 (e, π_ψ*)	←	231	0.293				
	247 (e, π_ψ*)	←	231	0.415				

excited state	orbital composition			coefficient	excitation			oscillator strength
					eV	nm	cm^{-1}	
	246 (e, π_ψ*)	←	232	0.220				
	247 (e, π_ψ*)	←	232	0.216				
69	245 (a_2, π_ψ*)	←	227	–0.238	4.49	276	36190	0.0944
	245 (a_2, π_ψ*)	←	228	–0.108				
	246 (e, π_ψ*)	←	228	0.320				
	245 (a_2, π_ψ*)	←	229	–0.153				
	246 (e, π_ψ*)	←	229	0.147				
	247 (e, π_ψ*)	←	230	–0.278				
	246 (e, π_ψ*)	←	231	0.205				
	247 (e, π_ψ*)	←	231	0.193				
	245 (a_2, π_ψ*)	←	232	0.121				
	246 (e, π_ψ*)	←	235	0.107				
70	247 (e, π_ψ*)	←	227	–0.211	4.50	276	36279	0.0149
	247 (e, π_ψ*)	←	228	0.296				
	247 (e, π_ψ*)	←	232	0.105				
	247 (e, π_ψ*)	←	233	0.335				
	257	←	242 (e, $d\pi$)	–0.210				
	258	←	243 (e, $d\pi$)	0.196				
	258	←	244 (a_1, $d\pi$)	–0.214				
71	245 (a_2, π_ψ*)	←	227	–0.179	4.51	275	36361	0.0505
	246 (e, π_ψ*)	←	227	0.416				
	247 (e, π_ψ*)	←	228	0.142				
	247 (e, π_ψ*)	←	233	0.254				
	257	←	242 (e, $d\pi$)	0.149				
	258	←	243 (e, $d\pi$)	–0.165				
	257	←	244 (a_1, $d\pi$)	0.123				
	258	←	244 (a_1, $d\pi$)	0.147				
72	246 (e, π_ψ*)	←	227	–0.353	4.51	275	36388	0.0302
	247 (e, π_ψ*)	←	233	0.415				
	247 (e, π_ψ*)	←	234	0.131				
	257	←	242 (e, $d\pi$)	0.170				
	258	←	243 (e, $d\pi$)	–0.161				
	258	←	244 (a_1, $d\pi$)	0.182				
73	246 (e, π_ψ*)	←	227	–0.142	4.52	274	36442	0.0066
	247 (e, π_ψ*)	←	227	–0.116				
	247 (e, π_ψ*)	←	228	0.160				
	247 (e, π_ψ*)	←	233	–0.138				
	247 (e, π_ψ*)	←	235	0.138				
	258	←	242 (e, $d\pi$)	0.302				
	257	←	243 (e, $d\pi$)	0.326				
	257	←	244 (a_1, $d\pi$)	0.309				
74	247 (e, π_ψ*)	←	227	–0.228	4.53	274	36515	0.0261
	246 (e, π_ψ*)	←	228	0.140				
	247 (e, π_ψ*)	←	228	0.355				
	247 (e, π_ψ*)	←	233	–0.246				
	247 (e, π_ψ*)	←	235	0.117				
	247 (e, π_ψ*)	←	237	–0.132				
	257	←	242 (e, $d\pi$)	0.127				
	258	←	242 (e, $d\pi$)	–0.181				
	257	←	243 (e, $d\pi$)	–0.155				
	258	←	243 (e, $d\pi$)	–0.117				
	258	←	244 (a_1, $d\pi$)	0.201				
75	245 (a_2, π_ψ*)	←	227	0.229	4.55	273	36686	0.5214

excited state	orbital composition			coefficient	excitation			oscillator strength
					eV	nm	cm^{-1}	
	245 (a_2, π_ψ*)	←	228	–0.128				
	246 (e, π_ψ*)	←	228	0.392				
	247 (e, π_ψ*)	←	229	0.172				
	247 (e, π_ψ*)	←	230	0.195				
	247 (e, π_ψ*)	←	231	–0.102				
	247 (e, π_ψ*)	←	232	0.188				
76	247 (e, π_ψ*)	←	227	–0.251	4.56	272	36796	0.0885
	246 (e, π_ψ*)	←	229	–0.188				
	247 (e, π_ψ*)	←	229	0.569				
77	246 (e, π_ψ*)	←	227	–0.105	4.60	269	37133	0.0091
	247 (e, π_ψ*)	←	227	0.463				
	247 (e, π_ψ*)	←	228	0.306				
	247 (e, π_ψ*)	←	229	0.289				
	247 (e, π_ψ*)	←	230	0.112				
	247 (e, π_ψ*)	←	231	0.103				
	247 (e, π_ψ*)	←	232	–0.174				
78	257	←	242 (e, $d\pi$)	0.310	4.65	267	37474	0.0003
	258	←	242 (e, $d\pi$)	0.321				
	257	←	243 (e, $d\pi$)	–0.313				
	258	←	243 (e, $d\pi$)	0.310				
	254	←	244 (a_1, $d\pi$)	–0.106				
79	248	←	238	0.341	4.76	260	38393	0.0075
	251	←	238	0.167				
	248	←	239	0.456				
	251	←	239	0.225				
	252	←	239	–0.114				
	248	←	241	–0.105				
80	248	←	241	0.616	4.80	258	38736	0.0456
	250	←	241	0.174				
	253	←	241	–0.192				
81	248	←	235	–0.387	4.81	258	38782	0.0034
	249	←	235	0.208				
	248	←	237	0.391				
	249	←	237	–0.178				
	248	←	238	0.186				
82	248	←	232	0.171	4.85	256	39079	0.0370
	248	←	235	–0.254				
	248	←	237	–0.196				
	248	←	240	0.477				
	250	←	240	0.134				
	253	←	240	–0.159				
83	248	←	230	0.111	4.85	256	39102	0.0124
	248	←	235	0.345				
	250	←	235	–0.111				
	248	←	237	0.294				
	250	←	237	–0.116				
	248	←	238	0.114				
	248	←	240	0.350				
	250	←	240	0.100				
	253	←	240	–0.129				
84	248	←	233	–0.102	4.85	255	39148	0.0271
	248	←	234	0.352				
	251	←	234	0.191				

excited state	orbital composition		coefficient	excitation			oscillator strength
				eV	nm	cm^{-1}	
	248	← 237	0.156				
	248	← 238	–0.310				
	252	← 238	0.113				
	248	← 239	0.292				
	251	← 239	–0.115				
85	248	← 233	–0.142	4.86	255	39167	0.0127
	248	← 234	0.412				
	251	← 234	0.211				
	252	← 234	–0.115				
	248	← 237	–0.157				
	248	← 238	0.273				
	251	← 238	–0.106				
	248	← 239	–0.212				
86	248	← 231	–0.220	4.87	255	39253	0.0662
	248	← 232	0.442				
	249	← 232	0.114				
	248	← 235	0.112				
	250	← 235	–0.122				
	248	← 238	0.117				
	248	← 240	–0.110				
	254	← 244 (a_1, $d\pi$)	–0.100				
87	248	← 231	0.383	4.89	254	39417	0.0005
	249	← 231	–0.249				
	248	← 232	0.249				
	249	← 232	–0.142				
	248	← 233	0.322				
	250	← 233	–0.139				
	248	← 234	0.103				
	254	← 244 (a_1, $d\pi$)	0.106				
88	248	← 231	–0.320	4.89	254	39427	0.0033
	249	← 231	0.160				
	248	← 232	–0.109				
	249	← 232	0.104				
	248	← 233	0.444				
	249	← 233	0.124				
	250	← 233	–0.210				
	251	← 233	–0.124				
	248	← 234	0.137				
89	248	← 236	0.581	4.90	253	39490	0.0032
	249	← 236	–0.109				
	250	← 236	0.150				
	251	← 236	–0.236				
	252	← 236	–0.200				
90	248	← 231	–0.109	4.91	253	39571	0.0048
	248	← 233	–0.103				
	248	← 237	0.116				
	254	← 244 (a_1, $d\pi$)	0.601				
91	248	← 229	0.541	4.93	252	39733	0.0049
	249	← 229	0.224				
	250	← 229	0.239				
	252	← 229	0.106				
	253	← 229	0.143				
92	248	← 230	0.594	4.93	251	39771	0.0155

excited state	orbital composition		coefficient	excitation			oscillator strength
				eV	nm	cm^{-1}	
	253	← 240	0.148				
	254	← 243 (e, $d\pi$)	0.104				
93	245 (a_2, π_ψ*)	← 226	–0.122	4.97	250	40047	0.0037
	246 (e, π_ψ*)	← 226	–0.155				
	248	← 228	–0.134				
	250	← 232	0.137				
	250	← 239	0.104				
	254	← 243 (e, $d\pi$)	0.121				
	255	← 244 (a_1, $d\pi$)	0.427				
94	245 (a_2, π_ψ*)	← 226	0.144	4.97	249	40121	0.0449
	248	← 227	–0.138				
	248	← 228	0.394				
	249	← 235	–0.182				
	248	← 237	0.136				
	249	← 237	0.149				
	254	← 242 (e, $d\pi$)	0.216				
	254	← 244 (a_1, $d\pi$)	–0.121				
	255	← 244 (a_1, $d\pi$)	0.183				
95	245 (a_2, π_ψ*)	← 225	–0.147	5.00	248	40315	0.0278
	246 (e, π_ψ*)	← 225	0.108				
	245 (a_2, π_ψ*)	← 226	0.138				
	246 (e, π_ψ*)	← 226	0.117				
	248	← 227	0.323				
	249	← 228	0.178				
	250	← 232	–0.110				
	254	← 243 (e, $d\pi$)	0.247				
	255	← 244 (a_1, $d\pi$)	0.164				
	256	← 244 (a_1, $d\pi$)	0.178				
96	247 (e, π_ψ*)	← 224	–0.109	5.01	247	40425	0.0198
	248	← 227	–0.169				
	248	← 228	–0.158				
	251	← 230	0.148				
	253	← 230	–0.142				
	248	← 239	–0.122				
	251	← 239	0.145				
	248	← 241	0.172				
	251	← 241	–0.121				
	253	← 241	0.212				
	254	← 242 (e, $d\pi$)	0.102				
	254	← 243 (e, $d\pi$)	–0.102				
	256	← 244 (a_1, $d\pi$)	0.302				
97	248	← 227	–0.141	5.02	247	40516	0.0048
	249	← 235	–0.130				
	248	← 237	0.141				
	249	← 237	0.104				
	248	← 238	–0.119				
	251	← 238	0.134				
	248	← 239	–0.120				
	251	← 239	0.146				
	252	← 239	–0.130				
	248	← 241	–0.101				
	250	← 241	0.101				
	253	← 241	–0.172				

excited state	orbital composition			coefficient	excitation			oscillator strength
					eV	nm	cm^{-1}	
	254	←	242 (e, $d\pi$)	0.105				
	254	←	243 (e, $d\pi$)	0.352				
	255	←	244 (a_1, $d\pi$)	–0.157				
98	245 (a_2, π_ψ*)	←	225	0.128	5.03	246	40573	0.0157
	248	←	228	0.103				
	248	←	241	0.139				
	250	←	241	–0.139				
	253	←	241	0.230				
	254	←	243 (e, $d\pi$)	0.419				
	255	←	244 (a_1, $d\pi$)	–0.242				
99	245 (a_2, π_ψ*)	←	226	–0.148	5.04	246	40629	0.0089
	249	←	235	0.111				
	253	←	241	–0.141				
	254	←	242 (e, $d\pi$)	0.562				
100	245 (a_2, π_ψ*)	←	225	0.163	5.05	246	40698	0.0110
	251	←	230	0.123				
	248	←	241	–0.126				
	250	←	241	0.121				
	251	←	241	0.175				
	253	←	241	–0.286				
	254	←	242 (e, $d\pi$)	–0.202				
	254	←	243 (e, $d\pi$)	0.104				
	256	←	244 (a_1, $d\pi$)	0.358				
101	245 (a_2, π_ψ*)	←	225	0.214	5.06	245	40820	0.0006
	246 (e, π_ψ*)	←	225	–0.147				
	245 (a_2, π_ψ*)	←	226	0.194				
	246 (e, π_ψ*)	←	226	0.192				
	249	←	235	0.127				
	249	←	237	–0.165				
	248	←	238	–0.132				
	251	←	238	0.105				
	248	←	239	–0.111				
	251	←	239	0.165				
	254	←	243 (e, $d\pi$)	0.171				
	255	←	244 (a_1, $d\pi$)	0.277				
102	245 (a_2, π_ψ*)	←	226	0.189	5.08	244	40982	0.0144
	248	←	232	–0.150				
	250	←	239	0.200				
	248	←	240	0.213				
	249	←	240	0.110				
	250	←	240	–0.116				
	251	←	240	–0.162				
	253	←	240	0.344				
	255	←	244 (a_1, $d\pi$)	–0.105				
	256	←	244 (a_1, $d\pi$)	0.136				
103	245 (a_2, π_ψ*)	←	225	–0.131	5.08	244	40985	0.0154
	245 (a_2, π_ψ*)	←	226	0.243				
	246 (e, π_ψ*)	←	226	0.102				
	248	←	232	–0.129				
	250	←	232	0.113				
	250	←	238	0.129				
	249	←	239	0.105				
	250	←	239	0.134				

excited state	orbital composition		coefficient	excitation			oscillator strength
				eV	nm	cm^{-1}	
	248	← 240	–0.185				
	250	← 240	0.150				
	251	← 240	0.154				
	253	← 240	–0.275				
	254	← 243 (e, $d\pi$)	–0.112				
	255	← 244 (a_1, $d\pi$)	–0.149				
104	248	← 227	0.162	5.09	244	41054	0.0406
	250	← 235	–0.101				
	248	← 238	0.116				
	249	← 238	0.189				
	250	← 238	–0.125				
	251	← 238	0.249				
	252	← 238	0.118				
	248	← 239	–0.234				
	252	← 239	–0.195				
	251	← 241	–0.115				
	256	← 244 (a_1, $d\pi$)	–0.114				
105	245 (a_2, π_ψ*)	← 225	–0.100	5.10	243	41109	0.0048
	245 (a_2, π_ψ*)	← 226	–0.125				
	248	← 227	0.212				
	248	← 235	–0.138				
	250	← 235	–0.153				
	249	← 237	0.119				
	248	← 238	–0.198				
	251	← 238	–0.139				
	252	← 238	–0.210				
	249	← 239	0.134				
	250	← 239	–0.106				
	251	← 239	0.215				
	256	← 244 (a_1, $d\pi$)	0.154				
106	246 (e, π_ψ*)	← 224	–0.101	5.11	243	41202	0.0093
	245 (a_2, π_ψ*)	← 226	–0.127				
	246 (e, π_ψ*)	← 226	0.244				
	248	← 227	–0.146				
	248	← 228	–0.159				
	249	← 228	–0.127				
	251	← 228	0.103				
	248	← 231	0.102				
	251	← 232	0.115				
	248	← 235	–0.198				
	250	← 235	–0.195				
	252	← 235	0.115				
	249	← 237	0.209				
	255	← 244 (a_1, $d\pi$)	0.121				
107	247 (e, π_ψ*)	← 225	0.108	5.13	242	41344	0.0002
	249	← 230	–0.107				
	251	← 230	–0.141				
	249	← 235	0.171				
	248	← 236	–0.120				
	251	← 236	–0.117				
	248	← 237	–0.129				
	249	← 237	0.103				
	250	← 237	–0.165				

excited state	orbital composition		coefficient	excitation			oscillator strength
				eV	nm	cm^{-1}	
	249	← 240	–0.108				
	251	← 240	–0.132				
	249	← 241	–0.178				
	251	← 241	–0.191				
	252	← 241	–0.104				
	255	← 243 (e, $d\pi$)	–0.107				
	256	← 244 (a_1, $d\pi$)	0.244				
108	245 (a_2, π_ψ*)	← 226	–0.155	5.13	242	41366	0.0074
	246 (e, π_ψ*)	← 226	0.106				
	249	← 230	0.123				
	249	← 235	–0.200				
	248	← 237	0.179				
	249	← 237	–0.206				
	250	← 237	0.249				
	250	← 240	0.104				
	249	← 241	–0.163				
	251	← 241	–0.182				
	256	← 244 (a_1, $d\pi$)	0.134				
109	248	← 228	–0.126	5.13	242	41399	0.0012
	249	← 230	0.337				
	250	← 230	0.164				
	249	← 232	0.150				
	250	← 235	0.113				
	250	← 237	–0.129				
	249	← 239	0.123				
	249	← 240	0.270				
	250	← 240	0.141				
	249	← 241	–0.131				
110	248	← 233	0.102	5.14	241	41427	0.0011
	248	← 234	–0.320				
	250	← 234	–0.260				
	251	← 234	0.328				
	252	← 234	–0.265				
	250	← 241	0.114				
	251	← 241	–0.152				
111	250	← 230	0.113	5.14	241	41448	0.0055
	248	← 234	–0.113				
	251	← 234	0.131				
	252	← 234	–0.102				
	251	← 236	–0.115				
	251	← 238	0.151				
	250	← 240	0.111				
	249	← 241	0.203				
	250	← 241	–0.253				
	251	← 241	0.367				
112	245 (a_2, π_ψ*)	← 225	–0.130	5.14	241	41472	0.0042
	248	← 228	0.103				
	249	← 230	0.185				
	250	← 230	0.167				
	248	← 231	–0.161				
	249	← 231	–0.193				
	252	← 231	0.102				
	249	← 240	0.185				

excited state	orbital composition		coefficient	excitation			oscillator strength
				eV	nm	cm^{-1}	
	250	← 240	0.147				
	249	← 241	0.257				
	250	← 241	0.288				
113	248	← 231	0.126	5.14	241	41483	0.0024
	249	← 231	0.162				
	248	← 236	–0.230				
	249	← 236	–0.116				
	251	← 236	–0.251				
	252	← 236	–0.214				
	249	← 241	0.273				
	250	← 241	0.278				
114	248	← 231	0.208	5.15	241	41501	0.0001
	249	← 231	0.256				
	252	← 231	–0.128				
	249	← 232	0.133				
	248	← 236	0.223				
	249	← 236	0.101				
	251	← 236	0.246				
	252	← 236	0.212				
	249	← 241	0.193				
	250	← 241	0.111				
115	247 (e, π_ψ*)	← 224	0.141	5.15	241	41566	0.0056
	250	← 230	–0.200				
	253	← 230	0.121				
	249	← 231	–0.164				
	248	← 232	–0.103				
	249	← 235	–0.119				
	249	← 238	0.173				
	249	← 239	0.226				
	251	← 239	–0.116				
	253	← 239	0.127				
	249	← 241	0.214				
	253	← 241	0.113				
	256	← 242 (e, $d\pi$)	0.108				
	256	← 244 (a_1, $d\pi$)	0.160				
116	245 (a_2, π_ψ*)	← 225	–0.154	5.16	240	41594	0.0050
	246 (e, π_ψ*)	← 225	0.104				
	248	← 227	–0.173				
	248	← 228	0.136				
	249	← 228	0.125				
	250	← 230	–0.103				
	248	← 231	0.102				
	249	← 231	0.116				
	249	← 232	0.156				
	248	← 233	0.136				
	249	← 233	–0.117				
	250	← 233	0.122				
	249	← 235	0.107				
	249	← 237	–0.129				
	250	← 237	0.145				
	249	← 239	0.222				
	250	← 240	–0.100				
	255	← 242 (e, $d\pi$)	0.113				

excited state	orbital composition			coefficient	excitation			oscillator strength
					eV	nm	cm^{-1}	
117	245 (a_2, π_ψ*)	←	224	0.113	5.16	240	41653	0.0087
	247 (e, π_ψ*)	←	224	–0.113				
	249	←	227	0.129				
	248	←	228	–0.134				
	249	←	230	–0.140				
	250	←	230	0.148				
	253	←	230	–0.188				
	250	←	232	–0.121				
	249	←	238	0.244				
	249	←	239	0.204				
	249	←	240	–0.123				
	251	←	240	–0.122				
	251	←	241	0.129				
	256	←	242 (e, $d\pi$)	–0.104				
	255	←	243 (e, $d\pi$)	–0.128				
	256	←	243 (e, $d\pi$)	–0.125				
118	245 (a_2, π_ψ*)	←	226	–0.120	5.17	240	41667	0.0075
	248	←	233	–0.243				
	249	←	233	0.337				
	250	←	233	–0.203				
	251	←	233	–0.141				
	253	←	233	–0.102				
	250	←	238	0.109				
	250	←	239	0.105				
	255	←	242 (e, $d\pi$)	0.146				
	255	←	243 (e, $d\pi$)	–0.191				
119	246 (e, π_ψ*)	←	226	–0.111	5.17	240	41697	0.0092
	250	←	227	0.128				
	248	←	229	0.124				
	250	←	229	–0.156				
	249	←	232	–0.133				
	250	←	232	–0.144				
	248	←	233	0.122				
	249	←	233	–0.179				
	250	←	233	0.162				
	250	←	237	–0.107				
	249	←	238	0.108				
	250	←	238	0.155				
	251	←	238	0.113				
	250	←	239	0.219				
	251	←	239	0.135				
	250	←	241	–0.110				
	255	←	242 (e, $d\pi$)	–0.125				
120	245 (a_2, π_ψ*)	←	226	–0.158	5.18	240	41750	0.0029
	248	←	228	0.134				
	251	←	228	0.130				
	250	←	235	0.114				
	251	←	235	–0.271				
	251	←	237	0.263				
	249	←	239	0.127				
	255	←	243 (e, $d\pi$)	0.371				